

GEOLOGICALLY-CONSTRAINED UBC–GIF GRAVITY AND
MAGNETIC INVERSIONS WITH EXAMPLES FROM THE
AGNEW-WILUNA GREENSTONE BELT, WESTERN
AUSTRALIA

by

Nicholas Cory Williams

B.Sc., Monash University, 1999

B.Sc. (Honours), University of Tasmania, 2000

A THESIS SUBMITTED IN PARTIAL FULFILLMENT OF THE
REQUIREMENTS FOR THE DEGREE OF

DOCTOR OF PHILOSOPHY

in

The Faculty of Graduate Studies

(Geophysics)

THE UNIVERSITY OF BRITISH COLUMBIA

(Vancouver)

October 2008

© Nicholas Cory Williams, 2008

Abstract

Geologically-constrained inversion of geophysical data is a powerful method for predicting geology beneath cover. The process seeks 3D physical property models that are consistent with the geology and explain measured geophysical responses. The recovered models can guide mineral explorers to prospective host rocks, structures, alteration and mineralisation. This thesis provides a comprehensive analysis of how the University of British Columbia Geophysical Inversion Facility (UBC–GIF) gravity and magnetic inversions can be applied to subsurface mapping and exploration by demonstrating the necessary approach, data types, and typical results.

The non-uniqueness of inversion demands that geological information be included. Commonly available geological data, including structural and physical property measurements, mapping, drilling, and 3D interpretations, can be translated into appropriate inversion constraints using tools developed herein. Surface information provides the greatest improvement in the reliability of recovered models; drilling information enhances resolution at depth. The process used to prepare inversions is as important as the geological constraints themselves. Use of a systematic workflow, as developed in this study, minimises any introduced ambiguity. Key steps include defining the problem, preparing the data, setting inversion parameters and developing geological constraints.

Once reliable physical property models are recovered they must be interpreted in a geological context. Where alteration and mineralisation occupy significant volumes, the mineralogy associated with the physical properties can be identified; otherwise a lithological classification of the properties can be applied. This approach is used to develop predictive 3D lithological maps from geologically-constrained gravity and magnetic inversions at several scales in the Agnew-Wiluna greenstone belt in Australia's Yilgarn Craton. These maps indicate a spatial correlation between thick mafic-ultramafic rock packages and gold deposit locations, suggesting a shared structural control. The maps also identify structural geometries and relationships consistent with the published regional tectonic framework.

Geophysical inversion provides a framework into which geological and geophysical data sets can be integrated to produce a holistic prediction of the subsurface. The best possible result is one that cannot be dismissed as inconsistent with some piece of geological knowledge.

Such a model can only be recovered by including all available geological knowledge using a consistent workflow process.

Table of Contents

Abstract.....	ii
Table of Contents	iv
List of Tables	viii
List of Figures.....	x
Acknowledgments	xvii
Dedication	xix
Co-Authorship Statement.....	xx
Chapter 1: Introduction	1
1.1 Introduction	1
1.1.1 Inversion	1
1.1.2 Physical properties.....	2
1.1.3 The Agnew-Wiluna greenstone belt	5
1.2 Thesis objectives	6
1.3 Thesis structure.....	7
1.4 References	11
Chapter 2: A review of the application of UBC–GIF 3D potential field inversions for mineral exploration	16
2.1 Introduction	16
2.2 Previous work using geologically-constrained UBC–GIF inversions	19
2.3 The UBC-GIF inversion method.....	21
2.3.1 Model objective function	22
2.3.2 Depth & distance weighting	23
2.3.3 Data misfit	24
2.3.4 Obtaining a solution.....	25
2.4 Preparing inversions	26
2.5 Choosing optimal parameters	27
2.5.1 Data uncertainty	27
2.5.2 Alphas.....	29
2.6 Supplying geological constraints.....	30
2.6.1 Types of geological constraints	31
2.6.2 Implementing located geological constraints.....	32
2.6.3 Defining gross geometry using aspect ratios	39
2.7 Synthetic geologically-constrained inversion example	41
2.7.1 Default, geologically-unconstrained inversion	44
2.7.2 Inversion constrained by mapping	45
2.7.3 Inversion constrained with the addition of aspect ratios.....	46
2.7.4 Inversion constrained with the addition of 1 drill hole	49
2.7.5 Inversion constrained with the addition of a second drill hole	50
2.7.6 Extrapolation of constraints	52
2.7.7 Inversion example summary	55
2.8 Real geologically-constrained inversion example	58
2.9 Conclusions	60
2.10 References	63
Chapter 3: A workflow for preparing and applying UBC–GIF gravity and magnetic inversions	65
3.1 Introduction	65
3.2 Inversion workflow checklist	67
3.3 Getting started	68

3.3.1 Assumptions and expectations	68
3.3.2 Clarify the problem	70
3.3.3 Basic components of an inversion setup	74
3.3.4 Advanced components of an inversion setup	76
3.4 Defining the mesh	77
3.4.1 Local versus regional meshes	78
3.4.2 Default mesh design	79
3.4.3 Rigorous mesh design	80
3.5 Data preparation	87
3.5.1 Topography data	87
3.5.2 Gridding and upward continuation	88
3.5.3 Gravity data	91
3.5.4 Magnetic data	97
3.5.5 Removing regional data contributions	101
3.6 First inversion	104
3.6.1 Graphic user interface (GUI)	105
3.6.2 Essential input files	105
3.6.3 Setting the model objectives	106
3.6.4 Misfit and trade-off parameters	109
3.6.5 Compression	110
3.6.6 Running the inversion	111
3.7 Evaluating and displaying the results	111
3.7.1 Did the inversion finish?	111
3.7.2 Did the recovered model adequately reproduce the geophysical data?	112
3.7.3 Does the recovered model satisfy conditions of smoothness and closeness to the reference model?	114
3.8 Subsequent inversions	117
3.8.1 Adjusting inversion parameters	118
3.8.2 Restarting an inversion	122
3.9 Incorporating geological constraints	123
3.9.1 How constraints are implemented	125
3.9.2 Using constraints to define data levels	129
3.9.3 Smooth model, or smooth model difference	132
3.9.4 The hypothesis-testing approach to constraints	133
3.9.5 The data-based approach to constraints	142
3.10 Conclusions	152
3.11 References	153
Chapter 4: Mass and magnetic properties of the southern Agnew-Wiluna greenstone belt and Leinster nickel deposits, Western Australia	155
4.1 Introduction	155
4.1.1 Geology of the Agnew-Wiluna greenstone belt	157
4.2 Methods	162
4.2.1 Mass properties	163
4.2.2 Magnetic properties	165
4.3 Results	167
4.3.1 XRD and basic physical properties	167
4.3.2 Thermomagnetic analysis	182
4.3.3 Natural remanent magnetisation directions	184
4.3.4 Physical property cross-plots	193
4.4 Discussion	199
4.4.1 Massive sulphides	200
4.4.2 Ultramafic rocks	203
4.4.3 Other greenstone and granitoid rocks	208
4.5 Conclusions	209
4.6 References	211
Chapter 5: An automated approach for building geological constraints for potential field inversions using sparse observations	218

5.1 Introduction	218
5.2 Method overview	221
5.3 Linking property measurements to inversion property models	223
5.4 Creating a physical property database	227
5.4.1 Drilling information	228
5.4.2 Translation table for geology labels	230
5.4.3 Calculating physical property estimates for geology labels	230
5.4.4 Manually-specified properties	231
5.5 Input data types	231
5.5.1 Drilling information	231
5.5.2 Maps	232
5.5.3 Three-dimensional geological and domain models	233
5.6 Assigning data properties to the model	234
5.6.1 Point observations	234
5.6.2 Maps and 3D models	240
5.7 Extrapolating properties	240
5.7.1 Defining ellipsoidal extrapolation buffers	241
5.7.2 Assigning properties within single buffers	244
5.7.3 Assigning properties within overlapping buffers	246
5.8 Calculating smoothness weights	250
5.8.1 Defining smoothness weights using reference model gradients	252
5.9 Example of developing geological constraints	256
5.9.1 Basic model of surface constraints	257
5.9.2 Complete model of sparse 3D constraints	259
5.10 Summary	266
5.11 References	268
Chapter 6: Mapping subsurface alteration using gravity and magnetic inversion models	270
6.1 Introduction	270
6.2 Method	273
6.3 Linear Programming	274
6.3.1 Inequality constraint equations	274
6.3.2 Model objective function	276
6.4 Application to drill core samples	277
6.4.1 Components, their properties and bounds	277
6.4.2 Objective functions	280
6.4.3 Additional constraint equations	280
6.4.4 Results	282
6.4.5 Summary	284
6.5 Application to 3D inversion models	284
6.5.1 Olympic Dam	285
6.5.2 Estimating mineral abundances from inversion models	286
6.6 Conclusions	291
6.7 References	293
Chapter 7: Geologically-constrained gravity and magnetic inversions over the Agnew-Wiluna greenstone belt and Perseverance nickel deposit, Western Australia	296
7.1 Introduction	296
7.2 Geology and architecture of the Eastern Goldfields	299
7.2.1 Geology of the Agnew-Wiluna greenstone belt	303
7.2.2 Mineral deposits of the Agnew-Wiluna greenstone belt	308
7.3 Physical properties	310
7.4 Agnew-Wiluna greenstone belt geophysical data	314
7.5 UBC-GIF inversion background	318
7.6 Methods	321
7.6.1 General inversion procedure	321
7.6.2 Geological constraints	327

7.6.3 Regularisation parameters.....	336
7.6.4 Extrapolating constraints	338
7.6.5 Predictive rock models	339
7.7 Inversion modelling.....	341
7.7.1 Regional-scale: Agnew-Wiluna greenstone belt.....	341
7.7.2 District-scale: Agnew-Leinster district.....	351
7.7.3 Deposit-scale: Perseverance nickel deposit	361
7.8 Discussion	371
7.8.1 Limitations.....	371
7.8.2 Geological interpretations.....	373
7.9 Conclusions	378
7.10 References	381
Chapter 8: Conclusions.....	389
8.1 Summary of research.....	389
8.1.1 Use of geological constraints.....	389
8.1.2 Physical properties.....	392
8.1.3 Performing inversions.....	393
8.1.4 Geological interpretation of inversion results	394
8.2 Limitations of the research and methods.....	397
8.3 Future research opportunities	400
8.4 Concluding statement	403
8.5 References	404
Appendix A: Mass and magnetic property measurements	407
Appendix B: GIFtools:ModelBuilder user manual.....	418
Introduction	420
Method Overview.....	422
User Manual	424
Requirements.....	424
Installation	425
Getting Started.....	425
ModelBuilder Settings.....	426
Input files and data	472
Mandatory For All Models	472
For Surface Samples (or any samples that have X-Y-Z coordinates):.....	472
For Drilling.....	472
For Outcrop or Basement Maps.....	474
For a 3D Domain Model.....	475
For a 3D Geological Model	476
Rock Properties Data	477
Output files.....	480
Reference Model and Weights.....	481
Bounds Model.....	482
Informational Text Files	484
MATLAB Binary Data Files	485
References	487

List of Tables

Table 2.1. Buffer parameters used to automatically extrapolate constraints prior to inversion.	55
Table 2.2. Quantification of the differences between the various recovered models and the true density model.	58
Table 3.1. Summary guide for defining the appropriate coordinates for the data and padding zones using the rigorous mesh design.	81
Table 4.1. Physical properties, and XRD and thermomagnetic mineralogy estimates for a massive sulphide sample and variously serpentinised ultramafic rock samples.	168
Table 4.2. Lithological summary of mass and magnetic properties obtained in this study.	170
Table 4.3. Lithological summary of mass and magnetic properties supplied by BHP Billiton.	171
Table 4.4. Summary of the densities and magnetic properties of the ultramafic host rocks and massive sulphide ore at Leinster, according to sulphide content.	177
Table 4.5. Summary of the densities and magnetic properties of the ultramafic host rocks, separated by protolith style.	179
Table 4.6. Summary of the density and magnetic properties associated with different ultramafic alteration and metamorphic styles.	181
Table 5.1. List of the data types handled by the model building application.	222
Table 5.2. Available methods for assigning reference properties to cells when the cells contain a combination of measurements from surface samples and drill holes and property estimates from drilling geology logs.	236
Table 5.3. Parameters assigned to data types based on data reliability.	262
Table 5.4. Model building parameters assigned to each domain.	263
Table 5.5. Breakdown of the number of cells constrained with each data type and whether the constraint came directly from the data or via buffer extrapolation.	266
Table 6.1. Summary of the physical properties of the components that will control the physical properties of rocks associated with komatiite-hosted nickel sulphide deposits.	279
Table 6.2. Expected minimum and maximum abundances of each mineral for rocks from the Leinster area.	279
Table 6.3. Summary of the physical properties of common minerals associated with iron oxide copper gold (IOCG) deposits.	287
Table 7.1. Statistical summary of densities and magnetic susceptibilities for different rock types observed in the southern Agnew-Wiluna greenstone belt.	312
Table 7.2. Details of the core, data and padding for each scale of inversion.	322
Table 7.3. Summary of the data used in this study and their sources.	323
Table 7.4. Summary of the geological constraints used in all inversions in this study.	328

Table 7.5. Manually-assigned physical property estimates for the most commonly encountered basement rock codes identified in the supplied surface geology map.....	330
Table 7.6. Densities and magnetic susceptibilities assigned to domains in the regional-scale domain model.	332
Table 7.7. Densities and magnetic susceptibilities assigned to domains in the district-scale domain model.	332
Table 7.8. Densities and magnetic susceptibilities assigned to domains in the deposit-scale domain model.	333
Table 7.9. Percentage of the 1,027,324 below ground cells in the full padded deposit-scale density model with various non-default constraints, with and without buffer extrapolation. ..	365
Table A.1. Physical property measurement sample locations.	408
Table A.2. Physical property measurements acquired in this study.	411
Table B.1. List of the data types handled by the model building application.	424
Table B.2. Differences between 3D geological and domain models.....	429
Table B.3. Summary of the effect of the three available types of weight scaling on constrained and unconstrained cells.....	456
Table B.4. Output filename abbreviations and ID flags for different data types.....	481

List of Figures

Figure 1.1. Physical properties of common silicate (green), sulphide (red) and oxide (grey) minerals associated with Archean greenstone-hosted nickel deposits, and trends of various geological processes acting upon them.....	4
Figure 1.2. Terranes (coloured polygons) and domains (white boundaries) of the Archean Yilgarn Craton.	5
Figure 2.1. Typical relationships between recovered models and specified data uncertainties for a set of inversions using 2025 synthetic data points.....	28
Figure 2.2. Schematic representations of the styles of geological constraints that can be included in a reference model.....	32
Figure 2.3. Example of determining a reference property and bounds using confidence intervals for 100 magnetic susceptibility measurements distributed within a single model cell and showing a lognormal distribution.	34
Figure 2.4. 3D view of a $2 \times 2 \times 2$ mesh indicating how the smoothness weight parameters are set.....	34
Figure 2.5. 2D slice through a model where the position of a unit is known or inferred, but its properties are too poorly known to include as constraints.	35
Figure 2.6. Schematic examples demonstrating the character of models obtained using smooth model or smooth model-difference formulations.	37
Figure 2.7. Synthetic inversion modelling of plate-like bodies with different aspect ratios.	42
Figure 2.8. Perspective view of the actual synthetic geology model, looking down to the north.	43
Figure 2.9. Synthetic gravity data calculated from the geology model shown in Figure 2.8.	44
Figure 2.10. A default, geologically unconstrained inversion result compared against the true density model.....	45
Figure 2.11. An inversion result constrained by outcrop mapping.....	47
Figure 2.12. Perspective view of assigned smoothness weights set using different aspect ratios in the regolith and basement regions.	48
Figure 2.13. The inversion result obtained when inferred aspect ratios indicating the gross geometry in the regolith and basement are included.	49
Figure 2.14. The addition of a single drill hole further enhances the recovered model.	51
Figure 2.15. The addition of a second deep drill hole further enhances the recovered model. ...	52
Figure 2.16. This final result uses an orientation-based extrapolation of the same constraints used in the previous example.....	54
Figure 2.17. A comparison of the actual densities against all six increasingly geologically-constrained inversion results.	57
Figure 2.18. The surface layer of the reference density model and smallness weights used to constrain the real gravity inversion example.....	59

Figure 2.19. Comparison of the improvement gained by including geological constraints in a real gravity inversion.	61
Figure 3.1. Perspective view of a default mesh created from a supplied data file.	80
Figure 3.2. Cross section view of the layout of the rigorous mesh design including local and regional meshes and padding.	81
Figure 3.3. Schematic, but accurately scaled example cross section showing the necessary data extent to accurately reproduce a source at depth within the local core.	83
Figure 3.4. Application of the method of Nettleton (1939) to determine an appropriate Bouguer slab and terrain correction density for an area based on a suite of gravity profiles.	94
Figure 3.5. Example demonstrating how incorrect magnetic data levels can be identified and corrected for problems in the northern hemisphere.	102
Figure 3.6. Example demonstrating how incorrect magnetic data levels can be identified and corrected for problems in the southern hemisphere.	103
Figure 3.7. The interface of the GRAV3D GUI for running inversions.	105
Figure 3.8. Examples for a synthetic gravity data set showing how different data uncertainties affect the data misfit associated with recovered inversion models.	113
Figure 3.9. Vertical slices through a set of inversion models indicating typical relationships between the character of recovered models and the allowed data uncertainties for the same 2025 gravity data and inversions used in Figure 3.8.	115
Figure 3.10. Example of the linear or checkerboard artefacts than can occur at depth within a model when there is too much compression of the sensitivity matrix.	116
Figure 3.11. A synthetic example (from Chapter 2) demonstrating the use of geological constraints from surface mapping and two drill holes using the data-based, smooth model style of constraints.	124
Figure 3.12. Smoothness weights are assigned to each internal cell face.	128
Figure 3.13. A synthetic example showing how an appropriate background density value for a model can be determined using map constraints.	131
Figure 3.14. Schematic examples of the impact of various styles of constraints on an inversion.	134
Figure 3.15. Example of bounding surfaces used to create a constraining reference model in Gocad.	136
Figure 3.16. Assigning smoothness weights to a mesh based on the positions and orientations of interpreted fault surfaces in Gocad.	139
Figure 4.1. Basement geology of the southern Agnew-Wiluna greenstone belt.	158
Figure 4.2. Detailed basement geology around the Leinster nickel deposits.	160
Figure 4.3. Relationship between different density determinations used in this study.	165
Figure 4.4. Plot of lab-determined magnetic susceptibilities collected in this study versus susceptibilities measured in the field and supplied by BHP Billiton for those samples where both were available.	167

Figure 4.5. Representative photos of samples used in this study.	169
Figure 4.6. Histograms of wet bulk density by rock type from this study.	173
Figure 4.7. Histograms of BHP Billiton specific gravities by rock type.	173
Figure 4.8. Histograms of magnetic susceptibility by rock type obtained in this study.	174
Figure 4.9. Histograms of BHP Billiton magnetic susceptibilities by rock type.	174
Figure 4.10. Histograms of the intensity of natural remanent magnetisation by rock type.	175
Figure 4.11. Histograms of the Koenigsberger ratio (Q) by rock type.	175
Figure 4.12. Histograms of the densities associated with increasing sulphide content in ultramafic host rocks.	176
Figure 4.13. Histograms of the susceptibilities associated with increasing sulphide content in ultramafic host rocks.	176
Figure 4.14. Physical properties of ultramafic host rocks according to sulphide content.	178
Figure 4.15. Histograms of the densities associated with different ultramafic rock types.	180
Figure 4.16. Histograms of the magnetic susceptibilities associated with different ultramafic rock types.	180
Figure 4.17. Histograms of densities of altered/metamorphism ultramafic rock divided by the dominant alteration/metamorphic minerals or assemblages.	182
Figure 4.18. Histograms of susceptibilities of altered/metamorphism ultramafic rock divided by the dominant alteration/metamorphic minerals or assemblages.	182
Figure 4.19. Thermomagnetic curves showing the temperature dependence of magnetic susceptibility for selected samples.	185
Figure 4.20. Zijderveld plots of remanence vectors (left) and demagnetisation intensities (right) for representative axially-oriented massive sulphide samples.	187
Figure 4.21. Equal area stereographic projection of remanent magnetisation components for axially oriented massive sulphide samples in geographic coordinates.	188
Figure 4.22. Zijderveld plots of remanence vectors (left) and demagnetisation intensities (right) for axially-oriented ultramafic rock samples.	190
Figure 4.23. Equal area stereographic projections of remanent magnetisation components attributed to drilling IRM for axially-oriented ultramafic rock samples in geographic coordinates.	191
Figure 4.24. Equal area stereographic projections of remanent magnetisation components attributed to VRM for axially-oriented ultramafic rock samples in geographic coordinates. ...	192
Figure 4.25. Equal area stereographic projections of ChRM components in geographic coordinates for axially-oriented ultramafic rock samples.	193
Figure 4.26. Densities versus magnetic susceptibilities for all samples in this study plotted with expected property ranges of associated minerals.	195
Figure 4.27. Densities and magnetic susceptibilities plotted by rock type for samples from this study.	196

Figure 4.28. Magnetic susceptibilities and NRM intensities plotted by rock type for samples from this study.	196
Figure 4.29. Cross-plots of density and magnetic properties associated with serpentinised and olivine-bearing ultramafic rocks.	198
Figure 4.30. Cross-plots of density and magnetic properties associated with ultramafic rocks and massive sulphides plotted according to sulphide content.	199
Figure 4.31. A physical property discriminant diagram for rocks found in the Leinster area.	201
Figure 5.1. Histograms of the lognormal probability density function used to populate 4 million cells.	224
Figure 5.2. Synthetic susceptibility model and calculated magnetic response.	224
Figure 5.3. Schematic depiction of the data inputs and stages for preparing the physical property database to be used to assign physical property estimates to geological observations throughout the model.	228
Figure 5.4. Schematic example showing how overlapping observation intervals in drill holes are handled.	229
Figure 5.5. Schematic example showing how different geology observations (rocks A, B, and C) and property measurements (ρ_1 , ρ_2 , and ρ_3) are matched to correctly assign the measurements to the corresponding geological observations.	230
Figure 5.6. A real example of assigning properties to a cell that contains many more property measurements (367) than geology observations (33).	237
Figure 5.7. A real example of assigning properties to a cell that contains many more geology observations (302) than property measurements (28).	238
Figure 5.8. Example of assigning smallness weights to a cell based on the distribution of point observations within the cell.	239
Figure 5.9. Definition of ellipsoidal buffer based on geological orientations.	243
Figure 5.10. Unidirectional example of property values assigned within a 100-m-wide buffer surrounding a single data-bearing cell at 0 m.	246
Figure 5.11. Two-dimensional example of how the size of a spherical buffer around a data-bearing cell (centre cell) is reduced when other data-bearing cells lie within the buffer zone.	248
Figure 5.12. Example of ellipsoidal buffers surrounding 15 random data points in a slice through a 3D model.	249
Figure 5.13. Unidirectional example of property values assigned within buffer zones surrounding three data-bearing cells marked with circles at 122.5 m, 147.5 m, and 222.5 m.	249
Figure 5.14. Schematic example demonstrating the uses of smoothness weights (coloured along cell faces) with respect to a reference model.	251
Figure 5.15. Schematic example of the physical property gradients necessary to define the smoothness weight for the cell face separating cells 1 and 2.	253
Figure 5.16. Mapping function to convert calculated gradient components into appropriate smoothness weights.	255

Figure 5.17. Constraint models recovered for the Perseverance case study area using readily available surface data only.....	257
Figure 5.18. Experimental semivariograms of density in the case study area.....	261
Figure 5.19. Cutaway perspective views of the final constraint models.	264
Figure 5.20. Cutaway perspective view along strike to the NNW zoomed to the central portion of Figure 5.19A.....	267
Figure 6.1. Graphical representation of equations 6.1-6.3 depicting how the density and susceptibility of a sample may be used to estimate the volume proportions of each of three end-members.....	272
Figure 6.2. Densities and magnetic susceptibilities of the 144 drill core samples in this study (black circles), and seven controlling components.....	278
Figure 6.3. Results of the mineral estimate calculation on drill core samples from Leinster.	282
Figure 6.4. An alternate representation of the results from Figure 6.3.....	283
Figure 6.5. Graph showing the accuracy of the mineral predictions when using a cut-off of 0.001 volume fraction pyrrhotite and pentlandite (top of Figure 6.4).	284
Figure 6.6. Maps and models of the calculated alteration mineralogy in the Olympic province inversion volume.	290
Figure 7.1. Terranes (coloured polygons) and domains (white boundaries) of the Archean Yilgarn Craton.	300
Figure 7.2. Outcropping Archean basement rocks of the Agnew-Wiluna greenstone belt and surrounding areas.....	301
Figure 7.3. Basement geology of the Agnew-Wiluna greenstone belt.	302
Figure 7.4. Deep reflection seismic profiles across the EGST.....	304
Figure 7.5. Basement geology surrounding the Perseverance Ni-deposit showing the deposit-scale inversion core.....	307
Figure 7.6. Total magnetic intensity data over the Agnew-Wiluna greenstone belt.	315
Figure 7.7. Bouguer gravity data over the Agnew-Wiluna greenstone belt.	316
Figure 7.8. Total magnetic intensity response over the Perseverance deposit.	318
Figure 7.9. Gravity response over the Perseverance deposit.....	319
Figure 7.10. Application of the Nettleton (1939) method to determine an appropriate Bouguer slab and terrain correction density for one profile across the deposit.	326
Figure 7.11. Simplified discriminant diagram for identifying certain distinct lithologies based on densities and susceptibilities.....	340
Figure 7.12. The surface layer of the reference density model and smallness weights used to constrain the regional-scale gravity inversion.	342
Figure 7.13. The surface layer of the reference susceptibility model and smallness weights used to constrain the regional-scale magnetic inversion.....	343

Figure 7.14. Horizontal slices at increasing depths through the regional-scale geologically-constrained gravity inversion model.....	344
Figure 7.15. Horizontal slices at increasing depths through the regional-scale geologically-constrained magnetic inversion model.	346
Figure 7.16. East-west cross sections through the regional-scale geologically-constrained gravity and magnetic inversions.	347
Figure 7.17. Predicted rock model for the Agnew-Wiluna greenstone belt based on the available geophysical data, geological constraints, and physical property data.....	349
Figure 7.18. Predicted distribution of mafic and ultramafic rocks throughout the Agnew-Wiluna greenstone belt based on the rock model presented in Figure 7.17.	350
Figure 7.19. The surface layer of the reference density model and smallness weights used to constrain the district-scale gravity inversion.	351
Figure 7.20. The surface layer of the reference susceptibility model and smallness weights used to constrain the district-scale magnetic inversion.....	352
Figure 7.21. Comparison of the improvement gained by including geological constraints in the district-scale gravity inversion.....	353
Figure 7.22. Horizontal slices at increasing depths through the district-scale geologically-constrained gravity inversion model.....	355
Figure 7.23. Horizontal slices at increasing depths through the district-scale geologically-constrained magnetic inversion model.	356
Figure 7.24. East-west cross sections through the district-scale geologically-constrained gravity and magnetic inversions.	357
Figure 7.25. Best estimate predicted rock model for the southern Agnew-Wiluna greenstone belt based on the available geophysical data, geological constraints, and physical property data.	359
Figure 7.26. Predicted distribution of mafic and ultramafic rocks throughout the Agnew-Leinster district based on the rock model presented in Figure 7.25.	361
Figure 7.27. Surface map constraints for the deposit-scale gravity inversions.	363
Figure 7.28. Surface map constraints for the deposit-scale magnetic inversions.....	364
Figure 7.29. Density constraint models for the core of the Perseverance inversion volume based on drilling geology logs, density measurements and surface information.	366
Figure 7.30. Apparent magnetic susceptibility constraint models for the core of the Perseverance inversion volume based on drilling geology logs, density measurements and surface information.	367
Figure 7.31. Comparison of the observed magnetic data with the magnetic response of the full reference model based on drilling and surface information.	368
Figure 7.32. Results of the Perseverance gravity and magnetic inversions, with interpreted geology.	369
Figure 8.1. Publicly available ground gravity station coverage over Australia as of October 2007 from Geoscience Australia (2007).....	399

Figure B.1. Schematic 2D cross-section examples of the available constraint cropping options.	436
Figure B.2. Definition of ellipsoidal buffer based on geological orientations.	441
Figure B.3. Demonstration of distance weight scaling of smallness weights for a simple synthetic example with a single vertical drill hole (dotted line) passing through an anomalous block (outlined with dashed line).	454
Figure B.4. Examples of how smoothness weights can be assigned for a simple synthetic example with a single vertical drill hole (dotted line) passing through an anomalous block (outlined with dashed line).	460
Figure B.5. Schematic example of ellipsoidal buffers applied around 15 random cells containing simulated surface sample property measurements (white dots) using the nearest neighbour buffer option.	462
Figure B.6. Schematic example of ellipsoidal buffers applied around the same data as used in Figure B.5 except using the most reliable nearby data buffer option.	463
Figure B.7. Schematic example of ellipsoidal buffers applied around the same data as used in Figure B.5 except using the smooth interpolation option based on distance weights.	464
Figure B.8. Schematic example of ellipsoidal buffers applied around the same data as used in Figure B.5 except using the smooth interpolation option based on distance- and smallness-weights.	466
Figure B.9. Schematic example using ellipsoidal buffers to extrapolate bounds around the same data as used in Figure B.5.	467
Figure B.10. Schematic example using ellipsoidal buffers to extrapolate bounds around the same data as used in Figure B.5.	468
Figure B.11. Schematic example using ellipsoidal buffers to extrapolate bounds around the same data as used in Figure B.5.	470

Acknowledgments

This thesis represents a conflux of disciplines and supporters, and I'm deeply indebted to all who helped out along the way. I especially thank my supervisors, Dick Tosdal and Doug Oldenburg, for bringing it together. Dick made things happen and pushed me forward. Doug challenged and inspired me to do great things. Both provided exactly the guidance and advice I needed. Greg Dipple was also part of my committee and I am grateful for his enthusiasm and for introducing me to new ways of thinking about numbers in geology such as the linear programming technique used in Chapter 6.

The project was a collaboration between UBC's Mineral Deposit Research Unit and Geophysical Inversion Facility, Geoscience Australia, the Predictive Mineral Discovery Cooperative Research Centre, and WMC Resources (now BHP Billiton). At MDRU I thank Karie Smith and Arne Toma for taking care of the details. The GIF group are a tremendous close-knit team full of ideas, experience and support. This thesis took shape out of innumerable discussions with Nigel Phillips, Peter Lelièvre, Francis Jones, and perhaps most importantly Roman Shekhtman. Without Roman's incredible knowledge, support and responsiveness to obscure program tweaks and bug fixes, the inversions would never have worked.

I owe much to Geoscience Australia for their support and belief that I warranted this opportunity. Chris Pigram and Peter Southgate made the PhD a possibility, and Richard Blewett, Russell Korsch, and James Johnson kept it alive. Richard has been an inspirational leader and always came through with field support, edits and ideas when I needed them. WMC Resources, and later BHP Billiton, willingly provided the data a project of this scope requires. Without the support of Jon Hronsky, Howard Golden, and Troy Herbert this thesis would only have consisted of ideas. In addition Graeme Thompson provided enormous data assistance, and Ian Lowry and Ria Brabham helped me obtain the rocks for the physical property analyses. Additional sponsorship came from Anglo American, Anglo Gold Ashanti, Barrick Gold, Falconbridge (now Xstrata), Geoinformatics Exploration Canada, Inco (now CVRD-Inco), Placer Dome (now Barrick Gold), and Teck Cominco. Matching funds were provided by the Natural Sciences and Engineering Research Council of Canada Collaborative Research and Development program. The Society of Economic Geologists supported the physical property analyses with a generous grant from the Hugo Dummett Mineral Discovery Fund. The pmd*CRC provided an Associate Scholarship to defray travel costs.

Brad Pillans and especially Chris Klootwijk at the Australian National University Palaeomagnetic Laboratory are thanked for providing access to their lab, training in palaeomagnetic analysis, performing some analyses, and helping me understand the results. At Geoscience Australia I thank Mike Smith for performing the density measurements and Peter Milligan for preparing the original magnetic data grids. At UBC, Elisabetta Pani, Sasha Wilson, and Mati Raudsepp are thanked for undertaking X-ray diffractions analysis on difficult samples. Dianne Mitchinson and Michael McMillan are thanked for testing early versions of the ModelBuilder software, and I am grateful to Victoria Sterritt for testing an early version of the mineralogy estimator software. Rick Allmendinger of Cornell University provided helpful advice on digitally plotting stereonet.

Without the amazing mentoring of Richard Lane at Geoscience Australia I would never have been introduced to geophysics, and especially inversions. I thank him deeply for the inordinate amount of time he has invested in training me, supporting me, and providing seemingly limitless advice over the last six years.

Finally I am heavily indebted to my friends and family. My parents, Cory and Gwynn, gave me every opportunity. They led by example and inspired me to see the world, following my dreams wherever they led. I could only have done that knowing they completely support me and are always there with advice and encouragement. My friends, both in Canada and Australia, have constantly been there despite my infrequent appearances. Claire, Elspeth and Dianne have always been willing ears for which I am most grateful. The most important person in my life is my amazing fiancée, Kylie. This thesis and adventure would not have been possible without her love, support, and laughter, which always lights my day. I can't wait to start our next adventure, together!

This thesis was printed on 100 % recycled paper.

*For Megan, Garry, and the
memories of Bruce and Ross*

May strength flow from your courage fighting cancer

and for Kylie

Let's laugh and love and play. We're free!

Co-Authorship Statement

The six manuscripts presented in this thesis are primarily my own work and design except as outlined below. My supervisors Dick Tosdal and Doug Oldenburg identified the initial project, sponsors, and collaborators, but I scoped, developed and planned the thesis outline, and identified the core issues to be addressed. I was also responsible for managing data acquisition and analysis, and for writing the full thesis. Doug Oldenburg and Dick Tosdal provided editorial assistance on all chapters.

Chapter 2: A review of the application of UBC–GIF 3D potential field inversions for mineral exploration

Authors: Nicholas C. Williams and Douglas Oldenburg

This chapter contains a review of the current state of the art of UBC–GIF gravity and magnetic inversions. Most of the methodology was developed by UBC–GIF prior to this thesis and Douglas Oldenburg is acknowledged for his leadership of that development and for enhancing my understanding of the issues. But the chapter includes several new ideas and approaches introduced in this study, and presents completely new examples that I developed.

Chapter 3: A workflow for preparing and applying UBC–GIF gravity and magnetic inversions

Authors: Nicholas C. Williams, Richard Lane, Douglas Oldenburg, Peter Lelièvre, Nigel Phillips, Francis Jones, and Roman Shekhtman

This chapter provides a best practice workflow for performing UBC–GIF inversions and includes ideas developed by many people over the years. The initial idea and basic concepts were developed with Richard Lane (Geoscience Australia). The present outline was proposed in discussion with Francis Jones and Nigel Phillips (UBC–GIF). All authors contributed unique ideas and techniques they had developed individually. I was responsible for synthesising all of the information, which was sometimes conflicting. I assessed, tested and improved upon the techniques and added my own developments from this thesis.

Chapter 4: Mass and magnetic properties of the southern Agnew-Wiluna greenstone belt and Leinster nickel deposits, Western Australia

Author: Nicholas C. Williams

This chapter was primarily my own work and research, including sample selection, preparation and interpretation.

Chapter 5: An automated approach for building geological constraints for potential field inversions using sparse observations

Author: Nicholas C. Williams and Douglas Oldenburg

This chapter was primarily my own work and research, including outlining the problem, and the solutions, and all programming and development. Douglas Oldenburg provided guidance and helped identify some key challenges that needed to be addressed.

Chapter 6: Mapping subsurface alteration using gravity and magnetic inversion models

Authors: Nicholas C. Williams and Gregory Dipple

This chapter was developed as a term project in a graduate class taught by Gregory Dipple. I proposed the original problem, and Gregory suggested a solution using linear programming and assisted with further development of the technique. I performed all programming and testing. I applied the technique to inversion results that I completed and published prior to commencing this PhD (Williams et al., 2004: reference in Chapter 6).

Chapter 7: Geologically-constrained gravity and magnetic inversions over the Agnew-Wiluna greenstone belt and Perseverance nickel deposit, Western Australia

Author: Nicholas C. Williams and Douglas Oldenburg

This chapter was primarily my own work and research using geophysical and geological data provided by various external sources acknowledged in the chapter. Most of the constraint capabilities were previously developed by Douglas Oldenburg's research group, and he provided valuable understanding of some of the issues associated with the use of inversions and constraints.

Chapter 1: Introduction

1.1 INTRODUCTION

Mineral exploration is making a transition from dominantly surface-based exploration to exploration of the subsurface. Such a move is mandated as it becomes increasingly less likely to discover large outcropping orebodies. The declining rate of discovery of large ore deposits, and the increasing cost of discovery for each new deposit have been well documented (Blain, 2000; Paterson, 2003; Taufen et al., 2003; Schodde, 2004). The solution appears to be to “expand the search space” to include higher risk or more challenging environments such as below cover (Whiting, 2006). But successful exploration in such environments will require several key advances: more effective quantification and management of exploration risk, cheaper and more effective drilling technology, enhanced geochemical tracers, more predictive conceptual targeting, and improved geophysical 3D imaging capability (Hedger, 2008; Hronsky and Groves, 2008; Williams, 2008). This thesis addresses the last of these aspects. It seeks to improve the effectiveness of subsurface geological mapping for mineral exploration through integrated use of geological observations, physical properties, and 3D inversion of gravity and magnetic data. Examples are drawn from nickel mineral exploration applications in an Archean granite-greenstone terrane in Western Australia’s Yilgarn Craton.

1.1.1 Inversion

Inversion is a mathematical procedure for deriving a set of parameters describing a model which can explain a set of observations. Where the observations are measured geophysical data the model parameters are usually a set of physical properties distributed within a particular space. For gravity and magnetic data, the two most widely used and cheaply acquired geophysical datasets in mineral exploration, the geophysical response can be readily calculated from a model of densities or magnetic susceptibilities, based on the physics of potential fields. The inverse calculation, deriving a physical property model from the data, is hampered by numerical problems and non-uniqueness. There may be an infinite number of models that explain the observed potential field data equally well. One approach is to seek a model that fulfills certain criteria based on the geological character expected in the model. An extremely diverse array of approaches has been proposed. A selection includes: smooth and small model inversion (Li and Oldenburg, 1996, 1998); focused inversions (Portniaguine and

Zhdanov, 1999, 2002); building models by growing source bodies (Camacho et al., 2000); inversion using combinations of mathematical model forms (Boulanger and Chouteau, 2001); covariance-based inversion (Chasseriau and Chouteau, 2003); recovery of arbitrary layers of variable properties (Gallardo-Delgado et al., 2003); stochastic lithology-based inversion (Guillen et al., 2004); structural inversion using linear programming (van Zon and Roy-Chowdhury, 2006); bimodal lithotype inversion for arbitrary geometries (van Zon et al., 2007); and inversion using an adaptive mesh (Fullagar and Pears, 2007). This thesis uses The University of British Columbia – Geophysical Inversion Facility (UBC–GIF) 3D gravity and magnetic inversion algorithms (Li and Oldenburg, 1996, 1998). Their method was chosen, partially due to its more common usage within the industry, but also because its flexibility for including varied geological information makes it particularly well suited to early stages of exploration where prior geological knowledge is limited.

The UBC–GIF gravity and magnetic inversion software packages seek a model that is as close as possible to some physical property reference model, which can be based on the expected geology, with a measure of smoothness between cells (Li and Oldenburg, 1996, 1998). The recovered model may be viewed as the simplest model that can satisfy the available geological information and the geophysical data. The inversions can be run without any geological information using default settings and a reference model that is zero everywhere to recover a physical property model that captures the key characteristics needed to reproduce the geophysical data. To date this has been the main use of the UBC–GIF software for mineral exploration problems, and has provided some success stories (Watts, 1997; Macdonald, 2002; Hart and Freeman, 2003). However, when detailed geological information is included, the recovered physical property models can contain as much detail as necessary to satisfy all the available information, and will provide much more reliable predictions of the subsurface physical property distribution.

1.1.2 Physical properties

Physical property knowledge is required at two stages of any geophysical inversion process. Geological information to be included in an inversion must be explicitly or implicitly converted into an input physical property model. But even where no geological information is available, knowledge of the expected physical properties is required to interpret the recovered model. Expectations of the physical properties allow the user to identify which features are

anomalous, which features are unrealistic, and which features indicate problems in the model, but also allow correlation with geology. Physical property data can be derived from several sources: direct measurements, measurements in analogous or neighbouring areas (such as nearby mine sites), public databases (Parsons and McGaughey, 2007), and published literature values (Telford et al., 1990; Hunt et al., 1995; Schön, 2004).

Actual measurements of the rocks to be modelled are the most reliable because of the complex effects of geological processes on physical properties (Henkel, 1976; Planke et al., 1999; Sterritt, 2006; Mitchinson, in prep). As an example, Figure 1.1 shows densities and susceptibilities for various common minerals in Archean greenstone belts, and the effects of some of the geological processes acting upon them. Serpentinisation is a hydration reaction that replaces olivine with serpentine and magnetite. Both minerals may be replaced by carbonate and amphibole during carbonatisation by CO₂-rich fluids. Amphibolite grade metamorphism may create new olivine and form a suite of new silicate minerals. Further post-metamorphic serpentinisation creates more magnetite and serpentine at the expense of metamorphic olivine. The physical properties of the ultramafic rocks will therefore be controlled by the geochemistry of the rocks (and the igneous processes which formed them), alteration fluid chemistry, fluid/rock ratios, and the pressure, temperature, and duration of each metamorphic stage. Depending on their histories, other rock types in the belt, such as the felsic and mafic volcanics and intrusives, and sedimentary rocks, might have escaped such dramatic changes, but metamorphism, deformation and fluid flow may still have an effect.

A further justification for measuring magnetic properties on rocks in an area of interest is the common presence of remanent magnetisation. Remanent magnetisation is a preserved magnetisation in addition to any magnetisation induced by the present earth field. It is also strongly affected by geological processes, especially the thermochemical history of the rocks in a particular area (Clark, 1997; Dunlop and Özdemir, 1997; Yu and Tauxe, 2006). Its presence can introduce major complications for magnetic inversions. Instead of solving for a single set of scalar model parameters, susceptibilities, the inversion must solve for at least three magnetisation components to capture the direction and magnitude of remanent magnetisation. Additional ambiguity is introduced because of the inability to distinguish between induced magnetisation and remanent magnetisation based solely on observed total magnetic intensity data. Because of these complications, the UBC–GIF magnetic inversion code assumes that

remanent magnetisation is negligible within the volume of interest, and that the magnetic response is entirely due to induced magnetisation. If this assumption is violated, major artefacts and errors can be introduced into the recovered susceptibility models. It is important to identify and understand the character of remanent magnetisation in an area to assess the reliability of recovered induced susceptibility models.

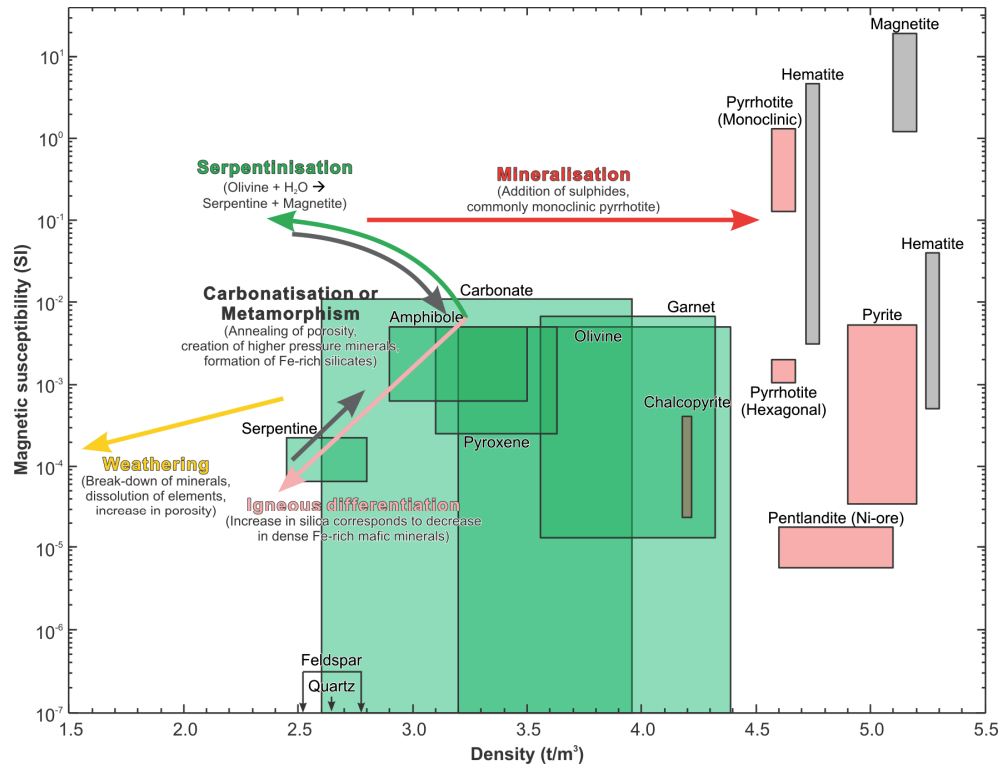


Figure 1.1. Physical properties of common silicate (green), sulphide (red) and oxide (grey) minerals associated with Archean greenstone-hosted nickel deposits, and trends of various geological processes acting upon them. Igneous processes lead to a trend from high density and susceptibility ultramafic and mafic rocks through to low density and susceptibility felsic rocks. Serpentinisation replaces ultramafic olivine with serpentine and magnetite. Carbonatisation is magnetite-destructive and will anneal any primary or secondary porosity. Metamorphism also removes porosity and at amphibolite grades can produce abundant metamorphic olivine. The impact of nickel sulphide mineralisation will depend on the host rock and the ore mineralogy (commonly monoclinic and hexagonal pyrrhotite, plus nickel-bearing pentlandite). Feldspar, quartz, and other non-iron-bearing minerals are diamagnetic with slight negative susceptibilities that plot off the diagram as indicated by arrows. The mineral physical property ranges are sourced from Chesterman and Lowe (1979), Bleil and Petersen (1982), Telford et al. (1990), Hunt et al. (1995), Clark (1997), Emerson et al. (1999), and Schön (2004).

In early exploration stages, large physical property databases are usually unavailable and other sources of physical property information are necessary. However, densities and magnetic properties measured as part of routine field reconnaissance, mapping and geochemical sampling can be used to validate data from other sources until a larger database can be acquired during systematic sampling and drilling.

1.1.3 The Agnew-Wiluna greenstone belt

The examples in this study are all from the Agnew-Wiluna greenstone belt in the Eastern Goldfields Superterrane of Western Australia's Yilgarn Craton (Figure 1.2), but the techniques and approaches presented are equally applicable to other areas. The Eastern Goldfields boasts several key characteristics that make it a suitable for such integrated geophysical and geological studies:

- A sizeable endowment of nickel sulphide mineralisation with a pronounced gravity and magnetic signature, and abundant gold mineralisation
- A variety of rock types with moderately large physical property contrasts
- Well mineralised and understood localities and wide areas of covered and poorly known rocks with high potential for additional sulphide mineralisation
- Availability of large amounts of high quality geological and geophysical data, at a range of scales, courtesy of BHP Billiton (formerly WMC Resources), Geoscience Australia (GA), and the Geological Survey of Western Australia (GSWA)

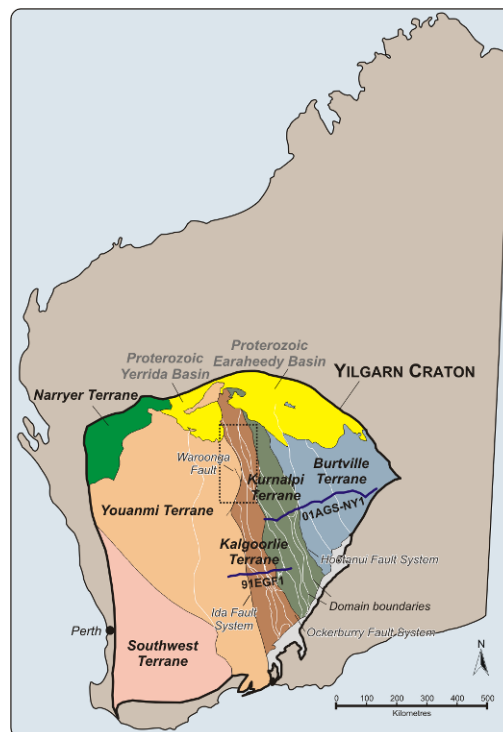


Figure 1.2. Terranes (coloured polygons) and domains (white boundaries) of the Archean Yilgarn Craton as defined by Cassidy et al. (2006). The Eastern Goldfields includes the Kalgoorlie, Kurnalpi, and Burtville Terranes. Blue lines show the locations of two deep reflection seismic lines, 91EGF1 (Goleby et al., 1993) through Kalgoorlie and 01AGS-NY1 (Goleby et al., 2003) through Leonora and Laverton. Dotted black box surrounds the Agnew-Wiluna greenstone belt.

The Agnew-Wiluna greenstone belt is located in the northwest of the Eastern Goldfields province. It possesses each of the above characteristics, including four of the world's largest nickel sulphide deposits (Mt. Keith, Perseverance, Yakabindie, and Honeymoon Well: Jaireth et al., 2005). It represents a fault-bounded sliver of structurally complex greenstone rocks, including metavolcanic and metasedimentary rocks, intruded by and juxtaposed against voluminous granitic and gneiss rocks.

Three main stratigraphic associations have been identified in the belt: komatiite – felsic volcanic, komatiite – basalt, and komatiite – black shale (Naldrett and Turner, 1977; Eisenlohr, 1989; Liu et al., 2002; Beresford et al., 2004; Beresford and Rosengren, 2004). The komatiitic rocks are defined as intrusive or extrusive ultramafic rocks with > 18 wt. % MgO (Leshner and Keays, 2002). The komatiite – felsic volcanic association is restricted to the east side of the belt and contains most of the known nickel deposits. The western portions of the belt contain the komatiite – basalt association which hosts most of the known gold deposits, notably at Agnew, Lawlers and Wiluna, with several smaller occurrences. The komatiite – black shale association is limited in extent and has been inferred to be a deep water equivalent of the komatiite – felsic volcanic association (Trofimovs et al., 2003).

1.2 THESIS OBJECTIVES

The main challenge facing explorers in the Agnew-Wiluna greenstone belt, as well as in the Yilgarn Craton and many other environments around the world, is the ubiquitous presence of overburden covering the prospective basement rocks. Less than 5 % of the Yilgarn Craton Archean basement rocks are exposed (Griffin, 1990); the remainder are deeply weathered or obscured by transported sediment and salt lakes. The greenstone rocks that host most of the gold and nickel mineralisation have strong potential field responses: the basaltic rocks are dense and well delineated by gravity data, and the ultramafic rocks are magnetic and well delineated by magnetic data. Even regional-scale gravity and magnetic data images clearly show the continuity of the greenstone belts beneath cover highlighting the further potential for mapping and targeting prospective greenstone rocks at depth. In recent years both regolith geochemistry and identification and modelling of geophysical anomalies have been successfully used to identify new gold and nickel deposits beneath 20-200 m of cover in greenstone belts adjacent to the Agnew-Wiluna belt, including Bronzewing (Anand et al.,

2001), Wallaby (Coggon, 2003), Sunrise Dam (Gray and Britt, 2005), Thunderbox (Bennett, 2004), and Waterloo (Bennett, 2004), among others. Although such techniques can be highly effective when applied close to an unknown ore body, selecting the appropriate ground for the necessary detailed sampling or data acquisition remains more of a challenge. Better area selection and targeting tools are necessary.

Despite the potential of geophysical inversion methods to provide such tools, there have been very few documented cases of the use of geological information to enhance the quality of inversion results for mineral exploration problems (Phillips, 1996; Williams et al., 2004; Ash et al., 2006; Farquharson et al., 2008). The roadblocks that have prevented more widespread adoption of geologically-constrained inversion for mineral exploration and targeting are the following questions:

1. If geological knowledge is already available why is geophysics required?
2. What is the benefit of incorporating geological information?
3. How much geological information is required?
4. How is geological information included in inversions?
5. Can it be done quickly and efficiently?
6. Once a reliable physical property model is recovered how can it be used for mineral exploration?

A few existing studies have addressed some of these questions, but many of the details remain elusive. This thesis aims to provide answers to each of these questions by presenting a comprehensive guide for the application of gravity and magnetic inversions for mineral exploration, including the use of geological constraints. It is targeted as a practical guide that focuses on the application of UBC–GIF inversions and does not seek to modify the theoretical basis for the algorithms chosen. Although the UBC–GIF method is used exclusively throughout the thesis, many of the principles and procedures could be applied to other inversion algorithms, once various input formats and parameterisations are accounted for.

1.3 THESIS STRUCTURE

The project was initiated in 2004 with logistical support from WMC Resources. BHP Billiton completed acquisition of WMC Resources in August 2005 and continued to provide

logistical support for the duration of the research. The research included one week of field work in November 2005, based at the Perseverance nickel mine in the Agnew-Wiluna greenstone belt, collecting rock samples from drill core and outcropping rocks throughout the district. During July 2006 I spent three weeks at the Australian National University Palaeomagnetic Laboratory in Canberra preparing and analysing magnetic properties on a selection of samples.

The thesis is presented as a series of six individual manuscripts which will be published in refereed scientific journals or publications. Although each manuscript addresses a specific and unique topic, they may contain unavoidable repetition in the background information presented in each. Chapter 2 presents a general introduction to the UBC–GIF inversion approach, and identifies the key aspects and parameters that need to be considered. It includes a review of the limited existing literature describing the use of geological constraints in UBC–GIF inversions. A synthetic geological model and gravity data are used to demonstrate the impact of including increasingly more geological information in a gravity inversion for mineral exploration. By comparing the various recovered density models to the true geological model, the value of the geological information is clearly evident. Surface mapping and physical property measurements appear to be the simplest and most powerful information to include, but even limited drilling information can also help enhance the result.

Due to the non-uniqueness of inversion solutions, it is important that minimal additional ambiguity is introduced into the inversions using inappropriate data or settings. Chapter 3 presents a detailed workflow for preparing and performing gravity and magnetic inversions with the UBC–GIF software. It represents a more detailed, expanded and updated version of a basic workflow previously presented on the internet (UBC-GIF, 2007). It is intended to be used as a step-by-step guide and is not presented in standard journal format. Instead, it is mainly a list of issues, decisions, and techniques, with expanded descriptions as required. It covers the whole process from identifying the problem to be addressed to how geologically-constraints can be created, how the inversions parameters should be set, how the inversions are run, and how the results should be assessed. Although it documents established inversion procedures it also outlines several new approaches for preparing data, defining a mesh, setting inversion parameters, and creating geological constraints. The construction of

geological constraints is covered in two different ways, each suitable for different problems with different available information.

In Chapter 4, the mass and magnetic properties of the rocks in the southern Agnew-Wiluna greenstone belt are assessed. The Chapter provides necessary background information for translating the geological observations into physical property constraints for the inversions presented in Chapter 7. Included is a synthesis of available WMC Resources and BHP Billiton physical property data which is validated using new physical property measurements acquired as part of this study. Some data are available for most of the rock types present, including the various nickel sulphide ore assemblages, and their host rocks. An emphasis is placed on the physical property distinctions between different lithologies and the effect of serpentinisation and mineralisation on the physical properties. The character of remanent magnetisation is also identified in each of the different rock types, which proves critical in performing reliable magnetic inversion in Chapter 7. The mass and magnetic property measurements are tabulated in Appendix A.

The question of how geological constraints can be constructed effectively is addressed in Chapter 5, which presents a new approach for automatically building physical property models for use as constraints in inversions using standard geological observations. Unlike those used in existing 3D modelling packages such as GeoModeller (Intrepid Geophysics) and Gocad (Paradigm), this data-based approach is specifically design for sparse geological observations that are restricted to the surface or small areas, and accommodates both geological observations (text labels) and physical property measurements (scalar numbers). Physical property measurements on surface samples, measurements and geological observations along drill holes, geological polygon-based maps, and 3D models created in external modelling packages can all be utilised within the approach. A new method for automatically extrapolating physical properties based on observed structural orientations is included. The approach is implemented in a complete MATLAB-based software package that handles all the data types listed above; its user manual is included in Appendix B. It automatically creates statistically-based physical property estimates for observed rock type labels, or uses manually assigned property estimates if insufficient measurements are available. It performs all necessary data management and file transformations, including basic coordinate projections. Options for extrapolating the observations are included, as well as other new

advanced options which improve the effectiveness of the constraints in the existing UBC–GIF codes. The software outputs all of the constraint files required by the UBC–GIF inversion codes.

Chapter 6 describes a new method for extracting an estimate of the mineralogy in either a rock sample or an inversion model cell based on its density and magnetic susceptibility. The technique uses a linear programming algorithm to calculate the possible range of abundances of any number of minerals subject to various linear constraints. The constraints will generally be based on the possible range of abundance of each mineral, but can also include limits imposed by geochemical or mineralogical processes, or petrographic relationships. The technique is developed using physical property measurements from actual rocks to estimate their sulphide content. The results are compared to visual estimates of the sulphide content. The method is also applied to previously published 3D geologically-constrained inversion results from the Olympic iron oxide copper gold prospect in South Australia (Williams et al., 2004), to identify possible exploration targets.

The various methods and techniques developed throughout this thesis are applied to real inversion problems for the Agnew-Wiluna greenstone belt in Chapter 7. The Chapter places equal emphasis on demonstrating the method and interpreting the geology, and is presented as an example of how geologically-constrained inversions can be used in mineral exploration at a range of scales. It describes the preparation of geophysical data, geological constraints, and the inversions for regional, district, and deposit scale models. The physical property models are interpreted directly, but are also converted into 3D predicted rock models based on the physical property relationships identified in Chapter 4. The results provide the first 3D geological models of the greenstone belt and provide an estimate of the thickness of the greenstones along the length of the belt. The models clearly identify the depth, geometry and extent of greenstone sequences under cover, but the resolution is severely limited by the wide spacing of the available gravity data stations.

A synthesis of the contributions and limitations of this thesis is presented in Chapter 8. Opportunities for future research and development regarding the application of gravity and magnetic inversions for mineral exploration are also identified.

1.4 REFERENCES

- Anand, R.R., Wildman, J.E., Varga, Z.S., and Phang, C., 2001, Regolith evolution and geochemical dispersion in transported and residual regolith - Bronzewing gold deposit: *Geochemistry: Exploration, Environment, Analysis*, v. 1, p. 265-276.
- Ash, M.R., Wheeler, M., Miller, H., Farquharson, C.G., and Dyck, A.V., 2006, Constrained three-dimensional inversion of potential field data from the Voisey's Bay Ni-Cu-Co deposit, Labrador, Canada: SEG Annual Meeting, New Orleans, October 1-6, p. 1333-1337.
- Bennett, M., 2004, Thunderbox gold and Waterloo nickel deposits, *in* Neumayr, P., Harris, M., and Beresford, S.W., eds., *Gold and nickel deposits in the Archaean Norseman–Wiluna greenstone belt, Yilgarn Craton, Western Australia — a field guide: Geological Survey of Western Australia, Record 2004/16*, p. 77-86.
- Beresford, S.W., Duuring, P., Rosengren, N.M., Fiorentini, M., Bleeker, W., Tait, M.A., Barley, M.E., Cas, R.A.F., and Wallace, H., 2004, Structural and stratigraphic reconstruction of the Agnew-Wiluna belt, Western Australia, *in* Beresford, S.W., Duuring, P., Fiorentini, M., Rosengren, N.M., Bleeker, W., Barley, M.E., Cas, R.A.F., Tait, M.A., and Wallace, H., eds., *P710 final report: The structural and stratigraphic architecture of the Agnew/Wiluna Belt, WA: Melbourne, AMIRA International*, p. 1-7.
- Beresford, S.W., and Rosengren, N.M., 2004, Komatiite-hosted Ni-Cu-PGE deposits of the Agnew-Wiluna greenstone belt - an overview, *in* Neumayr, P., Harris, M., and Beresford, S.W., eds., *Gold and nickel deposits in the Archaean Norseman–Wiluna greenstone belt, Yilgarn Craton, Western Australia — a field guide: Geological Survey of Western Australia, Record 2004/16*, p. 87-91.
- Blain, C., 2000, Fifty-year trends in minerals discovery - commodity and ore-type targets: *Exploration and Mining Geology*, v. 9, p. 1-11.
- Bleil, U., and Petersen, N., 1982, Magnetic properties of natural minerals, *in* Angenheister, G., ed., *Physical properties of rocks, Vol. 1b: Berlin, Springer-Verlag*, p. 308-365.
- Boulanger, O., and Chouteau, M., 2001, Constraints in 3D gravity inversion: *Geophysical Prospecting*, v. 49, p. 265-280.
- Camacho, A.G., Montesinos, F.G., and Vieira, R., 2000, Gravity inversion by means of growing bodies: *Geophysics*, v. 65, p. 95.
- Cassidy, K.F., Champion, D.C., Krapež, B., Barley, M.E., Brown, S.J.A., Blewett, R.S., Groenewald, P.B., and Tyler, I.M., 2006, A revised geological framework for the Yilgarn Craton, Western Australia: *Geological Survey of Western Australia, Record 2006/8*, 9 p.
- Chasseriau, P., and Chouteau, M., 2003, 3D gravity inversion using a model of parameter covariance: *Journal of Applied Geophysics*, v. 52, p. 59-74.
- Chesterman, C.W., and Lowe, K.E., 1979, *The Audubon Society field guide to North American rocks and minerals: New York, Alfred A. Knopf*, 850 p.

- Clark, D.A., 1997, Magnetic petrophysics and magnetic petrology; aids to geological interpretation of magnetic surveys: AGSO Journal of Australian Geology and Geophysics, v. 17, p. 83-103.
- Coggon, J., 2003, Magnetism - key to the Wallaby gold deposit: Exploration Geophysics, v. 34, p. 125-130.
- Dunlop, D.J., and Özdemir, Ö., 1997, Rock magnetism: fundamentals and frontiers: Cambridge, University Press, 573 p.
- Eisenlohr, B.N., 1989, The structural development and controls on mineralisation of the northern sector of the Norseman-Wiluna Belt, Western Australia: Unpub. Ph. D. thesis, University of Western Australia, 189 p.
- Emerson, D.W., Martin, K., and Williams, P.K., 1999, Electrical, magnetic and mass properties of the nickeliferous komatiite sequence near Leinster, Western Australia: Preview, v. 81, p. 13-22.
- Farquharson, C.G., Ash, M.R., and Miller, H.G., 2008, Geologically constrained gravity inversion for the Voisey's Bay ovoid deposit: The Leading Edge, v. 27, p. 64-69.
- Fullagar, P.K., and Pears, G.A., 2007, Towards geologically realistic inversion, *in* Milkereit, B., ed., Proceedings of Exploration 07: Fifth Decennial International Conference on Mineral Exploration, p. 444-460.
- Gallardo-Delgado, L.A., Pérez-Flores, M.A., and Gómez-Treviño, E., 2003, A versatile algorithm for joint 3D inversion of gravity and magnetic data: Geophysics, v. 68, p. 949.
- Goleby, B.R., Blewett, R.S., Groenewald, P.B., Cassidy, K.F., Champion, D.C., Korsch, R.J., Whitaker, A.J., Jones, L.E.A., Bell, B., and Carlson, G., 2003, Seismic interpretation of the northeastern Yilgarn Craton seismic data, *in* Goleby, B.R., Blewett, R.S., Groenewald, P.B., Cassidy, K.F., Champion, D.C., Jones, L.E.A., Korsch, R.J., Shevchenko, S., and Apak, S.N., eds., The 2001 northeastern Yilgarn deep seismic reflection survey: Geoscience Australia, Record 2003/18, p. 85-112.
- Goleby, B.R., Rattenbury, M.S., Swager, C.P., Drummond, B.J., Williams, P.R., Sheraton, J.E., and Heinrich, C.A., 1993, Archaean crustal structure from seismic reflection profiling, Eastern Goldfields, Western Australia: Australian Geological Survey Organisation, Record 1993/15, 54 p.
- Gray, D.J., and Britt, A.F., 2005, Sunrise Dam gold deposit, Eastern Goldfields, WA, *in* Butt, C.R., Robertson, I.D., Scott, K.G., and Cornelius, M., eds., Regolith Expression of Australian Ore Systems: Perth, CRC LEME.
- Griffin, T.J., 1990, Eastern Goldfields Province, *in* Geology and mineral resources of Western Australia: Western Australia Geological Survey, Memoir 3, p. 77-119.

- Guillen, A., Courrioux, P., Calcagno, P., Lane, R., Lees, T., and McInerney, P., 2004, Constrained gravity 3D litho-inversion applied to Broken Hill: ASEG 17th Geophysical Conference & Exhibition, Sydney, 15-19 August.
- Hart, J., and Freeman, H., 2003, Geophysical responses of the Prominent Hill Fe-Cu-Au-U deposit: ASEG 16th Geophysical Conference & Exhibition, Adelaide, South Australia, 16-19 February.
- Hedger, D.C., 2008, Quantification of economic risk in mineral exploration: A case study on exploration in the Yarrol region, Queensland, Australia: Unpub. Ph.D. thesis, The University of Queensland, 467 p.
- Henkel, H., 1976, Studies of density and magnetic properties of rocks from northern Sweden: *Pure and Applied Geophysics*, v. 114, p. 235-249.
- Hronsky, J.M., and Groves, D.I., 2008, Science of targeting: definition, strategies, targeting and performance measurement: *Australian Journal of Earth Sciences*, v. 55, p. 3-12.
- Hunt, C.P., Moskowitz, B.M., and Banerjee, S.K., 1995, Magnetic properties of rocks and minerals: *AGU Reference Shelf*, v. 3, p. 189-204.
- Jaireth, S., Hoatson, D., Jaques, L., Huleatt, M., and Ratajkoski, M., 2005, Nickel sulphide metallogenic provinces: resources and potential: *Geoscience Australia, AusGeo News*, n. 79.
- Leshner, C.M., and Keays, R.R., 2002, Komatiite-associated Ni-Cu-PGE deposits: geology, mineralogy, geochemistry, and genesis, *in* Cabri, L.J., ed., *The geology, geochemistry, mineralogy and mineral beneficiation of platinum-group elements*: Canadian Institute of Mining, Metallurgy and Petroleum, Special Volume 54, p. 579-617.
- Li, Y., and Oldenburg, D.W., 1996, 3-D inversion of magnetic data: *Geophysics*, v. 61, p. 394-408.
- Li, Y., and Oldenburg, D.W., 1998, 3-D inversion of gravity data: *Geophysics*, v. 63, p. 109-119.
- Liu, S.F., Champion, D.C., and Cassidy, K.F., 2002, Geology of the Sir Samuel 1:250,000 sheet area, Western Australia: *Geoscience Australia, Record 2002/14*, 57 p.
- Macdonald, J., 2002, The role of geoscience in attracting investment: *World Mines Ministries Forum*, Toronto, 13-15 March.
- Mitchinson, D., in prep, Targeting Archean orogenic gold mineralization using physical properties and integrated geophysical methods: Unpub. Ph.D. thesis, The University of British Columbia.
- Naldrett, A.J., and Turner, A.R., 1977, The geology and petrogenesis of a greenstone belt and related nickel sulfide mineralization at Yakabindie, Western Australia: *Precambrian Research*, v. 5, p. 43-103.

- Parsons, S., and McGaughey, J., 2007, Rock property database system, *in* Milkereit, B., ed., Proceedings of Exploration 07: Fifth Decennial International Conference on Mineral Exploration, p. 933-938.
- Paterson, N.R., 2003, Geophysical developments and mine discoveries in the 20th century: The Leading Edge, v. 22, p. 558-561.
- Phillips, N.D., 1996, Geophysical inversion in an integrated exploration program: examples from the San Nicolás deposit: Unpub. Masters thesis, University of British Columbia, 237 p.
- Planke, S., Cerney, B., Bucker, C.J., and Nilsen, O., 1999, Alteration effects on petrophysical properties of subaerial flood basalts: Site 990, Southeast Greenland margin: Proceedings of the Ocean Drilling Program Scientific Results, v. 163, p. 17-28.
- Portniaguine, O., and Zhdanov, M.S., 1999, Focusing geophysical inversion images: Geophysics, v. 64, p. 874-887.
- Portniaguine, O., and Zhdanov, M.S., 2002, 3-D magnetic inversion with data compression and image focusing: Geophysics, v. 67, p. 1532-1541.
- Schodde, R.C., 2004, Discovery performance of the Western World gold industry over the period 1985–2003: Proceedings of PACRIM 2004 Congress, p. 367-380.
- Schön, J.H., 2004, Physical properties of rocks: Fundamentals and principles of petrophysics: Oxford, Elsevier, 583 p.
- Sterritt, V., 2006, Understanding physical property-mineralogy relationships in the context of geologic processes in the ultramafic rock-hosted mineral deposit environment: aiding interpretation of geophysical data: Unpub. Masters thesis, University of British Columbia, 174 p.
- Taufen, P., Baker, P., Kelley, D., and Schodde, R., 2003, Enhancing effectiveness and success rates in modern exploration: Geochemistry - Exploration, Environment, Analysis, v. 3, p. 79-84.
- Telford, W.M., Geldart, L.P., and Sheriff, R.E., 1990, Applied Geophysics: New York, Cambridge University Press, 770 p.
- Trofimovs, J., Tait, M.A., Cas, R.A.F., McArthur, A., and Beresford, S.W., 2003, Can the role of thermal erosion in strongly deformed komatiite-Ni-Cu-(PGE) deposits be determined? Perseverance, Agnew-Wiluna Belt, Western Australia: Australian Journal of Earth Sciences, v. 50, p. 199-214.
- UBC-GIF, 2007, 3D inversion: magnetic or gravity data:
<http://www.eos.ubc.ca/ubcgif/iag/workflow/3D-mag/index.htm>, accessed March 2007.
- van Zon, T., Ditmar, P., Chowdhury, K.R., and Mondt, J., 2007, Lithotype discrimination within a gridded model by inverting gravity data: Geophysical Journal International, v. 170, p. 481-491.

- van Zon, T., and Roy-Chowdhury, K., 2006, Structural inversion of gravity data using linear programming: *Geophysics*, v. 71, p. J41-J50.
- Watts, A., 1997, Exploring for nickel in the 90s, or 'til depth us do part', *in* Gubins, A.G., ed., *Proceedings of Exploration 97: Fourth Decennial International Conference on Mineral Exploration*, 97, p. 1003–1014.
- Whiting, T.H., 2006, Tomorrow's exploration challenges for today's megaminer(s): Australian Earth Science Convention, Melbourne, 2-6 July, GSA Conference Abstract Series, p. 63-64.
- Williams, N., 2008, The exploration crisis - an industry perspective: *SEG Newsletter*, April, p. 7.
- Williams, N.C., Lane, R., and Lyons, P., 2004, Towards 3D maps of alteration under cover: Regional constrained 3D inversion of potential field data from the Olympic Cu-Au province, South Australia: *Preview*, p. 30-33.
- Yu, Y., and Tauxe, L., 2006, Acquisition of viscous remanent magnetization: *Physics of The Earth and Planetary Interiors*, v. 159, p. 32-42.

Chapter 2: A review of the application of UBC–GIF 3D potential field inversions for mineral exploration¹

2.1 INTRODUCTION

Mineral exploration produces a large amount of diverse geological and geophysical data, yet it has proved difficult to combine all of this information into consistent holistic models of subsurface geology. Traditionally, geophysical forward modelling along 2D profiles has been used to calculate the geophysical response of a physical property model based on observed or expected geology. Discrepancies between the calculated and observed geophysical data are interpreted to indicate differences between the inferred geological scenario built into the model and the geology that is actually present. In recent years advances in computing power have facilitated the forward computation of geophysical responses for very large 2D and 3D models. Methods have also been developed to calculate inverse solutions that predict the distribution of physical properties required to explain the observed geophysical responses.

Gravity and magnetic data are two of the most common geophysical datasets used in ore deposit exploration. Even in greenfields exploration these datasets may be available from government agencies or from work carried out by previous explorers. The application of inversion methods to obtain estimated models of physical properties within a subsurface region from these gravity and aeromagnetic datasets is a common step in many exploration programs, especially in areas where prospective basement rocks are covered. The recovered inverse models can be used to target regions of anomalous physical properties for further data acquisition or drilling.

Inversion of potential field data is impeded by several numerical difficulties:

1. Non-existence: Due to the ubiquitous presence of noise in geophysical and geological observations, there may not exist a single model capable of fitting the measured data.
2. Instability: Small changes in the data, such as noise, can result in large changes in the recovered model since the inverse problem is ill-conditioned.

¹ A version of this chapter will be submitted for publication. Williams, N. C., and Oldenburg, D. W. A review of the application of UBC–GIF 3D potential field inversions for mineral exploration

3. Non-uniqueness: There are two sources of non-uniqueness; the data are limited to a finite number of point observations, and the source distribution for potential fields is intrinsically non-unique.

The first problem is handled by allowing for noise in the geophysical data and seeking a model that explains the observed data to within some specified tolerance. Instability of the inversion problem is mitigated by some type of conditioning or regularisation. Regularisation typically imposes a set of mathematical constraints that stabilise the problem and recover a model that fulfils certain criteria. The non-uniqueness of inversion results is tackled either by including existing geological information in the geophysical inversion to guide the solution towards one that is consistent with all available knowledge, or by imposing a set of mathematical constraints that approximate geological expectations for the model when geological data is lacking. As pointed out by Silva et al. (2001), the diversity of methods available requires careful selection of an appropriate method for the specific geological problem to be addressed. To demonstrate the available variety, some examples of proposed potential field inversion algorithms are: smooth and small model inversion (Li and Oldenburg, 1996, 1998a); building models by growing source bodies (Camacho et al., 2000); inversion using combinations of mathematical model forms (Boulianger and Chouteau, 2001); focused inversions (Portniaguine and Zhdanov, 1999, 2002); covariance-based inversion (Chasseriau and Chouteau, 2003); recovery of arbitrary layers of variable properties (Gallardo-Delgado et al., 2003); stochastic lithology-based inversion (Guillen et al., 2004); structural inversion using linear programming (van Zon and Roy-Chowdhury, 2006); bimodal lithotype inversion for arbitrary geometries (van Zon et al., 2007); and inversion using an adaptive mesh (Fullagar and Pears, 2007).

Despite the variety of approaches, only a limited number of algorithms have been adopted in the mineral exploration industry, namely the University of British Columbia – Geophysical Inversion Facility’s (UBC–GIF) GRAV3D and MAG3D packages (Li and Oldenburg, 1996, 1998a), the University of Utah Consortium for Electromagnetic Modeling and Inversion’s GRMAG3D package (Portniaguine and Zhdanov, 1999, 2002), the Bureau de Recherches Géologiques et Minières (BRGM) & Intrepid Geophysics’ GeoModeller package (Guillen et al., 2004) and Fullagar Geophysics’ VPmg package (Fullagar and Pears, 2007). Each of the programs has benefits and limitations and most are suited to slightly different sets

of geological data and problems. This review focuses on the UBC–GIF GRAV3D and MAG3D inversion packages, partially due to their more common usage within the industry, but also because they are particularly well suited to early stages of exploration where prior geological knowledge is limited.

The regularisation imposed by the UBC–GIF inversion approach seeks a model that is small, containing as little deviation from a reference model as possible, and has certain smoothness characteristics. Smoothness can have one of two forms: either the model itself can vary smoothly (smooth model), or deviations from the reference model can be spread smoothly over a number of cells (smooth model-difference). This smooth and small implementation provides a robust, general solution that is relatively easy to parameterise, and efficient to calculate. A limitation of such an approach is that recovered models will generally be smooth, and won't delineate sharp geological boundaries. The recovered source features also tend to be larger in size with smaller physical property variations than are actually present. However for many applications, the smoothness constraint provides a good approximation of the distribution of properties within homogeneous bodies. The smooth gradients recovered along geological contacts can be attributed to the inherent non-uniqueness of inversion of potential field data and are a reminder of the resulting uncertainty in the exact position of those contacts based on potential field data alone.

While these mathematical constraints can be used to recover physical property models that may provide insight into the broad geological architecture, used in isolation they can never recover an accurate physical property model because there is no direct link between the mathematics and the geology. A holistic model, consistent with all observed information, can only be recovered by including geology-based constraints in addition to the mathematical constraints. While all of the available inversion packages allow or require constraints, a strength of the UBC–GIF inversion programs is that they allow the inclusion of as much or as little geological information as is available, in the form of a reference model of physical properties or bounds on the range of expected physical properties, and a set of weighting functions. The inversions return solutions that are within the bounds and as close as possible to the imposed reference model while still fitting the geophysical data to within the accepted uncertainty levels. Intelligent use of these forms of constraints can easily recover sharp

geological boundaries where they are known to exist, despite the general smoothness requirements.

This review begins with an overview of published examples of geologically-constrained UBC–GIF inversions. It then outlines the basic inversion method used by the UBC–GIF programs GRAV3D and MAG3D, describes the inversion parameters used in these programs, and provides some guidance on parameter settings for mineral exploration problems. The types of geological constraints that can be used are described and illustrated using a synthetic gravity inversion example. This example demonstrates the iterative nature of constraining inversions to ensure that the recovered models are consistent with the best available geological information at any stage of the exploration process. Finally, the impact of geological constraints based on surface mapping is further demonstrated using a real gravity inversion example taken from Chapter 7.

2.2 PREVIOUS WORK USING GEOLOGICALLY-CONSTRAINED UBC–GIF INVERSIONS

There are only a handful of publicly available studies using geologically-constrained UBC–GIF potential field inversions and even fewer related to mineral exploration. This is likely due to the strategic and confidential nature of much of the work undertaken in the mineral exploration industry, but is probably also due to the perceived difficulty in understanding and building appropriate constraints. However, several useful examples are available that demonstrate real applications of geological constraints, and the results that can be expected given different data sets and problems.

Phillips (1996; and also mentioned by Phillips and Oldenburg, 2002) provides the first example of geologically-constrained UBC–GIF gravity and magnetic inversions in a study of inversion of a full suite of geophysical datasets over the San Nicolás volcanic-hosted massive sulphide deposit in Mexico. One component of their study used density and magnetic susceptibility measurements on up to 60 drill holes through and adjacent to the deposit to define lower and upper bounds on the properties within each intersected cell to use as constraints for gravity and magnetic inversions. They used a uniform zero reference model throughout the inversions, so the use of bounds created a smooth model style of inversion (described in Section 2.6.2); this remains the only published application of smooth model inversions. All other studies use the default smooth model-difference style of inversion. Their

results show a dramatic improvement in the quality of the delineation of the deposit. They also include examples where density and magnetic susceptibility measurements from only a single drill hole are used to define the constraints, as might be available in an early exploration program, and found that the results were clearly more reliable than for the geologically-unconstrained gravity and magnetic inversions.

Farquharson et al. (2008) present a similar application of drill hole data to delineate the extent of sulphide ore in a known target using geologically constrained gravity inversions, however they derive and apply their constraints in a very different way from Phillips (1996). Their study is based on the Voisey's Bay nickel-copper-cobalt sulphide ovoid deposit in Labrador, Canada. They use iron, sulphide and copper assay percentages obtained from > 500 drill holes to calculate density estimates for the deposit using regression analysis. Drill hole intercepts are used to construct wireframe models of the known limits of the ore body and overburden. By kriging the density estimates within each wireframe body they are able to produce a robust 3D density reference model for use in constraining their inversions. Because it is rare to have such a comprehensive drilling database from which to derive constraints, they also prepare a kriged density reference model using density estimates from just six drill holes. The reference models are used to constrain gravity inversions over the deposit to attempt to map the density variations, and therefore the relative sulphide contents within the deposit itself.

A comprehensive overview of the full range of geophysical inversion methods for mineral exploration problems is provided by Oldenburg and Pratt (2007). Of particular relevance for this review is a brief example they present for the Joutel gold and base metal sulphide deposit in Quebec, Canada. There an inversion of magnetic data was constrained by a reference model populated from a full 3D geological interpretation of wireframe surfaces and lithological packages based on mapping, structural measurements and geological cross-section interpretations. Although the model would have been time-consuming to build, this provides a highly constrained result that can rigorously test the validity of the interpreted geology. In their example, portions of the recovered inversion model indicated that the geological interpretation was consistent with the observed magnetic data but in other locations there were significant discrepancies which may indicate alteration or mineralisation. Williams et al. (2004) use a similar approach to develop gravity and magnetic inversions constrained by a basic 3D wireframe geological model at a regional scale surrounding the Olympic Dam iron oxide

copper gold deposit in South Australia. They then calculate estimates of the abundance of different ore and alteration minerals that would be required to account for the observed differences between the density and magnetic susceptibility reference models and the recovered models. Their mineralogy estimates are further improved for the same constrained inversion results by Williams and Dipple (2007).

Apart from mineral exploration applications there are a couple more studies that show applications of geologically-constrained UBC–GIF inversions that could be useful examples for developing constraints for mineral exploration. Welford and Hall (2007) present a study where they use a combination of onshore and offshore gravity data in constrained inversions to determine the crustal structure and thickness beneath the continental shelf off the southeast coast of Newfoundland, Canada. Although this was a large-scale study covering an area of $975 \text{ km} \times 975 \text{ km}$ to a depth of 25 km, it faced issues familiar to mineral explorers needing to image below “overburden” material – in this case the ocean and sediments overlying the crustal basement of interest. They built a set of layered constraints in the top portions of the inversions to enhance resolution of the relevant features at depth. The topmost layer represented the ocean, with the bottom of the layer defined by bathymetric data. Below that they included a layer of sediments with a base defined by seismic reflection data acquired during oil and gas exploration. Within these layers they assign best estimate reference densities, and used appropriate bounds to allow for expected variability and stratification within those layers. The basement rocks of interest in their study were only constrained to lie within wide but realistic bounds. Their inversions provided good corroboration for the depth of Moho determined by seismic methods, with the benefit that the Moho could be mapped in 3D rather than along isolated 2D seismic profiles. For mineral exploration problems where seismic reflection data or other reliable depth-to-basement estimates are available, they could be used in a similar way to remove the ambiguity introduced by an unknown thickness and geometry of overburden. Cella et al. (2007) also use seismic reflection data and deep wells to build a constraint layer in gravity inversions over the Somma–Vesuvius volcano in Italy. In contrast to the study by Welford and Hall (2007), they use the constraints to control the influence of carbonate basement rocks so they could better image variations in the covering lavas.

2.3 THE UBC-GIF INVERSION METHOD

Linear inversion methods can be used to find a model, **m**, which satisfies:

$$\mathbf{G}\mathbf{m} = \mathbf{d}^{\text{obs}} \quad 2.1$$

where \mathbf{G} is the forward operator, or kernel, that describes the physics of the problem, and \mathbf{d}^{obs} is the observed data. For potential field data in mineral exploration, we discretise the subsurface into a model (\mathbf{m}) containing M individual cells, where M is typically greater than the number of data, N , available (\mathbf{d}^{obs}). This results in an $N \times M$ ($M > N$) matrix \mathbf{G} that is not square and therefore not invertible. Instead, the problem becomes an optimisation problem, seeking a solution that minimises both a numerical measure of the model and the misfit between the observed and predicted data.

The details of the UBC–GIF inversion approach for potential field data as implemented in the MAG3D and GRAV3D programs are given in Li and Oldenburg (1996; 1998a), and in the software user manuals UBC–GIF (2005a; 2005b). A brief summary is included here. In both of the inversion programs and the following method and discussion, all distance quantities are measured in metres, all gravity observations and predictions are in mGal, all densities are in g/cm^3 or t/m^3 , all magnetic field observations are in nT, and all magnetic susceptibilities are induced susceptibilities with units of SI. All other quantities (such as weightings) are effectively unit-less.

2.3.1 Model objective function

The UBC–GIF magnetic and gravity inversion codes use a model objective function to quantify various characteristics of the model. The function includes a term that measures the smallness, or difference between the recovered model and a reference model, and terms that measure how the difference between recovered and reference models varies between cells in each of three orthogonal directions. The reference model may be as simple as a uniform (commonly zero) half-space, in which case the returned model may be expected to contain the minimum amount of detail necessary to reproduce the observed data. However, the prior geological knowledge portrayed in the reference model may be more substantial, to the point where a full model of the expected physical properties could be used where there is a strong understanding of the subsurface physical property distribution. The model objective function is designed so that minimisation leads to a recovered inverse model that has characteristics that are as close as possible to those in the supplied reference model. The model objective function used is:

$$\begin{aligned}
\phi_m(m) = & \alpha_s \int_V w_s \left[w_r(z)(m - m_{ref}) \right]^2 dV + \dots \\
& \alpha_x \int_V w_x \left[\frac{\partial}{\partial x} (w_r(z)(m - m_{ref})) \right]^2 dV + \dots \\
& \alpha_y \int_V w_y \left[\frac{\partial}{\partial y} (w_r(z)(m - m_{ref})) \right]^2 dV + \dots \\
& \alpha_z \int_V w_z \left[\frac{\partial}{\partial z} (w_r(z)(m - m_{ref})) \right]^2 dV
\end{aligned} \tag{2.2}$$

The first integral component measures the smallness. The last three integral components measure the smoothness of the difference between the recovered model, m , and the reference model, m_{ref} , measured in the direction of each of the three orthogonal axes. These components ensure that any discrepancies between the recovered model and the reference model are spread over a region rather than concentrated in individual cells. The user-defined parameters α_s , α_x , α_y , and α_z are used to balance the contributions of the smallness and smoothness components. The weighting function w_s may be used to force the physical property of cells to be closer to the supplied reference model at specific cell locations where the physical properties are better understood. Similarly, the parameters w_x , w_y , and w_z , can be used to make the model-difference vary more or less smoothly across cell boundaries in the east, north, and vertical directions to reproduce geological continuity or boundaries. The function $w_r(z)$ is a depth or distance weighting function.

2.3.2 Depth & distance weighting

The depth or distance weighting function is designed to counteract the decay of the potential field response with distance from the source so that all cells have an equal likelihood of containing sources. Where no other geological information exists, this is necessary as there is no inherent depth information contained in the observed potential field response and a default solution to the inverse problem would result in a model with sources clustered near the surface where the data has the most sensitivity. The weighting function has two possible forms (Li and Oldenburg, 1996, 1998a).

A true depth weighting form takes into account only the distance below the observed geophysical data:

$$w_r^2(z_j) = \frac{1}{(z_j + z_0)^\beta} \quad 2.3$$

where z is the depth to the j th cell and z_0 and β are adjustable parameters used to match the weighting function to the kernel's decay with depth. β is usually chosen to reproduce the exponential decay of the gravity or magnetic response of a sphere with distance: $\beta = 2$ for gravity data and $\beta = 3$ for magnetic data. The parameter z_0 is usually calculated automatically to match the decay of the geophysical kernel in the center of the supplied mesh. This form is a suitable first order approximation of the decay of potential fields where there is a high density of data observations and topography is flat.

A more robust form of the weighting function is required where geophysical data are irregularly or sparsely distributed and/or where any topography is present. It allows for the true 3D separation of observations and cells. This distance weighting function accommodates lateral variations in data sensitivity as well as vertical variations and is related to the sensitivity of the gravity or magnetic data to a unit density or susceptibility at a particular source-observation separation:

$$w_r^2(r_j) = \sqrt{\sum_{i=1}^N \left(\frac{1}{(R_{ij} + R_0)^\beta} \right)^2} \quad 2.4$$

where R_{ij} is the distance between cell j and observation i , and R_0 is a small stabilising constant. For each cell, the distance weight is the best-fitting least squares data sensitivity of a unit source for all observation locations. As for depth weighting, β is usually chosen to reproduce the exponential decay of the gravity or magnetic response of a sphere with distance: $\beta = 2$ for gravity data and $\beta = 3$ for magnetic data. The parameter R_0 is taken as one-quarter of the smallest cell dimension to ensure that the distance weight is always defined.

2.3.3 Data misfit

For the recovered inverse model to be capable of reproducing the observed data there must also be a measure of how closely the predicted response of the recovered model matches the observed data. Geophysical experiments will obtain measurements:

$$\mathbf{d}^{\text{obs}} = \mathbf{d}^{\text{true}} + \boldsymbol{\varepsilon} \quad 2.5$$

where the observed data, \mathbf{d}^{obs} , includes noise, $\boldsymbol{\varepsilon}$, as well as the true response, \mathbf{d}^{true} . As discussed in a later section, the noise may include other contributions besides the uncertainty in the measurements themselves. A model that provided an exact match between the observed noisy data and the predicted data would almost certainly be incorrect because the model would be required to accurately reproduce the noise as well as the true geophysical response. To allow for uncertainty in the observed data, the data are only reproduced to a specified level of accuracy. The resulting data misfit is assessed by weighting the difference between the observed and predicted data by the uncertainty in those data:

$$\phi_d = \left\| \mathbf{W}_d (\mathbf{G}\mathbf{m} - \mathbf{d}^{\text{obs}}) \right\|^2 \quad 2.6$$

$$\mathbf{W}_d = \text{diag} \left(\frac{1}{\sigma_i} \right) \quad 2.7$$

where $\mathbf{G}\mathbf{m}$ is the predicted response of the recovered model, and σ_i is the standard deviation of noise attributed to the i th data point.

2.3.4 Obtaining a solution

A suitable model is found by solving the optimisation problem:

$$\begin{aligned} &\text{minimize } \phi = \phi_d + \mu\phi_m \\ &\text{such that } \phi_d = \phi_d^* \end{aligned} \quad 2.8$$

where ϕ is the objective function and μ is a trade-off parameter to balance the importance of low data misfit versus a small model objective function, and ϕ_d^* is the target data misfit which, assuming that the data noise is Gaussian with zero mean and standard deviation σ_i , will be equal to the number of data observations, N .

When discretised over a 3D mesh, the problem becomes one of minimising:

$$\phi = \left\| \mathbf{W}_d (\mathbf{G}\mathbf{m} - \mathbf{d}^{\text{obs}}) \right\|^2 + \mu \left\| \mathbf{W}_m (\mathbf{m} - \mathbf{m}_{\text{ref}}) \right\|^2 \quad 2.9$$

The minimum occurs at:

$$\begin{aligned} &\nabla_m \phi = \mathbf{0} \\ &(\mathbf{G}^T \mathbf{W}_d^T \mathbf{W}_d \mathbf{G} + \mu \mathbf{W}_m^T \mathbf{W}_m) \mathbf{m} = \mathbf{G}^T \mathbf{W}_d^T \mathbf{W}_d \mathbf{d}^{\text{obs}} + \mu \mathbf{W}_m^T \mathbf{W}_m \mathbf{m}_{\text{ref}} \end{aligned} \quad 2.10$$

where:

$$\begin{aligned} \mathbf{W}_m^T \mathbf{W}_m = & \alpha_s \mathbf{W}_r^T \mathbf{W}_s^T \mathbf{W}_s \mathbf{W}_r + \alpha_x \mathbf{W}_r^T \mathbf{W}_x^T \mathbf{W}_x \mathbf{W}_r + \dots \\ & \alpha_y \mathbf{W}_r^T \mathbf{W}_y^T \mathbf{W}_y \mathbf{W}_r + \alpha_z \mathbf{W}_r^T \mathbf{W}_z^T \mathbf{W}_z \mathbf{W}_r \end{aligned} \quad 2.11$$

and \mathbf{W}_r is a discretised form of the depth weighting function, \mathbf{W}_s , \mathbf{W}_x , \mathbf{W}_y , and \mathbf{W}_z are discretised forms of the weights \mathbf{w}_s , \mathbf{w}_x , \mathbf{w}_y , and \mathbf{w}_z . A solution for \mathbf{m} is found by solving the problem using iterative techniques for a range of μ until a solution is located with $\phi_d = \phi_d^* = N$ is located.

Several additional non-linear constraints, the implementation of which is described by Li and Oldenburg (1996; 1998a), are also applied when calculating a solution: positivity and bounds. Logarithmic barrier functions are used in the MAG3D code to ensure that only positive magnetic susceptibilities are obtained. They are also applied in both MAG3D and GRAV3D to ensure that the recovered properties lie between specific bounds. In default inversions, wide bounds are allowed, but when including geological constraints, narrow bounds can be supplied to restrict the properties to some expected range. The bounds can be set for the whole model or for individual cells and are strictly enforced.

2.4 PREPARING INVERSIONS

A number of steps are required to prepare data and a mesh for an inversion. These steps are covered by Li and Oldenburg (1996; 1998b; 1998a), UBC–GIF (2005a; 2005b), and Chapter 3. In summary they include:

- Definition of the problem to be addressed
- Definition of the volume of interest (depth, width and length of desired mesh)
- Definition of the data area
- Definition of the cell sizes to match the resolution of the data, the desired resolution of the recovered model, and available computing power (currently several million cells is a reasonable upper limit for tenable computation on standard desktop PCs)
- Padding the mesh with a buffer of additional cells to prevent boundary effects where anomalies are located near the edge of the mesh
- Upward continuation of the potential field data to the width of the cells to ensure that high frequency information that could only be reproduced by smaller cell sizes is not included

- Calculation and removal of a regional data trend that accounts for the contribution to the response of all sources located outside the volume of interest.

2.5 CHOOSING OPTIMAL PARAMETERS

The implementation of the UBC–GIF inversion method requires selection of appropriate values for a large number of parameters. Each choice can cause large differences in the model, and although use of the default values may be acceptable in some situations, more reliable models will be obtained by tuning the parameters to a particular problem. One exception is the depth or distance weighting which have their basis in the physics of potential fields; the default distance weighting values are usually best, and if the results are deemed to be inappropriate then some geological information or inference is available that could be included with constraints instead.

2.5.1 Data uncertainty

It is critical to assign an appropriate level of uncertainty to the observed data used in the inversion. If the assigned uncertainties are too high then too much of the observed data will be treated as unwanted noise, and information will be lost in the model (Figure 2.1A). If the assigned uncertainties are too low, much of the noise in the observed data will be reproduced as artefacts in the model (Figure 2.1D). Unfortunately potential field data rarely come with robust uncertainty estimates and the estimates must also account for less tangible attributes such as the effects of data processing, use of a discretised representation of the earth, and numerical inaccuracies.

If an estimate of the data uncertainty or noise level is available it can be included in the data file. For inversions gravity will commonly have standard deviations of 1–2 % of the data range, expressed as a constant (i.e. 0.05 mGal). Due to its higher dynamic range, aeromagnetic data may have standard deviations on the order of a couple of percent plus a couple of nT (i.e. 5 % + 5 nT). Older surveys may require higher uncertainty levels than newer surveys, depending on the methods used, and this can be accommodated in the UBC–GIF inversions where data from the two surveys are combined. Likewise, upward continued data will have a lower dynamic range and should have lower uncertainties applied.

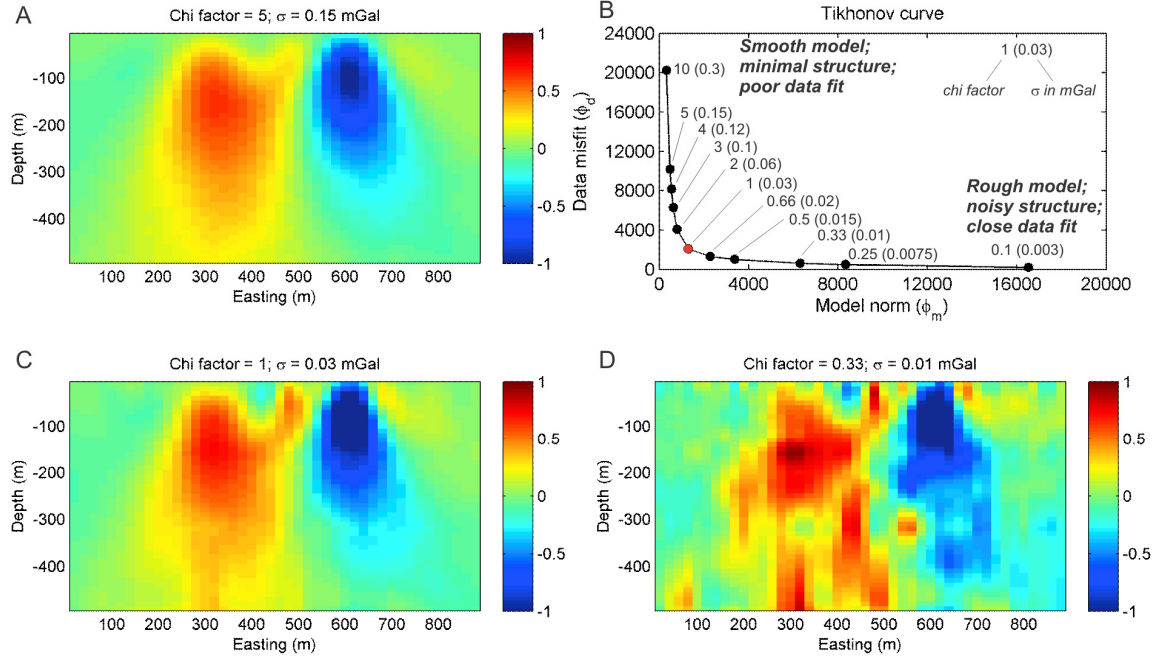


Figure 2.1. Typical relationships between recovered models and specified data uncertainties for a set of inversions using 2025 synthetic data points with 0.03 mGal of random Gaussian noise. The actual noise level of 0.03 mGal was specified in the data file as the standard deviation for each point. The effective data uncertainty allowed in each inversion was specified by adjusting the *chi factor* parameter as indicated; the effective data uncertainty is equal to $chi\ factor \times \sigma$. The Tikhonov curve (B) indicates the achieved model norm versus the achieved data misfit for each inversion. If the data noise is truly Gaussian and the correct data uncertainty is allowed, $\phi_d = N$ (the number of data points) provides a balanced solution. The red circle indicates that ideal result for this example, obtained using the actual noise level (C). If the specified data uncertainty is too high, the data will be poorly fitted, and an excessively smooth model will be recovered (A). If the specified data uncertainty is too low, the data will be tightly fitted, and an excessively noisy model will be recovered (D).

One approach to estimating the appropriate data uncertainty in the absence of good estimates is to perform a Generalised Cross Validation (GCV) inversion (Farquharson and Oldenburg, 2004), an option within the UBC–GIF codes, and supplying a best estimate of the standard deviation for all data, $\tilde{\sigma}$. This chooses a trade-off parameter μ based on how dependent the model is on individual data points. The completed inversion log file reports a final Achieved Misfit. An estimate of the likely standard deviation appropriate for the dataset is then obtained using:

$$\sigma_{gcv} = \tilde{\sigma} \cdot \sqrt{\frac{\text{achieved misfit}}{\text{number of observations}}} \quad 2.12$$

However, GCV inversions commonly fit the data too closely and estimates of the standard deviation derived from the results can sometimes underestimate the appropriate uncertainty level. The estimates must be compared to other estimates of the noise in the data.

2.5.2 Alphas

The balance of smoothness versus smallness for the whole model is controlled by the α values in the model objective function (equation 2.2): α_s for smallness, and α_x , α_y , and α_z for smoothness. A higher ratio of smallness to smoothness will serve to reproduce the supplied reference model more closely, at the expense of smoothness, but may also introduce excess structure similar to that observed when the supplied geophysical data are reproduced too closely. A lower ratio of smallness to smoothness will create a smoother model with less structure. Since the values are all scaled by the trade-off parameter, μ in equation 2.8, it is only the balance between them that is important. By simplifying the model objective function to ignore the reference model, and considering the case of only two cells that are adjacent in the x direction, the balance between smoothness and smallness can be evaluated from:

$$\phi_m(m) = \alpha_s \int m^2 dA + \alpha_x \int \left(\frac{\partial m}{\partial x} \right)^2 dA \quad 2.13$$

If each cell is the same size, with area $A = \Delta x \cdot \Delta z$ (where Δx is the cell width and Δz is the cell height, in metres) and physical properties m_1 and m_2 , the integrals transform into summations and the model objective function for the two cells becomes:

$$\phi_m = \alpha_s (m_1^2 + m_2^2) A + \alpha_x \left[\frac{m_2 - m_1}{\Delta x} \right]^2 A \quad 2.14$$

It is possible to evaluate the α 's so as to balance smallness and smoothness by equating the two terms:

$$\alpha_s (m_1^2 + m_2^2) A = \alpha_x \left[\frac{m_2 - m_1}{\Delta x} \right]^2 A \quad 2.15$$

Equality is reached when their ratio is unity:

$$\alpha_x = \frac{\alpha_s (m_1^2 + m_2^2) A}{\left[\frac{m_2 - m_1}{\Delta x} \right]^2 A} = \alpha_s (c_x \cdot \Delta x)^2 \quad 2.16$$

where:

$$c_x = \sqrt{\frac{m_1^2 + m_2^2}{(m_2 - m_1)^2}} \quad 2.17$$

The constant factor c_x controls the desired proportionality of the properties of the two cells, subject to all other constraints. For a full 3D mesh, the constant is more complex and is generalised to an arbitrary tuneable model smoothness parameter which can be applied in each direction to also yield:

$$\alpha_y = \alpha_s (c_y \cdot \Delta y)^2 \quad 2.18$$

$$\alpha_z = \alpha_s (c_z \cdot \Delta z)^2 \quad 2.19$$

Rearranging equation 2.16 gives the original form of the length scale definition given in the GRAV3D user manual (UBC–GIF, 2005a):

$$L_x \equiv c_x \cdot \Delta x = \sqrt{\frac{\alpha_x}{\alpha_s}} \quad 2.20$$

Values of 2-5 are usually recommended for c in each of the three directions. The c values are not actually supplied to the inversion algorithm directly, but provide a guide to allow users to decide on appropriate length scales or α coefficients. Although length scales can be supplied to the inversion, they are converted into appropriate α values internally. The crucial aspect of the above analysis is that the balance of smoothness versus smallness is primarily controlled by the square of the cell sizes, so it is critical to adjust the α parameters to suit the size of the cells in the centre of the model. But the concept of length scales also provides an important opportunity to include information about the gross geometry expected within a model as will be discussed in Section 2.6.3.

2.6 SUPPLYING GEOLOGICAL CONSTRAINTS

Without including prior information no inversion method will return a model that is entirely consistent with existing geological knowledge since there are an infinite number of mathematically-feasible but geologically-unlikely physical property models available. However, by limiting the suite of possible models to those that are also consistent with existing geological knowledge, predictions of the subsurface physical property distributions may be possible in areas where no other information is available. The UBC–GIF inversion approach is flexible enough to include a wide range of geological information, if available. The formulation provides for several global mathematical constraints that affect the whole model,

including depth/distance weighting and α coefficients, together with located geological constraints that apply to individual cells in the form of a reference model, smallness and smoothness weights, and model bounds. The reference model supplies the best estimate of the properties in the model and smallness weights are used to indicate the reliability of the estimated reference model properties. Smoothness weights define how smoothly the recovered model properties vary between adjacent cells in each direction. The bounds model indicates the minimum and maximum property allowed within each cell.

2.6.1 Types of geological constraints

In general, the located geological information that can be included as constraints falls into the five types illustrated in Figure 2.2. All five types can provide geometrical and lithological constraints indicating the positions and extents of particular units or types of rocks. Surface samples, maps, and drill holes may supply actual physical property measurements, or geological observations and interpretations from which physical property estimates can be derived, in each model cell. Cross sections and lithological volumes represent 2D and 3D interpretations of subsurface geology which can also be translated into physical property estimates. Broad constraints based on geological principles or concepts can also be included in particular regions of a model. These will typically be used to limit the expected range of properties possible in each region. An example would be where there is weathering at surface, but the thickness of the weathering profile is not known. Based on an understanding of the regolith, drilling, or seismic data, an inference might be made that all rocks below a certain depth (perhaps 100 m) are likely to be unweathered basement rocks and will not have the low densities typical of weathered material. Although the actual geology of the basement may be poorly known, densities $< \sim 2 \text{ g/cm}^3$ are unlikely for unweathered basement rocks, and this can be included as a constraint by applying a narrower range of bounds than the default. In another example, dense carbonate rocks may only be expected in a particular portion of a basin, based on sequence stratigraphic work, and this can be reflected in the inversion by allowing higher densities in that region, even if the exact location and properties of the carbonate rocks are unknown.

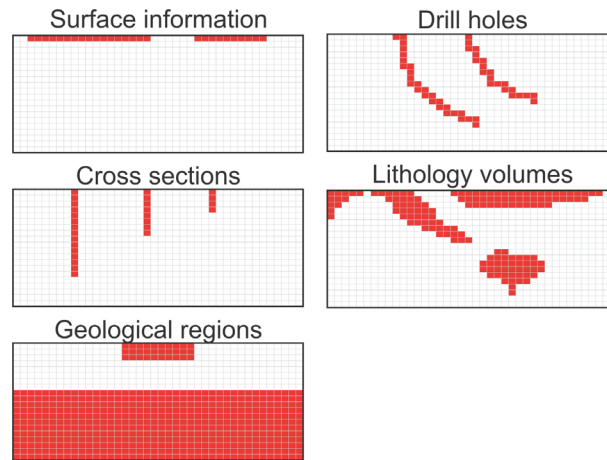


Figure 2.2. Schematic representations of the styles of geological constraints that can be included in a reference model as viewed in a 2D cross section through a 3D mesh. Red cells are those where information is available to assign either property bounds or a reference property, while white cells remain geologically-unconstrained using default values.

One further piece of geological information that may be available in certain settings is an expectation of the gross geometry in different parts of a model. There may be a pervasive strike orientation, or units may be known to be relative flat but expansive features, such as lava flows. This is not considered a located constraint, because it is not applied to a specific cell, but relates to the general form of the model.

2.6.2 Implementing located geological constraints

A reference model, bounds, and w_s , w_x , w_y , and w_z weightings are used in every inversion, but are assigned default values if not explicitly provided by the user. If located geological constraint information is available, it can be used to create detailed non-default reference models, bounds, or weightings. If any one of these is to be supplied, it must be defined for every cell in the model, but appropriate default values can be used in those cells that lack geological information.

The reference model consists of a single physical property value in each cell in the model; default values are a density contrast of 0 t/m³ or magnetic susceptibility of 0 SI. The principle of superposition of potential fields indicates that the observed potential field response associated with any physical property distribution inside a small cell will be the same as that observed if the cell contained a single physical property value equal to the arithmetic mean value. The reference model property in each cell is therefore a best estimate of the arithmetic mean property contained in that cell, and not necessarily the most likely or most common value

(Chapter 5). The reference model property values are used in conjunction with a set of w_s smallness weights, also defined for each cell in the model. These weights indicate a level of confidence in the reference model properties. The w_s values are unit-less; the default is unity, but increased confidence in the reference property estimate for each cell can be indicated with higher values.

Bounds provide a powerful means of enforcing a particular range of properties within a region or unit where the physical properties are known to vary, or are difficult to define exactly. They can be supplied with or without a non-default reference model and are assigned for each cell. If a reference model is not supplied, or default values are used for a particular region within the reference model, then bounds can be supplied to restrict the physical properties in that region to some approximate limits based on known, or expected, geology. Where a reference model is supplied, the reference model might be used to define the expected mean physical property value (perhaps with a low certainty, or w_s value), but the bounds can be used to define the most likely range of values, even if the physical properties are skewed or bimodal. Since the reference property in each cell should be an estimate of the mean property, it is useful to consider the bounds as a confidence interval on that estimate of the mean at a particular confidence level. Confidence intervals on a population mean are usually defined at a $100(1-\alpha)$ % confidence level using:

$$\bar{x} \pm Z_{\alpha/2} \frac{\sigma}{\sqrt{n}}, \quad (n \geq 30) \quad 2.21$$

where \bar{x} is the sample mean, $Z_{\alpha/2}$ is the critical Z value for the confidence level, σ is the sample standard deviation, and n is the number of measurements (Borradaile, 2003; Shi and Golam Kibria, 2007). For a 95 % confidence level ($\alpha = 0.05$) the critical $Z_{\alpha/2}$ value is 1.96. An example of a suitable reference property and bounds for a set of 100 magnetic susceptibility measurements distributed through a single cell is given in Figure 2.3. The true mean property should lie within the specified confidence interval in approximately 95 % of such trials. It is hoped that in the other 5 % of trials, the true mean value will still be close to the specified confidence interval. If this level of accuracy is not acceptable, then a higher confidence level should be used. Where actual property measurements are unavailable this approach indicates that the bounds should be defined as a best estimate of the limits on the range of the mean property, and not the maximum range of possible properties within the cell.

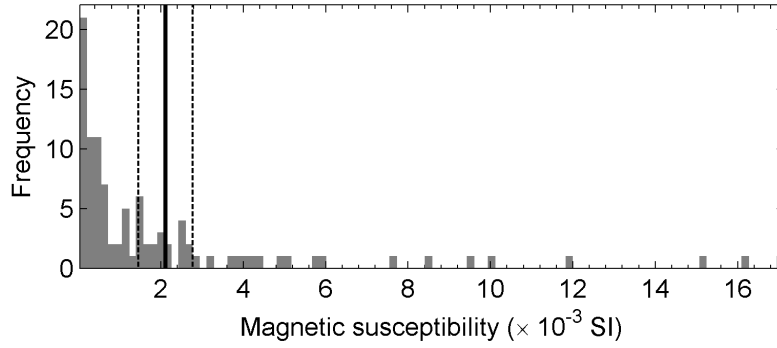


Figure 2.3. Example of determining a reference property and bounds using confidence intervals for 100 magnetic susceptibility measurements distributed within a single model cell and showing a lognormal distribution. The solid line indicates the arithmetic mean susceptibility which is used as the reference property for the cell ($\bar{x} = 2.1 \times 10^{-3}$ SI). The dashed lines are the confidence interval on that mean at a 95 % confidence level calculated using equation 2.21 and the observed standard deviation ($\sigma = 3.4 \times 10^{-3}$ SI). These confidence interval values (1.4×10^{-3} SI and 2.8×10^{-3} SI) are taken as the bounds for the cell. They indicate that in 95 % of trials the desired mean property for the cell should fall between those limits.

The directional smoothness weighting factors, w_x , w_y , and w_z , can be more difficult to apply since they must be defined for each individual cell face (Figure 2.4). The default values are unity. Values < 1 can be used to encourage breaks in smoothness of the model across known faults or lithological boundaries; values > 1 can be used to define regions where geological strike has different orientations on either side of a contact or fault. Their effect is similar to that of α values except on a local scale.

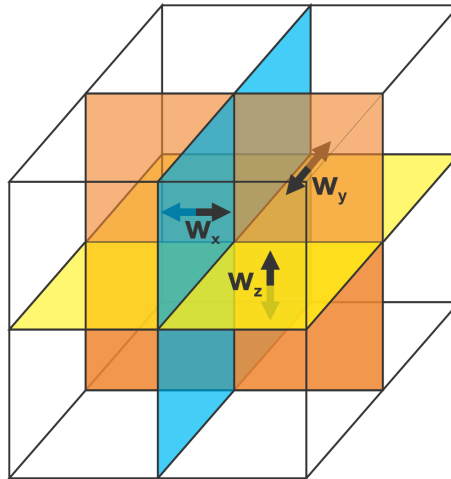


Figure 2.4. 3D view of a $2 \times 2 \times 2$ mesh indicating how the smoothness weight parameters are set. The smoothness weights, w_x (four blue faces), w_y (four orange faces), and w_z (four yellow faces), indicate the smoothness to be assigned to each cell boundary. The reference model properties, bounds, and w_s values are defined for the centers of the cells.

Positions of geological boundaries and contacts can also be recovered in the absence of physical property information by applying breaks in smoothness between cells. Assigning low

values (< 1) to the w_x , w_y , and w_z parameters along the boundary or contact will allow the overall model smoothness to “break” across the boundary as required to fit the geophysical data and any other geological constraints (Figure 2.5). This technique is most effective where the bounding surface completely separates two volumes of rock.

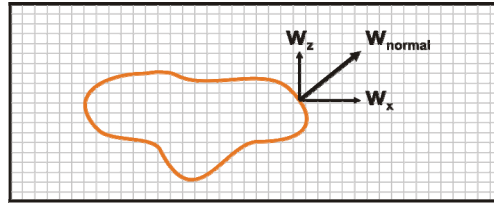


Figure 2.5. 2D slice through a model where the position of a unit is known or inferred, but its properties are too poorly known to include as constraints. The boundary can be encouraged by assigning a low ($0 \leq w_{\text{normal}} \ll 1$) smoothness in the direction of the surface’s normal vector (a default property of any surface in the Gocad modelling package) and separating that into east-west, north-south, and vertical components at each surface vertex (using a trigonometric script within Gocad). These smoothness components can then be “painted” into the appropriate smoothness dual meshes.

Reference properties, bounds, and weights can be assigned using a number of different software packages. The two recommended methods are to use the UBC–GIF GIFtools ModelBuilder (Chapter 5 and Appendix B), or to use Paradigm’s Gocad 3D modelling package with the Mira Geoscience Gocad for Mining suite. Within Gocad, regions are defined based on bounding surfaces, and properties are set for each of those regions or surfaces within a 3D mesh. Sample or drill-hole information can be “painted” into the appropriate intersected cells of the 3D mesh. The mesh can then be translated into appropriate UBC–GIF inversion file formats.

Depth and distance weighting with geological constraints

As discussed in Section 2.3.2, depth or distance weighting is used to ensure all cells are equally likely to contain sources, not just those at shallow levels that are most sensitive to the observed data. Where no geological constraints are available the use of depth or distance weighting provides a tremendous improvement in the quality of the recovered models. However, they should be considered a mathematical constraint that is only useful when no geological constraints are available. Inspection of equation 2.2 reveals that the depth or distance weighting, $w_r(z)$, scales the contribution of the $m - m_{\text{ref}}$ terms in the model objective function. At large distances or depths, $w_r(z)$ is very small (equations 2.3-2.4) and large deviations from the reference model contribute little to the model objective function so can be readily accommodated. Inversions with geological-constraints imposed by a reference model

therefore appear to ignore constraints at depth. The solution is to turn off depth or distance weighting in only those cells where geological constraints exist in the reference model and keep depth or distance weighting as a constraint in the remaining cells. This can be approximately achieved by multiplying the desired w_s , w_x , w_y , and w_z values by the squared inverse of the depth or distance weighting, w_r^{-2} , in those cells that contain geological constraints, and leaving the remaining unconstrained cells unscaled. The scaled weighting values will increase dramatically with increasing depth or distance from the data. This scaling technique is used in the example described in Section 2.7.

Smooth model or smooth model-difference?

The model objective function specified in equation 2.2 smoothes differences between the recovered model and the reference model over a number of cells. Where the reference model is the default zero model, or is constant throughout the model, this recovers smoothly varying physical properties everywhere. However, if the reference model is defined differently in adjacent cells, the model recovered using smooth model-differences can have step discontinuities in the property values (Figure 2.6). In some situations this may be desirable, but for mineral exploration problems the available geological information is commonly restricted to incomplete surface exposure and a limited number of drill holes. Where this is the case, a solution that produces a smooth extrapolation of the assigned reference properties some distance out into the model may be preferred (Figure 2.6).

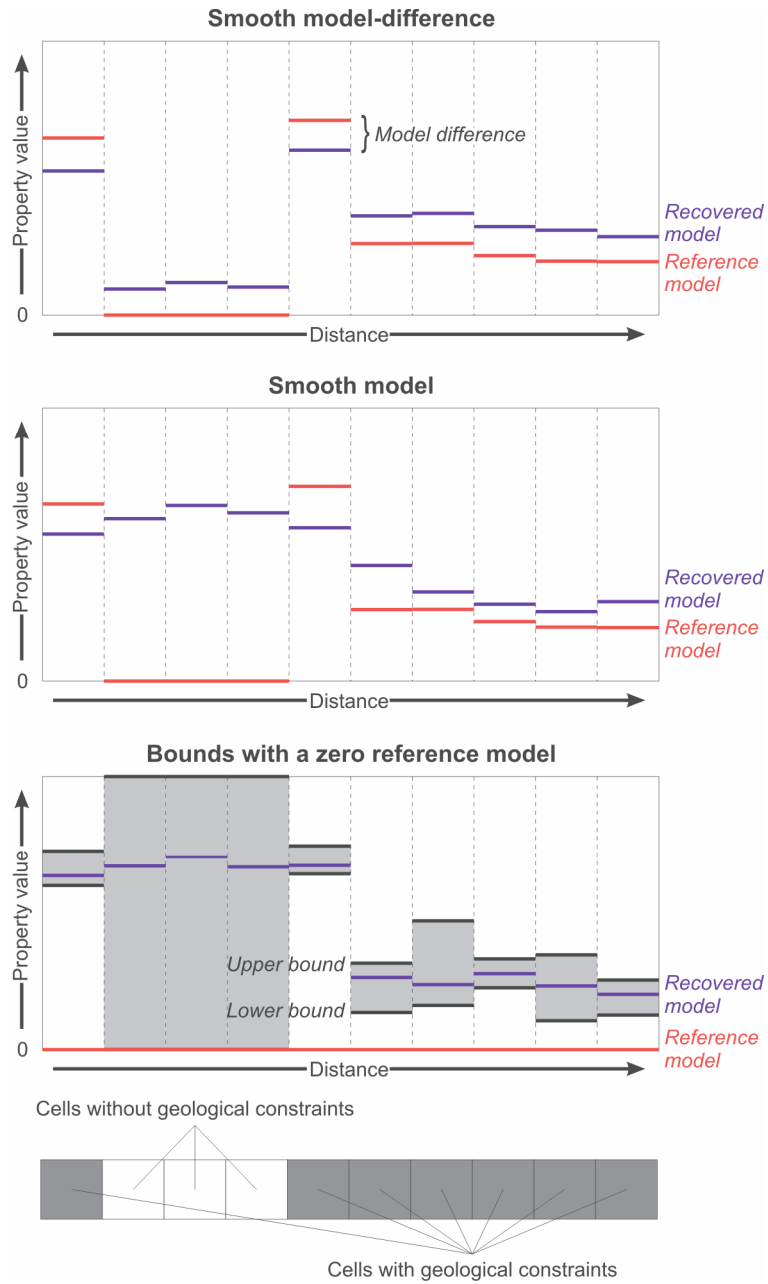


Figure 2.6. Schematic examples demonstrating the character of models obtained using smooth model or smooth model-difference formulations. Ten cells are shown: seven contain observations warranting physical property constraints and three have no information as depicted at the bottom of the figure. Above are three graphs plotting the constraints in the form of either a reference model (red lines) or bounds (grey boxes indicate the property range allowed by the bounds defined in black lines), versus the recovered model (blue lines) that might be recovered using those constraints. In smooth model-difference inversions (equation 2.2), the difference between the reference model and recovered model will vary smoothly between cells which can cause large changes in recovered properties where the reference model changes. Smooth model inversions (equation 2.22) recover a model that is smooth throughout while matching the reference model as closely as possible. By using bounds instead of a non-zero reference model it can be possible to recover a smooth model that also contains sharp property changes where defined.

To encourage this smooth model extrapolation behaviour, newer versions of the inversion software include a user option to select whether to use the “smooth model” or

“smooth model-difference” calculations. In older versions of the programs, smooth model-difference was the only possibility. Selecting the smooth model option modifies the objective function by removing the reference model term from the smoothness components. Equation 2.2 becomes:

$$\begin{aligned}
\phi_m(m) = & \alpha_s \int_V w_s \left[w_r(z)(m - m_{ref}) \right]^2 dV + \dots \\
& \alpha_x \int_V w_x \left[\frac{\partial}{\partial x} (w_r(z)(m)) \right]^2 dV + \dots \\
& \alpha_y \int_V w_y \left[\frac{\partial}{\partial y} (w_r(z)(m)) \right]^2 dV + \dots \\
& \alpha_z \int_V w_z \left[\frac{\partial}{\partial z} (w_r(z)(m)) \right]^2 dV
\end{aligned} \tag{2.22}$$

When a uniform reference model is used, such as the default zero model, the recovered models obtained with these two techniques (equation 2.2 and 2.22) are identical. The results only differ when non-uniform reference models are used. All other aspects of the inversion remain unchanged, and the reference model, w_s weights, and bounds perform the same way. However, the directional w_x , w_y , and w_z weights now control the smoothness of the model between cells, not the smoothness of the model difference between cells. For many applications this is also a more intuitive and easier to define behaviour.

In older versions of the codes that lack this smooth model option, the best way to mimic this smooth model extrapolation of constraints is to use the default zero reference model everywhere with default smallness and smoothness weights and supply the geological constraints using only lower and upper bounds. The bounds can be made very narrow if the property for a particular cell is well known, or wider if the property is less well known, equivalent to using w_s values to assign certainty to a the property. This also allows rigorous assignment of uncertainty in the properties with the use of confidence intervals. In areas where no constraints are available, appropriate wide bounds are used.

A drawback of using the smooth model formulation is that the inversion is less able to recover sharp boundaries in the model. However, where the positions of boundaries are known, they can be readily recovered by defining different bounds ranges on either side of the boundaries, or by enforcing a break in smoothness with the w_x , w_y , and w_z weighting functions. In other situations, the physical properties are not known well enough to enforce bounds so

using a reference model and weightings would provide a better solution. In general, the smooth model-difference approach using a non-zero reference model is ideal for regions where a full 3D geology model exists or one can be constructed. In other regions where the raw geological information (mapping, sampling, drill holes, cross sections, etc.) is all that is available, smooth model inversions are preferable.

2.6.3 Defining gross geometry using aspect ratios

The contributions of smallness and smoothness in each of the three mesh directions are defined by the four α coefficients specified for the whole model. As described in Section 0, these are usually defined using three length scales, again specified for the whole model, which determine appropriate ratios of the four α coefficients relative to the size of the cells being used in each direction (equation 2.20). Disproportionately increasing the length scales in one or two directions by increasing the value of c can bias the smoothness in those directions to recreate an expected gross geometry within the model, such as a favoured strike orientation. A limitation of this approach is that it cannot account for different preferred orientations and gross geometries in different regions within a model. There is also little guidance for how to tune the c parameter.

A better way to implement expectations of the gross overall geometry is to use the notion of aspect ratios, which define the general shape of the expected bodies. For example small spherical bodies would have the default east-north-vertical (x-y-z) aspect ratio of 1:1:1 ($A_x = A_y = A_z = 1$, where A is the aspect ratio in a given direction). Flat lava flows might be associated with aspect ratios of 10:10:1 to indicate properties are likely to be 10 times smoother in the east-west and north-south directions than in the vertical direction. If the underlying basement geology is elongated in the north-south direction relative to the east-west and vertical directions, it might have an aspect ratio of 2:10:1.

Aspect ratios can be implemented by noting that in equation 2.20, the α coefficients actually perform two roles. The first is to ensure that the ratio of smallness to smoothness is appropriate for the size of the cells being used in a particular problem (from equation 2.16). The second applies when disproportionately larger length scales are applied by increasing the value of c to recover a preferred orientation and smoothness within the model. This can be formalised by modifying the definition of length scales to separate the tuneable component

from the cell-size based component. A standard default value of $c = 2$ provides length scales appropriate for the cell sizes being used. Removing this variable from equation 2.20 and introducing the aspect ratio gives:

$$L_x \equiv A_x \cdot 2\Delta x = \sqrt{\frac{A_x^2 \cdot \alpha_x}{\alpha_s}}, \quad A_x = \frac{c_x}{2} \quad 2.23$$

The aspect ratio multiplies all terms and becomes the new tuneable parameter, and is based on geological observations and expectations.

This implementation provides a clearer way to estimate the appropriate length scales based on the expected aspect ratios. It also provides the means to assign different aspect ratios in different parts of a model. In the model objective function (equation 2.2), the three smoothness α coefficients, defined for the whole model, scale the individual smoothness weights for each cell face (w_x , w_y , and w_z), so the aspect ratios can be extracted from the length scales and applied directly within the model by explicitly multiplying the smoothness weights by the appropriate A^2 values in different parts of the model. In this way the aspect ratios are incorporated into the smoothness weights, and the inversion should be run with uniform default lengths of $2 \times$ the cell dimension.

A simple synthetic example is used to demonstrate the benefit of using aspect ratios to overcome a limitation of potential field data: their limited response over homogenous plate-like bodies. The magnetic response over an infinite uniform layer is zero, and the gravity response is just a constant (equivalent to a Bouguer slab). Although such bodies are unlikely to occur naturally, there may be situations that approach this extreme. Blanket cover rocks, such as sedimentary basins, expansive lava flows, or regolith, may have an overall geometry that resembles a plate-like body. At a larger scale, there may be entire supercrustal sequences, such as Archean greenstone belts, that show similar plate-like geometries. There may be significant potential field responses along their margins and associated with internal structure, but if the bodies are extensive enough the observed potential field response may be limited towards the centre of the body. The limited information contained in the potential field response leads to poor resolution of the features in inversions.

The limitation is demonstrated in Figure 2.7. The observed magnetic data (A) over a synthetic 3D model (B), containing four thin flat bodies with an extensive strike length

perpendicular to the cross section, is shown. The standard default magnetic inversion result (C) adequately recovers the narrower bodies (left), but fails to reproduce the more expansive bodies (right) due to the reduced magnetic response over the centres of the bodies (A). One approach to improving the recovered model is to use geological constraints from mapping. By assigning a single surface layer of constraints from mapping using a reference model (G), smallness weights and bounds (not shown), the surface of the bodies is better reproduced (D), but they still show keels extending to depth. An alternate approach is to supply information about the expected gross geometry via aspect ratios. An aspect ratio of 5:10:1 is applied using equation 2.23 to determine appropriate length scales for the model. Even though the supplied aspect ratio is not consistent with all of the bodies, the result (E) is far superior even to the model constrained by mapping. Combining both the mapping constraints and the aspect ratios gives an even better reproduction of the true model (F) by providing observational constraints as well as an understanding of the expected geometry.

2.7 SYNTHETIC GEOLOGICALLY-CONSTRAINED INVERSION EXAMPLE

A synthetic example based on a geological scenario of nickel exploration in Western Australia's Yilgarn Craton is developed in this section to demonstrate the benefits of including even a small number of typical geological constraints in a gravity inversion for mineral exploration. The area has a dipping, north-south-striking granite-greenstone basement, but extensive regolith cover limits basement outcrop. To simplify building the true geology for this example, and to simplify visualisation of the results using cross-sections, the north-south-strike is made perfect (similar to a 2.5D model) but full 3D constraints, data, and inversions are used. The topography is flat.

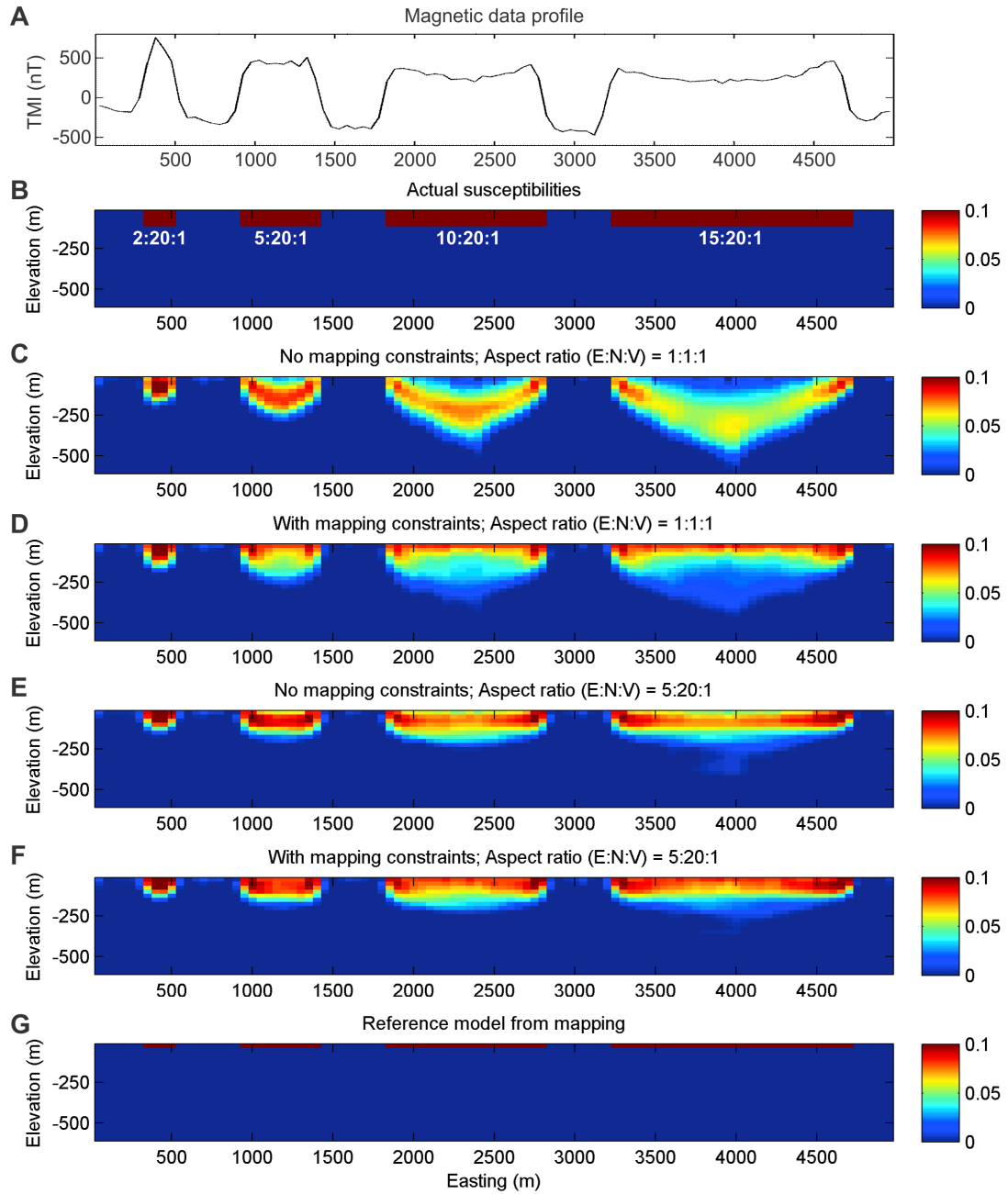


Figure 2.7. Synthetic inversion modelling of plate-like bodies with different aspect ratios. A profile through the observed data is shown in A. All remaining images show vertical slices through the middle of 3D magnetic susceptibility models using the same color scale with units of SI. Cells are $50 \text{ m} \times 50 \text{ m} \times 25 \text{ m}$ throughout so the default length scales are $L_x = 100 \text{ m}$, $L_y = 100 \text{ m}$, $L_z = 50 \text{ m}$. B. True magnetic susceptibility model with four flat bodies. The actual east:north:vertical aspect ratios of each are indicated. C. Recovered susceptibility model using default settings. Note that as the separation between the edges of the bodies increases from left to right, the quality of the recovered model decreases since there is a less data response over the central portion of the plates (A). D. Recovered model using simulated mapping constraints in only the top layer of cells. A reference model (shown in G), smallness weights, and bounds were used. The result is good near the constrained cells, but become less effective with depth. E. Recovered model using no observation constraints, but instead applying an aspect ratio of 5:20:1, equivalent to length scales of $L_x = 500 \text{ m}$, $L_y = 2000 \text{ m}$, $L_z = 50 \text{ m}$, for the whole model. F. Result obtained when using the same mapping constraints (G) in combination with the same 5:20:1 aspect ratio length scales. Combining the mapped lateral extents of the bodies with an inference regarding their shape using aspect ratios gives the best result.

The actual 3D synthetic geology of the area is shown in Figure 2.8. At the start of exploration in this area, the only geological information available to the explorer is from basic surface mapping and some density measurements. A greenstone belt outcrops above the centre of the volume to be modelled. An ultramafic unit with significant massive sulphide Ni-mineralisation is present in this belt, but rocks are deeply weathered on both sides. The explorer wants to delineate the main sulphide body, and hopes to identify whether ultramafic horizons identified to the north and south continue into this area at depth. These may be associated with additional mineralisation. There may also be massive sulphide lenses that have been structurally detached from their original ultramafic host rocks. A uniform cell size of $100\text{ m} \times 100\text{ m} \times 50\text{ m}$ is used throughout the model. All UBC–GIF gravity forward and inverse modelling is performed with respect to density contrasts; for this example the conversion between densities and density contrasts is made by adding or subtracting an inferred background density value of 2.8 t/m^3 . All subsequent descriptions will refer to results and constraints in densities; the necessary conversions to and from density contrasts are implicit. The gravity data for the area was calculated from the true density contrast model on a regular 100 m grid 50 m above ground to replicate upward continued ground gravity data. Such upward continuation is necessary to remove high frequency information that cannot be accommodated by the cell sizes used in the inversion. The data had Gaussian noise with a standard deviation of 0.03 mGal added.

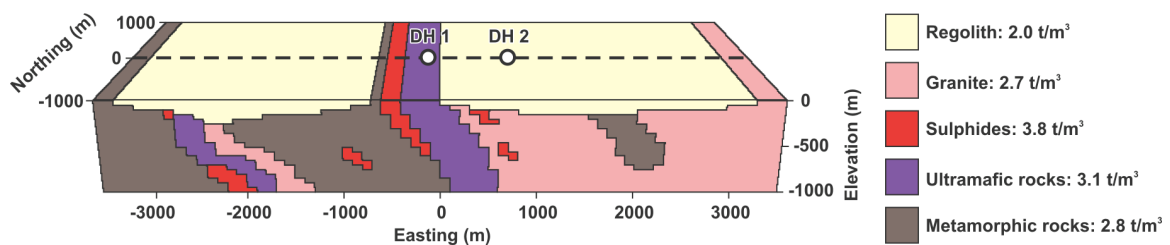


Figure 2.8. Perspective view of the actual synthetic geology model, looking down to the north. The dashed black line shows the position of the cross-sections shown in later figures, and the two white circles indicate the collar locations of two drill holes. The legend indicates the actual densities assigned to each rock unit in the true density model. The UBC–GIF inversion and forward modelling packages expect density contrasts rather than densities; density contrasts are obtained by subtracting a constant 2.8 t/m^3 from all densities prior to modelling.

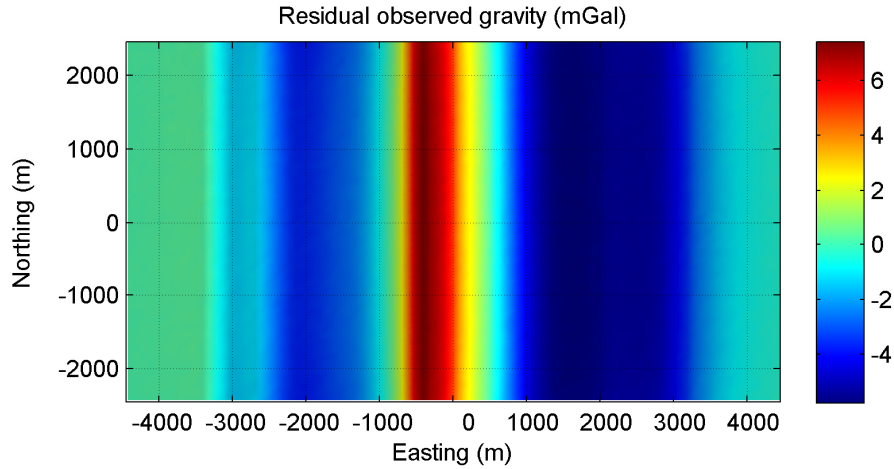


Figure 2.9. Synthetic gravity data calculated from the geology model shown in Figure 2.8. The data covers a larger area to ensure adequate data coverage throughout the desired inversion volume. Gaussian noise with a standard deviation of 0.03 mGal was added everywhere.

Appropriate padding cells were added to the inversion volume. Default distance weighting was used in all inversions. Default length scales of $2\times$ the cell dimension, $L_x = 200$, $L_y = 200$, and $L_z = 100$, are used in all inversions. Unless otherwise indicated, the inversions use a default reference model density contrast of 0 t/m^3 (a density of 2.8 t/m^3), default lower and upper bounds of $\pm 1.5 \text{ t/m}^3$ (densities of $1.3\text{--}4.3 \text{ t/m}^3$), and default w_s , w_x , w_y , and w_z values of 1. All inversions are performed using the smooth model option. In older versions of the codes that only use the smooth model-difference approach, similar results can be obtained by using the default zero reference model and supplying constraints via lower and upper bounds only. All inversions presented below show acceptable data misfits and reproduction of the observed gravity data.

2.7.1 Default, geologically-unconstrained inversion

Using all the default settings outlined above, a geologically-unconstrained inversion was performed. A vertical east-west cross-section through the result is shown in Figure 2.10 alongside the true densities from the geological model. The result is an acceptable first pass reproduction of the real geology. In particular it captures the position and dip, but not the shape and size of the main sulphide body (A). It also has some suggestion of the presence of the central main ultramafic that hosts the main sulphide body, but its extent, properties and dip are poorly defined. An explorer's interest may be drawn to the location and extents of any shallow density anomalies which might provide prospective mineralisation targets. Anomalies at positions B-C do correspond to buried sulphide bodies, but there are several anomalies of

similar size and magnitude that do not correspond to sulphide bodies (D). These are false positive targets: if every target (A-D) was drilled, the exploration program would only have a 50 % success rate in this well-endowed area. Without any knowledge of the subsurface, the most obvious deficiency in this recovered model is the absence of low density zones at surface where well developed regolith profiles are known to exist at surface (E). The extremely large low density features at depth (F) also appear to be geologically unrealistic as does the extreme size and depth extent of the density anomaly associated with the main sulphide body (G). Although the result could be used to plan exploration targets (A-D), it seems unwise given that the result is not consistent with the geological information that is available from mapping, even at shallow levels (E).

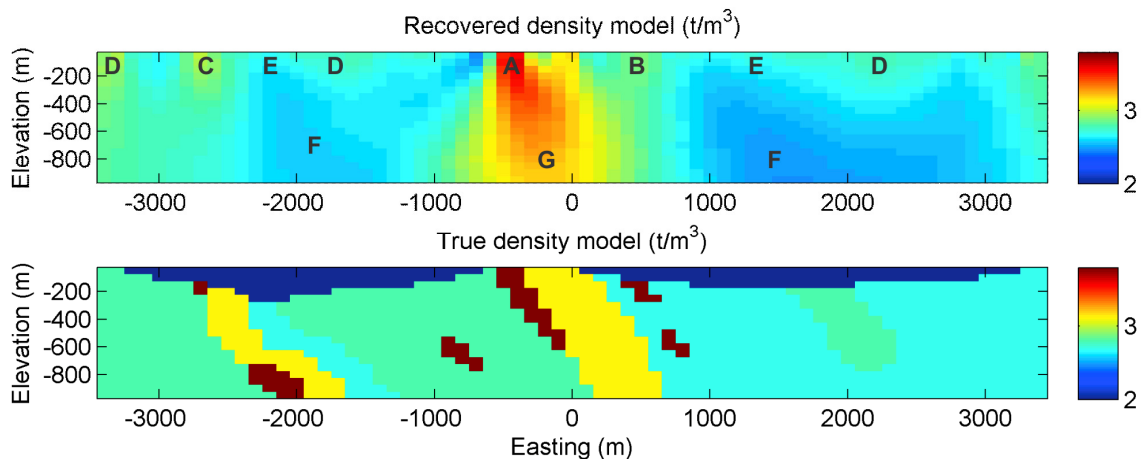


Figure 2.10. A default, geologically unconstrained inversion result compared against the true density model. Cross section is in the position of the dashed line in Figure 2.8. The result does capture some of the key features of the geology. Locations A-D shows possible target anomalies, however the three D locations represent false positive anomalies with no sulphides present. Locations E-G show major discrepancies between the two models. See text for discussion.

2.7.2 Inversion constrained by mapping

The most commonly available source of geological constraint information is mapping. With some measurements or estimates of the physical properties associated with each map unit, the map can be translated into a layer of constraints in surface cells. The reference model properties in the top layer of cells are taken as the mean of available measurements or best estimates of the mean for each geological unit observed in the map (listed in Figure 2.8 and shown Figure 2.11). The lower and upper property bounds in the top layer of cells are assigned to be the reference property $\pm 0.15 \text{ t/m}^3$ based on an estimate of the 95-99 % confidence interval on the mean properties. In addition, two rectangular regions are defined down to 250 m below the lateral extent of mapped regolith. This depth is inferred to be the maximum likely depth of

weathering and the regions identify those cells which may contain low density regolith, or higher density basement rocks. They are assigned lower and upper bounds that reflect either possibility: the lower bound indicates the minimum regolith density of 1.9 t/m^3 and the upper bound indicates the maximum likely density of 4.3 t/m^3 . The remaining cells are most likely to contain basement rocks and are assigned appropriate basement rock bounds: a lower bound of 2.6 t/m^3 and an upper bound of 4.3 t/m^3 . The w_s smallness weights are set to 5 in each of the surface layer cells and the default value of 1 everywhere else. The smoothness weights w_x , w_y , and w_z are not shown, but are set to default values of 1.

The result in Figure 2.11 is a dramatic improvement on the default result obtained in Figure 2.10. The most striking difference is the presence of extensive low density material near surface in those areas where regolith was known to be present (A). Without including any definitive interpretation about the actual depth to basement in the constraints, the inversion has derived a fairly accurate prediction of the depth to basement throughout the model. The inversion has refined the density anomalies associated with sulphides at B-D. It is critical to note that every one of the false positive targets identified in the default inversion result (marked D in Figure 2.10) has been eliminated. Drilling the remaining three targets would result in a 100 % success rate, although those targets are still poorly defined. Including simple map-based constraints has doubled the possible effectiveness of any exploration program in this area. The model also looks more reliable: the unrealistic density high at depth below the main sulphide body (E) has been subdued (but not removed) as have the surrounding deep low density features. The model must be considered entirely plausible without additional geological data.

2.7.3 Inversion constrained with the addition of aspect ratios

An additional piece of information is actually available, in the form of an understanding of the expected geometries in the model. The regolith is a blanket feature across the area. Within any horizontal zone in the regolith profile, the densities might be consistent, but there will be more variation between layers. This suggests a possible east-north-vertical aspect ratio of 2:2:1. In contrast, the basement outcrop suggests that the basement has a strong north-south strike and relatively narrow dipping units. An aspect ratio of 1:5:1 is thought to be appropriate. Since the expected aspect ratios are different in different parts of the model, they are not supplied using length scales as in equation 2.23, but are instead applied directly to the

smoothness weights used within the model by multiplying the default smoothness weights by the squared aspect ratio values in each direction as shown in Figure 2.12. All other constraints remain the same.

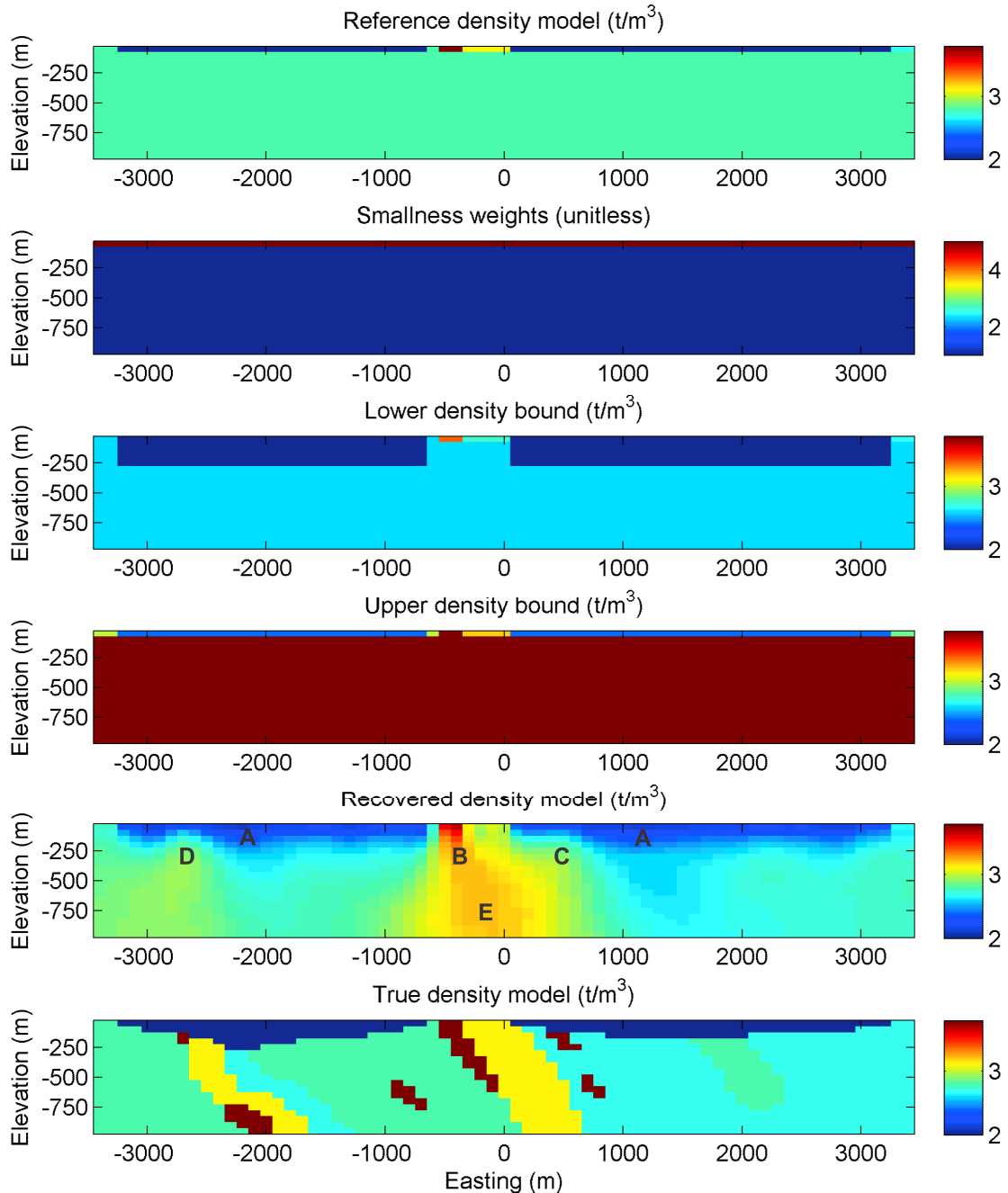


Figure 2.11. An inversion result constrained by outcrop mapping. Non-default reference properties, bounds, and smallness weights are defined in only the top layer of cells based on surface mapping and physical property measurements. In addition, the lower bounds are adjusted to include two subsurface regions to reflect the possible occurrence of regolith below mapped occurrences. All other cells and parameters retain their previously defined values. The recovered model is dramatically improved and looks more realistic due to the reasonably accurate reproduction of the depth the basement (A). Potential targets are still present at locations B-D, however the false positive anomalies (marked D in Figure 2.10) have been eliminated. The feature at E has notably higher densities than the true geology, but cannot be eliminated without additional geological information.

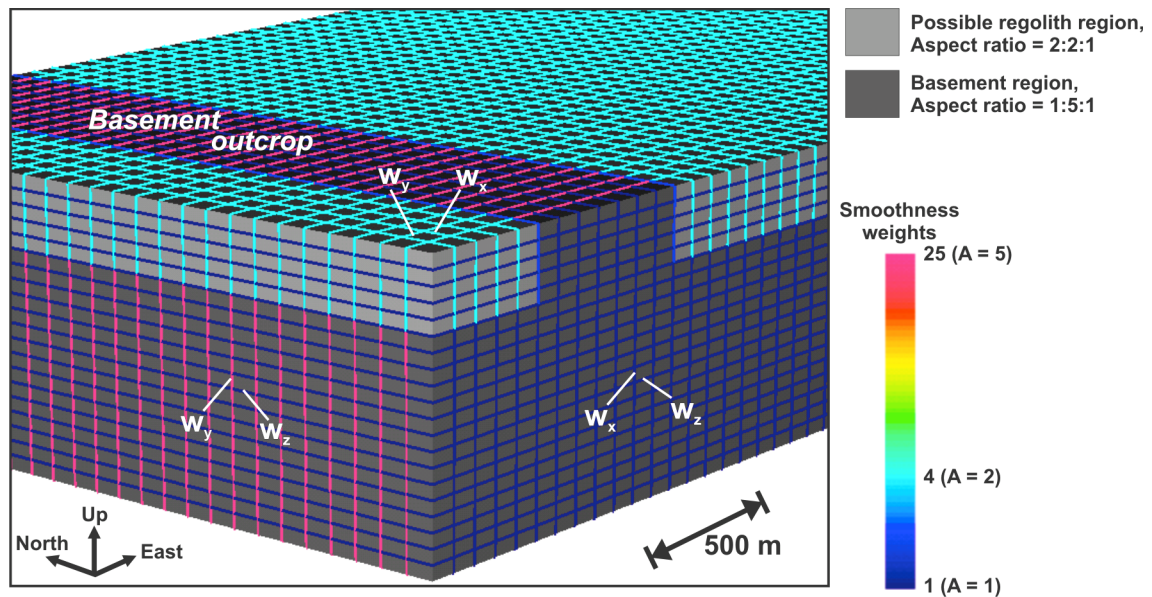


Figure 2.12. Perspective view of assigned smoothness weights set using different aspect ratios in the regolith and basement regions. The smoothness weights are multiplied by the squared aspect ratios in each direction. Each cell is coloured in greys to indicate which region it belongs in. The cell faces are coloured to indicate the values specified for the smoothness weight on each face in the inversions, according to their definitions in Figure 2.4.

The result when including these aspect ratio constraints is shown in Figure 2.13. Although in general only a slight improvement, the two most notable features are the enhanced resolution of the density anomalies at A and B; both are closely associated with massive sulphide mineralisation. Crucially, the strength of the anomaly at B provides the first solid evidence that there is another greenstone package buried below the regolith.

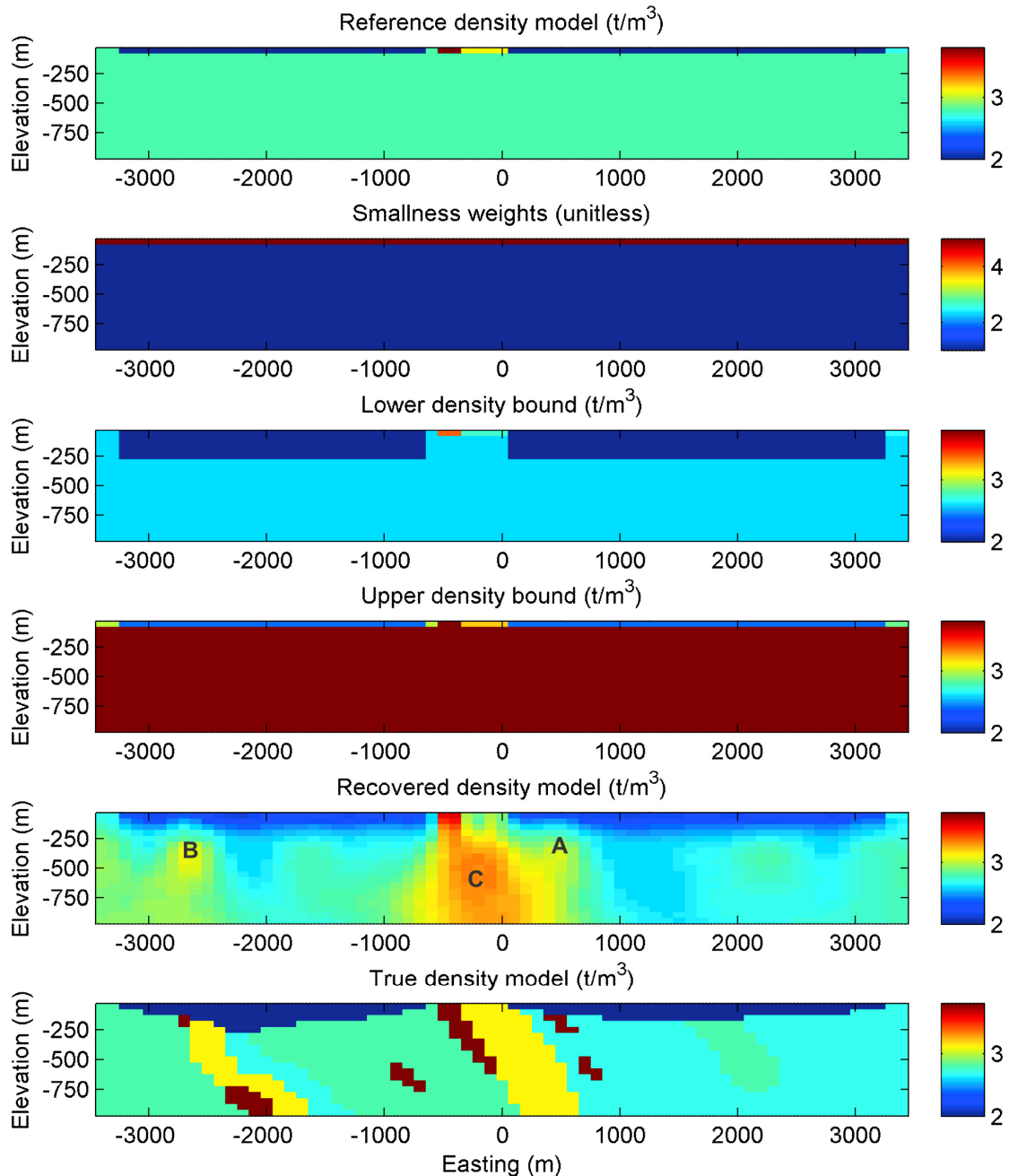


Figure 2.13. The inversion result obtained when inferred aspect ratios indicating the gross geometry in the regolith and basement are included. The improvement is less dramatic than in the previous example, but contains some important improvements. The density anomalies at A and B have been enhanced, and both are closely associated with massive sulphides bodies. Interestingly, the deep dense anomaly at C is stronger in this result – this provides better density estimates for the bottom of the main sulphide zone, but also exacerbates the spurious mass at depth.

2.7.4 Inversion constrained with the addition of 1 drill hole

Heartened by assay results on the outcropping sulphide body and the apparent depth extent of the sulphides inferred from the last inversion result, the explorer proceeds to the drilling stage and drills a single 800-m-long hole in the plane of the cross section to test the

primary density anomaly. Physical properties are measured regularly down the length of the drill core. The mean density in each cell intersected by the drill hole is taken as the reference model value for that cell. For consistency with the mapping constraints in this synthetic example, the bounds in the intersected cells are assigned as the reference density $\pm 0.15 \text{ t/m}^3$. It should be noted that this is a conservative bounds estimate. Equation 2.21 indicates that such a confidence interval would be roughly appropriate for a set of 5-10 measurements with a standard deviation of 0.1 t/m^3 , at a 99.7 % confidence level. More measurements, a lower standard deviation, or a lower confidence level would all significantly tighten the bounds, further improving the result. All intersected cells are assigned a smallness weight of 10 (as they are based on a larger number of density measurements than the mapping constraints), and the w_x , w_y , and w_z smoothness weights are set to 2 on all cell faces that separate constrained cells from unconstrained cells. As discussed in Section 2.6.2 the smallness and smoothness weights are scaled by the squared inverse of the distance weights where geological constraints exist in the map layer and along the trace of the drill hole. This effectively turns off the distance weighting constraint in those cells where more reliable geological information exists. This further modifies the values obtained by applying the aspect ratios to the smoothness weights. All other parameters are set the same as for the previous example. The constraints and result are shown in Figure 2.14. The result is a slight improvement with enhanced resolution of the sulphide anomalies at A-C, and a decrease in the strength of the spurious mass at depth (D).

2.7.5 Inversion constrained with the addition of a second drill hole

To demonstrate the impact of additional drill hole constraints, a second hypothetical 2-km-long hole is drilled to test the maximum depth extent of the main sulphide body. Such long holes may be unrealistic in most exploration programs, but provide the only reliable way to obtain reliable geological inversion constraints at depth. Density measurements are again taken at regular intervals. Constraints are assigned in exactly the same way as for the first drill hole and are shown in Figure 2.15 with the recovered model. The additional hole has significantly improved the resolution of the main ultramafic body at depth (A), and also shows the first signs of density anomalies associated with the deep sulphide bodies at C and D. Since these small bodies are likely to be on the limit of detection with the supplied gravity data, the use of deep constraints is critical in any attempt to target such features.

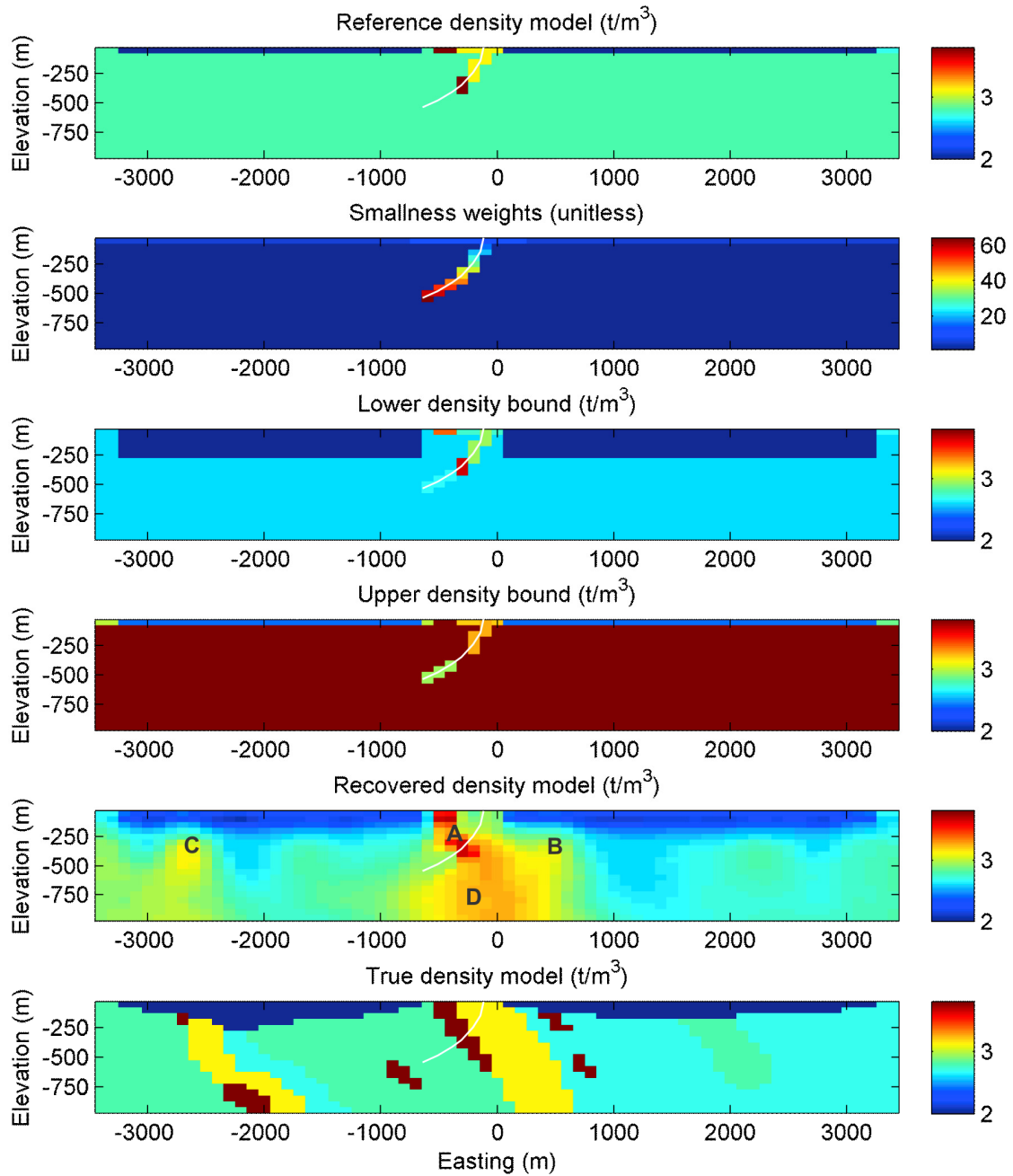


Figure 2.14. The addition of a single drill hole further enhances the recovered model. The drill hole is 800-m-long in the plane of the section and is marked by the white line. All constraints are the same as in the previous iteration, except for the measured physical properties along the drill hole. The smallness weights are increased with depth to effectively turn off distance weighting in those cells. The new constraints have further enhanced the resolution of the sulphide anomalies at A-C and subdued the deep density anomaly at D.

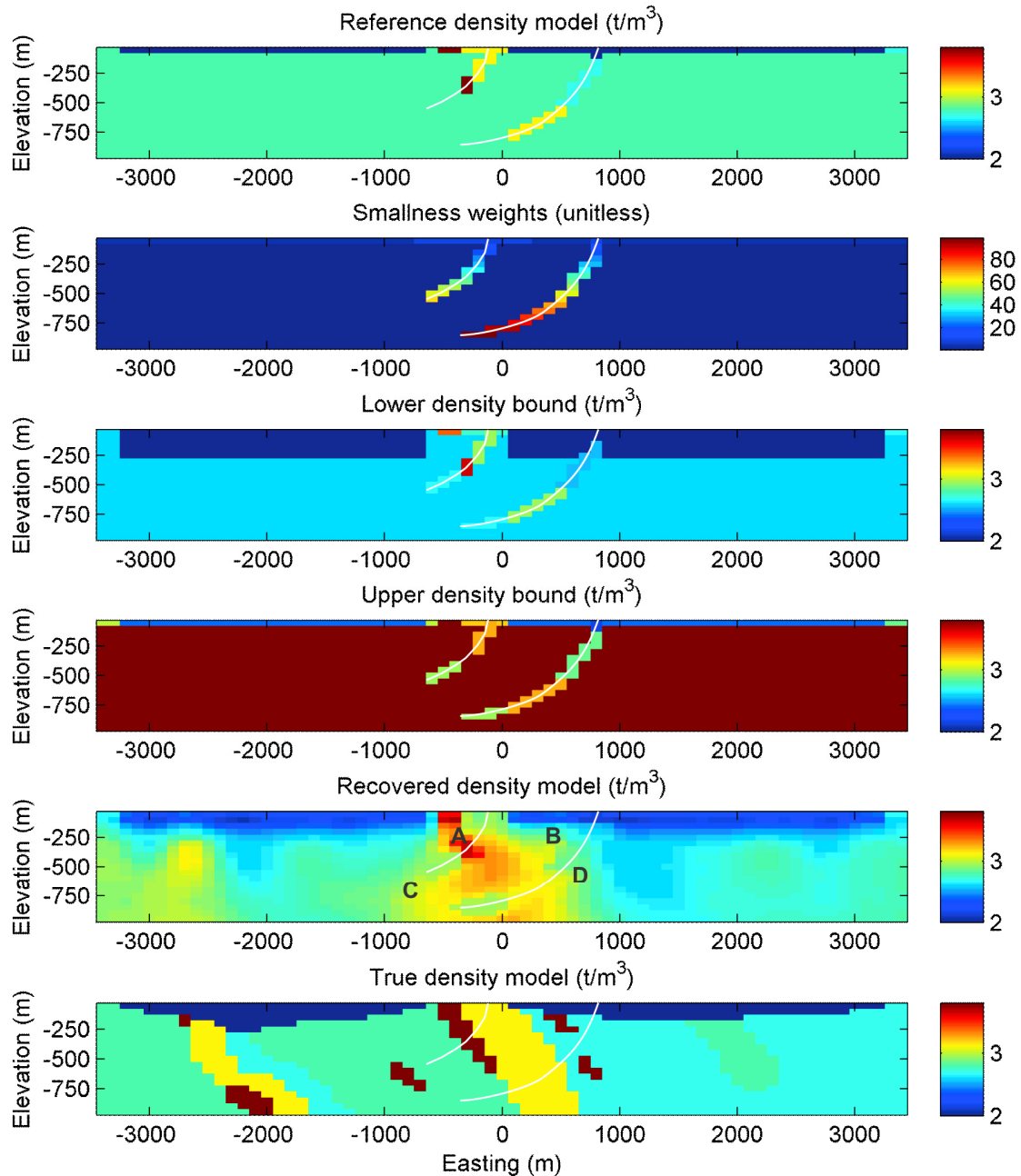


Figure 2.15. The addition of a second deep drill hole further enhances the recovered model. The second drill hole is an unlikely 2-km-long, but is included to indicate the importance of deep drilling as constraints. Anomalies A-B continue to improve. In addition, weak density anomalies are now apparent in association with the deeper sulphide bodies at C and D. The smallness weights along the drill hole traces are again increased with depth using the same scheme, but the color scale is different from in Figure 2.14.

2.7.6 Extrapolation of constraints

Up to this stage all of the example inversions have been constrained by raw geological data and observations and a basic understanding of the gross geometry. No significant geological interpretations have been prepared or included. The importance of such simple data-based constraints is clear from the results. However, in the previous example with two drill

holes and a map, only 5.0 % of the 42,000 cells in the volume of interest contain non-default constraints. The map accounts for 4.9 % of the model and the two drill holes add constraints in just 0.1 % of the model. Geological experience, structural observations, and other evidence will likely suggest that the observations in one model cell may tell us something about adjacent cells in the directions of the observed structural orientations. In measurement-rich environments geostatistical analysis and kriging will provide robust estimates of the physical property values in nearby cells, but in most early exploration programs there is insufficient data for this analysis. Instead, simpler forms of extrapolation must be used. Chapter 5 describes an automated method specifically designed for sparse geological constraints in UBC–GIF inversions. It extrapolates the properties using ellipsoidal buffers defined according to observed structural orientations. All cells within an ellipsoidal buffer surrounding a cell that contains geological observations are assigned that cell's reference property as a best estimate. The smallness weights decrease and the bounds widen towards default values with distance from the observations within the buffer. Where adjacent buffers overlap, a weighted average property is computed based on the squared distance from observations and the smallness weight associated with each constrained cell.

This buffering method has been applied to the same constraints used in the previous example as indicated in Figure 2.16. The orientations and sizes of the buffers are listed in Table 2.1. The only assumptions made in using these buffers are that the observed structural orientations are consistent throughout the buffer zone around each cell, and that properties of different cells within the buffer are roughly related. This could be concluded from *in situ* structural measurements in outcrop and drill core, as well as by correlation of geological units in the drill to those observed at surface. A comparison of the new extrapolated reference model with the actual density model shows an excellent correspondence where constraints are applied. Also note that the bounds widen outwards, and the smallness weights decrease outwards. Only those smallness weights that are based on actual observations along the drill hole traces and maps are scaled with depth. This is a conservative approach that will only strongly enforce the constraints where they are based on actual observations within the cells. The buffers are intended to represent a milder form of constraint than provided by the observations. In this new set of constraints, 14.7 % of cells have some form of constraint imposed, compared to 5.0 % without the buffers. Even though the buffers are only imposed as

mild constraints, they provide significantly more constraints and provide a level of geological intuition regarding the continuity of the observed geology.

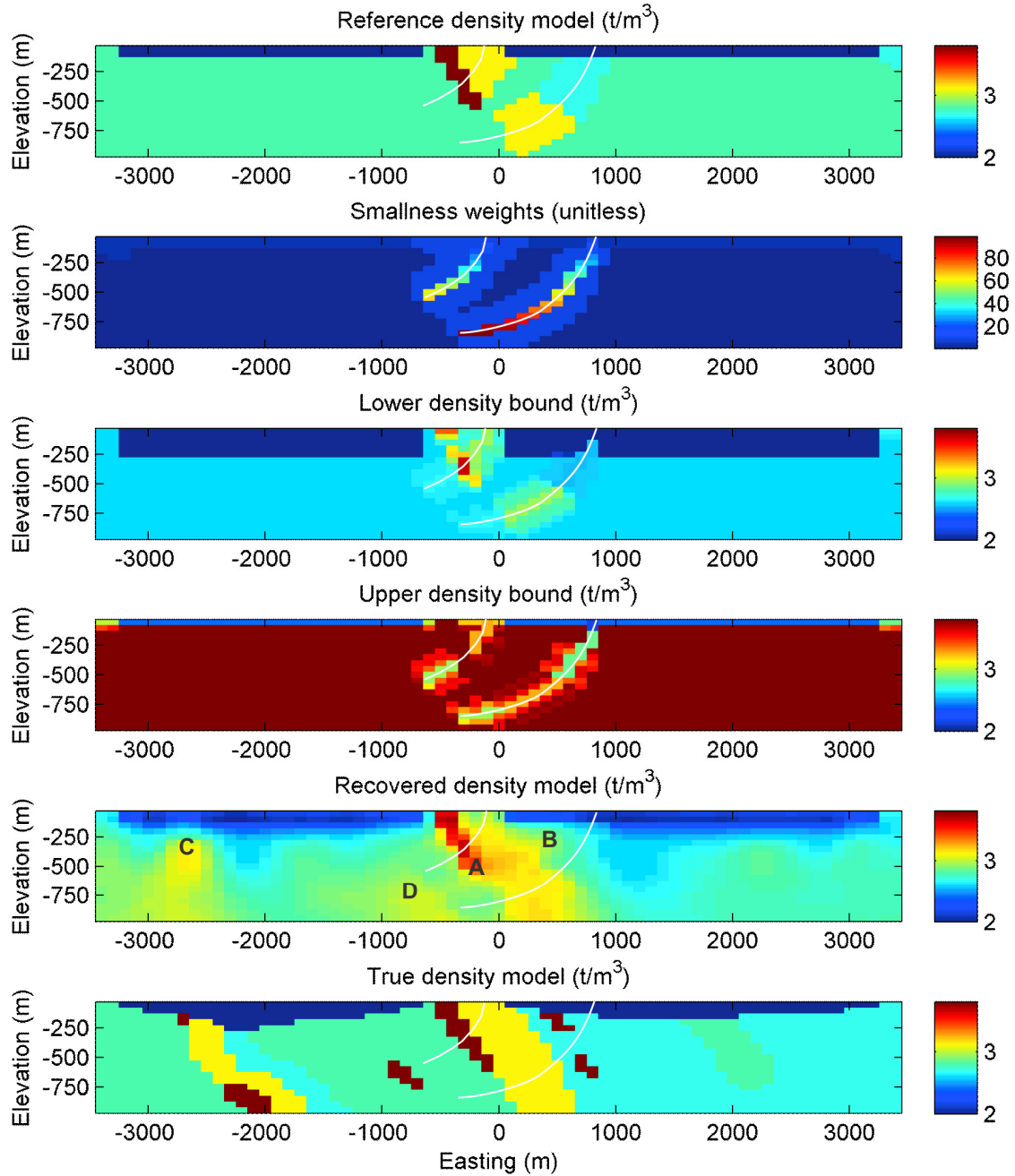


Figure 2.16. This final result uses an orientation-based extrapolation of the same constraints used in the previous example. The geological observations are automatically extrapolated within buffer zones around the observations using the method developed in Chapter 5. The buffers represent ellipsoids defined by the measured or inferred strike and dip in each location as indicated Table 2.1. The strength of the constraints decreases with distance from the observation locations to indicate increasing uncertainty. The resolution of anomaly A continues to improve. Anomalies B-C show little change from previous iterations, but the anomaly at D is enhanced and may provide sufficient evidence of the presence of an additional prospective anomalous mass that existing drilling cannot explain.

Table 2.1. Buffer parameters used to automatically extrapolate constraints prior to inversion. All are based on interpretation of the structural orientation and continuity in each cell.

Buffer parameter	Values for cells in possible regolith regions	Values for cells in basement regions
Strike	0°	0°
Dip	0°	50° E
Pitch	0°	0°
Ellipsoid radius in strike direction	500 m	500 m
Ellipsoid radius in dip direction	100 m	200 m
Ellipsoid radius perpendicular to strike and dip	50 m	100 m

The result in Figure 2.16 is an even more reliable reproduction of the true densities. The anomaly associated with the main sulphide body (A) is almost entirely recovered, albeit with slightly lower densities (3.65 t/m^3 , instead of the true 3.8 t/m^3). The secondary anomalies at B and C show little improvement from previous results, but still provide moderately reliable targets. The resolution of anomaly D at depth is much improved. There is likely sufficient evidence for excess mass accumulations at all three anomalies B-D that cannot be explained given the available geological understanding. These should be considered as quality targets worthy of follow up.

2.7.7 Inversion example summary

A comparison of all the recovered inversion models with the true density model is shown in Figure 2.17. The images are arranged in order of increasing number of constraints, and each is shown with the outlines of the actual geological units for comparison. The similarity between the recovered model and the true model in each case is also quantified using the L_2 norm of model differences and the correlation coefficient between the two in Table 2.2. Although this is a relatively simple synthetic example with relatively large sulphide bodies, there is no doubt that additional constraints improve the reliability of the recovered model. All of the constraints are relatively simple and are based only on the best available geological knowledge at each stage of the exploration program. The most complicated aspects are creating the buffers and applying the inverse distance weighing to turn off distance weighting in geologically-constrained cells, but both of these tasks can be automated (Chapter 5). There was no need for rigorous 3D model building and interpretation to obtain these results; although there is no doubt that inclusion of reliable interpreted 3D geometrical models would add extra detail.

Comparison of the images in Figure 2.17 and the similarity scores in Table 2.2 reveals that a couple of stages proved to be more beneficial than others. The most dramatic improvement is obtained using the simplest of constraints: those determined from surface mapping. Such surface constraints are critical in recovering reliable models as the surface cells have the highest sensitivity to the geophysical data. Small discrepancies between the true densities and the recovered densities in those shallow layers are readily accommodated at depth where the reduced data sensitivity will allow much larger deviations. This is demonstrated by the large low density features at depth in the default recovered model. The numerical measures suggest that introducing aspect ratios actually reduces the quality of the model slightly. Qualitative comparison of the results with and without aspect ratios shows that the resolution of the important small features, such as the buried greenstones rocks at the west end, is improved by use of aspect ratios. The numerical measures are mainly responding to the expanded anomalous mass at depth in the centre of the model. Further investigation reveals that the positive effect of aspect ratios increases with increasing numbers of constraints, and this outweighs the slight deterioration observed when only map constraints are used in this example.

Because only a small number of cells are intersected by individual drill holes, their benefit is generally limited to a small number of cells directly adjacent to the drill holes. The two drill holes combined only provide constraints in 42 out of 42,000 cells so provide very little additional information above that provided by the mapping. As a result, the L_2 norms and correlation coefficients show only marginal improvement. Using buffered extrapolation to increase the number of constrained cells provides a significant increase in the quality of the recovered model and must be considered a useful approach for quickly developing larger numbers of constraints where data are limited, without the need for detailed 3D model building and interpretation.

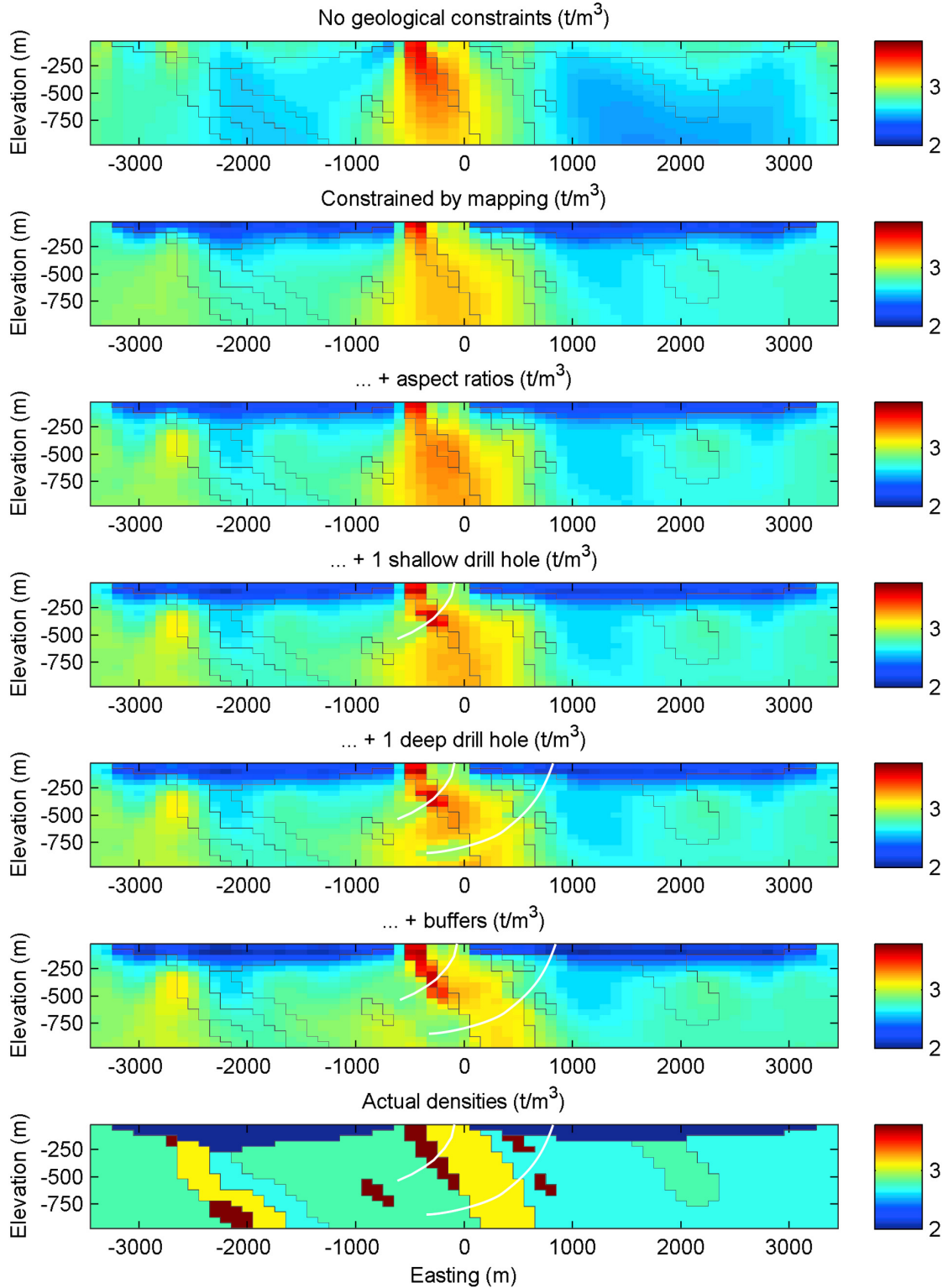


Figure 2.17. A comparison of the actual densities against all six increasingly geologically-constrained inversion results. The biggest improvement is achieved by including constraints from mapping. Aspect ratios help enhance parts of the model without any additional expenditure. Drilling gives excellent constraints in a small number of cells, so the results improve when there are a large number of drill holes, or when buffers are used to extrapolate the constraints based on geological orientations. Even the best results do not recover the extreme density values of the regolith or sulphides. This is due to the inherent smoothing creating larger more subdued anomalies, as well as being a further indication of the non-uniqueness of the inverse solutions even with constraints.

Table 2.2. Quantification of the differences between the various recovered models and the true density model. Decreasing L_2 norms and increasing correlation coefficients indicate better reproduction of the true geology model.

Inversion	L_2 norm	Correlation coefficient
	$\left(\sqrt{\sum_{i=1}^M (m_{true} - m)^2} \right)$	
Default	70.7	0.308
With mapping	51.3	0.689
With aspect ratios	54.2	0.645
With 1 drill hole	53.0	0.667
With 2 drill holes	52.5	0.674
With buffer extrapolation	48.4	0.731

Only one of the three sulphide bodies below 500 m depth is resolved sufficiently well to be considered a target, but that is to be expected given their depth and size relative to the size of the cells in the mesh, and the geophysical data spacing. Even so, comparison of the best inversion result and the true model suggests that there is some indication that the data might require additional anomalous features in the position of the two deep sulphide bodies in the centre of the model. They are on the cusp of the data sensitivity and the combination of these results with additional geophysical techniques, such as down-hole electromagnetic measurements, may confirm these features as legitimate exploration targets.

2.8 REAL GEOLOGICALLY-CONSTRAINED INVERSION EXAMPLE

In Chapter 7 a comprehensive inversion modelling study of the Archean Agnew-Wiluna greenstone belt in Western Australia is presented. The area is richly endowed with gold and nickel, and the study sought to identify some of the stratigraphic and structural controls on mineralisation in the area. The geology consists of a roughly north-south striking greenstone sequence composed of ultramafic, mafic, and felsic rock packages, bounded and surrounded by granitic intrusions. The mafic rocks are mapped well by the gravity data. Geologically-constrained gravity and magnetic inversions were performed at a range of scales to develop new 3D geological models of the subsurface.

To demonstrate the effectiveness of real geological constraints, a district scale inversion result from Chapter 7 is presented here. The model measures 51 km east-west by 84 km north-south with $400 \text{ m} \times 400 \text{ m} \times 200 \text{ m}$ cells. Surface constraints are derived from publicly

available mapping data (GSWA, 2004) with appropriate density estimates based on available measurements. A basic two layer earth model is also included based on nearby seismic reflection data that indicates the greenstone rocks are typically only 6 km thick. Aspect ratios of 2:5:1 are applied throughout the model to recover the observed north south strike. Spherical buffers with a radius of 500 m are used to extrapolate the observed constraints slightly using the method developed in Chapter 5. The reference densities and smallness weights used in the surface layer of cells in the inversion are shown in Figure 2.18. Most of the dark blue cells in the smallness weight model lie beneath regolith, the remainder are associated with lithologies for which there are no reliable physical property measurements. Bounds and smoothness weights were also used to constrain the inversion, but are not shown here.

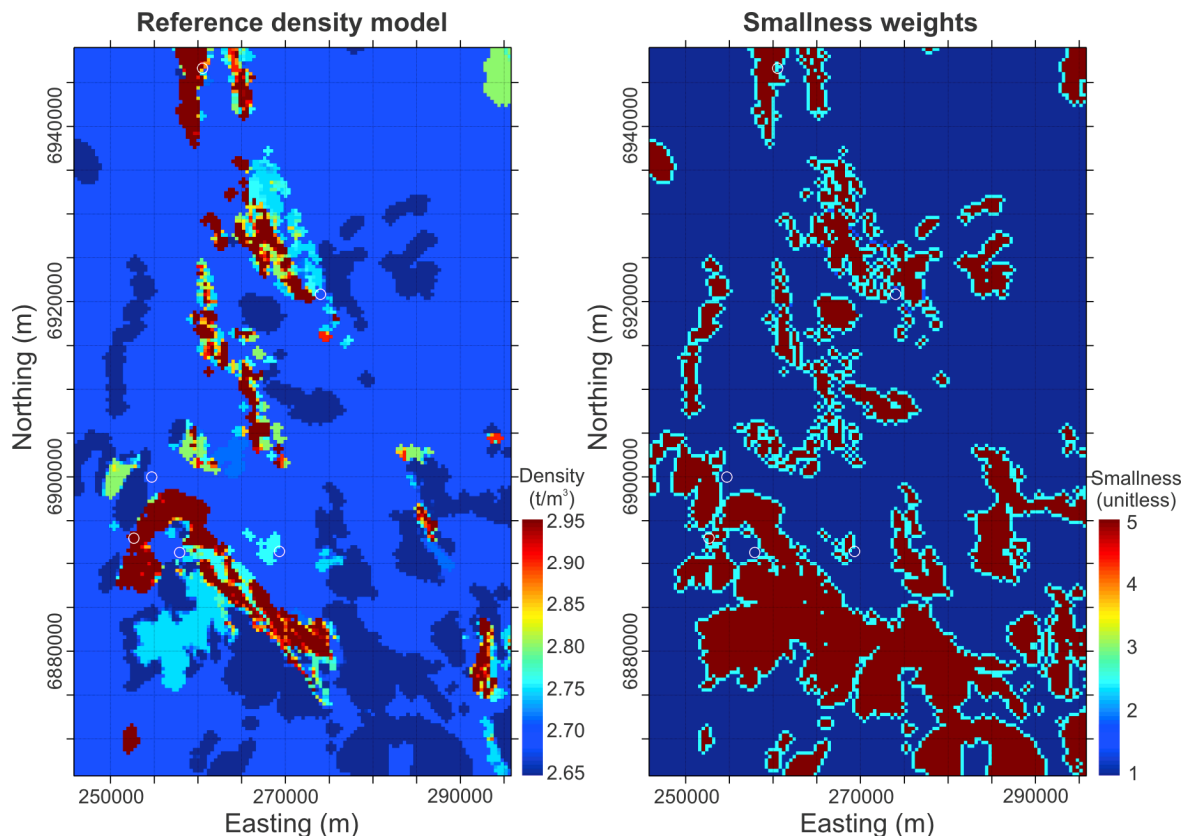


Figure 2.18. The surface layer of the reference density model and smallness weights used to constrain the real gravity inversion example. The constraints are based on surface mapping, a basic layered earth model, and best estimate physical properties. The densities are converted to density contrasts using a background density of 2.70 t/m^3 ; this background value was used as the default reference property where no geological information was available. The smallness weights indicate the relative reliability of the supplied reference model: blue cells are effectively unconstrained (default values); brown cells contain mapped basement outcrops. The cyan cells indicate cells where the properties have been extrapolated outwards using 500-m-radius buffers; these cells are assigned slightly lower smallness weights to reflect their lower reliability. Modified from Chapter 7.

The result of the gravity inversion using these constraints is shown in Figure 2.19 with the equivalent default, unconstrained gravity inversion result. Since the gravity data are

unevenly distributed, and widely spaced in some areas, the default result tends to identify individual, isolated density anomalies scattered throughout the model. Adding constraints from mapping and aspect ratios causes these distinct anomalies to link into coherent bodies, consistent with mapped trends. The layer-based constraints help focus the recovered anomalies into realistic shapes and volumes. The model shows a vertical slice which passes through some of the best outcrop in the district. The default inversion result provides a very poor reproduction of the mapped surface geology, and doesn't reproduce outcropping dense gabbro in the area, a representative sample of which has a measured density of 2.97 t/m^3 . Including the mapping constraints ensures that these outcropping rocks are reproduced in the result and shows that they can only be accommodated if they are relatively thin and underlain by a less dense unit. Comparison of Figure 2.18 and Figure 2.19 also shows that the geologically-constrained inversion results clearly map the dense mafic rocks where they extend beneath regolith. Even though the actual 3D geology is not well known, there is no doubt that the geologically-constrained result provides a more realistic and reliable depiction of the subsurface density distribution than the default result.

2.9 CONCLUSIONS

This paper has reviewed how the UBC-GIF inversion software works and provided some guidance on the careful preparation required for developing inversions and building constraints. A specific capacity of the UBC-GIF inversion approach is its flexibility to include as much or as little geological information as is available using a best estimate reference property model, limiting bounds, and weights for controlling smoothness or roughness. In early phases of exploration, default inversions may be used to locate possible anomalous regions. As more geological data becomes available during exploration, more constraints can be included to further refine the recovered physical property models, and therefore enhance their potential for targeting. Full 3D geological models are clearly a powerful dataset to include if available, but constraints based on the raw geological data can be included without the additional interpretation required to build a full 3D model.

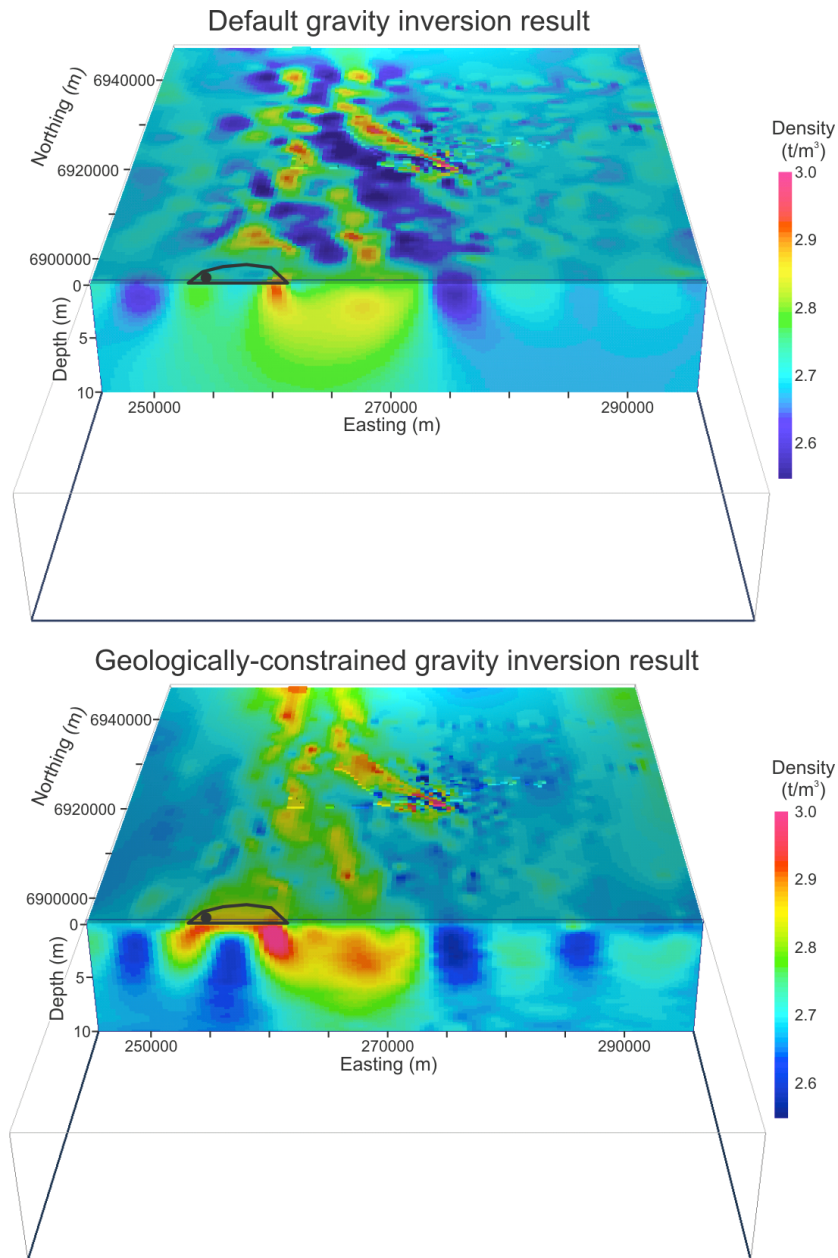


Figure 2.19. Comparison of the improvement gained by including geological constraints in a real gravity inversion. The top model shows the default, geologically unconstrained result. The bottom model shows the result when constraints from mapping, a layered earth model, and aspect ratios are included. Both models explain the observed gravity data equally well, and the same view is shown for both with the same colour scale. Density contrasts have been converted to densities using a background density of 2.7 t/m^3 in both models. The area outlined in black contains outcropping gabbroic rocks; the black circle marks the location of an outcropping gabbro sample collected in this study with a measured density of 2.97 t/m^3 . This unit is not recovered in the default inversion result. Also note that in the geologically-constrained result the anomalies link-up into coherent bodies rather than isolated anomalies.

A synthetic example of inversion using geological constraints in the early stages of an exploration program shows the importance of including surface mapping information, even if that surface information doesn't come from outcropping basement rocks. The input of weathered material, or other overburden, as a constraint is just as important as delineating

basement units due to the low density (and commonly low magnetic susceptibility) of weathered material relative to basement rocks. The addition of deep drill hole data is the only means for deriving reliable geological constraints at depth, provided they are adequately sampled for physical properties. Used in isolation such drilling constraints will locally improve the quality of the recovered model, but by using buffered extrapolation of the constraints based on structural orientations as described in Chapter 5 and demonstrated in this example, individual drill holes can have a much stronger influence on the recovered models. When more comprehensive information is available, full or partial 3D geology or property models, such as those outlined in Section 2.2, provide tight restrictions on the physical properties of a large volume of rock and tightly restrict the range of possible inverse solutions. The value of geological constraints is further emphasised using a real gravity inversion example from Chapter 7. Even with relatively limited constraints derived from surface mapping, a layered earth model and aspect ratios, a much more realistic looking density model is recovered.

Whenever an inversion result is obtained, with or without geological constraints, it must be assessed in the context of the known or expected geology or physical property distribution. If the inversion does not look plausible, the reasons why must be identified. Perhaps the geophysical data was not prepared correctly, or the inversion parameters were not set to appropriate values. Commonly, however, the interpreter will base their assessment on some intangible piece of geological knowledge that should have been included in the inversion as a constraint. Careful use of bounds, reference models, and weightings can allow this information to be included with the more specific located constraints. Together, these constraints help recover not only a more geologically-realistic model, but one that is also more accurate. The key to successful development and refinement of geophysical inverse models is to include all available information and to update the constraints as soon as new information becomes available.

2.10 REFERENCES

- Borradaile, G., 2003, Statistics of earth science data: Their distribution in space, time, and orientation: Berlin, Springer-Verlag, 351 p.
- Boulanger, O., and Chouteau, M., 2001, Constraints in 3D gravity inversion: Geophysical Prospecting, v. 49, p. 265-280.
- Camacho, A.G., Montesinos, F.G., and Vieira, R., 2000, Gravity inversion by means of growing bodies: Geophysics, v. 65, p. 95.
- Cella, F., Fedi, M., Florio, G., Grimaldi, M., and Rapolla, A., 2007, Shallow structure of the Somma–Vesuvius volcano from 3D inversion of gravity data: Journal of Volcanology and Geothermal Research, v. 161, p. 303-317.
- Chasseriau, P., and Chouteau, M., 2003, 3D gravity inversion using a model of parameter covariance: Journal of Applied Geophysics, v. 52, p. 59-74.
- Farquharson, C.G., Ash, M.R., and Miller, H.G., 2008, Geologically constrained gravity inversion for the Voisey's Bay ovoid deposit: The Leading Edge, v. 27, p. 64-69.
- Farquharson, C.G., and Oldenburg, D.W., 2004, A comparison of automatic techniques for estimating the regularization parameter in non-linear inverse problems: Geophysical Journal International, v. 156, p. 411-425.
- Fullagar, P.K., and Pears, G.A., 2007, Towards geologically realistic inversion, *in* Milkereit, B., ed., Proceedings of Exploration 07: Fifth Decennial International Conference on Mineral Exploration, p. 444-460.
- Gallardo-Delgado, L.A., Pérez-Flores, M.A., and Gómez-Treviño, E., 2003, A versatile algorithm for joint 3D inversion of gravity and magnetic data: Geophysics, v. 68, p. 949.
- GSWA, 2004, East Yilgarn DVD: Western Australia 1:100,000 geological information series, Government of Western Australia, Department of Industry and Resources.
- Guillen, A., Courrioux, P., Calcagno, P., Lane, R., Lees, T., and McInerney, P., 2004, Constrained gravity 3D litho-inversion applied to Broken Hill: ASEG 17th Geophysical Conference & Exhibition, Sydney, 15-19 August.
- Li, Y., and Oldenburg, D.W., 1996, 3-D inversion of magnetic data: Geophysics, v. 61, p. 394-408.
- Li, Y., and Oldenburg, D.W., 1998a, 3-D inversion of gravity data: Geophysics, v. 63, p. 109-119.
- Li, Y., and Oldenburg, D.W., 1998b, Separation of regional and residual magnetic field data: Geophysics, v. 63, p. 431-439.

- Oldenburg, D.W., and Pratt, D.A., 2007, Geophysical inversion for mineral exploration: A decade of progress in theory and practice, *in* Milkereit, B., ed., Proceedings of Exploration 07: Fifth Decennial International Conference on Mineral Exploration, p. 61-95.
- Phillips, N.D., 1996, Geophysical inversion in an integrated exploration program: examples from the San Nicolás deposit: Unpub. Masters thesis, University of British Columbia, 237 p.
- Phillips, N.D., and Oldenburg, D.W., 2002, Geophysical inversion in an integrated mineral exploration program: examples from the San Nicolás deposit: SEG Annual Meeting, Salt Lake City, October 6-10.
- Portniaguine, O., and Zhdanov, M.S., 1999, Focusing geophysical inversion images: *Geophysics*, v. 64, p. 874-887.
- Portniaguine, O., and Zhdanov, M.S., 2002, 3-D magnetic inversion with data compression and image focusing: *Geophysics*, v. 67, p. 1532-1541.
- Shi, W., and Golam Kibria, B.M., 2007, On some confidence intervals for estimating the mean of a skewed population: *International Journal of Mathematical Education in Science and Technology*, v. 38, p. 412-421.
- Silva, J.B.C., Medeiros, W.E., and Barbosa, V.C.F., 2001, Potential-field inversion: Choosing the appropriate technique to solve a geologic problem: *Geophysics*, v. 66, p. 511-520.
- UBC–GIF, 2005a, GRAV3D version 3.0: A program library for forward modelling and inversion of gravity data over 3D structures: The University of British Columbia–Geophysical Inversion Facility, 46 p.
- UBC–GIF, 2005b, MAG3D version 4.0: A program library for forward modelling and inversion of magnetic data over 3D structures: The University of British Columbia–Geophysical Inversion Facility, 41 p.
- van Zon, T., Ditmar, P., Chowdhury, K.R., and Mondt, J., 2007, Lithotype discrimination within a gridded model by inverting gravity data: *Geophysical Journal International*, v. 170, p. 481-491.
- van Zon, T., and Roy-Chowdhury, K., 2006, Structural inversion of gravity data using linear programming: *Geophysics*, v. 71, p. J41-J50.
- Welford, J.K., and Hall, J., 2007, Crustal structure of the Newfoundland rifted continental margin from constrained 3-D gravity inversion: *Geophysical Journal International*, v. 171, p. 890-908.
- Williams, N.C., and Dipple, G.M., 2007, Mapping subsurface alteration using gravity and magnetic inversion models, *in* Milkereit, B., ed., Proceedings of Exploration 07: Fifth Decennial International Conference on Mineral Exploration, p. 461-472.
- Williams, N.C., Lane, R., and Lyons, P., 2004, Towards 3D maps of alteration under cover: Regional constrained 3D inversion of potential field data from the Olympic Cu-Au province, South Australia: Preview, p. 30-33.

Chapter 3: A workflow for preparing and applying UBC–GIF gravity and magnetic inversions¹

3.1 INTRODUCTION

The UBC–GIF gravity and magnetic inversion programs, MAG3D and GRAV3D, provide powerful frameworks for recovering models of the subsurface magnetic susceptibilities and density contrasts that explain observed geophysical data. The recovered models will satisfy three criteria:

1. Reproduce the observed geophysical data to within some specified level of uncertainty
2. Reproduce supplied prior geological knowledge as closely as the data allow
3. Satisfy mathematical constraints of smoothness and smallness

In general, such solutions provide models of the subsurface physical properties that explain the geophysical anomalies, without introducing unnecessary detail. Although such smooth and small models may not be ideal for all types of problems, they provide a general solution that is relatively easy to compute, and is flexible enough to accommodate as much or as little prior geological knowledge as is available.

Due to the fundamental non-uniqueness of inversion problems, it is important to remove as many sources of ambiguity as possible. Ambiguity can be introduced at every stage of the inversion process, from defining the problem, the data, the model, appropriate parameters, and available constraints. The workflow outlined here aims to provide a “best practice” procedure for preparing and performing UBC–GIF gravity and magnetic inversions so as to limit the uncertainties that can be introduced during different stages of the inversion problem. It also seeks to facilitate efficient use of inversions by distinguishing those aspects which must be addressed from those that are less important for obtaining the most reliable results. The workflow is based on inversion and potential field theory, and experience in applying inversions to mineral exploration problems at a range of scales. Most of the recommendations will apply equally well to engineering or environmental applications.

¹ A version of this chapter will be submitted for publication. Williams, N.C., Lane, R., Oldenburg, D., Lelièvre, P., Phillips, N., Jones, F., and Shekhtman, R. A workflow for preparing and applying UBC–GIF gravity and magnetic inversions.

Inversion of geophysical data is a highly technical endeavour, and although this workflow is presented for both novice users as well as advanced users, a particular level of background knowledge is assumed. This guide is not a replacement for the GRAV3D and MAG3D user manuals (UBC–GIF, 2005a, b) and it is expected that a user will have read them to understand the basic concepts and terminology associated with the UBC–GIF style of inversion. The original publications on the inversion method (Li and Oldenburg, 1996, 1998a) may also be helpful references. Recovered models are highly dependent on the supplied geophysical data which must satisfy certain criteria. It is expected that the user has access to geophysical processing knowledge and software, or is working in a team that can provide such support. For many applications it will become apparent that geological constraints are required to obtain reliable subsurface models. These constraints can take a variety of forms. Developing some types of constraints will require specialised 3D modelling software and expertise that is beyond the scope of this workflow. Again it is recommended that access to such capability is available.

3.2 INVERSION WORKFLOW CHECKLIST

1. Preliminaries

- ☐ Define the inversion goals and expectations (p. 68)
- ☐ Define volume of interest: area and depth (p. 70)

2. Data

- ☐ Identify sources of data uncertainty (p. 73)
- ☐ Decide if a regional data trend should be removed (p. 78)
- ☐ Extract appropriate topography data: local and regional (p. 87)
- ☐ Extract geophysical data: local and regional (p. 91, 97)
- ☐ Gravity data: apply terrain corrections (p. 92)
- ☐ Apply upward continuation if required (p. 89)
- ☐ Define data levels: subtract mean value (p. 97, 100)
- ☐ Ensure appropriate data uncertainties are specified (p. 94, 99)

3. Meshes

- ☐ Determine appropriate cell sizes (p. 72, 79, 80)
- ☐ Define meshes: local and regional (p. 80)

4. Regional-removal inversions

- ☐ Prepare regional-removal inversions (follow standard inversion procedure) (p. 101)
- ☐ Scoop (zero) out the local padding volume from the regional model
- ☐ Forward model scooped model to local data
- ☐ Subtract scooped regional response from observed data
- ☐ Define data levels: subtract mean value
- ☐ Ensure data uncertainties are specified

5. Standard default inversions

- ☐ Identify input files (p. 105)
- ☐ Define length scales based on cell sizes (p. 106)
- ☐ Choose distance weighting option (or depth weighting if required) (p. 107)
- ☐ Check default bounds values

- ☐ Choose ‘*chifact*’ or ‘GCV’ mode as required (p. 109, 118)
- ☐ Check sensitivity compression settings (p. 110, 121)

6. Evaluating inversion results

- ☐ Did the inversion finish? Check logs and files (p. 111)
- ☐ Did the inversion reproduce the data? Check achieved misfit and normalised data difference (p. 112)
- ☐ Is the model appropriately smooth and small? (p. 114)
- ☐ Check if data levels were appropriate: adjust if required and update data uncertainties (p. 102)

7. Subsequent inversions

- ☐ Adjust data uncertainties (p. 118)
- ☐ Adjust length scales / alpha coefficients (p. 119)
- ☐ Adjust sensitivity compression if necessary (p. 121)

8. Geological constraints

- ☐ Choose approach: hypothesis-testing or data-based (p. 133, 142)
- ☐ Decide on smooth-model difference or smooth model style (p. 129)
- ☐ Build constraints (p. 136, 144)
- ☐ Invert
- ☐ Iterate!

3.3 GETTING STARTED

To get a predicted model that will be useful, the inversion problem must be defined carefully according to stated goals. The problem or question to be addressed must be carefully defined before any decisions can be made regarding the inversion setup. Its definition will mandate certain aspects of the inversion. As preparing, running, and interpreting geophysical inversions can be time consuming, it is also important that expectations are appropriate. Certain features may never be recovered through inversion, due to lack of data, lack of sensitivity to the data, incorrect parameterisation, or invalid assumptions. Much time can be saved by identifying whether the inversion goals are compatible with realistic expectations.

3.3.1 Assumptions and expectations

General assumptions

- Consistent processing and corrections have been applied to the data. Multiple datasets may be combined so long as they have been processed in a similar way, are reported relative to the same datum, and have similar background data levels.
- Noise in the observed data is Gaussian with zero mean and is not spatially correlated.
- The geophysical data can be reproduced with the supplied mesh and topography. This assumption requires that:
 - The resolution of the mesh is consistent with the resolution of the geophysical data. Potential field anomalies with a 10 m wavelength cannot be reproduced by 100-m-wide cells.
 - The data do not contain responses from any sources that lie outside of the supplied mesh volume.

Assumed units

- Gravity data are in milli-Gals (mGal). Densities are in g/cm^3 ($= \text{t/m}^3$).
- Magnetic data are in nano-Teslas (nT). Magnetic susceptibilities are in SI.
- Positions and elevations are in metres. UTM or local coordinates are allowed.

Assumptions for gravity inversions

- The data contain vertical gravity anomalies caused by local density variations only.

- Appropriate data reduction (e.g., latitude, drift, free air and Bouguer slab) has been applied.

Assumptions for magnetic inversions

- The data represent total magnetic intensities.
- The defined incident magnetic field direction and intensity is appropriate for the whole area being considered. This implies that there is a negligible gradient in the field direction and intensity for the whole area and time over which the survey(s) were acquired. If the data has been reduced to the pole then the defined incident magnetic field is vertical.
- If a local coordinate system is used that is not aligned with true north, then the defined incident magnetic field declination must be converted into the local coordinate reference frame.
- Remanent magnetisation is insignificant relative to induced magnetisation.
 - Koenigsberger ratios for the rocks are much less than unity.
- Magnetic susceptibilities are sufficiently low that self-demagnetisation is not significant. Typically this requires susceptibilities $< \sim 0.13$ SI (Clark and Emerson, 1999) throughout the model.
- Anisotropy of magnetic susceptibility is minimal.

General expectations for inversions

- Models will be close to a reference model (possibly zero everywhere) and smooth, according to the parameters set during inversion. Features that are "blocky" in reality will have their edges smoothed in models recovered by inversion. Sharp boundaries are unlikely to be recovered without including geological constraints.
 - Smoothness in recovered models should be interpreted as uncertainty in the positions of contacts, and not an indication that the actual properties are smooth.
- The smoothing that occurs within the inversion tends to create larger bodies with lower magnitude physical properties than might be expected. This may be alleviated by including geological constraints.
- Because of the fundamental non-uniqueness of inversion, and the lack of depth information in potential field data, the recovered model will only be one of an infinite number of models that explain the observed data equally well. A preferred solution can only be

identified after exploring some of the range of acceptable models to develop an understanding of the variability of the results.

Specific expectations for gravity inversions

- The inversion will return a density contrast for each cell. The density contrast may be positive or negative and is relative to some unknown background value.
 - The background value represents some average of the true densities of the rocks within the inversion volume. It is related to the average data level which may be determined by the data processing applied prior to inversion.
- The density contrasts will represent *in situ* densities. These will typically be equivalent to wet bulk densities, or saturated densities, which take into account the composition of the rocks, their porosity, and the composition of any pore fluids or gases.

Specific expectations for magnetic inversions

- The inversion will return a positive magnetic susceptibility for each cell.
- Recovered susceptibilities will represent apparent susceptibilities and won't account for the impact of anisotropy of magnetic susceptibility or self-demagnetisation which can be significant for rocks with susceptibilities $> \sim 0.13$ SI (Clark and Emerson, 1999).

3.3.2 Clarify the problem

Establish the area of interest

- The area of interest will commonly be based on the extent of available data, and especially the extent of detailed or high resolution data. Detailed models will require detailed data, which may place restrictions on the inversion extents. The most critical data sets are:
 - Potential field data
 - The data must capture most of the geophysical anomaly.
 - Data should also extend far enough outside area of interest to establish regional trends. How far depends on the depth of interest.
 - Topography
 - Shuttle Radar Topography Mission (SRTM: <http://www2.jpl.nasa.gov/srtm/>) data is freely available worldwide at a grid spacing of ~ 90 m (3 arc-seconds), so the extent of local topographic data from other sources is only important to consider for

detailed inversions with cell widths < 90 m. In the United States SRTM data is available at a grid spacing of ~ 30 m (1 arc-second).

- Mapping, sampling, drilling, etc.
 - This data provides necessary ground truth or geological constraints which can be used to guide the inversion.
- Other factors that are important for defining the area of interest include:
 - Relevant geology, either known, expected, or hypothesised
 - Likely extent of known units, domains, districts, rock packages
 - Prospective target areas
- It is recommended that if both gravity and magnetic inversions are to be performed, they cover the same area of interest.

Determine the maximum depth of interest

- This will be guided by the questions to be addressed by the inversion. Some options are:
 - Depth of cover/depth to basement
 - Depth of target
 - Depth to an unconformity or rock boundary
 - Maximum depth of existing or future drilling
 - Depth penetration of other geophysical data
 - Depth to magnetic Curie temperature
 - For magnetite, the Curie temperature is ~ 580 °C, so for typical continental geothermal gradients (30 °C/km), a depth of around 20 km below surface might be a reasonable maximum limit for magnetic inversions (and therefore for gravity inversions intended to cover the same area). The depth of the Curie temperature may be deeper or shallower if the crustal heat flow, and therefore the geothermal gradient, is lower or higher, respectively.
 - Thickness of crust
 - Maximum depth of data sensitivity. This can be based on forward modelling of features with similar size and physical properties to those expected in the model at a range of depths. The maximum depth of data sensitivity is the depth at which those features no longer have a significant impact on the observed data or have anomalies that are consistently well below the specified data uncertainty level.

- It is recommended that if both gravity and magnetic inversions are to be performed, they have the same depth extent.

What physical property contrasts are expected and what magnitude should they be?

- This is fundamental to any geophysical survey and should be understood before attempting any inversions. This understanding can be derived from:
 - Compilations of available physical property measurements.
 - 2D or 3D forward modelling which allows testing of the sensitivity of the data to a variety of physical property contrasts at a range of depths.
- Is it reasonable to expect to detect these contrasts given the available data and desired depth of investigation?
 - Again, this can be addressed by synthetic forward modelling of appropriate bodies and appropriate contrasts.

What resolution is required?

The inversion model is defined by a finite number of cells with each assigned a single property value. The maximum resolution of a model is directly related to the size of the cells used, but is also affected by a number of other factors listed below. While the most desirable model may be the one with the most detail and the highest resolution, and thus very small cells, this is not always practical to achieve. The speed and required computing resources of an inversion is related to the number of data and model cells, and increasing the number of cells can dramatically slow down the inversions. If the volume of interest is large, the resolution of the inversion may need to be decreased by increasing the cell sizes to facilitate computation. At present, inversions up to several million cells are tractable on high performance PCs. Factors to consider are:

- Size of the target
 - At shallow levels the smallest features that may be resolved will be > 2 -5 cells across. This minimum size will increase with depth.
- Spacing of geophysical data/observations
 - The maximum resolution will be obtained when there is roughly one geophysical observation per column of cells in the model. Therefore the average data spacing provides a good guide to the width of cells to be used.

- Grain and continuity of geology
 - If the geology is expected to contain many small units with high physical property contrasts, then smaller cells might be required. Larger cells may be sufficient to represent geology consisting of large homogeneous bodies.
- Size of the volume of interest
 - Larger volumes will usually require larger cell sizes to maintain a manageable total number of cells.
- Steepness and height of the topography
 - Steep, rugged, or variable topography requires smaller cell sizes to reproduce it accurately within the model. Larger cell sizes can be used below the lowest point of topography.

Sources of data uncertainty

Although the precision of gravity meters and magnetometers is extremely high, they must measure extremely weak signals. No geophysical data set will be absolutely accurate. If an inversion were to exactly reproduce the supplied geophysical data, it would also exactly reproduce noise in that data. Therefore inversions make allowance for data uncertainty, but the degree of uncertainty must be quantified. Common sources of uncertainty that must be considered include uncertainty in the data itself, but also less tangible uncertainty associated with representing a continuous geophysical response and a continuous physical property distribution with a discrete mesh composed of a finite number of cells using a finite number of observations.

- Potential field data collection uncertainty
 - Instrument accuracy, calibration, and drift
 - External noise
 - Gravity: wind, storms, unstable ground, distant earthquakes, water flow
 - Magnetism: cultural and atmospheric magnetic and electrical fields
- Data correction, levelling, and processing errors or artefacts
 - Gravity:
 - Choice of Bouguer slab and terrain correction densities
 - Inclusion and accuracy of gravity terrain corrections
 - Magnetism:

- Approximation of ambient magnetic field direction and intensity over the entire areal extent of the data
- Location accuracy
 - Measurement uncertainty (GPS versus surveyed locations)
 - Accuracy when converting between different geographic projections
 - Incorrect elevation reference frames (geoid versus ellipsoid)
- If using data from a grid, then inaccuracies introduced by gridding, smoothing, warping, drape, and interpolation must be considered
- Errors due to discretisation of the model
 - Observed data reflects continuous earth, whereas forward modelled data from inversion represents a blocky earth (regardless of cell sizes)
 - Larger cells will be less capable of reproducing a continuous earth, and may therefore may be associated with larger uncertainties
- Incorrect removal of regional data trends
- Uncertainties in physical property measurements and geological uncertainty using constraints in the inversion

3.3.3 Basic components of an inversion setup

All inversions will use the following components. Preparation of each of these will be discussed in the following sections.

Geophysical data

- The geophysical observations are the primary control on the inversion. The inversion will seek a model that can explain the supplied data.

Mesh

- A 3D mesh defines the physical distribution of cells within the model to be recovered. It specifies the number of cells, their lateral and vertical extents, their sizes, and their position.

Topography data

- Topography data defines the position of the earth's surface which separates air cells from ground cells. The inversion will only recover properties for cells that lie below the topographic surface.
- Although optional, most inversions of real data should include topographic data to avoid recovering properties in cells that lie above ground, or ignoring possible anomalies inside topographic highs. Gravity data is critically sensitive to even small topography changes of < 1 m.

Inversion control files

- Two text input files must be defined to identify relevant input files, and to control how the inversion seeks a solution. Usually these files will be created automatically by the GRAV3D or MAG3D graphical user interface (GUI), but advanced users can edit the files manually to gain enhanced control of the inversion.

Sensitivity matrix

- A large component of any inversion process is calculating the relationship, or sensitivity, between each observation and every cell within the mesh. Even for moderate sized problems this can be a large calculation.
 - For example, a $50 \times 50 \times 50$ cell mesh with 1000 observations will have 125 million cell to observation point pairs and could require up to 0.47 GB of computer RAM to store.
 - Compression is applied to the matrix to reduce its size to allow manageable computation, but this can also result in a loss of information.
- Once calculated for a particular combination of mesh and geophysical data, the sensitivity matrix can be reused for any inversion using that combination, so it is saved as an output file with an '.mtx' filename extension.

Recovered physical property model

- This is the physical property model recovered by the inversion for the specified data, mesh, and assigned parameters. For gravity inversions the result will be a model of density

contrasts relative to some unknown background density. For magnetic inversions the result will be a model of magnetic susceptibilities.

3.3.4 Advanced components of an inversion setup

The following components will only be modified in specialised or advanced inversion problems. Most relate to including geological constraints into the inversion. Constraints are used to recover a physical property model that explains the observed geophysical data and is also consistent with available geological knowledge. Such inversions will be more reliable representations of the subsurface physical property distributions.

Reference property model

- A reference model of physical properties can be supplied to indicate the best available estimate of the average physical property in each cell. The inversion will seek a physical property model that is as close as possible to this reference model while satisfying other inversion parameters and explaining the geophysical data. The reference model used by default in gravity inversions has a density contrast of 0 g/cm^3 . In magnetic inversions it has a value of 0 SI.

Weighting models

- This single file contains several sets of weights that are used to control the importance of different aspects of the recovered model. Its format is described in detail in the GRAV3D and MAG3D manuals (UBC–GIF, 2005a, b). Briefly, it contains weights controlling how closely the supplied reference property model should be matched by the recovered model, and how smoothly the recovered properties should vary across the face of each cell.

Property bounds model

- Default inversions allow a relatively wide range of properties to be recovered in each cell. If particular knowledge is available regarding the possible range of properties in particular cells or areas, this can provide a very powerful constraint on the inversion. Restriction of the properties allowed in each cell can be incorporated via a property bounds file. These bounds are inviolate, and the recovered model will always lie within the specified upper and lower bounds.

Initial model

- This defines a starting physical property model for the inversions and all values must fall between any specified bounds. Its sole purpose is to speed up some inversions where the desired recovered model is expected to be similar to the specified initial model. It has negligible affect on the properties recovered.

3.4 DEFINING THE MESH

All UBC–GIF inversion models are defined on a right rectangular prism mesh consisting of right rectangular prism cells. Ideally a continuous earth should be represented by infinitesimally small cells in the model so that the details of the discretisation do not influence the result. Such computation is not practical and larger cells are required. The use of larger cells to represent a continuous earth may affect the inversion result so care must be taken to define an appropriate mesh for the problem being addressed.

- Cells within the mesh can have different sizes and aspect ratios. Each column, row, or tube of cells will share at least two dimensions with the same width throughout. A decision must be made whether all cells in the mesh will have the same size and aspect ratios, or whether different sizes and aspect ratios will be used in different areas.
 - Using different cell sizes in different areas of the mesh, for instance using larger cells in padding zones, can reduce the number of cells and make the inversion run faster and use less memory without sacrificing detail in the areas of interest. The nature of potential fields results in less resolution with increasing depth, so larger cells can be used at depth without sacrificing resolution.
 - Uniform cell sizes are favoured where practical because they ensure that the mathematical measures of smoothness and smallness, which are defined relative to cell size, are consistent throughout the model.
 - Manipulating meshes with non-uniform cell sizes can be more difficult than for uniform meshes. In the Gocad (Paradigm) 3D modelling package, meshes with uniform cell sizes can be stored as Voxets or SGrids allowing more computational flexibility. Variable cell sizes can only be accommodated by Gocad SGrids.
- The areal extent and the depth of the mesh will be based on issues previously raised in Section 3.3.2.

- The top of the mesh should be just above the highest topographic point. Cells that lie above topography will be assigned a large negative value to indicate they are in the air.
 - Geophysical observations can extend above the top of the mesh.
- There are two recommended methods for designing a mesh, and each is explained in a separate section:
 - The default method implemented within the UBC-GIF inversion and utility software. This will be acceptable for most problems where there are no anomalies near the edge of the supplied geophysical data, and there are no data contributions from sources outside the mesh.
 - A more rigorous method designed to ensure no erroneous features are introduced near the edge of the model where anomalies are incompletely captured at the edges of the supplied data. This is a more conservative style of mesh that will typically cover a larger area and contain more cells than the default but may give a more reliable result.

3.4.1 Local versus regional meshes

Simple, small, isolated anomalies can be modelled directly within a single mesh. However, most potential field data will be complicated by multiple sources at multiple depths, and may have contributions from below or outside the volume of interest defined by the local mesh. It is necessary to remove those external, or regional, contributions to satisfy the assumption that the data can be reproduced by the supplied mesh (Section 3.3.1). If inversion results are deemed to provide an appropriate representation of the subsurface physical property distribution, then it would be reasonable to use inversion to calculate the regional contribution as described by Li and Oldenburg (1998b). Their method, which is based on a local mesh nested within a larger regional mesh, is favoured because it ensures that the calculated regional contribution is consistent with the physical property distribution calculated by the inversion. It is outlined in Section 3.5.4.

Local mesh

- The local mesh will be defined for the desired volume of interest for the problem to be addressed, as described above.

Regional mesh

- The regional mesh must be large enough to include all possible sources for the observed geophysical data. As a result, it will cover a much larger area than the local mesh and extend to greater depth.

3.4.2 Default mesh design

This is a simple, automatically-defined mesh that will accommodate datasets that don't have anomalies near their edges. It is particularly useful for synthetic examples and forward modelling tests. Most of the procedure outlined in this document is specifically based on using the more rigorous mesh design (Section 3.4.3); however it applies just as well for the default mesh design.

- The default mesh can be created from a UBC–GIF gravity data file in the GRAV3D or MAG3D GUI; it requires only three user inputs: 1) the data file, 2) a user-defined cell width in the middle of the mesh, and 3) a user-defined elevation for the top of the mesh. An example is shown in Figure 3.1. The resulting mesh will:
 - Cover the area of input data
 - Have a central main mesh volume with the same areal extent as the supplied data and cells that have widths equal to their lengths, and heights equal to half their widths.
 - Have an additional 3 padding cells on each side of the data area
 - First padding cell will be the same width as the cells in the middle of the data area.
 - Second padding cell will be double width of the first padding cell.
 - Third padding will be double the width of the second padding cell.
 - Have a depth based on the areal extent of the data
 - Depth of the mesh will be equal to the maximum dimension of the data area.
 - Have two zones of padding cells below the main mesh volume
 - The main portion of mesh will have a thickness of one quarter the maximum dimension of the data area with cells that have a height equal to half their width.
 - The first padding zone will have a thickness of one quarter the maximum dimension of the data area with cells that have a height equal to their width.
 - The bottom padding zone will have a thickness of one half the maximum dimension of the data area and will be three cells high.
- Defining the elevation of the top of the mesh

- If topography data is supplied:
 - The top of the mesh must lie just above the highest point in the topography file.
 - Every data point must lie above the topography, but may lie above or below the top of the mesh.
 - Any cell that is within the mesh, but above topography will be marked with a large negative value in the output model file.
- If topography data is not supplied
 - Every data point must lie above the top of the mesh which is assumed to represent the ground surface.
- This mesh design can be applied to create either regional or local meshes separately. There is no explicit link between the extents of the two meshes.

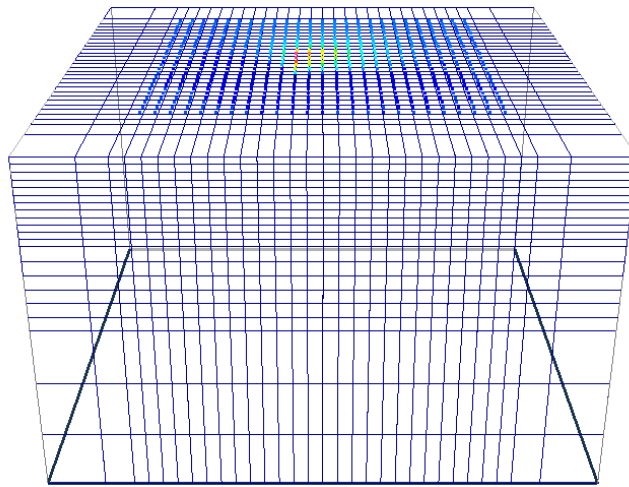


Figure 3.1. Perspective view of a default mesh created from a supplied data file. Note the increasing cells sizes in padding zones surrounding the supplied data, and also at depth where resolution decreases.

3.4.3 Rigorous mesh design

The more rigorous mesh design suggested here is appropriate where there is some unknown regional contribution to the observed data and the data includes anomalies near the edges of the mesh that are not of direct interest but cannot be removed or filtered out of the data. Such anomalies might be attributed to through-going structures or geological units that provide the architecture of the general model but are not the specific target for modelling, or are only of interest in a particular portion of the model. The rigorous mesh layout explicitly links the extents of the regional and local meshes to create a full system of meshes and extents for a given problem (Figure 3.2) and provides an easy set of relationships for calculating the extents of the various data and mesh components (Table 3.1).

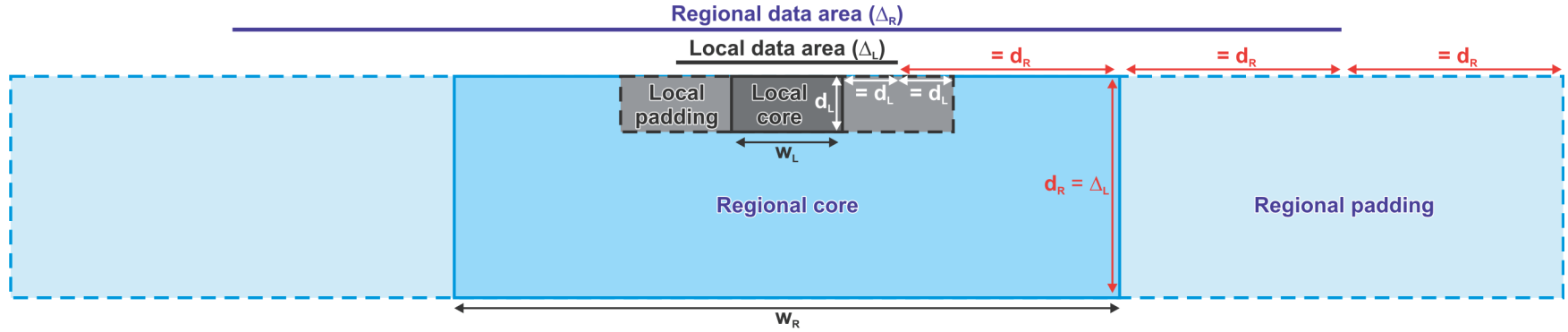


Figure 3.2. Cross section view of the layout of the rigorous mesh design including local and regional meshes and padding. The image is drawn to scale. The width (w_L) and depth (d_L) of the local core defines the width of the local data (Δ_L) and the extent of the local padding. Likewise the width (w_R) and depth (d_R) of the regional core defines the width of the regional data (Δ_R), and the regional padding. One suggestion for the depth of the regional core is the width of the local data area (Δ_L) as shown. The regional meshes are used to determine the regional data contribution to the local data.

Table 3.1. Summary guide for defining the appropriate coordinates for the data and padding zones using the rigorous mesh design. The coordinates can be defined starting with the local core extent or the local data extent (shaded), depending on which is appropriate for a particular problem. x_{SW} = easting for starting southwest corner; y_{SW} = northing for starting southwest corner; x_{NE} = easting for starting northeast corner; y_{NE} = northing for starting northeast corner; z_{top} = elevation of the top of the local core; z_{bot} = elevation of the bottom of the local core; d_L = depth of the local core; d_R = depth of the regional core.

	Local core		Local data		Local padding		Regional core		Regional data		Regional padding	
Starting with the local core volume												
Easting	x_{SW}	x_{NE}	x _{SW} − d _L	x _{NE} + d _L	x _{SW} − 2d _L	x _{NE} + 2d _L	x _{SW} − d _L − d _R	x _{NE} + d _L + d _R	x _{SW} − d _L − 2d _R	x _{NE} + d _L + 2d _R	x _{SW} − d _L − 3d _R	x _{NE} + d _L + 3d _R
Northing	y_{SW}	y_{NE}	y _{SW} − d _L	y _{NE} + d _L	y _{SW} − 2d _L	y _{NE} + 2d _L	y _{SW} − d _L − d _R	y _{NE} + d _L + d _R	y _{SW} − d _L − 2d _R	y _{NE} + d _L + 2d _R	y _{SW} − d _L − 3d _R	y _{NE} + d _L + 3d _R
Elevation	z_{top}	z_{bot}	−	−	z _{top}	z _{bot} [*]	z _{top}	z _{top} − d _R	−	−	z _{top}	z _{top} − d _R
Starting with the local data area												
Easting	x _{SW} + d _L	x _{NE} − d _L	x_{SW}	x_{NE}	x _{SW} − d _L	x _{NE} + d _L	x _{SW} − d _R	x _{NE} + d _R	x _{SW} − 2d _R	x _{NE} + 2d _R	x _{SW} − 3d _R	x _{NE} + 3d _R
Northing	y _{SW} + d _L	y _{NE} − d _L	y_{SW}	y_{NE}	y _{SW} − d _L	y _{NE} + d _L	y _{SW} − d _R	y _{NE} + d _R	y _{SW} − 2d _R	y _{NE} + 2d _R	y _{SW} − 3d _R	y _{NE} + 3d _R
Elevation	z_{top}	z_{bot}	−	−	z _{top}	z _{bot} [*]	z _{top}	z _{top} − d _R	−	−	z _{top}	z _{top} − d _R

* Note that these depths for the local padding assume that a regional field has been (or will be) removed from the data. If this is not the case the depth of the local padding may need to be considerably deeper than for the local core. See discussion for ‘Regional core’.

The method is heavily based on standard depth estimates for spherical bodies, in particular the half-width method for estimating depths (Telford et al., 1990; Goussev and Peirce, 2000). Such estimates are appropriate because, in the absence of other information, the source features recovered using a smooth and small style of inversion will commonly be roughly spherical. These estimates provide a means of determining the approximate wavelengths that can be attributed to sources at particular depths and so provide a useful rule-of-thumb for defining how much padding is required to avoid any edge effects caused by truncating the data or the model.

- For an isolated gravity anomaly attributable to a spherical source, the half-width method states that the depth to the gravity center of mass is 1.3 times half the horizontal distance across the anomaly peak at the level of half the maximum amplitude.
- For an isolated magnetic anomaly attributable to a spherical source the depth to the centre of the magnetic body is 2.0 times half the horizontal distance across the anomaly peak at the level of half the maximum amplitude.

Local core: the main volume of interest

- This volume will be the only volume to contain reliable information after the inversion; all other volumes and pads should be removed when the inversion is complete as they are only required to avoid edge effects.
- Define the areal extent, depth and cell sizes for the local core based directly on the definition of the problem to be addressed (Section 3.3.2).
 - The cell widths should be comparable with the data spacing – preferably use the worst observation spacing in the area to determine the cell size. It is advisable to have roughly one data point per column of cells; this may require decimating the data where data observations are densely spaced.
 - If processing time permits, use equal cell sizes.
 - At shallow levels try a cell height/width ratio of 0.5, and if the number of cells is large increase the ratio to 1.0 at depth.
 - If a reliable regional response has been (or will be) removed from the data then the depth of the core can be based on the geological problem to be addressed. If no regional response has been removed then the maximum depth should be at least half the width of

the longest side, and more likely equal to the width of the longest side, to account for the longest wavelengths possibly captured in the supplied data.

- Alternately, the local core can be defined by the extent of high resolution geophysical data to be used in the inversion using the relationships identified in Table 3.1 and described below.

Local data

This is the extent of the data used in the inversion. Since observations just outside the edge of the core will contain information about source features within the local core, the data should extend some distance beyond the core. The width of extra data required is determined from the depth of the local core (d_L) by the half-width method as demonstrated for a gravity example in Figure 3.3.

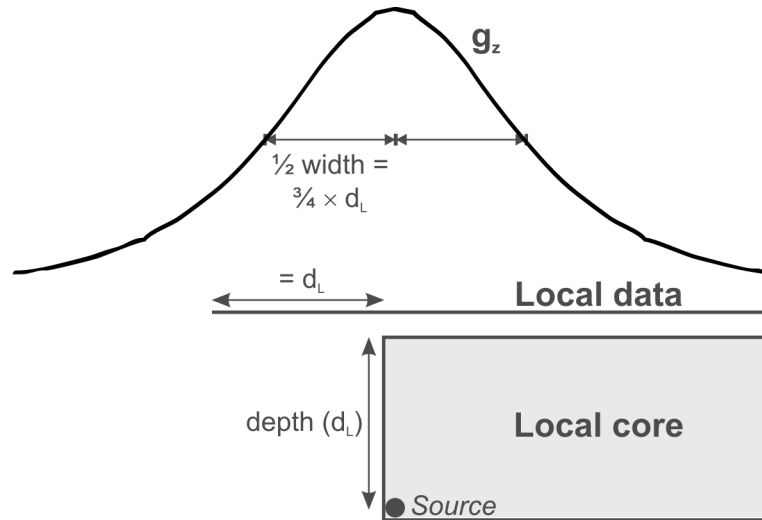


Figure 3.3. Schematic, but accurately scaled example cross section showing the necessary data extent to accurately reproduce a source at depth within the local core. The source in the bottom corner of the local core has a gravity anomaly profile, g_z , as shown. The wavelength of the anomaly can be determined using the half-width method and this indicates the extent of data required to capture the full anomaly. For gravity data, the half-width of the anomaly is expected to be $\frac{3}{4}$ of the depth to the source. It is recommended that the data extend past the edge of the local core by a distance equal to the depth of the core volume.

- For gravity: half-width of peak at half amplitude = depth/1.3
 - Anomalies from sources within the core may extend to $1/1.3 \approx \frac{3}{4}$ the depth of the core ($\sim 0.75d_L$) beyond the edge of the core.
- For magnetics: half-width of peak at half amplitude = depth/2.0
 - Anomalies from sources within the core may extend to $\frac{1}{2}$ the depth of the core ($\sim 0.5d_L$) beyond the edge of the core.

- If the desired local core has a width w_L and a depth d_L , then the appropriate total width of the local data area, Δ_L , would be:

$$\Delta_L = w_L + 2\beta d_L \quad 3.1$$

with $\beta > 1/2$ for magnetic data or $\beta > 3/4$ for gravity data. A value of $\beta = 1$ is recommended for both data types giving a local data width of:

$$\Delta_L = w_L + 2d_L \quad 3.2$$

This provides a conservative and easy to calculate data extent. The appropriate coordinates for the edges of the data area are indicated in Table 3.1.

Local padding

Although the data extent is designed to capture all the information available for sources within the local core, it may also contain information from sources outside the core. For the inversion to adequately reproduce the supplied data it must be able to account for these features within the mesh. This requires the addition of padding cells. These padding cells will be included in the inversion but should be removed from the resulting models as they may not contain reliable property distributions. It is expected that the physical property distribution recovered within the padding cells will approach zero along the lateral margins. The width of padding required can again be determined using the half-width method as for the data extent above.

- The half-width depth estimate implies that data at the edge of the supplied data extent may contain information from sources up to a width d_L (depth of the local core) beyond the supplied data in each direction.
- The total width of the local padded mesh can be defined in terms of the core volume extent:

$$\text{local padding width} = w_L + 4d_L \quad 3.3$$

or the supplied data extent:

$$\text{local padding width} = \Delta_L + 2d_L \quad 3.4$$

- The appropriate coordinates of the margins of the padding can therefore be determined from the coordinates of the local core or the local data as indicated in Table 3.1.
- If a reliable regional response accounting for sources below the local core has been (or will be) removed, then the depth of the padding is the same as the depth of the core (d_L).

Otherwise the depth of the padding must be greater than the core depth to allow for long wavelength sources that cannot be accommodated inside the core.

- In this situation the depth of the local padding should be equivalent to the depth of the regional core that would be required. See discussion for ‘Regional core’ below.
- For large problems it may be necessary to increase the cell sizes used in the padding zones to speed processing. This is best done gradually by having concentric rings of cells with double the widths of the cells inside.
 - In the padding cells directly below the local data, try using double the dimension of the cells in a local core.
 - In the padding cells beyond the local data, try using double the dimension of the cells under the data (quadruple the dimension of the cells in the core).

Regional core

If using regional inversions to define the regional data contribution to the observed data, then a regional inversion mesh must be defined. This is equivalent to the local mesh but on a larger scale. The goal is to create a reasonable approximation of the actual physical property distribution surrounding the local meshes from which to calculate the regional contribution to local data. The regional core contains the main reliable portion of the regional model just as for the local core. The primary differences between them will be their lateral extents, depths, and cell sizes.

- The regional core must be deep enough to allow adequate representation of the longest wavelengths in the observed local data. Several options are available. To speed processing, choose the smallest option for a given problem.
 - Regional core depth (d_R) = width of local data (Δ_L)
 - The longest wavelength that can be captured by the local data has a peak wavelength equal to the width of the local data. It therefore has a half-width at half the peak amplitude equal to half the width of the local data. Longer wavelengths cannot be attributed to a discrete spherical source within the mesh and will instead be represented by gradients in the physical property distribution.
 - The half-width depth estimate indicates that a gravity anomaly with this half-width would have a spherical source depth estimate of:

$$\text{depth} = 1.3 \cdot \frac{1}{2} \cdot \Delta_L = 0.65 \Delta_L \quad 3.5$$

- A similar magnetic anomaly would have a spherical source depth estimate of:

$$\text{depth} = 2 \cdot \frac{1}{2} \cdot \Delta_L = \Delta_L \quad 3.6$$

- To capture the spherical source of such an anomaly a reasonable minimum depth for the regional core would therefore be Δ_L , as shown in Figure 3.2.
- Regional core depth (d_R) = depth to a layered earth
 - If there is a reasonable geological expectation that the crust can be approximated by layers with uniform properties below some depth, then there is no need to model below that depth as the potential field response of each layer will only contribute a uniform constant everywhere.
- Regional core depth (d_R) = Curie depth
 - Below the Curie depth (at which the temperature is $\geq 580^\circ\text{C}$) magnetite becomes paramagnetic and contributes no significant anomaly. A standard continental crust geothermal gradient of $\sim 30^\circ\text{C}/\text{km}$ suggests a typical Curie depth of ~ 20 km, but in cooler cratons it can be as deep as 60 km (Frost and Shive, 1986).
- Regional core depth (d_R) = crust thickness
 - There is no point attempting to model the mantle: processing time is prohibitive, it is geologically unreasonable to do so, and gravity data is processed to remove the whole earth contribution anyway.
- The regional core must be wide enough so that sources just beyond the edges of the regional core do not influence the local data. A spherical source just outside the bottom of the regional of the regional core will have a wavelength half-width roughly equal to its depth. Therefore as shown, in Figure 3.2, the regional core should have a width, w_R , related to the width of the local core (w_L) by:

$$w_R = w_L + 2d_R \quad 3.7$$

to ensure that the anomaly is not contained in the local data. This gives coordinates relative to the local core and local data as specified in Table 3.1.

- Since the RV covers a much larger area than the LV, much larger cells must be used to facilitate processing in reasonable times. The detail of the recovered potential field

distribution is not critical, only that the data is reproduced accurately and that sources are approximately in the correct position.

- Regional inversion cell sizes 2-5 times the local inversion cell sizes are good. Try 4×

Regional data

- The width of data required is defined based on the width (w_R) and depth (d_R) of the regional core in exactly the same way as for the local data:

$$\Delta_R = w_R + 2d_R \quad 3.8$$

This gives coordinates relative to the local core and local data as specified in Table 3.1.

Regional padding

- This is defined based on the width (w_R) and depth (d_R) of the regional core in exactly the same way as for the local data:

$$\text{regional padding width} = w_R + 4d_R \quad 3.9$$

- It can be defined in term of the local data by:

$$\text{regional padding width} = \Delta_L + 6d_R \quad 3.10$$

This gives coordinates relative to the local core and local data as specified in Table 3.1.

- If necessary, the cell size in these padding cells can be increased to speed up processing. Follow the guidelines as for the local padding, above.

3.5 DATA PREPARATION

3.5.1 Topography data

- Any topography data needs to be converted into appropriate UTM or local coordinates relative to the appropriate height datum. This must be the same datum as used for the potential field data locations.
- When combining data from multiple data sources remove duplicate data points. Warnings are provided if there are multiple data points.
- Large detailed topography datasets can be very large files. They can be down-resampled to reduce the file size, but ensure that there are >1-3 topography points above each column of cells.

- Gridded topography data is generally not recommended, especially for gravity inversions which rely on highly accurate and reliable topography values.

Data sources

- Shuttle Radar Topography Mission (SRTM)
 - This is an excellent worldwide dataset providing a ~90 m (3 arc-second) grid of topography points that can be freely downloaded from <http://seamless.usgs.gov/> by defining the desired area of interest and selecting a file format. The data is provided in WGS84 geocentric coordinates relative to the EGM96 geoid, and can be downloaded in the following formats: ArcGrid, BIL, GridFloat, and Geotiff. Further details, including accuracy estimates, can be obtained from Farr et al. (2005).
- Government geological surveys' websites commonly have freely available topography data downloads.
- Local data associated with other geophysical surveys
 - If ground gravity data will be used, then the positions of the gravity stations should also be included in the topography data file, to ensure that the topography is represented as accurately as possible near the gravity stations.

Data extent

- Topography data must cover the full extent of the local padding mesh. If performing a regional-removal inversion then topography data must be available for the full extent of the regional padding mesh.

3.5.2 Gridding and upward continuation

Original observations or gridded data?

Ideally, potential field inversions should be performed using potential field data at the original observation locations rather than an imposed regular grid of interpolated data. The observed data points provide the highest amount of detail about the subsurface without introducing any non-geological information. However, data will often only be provided as a grid, without access to the original observations.

- Problems with gridded data:

- Gridding can create data in regions where there are no observations. These interpolated data can be quite incorrect. Artefacts are particularly numerous and problematic where the distance between observations is greater than the distance between grid points.
- The values assigned to these interpolated points will be highly dependent on the gridding algorithm used.
- Due to aliasing, gridded data may contain longer wavelengths than are actually present. These will tend to increase the depth of features within the recovered model.
- If using previously gridded data, it is important to ensure that the grid spacing is appropriate for the mesh cell sizes being used. Data should never be re-gridded at different grid spacings as this will seriously degrade the reliability of the data locations and values.

Upward continuation

In practice, a critical problem with using potential field data acquired in ground surveys or at low altitudes is that these data may record the effect of small, shallow, short-wavelength features too small to be accurately reproduced by the size of the cells used in the model. Since these features cannot be reproduced by the inversion, they contribute unnecessary errors to the data misfit. This in turn can bias the result and introduce noise into the recovered model that is manifested as spurious large high frequency property variations.

- These artefacts can be prevented by upward continuing the observed data to a height of 0.5-1 times the width of the mesh cells in the center of the model. This removes short wavelengths too small to be accommodated by the chosen cell size.
 - There is currently no reliable method for upward continuing scattered data. Upward continuation, performed in the frequency domain, must be done on gridded data.
- Inversions using ground data will commonly report that observations lie below topography. This occurs because of the discretisation of topography imposed by the mesh cells is an approximation of the true ground surface and may sometimes lie above ground data observation locations. The only ways to alleviate this problem are to:
 - Decrease the mesh cell sizes for near surface layers to produce a better representation of topography.
 - Increase the apparent height of the observations by upward continuing the observed data.

Recommendations

- In some situations, irregularly distributed ground and near-surface data may be used in an inversion without gridding and upward continuation by allowing larger data uncertainties. If an excessive increase in data uncertainty is required to get an acceptable model then upward continuation may be necessary.
- Gridding and upward continuation should be performed if the observation height of the potential field data is much less than the width of the mesh cells.
- A strategy to minimise the influence of the spurious non-data points introduced during gridding is to grid the data, apply upward continuation, and then extract the upward continued data values from the grid at the original observation points via interpolation. In this way, the gridded data is only used as an intermediate step, and the inversion uses as close as possible to upward continued scattered data at the original observation locations.

Gridding tips

- Use any gridding algorithm that gives a smooth result and honours the original data. Equivalent layer, minimum curvature or spline interpolators are fine.
- If only using the gridded data temporarily to calculate upward continuation, then use the smallest grid cell size that is realistically possible to ensure the most accurate reproduction of the original observation points.
- If the grid will be used in the inversions, rather than as an intermediate step to extract upward continued observation values:
 - Match the grid cell size to the mesh cell size in the centre of the model to ensure that there is one grid point over every column in the mesh.
 - Ensure that the grid points are located roughly in the centre of each mesh cell in the central region of the mesh. This can be achieved by preparing a grid and comparing the positions of the grid points to the positions of the mesh cells and determining the amount of offset required to centre the grid points above the cells. Re-grid the original data with lateral extents that are offset by that distance.
- To avoid any edge effects due to gridding and upward continuation, prepare the grid over at least the full padded mesh before trimming the grid to the desired data extent (local or regional).

- Once the data have been gridded, it should be upward continued to a height of at least half the width of cells in the core of the mesh using standard geophysical processing methods. An upward continuation height equal to the cell width is recommended.
- The resulting grid will usually have lost elevations and assigned data uncertainties during the gridding process. To recover the station elevations and uncertainties, and to remove spurious interpolated points that could introduce artefacts, the following procedure is recommended.
 - Interpolate the new upward continued grid at the original data observation locations to extract the gridded and upward continued data values at those locations as well as the original observation elevations.
 - Alternatively use 3D modelling software (such as Gocad) to drape the gridded data onto a high resolution topography surface to recover the elevations.
 - Be sure to add the height of upward continuation to the data elevations to ensure they are in the correct position.

3.5.3 Gravity data

Data extent

- The gravity data should extend beyond the margins of the core volume. As defined in Section 3.4.3, the width of data required for local (Δ_L) or regional (Δ_R) inversions can be determined from the width of the core volume and the depths of the local and regional cores, respectively:

$$\Delta_L = w_L + 2d_L \quad 3.11$$

$$\Delta_R = \Delta_L + 6d_R \quad 3.12$$

Acquisition

- Ensure data is in appropriate units: gravity in mGal ($1 \text{ mGal} = 10 \mu\text{m/s}^2$) and locations in metres.
- Remove duplicate data points.
- Identify what the gravity data represent and what data corrections have been applied.

- Gravity data are commonly reported as “simple Bouguer” or “Bouguer slab” processed data. Such data will have had standard gravity correction procedures applied to the observed gravity measurement (Blakely, 1995), including:
 - Removal of the reference ellipsoid
 - Free-air correction
 - Bouguer slab correction
 - Correction for time-dependent variations (e.g., tides)
 - Correction for a moving observation platform (e.g., aircraft or boat)
- Some data may be reported as “complete Bouguer” or “terrain corrected”. These data have undergone an additional terrain correction based on surrounding topography data.

Gravity data corrections

- Gravity inversions should be performed using the best gravity corrections possible. In most cases this will mean using fully terrain corrected Bouguer gravity data that removes the influence of topography, mass between the observation point and the geoid, distance above the geoid, and tidal effects.
 - These data will usually be referred to as ‘complete Bouguer gravity’ or ‘terrain corrected gravity’ data.
 - These data will accurately depict the anomalous masses within the volume of interest without spurious effects from terrain.
 - Although the inversion accounts for topography, the use of a discrete mesh prevents the inversion from reproducing the actual topographic surface in sufficient detail to account for all terrain effects. Where terrain is significant this demands fully terrain corrected data to obtain accurate results.
 - Simple Bouguer slab, or non-terrain corrected, data is not ideal because it is an incomplete, or approximate terrain correction that only partially removes the influence of terrain. Gravity lows will still be present over hills and valleys and adjacent to those features, and these will be manifest as density lows below those features in density models
 - Free air anomaly data is not appropriate because it treats masses above some reference level, including positive topography, as densities, but treats masses below that reference level as density contrasts (Fig. 7.5 in Blakely, 1995). The UBC–GIF

inversion method treats everything below the topography surface as density contrasts.

- In practice, terrain corrections are difficult to perform accurately due to the accuracy required in defining and modelling the topographic surface, and the required estimate of a correction density.
 - Topography accuracy
 - A topographic inaccuracy of 1 m within 1-2 m of a gravity station can result in 0.01-0.05 mGal error in the terrain correction (Leaman, 1998).
 - If the maximum terrain correction values for an area are likely to be less than the specified gravity data uncertainty, such as where topography is basically flat, simple non-terrain corrected Bouguer data may be acceptable.
 - If gridded data is required (see below) and topography is present, fully terrain-corrected data should be used to remove the influence of topography that will be ignored by the gridding procedure.
 - Bouguer slab and terrain correction density estimate
 - The density used for Bouguer slab and terrain corrections should be an estimate of the average density between the ground surface and the level of the lowest topographic point in the model area.
 - Although standard Bouguer slab and terrain corrections require an estimate of the crustal density between the topographic surface and the geoid, the Bouguer slab contribution from the lowest point of topography to the geoid is a constant for all data. This constant can be ignored here because a mean data trend is removed prior to any inversion (see 'Data levels' below).
 - This density is particularly difficult to estimate where there are regions of weathering or transported cover at surface that cause a significant and non-uniform density variation with depth that overprints lateral variations in geology.
 - In weathered terrain, this density may be considerably lower than the standard terrain correction value of 2.67 g/cm³.
 - A useful method for estimating the Bouguer slab and terrain correction density is to apply the method of Nettleton (1939) and plot data profiles over topographic features processed at a range of terrain correction densities. The best terrain density

is that which minimises the correlation between the gravity profile and the topographic profile for most topographic features (Figure 3.4).

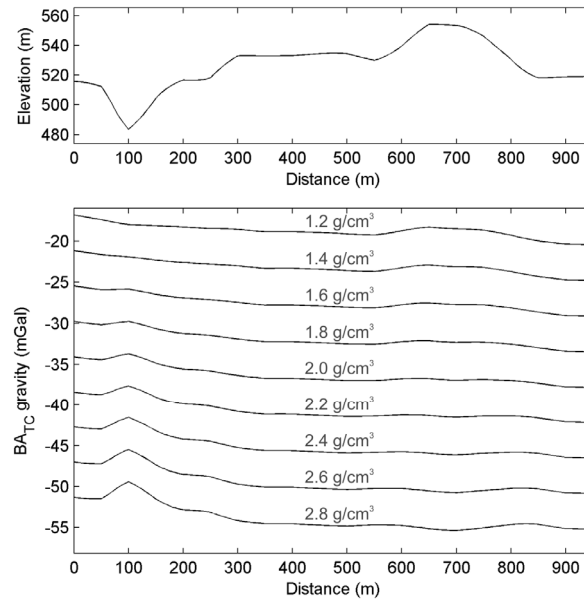


Figure 3.4. Application of the method of Nettleton (1939) to determine an appropriate Bouguer slab and terrain correction density for an area based on a suite of gravity profiles. The total topographic relief is ~ 70 m and there is pervasive low density regolith developed at shallow levels. Bouguer slab and terrain corrections were applied to the data using the suite of correction densities shown. The most appropriate correction density is that which minimises correlations between topography and the gravity value. A value of $1.8\text{--}1.9\text{ g/cm}^3$ might be best for this example.

- If there is reason to doubt the validity of terrain corrections applied to data, better results may be obtained by changing the Bouguer slab and terrain correction density to more appropriate values or by using simple non-terrain corrected Bouguer data for the inversion.
- Where the terrain correction density is too high, inversions will recover high density contrast anomalies at shallow levels that will correlate with the location of the highest terrain correction values. Conversely where the terrain correction density is too low, low density anomalies will occur below observations that have insufficient terrain correction applied.

Data uncertainty

It is important to allow for some uncertainty in the observed geophysical data because the data will never be exactly accurate. Various sources of uncertainty are identified in Section 3.3.1, and many will be present in any collected data. Since such uncertainty is unavoidable in

geophysical data, there is no use in an inversion reproducing the observed geophysical data exactly. Doing so would reproduce noise in the data as noise in the model.

- The required uncertainties are an estimate of the standard deviation of the noise and errors associated with each observation.
- Uncertainty can depend on measurement and location methods, reduction/corrections/processing, data spacing, and especially the quality of gridding (if used) since gravity data tends to be sparsely distributed.
 - Upward continued data will likely require a smaller uncertainty than ground data because high frequency noise in the data has been filtered out and the dynamic range of the data reduced.
- Gravity data uncertainties should be assigned as a constant value regardless of the observed gravity value.
 - Useful estimates may be: ~0.01-0.05 mGal for new/high quality data, ~0.05-0.1 mGal for average quality data; ~0.1-0.15 mGal for old/poor quality data.
 - If the assigned uncertainty is too small, the inversion will take longer to process and will recover a model that contains excess structure or fine detail at depth that cannot reasonably be supported by the observed data (since resolution decreases with depth). If the assigned uncertainty is too high, the inversions will run too quickly and recover a model that is excessively smooth and lacks detail. The difference between the observed and predicted gravity response may also contain geological features or trends that are not accounted for by the model.
 - If an inversion is taking a long time, and the misfit values reported in the inversion window are not changing much, open the model in Meshtools3D and check if there is excess structure appearing at depth. Terminating an inversion process early and restarting it with increased data uncertainties will save a lot of processing time.
- If merging multiple data sets, consider assigning different uncertainties to each dataset before combining them. Larger uncertainties may be required for older data, or data from less reliable sources.

Gravity data preparation workflow

The following workflow assumes that the gravity data is available only as standard non-terrain corrected Bouguer gravity data that has not been gridded. If the data have already been

gridded and the original observation locations are unavailable, skip step 5, and replace step 7 with some method for recovering the elevations of the observations, usually by draping the observations on a topographic surface in a 3D modelling package.

1. Extract data for the full local or regional padding volume (depending on whether the data is to be used for local or regional inversions, respectively).
2. If the Bouguer slab density needs to be changed to be more appropriate for the terrain densities in the area of interest, adjust the gravity data using the following equation based on the standard Bouguer slab correction equation:

$$g_{z_{new}} = g_{z_{old}} + 0.041935 \cdot Z \cdot (\rho_{BA_{old}} - \rho_{BA_{new}}) \quad 3.13$$

where $g_{z_{new}}$ is the new Bouguer anomaly, $g_{z_{old}}$ is the old Bouguer anomaly, Z is the elevation of the observation, $\rho_{BA_{old}}$ is the old Bouguer slab density, and $\rho_{BA_{new}}$ is the new Bouguer slab density, and units are in m, g/cm³, and mGal.

3. Assign data uncertainties
 - This step is useful here if combining multiple datasets of differing quality. If using a single dataset with uniform uncertainty, then this step can be postponed until step 7.
4. Merge multiple datasets into a single file (if necessary)
 - Remove duplicate data points.
5. Apply full terrain corrections, usually using the new Bouguer slab correction density, with the best available topography data.
6. Grid the data using the best available method and the smallest grid cell size that can be realistically managed given the number of data and their lateral extent. Equivalent layer, minimum curvature and spline methods work well.
7. Upward continue the gridded data using Fourier transform techniques.
8. Interpolate the upward continued gridded and terrain corrected gravity data at the original observation locations to recover the upward continued gravity values at those original observations as well as the original observation elevations and data uncertainties.
9. Add the upward continuation height to the data observation heights.
10. Subtract the mean observation value from the data (see ‘Data levels’ below).

Data levels

An important step before any inversion is to ensure the geophysical data is at the correct data level. Gravity data show the observed gravity value relative to some reference, typically the whole earth. The data will therefore contain some zero order trend that indicates whether the data are higher or lower than that reference. This trend cannot be explained solely by the density distribution within the inversion mesh, violating the assumption that the mesh can reproduce the data (Section 3.3.1), and so must be removed.

- After gridding and upward continuation, subtract the mean observation value from every data point.
 - This should be done for both regional and local data sets and after any processing has been applied that would change the data values.
 - Subtracting the mean value may change the magnitudes of the recovered density contrasts, but the relative contrasts between highs and lows will be the same.
- The mean value should be removed even if a regional trend has already been removed. Removal of a regional trend will still leave a constant value in the local data that indicates whether it is higher or lower on average than the regional trend. This constant is not relevant within the local mesh and should be removed.
- If data uncertainties have been assigned as a constant (e.g., ± 0.05 mGal), then they do not need to be adjusted after the data level has been changed.

3.5.4 Magnetic data

Data extent

- The magnetic data should extend beyond the margins of the core volume. As defined in Section 3.4.3, the width of data required for local or regional inversions can be determined from the width of the core volume (w_L) and the depths of the local (d_L) and regional (d_R) cores respectively:

$$\Delta_L = w_L + 2d_L \quad 3.14$$

$$\Delta_R = \Delta_L + 6d_R \quad 3.15$$

Acquisition

- Ensure data is in appropriate units: total magnetic intensity in nT and locations in metres.

- Analytical signal and derivative products are not supported.
- Remove duplicate data points.
- The magnetic data should have undergone standard processing procedures:
 - Manual quality control on the raw data, including removal of spikes and assorted instrument errors.
 - Removal of time-dependent variations using a base station.
 - Levelling to remove tie-line crossover discrepancies
 - Micro-levelling to remove other unaccounted for residual errors. Although important when preparing gridded magnetic data, these errors may be accommodated in inversions by allowing larger data uncertainties in the inversions.
- Ground magnetic data may be combined with aeromagnetic data acquired at different altitudes, but care must be taken to assign appropriate data uncertainties to each dataset prior to combining them, and it is important that the true observation locations are used for each dataset to allow for varying acquisition heights.
- If un-gridded aeromagnetic data is available and is to be used directly (rather than gridded), the data should be down-sampled along the flight lines if the data spacing along the flight lines is significantly less than the desired mesh cell widths. The detailed along-line data will contain high frequency information that cannot be accommodated by larger cell sizes.
 - If the spacing between flight lines is much less than the cell widths, whole flight lines may also need to be removed to limit the impact of small wavelength anomalies on the data misfit.
 - Alternatively, the data can be gridded and upward continued as for gravity data.
- Magnetic data must be supplied with a single magnetic field direction and intensity appropriate for the time and location of the supplied data survey. This should be based on the IGRF/DGRF standard. One source for such magnetic field information is the NOAA National Geophysical Data Center (<http://www.ngdc.noaa.gov/geomag/magfield.shtml>). For large surveys, the field direction and intensity may vary over the survey area. The field parameters appropriate for the center of the survey at the average time the survey was acquired should be used, and variations may need to be accommodated in the specified data uncertainty.
 - Data that has been reduced to the pole may be used if the incident magnetic field direction is set as vertical.

Data uncertainty

It is important to allow for some uncertainty in the observed geophysical data because the data will never be exactly accurate. Various sources of uncertainty are identified in Section 3.3.1, and many will be present in any collected data set. Since such uncertainty is unavoidable in geophysical data, there is no use in an inversion reproducing the observed geophysical data exactly. Doing so would reproduce noise in the data as noise in the model.

- Uncertainties are an estimate of the standard deviation of the noise contained in the data.
- Uncertainty can depend on measurement and location methods. Magnetic data has a high dynamic range and good precision (≤ 0.1 nT), but accuracy may be uncertain due to remanent magnetisation, self-demagnetisation, approximation of the earth field, navigation and position errors, topographic drape, gridding, etc.
 - Upward continued data will likely require a smaller uncertainty than ground data because high frequency noise in the data has been filtered out and the dynamic range of the data reduced.
- Uncertainties should generally be assigned as a percentage of each data value plus a constant.
 - Useful estimates will typically be on the order of 3 % + 3 nT to 5 % + 5 nT.
 - This form of data uncertainty is easily assigned within the gm-data-viewer software.
 - If the assigned uncertainty is too small, the inversion will take longer to process and will recover a model that contains excess structure or fine detail at depth that cannot reasonably be supported by the observed data (since resolution decreases with depth). If the assigned uncertainty is too high, the inversions will run too quickly and recover a model that is excessively smooth and lacks detail. The difference between the observed and predicted magnetic response may also contain geological features or trends that are not accounted for by the model.
 - If an inversion is taking a long time, and the misfit values reported in the inversion window are not changing much, open the model in Meshtools3D and check if there is excess structure appearing at depth. Terminating an inversion process early and restarting it with increased data uncertainties will save a lot of processing time.

- If merging multiple data sets, consider assigning different uncertainties to each dataset before combining them. Larger uncertainties may be required for older data, or data from less reliable sources.

Data levels

- Magnetic data are generally processed relative to some arbitrary regional level. This level has little importance for the desired inversion volume, and will not likely be reproducible within the specified inversion volume, violating a key assumption of the inversions.
- Due to the dipolar response of magnetic bodies, it can be difficult to determine the most appropriate data level for a given data set. The best strategy is as follows:
 - After all data processing has been completed, subtract the mean magnetic value from the data.
 - Perform an inversion at the appropriate scale (regional or local) using the zero-mean data following standard procedures.
 - Open the recovered model in Meshtools3D and slice through the model towards the bottom layers of cells using horizontal slices. Look at the distribution of source material at depth. If there are accumulations or “puddles” of extreme magnetic susceptibilities at the bottom of the model at either the north or south end within the padding cells, then the data level will need to be shifted up or down accordingly. The relationships indicated here are based on treating the entire model volume as a single dipole source and ensuring that the data levels are appropriate given the relative position of that source.
 - If the earth field is inclined down to the north (northern hemisphere, Figure 3.5):
 - Puddles at the north end of the model indicate the data level is too high and a bias needs to be subtracted from the data. To achieve such high data values in a dipole response, the inversion expects the full source to lie to the north of the model and it adds source material there where there is poor data sensitivity.
 - Puddles at the south end of the model indicate the data level is too low and a bias needs to be added to the data. To achieve such low data values in a dipole response, the inversion expects the full source to lie to the south of the model and it adds source material there where there is poor data sensitivity.
 - If the earth field is inclined up to the south (southern hemisphere, Figure 3.6):

- Puddles at the north end of the model indicate the data level is too low. To achieve such low data values in a dipole response, the inversion expects the full source to lie to the north of the model and it adds source material there where there is poor data sensitivity.
- Puddles at the south end of the model indicate the data level is too high. To achieve such high data values in a dipole response, the inversion expects the full source to lie to the south of the model and it adds source material there where there is poor data sensitivity.
- Ideally, susceptible material at the base of the model should be evenly distributed from north to south, or focussed in a few central locations according to the geology.
- Initial adjustments of ± 5 -10 % of the total magnetic data range should be added or subtracted from the data as indicated, before repeating the inversion process.
- Once the data level is close to achieving an even distribution of susceptibilities at depth, finer adjustments of ~ 1 % may be useful.
- It is important to recalculate the magnetic data uncertainties every time the data level is adjusted because the uncertainties are calculated as a percentage of the data value (e.g. 5 % + 5 nT). Changing the data value will change the required uncertainty level.

3.5.5 Removing regional data contributions

To ensure that the supplied mesh is capable of reproducing the observed geophysical data, the contribution of all sources lying outside the local mesh must be removed from the data. Although a first order mean trend will be removed, this does not account for the variable distribution of sources outside the local mesh. There are many published regional trend removal methods and all have merit in particular problems. Common examples include polynomial-trend removal (Agocs, 1951; Skeels, 1967), Fourier domain filtering (Spector and Grant, 1970), and minimum curvature gridding (Mickus et al., 1991). Since inversions are being used to predict subsurface physical properties at a local scale, it is reasonable that they could be used to predict the regional distribution of physical properties outside the local volume of interest. Li and Oldenburg (1998b) describe this method in detail. It is summarised here.

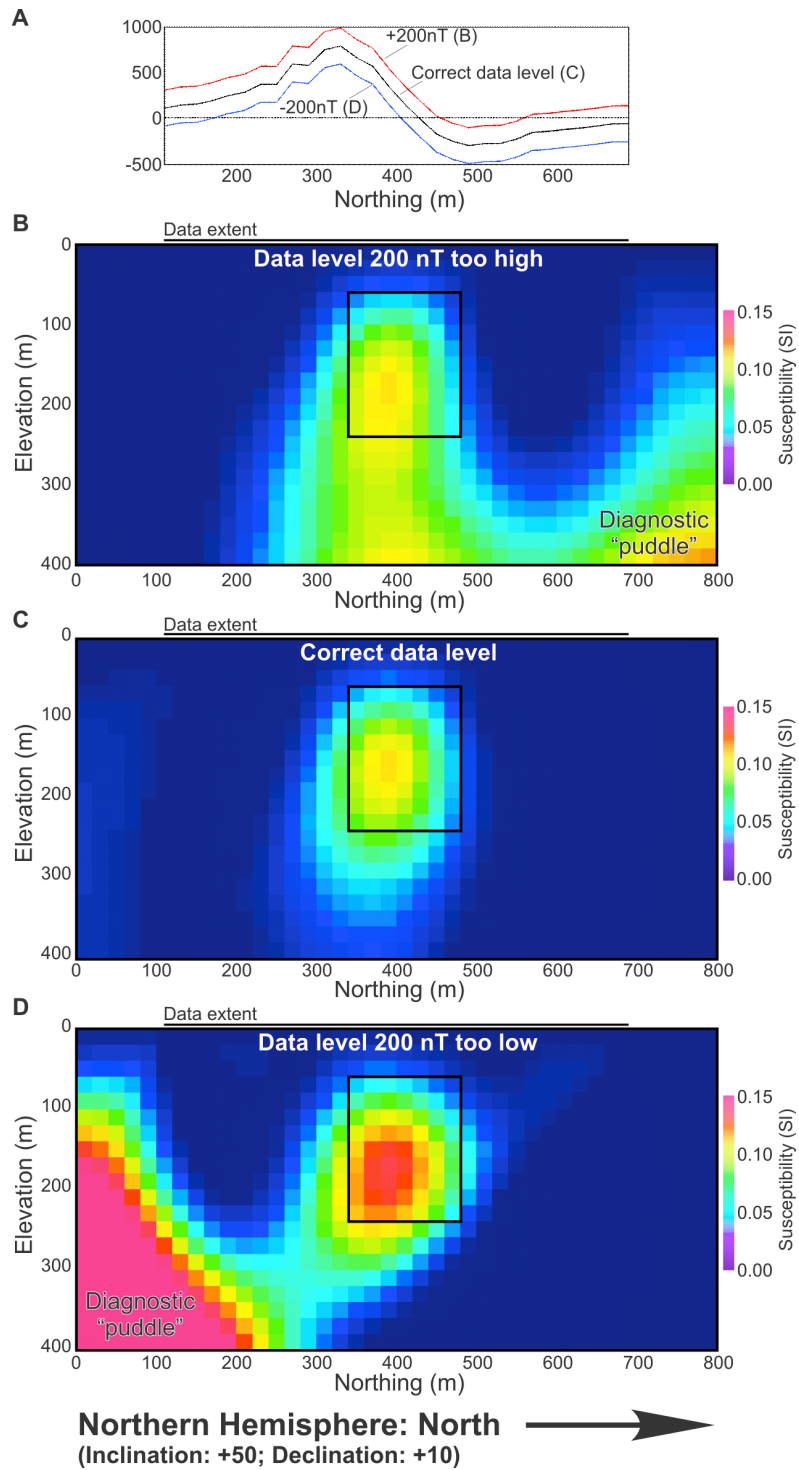


Figure 3.5. Example demonstrating how incorrect magnetic data levels can be identified and corrected for problems in the northern hemisphere. A. North-south profiles of the data used to derive the models shown in B-D. The two shifted data sets are identical except for a constant shift of ± 200 nT. B. North-south slice through the susceptibility model recovered when the data are 200 nT too high. The large “puddle” of susceptible material within the padding cells along the northern edge is diagnostic. The black box shows the location of the actual source feature, which has a true susceptibility of 0.1 SI. C. North-south slice through the susceptibility model recovered when actual data are used. D. North-south slice through the susceptibility model recovered when the data are 200 nT too low. The large “puddle” of susceptible material within the padding cells along the southern edge is diagnostic.

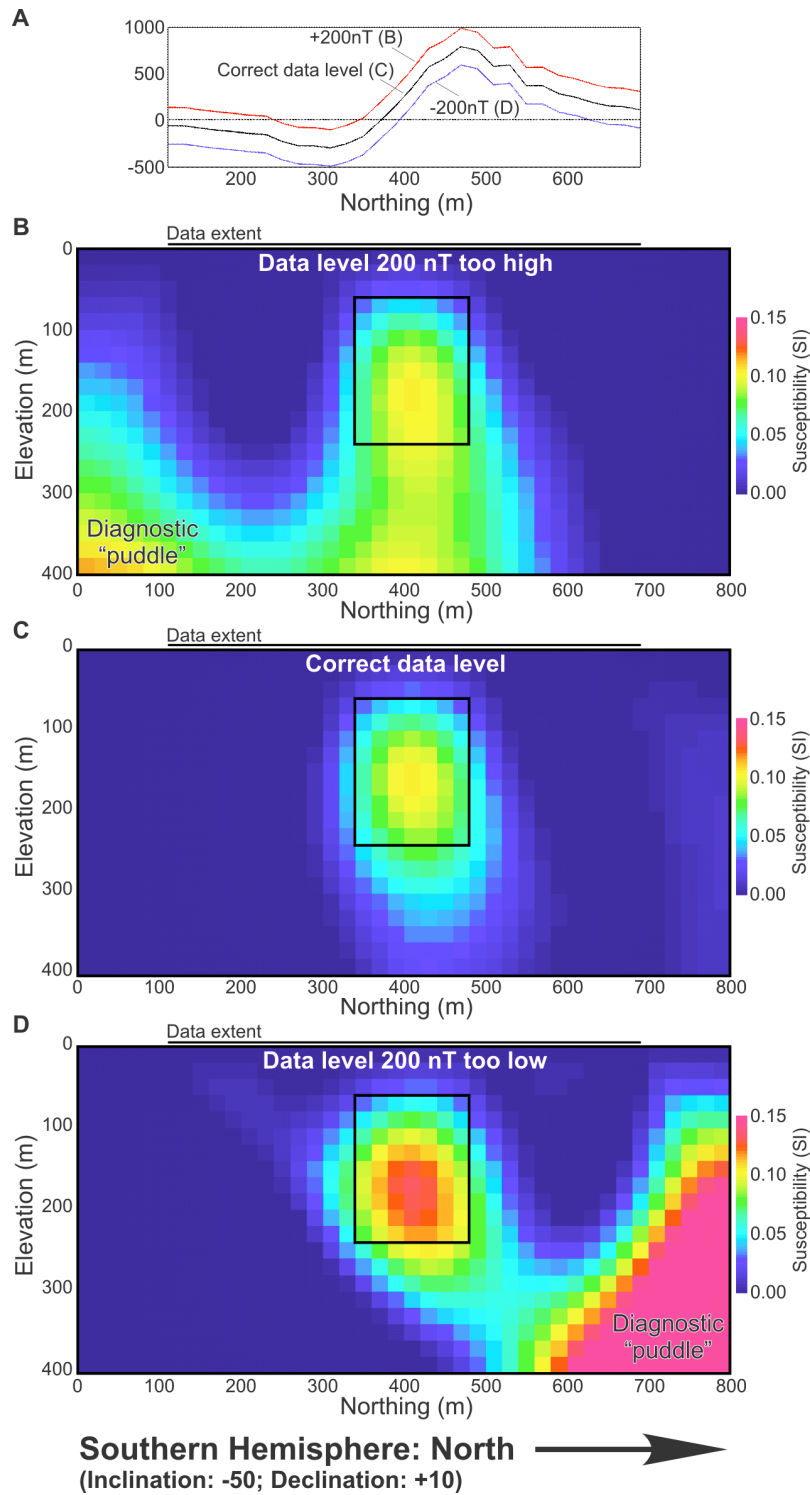


Figure 3.6. Example demonstrating how incorrect magnetic data levels can be identified and corrected for problems in the southern hemisphere. A. North-south profiles of the data used to derive the models shown in B-D. The two shifted data sets are identical except for a constant shift of ± 200 nT. B. North-south slice through the susceptibility model recovered when the data are 200 nT too high. The large “puddle” of susceptible material within the padding cells along the southern edge is diagnostic. The black box shows the location of the actual source feature, which has a true susceptibility of 0.1 SI. C. North-south slice through the susceptibility model recovered when actual data are used. D. North-south slice through the susceptibility model recovered when the data are 200 nT too low. The large “puddle” of susceptible material within the padding cells along the northern edge is diagnostic.

Basic regional trend removal

- Perform a regional scale inversion with the regional data and regional padding mesh.
 - Define default parameters as for normal default inversions (Section 3.6).
- Assess the recovered regional model according to standard criteria (Section 3.7) and consider adjusting inversion parameters to improve the model (Section 3.8).
- Advanced: Consider applying geological constraints to ensure the regional physical property distribution is consistent with geological expectations (Section 3.8.2).
- Set all cells within regional padding mesh that lie within the central local padding mesh to a property of zero.
 - This can be done in Meshtools3D by loading the regional model, using the Edit->Add Blocks command to create a block of zero property covering the lateral and vertical extent of the local padding mesh.
 - This creates a “scooped” out regional model.
- Forward model the scooped regional model to the local data observation locations.
 - This gives the regional contribution observed at the local data points.
- Subtract the calculated regional contribution from the observed (possibly upward continued) local data.
 - The result is the residual local data which can be used in the local inversions with the local padding mesh.
- Reset the local data level to zero by subtracting the mean observation value.

3.6 FIRST INVERSION

Once the mesh has been defined and the data have been pre-processed, inversions can be run. The act of running an inversion typically consists of identifying the locations of the appropriate input files and defining a set of parameters that control how the inversion should be calculated and what character the recovered property model should have. For many problems, the first inversions will actually be regional-scale inversions used to define the regional physical property distribution that will be used to calculate the regional trend associated with a local data set, prior to inverting that local data. The procedure for both local and regional inversions is the same, but with slightly different parameter settings. If a regional response is deemed to be zero, or has been determined using techniques other than inversion, then the first inversions will be local inversions to directly tackle the specific problem.

3.6.1 Graphic user interface (GUI)

Most basic inversions can be performed using the GRAV3D or MAG3D GUIs. The interface is shown in Figure 3.7; it automatically creates and manages the inversion control files that direct the inversion. It also provides useful shortcut buttons to view the geophysical data, create a default mesh based on the data, run or terminate an inversion, view log files, the recovered model and the predicted geophysical response of the recovered model. All of the functionality implemented in the GUIs can also be achieved manually by editing the text inversion control files. Advanced users may prefer to manage their own control files.

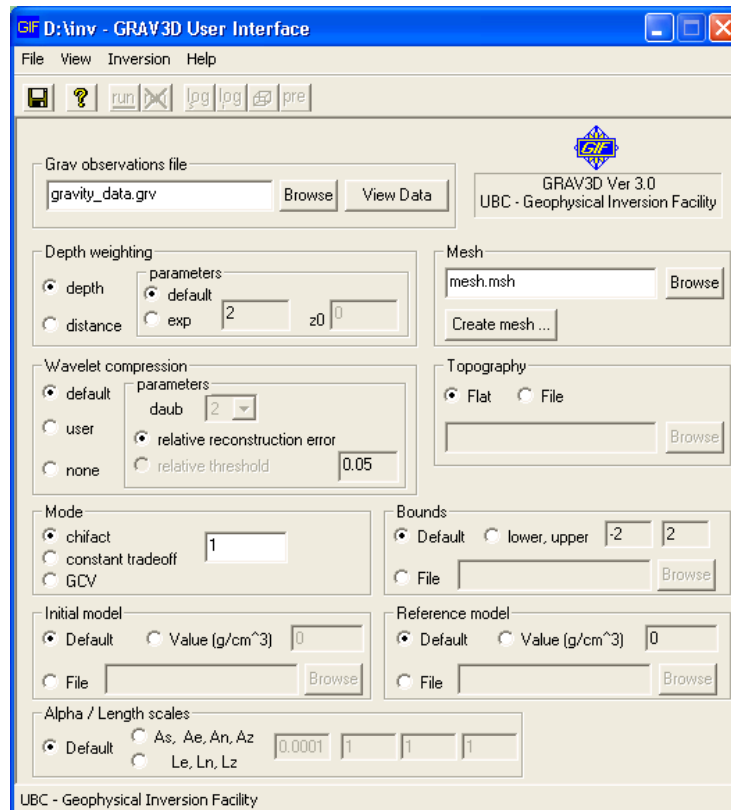


Figure 3.7. The interface of the GRAV3D GUI for running inversions. Most of the functionality of the inversions can be accessed using the GUI. The MAG3D GUI is identical except for the units for the physical property values.

3.6.2 Essential input files

All inversions must include:

- A geophysical data file in the correct format with data uncertainties defined.
- A mesh file in the correct format defining the geometry of the model to be recovered
- Most inversions of real data will include a topography file indicating the elevations of points on the ground surface.

- All three of the above files can be entered into the GUI interface by using the relevant browse buttons, or by dragging and dropping the file into the white input boxes.

3.6.3 Setting the model objectives

Due to the inherent non-uniqueness of potential fields and inversions the recovered physical property models will be heavily controlled by the mathematical style imposed by the inversions. The UBC–GIF inversions recover models that tend to be smooth and are as close as possible to a defined reference property model which is zero by default. They also apply a depth weighting function that allows the recovered properties to be distributed throughout the depth of the model. Each of these parameters can be controlled in the inversion. Initial inversions will usually use the default set of parameters that work well for many problems; however alpha coefficients/length scales must be adjusted to suit the mesh being used for each inversion. Advanced users can adjust the character of all of the following parameters to suit specific problems and prior knowledge.

Alpha coefficients / length scales

- These are fundamental parameters that should be adjusted in all inversions.
- They control the smoothness of the model relative to how closely the model fits the supplied reference model (that has a default value of zero everywhere).
- The values can be assigned in two different ways, but have the same effect. Length scales are recommended for initial inversions.
 - Length scales (L) are a simpler representation that specifically relates the relative amount of smoothness to the size of the cells in the mesh.
 - In the absence of a preferred orientation in the model, length scales should be set to 2-5× the dimensions of cells in the core of the model.
 - Larger length scales will create a smoother model which may deviate further from the reference model.
 - Advanced: Alpha (α) values directly specify the coefficients of each of the four components of the inversion model objective function:
 - α_s ('As' in the GUI) controls the importance of closeness of the recovered model to the reference model.

- α_e ('Ae' in the GUI) controls the importance of smoothness of the model in the east-west direction.
- α_n ('An' in the GUI) controls the importance of smoothness of the model in the north-south direction.
- α_z ('Az' in the GUI) controls the importance of smoothness of the model in the vertical direction.
- Only the ratios between the values are important, the actual values are not. Doubling one of the values relative to the other 3 doubles the importance of that component relative to the others.
- The default setting uses alpha values $\alpha_s = 0.0001$, $\alpha_e = 1$, $\alpha_n = 1$, $\alpha_z = 1$. These are equivalent to length scales of 100 m and are appropriate for problems using cells of ~20-50 m in each dimension. For other cell sizes use the length scale option and enter L values of 2-5× the cell dimension in each direction.
 - If the default settings are used with much larger cells, the model will appear too structured or “rough”. If they are used with smaller cells, the model will appear to smooth and lack detail.
- Advanced: Specifying larger length scales or α_e , α_n , α_z values for one or two of the directions will promote extra smoothness in that direction which can be used to help reproduce dominant strike or dip directions. For additional detail see Section 3.8.1.

Depth weighting

- Because potential field data contains no inherent depth information, a weighting function controls the vertical distribution of properties within a model. It is defined to compensate for the decay of the geophysical response of a spherical source with increasing depth in the model.
 - There are two types of depth weighting that are available.
 - True ‘depth weighting’ is an approximation based on the vertical depth of a cell below topography.
 - ‘Distance weighting’ is based on the physics of potential fields and indicates the proportional sensitivity of each cell to the observed data and takes into account lateral distances as well as vertical distances.
- Distance weighting should be used for all problems, especially where:

- Any topography is present
- Data are irregularly spaced, or contains gaps
- In the GUI select ‘distance weighting’ and leave the weighting parameters to the default values. These are defined by the physics of the problem.
 - Advanced: Distance weighting also must be used where borehole magnetic data is being used.
 - Advanced: Depth weighting is an approximation of distance weighting that only applies if there is a high density of data on a regular grid on a completely level surface. If this situation applies, depth weighting can be tried. It is slightly quicker to calculate the sensitivity matrix than for distance weighting.

Bounds

- The maximum range of properties allowed in each cell is defined by bounds. Bounds can be assigned for the whole model or for each individual cell.
- The default bounds for gravity inversions are -2 to +2 g/cm³ relative to some background or average density. For magnetics the defaults are 0 to 1 SI. These are acceptable default values for most problems.
 - Advanced: To allow a tighter or wider range of properties for every cell, choose the ‘lower, upper’ option and specify the new limits, or select ‘File’ and indicate an input file with bounds defined for every cell.

Reference model

- The recovered property model will be as close as possible to the specified reference model while still fitting the geophysical data.
- When a uniform reference model is used this will result in a model that has the minimum structure and property variability required to explain the observed geophysical data. It can be thought of as the simplest model.
- The default reference model of 0 (g/cm³ or SI) is an acceptable choice when no other geological information is available, and is usually used for the first few inversions to ensure that all other parameters are set appropriately.
 - Advanced: A uniform, non-zero reference model can be employed by selecting the ‘value’ option and specifying any property value. The value does not have to be within

the specified bounds, however if it is not between the bounds its value will not be recovered by the inversion.

- Advanced: When there is additional information about the subsurface distribution of physical properties, a best estimate of those properties can be supplied in a reference model file. This file can define a complex non-uniform physical property model that reflects the subsurface geology. Physical property models recovered by inversions using such constraints will not necessarily contain minimal structure, and sharp changes in recovered physical properties are possible.

Initial model

- This specifies the starting physical property distribution. It is only used to speed up inversions by supplying an existing model which only requires minimal adjustment. It has negligible affect on the recovered property model.
- All values in the initial model must lie between the specified bounds. Commonly the easiest way to ensure this is to also use the supplied reference model as the initial model. For default inversions the initial model will almost always be set as the default value of 0 (g/cm³ or SI).

3.6.4 Misfit and trade-off parameters

The inversion has three modes for defining the trade-off between finding a model that closely satisfies the smoothness and smallness constraints, and one that closely matches the geophysical data. The balance is directly controlled by a specific trade-off parameter, but that trade-off parameter is usually determined automatically by the inversion based on the specified data uncertainty.

- Inversions that have reliable data uncertainty estimates specified in the data file will usually use the default setting using the ‘chifact’ mode with a default value of 1.
 - Using different values for ‘chifact’ has the effective of scaling the specified data uncertainties, σ , giving an effective uncertainty:

$$\sigma_{effective} = chifact \cdot \sigma \quad 3.16$$

- An alternate way of achieving the same effective uncertainty is to multiply the data uncertainties specified in the data file by the value of ‘chifact’ and specify a new ‘chifact’ of 1 in the inversion control file.
- The main exception to this rule is when it is difficult to assign useful estimates of uncertainty to the data. In this situation, the ‘GCV’ (generalised cross-validation) mode should be used.
 - GCV mode uses a computationally intensive search to derive a trade-off parameter that recovers a model that fits the data adequately while satisfying the desired model characteristics of smoothness and closeness to a reference model.
 - GCV inversions should be run with an estimate of the appropriate relative data uncertainties assigned to every observation. This is particularly important where some data are known to have larger uncertainties than others but the actual values are not accurately known.
 - Advanced: GCV mode can be used to derive an estimate of the appropriate data uncertainty. Run a GCV inversion with a best estimate of the relative data uncertainties, $\tilde{\sigma}$. When finished, find the ‘achieved misfit’ reported at the end of the inversion log file. An updated estimate of the data uncertainties for each observation, σ_{gcv} , can be obtained using:

$$\sigma_{gcv} = \tilde{\sigma} \cdot \sqrt{\frac{\text{achieved misfit}}{\text{number of observations}}} \quad 3.17$$
 - This commonly underestimates the data uncertainty slightly, so may need to be rounded up.

3.6.5 Compression

Inversions with large numbers of cells and a large numbers of geophysical data consume a very large amount of memory and can be slow to process. The UBC–GIF inversion procedure uses wavelet compression to reduce the size of the problem. The compression makes the inversions tenable, but can lead to undesirable artefacts requiring adjustment of the compression ratio. These artefacts are usually evident as orthogonal lines or a checkerboard pattern at depth within the recovered physical property model.

- Most inversions can be run with the default compression settings. This will effectively balance the processing requirements with the quality of the result.
- Advanced: An easy way to slightly improve the quality of the recovered inversions with only a small processing penalty is to reduce the amount of compression slightly. Set the wavelet compression option to ‘user’. Select ‘relative reconstruction error’ and enter a value of about 0.025. Using values smaller than this will usually cause the sensitivity calculation to abort by failing to achieve the desired compression.
 - If the inversion fails to complete after adjusting this setting, increase the value slightly and try again.

3.6.6 Running the inversion

Once all the files have been identified and all the parameters set appropriately the control files need to be saved by clicking the save button. Then the inversion can be run using the run command. The first inversion will be performed in two parts. The first part will be the sensitivity matrix calculation. Once this has been completed the matrix will be saved to the same directory that the control files were stored in for use in subsequent inversions with the same mesh and data. The inversion calculation will then commence.

3.7 EVALUATING AND DISPLAYING THE RESULTS

Once an inversion has completed, a number of checks must be made to determine whether the inversion finished successfully and whether the recovered result is valid. If the inversion completed successfully, the primary criteria for judging the quality of the recovered model are based on how well the model met its objectives.

3.7.1 Did the inversion finish?

- Two text log files will be produced. These will be available by clicking the ‘log’ buttons in the GUI interface, or by opening the directory in which the control files were saved.
 - The first is ‘magsen3d.log’ (MAG3D) or ‘gzsen3d.log’ (GRAV3D). This indicates the progress of the sensitivity matrix calculation. It will indicate if any errors occurred.
 - The second is ‘maginv3d.log’ (MAG3D) or ‘gzinv3d.log’ (GRAV3D). This indicates the progress of the inversion calculation. It will indicate if any errors occurred.
- The following output files should also be present (among others):

- Recovered property model file: `maginv3d.sus/gzinv3d.den`
- Predicted data response file: `maginv3d.pre/gzinv3d.pre`
 - This shows the predicted geophysical response of the recovered model. It should be similar to the observed data as discussed below.

3.7.2 Did the recovered model adequately reproduce the geophysical data?

- The inversion log file will report an ‘achieved misfit’ at the end of the file.
- For inversions that use the ‘chifact’ mode:
 - This reported achieved misfit should be approximately equal to the number of data times the specified *chifact* value (usually 1).
- For inversions that use the ‘GCV’ mode:
 - Equation 3.17 shows how to calculate the GCV estimate of the appropriate uncertainties for the current data. If this estimate is unreasonably high or low it may suggest that the inversion did not fit the data appropriately.
- The predicted data should be compared to the input observed data. This can be done by loading both data files in the `gm-data-viewer` program, and using the difference functions to display the difference between the two datasets. Of particular importance is the normalised difference obtained by dividing the difference in the data by the specified data uncertainty, $\delta d/\sigma_i$. An example of various data misfits as a function of the allowed data uncertainty is shown in Figure 3.8.
 - The depicted differences should appear mostly as random noise (Figure 3.8B). If there appears to be too much geological structure present in the difference (Figure 3.8D), then the inversion did not adequately reproduce the observed data and the specified data uncertainty or *chifact* value should be decreased.
 - If there are problems with specific data points this may be apparent as spikes in the data misfit at those points.

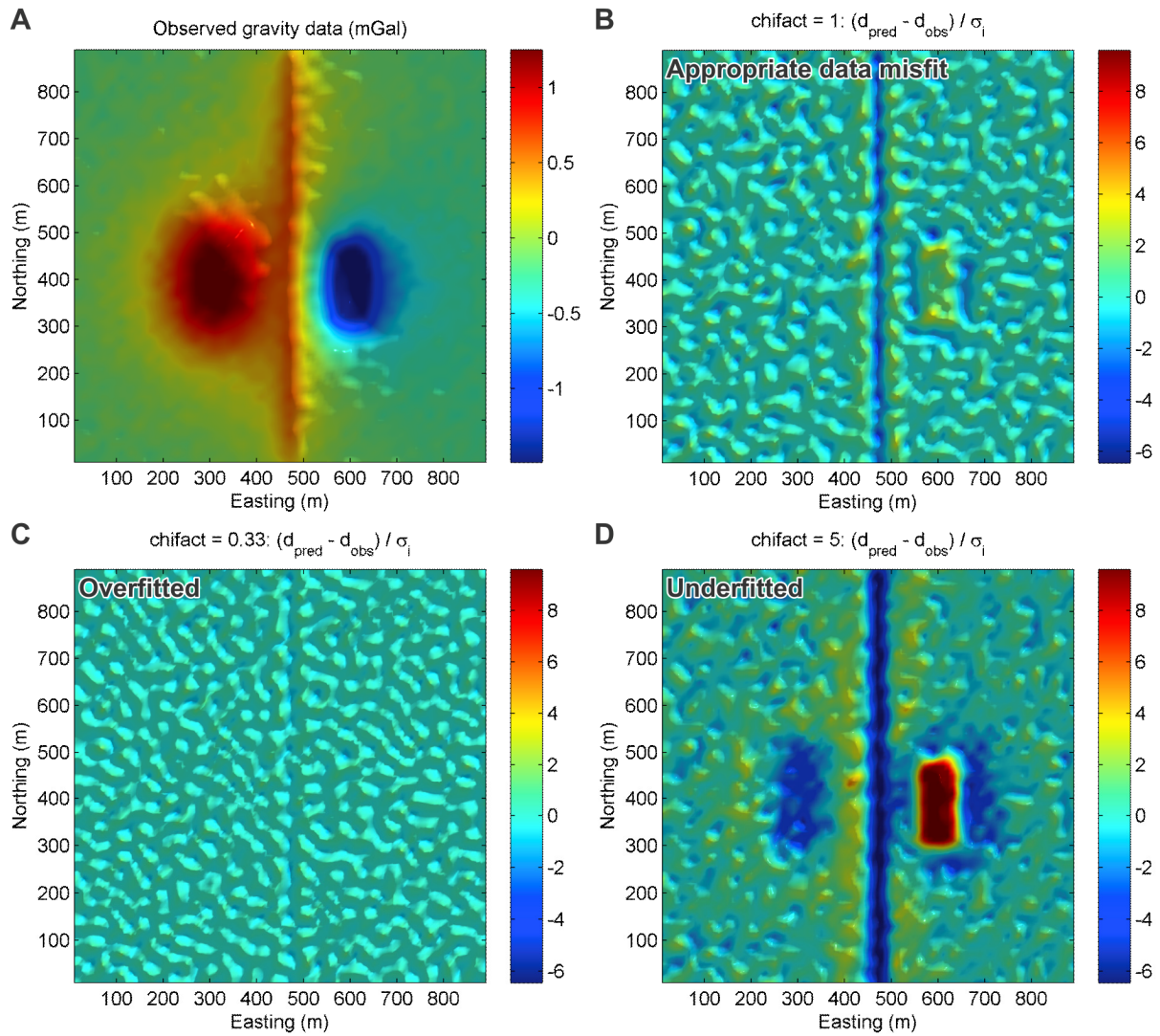


Figure 3.8. Examples for a synthetic gravity data set showing how different data uncertainties affect the data misfit associated with recovered inversion models. All inversions were run with the same data uncertainty of 0.03 mGal specified in the data file, but the effective data uncertainty ($chifact \times \sigma_i$) was modified using different values for $chifact$ as indicated. A. The observed gravity data shows three geological features and random noise with a standard deviation of 0.03 mGal. B. The difference between the observed and predicted data, normalised by the specified data uncertainties, when the effective data uncertainty was correctly specified as 0.03 mGal for all data points. The difference is mostly noise with only a slight geological signal present. C. The normalised data difference obtained when the effective data uncertainty is 0.01 mGal. The data is fitted too closely and noise in the data will have been reproduced in the model. As a result, the difference shows only noise. D. The normalised data difference obtained when the effective data uncertainty is 0.15 mGal. In this case the data is not reproduced well enough and a significant amount of geological information is discarded as noise. The model will not contain sufficient geological detail.

3.7.3 Does the recovered model satisfy conditions of smoothness and closeness to the reference model?

- This can only be assessed qualitatively by visually inspecting the recovered model. This step is easiest with some experience and with some understanding of what the recovered model should look like based on the problem being addressed (Section 3.3.1).
- Load the recovered model in Meshtools3D.
- Slice through the model vertically and horizontally to visually identify any problem areas.

Assess whether:

- The recovered properties are distributed uniformly through the model. Look for puddles of extreme property values (high or low) at depth and in the corners of the model, especially within padding cells beyond the lateral extent of the supplied data
 - These features typically indicate that the model is trying to reproduce long data wavelengths that cannot realistically be explained with the supplied mesh.
 - The mesh may not extend deep enough, the level of the data may be incorrect (especially for magnetic data: see Section 3.5.4, Figure 3.5 and Figure 3.6), a regional response was not removed from the data or was inappropriate, or there are other problems with the data processing.
- The model is excessively noisy (especially at depth) or unrealistically smooth. These problems are primarily the result of using inappropriate data uncertainties. Some examples of how the specified uncertainties affect the recovered models are shown in Figure 3.9.
 - The presence of small (< 2-5 cells wide) anomalies at depth within the model cannot be supported by potential field data which have very low sensitivity to small features at depth. These generally indicate that the specified data uncertainty is too low, and noise in the data is being reproduced as noise in the model (Figure 3.9D). Increase the specified data uncertainties or the *chifact* parameter.
 - If the model seems too smooth (Figure 3.9A) then the specified data uncertainties might be too high. An excessively smooth model will usually have a predicted response that does not adequately reproduce the observed data (Figure 3.8D). Decrease the specified data uncertainties or the *chifact* parameter.
 - Other possible causes include: mesh cell sizes that are too large or too small to reproduce the supplied data (change the cell sizes, down sample the data or upward

continued it to a higher level), or alpha coefficients/length scales that are not set appropriately (see Section 3.8.1).

- If the structure takes the form of orthogonal stripes or a checkerboard pattern (Figure 3.10), then the sensitivity matrix wavelet compression resulted in a loss of necessary information, and the amount of compression should be reduced.

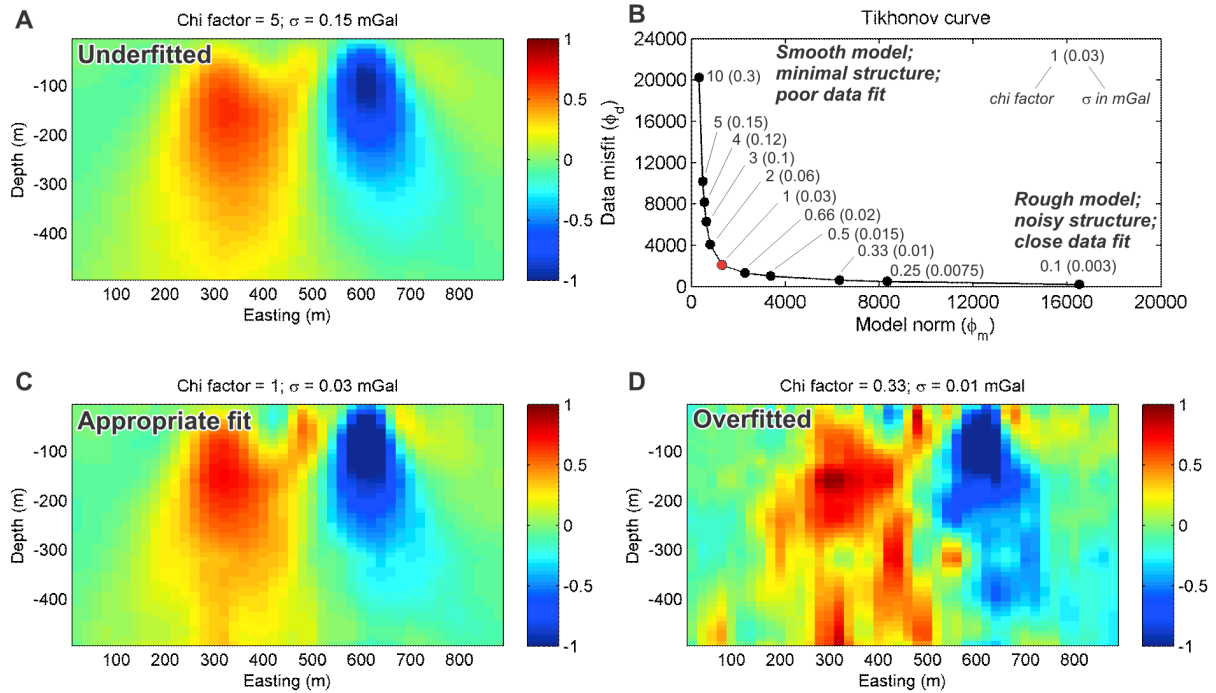


Figure 3.9. Vertical slices through a set of inversion models indicating typical relationships between the character of recovered models and the allowed data uncertainties for the same 2025 gravity data and inversions used in Figure 3.8. The observed data had the same 0.03 mGal of random Gaussian noise. The actual noise level of 0.03 mGal was specified in the data file as the standard deviation for each point. The effective data uncertainty ($chifact \times \sigma_j$) allowed in each inversion was specified by adjusting the $chifact$ parameter as indicated. The Tikhonov curve (B) indicates the achieved model norm versus the achieved data misfit for each inversion. If the data noise is Gaussian and the correct data uncertainty is specified, $\phi_d = N$ (the number of data points) = 2025 provides a balanced solution. The red circle indicates that ideal result for this example (and corresponds with the data misfit shown in Figure 3.8B), obtained using the actual noise level (C). If the specified data uncertainty is too high, the data will be poorly fitted (Figure 3.8D), and an excessively smooth model will be recovered (A). If the specified data uncertainty is too low, the data will be tightly fitted (Figure 3.8C), and an excessively noisy model will be recovered (D). Use of the GCV mode and equation 3.17 gives an uncertainty estimate of 0.024 mGal, which is a slight underestimate.

- There is excessive structure or noise at shallow levels associated with topography.
 - This is a common problem for gravity data and indicates that terrain correction has not been applied, or has been applied using an incorrect correction density, or that the mesh cell sizes and supplied topography data do not adequately reproduce the actual topography.

- If positive density anomalies correlate with topography then terrain corrections should be applied using a lower correction density. If topographic features correlate with density contrast lows, then a higher terrain correction density needs to be used.

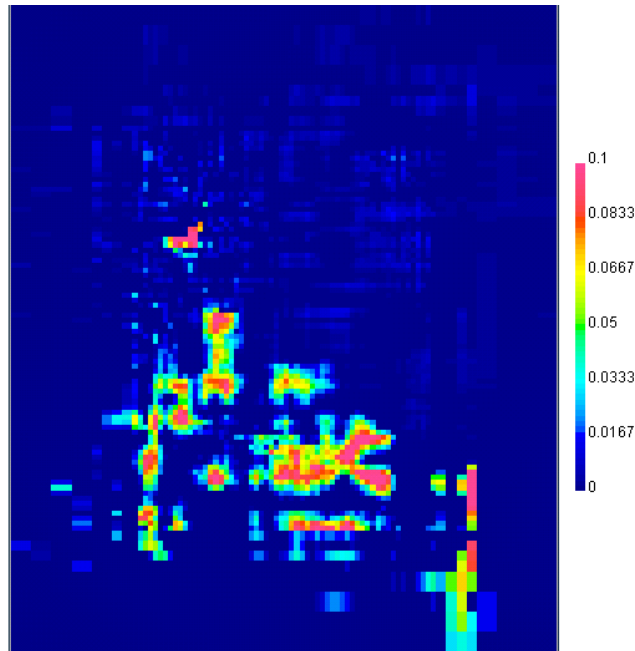


Figure 3.10. Example of the linear or checkerboard artefacts than can occur at depth within a model when there is too much compression of the sensitivity matrix. The displayed horizontal slice is from near the bottom of a magnetic inversion result.

- If there are no obvious problem areas like those outlined above, assess whether the model has the right overall character. Based on the assumptions and expectations outlined in Section 3.3.1, the model should be moderately smooth, without large property variations over short distance, but should also contain obvious geological structure. Due to the behaviour of potential fields it is expected that the resolution will decrease with depth
 - If there are unrealistic variations in properties that do not look geologically feasible (Figure 3.9D) then:
 - Increase the alpha coefficients/lengths scales to promote more smoothness.
 - Increase the allowed data uncertainty or *chifact* parameter.
 - If the model is too smooth and contains little structure (Figure 3.9A) then:
 - Decrease the alpha coefficients/length scales to promote a model that is less smooth.
 - Decrease the allowed data uncertainty or *chifact* parameter.

- If everything outlined above is acceptable, then the model represents one acceptable explanation of the observed data.
 - If the inversion was a regional-scale inversion for calculating the regional contribution to a local data set, then attempt to improve the result, if possible, by trying some of the steps outlined in Section 3.8 and 3.8.2 before following the regional-removal procedure outlined in Section 3.5.4.
 - If the inversion was a local-scale problem, then continue to improve the quality of the result and understanding of the range of possible results by following the steps outlined in Section 3.8 and 3.8.2.

3.8 SUBSEQUENT INVERSIONS

Having recovered a single model that explains the observed geophysical data and adequately satisfies the mathematical constraints of smoothness and closeness to a reference model, it is important to develop an understanding of the range of models that are possible. Commonly small changes in some of the inversion parameters can give strikingly different models, and a range of models can be developed using a range of parameters. The gathered suite of models provides an understanding of the uncertainty in the models. Features that are present in a range of models regardless of what parameters are used are likely to be more reliable than features that are only present in individual models. These dominant features are more strongly controlled by the data than by the mathematical parameterisation.

Whether recovered inversion models provide a reliable and accurate solution to the problem being addressed can really only be assessed by comparison of the models to some prior knowledge or expectation. Such assessment will be based on what property distributions are geologically reasonable, what geometries are acceptable, and what the range of physical properties is expected to be. In many problems, investigation of the suite of possible models will indicate that certain characteristics of the expected geology cannot be recovered by adjusting only the inversion parameters. Instead this prior knowledge must be formulated into a set of geological and physical property constraints on the inversion. These constraints will be covered in Section 3.8.2.

3.8.1 Adjusting inversion parameters

Although the inversions are controlled by a large number of parameters, there are only three sets that may benefit from routine adjustment to refine an inversion model. All broadly influence the trade-off between recovering a highly structured model containing lots of noise, and a model that is excessively smooth and lacks detail. They are listed below in decreasing order of importance. Making adjustments in this order will provide the most efficient method for obtaining a suite of suitable models based only on mathematical constraints. The resulting changes are better understood when only one parameter is changed at a time. Doing so will quickly identify which parameters have the greatest influence on the recovered models for a particular problem.

Some users of the inversion codes have found that adjusting the depth weighting parameters can give recovered models that are more consistent with their expectations. Such adjustments are not usually recommended and are not discussed in this workflow. The recommended distance weighting style of depth weighting is carefully designed to reproduce the theoretical decay of a potential field response with increasing distance from observations. It is based on the physics of potential fields. If the recovered depths and heights of source features are deemed to be unreliable or inaccurate, this indicates that the interpreter has some additional knowledge about the distribution of source features or the three dimensional geological architecture that should be included as geological constraints. Supplying appropriate constraints instead of “fudging” depth weighting parameters is more reliable, more robust, and more controllable.

Misfit and trade-off parameters

The amount of detail and structure present in the recovered property models is primarily controlled by how closely the recovered model reproduces the observed data. As discussed above, the observed data are assumed to contain a specified level of uncertainty, but the degree of uncertainty can be difficult to quantify and may vary from problem to problem even with similar data. Decreasing the specified level of uncertainty in the observed data will result in more structured models, but that additional structure may be a manifestation of noise in the data (Figure 3.9). Typically the misfit and trade-off parameters should only adjusted if there is doubt in the specified data uncertainties.

If the problem uses high resolution data and is designed to delineate small target anomalies which may have subtle geophysical responses, then the extra structure might be critical in satisfying the inversion goals, but too much will lead to a large number of false positive targets that are a manifestation of noise in the data. The reliability of these small targets must be assessed relative to the expectations for the potential field data being used: small targets at great depths are unlikely to be represented in potential field data. Other applications may seek to identify the broad trends and geometries in a model, and the results can be significantly easier to interpret if the model only reproduces the major features.

- To increase the amount of structure recovered by the inversion set the inversion mode to *chifact* and specify a value < 1 . This effectively multiplies the specified data uncertainties by this new *chifact* value, decreasing the uncertainty and resulting in a closer reproduction of the observed data.
 - When checking if the inversions acceptably reproduced the observed data at the new data uncertainty, the reported achieved misfit should be approximately equal to the number of observations times the specified *chifact* value.
- To decrease the amount of structure recovered set the inversion mode to *chifact* and specify a value > 1 . This effectively multiplies the specified data uncertainties by this new chi factor value, increasing the uncertainty and resulting in a lesser reproduction of the observed data.
 - The achieved misfit should be approximately equal to the number of observations times the specified chi factor value.

Alpha coefficients / length scales

If the data uncertainty is fairly well understood, the amount of smoothness observed in the model can be adjusted to increase or diminish the recovered detail of the model. As discussed in Section 3.6.3, smoothness can be controlled by sets of alpha coefficients or length scales. These parameters provide the most flexible and dramatic way to modify a model that has well defined data uncertainties.

Alpha coefficients are applied directly to the smallness and smoothness components in the model objective function used to seek the optimal solution. Length scales are a higher level representation of the alpha coefficients, and are converted to appropriate alpha coefficients in the inversion. Alpha coefficients are related to length scales by the following equations:

$$\alpha_e = \alpha_s (L_e)^2, \quad L_e = f_e \cdot \Delta E = \sqrt{\frac{\alpha_e}{\alpha_s}} \quad 3.18$$

$$\alpha_n = \alpha_s (L_n)^2, \quad L_n = f_n \cdot \Delta N = \sqrt{\frac{\alpha_n}{\alpha_s}} \quad 3.19$$

$$\alpha_z = \alpha_s (L_z)^2, \quad L_z = f_z \cdot \Delta Z = \sqrt{\frac{\alpha_z}{\alpha_s}} \quad 3.20$$

where f is some factor of the cell dimension (usually recommended to be 2-5), and ΔE , ΔN , ΔZ , are the east-west, north-south, and vertical dimensions of cells in the centre of the mesh.

- Higher values for α_e , α_n , and α_z (and consequently L_e , L_n , and L_z) will create a smoother model. Increasing one or two of the values will cause greater smoothness in those directions allowing a simple way of recovering broad geological trends.
- The actual value of α_s is not important, only its value relative to α_e , α_n , and α_z .
- One approach that is useful for defining appropriate length scales for a particular problem is to consider the aspect ratio associated with geological units within the model.
 - Choose an approximate aspect ratio that reflects the expected geological geometry and the relative dimensions of geological units in each direction. Some examples are:
 - Small spherical bodies would have the default E-N-Z aspect ratio of 1:1:1.
 - A layered earth might have geological units that are 10 times wider in the east-west and north-south directions than they are tall. This suggests an E-N-Z aspect ratio of 10:10:1.
 - If the geology is elongated in the north-south direction relative to the east-west and vertical directions, it might have an E-N-Z aspect ratio of 2:10:1.
 - If the geology has a steep dip then an aspect ratio of 1:10:5 might be appropriate.
 - To calculate the appropriate length scales to use for a desired aspect ratio use the following equations (from Chapter 2):

$$L_e = A_e \cdot 2\Delta E \quad 3.21$$

$$L_n = A_n \cdot 2\Delta N \quad 3.22$$

$$L_z = A_z \cdot 2\Delta Z \quad 3.23$$

where A is the desired aspect ratio in each direction.

- Applying an aspect ratio of 2:10:1 to cells sizes $\Delta E = 50$ m, $\Delta N = 50$ m, $\Delta Z = 25$ m, gives length scales of $L_e = 200$, $L_n = 1000$, $L_z = 50$.
- An alternate method uses an empirical rule of thumb to estimate the minimum f value for defining an appropriate length scale in a particular direction as per equations 3.18-3.20:

$$f_e \geq \sqrt{\frac{4r_e}{\Delta E} - 14}, \quad r_e \geq 4.5 \cdot \Delta E \quad 3.24$$

where r_e is the maximum east-west distance over which the properties of two cells might be related, and ΔE is the east-west cell dimension. In geostatistical terms r_e represents the range of correlation between the property estimates in the east-west direction. Equation 3.24 can be applied in the north-south and vertical directions to estimate f_n and f_v .

- Example: If properties are expected to be weakly correlated up to 500 m east-west and the cells are 50-m-wide in that direction then $f_e \geq 5.1$ should be used. This is a minimum estimate; higher values of f_e might be required to recover the expected strike continuity.
- The minimum amount of smoothness possible is defined by the size of individual cells, implying length scales equal to the cell widths and f factors = 1. For this reason using $f < 2$ will have negligible impact.
- Although using large length scales ($f > 2-5$) or alpha coefficients will tend to recover a smooth model, the model must always explain the observed data, so regardless of how much smoothness the parameters may define, the model will contain as much detail and roughness as is necessary to reproduce the data.

Sensitivity compression

As described in Section 3.6.5, wavelet compression is used to decrease the size of the sensitivity matrix and to speed the inversion process. Usually the default settings work well, but in some problems, especially with large depth extents, the sensitivity compression can introduce a large amount of excess noisy structure at depth (Figure 3.10). If there is difficulty finding an appropriate balance of data uncertainties, trade-off parameters, and smoothness weights that doesn't produce a great deal of unrealistic structure at depth in the models, try reducing the amount of compression used. The result may be dramatically smoother despite all other parameters being constant. Doing so will significantly increase the computing resources required and decrease the speed of the inversions.

- To test if compression is introducing errors in the modelling:
 - Calculate the exact data response associated with the problematic model using the GZFOR3D/MAGFOR3D programs given the model, mesh, observation locations, and topography.
 - Compare the exact forward modelled response to the predicted response produced during the inversion ('gzinv3d.pre' or 'maginv3d.pre'). This predicted response includes the sensitivity compression and although not the exact potential field response, it should be very similar. Any differences between the two are errors introduced by the sensitivity compressions. If the differences are significant, then the amount of sensitivity compression needs to be reduced.
- To reduce the amount of compression:
 - Open an existing sensitivity calculation log file and find the value reported for 'Estimated relative threshold' near the end of the file ('gzsen3d.log' or 'magsen3d.log').
 - Under the 'Wavelet compression' section of the inversion GUI, select 'user' and 'relative threshold' and enter a new relative threshold value that is up to one order of magnitude less than the value reported in the log file.
 - Run the sensitivity calculation and inversion as normal.
 - Because of the large increase in resources required, the sensitivity calculation may fail to complete due to out of memory errors. If this occurs, increase the assigned relative threshold value slightly towards the value reported in the original log file, and try again.

3.8.2 Restarting an inversion

Occasionally an inversion may end prematurely due to power outages, computer crashes, or user intervention. For large time consuming problems it may be desirable to start the inversion from where it left off. Restarting an inversion is only possible if the sensitivity matrix was calculated completely and saved in the inversion directory ('gzsen3d.mtx' or 'magsen3d.mtx') and if a valid model file ('gzinv3d.den' or 'maginv3d.sus') was also saved at some intermediate point during the inversion. If these files exist the inversion can be restarted.

- To restart an inversion:
 - Open the 'gzinv3d.log' or 'maginv3d.log' file and identify the last recorded value for 'multiplier'.

- In the inversion directory where the control files were saved, rename the existing unfinished ‘gzinv3d.den’ or ‘maginv3d.sus’ model file to ‘initial.den’ or ‘initial.sus’.
- Open the inversion control file in the inversion GUI.
- In the initial model box, select ‘file’ and identify the new ‘initial.den’ or ‘initial.sus’ file.
- In the ‘Mode’ box select ‘constant tradeoff’ and enter the value of ‘multiplier’ identified in the log file.
- Run the inversion. It will restart where it left off.

3.9 INCORPORATING GEOLOGICAL CONSTRAINTS

Once appropriate parameters have been defined for a particular inversion problem, the most powerful technique for enhancing the reliability of the recovered models is to include constraints based on geological observations and interpretations. Use of such constraints will require that the inversion is consistent with prior knowledge or expectations of the geology and physical properties where available, in addition to the usual requirements of explaining the data and satisfying the smoothness and smallness requirements. An example of the results that can be obtained by including simple geological constraints is shown in Figure 3.11.

Geological constraints can be defined using two different approaches depending on the type of problem to be addressed and the type of information available. The first is a hypothesis-testing approach in which a hypothetical model is built based on an interpretation of positions, geometries, and physical properties of the major features within the model volume. Physical property models recovered from inversions constrained in this way are assessed to see if the supplied constraints are consistent with the observed geophysical data. The second approach is a data-based approach which supplies constraints based only on actual geological observations and uses the inversions to predict what physical properties are required in the remaining areas to explain the observed geophysical data. Both approaches provide powerful ways of improving geological knowledge of the subsurface.

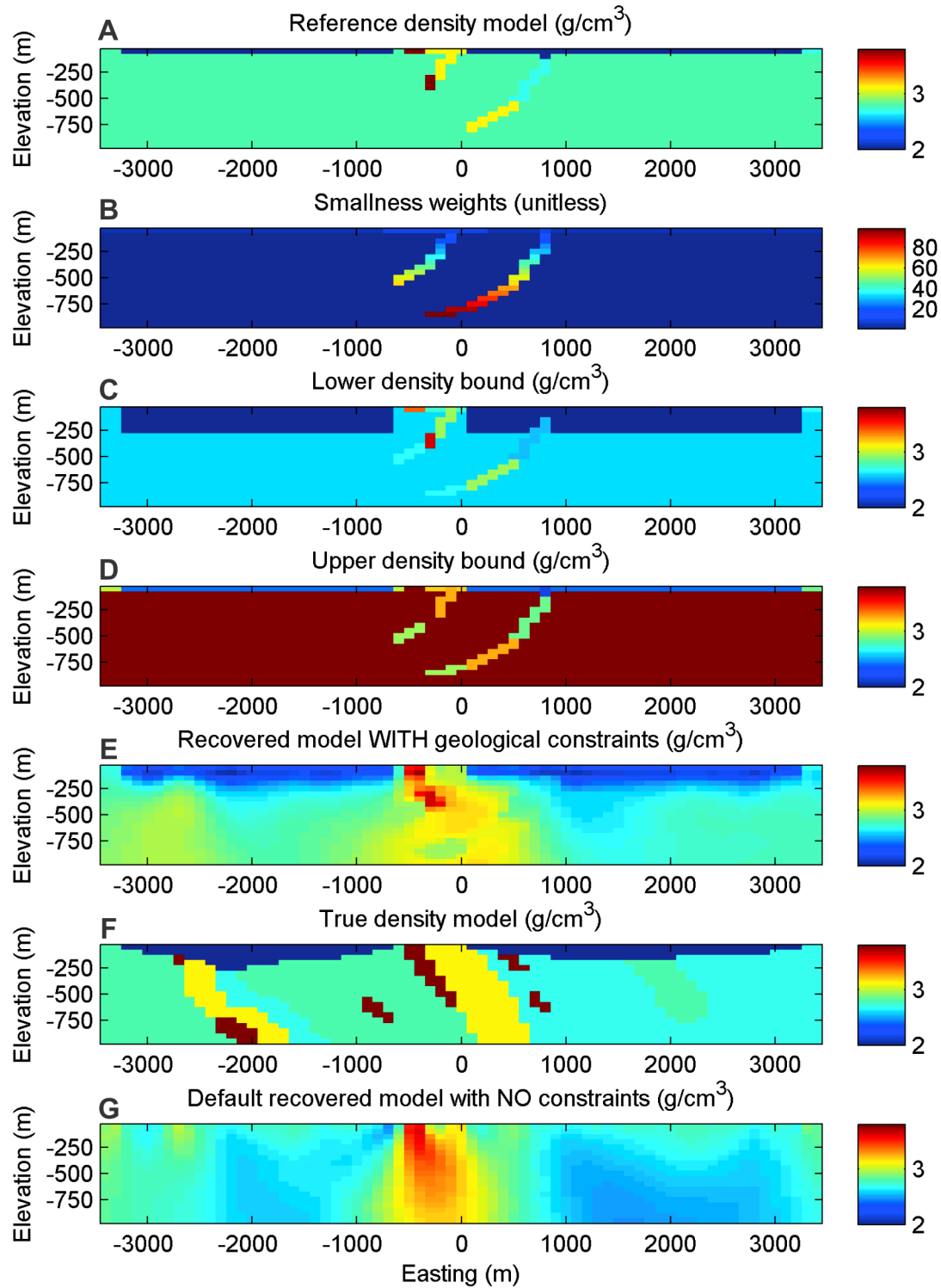


Figure 3.11. A synthetic example (from Chapter 2) demonstrating the use of geological constraints from surface mapping and two drill holes using the data-based, smooth model style of constraints. All images are vertical slices through the centre of a 3D model. The reference model, smallness weights and bounds constraints are shown A-D; non-default values are assigned along the map surface and the two drill hole traces and default values used elsewhere. The geologically constrained inversion result is shown in E. Comparison of the result with the true density model (F) and the default result obtained without geological constraints (G) shows that the constraints have dramatically improved the quality of the result. There is better representation of the near-surface low density features and enhanced resolution of the anomalous densities in the centre of the model.

3.9.1 How constraints are implemented

There are three ways in which geological constraints can be implemented in the UBC–GIF codes and the methods are the same for both magnetic and gravity inversions. The different implementations handle different forms of knowledge about the geology and physical properties within the model and can be used in any combination to suit the specified inversion goals. The required file formats for the constraints are defined in detail in the UBC–GIF GRAV3D and MAG3D user manuals (UBC–GIF, 2005a, b).

Reference property model and smallness weights

A reference property model defines the best estimate of the arithmetic mean physical property of rocks contained in each model cell based on prior knowledge. The model objective function that defines the optimal character of the recovered inverse model includes a measure of how closely the recovered model matches the supplied reference model. In default inversions that lack geological constraints, this reference model is usually zero everywhere and therefore contains no structure. A recovered model that satisfies the requirement of matching the reference model as closely as possible will therefore contain as little structure as necessary to reproduce the observed geophysical data.

If a non-uniform reference model is supplied, the result can be very different – structure in the reference model will be reproduced in the recovered model if it is consistent with the geophysical data. Reference models therefore provide a powerful method of defining the values of properties expected within each cell and how those properties vary throughout the model. Reference models act as a soft constraint on the inversion because large deviations between the reference model and recovered model are allowed if necessitated by the geophysical data.

The reliability of the reference model is specified by assigning a smallness weight to every cell. The weights are unitless, unbounded values typically ≥ 1 . The default smallness weight is unity; higher weights promote a recovered model that more closely matches the reference model. The actual smallness weight values required to enforce a particular reference model are problem-dependent. They depend on the defined alpha coefficients / length scales, the data sensitivity and depth within the model, the relative smallness weights assigned to other cells, smoothness weights defined across cell faces, and a range of other factors.

- Reference model properties and smallness weights must be defined in some external modelling package.
 - Basic geometries, such as layered earth or block models, can be built within the Meshtools3D software.
 - More complex or geologically realistic models will typically need specialised modelling and data manipulation packages such as Gocad (Paradigm) or GeoModeller (Intrepid Geophysics).
- Due to the law of superposition for potential fields (Blakely, 1995), the desired reference property in each cell is the arithmetic mean for rocks within that cell. Note that for lognormal, skewed, or bimodal physical property distributions this may be somewhat different from the most common measurement value.
- Reference properties should be in the same units as the recovered model.
 - For gravity inversions they should represent apparent wet bulk density contrasts in g/cm^3 relative to the expected average density within the model volume.
 - For details on how determine an appropriate conversion from densities to density contrasts, see Section 3.9.2.
 - For magnetic inversions they should represent expected magnetic susceptibilities in SI.
- The smallness weights are defined together with smoothness weights in a single weighting file. Note that this weighting file currently cannot be identified within the MAG3D/GRAV3D GUIs, and must be manually specified within the inversion control file using a text editor.
- Initial smallness weights of 1-10 are recommended for cells containing constraints. If models recovered using these weights do not sufficiently reproduce the supplied reference model, increase the smallness weights or adjust the constraints.
 - Consider that the reference property assigned to a single cell with a smallness weight of 10 will have the same importance as 10 cells assigned a smallness weight of 1.
 - Since smoothness and smallness are relative, excessively large smallness weights will reduce the smoothness of the model and may require larger length scales / alpha coefficients.
- Different smallness weights should be applied to different types of constraints. Large volumetric interpretations may have a relatively low confidence, and so should use lower

smallness weights (e.g., 1-5). Constraints in cells that are well understood from mapping or drilling observations may warrant higher smallness weights (5-10).

Property bounds

The lower and upper bound on the allowed properties in any cell can provide the strongest constraints in a model if those bounds can be tightly defined. Bounds provide a hard constraint which cannot be violated regardless of how they affect a model's calculated misfit between the observed and predicted data. Bounds also reflect a common geological scenario where it is possible to define the range of properties expected, but not their average value. Uniform lower and upper bounds can be specified for the whole model, or the bounds can be specified differently in every cell via a two column input file.

- Bounds must be defined in some external modelling package.
 - Basic geometries, such as layered earth or block models, can be built within the Meshtools3D software.
 - More complex or geologically realistic models will typically need specialised modelling and data manipulation packages such as Gocad (Paradigm) or GeoModeller (Intrepid Geophysics).
- Bounds should be in the same units as the recovered model.
 - For gravity inversions they should represent apparent wet bulk density contrasts in g/cm^3 relative to the expected average density within the model volume.
 - For details on how determine an appropriate conversion from densities to density contrasts, see Section 3.9.2.
 - For magnetic inversions they should represent magnetic susceptibilities in SI.
- Since bounds are strictly enforced, they should only be tightly defined where they are well known. But these cells will be guaranteed to match the prior knowledge.

Smoothness weights

The final set of constraints allows inclusion of prior information about how properties are expected to change between cells within the recovered model. Smoothness weights can be defined for every individual internal cell face in the east, north and vertical directions: w_e , w_n , and w_z (Figure 3.12). The weights are unitless unbounded values ≥ 0 . Their default value is unity. Values > 1 promote smooth variation of properties between adjacent cells, and can be

used to indicate geologically continuous trends of relatively homogeneous properties. Values < 1 allow sharp changes in properties between adjacent cells if required by the data, and are useful for replicating sharp boundaries such as faults or geological contacts.

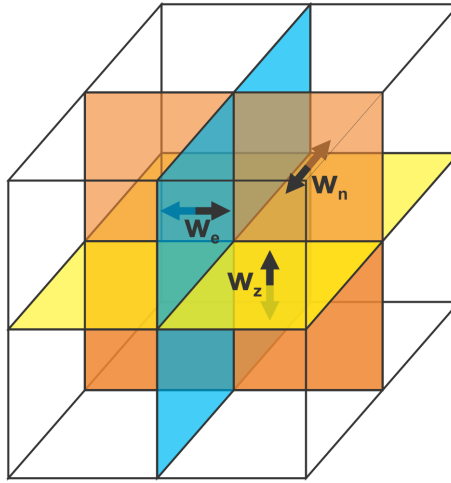


Figure 3.12. Smoothness weights are assigned to each internal cell face. In this $2 \times 2 \times 2 = 8$ cell cube, east-west w_e weights are assigned to 4 vertical blue faces, north-south w_n weights are assigned to 4 vertical orange faces, and vertical w_z weights are assigned to 4 horizontal yellow faces.

- It is useful to think of the weights as following a logarithmic scale.
 - A smoothness weight of 1 on a cell face will make smoothness across that face 10 times more important than the same amount of smoothness across a cell face assigned a weight of 0.1.
 - A smoothness weight of 10 on a cell face will make smoothness across that face 10 times more important than across a cell face assigned a weight of 1.
- The actual magnitude required (0.05 versus 0.01, 10 versus 20, etc.) will be influenced by many factors including the defined alpha coefficients / length scales, the data sensitivity and depth within the model, the smallness weights assigned to cells, the relative smoothness weights defined across other cell faces, and a range of other factors.
- Because smoothness weights are defined for each face, rather than each cell centre, they must be treated slightly differently from standard model formats. If the supplied mesh contains N_e cells in the east direction, N_n cells in the north direction and N_v cells in the vertical direction, then there will be:
 - $(N_e - 1) \times N_n \times N_v$ w_e weights associated with north-south oriented cell faces
 - $N_e \times (N_n - 1) \times N_v$ w_n weights associated with east-west oriented cell faces
 - $N_e \times N_n \times (N_v - 1)$ w_z weights associated with horizontal cell faces

- Smoothness weights are defined in the same file as the smallness weights used to enforce a reference model. If one set is to be specified then both must be specified. However, default smoothness weights of unity can be defined with non-default smallness weights, and vice-versa. Note that this weighting file cannot be identified within the MAG3D/GRAV3D GUIs, and must be manually identified within the inversion control file using a text editor.

3.9.2 Using constraints to define data levels

As discussed in Sections 3.5.3 and 3.5.4, it is important to establish appropriate data levels associated with the supplied geophysical data. However, to do this exactly would require knowledge of the actual gravity or magnetic response and data level of only that portion of the earth contained by the specified mesh. In general, subtracting the mean of the observed gravity or magnetic values from a dataset after a regional trend is removed provides a good estimate of the zero level associated with supplied data, relative to the volume of interest. For magnetic data, this can be further refined by identifying spurious “puddles” of high susceptibilities at the north or south end of the padding zones as shown in Figure 3.5 and Figure 3.6. For gravity inversions no such refinement is possible for default geologically-unconstrained inversions, and the resulting models of density contrast are relative to some unknown background average density which can only be guessed. Without any additional information, this is the best that can be achieved.

A more robust and conclusive result can be obtained if geological constraints are available. The constraints, posed as expected densities or susceptibilities, can provide a calibration to more accurately define the appropriate data level. They provide a direct link between the recovered density contrasts and susceptibilities and the actual densities and susceptibilities within the volume of interest, and therefore provide a means of estimating the actual geophysical response and data level of the portion of the earth contained by the mesh. For magnetic data, this refinement is achieved by including the constraints that estimate the actual susceptibilities in the inversion. This ensures that the recovered susceptibilities are representative of those that occur in the earth, making refinement of the data level as described in Section 3.5.4, Figure 3.5 and Figure 3.6 more accurate. The data level required may differ from the estimate made for the default geologically-unconstrained inversions results.

Densities, density contrasts, and data levels

For gravity data, the process is a little more complicated since changes in the data level can be accommodated by linear shifts in the recovered density contrasts and density constraints must be converted into appropriate density contrast constraints. The process is as follows and the results are demonstrated in Figure 3.13:

1. Ensure that the mean gravity observation has been subtracted from the supplied gravity data. This ensures that the data is directly related to the values within the mesh.
2. Prepare a set of reliable constraints using actual densities. Constraints from maps, which provide a near-surface layer of constraints, are particularly helpful for addressing this problem and will be used in the example below, but any type of constraints should work in a similar way.
3. Convert the constraint densities into density contrasts by subtracting an estimate of the actual mean density in the defined mesh.
4. Run the inversion as normal.
5. When completed, display the recovered density contrast model using various vertical slices.
 - If there are areas where the cells containing constraints appear to be biased towards higher values than the unconstrained cells (Figure 3.13A-B), this suggests that the density contrasts used in those constrained cells are too high. The inversion may compensate by adding surrounding regions with lower density contrasts. The specified data level requires that a higher background density be subtracted to convert the actual densities into appropriate density contrasts.
 - If there are areas where the cells containing constraints appear to be biased towards lower values than the unconstrained cells (Figure 3.13D-E), this suggests that the density contrasts used in those constrained cells are too low. The inversion may compensate by adding surrounding regions with higher density contrasts. The specified data level requires that a lower background density be subtracted to convert the actual densities into appropriate density contrasts.
6. Convert the constraint densities into updated density contrasts by adding or subtracting a new background density value and repeat the process. Typically adjusting the background

density in increments of $\pm 0.05 \text{ g/cm}^3$ is sufficient to identify an appropriate value. More detailed refinements of $\pm 0.01\text{--}0.02 \text{ g/cm}^3$ may be beneficial in some problems.

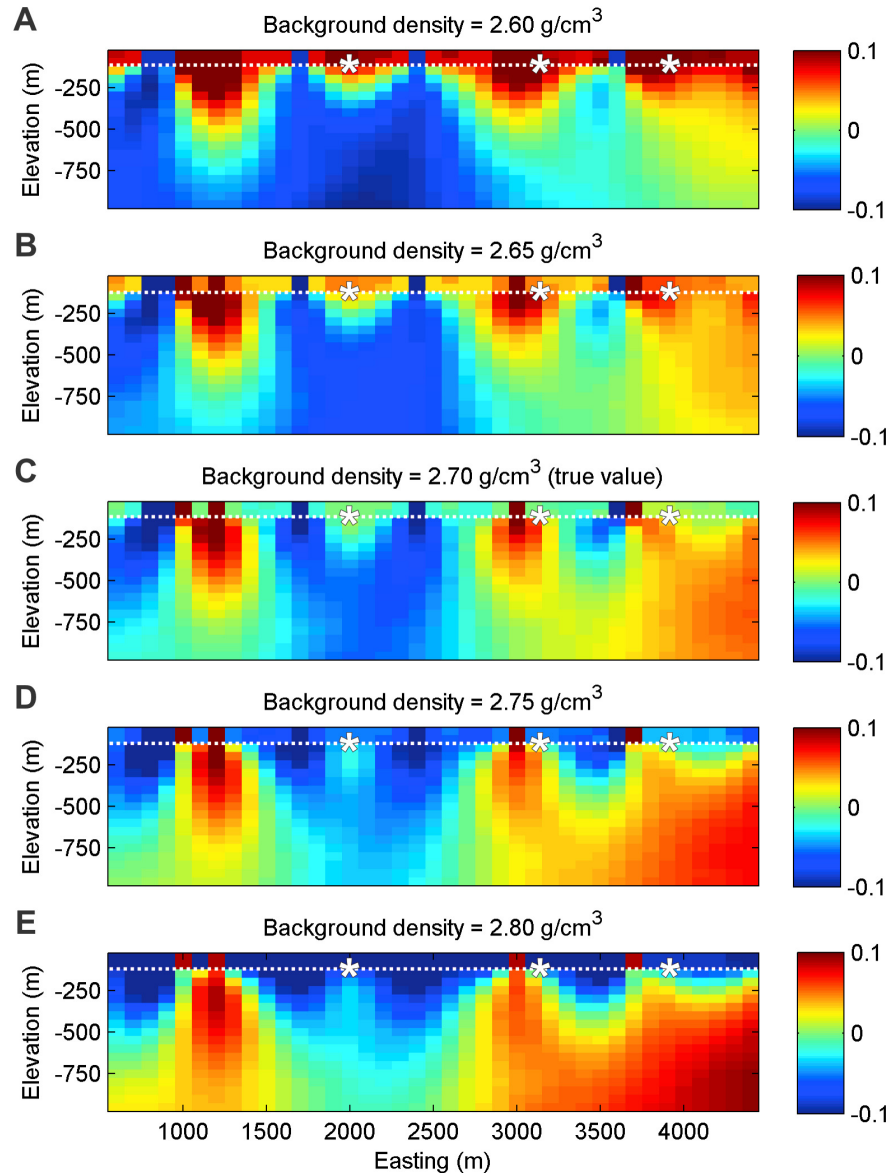


Figure 3.13. A synthetic example showing how an appropriate background density value for a model can be determined using map constraints. Images show vertical slices through five recovered density contrast models in g/cm^3 . Map constraints (implemented using a reference model, smallness weights, and bounds) are assigned in the top two layers of cells above the dotted white line; all cells below the white line were assigned default constraint values and were therefore unconstrained. All inversions were run with exactly the same gravity data (with mean value subtracted) and map densities. The map density constraints (notionally from density measurements) were converted into density contrasts for each inversion by subtracting the indicated background density value. By comparing the suite of recovered inversions, it is possible to estimate which of the background densities is the actual value appropriate for the supplied data and mesh. In A and B, the two map layers are biased to notably higher density contrasts than the layers immediately below. In D and E the two map layers are biased towards lower values than the layers below. In C, where the true background value was used, the map layers are sometimes higher and sometimes lower than the underlying layers. Locations marked with asterisks are particularly diagnostic of these relationships. The observation that the map constraints do not introduce a bias in C indicates the background density value of 2.70 g/cm^3 is likely correct.

7. An appropriate value is found where the constraints can be accommodated in the inversion without being compensated for by high or low density contrasts.
8. Once an appropriate background density value is found, it can be added on to the density contrasts recovered by the inversion to obtain an estimate of the actual densities.

3.9.3 Smooth model, or smooth model difference

The inversion codes actually include two very different ways of handling constraints supplied by a reference model. For any inversion which uses a uniform reference model the methods provide identical results. However, when a non-uniform reference model is used, a decision has to be made about how the reference model should be applied in the model objective function that quantifies the character of the recovered model. All of the constraints are defined in exactly the same way and with the same values, but get treated differently in each of the two methods.

Smooth model difference

This method was the only one available in earlier versions of the inversion programs (up to and including MAG3D v4 and GRAV3D v3). It specifies that the difference between the reference model and the recovered model should vary smoothly between cells (Figure 3.14). The smoothness weights specify how smoothly the difference between the recovered model and reference model should vary between adjacent cells.

- Choose the smooth model difference option where all cells within a model can be assigned reliable property estimates and blocks of cells with uniform properties are separated from each other by sharp contacts.
 - It is particularly well suited to the hypothesis testing approach outlined below, where the constraints are defined using a full 3D geological model.
- Models recovered by inversions using the smooth model difference method will usually recover very sharp property changes wherever there are changes in the reference property.
 - The inversion will not extrapolate properties outwards from constrained cells into cells without geologically-based constraints.

Smooth model

This is a recent addition to the inversion software introduced in MAG3D v5.0 and GRAV3D v4.0. With this method the model objective function specifies that the model properties themselves should vary smoothly between cells (Figure 3.14). Smoothness weights are used to define how smoothly the recovered model varies between adjacent cells.

- As the name implies, inversions using this method will tend to recover smoother models, but sharp property changes can still occur where required by the observed data, or where defined by other constraints.
- This method is the recommended method for the data-based approach to developing constraints. This approach places strong constraints only in those areas where the observations were made, and uses smoothness in the inversion to extrapolate those constraints out into cells for which no prior information is available.
- A slight modification of the smooth model style can be obtained by applying constraints only using bounds and a uniform zero reference model (Figure 3.14). The result maintains the smooth extrapolation of properties observed using the smooth model style, but also forces sharp changes in properties where properties are known to change as occurs in the smooth model difference style. This technique can also be applied to perform smooth model inversions in older versions of the inversion programs.

3.9.4 The hypothesis-testing approach to constraints

A hypothesis-testing approach supplies the inversion a full 3D model of constraints based on geological observations and interpretations to test the hypothesis that the interpretations are consistent with the geophysical data. Examples of such hypothesis testing inversions have been presented by McGaughey (2007), McInerney (2007) and Oldenburg and Pratt (2007). Typically a qualitative assessment of the result is made based on how far the recovered inversion model deviated from the supplied interpretations in order to explain the observed geophysical data. Large deviations indicate that the model might need to be adjusted to better explain the geophysical data, whereas small deviations indicate that the model may be consistent with the geophysical data. By testing different sets of interpreted constraints over a number of iterations, those interpretations that are not supported by the geophysical data can be identified and discarded.

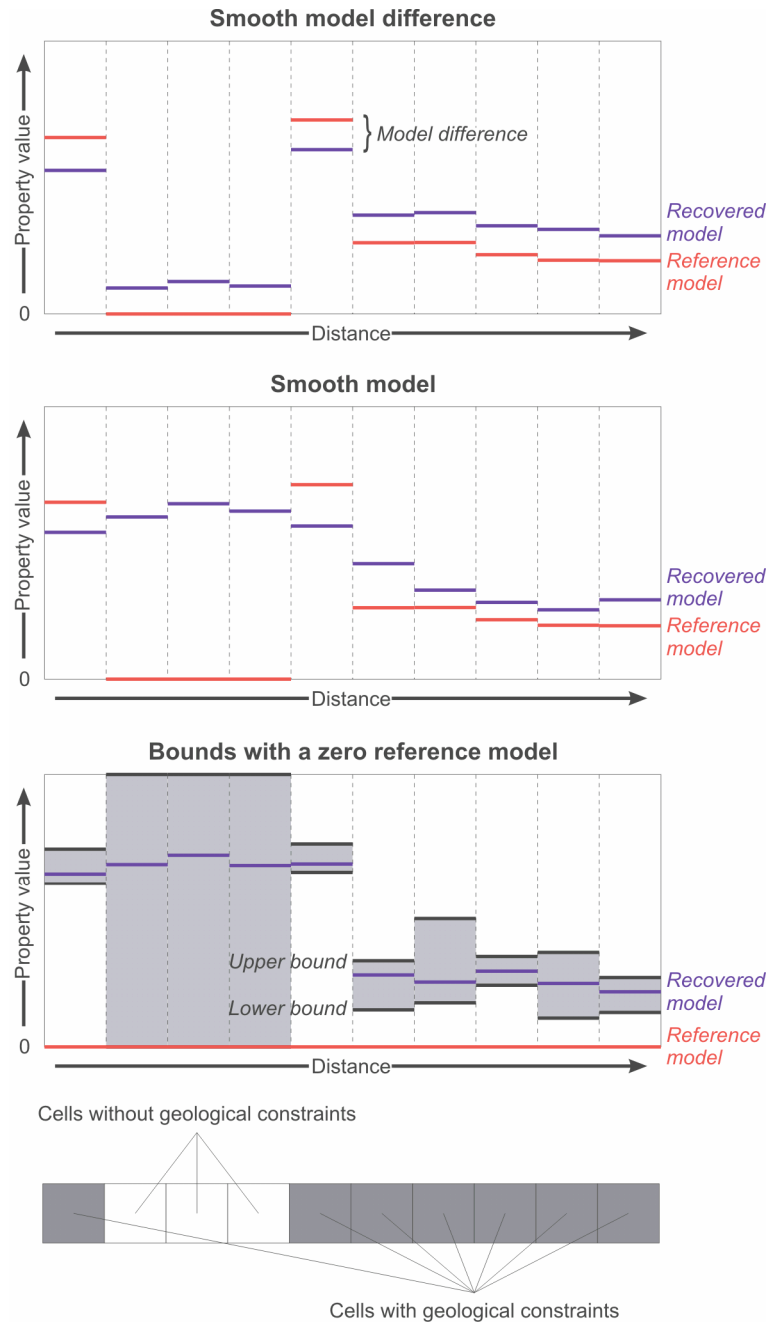


Figure 3.14. Schematic examples of the impact of various styles of constraints on an inversion. Ten cells are shown: seven contain observations warranting physical property constraints and three have no information as depicted at the bottom of the figure. Above are three graphs plotting the constraints in the form of either a reference model (red lines) or bounds (grey boxes indicate the property range allowed by the bounds defined in black lines), versus the recovered model (blue lines) that might be recovered using those constraints. In smooth model difference inversions, the difference between the reference model and recovered model will vary smoothly between cells which can cause large changes in recovered properties where the reference model changes. Smooth model inversions recover a model that is smooth throughout while matching the reference model as closely as possible. By using bounds instead of a non-zero reference model it can be possible to recover a smooth model that also contains sharp property changes where defined.

- This approach is best suited to problems where there is good 3D understanding of the likely geology and property distribution that needs to be verified.

- Observations and interpretations need to be developed into a 3D geological model in some external modelling package, and then translated into appropriate constraints for use in the inversion.
 - There may be a large time commitment required for geological interpretation and model building prior to running any geologically-constrained inversions.
- Although difficult and time consuming to develop, this approach facilitates testing of the geophysical viability of many geological ideas within a single model.
- Since constraints will usually be based on a 3D model defining the geometry and extent of discrete geological bodies separated by faults or contacts, this approach will usually use the smooth model difference style of inversion. This will recover sharp property changes wherever properties change in the reference model.
- Typical constraints for such a model will consist of the following components:
 - A reference model with an estimate of expected average properties in every cell,
 - A model of smallness weights defined in every cell. These will commonly be set to a uniform, relatively low value (> 1) in all cells that are based only on interpretations, especially at depth where there is little ground truth. High smallness weights should be reserved for those areas where there are reliable observations.
 - A non-default bounds model may be used, however it must be carefully specified because the constraints for many cells will be poorly defined and will not warrant the strict control imposed by bounds. Employing tight bounds over much of the model will only serve to reinforce a particular model even if there are more likely alternatives.
 - Non-default smoothness weights will not usually be necessary as the reference model will contain all the available information about where properties are relatively uniform and where they change sharply between geological units.
 - One exception is where the positions and orientations contacts and faults are defined but the physical properties of the intervening rocks are poorly understood. In this situation a uniform physical property model could be used with default smallness weights. Smoothness weights < 1 can be applied to cell faces that coincide with faults and contacts to recover blocks of relatively homogeneous properties separated by sharp property contrasts.

Suggestions for preparing constraints in Gocad for hypothesis-testing inversions

The challenge of creating full 3D geological models requires advanced 3D modelling software. The Gocad modelling package (Paradigm: <http://www.pdgm.com>) is often recommended because of its specialised capability in constructing geological models, and its available links to the UBC–GIF inversions software through the Mira Geoscience Gocad For Mining add-on (<http://www.mirageoscience.com>). Instruction on how to create models in Gocad and Gocad For Mining is beyond the scope of this workflow, but this section contains advice on how to effectively extract a Gocad 3D geology model consisting of surface-bounded geological bodies into UBC–GIF inversion constraints using the Gocad For Mining add-on. Figure 3.15 shows an example where bounding surfaces have been used to assign values to cells associated with different geological units.

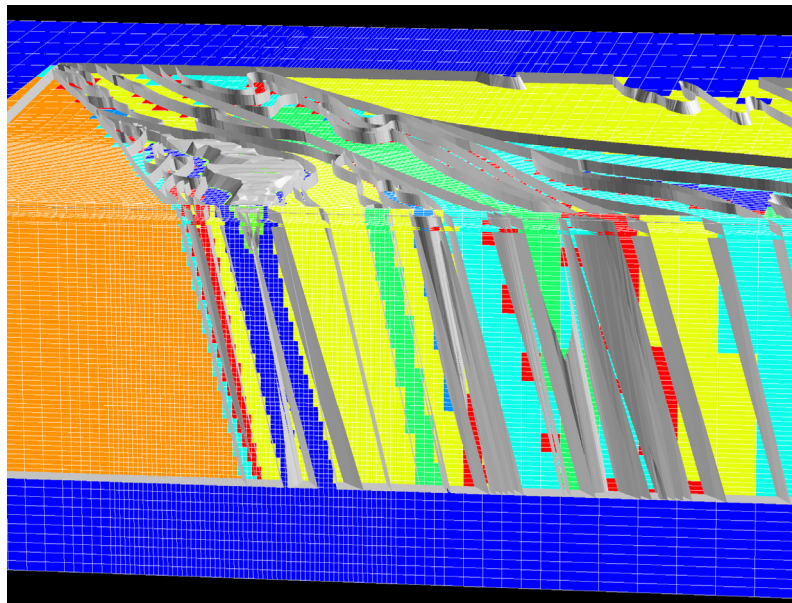


Figure 3.15. Example of bounding surfaces used to create a constraining reference model in Gocad. The surfaces (grey) divide the mesh into regions of cells in which an expected property can be defined. Blue cells lie outside the model and so are assigned default reference model properties and smallness weights. Note that the quality of the reference model derived from the surfaces depends on the relative size of the cells (outlined in white) and the thickness of the units. Towards the right of the model the cells are too large to adequately represent the interpreted geology, resulting in a blocky model.

- It is recommended that Gocad models be constructed with a single triangulated surface separating each geological package or unit. This means that each geological unit is not a self-contained entity that can be “turned on and off”, but its shape depends directly on the geometries of the adjacent units.

- This makes the model easier to update. Modifying a contact or fault only requires adjusting one adjoining surface rather than a pair of bounding surfaces.
- It also dramatically simplifies translation of the model into UBC–GIF constraints.
- The model should be constructed at an appropriate scale for the size of cells being used in the inversion mesh. Models containing geological bodies that are < 1-5 cells wide are difficult to manipulate and translate into constraints.
- Bounding surfaces must be “watertight” so that they exactly seal the enclosed volumes. This can be achieved by building the surfaces so that they extend beyond their desired boundaries, and then cutting one surface by another surface (Surface->Tools->Cut) and removing unwanted parts (Surface->Tools->Part->Delete Selection).
- Import the desired inversion mesh into Gocad using Gocad For Mining’s Potential Fields feature.
 - If the mesh has uniform cells throughout it can be imported as a Voxet (recommended) or an SGrid.
 - If the mesh contains variable cell sizes it must be imported as an SGrid.
- Create two properties on the imported mesh:
 - *ref*: used to assign the reference model physical properties. Set the default value appropriately – usually to zero density contrast or SI.
 - *ws*: used to assign the smallness weights indicating the confidence in the assigned reference model property for each cell. Set the default value to 1.
- There are two methods that can be used to translate surface-bounded volumes into discretised mesh regions. Each region will be a blocky representation of the geological unit and can be assigned properties associated with that unit. An automatic method exists which creates a single region of cells in the mesh for every volume of cells enclosed by the bounding surfaces. For many problems this is the best approach, and it can be applied to both Voxets and SGrids. For some problems, more control may be required, especially if there are relatively small geological units, or if only a small number of the geological model units need to be turned into regions. For these problems there is a manual method which allows the user to interactively create the regions one at a time. The manual method only applies if the mesh is represented as a Voxet, not an SGrid.
 - For the automatic method, turn on all of the bounding surfaces that will be used to divide the model into geological units. Use the command Voxet->Model3d-

- >AddSurfaces or SGrid->Model->FromSurfaces to define which surfaces should be used to build all the regions; selecting the inversion mesh, and the all the bounding surfaces. To actually create the regions use the Voxet->Model3d->Build or SGrid->Model->Build command on the selected mesh and turn off any check box options shown. A number of regions will be created on the inversion mesh. The regions can be merged if required (Voxet/SGrid->Region->Union). If there are many small regions consisting of only a few cells, they can automatically be joined to adjacent units by using the Voxet/SGrid ->Region->Filter->Automatically command.
- For the manual method, use the Voxet->Tools->CutWithSurfaces command and select all the bounding surfaces to be used, and the inversion mesh. Make the Voxet visible and turn on some sections through the mesh. Right-click on the Voxet name in the Object list tree in the panel on the left, and select 'Attributes'. On the 'Graphic' tab, turn on the 'Visible' check box under 'Cut lines on planes'. Green lines will be visible on the Voxet sections indicating where they are cut by the bounding surfaces. The volumes bounded by green cut lines represent cohesive rock packages. To create a discrete Voxet region from one of these volumes use the Voxet->Region->FromSeed command, assign the region a name, and then click on a Voxet cell that lies within the desired region. All cells contiguous with the selected cell will be assigned to the new region.
 - If the number of regions created by these methods is less than expected, it is likely that the surfaces are not “watertight”.
 - Once regions have been defined, use the Voxet/SGrid->Property->SetConstant command to assign desired reference property and smallness weight values to every region.
 - If it is desirable to assign low smoothness weights across defined fault or contact surfaces to allow sharp changes in properties across those surfaces, it is useful to base the weights on the orientations of the surfaces. A shallowly-dipping north-south trending fault surface will be smooth in the north-south direction ($w_n \geq 1$) but may have a sharp change in properties in the east-west and vertical directions (w_e and $w_z < 1$). An example is shown in Figure 3.16. Gocad automatically calculates the normal vector for every node on every triangulated surface and this can be utilised in the following way.

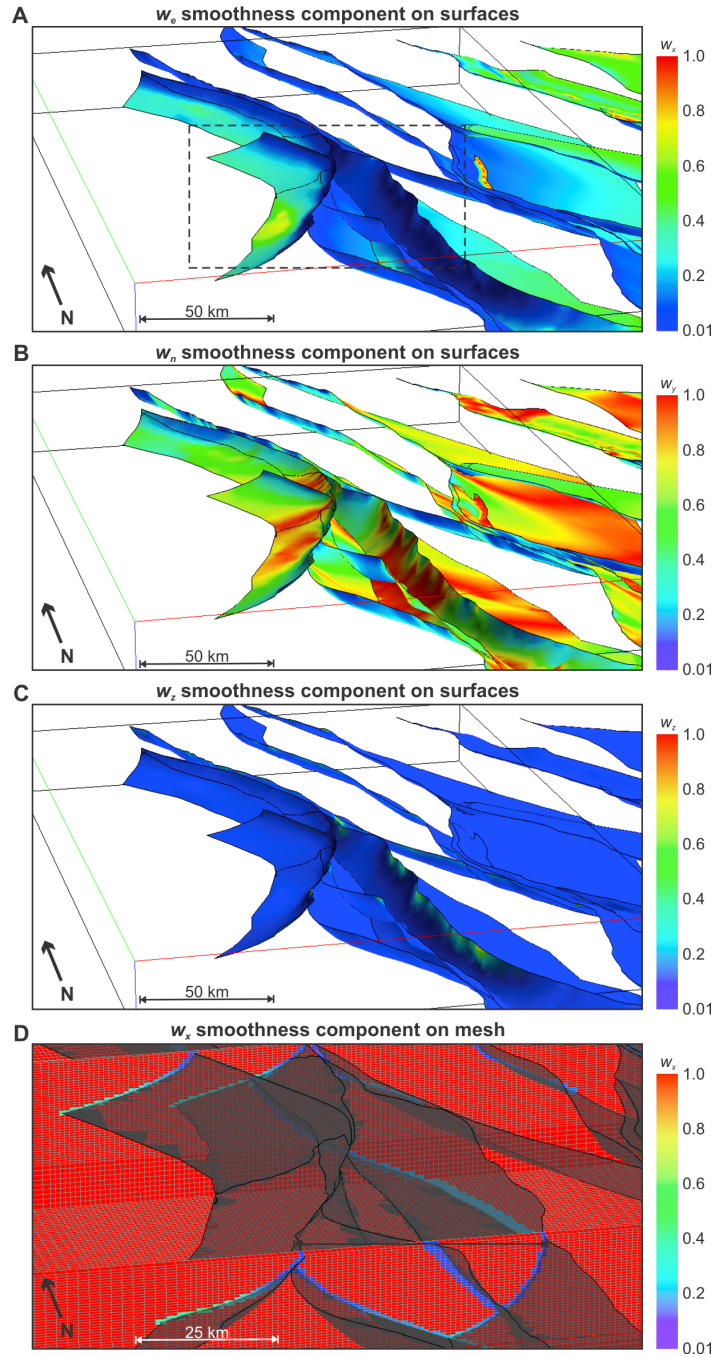


Figure 3.16. Assigning smoothness weights to a mesh based on the positions and orientations of interpreted fault surfaces in Gocad. The faults surfaces are from a regional-scale 3D model based on seismic reflection profiles and structural interpretation in the northern Yilgarn Craton of Western Australia (Henson and Hitchman, 2004). The surfaces were assigned a total smoothness weight of 0.01 (*weight* in equation 3.25) parallel to their normal vector. Equation 3.25 was used to calculate the east, north, and vertical (z) components of that smoothness weight as shown in A-C. Higher values occur where the faults are parallel to the component direction and low values occur where the faults are perpendicular to the component direction. As the faults generally trend north with shallow dips, the smoothness weight components are highest (smoother) north-south and lowest vertically (sharper). The values on the surfaces are painted onto the w_e , w_n , and w_z meshes. The populated w_e mesh is shown on several slices in D, zoomed in to the area outlined by the box in A. Along the faults the values increase where the faults become flatter. The values in red are the default values of 1 where there are no modelled faults.

- Create a set of three offset meshes with cells that are centred on the cell faces of the original inversion mesh. This is easy to accomplish for meshes with uniform cell sizes by making three copies of the original mesh file and using a text editor to edit the mesh definitions:
 - w_e mesh: subtract 1 cell off the original mesh in the east-west direction, and add half a cell width to the original origin easting.
 - w_n mesh: subtract 1 cell off the original mesh in the north-south direction, and add half a cell width to the original origin northing.
 - w_z mesh: subtract 1 cell off the original mesh in the vertical direction, and subtract half a cell width from the original origin elevation.
- Import the three offset meshes into Gocad as either Voxets (recommended) or SGrids.
- For each mesh create a single property corresponding to the meshes use, either w_e , w_n , or w_z .
 - Set the default values of all three properties to 1 for all cells in all three meshes.
- Create a new single surface from all the individual surfaces that need to be painted into the smoothness weight model. Use the Surface->New->Surfaces command and selecting all of the desired surfaces.
- Create four properties on this new combined surface:
 - *weight*: this overall smoothness weight will indicate how sharply properties might change between two cells perpendicular to the surface, e.g. 0.1 or 0.01.
 - w_e , w_n , and w_z : these will be assigned the relevant components of the overall smoothness weight for the surfaces in each of the three orthogonal directions (Figure 3.16A-C).
- A formula can be used to calculate the directional components of the smoothness contrast across a bounding surface:

$$w_{\phi} = 10^{n_{\phi} \log_{10}(\text{weight})} \quad 3.25$$

where w_{ϕ} is the smoothness in the ϕ direction (e – east, n – north, z – vertical) and n_{ϕ} is the smoothness component in the ϕ direction. This gives a range of values for each component from 1 when the surface is parallel to the specified direction to *weight* when the surface is perpendicular to that direction.

- The formula can be applied to the *we*, *wn*, and *wz* properties of the surface by selecting Surface->Compute->OnObject, identifying the new all-in-one surface, and entering these three commands in the main script box:

`we = pow(10,fabs(normal[0]) * log10(weight));` 3.26

`wn = pow(10,fabs(normal[1]) * log10(weight));` 3.27

`wz = pow(10,fabs(normal[2]) * log10(weight));` 3.28

- In Gocad, the notation `normal[n]` accesses the *n*th component of a vector quantity, in this case the surface normal vector. The property `normal` is calculated automatically for any surface in Gocad.
- With the smoothness weights now assigned to the surfaces, the values need to be “painted” into the appropriate mesh cells (Figure 3.16D). Use the command Voxet->Property->PaintWithSurface or SGrid->Property-AveragePaint (if using the AveragePaint command, set ‘Mean computation type’ to ‘arithmetic’). Ensure that all three check boxes for ‘Nodes’, ‘Segments’, and ‘Triangles’ are on. The command will need to be applied three times, once for each of the three meshes. Be sure to select the appropriate weight property for each mesh (*we*, *wn*, *wz*).
- The completed reference model and weight models can be exported using the Gocad For Mining UBC-GIF->CreateFiles menu.

Evaluating hypothesis testing inversion results

- Hypothesis testing inversions can only be assessed by comparing a suite of slightly different models.
 - Features that are common to many inversion results using a range of different reference models are likely to be real.
 - Features that are only present in some results are not likely to be essential to explain the geophysical data. They may be present but lack the necessary data sensitivity to resolve them accurately, or they may be artefacts that are introduced to compensate for erroneous constraints elsewhere in the model.
- Each recovered model must be compared to the supplied reference model to identify differences. Differences between the reference model and the recovered model may indicate discrepancies between the reference model and the true earth regarding the shapes,

positions, extents, or properties of the body. The Meshtools3D viewer allows the difference between two models to be displayed (Options->Difference, and show the second model in the display). This can also be done in 3D modelling packages like Gocad.

- The similarities between many recovered models and their respective reference models can be assessed numerically by calculating the sum of the squared differences between the reference model and recovered model. Smaller values indicate a closer overall match. Alternatively a correlation coefficient can be calculated.
- It is important to look for portions of the recovered model that are compensating for deficiencies in the constraints, especially at greater depths where sensitivity to the data is less. If the property or geometry of one body is wrong, the adjacent bodies may be forced to compensate by having exaggerated properties or distorted geometries.
 - The most common example is where the properties of a shallow body are wrong. If the reference property is too high the inversion may compensate by creating a low density or susceptibility feature below the body. Conversely, if the reference property for the shallow feature is too low, the inversion may compensate by placing a high density or susceptibility feature at depth.
 - Geometrical compensations are harder to identify. They usually take the form of geologically-unrealistic geometries which can only be identified using prior knowledge of the expected geological style.

3.9.5 The data-based approach to constraints

The data-based approach to preparing geological constraints skips the requirement for full 3D interpretation of the geology prior to performing the inversions. Instead it supplies only the available raw geological knowledge to the inversion to recover a prediction about the subsurface distribution of geological features in areas where no knowledge is available (Figure 3.11). This approach is particularly suited to problems where geological information is limited, sparsely distributed, or concentrated within restricted areas such as known ore bodies or along the ground surface. The limited and uneven distribution of data makes it difficult or impossible to build full 3D models that are reliable enough to be included in the hypothesis testing approach. By postponing much of the geological interpretation until after the inversions have been performed, the lead time to recovering an inversion result is reduced. Using this approach, geologically-constrained inversion results can be obtained relatively quickly and used in

decisions to acquire further geological and geophysical data or to assist with geological interpretation. Because only observed geological data are included, and the number of cells which contain observations is usually small, this approach creates weakly constrained models. These may or may not differ significantly from the default geologically-unconstrained results. As new information is gathered it must be included as new constraints in updated inversions to enhance the reliability of the recovered models.

- This approach should be used where geological data are limited or sparsely distributed and building a full 3D geological model is impractical.
- The approach is mainly based on data-management, identifying the appropriate geological data, translating the observations into useful physical property estimates and assigning those physical property estimates to the appropriate cells within the model.
- Data-based constraints must be implemented using the smooth model inversion option, otherwise the constraints will only affect those cells where constraints are enforced and will not be extrapolated out into unknown areas.
- If a non-default reference model is to be used to constraint an inversion, reference properties must be defined for every cell in the model. Likewise for weights and bounds: if even a single non-default value needs to be assigned, then all cells need to be assigned a value. This indicates a need to enforce constraints differently in different cells according to how reliable the constraints are.
 - Reference models
 - Cells with no information must be assigned some default reference property that will typically be the expected average property within the model, or within a particular portion of the model.
 - Cells containing observations should be assigned a best estimate of the mean physical property of rocks within in those cells.
 - Smallness weights
 - Cells with no information should be assigned a default smallness weight value of 1.
 - Cells containing observations should be assigned a weight > 1 commensurate with the reliability of the reference property estimate within that cell.
 - Bounds
 - Cells with no information should be assigned wide bounds to allow the likely natural range of properties within that cell.

- Cells with observations should be assigned as tight bounds as can be reasonably justified. A useful strategy is to define the bounds based on a calculated or inferred confidence interval on the expected mean property within each cell at a particular confidence level.
- Smoothness weights
 - Cell faces separating cells with no information will usually be assigned default smoothness weights of unity. This indicates that the properties are equally likely to vary in any direction.
 - Cell faces adjoining cells that contain observations should be assigned either high smoothness weights to promote extrapolation, or low smoothness weights to prevent extrapolation of the properties (for instance where the cell is adjacent to a geological contact). The use of smoothness weights is more important for data-based constraints than hypothesis-testing constraints because they must be implemented with smooth model style inversions which recover smoother models. If sharp physical property contrasts between cells are desired they need to be enforced using low smoothness weights where they are known to exist.

Preparing constraints for data-based inversions using GIFtools:ModelBuilder

The UBC–GIF GIFtools:ModelBuilder software provides a purpose built tool for preparing data-based constraints for UBC–GIF inversions (Chapter 5). It combines all available property measurements from surface samples or from drill holes with geological observations in the form of maps, drilling logs, or partial 3D models. Geological observations are converted into physical property estimates automatically using available property measurements or manually with user-specified estimates of the property values. The software handles all data management and applies any available observations or measurements as constraints in the appropriate cells. It builds reference property models, weights, and bounds and supplies all outputs in appropriate formats ready for inversion.

The ModelBuilder software works like a structured workflow that guides the user through the process of building constraints using a set of dialog boxes. Each dialog box acts as either an input interface for identifying various input files and options, or a prompt for a decision on how the constraints should be applied. For any particular problem, only those dialog boxes that are relevant to the supplied data and selected options are shown. The details

of the ModelBuilder process are discussed in Chapter 5 and in the ModelBuilder user manual (Appendix B). An overview of the important options is presented here; the dialog boxes are referred to by their numbers in the order in which they appear.

- Dialog box 1: Mesh definition, data types, buffers
 - Identify the mesh on which the model will be created, which data types will be used, and whether ellipsoidal buffers should be used to extrapolate the constraints outwards. How the buffers are applied is defined in dialogs 6 and 17-20. The first option in dialog box 1 allows identification of a pre-existing session file which contains all data loaded by dialog box 2-10 in a previous run. Using a prior session file can dramatically speed creation of constraint models using the same data but slightly different parameters.
- Dialog set 2: Which constraints to build
 - Select the types of constraints that should be built. Although it is possible to select constraints individually (i.e., build a reference model with smallness weights, but not bounds), it is usually easiest to build all available constraints at one time, and then decide which individual sets of constraints should be applied in a specific inversion.
- Dialog set 3: Physical properties
 - Up to six different dialog boxes can be available in this set, and all relate to defining the physical properties to be used in the constraint models. The first choice regards which fundamental property is being used. Density and susceptibility are the usual options and are the specific focus of the ModelBuilder, but chargeability and conductivity are available for experimentation. The selection made defines the default values for the constraints.
 - The next box allows customisation of these default values for different constraints. An option exists to supply a prior physical property model to be used as the default reference model in the absence of other information, rather than applying a single value throughout the model. A prior geologically-unconstrained inversion could be used if it is considered to be a reasonable approximation. Be aware that if the prior model is not reliable, using this option may serve to further reinforce incorrect parts of the model as constraints.
 - If drilling geology logs or maps are to be used in the model builder, then physical property estimates must be defined to translate the recorded geology names or codes into physical properties. They can be 1) supplied via a text file of manually-defined

property estimates, 2) automatically calculated from available property measurements, or 3) loaded from an existing file that saved the calculated property estimates in a previous run. A useful practice the first time the ModelBuilder is run with new map or drilling data is to not specify any property estimate files or calculate new estimates. No map or drilling geology constraints will actually be applied, but lists of all the geology codes will be created in the working directory, and these can be used as a basis for defining manual property estimates as required. These can then be supplied for future constraint building.

- If property estimates are to be calculated automatically, two dialog boxes will follow to identify the data sources for calculating the estimates. These can be surface sample measurements or drilling measurements. An option is also included to supply a text file translation table that can link measurements associated with geology labels or codes that are related. This has two main uses:

- To link drilling geology codes with mapping labels, as these commonly use different name formats. A ‘Felsic porphyry’ map unit may be logged in drilling as ‘FP’ or ‘FPQ’ or ‘Afp’ and it is important that all measurements associated with any of these labels are also applied to all occurrences of ‘Felsic porphyry’. This could be done by including the following line in the translation table file:

Felsic porphyry FP%, Afp

where ‘FP%’ matches all measurements associated with codes starting with the two letters ‘FP’.

- To link geology codes where a particular label is underrepresented in the available measurements. For instance, there may be no measurements on the quartz-bearing felsic porphyry ‘FPQ’ but many measurements on the more general ‘FP’. If ‘FPQ’ is expected to have similar properties to ‘FP’ then the measurements can be linked using the line:

FPQ FP

- Dialog set 4: Constraint cropping

- Options are provided to restrict constraints to core portions of the mesh. Generally this is not necessary. However, for some problems, especially those where a regional data trend has not been removed or there are other problems with the data, it can be useful to avoid applying tight constraints in the padding zones.

- Dialog set 5: Surface samples
 - If using surface sample property measurements as a constraint, the file is identified here. An additional option is available to fix the sample positions to the topography surface. This is necessary for surface samples because the discretisation of the topography in the mesh may result in some samples being placed in cells that are treated as air cells in the inversion and therefore the constraints will be lost. This can be avoided by selecting this option and supplying a model file containing a representation of the topography surface. The vertical position of the samples is then adjusted so that they always lie within the top ground cell in the model.
- Dialog set 6: 3D domain model
 - A domain model provides a means to identify different default constraint values in different parts of a model according to general inferences about the locations and extents of particular features. For instance, it can identify the range of properties expected in different regions, without exactly specifying the positions and properties in detail. A domain model might define a layered earth model on which more detailed constraint observations are overlain.
 - Domain models are also used to specify geological or structural orientations in different parts of the model. Aspect ratios are specified which effectively allow different length scales/alpha coefficients to be used in different parts of the model according to the inferred shapes of bodies in those regions. If bodies are expected to be twice as wide (east-west) and 5 times as long (north-south) than they are tall, then they would be assigned an aspect ratio like 2:5:1 and these values multiply the length scales specified in the inversion control files. If buffers will be used to extrapolate the constraints, then different shapes and orientations can be specified for the buffers in different domains. Doing so ensures that the extrapolation is consistent with known structural or stratigraphic orientations.
 - An option exists to automatically identify and populate a cover or weathering domain. This can be specified as a blanket layer of a certain thickness below present topography, or by supplying a model containing a representation of an inferred basement surface. The cover/weathering domain can have all the same parameters defined as for other domains and overprints any other domains or geological units in

those cells that are in the cover/weathering domain. In addition the cover/weathering domain allows two additional features:

- Ignore geology drilling logs in cover/weathering domain. Geologists commonly log the protolith associated with weathered rocks in drill core, but doing so will bias the property estimates towards the unweathered variants. These will not adequately represent the rocks that are actually present so it can be useful to ignore the geology logs in the cover/weathering zone and rely only on actual measurements.
 - In dialog box 16, an option is available to make the cover/weathering domain boundary a smooth transition or a sharp contact, and this can be used to differentiate between a gradual weathering interface and a sharp erosional contact.
- Dialog box 7: 3D geological model
 - A 3D geological model built in a 3D modelling package can be supplied. This allows very detailed property estimates to be defined in specific areas, and identifies the locations of geological boundaries that should correspond to sharp property contrasts in the recovered inversion model.
 - Dialog sets 8 & 9: Geology maps
 - Outcrop and basement geology maps, specified in ESRI shapefile format, are sampled in a user-specified number of locations in each cell in which they occur, and appropriate constraints are applied based on the geological labels present and the supplied physical property estimates. Outcrop and basement geology maps represent two different user-defined elevation levels, and multiple shapefiles can be specified on each level to ensure full coverage across the mesh. If multiple shapefiles are being used on a particular level, they should be specified in order of priority, with the most reliable, most detailed maps being identified first, and the more regional, less detailed maps specified last. An option is available to specify property estimates to be applied in cells that contain map “whitespace” or no geological codes. This can be useful if the whitespace is known to correspond with a particular unmapped unit.
 - Dialog box 10: Drilling options
 - The drilling data is handled fairly automatically, and once the files are identified, the only option is to specify a sample interval along the drill holes. Any geology logs and property measurements available at each sample point will be extracted. This should be a value less than the general reporting interval for the geology logs and property logs.

- Dialog box 11: Assigning reference properties from point observations
 - Where both geological observations and physical property measurements are available in a cell, choices are required as to which type of data is more reliable. Options exist to favour actual physical property measurements, or the physical property estimates derived from geological observations. If the choice is not clear which data type to favour in a cell, there are two ways to automate the decision. The first is to treat each individual observation equally, regardless of whether they are measurements or an estimate. This is the best option to use if the choice is not clear or there are a limited number of points. The second option is to base the choice on the type of observation that has the best spatial distribution within each cell. This option may be best when there is a large amount of data in the cells.
- Dialog box 12: Spatial sampling requirements
 - If point observations from surface samples or drilling are being used then this option specifies how representative each observation point is. The volume of rock that can be represented by a single point observation needs to be specified in terms of the length of a side of the represented cube. Using smaller volumes may increase the quality and reliability of the constraints, but will require more data for constraints to be applied. If bounds are being computed, then it is also necessary to specify the how well a cell has to be sampled by points before tight bounds will be applied.
- Dialog box 13: Bounds confidence level for point measurements
 - In cells that contain point observations from surface samples or measurements bounds are applied based on the confidence interval on the estimate of the mean property in the cell. The width of the confidence interval is defined by the specified confidence level. Higher confidence levels create wider, more reliable but less restrictive bounds.
- Dialog box 14: Smallness (w_s) weights for each constraint type
 - This box has two functions. It provides the opportunity to define the smallness weights associated with each of the supplied data types. For point observations from surface samples or drilling, the smallness weight assigned here will be the maximum possible, and the actual weight applied will be determined based on the quality of the spatial distribution of points in each cell.
 - It also includes an option to scale smallness and/or smoothness weights with depth or distance. This is a very powerful tool which ensures that geological constraints are

applied equally throughout the model. The scaling options are specified in Dialog set 15.

- Dialog set 15: Distance or depth weight scaling
 - Where no geological constraints are available, distance or depth weighting provides a powerful mathematical constraint which ensures that sources are equally likely to occur at any vertical position in the recovered model. However it works in such a way that reduces the effectiveness of supplied reference model, smallness and smoothness constraints with increasing depth in the model (it doesn't affect bounds constraints). Since geological constraints are much more reliable than the distance or depth weighting mathematical constraints, it is useful to effectively turn off distance or depth weighting in those cells that contain geological constraints. This is achieved by multiplying the specified smallness and smoothness weights by the squared inverse of the distance or depth weights in those cells. This increases the smallness and smoothness weight with depth and ensures they are reproduced equally well throughout the model.
 - For scaling to be applied, the distance or depth weights need to be determined; ModelBuilder can calculate the weights directly, or they can be loaded from pre-existing weighting files that are output by new versions of the GZSEN3D and MAGSEN3D sensitivity matrix calculation programs ('dist_weight.txt' or 'depth_weight.txt') or from previous ModelBuilder runs.
 - Scaling can be applied to just smallness weights or just smoothness weights, but usually it should be applied to both. The type of scaling to be used will be determined by whether distance or depth weights will be used in the actual inversion.
- Dialog box 16: Smoothness weight options
 - The values of smoothness weights to be applied to different features and interfaces can be specified here. The gradient-based weight calculation determines the smoothness weight on cell faces separating constrained cells based on the physical property gradient at each face. Faces associated with sharp property gradients will be assigned lower smoothness weights to promote sharper gradients in the recovered model. Where properties vary more smoothly, higher smoothness weights will be assigned. The weights will be assigned on the range 10^{-M} - 10^{+M} , where M is a user specified magnitude which would usually be 1 or 2. Use M = 0 to turn off the gradient

calculation. Options are also available to specify the smoothness weights associated with various interfaces: the edge of data constraints, the edge of buffer constraints, geological contacts (from the 3D geological model), and the cover/weathering domain boundary.

- Dialog box 17: Reference property buffers
 - Buffers provide a very powerful means of expanding the number of constrained cells in a model. The reference property buffers can be calculated in a number of ways, but the best method is usually the smooth interpolation based on smallness weights and distance. This reduces the smallness weights with distance from the observations and calculates a weighted average reference property from adjacent observations.
- Dialog box 18: Bounds property buffers
 - Buffers provide a very powerful means of expanding the number of constrained cells in a model. The bounds buffers can be calculated in a number of ways, but the best method is usually the smooth interpolation based on smallness weights and distance. This provides bounds that widen with distance from the observations using a weighted average from adjacent observations.
- Dialog box 19: Buffer distances
 - The maximum dimensions of the extrapolation buffers are defined here. The specified distance is applied as the length of the longest axis of an ellipsoid, and the shape and relative lengths of the remaining two axes are defined either from the domain model (dialog set 6) or the default settings for the model (dialog box 20).
 - Keep in mind that the buffer size might be better related to how widely applicable a type of observation is than how reliable the observation is. Surface samples might be the most reliable observations because they were carefully selected and measured, but they might only apply to a relatively small volume, whereas maps might show the dominant lithology over a large volume and can therefore justify a larger buffer size.
- Dialog box 20: Default buffer orientation
 - The default buffer shape and orientation specified here will be applied to buffers everywhere in the model that were not directly specified by the domain model (dialog box 6).

3.10 CONCLUSIONS

The workflow presented above aims to provide a comprehensive reference guide for taking the appropriate steps to obtain the best possible results from gravity and magnetic inversions using the UBC–GIF inversion codes. With the addition of geological constraints, complex predictions of subsurface physical property distributions can be obtained. Application of the advice and techniques outlined in this workflow should provide a level of confidence in the quality of the recovered models. However, at all times it must be remembered that inversion of potential field data is non-unique, and any obtained solutions will form only a small subset of the possible models, even if geological constraints are included. It is hoped that the use of constraints will limit the results to those that are geologically and geophysically likely, but there may still remain a large number of candidate models that satisfy those criteria. The resolution of any inversion model will also ultimately be determined by the quality and resolution of the supplied geophysical data. The detail contained within the recovered models must be judged accordingly. Inversions may recover small features, especially at depth, to which the potential field data cannot be sensitive. These features will usually be manifestations of noise in the data. All models must therefore be assessed to ensure that the features of interest can actually be justified by the supplied geophysical data, given the expected uncertainty in the data. The benefits of inversion methods, however, far outweigh the limitations: there remain very few other practical techniques for directly imaging and predicting subsurface geology in 3D.

3.11 REFERENCES

- Agocs, W.B., 1951, Least squares residual anomaly determination: *Geophysics*, v. 16, p. 686-696.
- Blakely, R.J., 1995, *Potential theory in gravity and magnetic applications*: Cambridge, Cambridge University Press, 441 p.
- Clark, D.A., and Emerson, D.W., 1999, Self-demagnetisation; "the rock doctor": *Preview*, v. 79, p. 22-25.
- Farr, T.G., Rosen, P.A., Caro, E., Crippen, R., Duren, R., Hensley, S., Kobrick, M., Paller, M., Rodriguez, E., and Roth, L., 2005, The Shuttle Radar Topography Mission: *Reviews in Geophysics*, v. 45, RG2004, p. 33.
- Frost, B.R., and Shive, P.N., 1986, Magnetic mineralogy of the lower continental crust: *Journal of Geophysical Research*, v. 91, p. 6513-6521.
- Goussev, S.A., and Peirce, J.W., 2000, Gravity and magnetics exploration lexicon, <http://www.gedco.com/lex/lex00.htm>, 2008: Calgary, Geophysical Exploration & Development Corporation (GEDCO).
- Henson, P., and Hitchman, A.P., 2004, An integrated geological and geophysical 3D map for the EYC, *in* Blewett, R.S., and Hitchman, A.P., eds., *Project Y2 Final Report: 3D geological models of the eastern Yilgarn Craton*: Perth, Predictive Mineral Discovery Cooperative Research Centre, p. 39-89.
- Leaman, D.E., 1998, The gravity terrain correction—practical considerations: *Exploration Geophysics*, v. 29, p. 476-471.
- Li, Y., and Oldenburg, D.W., 1996, 3-D inversion of magnetic data: *Geophysics*, v. 61, p. 394-408.
- Li, Y., and Oldenburg, D.W., 1998a, 3-D inversion of gravity data: *Geophysics*, v. 63, p. 109-119.
- Li, Y., and Oldenburg, D.W., 1998b, Separation of regional and residual magnetic field data: *Geophysics*, v. 63, p. 431-439.
- McGaughey, J., 2007, Geological models, rock properties, and the 3D inversion of geophysical data, *in* Milkereit, B., ed., *Proceedings of Exploration 07: Fifth Decennial International Conference on Mineral Exploration*, p. 473-483.
- McInerney, P., Goldberg, A., Calcagno, P., Courrioux, G., Guillen, A., and Seikel, R., 2007, Improved 3D geology modelling using an implicit function interpolator and forward modelling of potential field data, *in* Milkereit, B., ed., *Proceedings of Exploration 07: Fifth Decennial International Conference on Mineral Exploration*, p. 919-922.

- Mickus, K.L., Aiken, C.L.V., and Kennedy, W.D., 1991, Regional-residual gravity anomaly separation using the minimum-curvature technique: *Geophysics*, v. 56, p. 279-283.
- Nettleton, L.L., 1939, Determination of density for reduction of gravimeter observations: *Geophysics*, v. 4, p. 176-183.
- Oldenburg, D.W., and Pratt, D.A., 2007, Geophysical inversion for mineral exploration: A decade of progress in theory and practice, *in* Milkereit, B., ed., *Proceedings of Exploration 07: Fifth Decennial International Conference on Mineral Exploration*, p. 61-95.
- Skeels, D.C., 1967, What is residual gravity?: *Geophysics*, v. 32, p. 872-876.
- Spector, A., and Grant, F.S., 1970, Statistical models for interpreting aeromagnetic data: *Geophysics*, v. 35, p. 293-302.
- Telford, W.M., Geldart, L.P., and Sheriff, R.E., 1990, *Applied Geophysics*: New York, Cambridge University Press, 770 p.
- UBC–GIF, 2005a, GRAV3D version 3.0: A program library for forward modelling and inversion of gravity data over 3D structures: The University of British Columbia–Geophysical Inversion Facility, 46 p.
- UBC–GIF, 2005b, MAG3D version 4.0: A program library for forward modelling and inversion of magnetic data over 3D structures: The University of British Columbia–Geophysical Inversion Facility, 41 p.

Chapter 4: Mass and magnetic properties of the southern Agnew-Wiluna greenstone belt and Leinster nickel deposits, Western Australia¹

4.1 INTRODUCTION

The critical link between geological and geophysical interpretation is an understanding of the physical properties of the rocks and minerals involved. With 3D interpretation, modelling, and inversion of gravity and magnetic data becoming common practice in the mineral exploration industry, the importance of reliable physical property knowledge cannot be overstated. The ambiguity, uncertainty, and non-uniqueness of deriving predictive surface physical property models that explain observed geophysical data requires the most accurate and complete information available. Available geological knowledge must be translated into physical property constraints to limit the possible suite of models to those that are consistent with the geology. The recovered property models can only be validated by comparison with known or expected geology, which requires reliable physical property knowledge. Geophysical interpretation and modelling commonly applies standard or textbook physical property values due to a lack of actual measurements, especially in new or poorly explored areas. However, ancient rocks can have complex histories and standard values may not be representative. This study seeks to provide a reliable understanding of the density and magnetic properties of Archean greenstone and granitoid rocks surrounding the Leinster group of Ni-sulphide deposits in the Eastern Goldfields terrane in Western Australia's Yilgarn Craton. The results will be used in Chapter 7 to translate available geological information into physical property constraints for 3D gravity and magnetic inversions, and to interpret the inversion results.

The Leinster nickel deposits include Perseverance, Rocky's Reward, and Harmony, with a total underground resource of 31 Mt at 2.3 wt. % Ni and open pit resource of 155 Mt at 0.6 % Ni (BHP Billiton Ltd., 2007). They are hosted by a lower- to middle-amphibolite facies metamorphosed sequence of ultramafic and felsic volcanic rocks within the Agnew-Wiluna greenstone belt (Barnes et al., 1988; Binns et al., 1976; Gole et al., 1987; Martin and Allchurch, 1975; Trofimovs et al., 2003). The host rocks are associated with other

¹ A version of this chapter has been submitted for publication. Williams, N.C. Mass and magnetic properties of the southern Agnew-Wiluna greenstone belt and Leinster nickel deposits, Western Australia. Australian Journal of Earth Sciences.

metamorphosed mafic rocks within the greenstone belt, and juxtaposed against voluminous granitoid and gneissic rocks outside the greenstone belt. Such a collection of rocks would be expected to have large density and magnetic property contrasts suitable for geophysical modelling and interpretation; however the properties are complicated by complex changes in density and magnetic properties associated with alteration and metamorphism.

The most relevant previous study of physical properties was that of Emerson et al. (1999) for the Rocky's Reward deposit at Leinster. They analysed the magnetic, mass, and electrical properties of 104 samples and noted in particular the extreme conductivities and high magnetic susceptibilities and densities of the sulphide ores. Although they did measure the properties of several host rock samples, they did not discuss the results in detail. Emerson et al. (2000) and Emerson and Macnae (2001) analysed the magnetic, mass, and electrical properties of the regolith at Lawlers 30 km southwest of Leinster. McCall et al. (1995) provide a summary of a large dataset of magnetic properties associated with nickel sulphide deposits and their host rocks at Widgiemooltha in a greenstone belt 400 km SSE of Leinster. Bourne et al. (1993) provided an overview of published relationships between metamorphism and density and magnetic susceptibility, and supplied additional density and susceptibility data as a function of metamorphic grade for two other greenstone belts from the Yilgarn Craton. Studies outside of Australia may also be relevant for understanding the physical properties of ancient rocks, particularly associated with Archean and Proterozoic cratons in Canada (Fowler et al., 2005), Africa (Benn et al., 1993; Ferré et al., 1999; Yoshihara and Hamano, 2004), and Scandinavia (Henkel, 1976; Henkel, 1989, 1991; Puranen, 1989).

The present study seeks to describe the mass and magnetic properties associated with all major rock types in the Leinster region, with a particular emphasis on the relationships between the physical properties and alteration and mineralisation. Densities and magnetic susceptibilities collected in this study will be used to validate a large corporate database of density and susceptibility measurements provided by BHP Billiton. Synthesis of both of these data sets will provide robust rock property estimates that can be used in future modelling within the Agnew-Wiluna greenstone belt and the Yilgarn Craton in general. The densities and susceptibilities are augmented by remanent magnetisation measurements, thermomagnetic analysis, and demagnetisation data collected in this study. The results may also be applicable in

other greenstone belt terranes around the world where less information regarding physical properties is available to constrain geophysical modelling.

4.1.1 Geology of the Agnew-Wiluna greenstone belt

The Yilgarn Craton is composed of greenstone belts, containing metavolcanic and metasedimentary rocks, several granitoid suites, and granitic gneiss, all with ages generally ranging from 3.05 to 2.62 Ga (Myers, 1993). The craton is an agglomeration of at least six terranes (Cassidy et al., 2006) each containing several domains; each domain represents a dismembered fragment of relatively contiguous stratigraphy. The craton-wide north-south Ida Fault System separates the Youanmi Terrane from the Eastern Goldfields Superterrane (EGST) to the east. The EGST contains a majority of the Yilgarn Craton's greenstone belts and comprises three terranes; from west to east the Kalgoorlie, Kurnalpi, and Burtville Terranes.

The Agnew-Wiluna greenstone belt, the southern portion of which is shown in Figure 4.1, is the smaller of two greenstone belts in the northern Kalgoorlie Terrane, the other being the Yandal greenstone belt 50 km to the east. Both belts are well endowed with gold, but only the Agnew-Wiluna belt is known to contain significant nickel resources. Gold mining has occurred in the Agnew-Wiluna greenstone belt since the 1890s and the belt contains four of the world's 15 largest nickel sulphide deposits, Mt Keith, Perseverance, Yakabindie, and Honeymoon Well, representing the majority of the world's large komatiite-hosted Ni-Cu-(PGE) deposits (Jaireth et al., 2005). The Agnew-Wiluna belt is between 2 and 20 km wide and extends over 200 km north-south. It is bounded to the west by the Ida Fault System, the western edge of the EGST (Cassidy et al., 2006). The eastern margin of the Agnew-Wiluna belt is controlled by the Perseverance Fault.

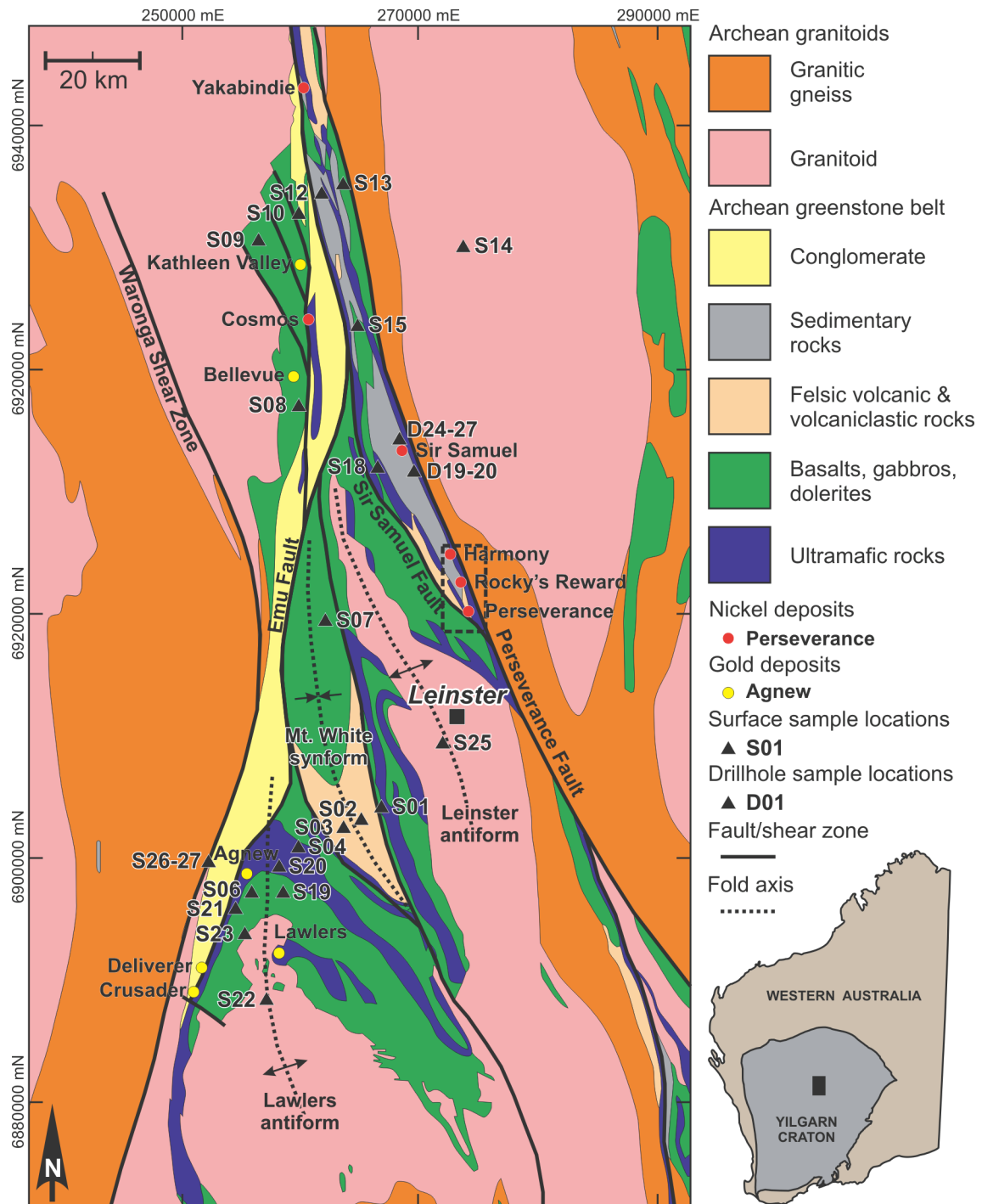


Figure 4.1. Basement geology of the southern Agnew-Wiluna greenstone belt, simplified and modified from Liu et al. (2000) indicating the locations of significant ore deposits, major structures, the town of Leinster, and the site locations of samples acquired in this study. The Ida Fault System, here consisting of the Emu Fault and Waroonga Shear Zone, marks the western boundary of the greenstone belt. The dashed box indicates the location of the detailed map of the Leinster deposits in Figure 4.2.

The accumulated work on the stratigraphy of the Agnew-Wiluna greenstone belt indicates that there are three ultramafic associations present in the belt: komatiite – felsic volcanic, komatiite – black shale, and komatiite – basalt, all below the unconformable Jones

Creek Conglomerate (Beresford et al., 2004; Beresford and Rosengren, 2004; Eisenlohr, 1989; Liu et al., 2002; Naldrett and Turner, 1977). All three associations should have characteristic physical properties and geophysical responses that may facilitate subsurface geophysical modelling. Naldrett and Turner (1977) provided the first basic stratigraphy for the Agnew-Wiluna belt south of Mt Keith. They identified a Lower Greenstone sequence, exposed in the hinges of the Lawlers and Leinster anticlines and between Yakabindie and Kathleen Valley, that consists of gabbros, and tholeiitic and high-Mg basalts, below sedimentary rocks; and an Upper Greenstone sequence along the eastern edge of the Agnew-Wiluna belt that consists of felsic volcanics and volcanoclastics, shales and cherts, basalts, more felsic volcanoclastics, and ultramafic flows intruded by mineralised dunite lenses. Although felsic facies are present in the upper greenstone sequences throughout the Kalgoorlie Terrane, only in the Mt Keith-Perseverance domain are they associated with komatiitic rocks and rich nickel mineralisation (Figure 4.2).

A characteristic of the komatiite – felsic volcanic association in the Agnew-Wiluna belt is the presence of large, up to 700 m wide and 2 km long, adcumulate dunite lenses amongst thin spinifex-textured komatiite flows. The dunite lenses host, or are adjacent to, most of the known major nickel occurrences in the belt, notably Perseverance and Mt Keith. The Perseverance orebody lies along the western margins of the vertical dipping Perseverance Ultramafic Complex (Figure 4.2). Despite debate on the extrusive versus intrusive origin of the dunite lenses (Barnes et al., 1988; Naldrett and Turner, 1977; Trofimovs et al., 2003), it is accepted that the ultramafics, especially those in the komatiite – felsic volcanic association, form a temporally-related horizon throughout the Mt Keith-Perseverance domain (Duuring et al., 2004b; Hill et al., 1995). The host felsic volcanics in the komatiite – felsic volcanic association are dated at c. 2706 Ma (R.I. Hill and I.H. Campbell, unpub. data, cited in Duuring et al., 2004b; Libby et al., 1998; Rosengren et al., 2004) providing a maximum age for the komatiites.

The komatiite – black shale association only occurs in the Mt Keith-Perseverance domain near the Sir Samuel Ni-Cu-(PGE) prospect 14 km north of Perseverance along the Perseverance Fault (Figure 4.1). Since the abundance of black shales increases northwards from Perseverance they are inferred to represent deep marine facies equivalents of sedimentary and volcanoclastic rocks near Perseverance (Trofimovs et al., 2003). The komatiite – basalt

association is restricted to the western domains of the Agnew-Wiluna belt (Figure 4.1), especially the Agnew domain where it is associated with mesothermal gold deposits, but no nickel deposits. The separation between the gold-bearing versus nickel-bearing, or equivalently the komatiite – basalt association versus the komatiite – felsic volcanic association, is either the north-northwest-plunging Leinster anticline which is intruded by the Leinster granodiorite (Duuring et al., 2004b; Eisenlohr, 1989), or the eastern limb of the anticline along the Sir Samuel Fault (Liu et al., 2002).

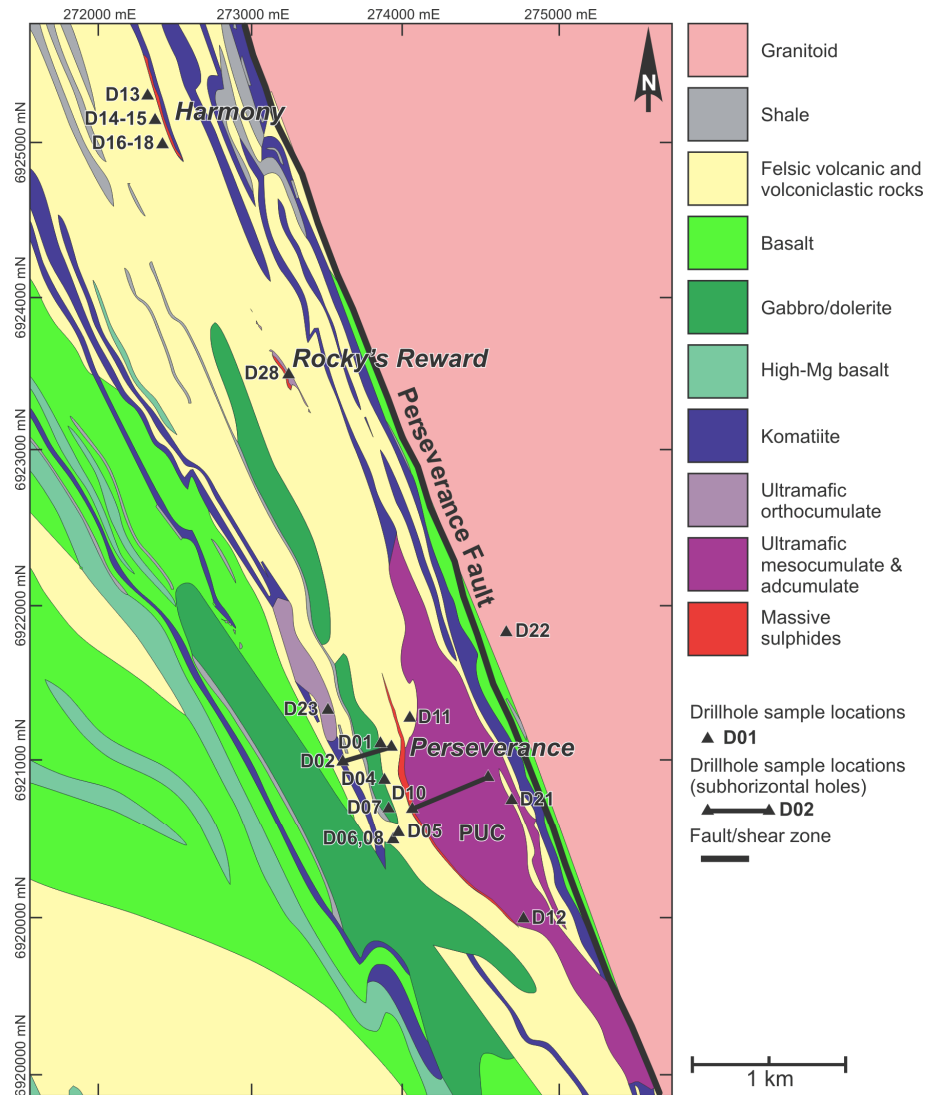


Figure 4.2. Detailed basement geology around the Leinster nickel deposits, modified from BHP Billiton unpublished data (C. Perring, pers. commun, 2005), and indicating the locations of the main Perseverance, Rocky's Reward and Harmony ore bodies, the Perseverance Ultramafic Complex, and the site locations of samples acquired in this study. The site locations are vertical projections from deeper positions on drill holes so some do not accurately indicate positions relative to the geology. Site locations D02 and D10 are on curved drill holes with samples spaced along the length shown. For clarity all structures are omitted except for the major Perseverance Fault.

The metamorphic grade increases from north to south ranging from prehnite-pumpellyite and lower-greenschist facies near Wiluna through middle-greenschist facies at Mt Keith up to lower- to middle-amphibolite facies ($< 550\text{ }^{\circ}\text{C}$) at Leinster (Barrett et al., 1977; Binns et al., 1976; Gole et al., 1987). Metamorphism and serpentinisation have substantially altered the ultramafic rocks throughout the belt. Deformation and infiltration of CO_2 -rich fluids, likely at several different times, has eradicated primary igneous textures in many rocks. The primary igneous mineralogy of the komatiitic rocks, intrusive or extrusive ultramafic rocks with $> 18\text{ wt. \% MgO}$ (Leshner and Keays, 2002), would have consisted of olivine, clinopyroxene, chromite and glass (Leshner, 1989). Serpentinisation involving hydration reactions prior to regional metamorphism converted olivine into serpentine with minor brucite and magnetite, with a dramatic volume increase and density decrease (Henkel, 1991). Increasing grades of prograde metamorphism formed chlorite, tremolite, talc, and eventually metamorphic olivine at amphibolite grades (Hill et al., 1990). Addition of CO_2 during metamorphism gave rise to anthophyllite-, enstatite-, and magnesite-bearing assemblages (Gole et al., 1987; Rödsjö and Goodgame, 1999). A second phase of serpentinisation may have occurred during or following retrograde metamorphism, resulting in production of more magnetite and serpentine (Hill et al., 1990). The complex and cyclic nature of the alteration and metamorphism of the belt may complicate any expected physical property relationships with lithology types.

The Leinster group of deposits, which includes Perseverance, Rocky's Reward, and Harmony, contains massive nickel sulphide basal horizons (Type I: Leshner and Keays, 2002), disseminated intercumulus nickel sulphides (Type IIb), and tectonically remobilised sulphides (Type V). Massive sulphide bodies at Perseverance are generally less than 5 m thick, and contain pyrrhotite (80 vol. %), pentlandite ($< 8\text{ vol. \%}$), with the remainder consisting of pyrite, chalcopyrite, and magnetite (Duuring et al., 2004a). The disseminated ore body at Perseverance, defined by a 1 wt. % Ni shell, is up to 50 m wide and can contain up to 45 vol. % sulphides, mainly pyrrhotite and pentlandite, with minor pyrite and chalcopyrite (Duuring et al., 2004a).

The granitoids surrounding the Agnew-Wiluna greenstone belt fall into the High-Ca group identified by Champion and Sheraton (1997) and consist mainly of biotite-hornblende monzogranite (Liu et al., 2002). Less voluminous Low-Ca and Mafic (tonalite) granitoids of

the Low-Ca and Mafic groups occur in the core of the Lawlers anticline southwest of Leinster (Champion and Sheraton, 1997; Vanderhor and Flint, 2001). Although the Mafic granitoids are distinctly different in appearance, Champion and Sheraton (1997) note that the High-Ca and Low-Ca granitoid groups are mineralogically similar and difficult to distinguish except with geochemistry. Whitaker (2003) also notes that the High-Ca and Low-Ca groups have nearly indistinguishable magnetic susceptibilities.

4.2 METHODS

A suite of 265 rock samples were collected from outcropping rocks and BHP Billiton drill core from the Leinster area. The sample set included 32 variously weathered surface samples from a variety of common rock types in 27 locations around the district where outcrop had been mapped by previous workers (Liu et al., 1996; Stewart, 2001). There were also 233 samples of drill core from 28 drill holes throughout the district. Following description of the samples, 157 of the most representative samples covering the full range of rock types were selected for physical property analysis, including 30 surface samples and 127 core samples. The locations used are indicated in Figure 4.1 and Figure 4.2. The 'S' prefix indicates surface sample locations and the 'D' prefix indicates sampled drill holes. The first pair of numbers indicates the site location; a second pair of numbers is added to indicate the sample number within each site. Detailed petrographical analysis is beyond the scope of this study, but 5 of the drill core samples were selected for quantitative Rietveld X-ray diffraction (XRD) analysis at The University of British Columbia Department of Earth and Ocean Sciences. The 5 sample splits were ground to $<5\ \mu\text{m}$ under ethanol in a vibratory McCrone Micronising Mill. Three of the samples (D0401, D2006 and D2611) were expected to contain abundant serpentine which is difficult to quantify using traditional Rietveld analysis. They were spiked with 10 wt. % annealed synthetic corundum and analysed following the methods of Wilson et al. (2006). Wilson et al. (2006) reported relative analytical uncertainties of $< 5\ \text{wt.}\%$ for serpentine estimates in serpentine-rich samples using this method. The remaining two samples were analysed using traditional Rietveld methods. Diffraction data were collected over a range of $3\text{--}80^\circ 2\theta$ on a standard Siemens D5000 Bragg-Brentano Diffractometer.

All physical property samples were prepared for analysis at the Australian National University Palaeomagnetic Laboratory. Samples from drill core were axially oriented by marking the down-hole direction on each specimen. Surface samples were unoriented, but the

relative orientation of each specimen within a sample was maintained and all specimens from a rock sample were measured in the same orientation. Drill core samples that had previously been split into half or quarter core were cut into four to five 22 mm × 22 mm × 22 mm cubes. Whole drill core samples and surface samples were drilled to extract four to five 22 mm long 25 mm diameter cylinders. For each sample the most representative three specimens were selected for analysis of magnetic properties and all specimens were analysed for mass properties. Mass and magnetic properties were measured on a total of 461 individual specimens. The sample locations and measurements for each sample are listed in Appendix A.

4.2.1 Mass properties

Density and porosity analysis of the samples collected in this study was performed at Geoscience Australia's geochemical laboratory following the procedures of Johnson and Olhoeft (1984) and Emerson (1990). All specimen cubes or cylinders were dried for two days at 110 °C to remove residual moisture, weighed in air, soaked in water for two days to fill pores with water, weighed in air, and then weighed suspended in water. The mass properties for each sample are taken as the mean of the measurements for all constituent specimens. Throughout this study densities will be reported as t/m³ (= g/cm³), rather than kg/m³, so that the densities can be directly compared to specific gravities; units of t/m³ also provide a clearer representation of the number of significant figures given the measurement uncertainty (below). The most common density measure used in geophysical interpretations is the saturated or wet bulk density (Grant and West, 1965), ρ_{WBD} , in which pores in the rock are filled with water:

$$\rho_{WBD} = \frac{M_{wet} \cdot \rho_w}{M_{wet} - M_{sub}} \quad 4.1$$

where M_{wet} is the mass of the rock weighed in air after saturation in water and M_{sub} is the mass of the saturated rock in water, and $\rho_w = 1.00 \text{ t/m}^3$ (at 25 °C) is the density of water (Emerson, 1990). The densities supplied by BHP Billiton are reported as unitless specific gravities, sg :

$$sg = \frac{M_{dry}}{M_{dry} - M_{sub}} \quad 4.2$$

where M_{dry} is the mass of the dry rock in air (Hutchison, 1974). Specific gravities can be directly converted to grain densities by multiplying by the density of water (Emerson, 1990):

$$\rho_{GD} = \frac{M_{dry} \cdot \rho_w}{M_{dry} - M_{sub}} = sg \cdot \rho_w \quad 4.3$$

Grain densities, and therefore specific gravities, report only the density of grains in the rock and ignore the mass and volume of pores. They are controlled only by the mineral composition of the rock and not its textural characteristics. The volume of accessible pores in a sample is indicated by the apparent porosity, ϕ_a (in %), by:

$$\phi_a = 100 \frac{V_w}{V_b} = 100 \frac{M_{wet} - M_{dry}}{M_{wet} - M_{sub}} \quad 4.4$$

where V_w is the volume of water that can be imbibed into a sample, V_b is the bulk volume of the sample (Emerson, 1990). This apparent porosity doesn't include occluded pores and may be underestimated without the use of vacuum techniques to imbibe water into the samples. For basement rocks with low apparent porosities, the difference between the wet bulk density and the grain density will be negligible. Repeated measurements on 16 specimens with a mean wet bulk density of 3.03 t/m³ gave an average measurement uncertainty of 0.07 t/m³ or 2 %. The mean apparent porosity for the repeated specimens was 0.7 % with an uncertainty of 0.7 %, or nearly 100 % relative uncertainty. This large uncertainty is partly due to not using vacuum techniques to completely saturate the samples. However, Fowler et al. (2005) reported 25 % uncertainties for low porosity determinations even when vacuum saturation was applied.

Figure 4.3 assesses the equivalency of the BHP Billiton specific gravity measurements and the wet bulk density measurements obtained in this study. Samples with both BHP Billiton specific gravity measurements and wet bulk density measurements from this study are plotted in Figure 4.3A to demonstrate their similarity. The data have a correlation coefficient of 0.96 and a slope of 0.96. For the low density samples that tend to have higher porosities, specific gravities slightly overestimate the density because they fail to account for the porosity. Figure 4.3B shows the magnitude of this difference in measurements for all specimens obtained in this study as a function of porosity. For porosities < ~4 % the difference between specific gravity and wet bulk density is less than the measurement uncertainty. Since porosities are unavailable for the BHP Billiton specific gravity measurements but are expected to be < 2 % based on the average of porosity measurements in this study, the specific gravities will be treated as equivalent to the wet bulk densities measured in this study. This may introduce a 1 % error, but this is less than the estimated measurement uncertainty of 2 %.

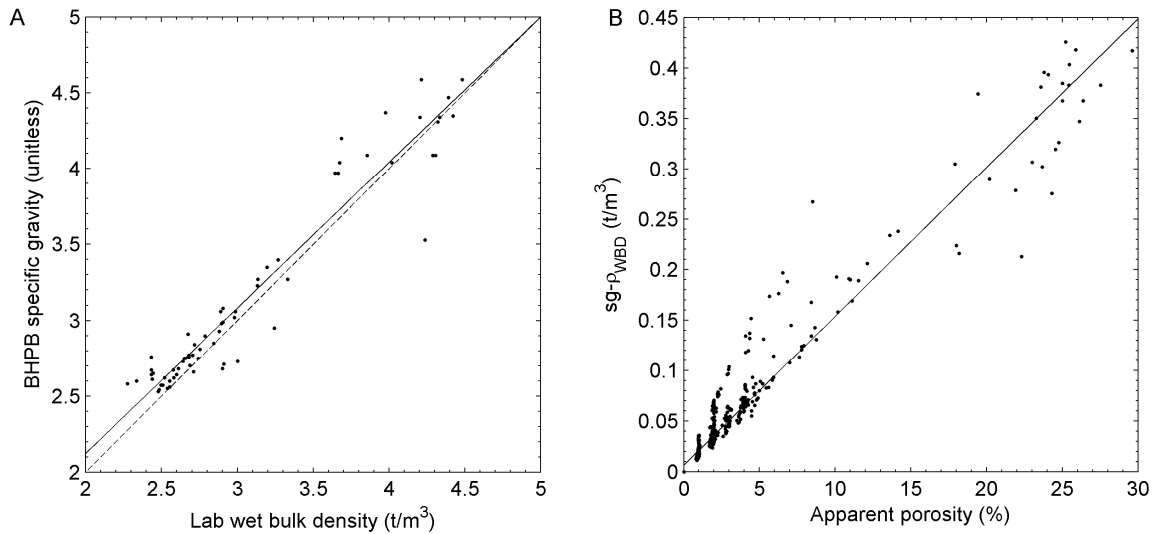


Figure 4.3. Relationship between different density determinations used in this study. A. Plot of lab-determined wet bulk densities collected in this study versus specific gravities measured by BHP Billiton for those samples where both were available. The solid line is a best-fitting regression line with a correlation coefficient of 0.96; the dashed line indicates a true 1:1 correlation. At low wet bulk densities the specific gravity measurements slightly overestimate the densities, likely due to slightly higher porosities, but the specific gravity and wet bulk density measurements are basically equivalent. B. Correlation of differences in the density estimates as a function of porosity for all specimens measured in this study. As porosity increases, the difference between specific gravity and wet bulk density increases. The solid line indicates a best fitting linear regression line with a correlation coefficient of 0.97. The density measurement uncertainty of 0.07 t/m^3 corresponds to a porosity of 4.4 %. Most samples have porosities less than this and so the density measurements should be equivalent to within uncertainty.

4.2.2 Magnetic properties

All magnetic properties were analysed at the Australian National University Palaeomagnetic Laboratory. The intensity and direction of natural remanent magnetisation (NRM) was measured on either a Molspin spinner magnetometer or a more sensitive semi-automated 2-axis cryogenic ScT magnetometer. The induced susceptibility of the specimens was measured either on a Digico susceptibility bridge (for lower susceptibilities) or an AGICO KLY-3 kappabridge (for higher susceptibilities). All instruments are cross-calibrated to ensure consistent results between instruments (C. Klootwijk, written commun., 2006). The bulk susceptibility for each sample was taken as the geometric mean of the three constituent specimens. The measurement uncertainty was determined to be $0.04 \times 10^{-3} \text{ SI}$ or about 0.3 %. The magnetic susceptibilities supplied by BHP Billiton were measured on drill core in the field using either Exploranium KT-5 or KT-9 handheld magnetic susceptibility meters. Figure 4.4 plots the BHP Billiton field measurements against those obtained in the lab in this study for those samples that had both available. There is a strong linear relationship with a correlation coefficient of 0.95 indicating that the results can be used interchangeably. The bulk NRM for each sample was taken as the vector average of the measurements for the constituent

specimens. The measurement uncertainty in the NRM intensities is 40 mA/m or ~18 %. Repeat measurements of bulk NRM orientations on several specimens gives an average 95% confidence angular standard deviation of ~11°. For core samples which are only axially-oriented the measured inclinations and declinations of NRM do not represent a discrete vector but define a small circle with axis of rotation along the direction of the drill hole. For unoriented surface samples the measured inclinations and declinations are arbitrary. The relative strength of induced magnetisation versus remanent magnetisation was determined using the Koenigsberger ratio:

$$Q = \frac{|\mathbf{NRM}|}{\kappa |\mathbf{H}_0|} \quad 4.5$$

where $|\mathbf{NRM}|$ is the measured intensity of remanent magnetisation, κ is the measured induced susceptibility, and $|\mathbf{H}_0|$ is the strength of the earth's magnetic field. Values < 1 indicate induced magnetisation is dominant; values > 1 indicate that remanent magnetisation is dominant.

To try to describe the character of the remanence in the rocks 99 specimens from representative samples were further analysed for their NRM components using fully automated alternating field (AF) demagnetisation on a 2G cryogenic magnetometer. This involved progressive step-wise demagnetisation of specimens with increasing AF strengths up to 140 mT, with measurement of the NRM components and intensity remaining after each step (after Giddings et al., 1997). Small rock chips were extracted from 65 samples and crushed to $< 150 \mu\text{m}$ using a hand crusher and sieve for thermomagnetic analysis to identify the minerals controlling the magnetic susceptibility. About 1 cm^3 of each sample powder was subjected to continuous induced susceptibility measurement on an AGICO KLY-3 kappabridge with water-cooled CS-3 furnace and CS-L cryostat over a range of temperatures. Each powder was cooled to $-196 \text{ }^\circ\text{C}$ in the cryostat with liquid nitrogen then slowly heated to $0 \text{ }^\circ\text{C}$ over the period of 1 hour while measuring susceptibility. The furnace was then used to heat the same powder to $700 \text{ }^\circ\text{C}$ in argon gas over a period of 1 hour, hold the sample at $\sim 700 \text{ }^\circ\text{C}$ for 20 minutes, and cool the sample back down to room temperature over another period of 1 hour while again measuring susceptibility over the range of temperatures.

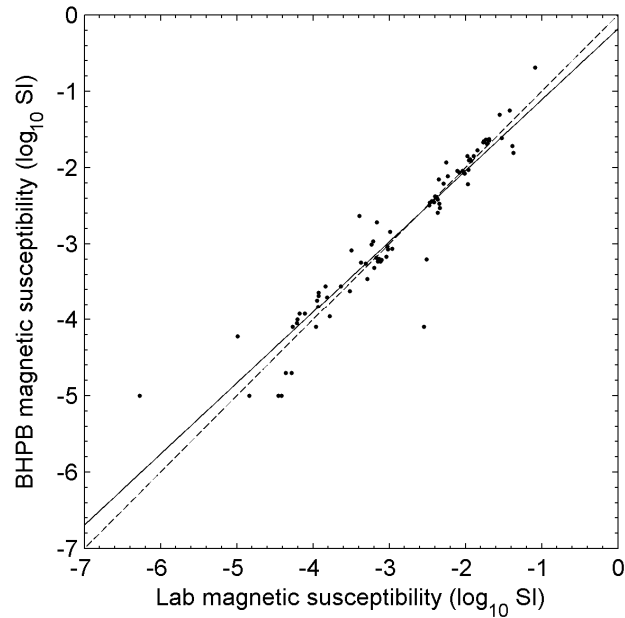


Figure 4.4. Plot of lab-determined magnetic susceptibilities collected in this study versus susceptibilities measured in the field and supplied by BHP Billiton for those samples where both were available. The solid line is a best fitting regression line with a correlation coefficient of 0.95; the dashed line indicates a true 1:1 correlation.

4.3 RESULTS

4.3.1 XRD and basic physical properties

The results of XRD, thermomagnetic, and petrophysical analysis for a massive sulphide sample and four ultramafic rock samples are shown in Table 4.1. Photos of the five XRD samples plus several other representative rocks are shown in Figure 4.5. The ultramafic samples were selected to cover a range of visually estimated serpentinisation intensities. Although the XRD analyses do show a range of serpentine contents, there is a bimodal distribution of serpentine contents either being low (< 5 wt. %; Figure 4.5D) or high (> 70 wt. %; Figure 4.5E-G). As the serpentine content increases, the density of the samples decreases strongly. There is less of a correlation between the magnetic properties and either magnetite or pyrrhotite content. All five samples have moderate to high susceptibilities, and high remanent magnetisation resulting in Koenigsberger ratios > 3. The highest NRM intensities and susceptibilities are observed in the two samples with the highest pyrrhotite and magnetite contents. The lowest NRM intensities and susceptibility occur in the least-serpentinised ultramafic sample with the least magnetite and pyrrhotite, but the same sample also has the highest Koenigsberger ratio. In some samples thermomagnetic analysis indicates the presence of magnetic minerals not identified by the XRD analyses. Notably these include magnetite and

titanomagnetite in the massive sulphide (D0701), titanomagnetite in two ultramafic samples (D1023 and D0401), and pyrrhotite in another ultramafic sample (D2611). These may be present in too small amounts (<1-2 %) and be too fine-grained (<1-2 μm) to be detected by XRD. Such phases can readily control the observed magnetic properties (Clark, 1997).

Table 4.1. Physical properties, and XRD and thermomagnetic mineralogy estimates for a massive sulphide sample and variously serpentinised ultramafic rock samples.

Sample number	D0701	D1023	D0401	D2006	D2611
Description	100 vol. % massive sulphide. Predominantly pyrrhotite with < 3 mm stringers of pentlandite. Trace chalcopyrite	Ultramafic mesocumulate with < 8 mm olivine crystals. Trace disseminated sulphides.	Ultramafic rock with retrograde serpentine pseudomorphs after bladed metamorphic olivine. Contains 10-20 vol. % disseminated sulphides plus sulphide stringers.	Ultramafic mesocumulate with < 5 mm serpentine pseudomorphs after olivine. Patchy weak sericite alteration. Disseminated sulphides 2-5 %.	Ultramafic rock with retrograde serpentine pseudomorphs after bladed metamorphic olivine. Possible chlorite alteration. Contains ~2 vol. % disseminated sulphides.
XRD mineralogy (wt. %)					
Quartz [SiO_2]	-	0.3	0.5	-	0.3
Muscovite [$\text{KAl}_2\text{AlSi}_3\text{O}_{10}(\text{OH})_2$]	-	-	-	9.4	-
Clinocllore [$(\text{Mg},\text{Fe}^{2+})_5\text{Al}(\text{Si}_3\text{Al})\text{O}_{10}(\text{OH})_8$]	-	2.0	3.5	3.2	2.5
Brucite [$\text{Mg}(\text{OH})_2$]	-	0.3	1.8	-	-
Hydrotalcite [$\text{Mg}_6\text{Al}_2(\text{CO}_3)(\text{OH})_{16} \cdot 4\text{H}_2\text{O}$]	-	-	-	-	1.2
Lizardite [$\text{Mg}_3\text{Si}_2\text{O}_5(\text{OH})_4$]	-	1.2	-	-	-
Serpentine [$(\text{Mg},\text{Fe})_3\text{Si}_2\text{O}_5(\text{OH})_4$]	-	-	75.6	81.3	93.3
Calcite [CaCO_3]	-	0.2	-	-	-
Magnetite [Fe_3O_4]	-	1.2	4.5	3.0	2.5
Pentlandite [$(\text{Fe},\text{Ni})_9\text{S}_8$]	19.8	0.3	4.4	3.1	0.1
Pyrrhotite 4M [Fe_{1-x}S]	80.2	-	9.6	-	-
Pyrite [FeS_2]	-	0.3	-	-	-
Forsterite [Mg_2SiO_4]	-	94.2	-	-	-
Total	100.0	100.0	100.0	100.0	100.0
Pentlandite:Pyrrhotite wt. ratio	1:4	-	1:2	-	-
Magnetite:Serpentine wt. ratio	-	1:1	1:17	1:27	1:37
Thermomagnetic mineralogy ¹	Monoclinic pyrrhotite; minor SD magnetite, titanomagnetite	MD magnetite, titanomagnetite	MD magnetite; minor pyrrhotite, titanomagnetite	Not analysed	MD magnetite; minor pyrrhotite
Physical properties					
Wet bulk density (t/m ³)	4.21	3.19	3.00	2.65	2.33
Magnetic susceptibility ($\times 10^{-3}$ SI)	224	10.7	119	41.1	77.0
Natural remanent magnetisation intensity (NRM: mA/m)	37,200	9,190	26,300	7,500	20,900
Koenigsberger ratio (Q: unitless)	3.6	18.5	4.8	3.9	5.8

¹ SD = single domain; MD = multidomain. Single domain magnetite cannot be identified in samples with multidomain magnetite even if present.

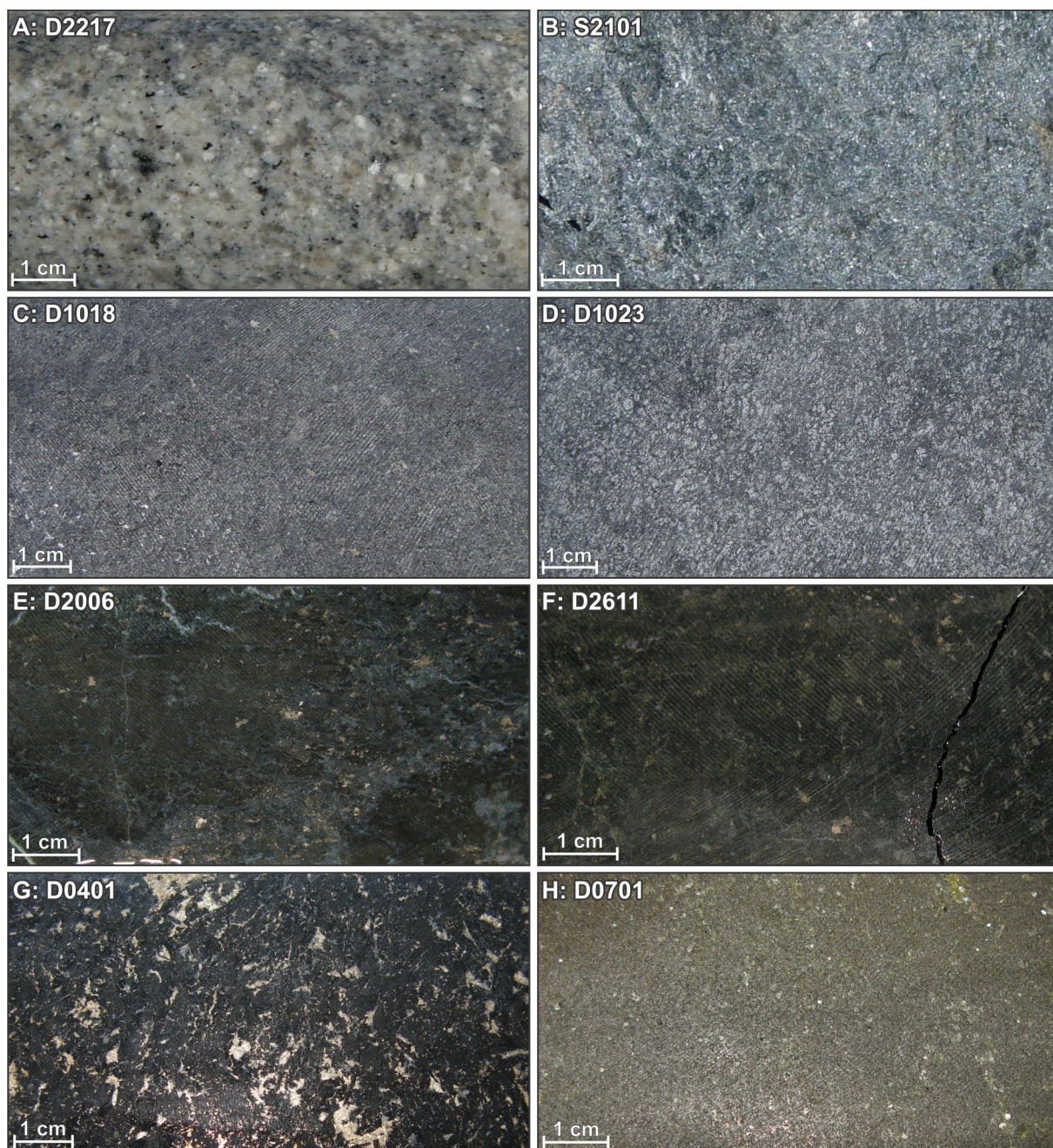


Figure 4.5. Representative photos of samples used in this study. A. Slightly strained granite from just east of the Perseverance Fault. B. Dolerite from the nose of the Lawlers Anticline south of Agnew. C. Coarse olivine-bearing ultramafic adcumulate with trace sulphides. This sample was one of two for which full remanent magnetisation orientations could be derived. D. Coarse olivine-bearing ultramafic mesocumulate with trace sulphides. E. Strongly serpentinised ultramafic mesocumulate with serpentine pseudomorphs after olivine and 2-5 vol. % disseminated pyrrhotite and pentlandite. Pale patches of sericite alteration. F. Ultramafic rock with retrograde serpentine pseudomorphs after bladed metamorphic olivine and ~2 vol. % disseminated pyrrhotite and pentlandite. G. Ultramafic rock with retrograde serpentine pseudomorphs after bladed metamorphic olivine. Contains 10-20 vol. % disseminated pyrrhotite and pentlandite. H. Massive sulphide with thin bands of pentlandite in dominantly pyrrhotite, with minor chalcopyrite.

Table 4.2. Lithological summary of mass and magnetic properties obtained in this study. With the exception of massive sulphide samples, all samples with > 1 vol. % sulphides are excluded from this table to indicate unmineralised rock properties. Means are listed with 1 σ standard deviations. Geometric means are the means of the log₁₀-transformed data and better indicate the most likely value than the arithmetic mean for lognormally-distributed data such as magnetic properties.

	Massive sulphides	Ultramafics	Basalts	Gabbros/ dolerites	Granitoids	Pegmatites	Felsic volcanics/ volcaniclastics	Fine-grained metamorphic rocks	Sedimentary	Regolith/ Quaternary
Number of samples	18	28	12	5	13 ¹	2	12	12	5	2 ¹
Wet bulk density (t/m ³)										
Mean \pm std	4.12 \pm 0.30	2.87 \pm 0.39	2.79 \pm 0.23	2.84 \pm 0.21	2.53 \pm 0.09	2.58 \pm 0.06	2.52 \pm 0.18	2.79 \pm 0.16	2.37 \pm 0.35	2.40 \pm 0.09
Median	4.23	3.02	2.83	2.94	2.53	2.58	2.57	2.83	2.47	2.40
Porosity (%)										
Mean \pm std	1.5 \pm 1.9	2.8 \pm 6.1	2.6 \pm 7.0	4.2 \pm 8.1	0.91 \pm 0.69	1.1 \pm 0.13	3.9 \pm 7.0	0.95 \pm 0.66	9.6 \pm 12	8.2 \pm 5.6
Median	1.0	1.1	0.54	0.59	0.93	1.1	1.4	0.81	1.7	8.2
Magnetic susceptibility ($\times 10^{-3}$ SI)										
Mean \pm std	128 \pm 80.2	24.2 \pm 22.8	1.03 \pm 1.07	1.46 \pm 1.55	4.01 \pm 3.04	0.0600 \pm 0.0704	0.0995 \pm 0.0607	1.10 \pm 0.668	0.0870 \pm 0.121	0.119
Median	131	17.3	0.835	0.794	3.72	0.0600	0.0948	1.10	0.0386	0.119
Geometric (log ₁₀) mean	70.3	14.7	0.763	1.07	2.63	0.0335	0.0631	0.815	0.0482	0.119
Natural remanent magnetisation intensity, (NRM: mA/m)										
Mean \pm std	124,000 \pm 137,000	6,740 \pm 10,300	15.6 \pm 38.8	159 \pm 203	923 \pm 2,420	0.256 \pm 0.121	4.43 \pm 11.1	83.4 \pm 91.1	8.16 \pm 14.7	22.4 \pm 28.6
Median	76,700	1,880	0.976	44.3	136	0.256	0.317	59.4	1.88	22.4
Geometric (log ₁₀) mean	42,900	1,780	1.50	35.5	99.5	0.242	0.852	27.0	2.75	9.66
Koenigsberger ratio, (Q: unitless)										
Mean \pm std	18 \pm 13	7.0 \pm 9.6	0.17 \pm 0.32	2.1 \pm 2.2	4.6 \pm 12	0.21 \pm 0.21	11 \pm 36	1.2 \pm 1.1	1.4 \pm 0.78	0.40
Median	17	2.0	0.028	1.5	0.86	0.21	0.063	1.1	1.2	0.40
Geometric (log ₁₀) mean	13	2.6	0.042	0.71	0.89	0.16	0.29	0.71	1.2	0.40

¹ Magnetic susceptibility and Koenigsberger ratios are only available for 12 granitoid samples and one regolith/Quaternary sample.

Table 4.3. Lithological summary of mass and magnetic properties supplied by BHP Billiton. With the exception of massive sulphide samples, all samples with > 1 vol. % sulphides are excluded from this table to indicate unmineralised rock properties. Means are listed with 1 σ standard deviations. Geometric means are the means of the log₁₀-transformed data and better indicate the most likely value than the arithmetic mean for lognormally-distributed data such as magnetic properties.

	Massive sulphides	Ultramafics	Basalts	Gabbros/ dolerites	Granitoids	Pegmatites	Felsic volcanics/ volcaniclastics	Fine-grained metamorphic rocks	Sedimentary	Regolith/ Quaternary
Specific gravity (unitless)										
Number of samples	10,427	63,074	2,072	501	20	414	6,041	9,664	723	13
Mean \pm std	3.85 \pm 0.68	2.80 \pm 0.27	2.97 \pm 0.25	2.96 \pm 0.24	2.69 \pm 0.19	2.71 \pm 0.21	2.76 \pm 0.28	2.86 \pm 0.32	2.86 \pm 0.33	2.26 \pm 0.30
Median	4.02	2.76	2.95	2.96	2.65	2.65	2.72	2.78	2.84	2.21
Magnetic susceptibility ($\times 10^{-3}$ SI)										
Number of samples	402	18,149	4,693	342	21	212	4,741	8,060	2,779	976
Mean \pm std	26.7 \pm 73.0	19.3 \pm 47.7	2.71 \pm 22.5	1.17 \pm 1.73	1.48 \pm 1.43	2.04 \pm 8.27	1.77 \pm 5.76	2.99 \pm 23.6	2.44 \pm 8.03	3.18 \pm 7.18
Median	6.76	5.92	0.770	0.795	0.950	0.485	0.690	0.600	0.800	0.905
Geometric (log ₁₀) mean	6.07	4.85	0.667	0.758	0.997	0.347	0.527	0.552	0.765	0.886

A summary of the basic mass and magnetic properties obtained in this study for each major rock type is given in Table 4.2. The equivalent values obtained from the BHP Billiton data are shown in Table 4.3. Histograms of the data grouped by lithology are presented in Figure 4.6 to Figure 4.11. All histograms in this study use bin widths defined by the data range and number of samples (Freedman and Diaconis, 1981). Magnetic properties typically follow a lognormal (base 10) distribution (Latham et al., 1989; Puranen, 1989) and so are presented on logarithmic axes. The arithmetic mean consistently overestimates the most likely value for lognormal distributions, so the median is provided to give a better estimate of the most likely value for skewed data, and the geometric mean is provided to indicate the most likely value associated with lognormal properties (Borradaile, 2003; Kirkwood, 1979). Comparison between the data collected in this study versus the BHP Billiton property measurements indicates that the two data sets are consistent. The average properties for some rock types diverge between the two datasets, notably the massive sulphide and sedimentary rock densities, but the histograms show that the values measured in this study always fall within the ranges shown in the much larger BHP Billiton datasets (Figure 4.6 versus Figure 4.7; and Figure 4.8 versus Figure 4.9). This is taken as further indicating the equivalence of the two datasets and subsequent plots and tables will combine the two to maximise the statistical reliability of the data.

All properties show high variability between rock types with magnetic properties showing several orders of magnitude difference, however there is also considerable overlap between the observed properties of each rock type. The massive sulphides have the most extreme densities and magnetic properties including strong remanent magnetisation with Koenigsberger ratios of 3-50. The supplied specific gravities for massive sulphides extend to much lower values (2.6-4.7, unitless) than the densities measured in this study (3.5-4.7 t/m³). This could be due to the patchy distribution of sulphides, especially in stringer zones where centimetre to decimetre zones of sulphides can be inter-layered with non-sulphide bearing rocks. Such intervals may have been logged by company geologists as containing massive sulphides but the actual specific gravity measurements happened to be obtained in the zones with fewer sulphides. The various ultramafic rocks have consistently high remanent magnetisation with Koenigsberger ratios of 1-50 (the most extreme values may be artefacts from drilling: see discussion) and the most variable densities (2.4-3.3 t/m³). All other rock types have Koenigsberger ratios ≤ 1 indicating that induced magnetisation is either equal to or

dominant over remanent magnetisation. Although the various mafic rock suites appear indistinguishable in most properties they do appear to have an order of magnitude difference in their observed NRM intensities. The granitoids have low densities and the most significant magnetic susceptibilities and remanent magnetisation of the remaining lithologies.

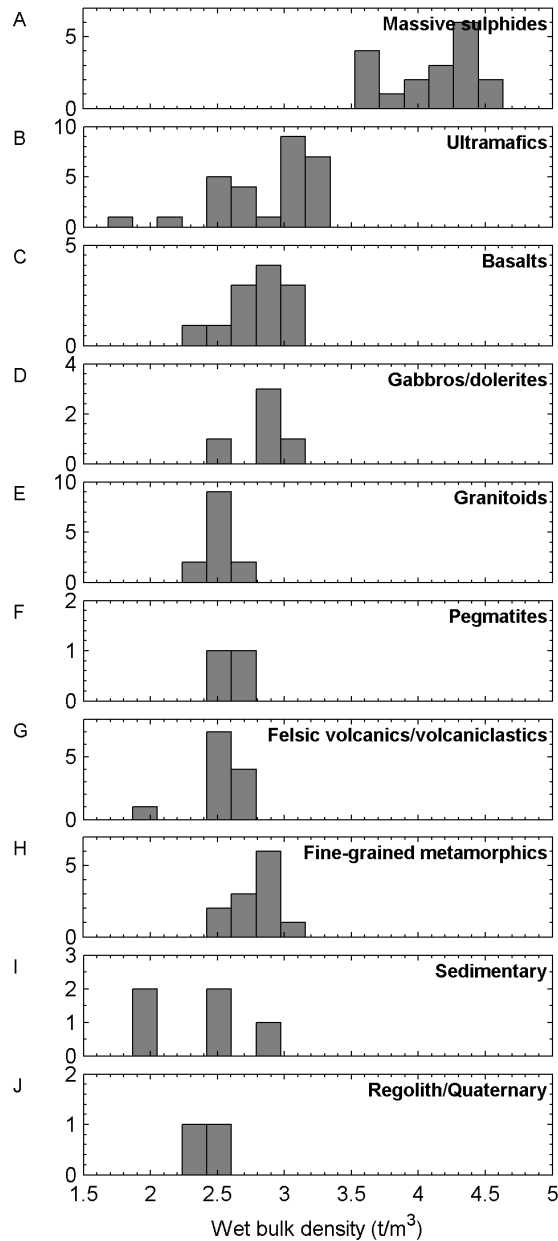


Figure 4.6. Histograms of wet bulk density by rock type from this study.

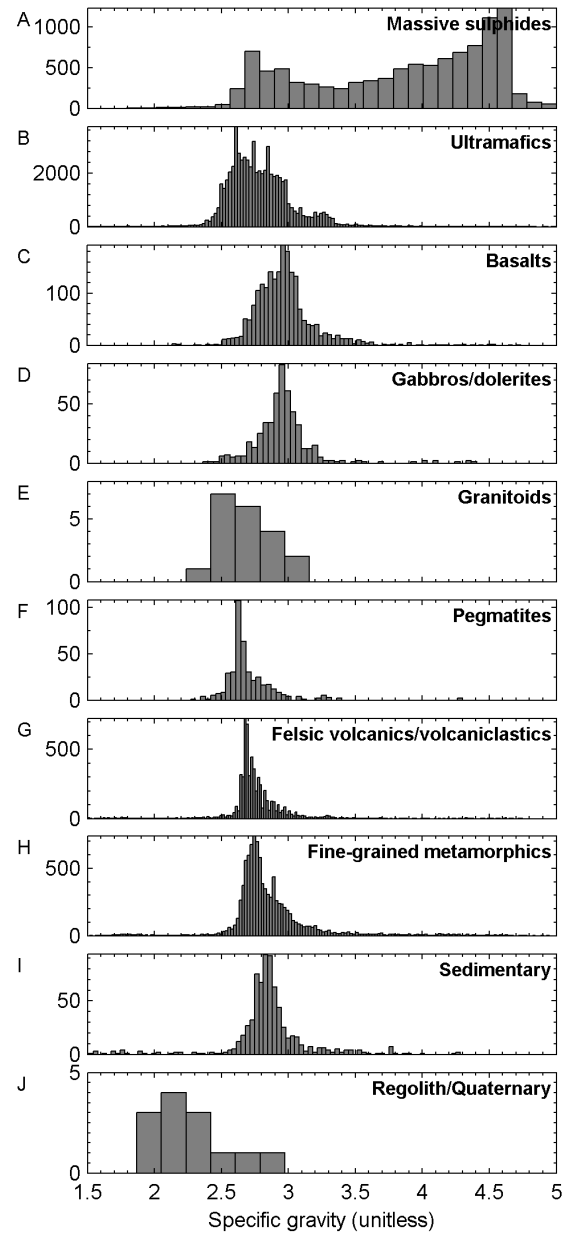


Figure 4.7. Histograms of BHP Billiton specific gravities by rock type.

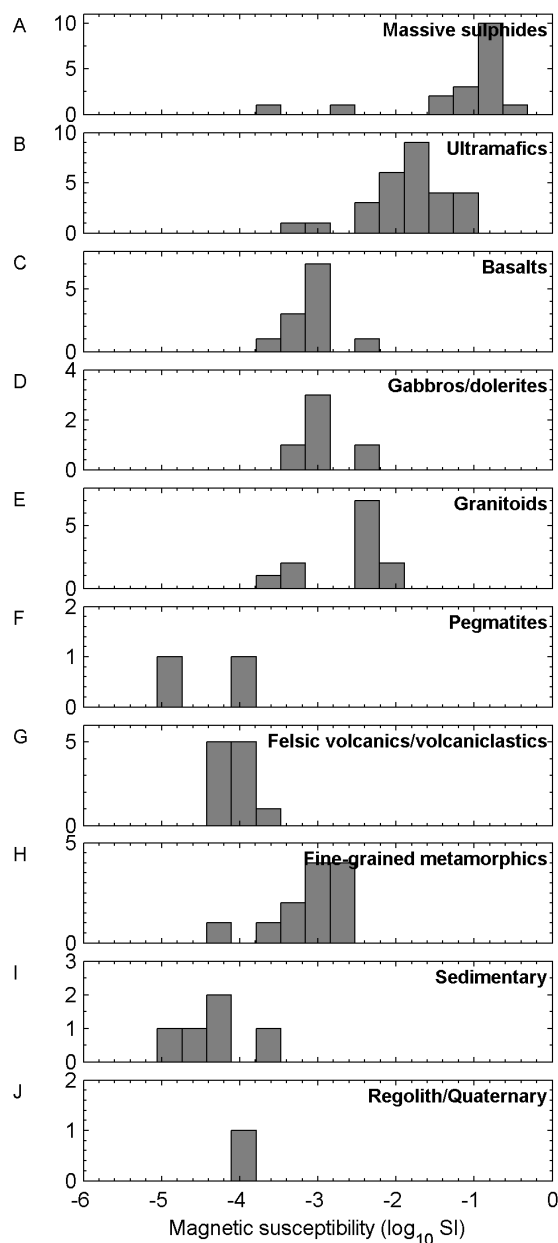


Figure 4.8. Histograms of magnetic susceptibility by rock type obtained in this study.

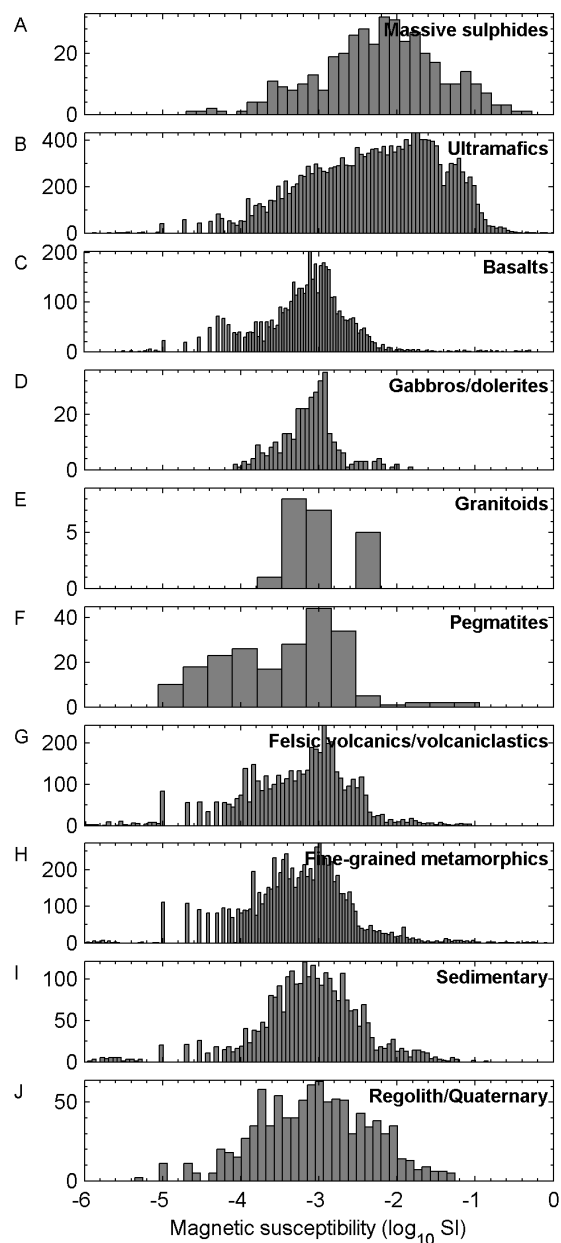


Figure 4.9. Histograms of BHP Billiton magnetic susceptibilities by rock type.

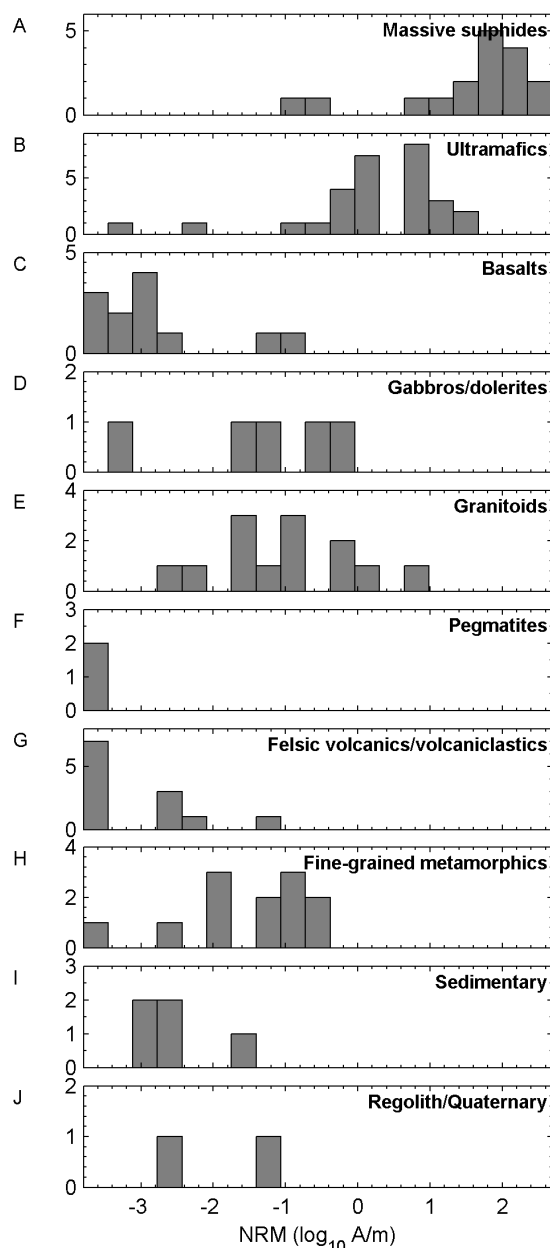


Figure 4.10. Histograms of the intensity of natural remanent magnetisation by rock type.

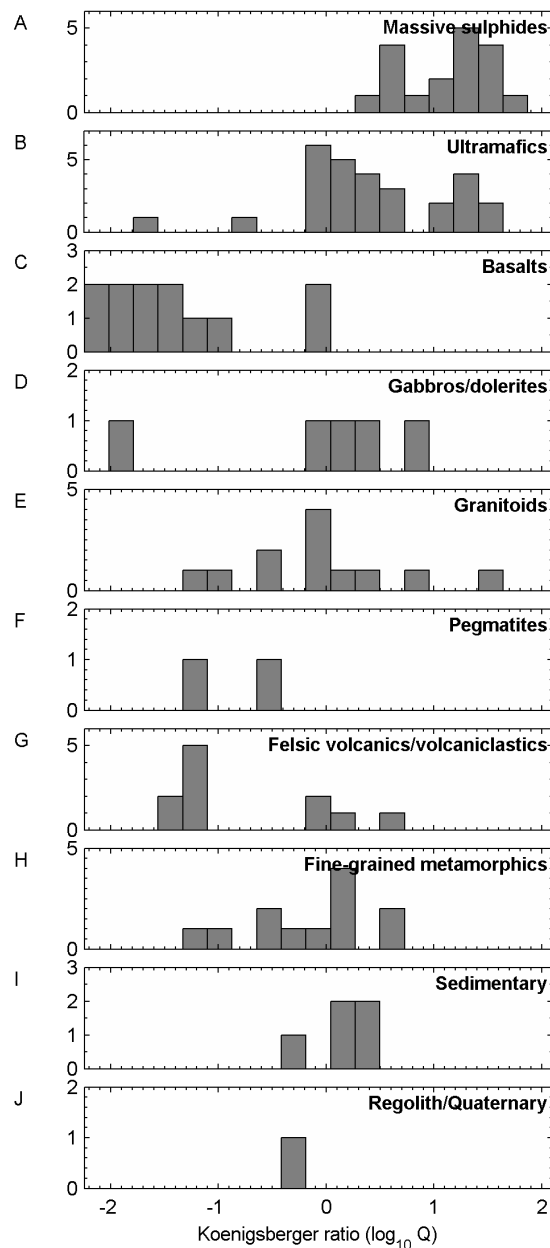


Figure 4.11. Histograms of the Koenigsberger ratio (Q) by rock type. A Q ratio of 1 ($\log_{10} Q = 0$) indicates that magnetic susceptibility and NRM intensity have equal magnitude. If $Q > 1$ remanent magnetisation dominates. If $Q < 1$ induced magnetisation dominates.

To identify possible relationships between sulphide content and physical properties the predominant ultramafic host rock measurements are grouped according to visually estimated sulphide content with properties summarised in Table 4.4, Figure 4.12 and Figure 4.13. There is a slight trend of increasing properties with sulphide content for all the plotted properties

(Figure 4.14); however the variations in properties between adjacent categories of sulphide content are not significant. Koenigsberger ratios are always > 1 regardless of the actual sulphide content, indicating strong remanent magnetisation in all ultramafic rocks.

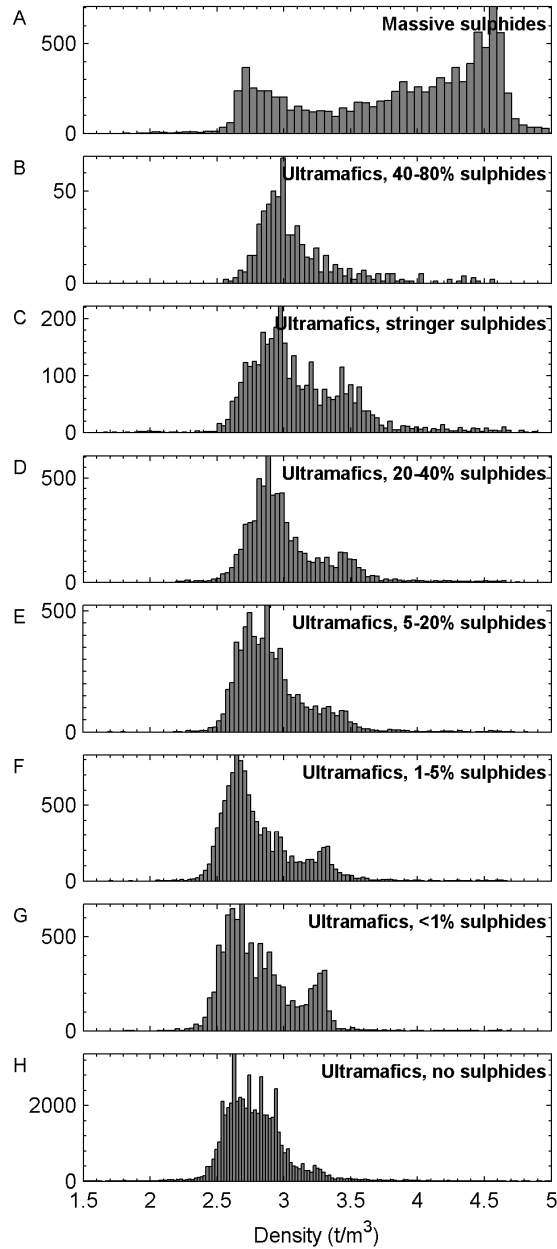


Figure 4.12. Histograms of the densities associated with increasing sulphide content in ultramafic host rocks. Includes both wet bulk densities from this study and specific gravities supplied by BHP Billiton.

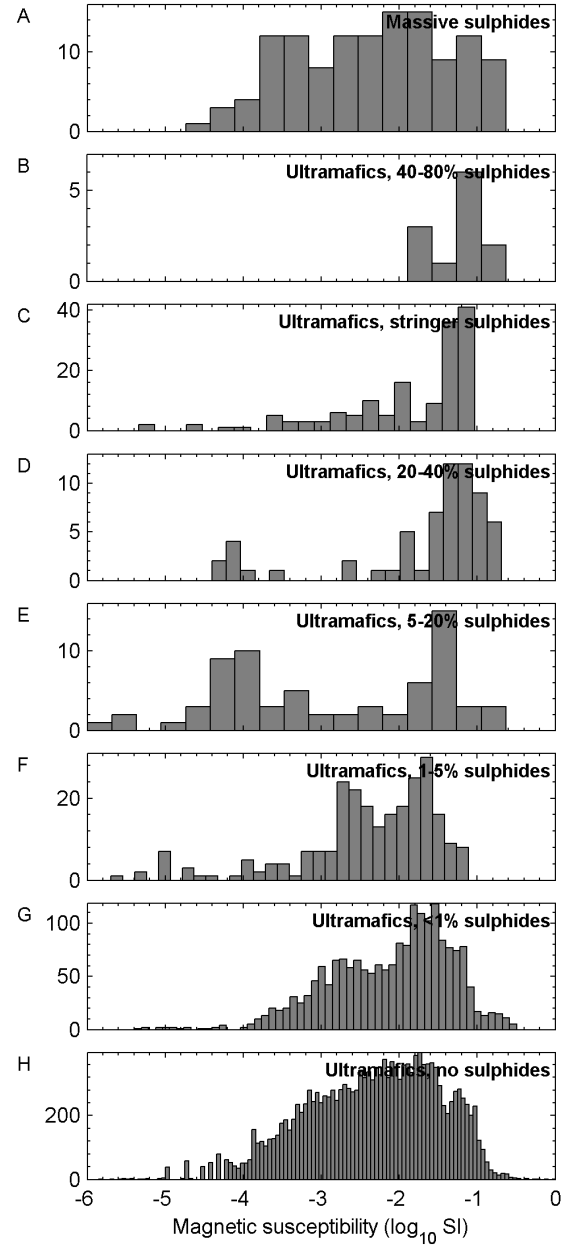


Figure 4.13. Histograms of the susceptibilities associated with increasing sulphide content in ultramafic host rocks. Includes susceptibilities from this study and those supplied by BHP Billiton.

Table 4.4. Summary of the densities and magnetic properties of the ultramafic host rocks and massive sulphide ore at Leinster, according to sulphide content. Sulphide content is determined by visual inspection of hand samples. Densities include both wet bulk densities from this study and specific gravities from BHP Billiton. Susceptibilities include both laboratory measurements from this study and field measurements from BHP Billiton. Means are listed with 1 σ standard deviations.

	Massive sulphides	Ultramafics with 40-80% sulphides	Ultramafics with stringer sulphides	Ultramafics with 20-40% sulphides	Ultramafics with 5-20% sulphides	Ultramafics with 1-5% sulphides	Ultramafics with <1% sulphides	Ultramafics with no sulphides
Density (t/m ³)								
Number of samples	9,802	599	3,559	6,763	6,781	11,176	9,174	53,928
Mean \pm std	3.86 \pm 0.68	3.11 \pm 0.35	3.12 \pm 0.40	3.02 \pm 0.31	2.92 \pm 0.29	2.82 \pm 0.29	2.82 \pm 0.28	2.79 \pm 0.26
Median	4.04	2.99	3.01	2.94	2.86	2.73	2.75	2.76
Natural remanent magnetisation intensity, (NRM: mA/m)								
Number of samples	13	0	3	8	19	6	16	12
Mean \pm std	140,000 \pm 152,000	-	10,100 \pm 14,100	15,300 \pm 14,500	10,900 \pm 14,000	4,800 \pm 7,990	4,920 \pm 4,120	9,170 \pm 15,000
Median	94,000	-	3,280	15,000	6,690	1,790	5,900	1,730
Geometric (log10) mean	53,000	-	3,930	7,260	3,970	1,520	2,460	1,150
Magnetic susceptibility ($\times 10^{-3}$ SI)								
Number of samples	125	12	160	66	71	256	1,922	16,255
Mean \pm std	26.0 \pm 46.1	77.5 \pm 38.0	39.0 \pm 32.9	63.7 \pm 60.8	19.1 \pm 32.9	13.3 \pm 17.2	24.3 \pm 41.8	18.6 \pm 48.3
Median	5.15	88.2	44.4	47.2	1.08	6.23	11.2	5.50
Geometric (log10) mean	4.08	66.1	14.9	22.8	1.16	4.18	7.85	4.54
Koenigsberger ratio, (Q: unitless)								
Number of samples	13	0	3	8	19	6	16	12
Mean \pm std	21 \pm 14	-	3.5 \pm 1.1	3.2 \pm 2.7	7.7 \pm 13	3.3 \pm 2.8	7.4 \pm 9.2	6.4 \pm 11
Median	19	-	3.3	3.4	3.1	2.5	2.7	1.9
Geometric (log10) mean	16	-	3.4	1.8	3.2	2.3	3.5	1.8

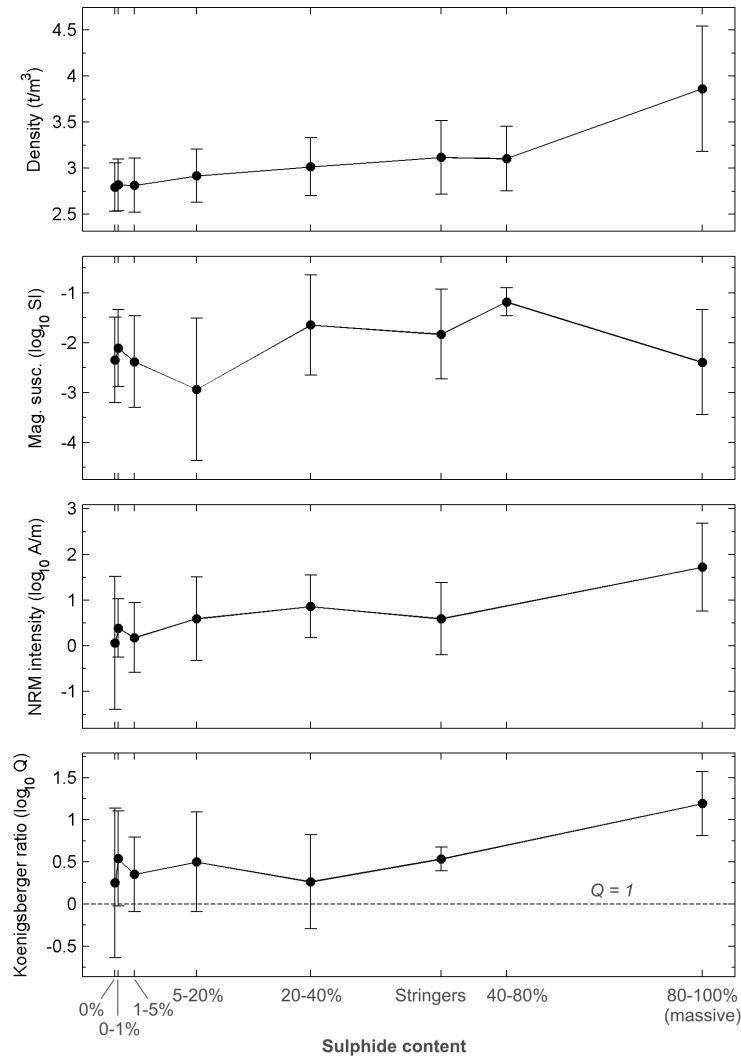


Figure 4.14. Physical properties of ultramafic host rocks according to sulphide content. Arithmetic mean densities are shown with 1σ standard deviations. Log-transformed magnetic properties are shown by plotting the geometric means and geometric 1σ standard deviations accordingly. Sulphide contents of 0-80 % consist of disseminated sulphides. Sulphide stringers are vein-like sulphides and are difficult to quantify visually as they are either present and approach massive sulphide contents, or absent, in different portions of samples that also may contain variously disseminated sulphides. Densities, remanent magnetisation, and Koenigsberger ratios all tend to increase with increasing sulphide content but the trend is only significant at $> 20\%$ sulphides. Most ultramafic rocks show Koenigsberger ratios > 1 regardless of their sulphide content.

To further characterise the properties associated with the ultramafic host rocks, they are also subdivided based on inferred protolith (Table 4.5, Figure 4.15 and Figure 4.16). This subdivision ignores the effects of alteration and metamorphism but still shows some clear trends. Ultramafic rocks that show preserved cumulate textures have a wider range of densities and higher susceptibilities than fine-grained komatiitic ultramafic rocks. Adcumulate ultramafic rocks, or dunites, have the lowest susceptibilities and highest Koenigsberger ratios, but show a bimodal density distribution with distinct peaks at 2.55 t/m^3 and 3.25 t/m^3 .

Table 4.5. Summary of the densities and magnetic properties of the ultramafic host rocks, separated by protolith style. All samples with > 1 vol. % sulphides are excluded from this table to indicate unmineralised rock properties. Densities include both wet bulk densities from this study and specific gravities from BHP Billiton. Susceptibilities include both laboratory measurements from this study and field measurements from BHP Billiton. Means are listed with 1 σ standard deviation.

	Ultramafic adcumulate	Ultramafic mesocumulate	Ultramafic orthocumulate	Olivine-phyric komatiite	Komatiite	Undivided ultramafics
Density (t/m ³)						
Number of samples	11,313	19,070	6,568	2,722	4,755	5,054
Mean \pm std	2.79 \pm 0.30	2.78 \pm 0.27	2.72 \pm 0.20	2.83 \pm 0.23	2.92 \pm 0.25	2.88 \pm 0.24
Median	2.69	2.72	2.68	2.81	2.91	2.87
Natural remanent magnetisation intensity, (NRM: mA/m)						
Number of samples	17	5	2	0	0	1
Mean \pm std	7,290 \pm 11,100	4,820 \pm 3,610	3,580 \pm 2,790	-	-	1,190
Median	1,960	4,880	3,580	-	-	1,190
Geometric (log10) mean	2,720	3,390	2,990	-	-	1,190
Magnetic susceptibility ($\times 10^{-3}$ SI)						
Number of samples	815	3,506	1,857	1,610	4,694	2,206
Mean \pm std	14.0 \pm 19.3	28.3 \pm 87.0	40.3 \pm 43.7	23.0 \pm 29.4	10.2 \pm 21.4	8.66 \pm 29.1
Median	7.88	16.3	23.2	11.2	2.62	2.26
Geometric (log10) mean	7.17	12.0	15.1	5.42	2.80	2.02
Koenigsberger ratio, (Q: unitless)						
Number of samples	17	5	2	0	0	1
Mean \pm std	7.5 \pm 8.7	5.2 \pm 7.5	1.3 \pm 0.57	-	-	2.8
Median	2.4	1.8	1.3	-	-	2.8
Geometric (log10) mean	3.9	2.5	1.2	-	-	2.8

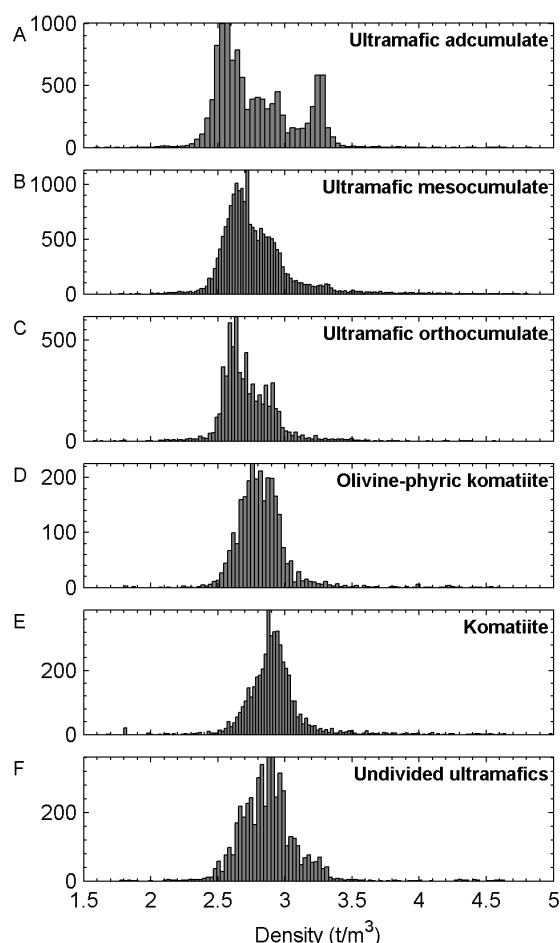


Figure 4.15. Histograms of the densities associated with different ultramafic rock types. Only rocks with < 1 % sulphides are included. Densities include both wet bulk densities from this study and specific gravities supplied by BHP Billiton.

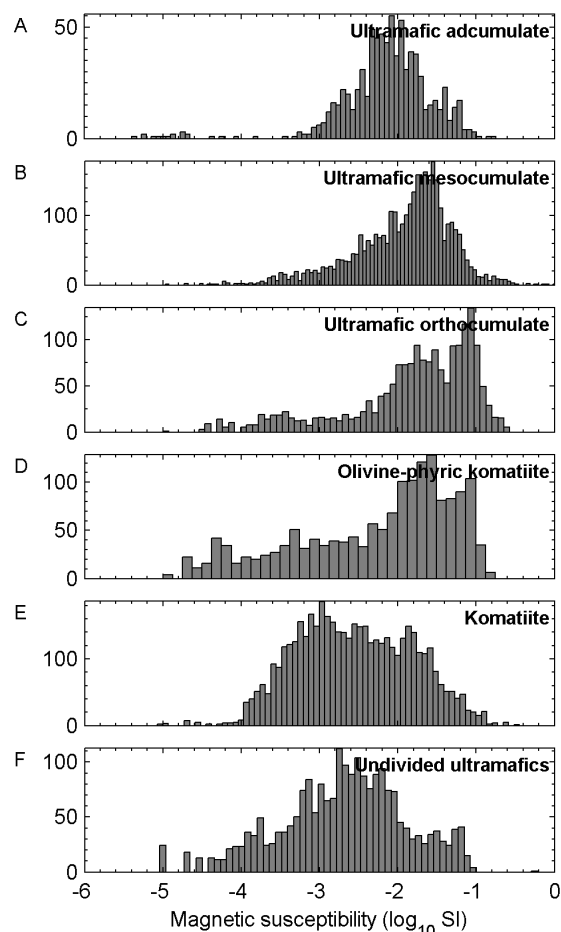


Figure 4.16. Histograms of the magnetic susceptibilities associated with different ultramafic rock types. Only rocks with < 1 % sulphides are included. Susceptibilities include those from this study as well as those supplied by BHP Billiton.

There is insufficient information to provide a rigorous analysis of the physical properties associated with different alteration styles and intensities, but a cursory summary of the properties associated with the presence of different alteration minerals and assemblages in the ultramafic rocks is presented in Table 4.6, Figure 4.17 and Figure 4.18. Serpentinised ultramafic rocks have the lowest densities and highest susceptibilities whereas olivine-bearing rocks have the highest densities. The serpentinised samples show bimodal densities with a main cluster at 2.65 t/m^3 and a smaller population at 3.25 t/m^3 , and the reverse is observed for the olivine-bearing samples. The similarity in densities of the two peaks possibly suggests some misidentification. All other assemblages lie between these two end-members.

Table 4.6. Summary of the density and magnetic properties associated with different ultramafic alteration and metamorphic styles. Only the dominant minerals are listed, as determined by visual inspection of hand samples, and only those samples with <1 % sulphides are included. Densities include both wet bulk densities from this study and specific gravities from BHP Billiton. Susceptibilities include both laboratory measurements from this study and field measurements from BHP Billiton. Means are listed with 1σ standard deviations.

	Serpentine	Serpentine with talc	Talc-chlorite- amphibole	Chlorite- biotite	Carbonate	Olivine with talc	Olivine
Density (t/m^3)							
Number of samples	3,389	959	686	1,519	1,689	746	1,147
Mean \pm Std	2.74 \pm 0.24	2.88 \pm 0.26	2.94 \pm 0.26	2.91 \pm 0.22	2.88 \pm 0.23	3.20 \pm 0.21	3.09 \pm 0.28
Median	2.65	2.87	2.91	2.89	2.86	3.25	3.21
Natural remanent magnetisation intensity, (NRM: mA/m)							
Number of samples	12	0	0	0	0	0	9
Mean \pm Std	8,100 \pm 12,900	-	-	-	-	-	3,990 \pm 4,250
Median	3,680	-	-	-	-	-	1,740
Geometric (log10) mean	2,920	-	-	-	-	-	2,080
Magnetic susceptibility ($\times 10^{-3}$ SI)							
Number of samples	166	17	23	44	0	0	14
Mean \pm Std	28.2 \pm 24.3	3.14 \pm 4.56	1.70 \pm 2.66	6.22 \pm 15.2	-	-	3.49 \pm 5.25
Median	22.8	1.10	0.720	0.750	-	-	0.0180
Geometric (log10) mean	11.0	1.18	0.879	1.07	-	-	0.132
Koenigsberger ratio, (Q: unitless)							
Number of samples	12	0	0	0	0	0	9
Mean \pm Std	5.9 \pm 6.6	-	-	-	-	-	8.4 \pm 11
Median	1.9	-	-	-	-	-	2.0
Geometric (log10) mean	3.1	-	-	-	-	-	3.6

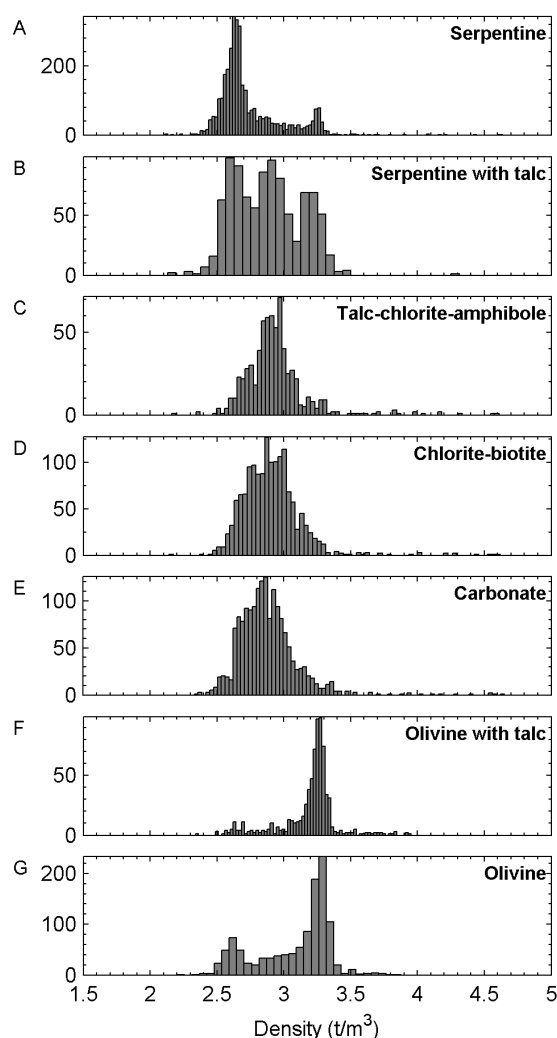


Figure 4.17. Histograms of densities of altered/metamorphism ultramafic rock divided by the dominant alteration/metamorphic minerals or assemblages. Densities include both wet bulk densities from this study and specific gravities supplied by BHP Billiton.

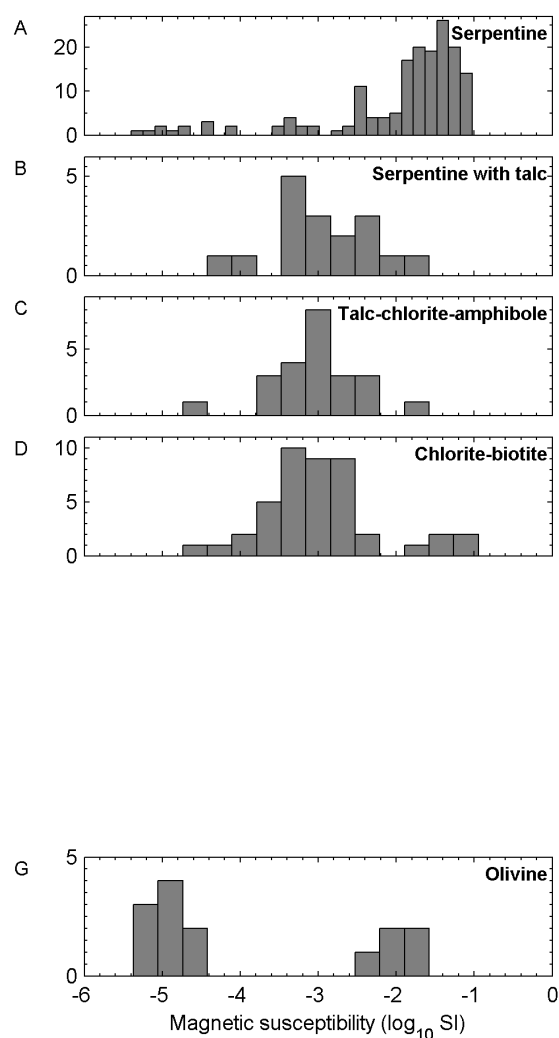


Figure 4.18. Histograms of susceptibilities of altered/metamorphism ultramafic rock divided by the dominant alteration/metamorphic minerals or assemblages. Susceptibilities include both wet bulk densities from this study and specific gravities supplied by BHP Billiton. No measurements were associated with carbonate or olivine + talc styles.

4.3.2 Thermomagnetic analysis

Thermomagnetic analysis is a reliable method for identifying specific magnetic minerals in a sample (Clark, 1997; Hunt et al., 1995). It is particularly useful for identifying extremely fine-grained magnetic phases ($<10\ \mu\text{m}$) that can't be readily identified in thin sections or XRD analyses. These fine grains may contribute significantly to the magnetic properties; single domain magnetite grains between $0.03\text{-}30\ \mu\text{m}$ account for most remanent magnetisation (Clark, 1997; Hunt et al., 1995; Schön, 2004). Representative thermomagnetic

curves for a range of rock types at Leinster are shown in Figure 4.19 indicating the measured susceptibilities over the temperature range -196 to +700 °C. Ferrimagnetic and antiferromagnetic minerals become paramagnetic when heated beyond their Curie or Néel temperatures, respectively, resulting in a sharp decrease in measured susceptibility. This decrease is usually preceded by an increase in susceptibility resulting in a Hopkinson peak (Dunlop and Özdemir, 1997). The Hopkinson peak will usually be more pronounced for single domain minerals (Dunlop and Özdemir, 1997). The cooling curves shown in Figure 4.19 (dashed lines) do not reproduce the susceptibilities measured during heating cycles (solid lines). This indicates that mineral reactions have occurred within the samples at elevated temperatures.

The magnetic minerals likely to be responsible for the thermomagnetic responses are identified based on the position of the Curie or Néel temperatures and Hopkinson peaks if present (based on compilations by Clark, 1997; Hunt et al., 1995). This study identified magnetite and ferrimagnetic monoclinic pyrrhotite as being the dominant magnetic phases. All magnetite-bearing samples contain coarse multidomain magnetite except for the massive sulphides which only contain fine-grained single domain magnetite (Figure 4.19E-F). Multidomain magnetite is distinguished from single domain magnetite by a characteristic peak in susceptibility at -155 °C (Clark, 1997; Hunt et al., 1995). In addition, titanomagnetite and ilmenite are indicated in several samples (Figure 4.19A, C, D). Titanomagnetite is identified by a Curie temperature lower than that of pure magnetite and related to the amount of Ti substitution (Clark, 1997; Hunt et al., 1995). Antiferromagnetic hexagonal pyrrhotite is the stable pyrrhotite phase at temperatures >230-295 °C in hydrothermal environments (Bennett and Graham, 1980; Kontny et al., 2000). At room temperature it has low magnetic susceptibility (Hunt et al., 1995). It can be identified by a distinctive increase in measured susceptibilities above 200-220 °C before demagnetising at a Curie temperature of 275-295 °C which is distinct from the Curie temperature of 310 °C for the monoclinic variety (Bennett and Graham, 1980; Rochette et al., 1990). Significant hexagonal pyrrhotite was observed in several massive sulphide samples, including the massive sulphide sample with the lowest measured magnetic susceptibility (Figure 4.19E). Trace amounts of hexagonal pyrrhotite are observed in several ultramafic samples with >20 vol. % disseminated pyrrhotite and pentlandite. When samples containing monoclinic pyrrhotite at low temperatures are cooled down from 700 °C,

the monoclinic pyrrhotite peak is absent or diminished and is commonly replaced by an increase in susceptibility around 250 °C diagnostic of hexagonal pyrrhotite (Figure 4.19F). In other samples the monoclinic pyrrhotite apparently converts to magnetite and presumably a non-magnetic sulphide phase, likely pyrite, upon cooling (Figure 4.19B). Most pyrrhotite-bearing samples have moderate to high NRM intensities and Koenigsberger ratios, however moderately high Koenigsberger ratios can also occur in the absence of pyrrhotite (Figure 4.19C).

4.3.3 Natural remanent magnetisation directions

NRM is common, especially in the ultramafic rocks and sulphidic rocks. Out of 461 specimen measurements, 64 % have Koenigsberger ratios >1.0 , but 78 % of those specimens are from ultramafic or massive sulphide samples. Q ratios > 10.0 (remanent magnetisation 10 times stronger than induced) are observed in 17 % of all specimens and 94 % of those are from ultramafic or massive sulphide samples. The lack of fully oriented samples prevents quantitative directional analysis of NRM. Instead, the measured remanent magnetisation directions form conical small circles of rotation around the sample axis which corresponds to the original drill hole axis for each sample. The true magnetisation direction will lie somewhere on the small circle.

Alternating field (AF) demagnetisation was applied to determine the character and components of remanent magnetisation present. Thermal demagnetisation was not used because most samples subjected to thermomagnetic study showed significant mineralogy changes during heating, as evidenced by the large differences between heating and cooling curves. Zijderveld vector component diagrams provide a projection based method of plotting the measured 3D magnetisation vectors at each demagnetisation step on a 2D diagram (Zijderveld, 1967). Individual vector components are identified on such plots by distinct straight line segments, and principal component analysis can be applied to the data points in each straight line segment to calculate the inclination and declination of each component (Butler, 1992; Kirschvink, 1980).

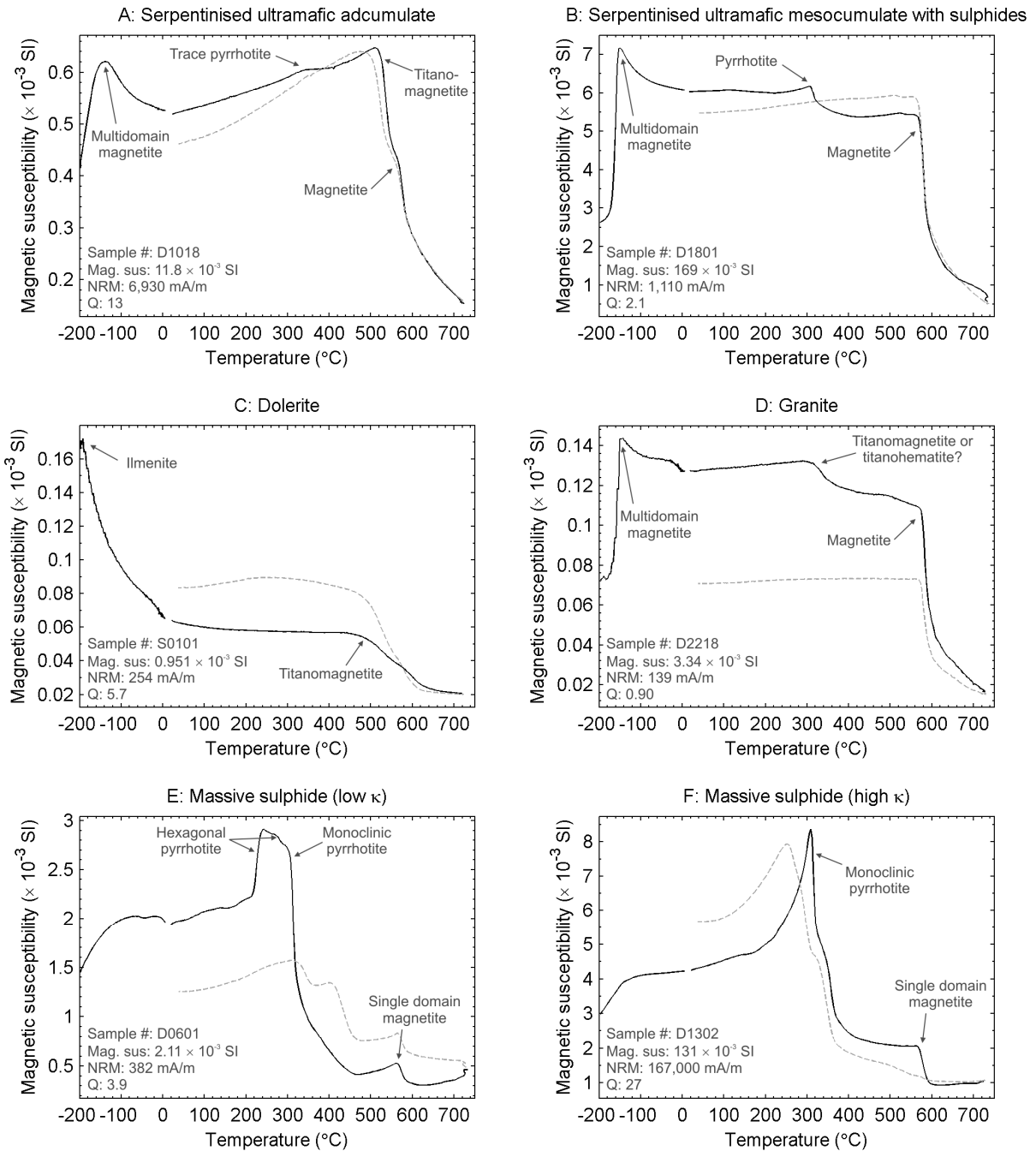


Figure 4.19. Thermomagnetic curves showing the temperature dependence of magnetic susceptibility for selected samples. Solid black lines indicate heating cycles; grey dashed lines indicate cooling cycles. Cooling curves will not match heating curves if chemical reactions have occurred during the heating cycles. Major mineral phases are identified from their Curie or Néel temperatures as indicated by Clark (1997) and Hunt et al. (1995). In C, ilmenite with a Néel temperature of -205°C is likely present although this lies below the minimum measurement temperature of -196°C . Hexagonal pyrrhotite is indicated in E with a transition to ferrimagnetic behaviour at $\sim 220^{\circ}\text{C}$ and a Curie point at $\sim 280^{\circ}\text{C}$ (indicated with arrows) below the monoclinic pyrrhotite Curie temperature of 310°C .

Zijderveld diagrams of the demagnetisation of three massive sulphide ore samples from Perseverance are shown in Figure 4.20 along with the remaining NRM intensities at each step. The diagrams are in sample coordinates with the vertical up-down axis parallel to the sample axis, which is parallel to the axis of the original drill core. The X and Y axes are arbitrary due to the unknown rotation around the sample axis. All three samples show consistent vertically-upward (relative to the sample) oriented remanence directions (open circles) but different demagnetisation intensity behaviours. Sample D1101.1 had the highest initial NRM intensity but was the most easily demagnetised with a peak field of < 12 mT. Thermomagnetic analysis indicated monoclinic pyrrhotite was the only magnetic phase in this sample. Sample D0102.1 also demagnetised easily up to 6 mT but the remaining 10 % of the remanent magnetisation could not be removed up to 80 mT. Thermomagnetic analysis was not performed on this sample, but its susceptibility is one of the lowest measured for massive sulphides in this study, and it may contain both monoclinic and hexagonal pyrrhotite. In contrast, sample D0403.1 had the weakest initial NRM but was the hardest to demagnetise with 40 % of its magnetisation still present at 18 mT and 16 % remaining at 140 mT. Its low magnetic susceptibility indicates that it contains dominantly hexagonal pyrrhotite (analogous to D0601 in Figure 4.19E). All three samples are inferred to contain single remanent magnetisation components and their orientations are plotted in geographic coordinates in Figure 4.21. Samples D0102.1 and D0403.1 both show normal to intermediate polarities, and the small circle for D0403.1 contains the direction of the present day earth field. The polarity of sample D1101.1 is indeterminate because the small circle crosses the horizon.

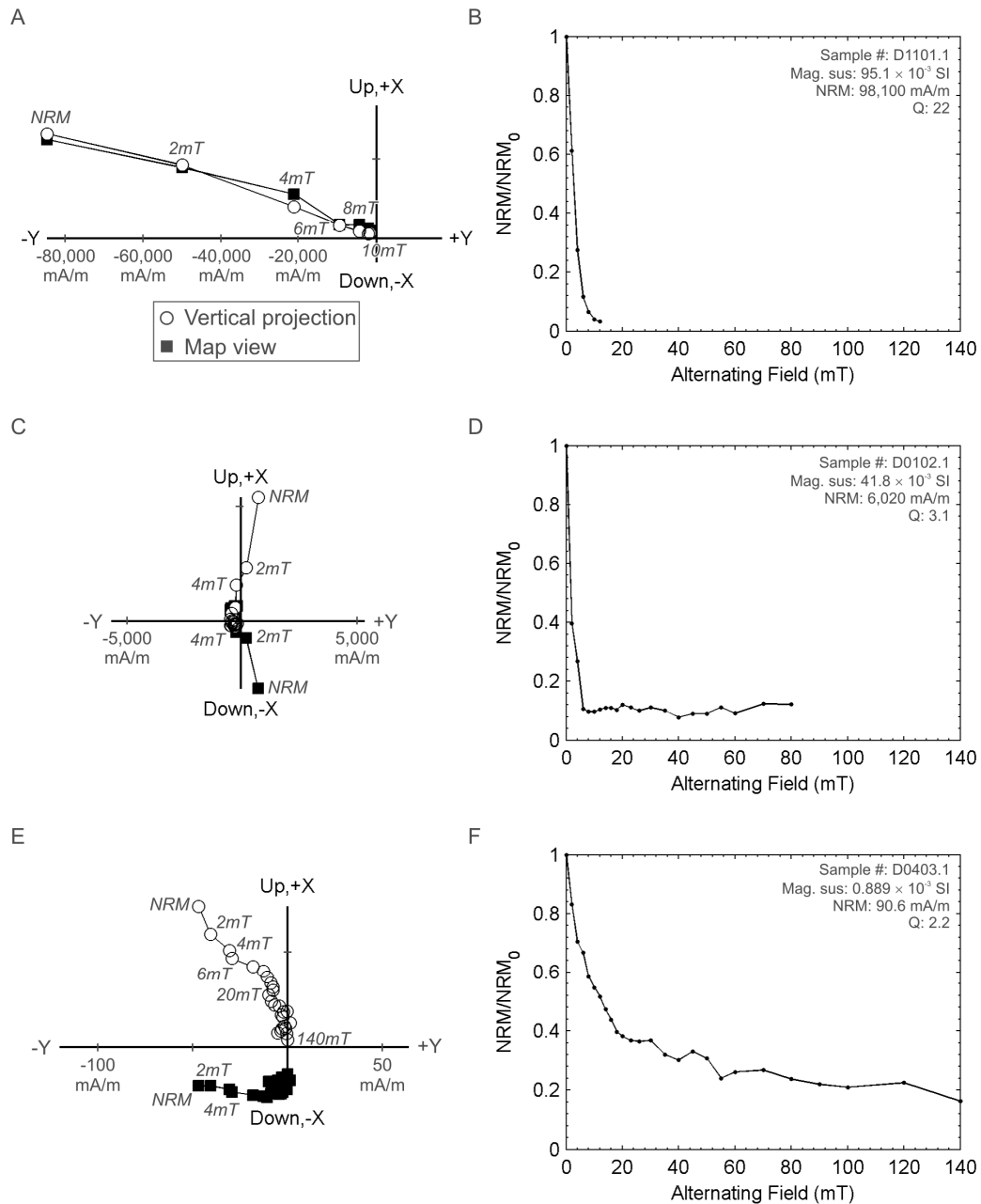


Figure 4.20. Zijderveld plots of remanence vectors (left) and demagnetisation intensities (right) for representative axially-oriented massive sulphide samples. All samples are from the Perseverance ore bodies and contain > 95 vol. % pyrrhotite and pentlandite. All Zijderveld plots are shown in sample coordinates with the legend as for A. The up/down axis is with respect to the sample axis which is aligned with the original drill hole axis; the X and Y axes are arbitrary due to unknown axial rotation of samples. Selected peak alternating field intensities are indicated in *italics*. Demagnetisation intensity plots for each sample show proportion of initial NRM intensity (NRM₀) remaining after demagnetisation at each frequency. A-B. D1101.1 has intense but low coercivity remanence associated with monoclinic pyrrhotite. It is inferred to represent a ChRM. C-D. D0102.1 contains an extremely soft coercivity component and a weak high coercivity component. It may contain a mixture of monoclinic and hexagonal pyrrhotite. E-F. D0403.1 shows a weak but moderate coercivity remanence with a small circle consistent with the direction of the current earth field direction and the inference that it records a VRM (Figure 4.21). Its low magnetic susceptibility suggests that hexagonal pyrrhotite is dominant.

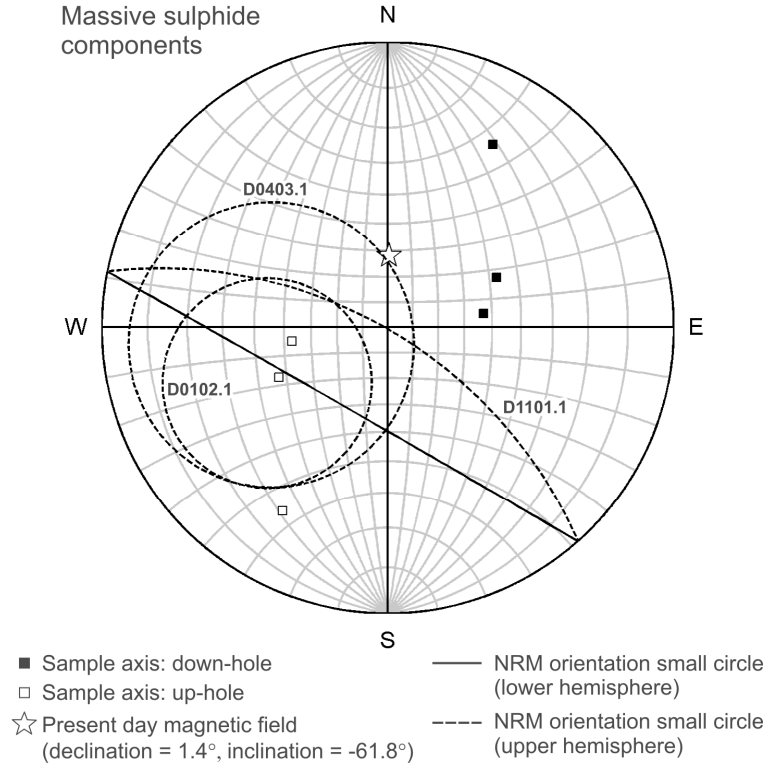


Figure 4.21. Equal area stereographic projection of remanent magnetisation components for axially oriented massive sulphide samples in geographic coordinates. Open symbols and dashed lines indicate upper hemisphere projections; solid symbols and lines indicate lower hemisphere projections. Each small circle is a rotation around the sample axis indicated by pairs of up-hole and down-hole sample axes. Samples D0403.1 and D0102.1 show normal to intermediate polarity. The polarity of remanence in sample D1101.1 cannot be determined without a full sample orientation.

The other rocks at Leinster that show strong remanent magnetisation are the ultramafic rocks. Their typical AF demagnetisation behaviours are shown in Figure 4.22. All samples contain ≤ 10 vol. % sulphides (mainly pyrrhotite and pentlandite). Sample D2003.1 is a serpentinised ultramafic mesocumulate and contains the most sulphides, ~ 10 %. It shows a distinct upwards vertical remanent magnetisation orientation $\sim 5^\circ$ from the sample axis and is easily demagnetised with a peak field < 20 mT. This behaviour is observed in many samples regardless of geographic position or orientation and is inferred to represent an isothermal remanent magnetisation (IRM) overprint acquired from a spinning magnetised drill core barrel (de Wall and Worm, 2001; Musgrave et al., 2006; Pinto and McWilliams, 1990). Such IRM overprints can completely replace any *in situ* NRM directions and all samples in this study that have measured remanence directions within 20° of the sample axis and peak destructive fields < 20 mT are treated as drilling IRM overprints (Figure 4.23). Sample D0229.1 in Figure 4.22 is an olivine-bearing ultramafic adcumulate with < 1 % sulphides. It shows a soft upwards component $\sim 18^\circ$ from the sample axis, inferred to be a drilling IRM, overprinting a harder

component that may represent a characteristic remanent magnetisation (ChRM). A peak field of 12 mT only removes half of the magnetisation and > 20 % initial NRM intensities persist until > 60 mT.

Extremely strong remanent magnetisation was measured in the sulphide-free serpentinitised ultramafic adcumulate sample D1704.1 but the magnetisation was easily removed with < 5 % of the initial NRM remaining after a peak field of 8 mT. The NRM direction is stable and the small circle is consistent with the present day earth field. This component and others with similar low coercivities and angles > 20° from the sample axes are plotted in Figure 4.24. Although the coercivities of these sample are similar to those observed in drilling IRM, the angles from the sample axes are too large to be the result of drilling IRM. Instead all lie < 20°, and usually < 6°, from the present day *in situ* earth field orientations and are likely to represent viscous remanent magnetisation (VRM) acquired during the current magnetic epoch.

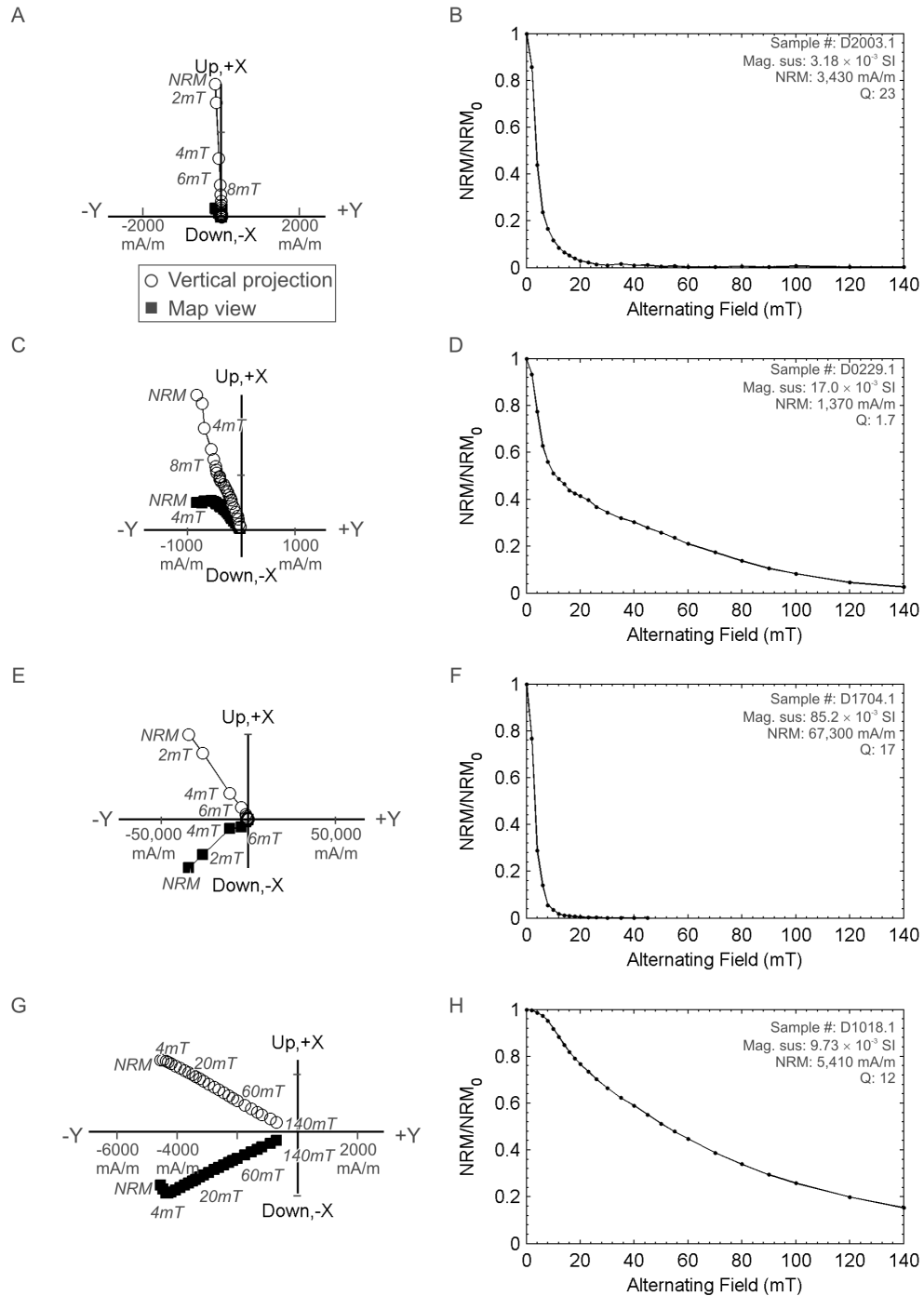


Figure 4.22. Zijderveld plots of remanence vectors (left) and demagnetisation intensities (right) for axially-oriented ultramafic rock samples. All plots are shown as described for Figure 4.20. A-B. D2003.1 shows an upwards-directed remanence aligned with the drill core barrel, suggesting a drilling IRM overprint. C-D. D0229.1 contains a soft component $\sim 18^\circ$ from the core axis which may be a drilling IRM overprinting a harder but low intensity component inferred to represent a ChRM. E-F. D1704.1 shows an intense but soft remanence with a small circle consistent with the present *in situ* earth field direction. It is inferred to represent a VRM acquired from a recent earth field. G-H. D1018.1 contains two components, a less stable component consistent with a recent earth field VRM, and a more stable component inferred to be a ChRM. This sample is one of two used to derive oriented remanence vectors (Figure 4.25).

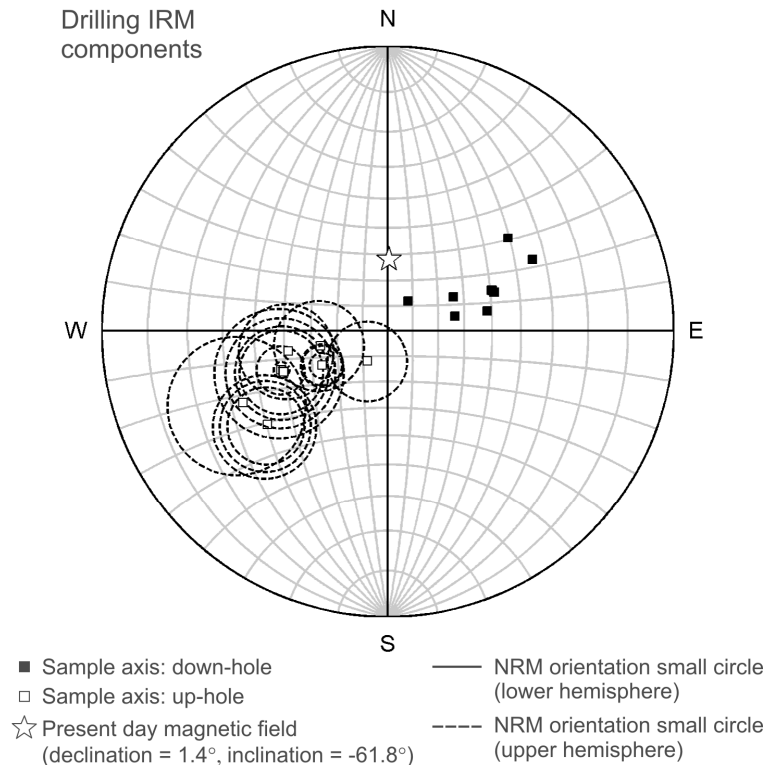


Figure 4.23. Equal area stereographic projections of remanent magnetisation components attributed to drilling IRM for axially-oriented ultramafic rock samples in geographic coordinates. Open symbols and dashed lines indicate upper hemisphere projections; solid symbols and lines indicate lower hemisphere projections. All of these components are the softest component in each sample, are demagnetised by peak fields < 20 mT (usually ~ 12 mT), and lie $< 20^\circ$ from the sample axis.

Sample D1018.1 in Figure 4.22 is a serpentinised ultramafic adcumulate with only trace sulphides (Figure 4.5C) and has moderate remanent magnetisation intensity. It proved to be one of the hardest samples to demagnetise in this study with $> 40\%$ of the initial intensity persisting to peak fields of 60 mT and $\sim 16\%$ remaining after 140 mT. It contains two magnetisation components, one from 0-4 mT and the other from 4-140 mT. The small circle associated with the softer component is plotted and labelled in Figure 4.24 with a similar component measured in sample D1009.1. The two samples are both from the Perseverance Ultramafic Complex, are similar in appearance, and were separated by 200 m along the same drill hole. The small circles identified for the soft components in each of these samples are both consistent with the present earth field orientation. If they are also VRM overprints acquired from the current earth field, the samples can be rotated around their axis until the soft VRM component is aligned with the current earth field direction to fully orient the samples (Kodama, 1984; Van der Voo and Watts, 1978). The measured orientation of the more stable remanent magnetisation component, inferred to be the ChRM, can be rotated by the same amount to

obtain a fully oriented ChRM direction. Applying this technique to sample D1018.1 gives a ChRM inclination of $+5^\circ$ and declination of 305° , or intermediate polarity. A ChRM inclination of $+42^\circ$ and declination of 235° is obtained for sample D1009.1, suggesting reverse polarity. These oriented remanence directions are plotted with the associated small circles in Figure 4.25 alongside all other small circles believed to record ChRM components in each sample based on having higher coercivities like those in Figure 4.22D and H.

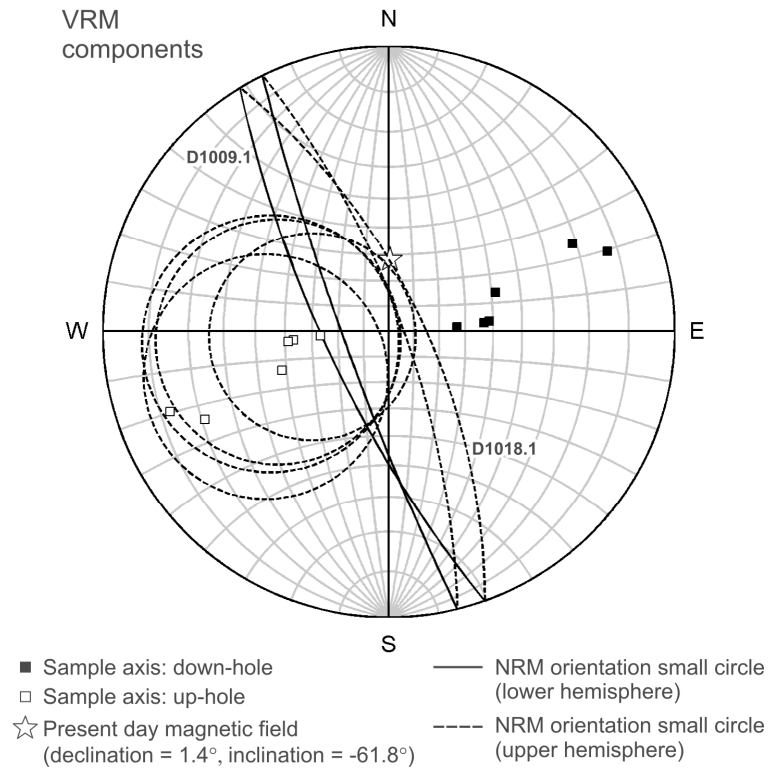


Figure 4.24. Equal area stereographic projections of remanent magnetisation components attributed to VRM for axially-oriented ultramafic rock samples in geographic coordinates. Open symbols and dashed lines indicate upper hemisphere projections; solid symbols and lines indicate lower hemisphere projections. All samples are serpentinitised. All of these components are demagnetised by peak fields < 20 mT and lie $> 20^\circ$ from the sample axis. Their larger angles to the sample axes make it unlikely that they are the result of drilling IRM, although their coercivities are similar. All pass within 20° of the present earth field orientation, and all but one lie within 6° . Based on the assumption that they do represent *in situ* VRM, full orientations can be identified for labelled samples D1009.1 and D1018.1 (Figure 4.25).

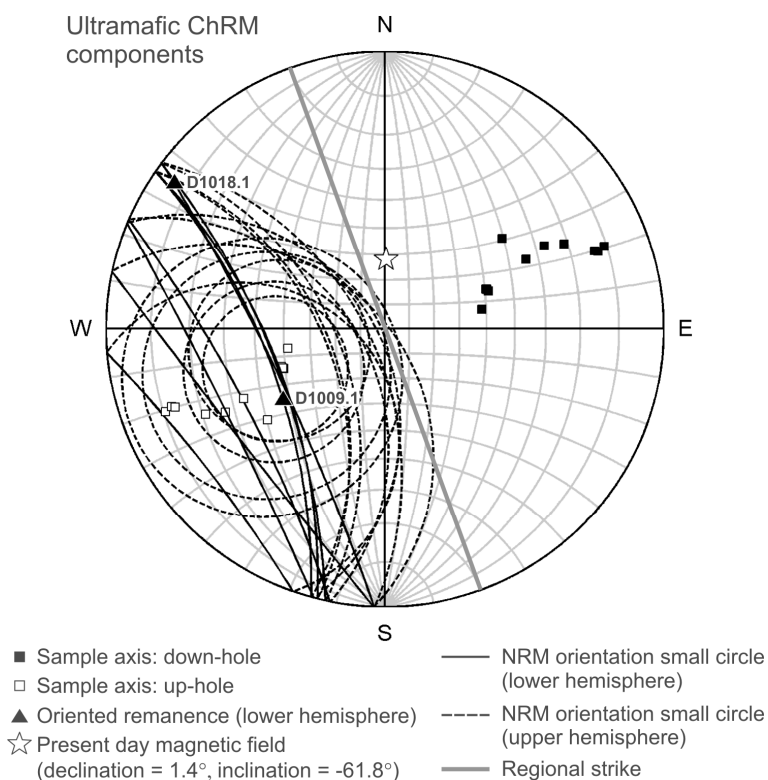


Figure 4.25. Equal area stereographic projections of ChRM components in geographic coordinates for axially-oriented ultramafic rock samples. Open symbols and dashed lines indicate upper hemisphere projections; solid symbols and lines indicate lower hemisphere projections. These components are the most stable components observed in each sample and show the highest coercivities with demagnetisation intensities similar to those in those in Figure 4.22D and H. Most show normal to intermediate polarity regardless of the sample orientation. Samples D1009.1 and D1018.1 have oriented remanence directions plotted assuming that their softer components identified in Figure 4.24 are associated with the present field direction.

The results from AF demagnetisation on other lithologies in this study, notably granitoids, mafic rocks, and felsic volcanoclastic rocks, are unreliable. The remanent magnetisation in those samples was either too low to give meaningful results, or the measured remanent magnetisation directions lie $< 20^\circ$ (and usually $< 10^\circ$) of the sample axis, indicating likely drilling-induced IRM.

4.3.4 Physical property cross-plots

Several previous studies have demonstrated the value of physical property cross plots for identifying trends and relationship between samples and their constituent minerals (Emerson et al., 1999; Emerson and Yang, 1997; Henkel, 1976; Henkel, 1994; Puranen, 1989). They are employed here to attempt to identify the major controls on the observed physical properties and to facilitate prediction of physical properties based on geological processes when measurements are lacking. Figure 4.26 provides an overview of the densities and

susceptibilities measured in this study in comparison to minerals commonly present in Archean granite-greenstone terranes and associated Ni-sulphide mineralisation. Also included is the field for Scandinavian Precambrian igneous and metamorphic rocks containing dominantly paramagnetic minerals, defined by Henkel (1994). The field corresponds well with the lowest measured susceptibilities for silicate rocks in this study. The densities and susceptibilities measured in this study cover much of the possible range of properties that could be attributed to the selected minerals. A more detailed plot with samples coloured by rock type is shown in Figure 4.27. The properties of granitoids, felsic volcanic rocks, and many sedimentary, metamorphic, and mafic igneous rocks have standard crustal densities controlled by abundant feldspar and quartz, but have a range of susceptibilities above paramagnetic values that can be attributed to small but variable oxide contents, especially magnetite and ilmenite. The remaining mafic igneous, metamorphic and sedimentary rocks have higher densities suggesting increasing control imposed by more mafic minerals or sulphides. Ultramafic rocks show the highest susceptibilities and the widest range of densities of all the silicate lithologies, and the properties of the massive sulphides are clearly controlled by their sulphide content, with monoclinic pyrrhotite apparently dominant in most samples.

Cross plots of magnetic properties are important for understanding observed aeromagnetic anomalies which are controlled by both induced susceptibility and NRM. Plotting magnetic susceptibility versus NRM intensity (Figure 4.28) allows discrimination of the rock types that may control observed magnetic anomaly maps. Such plots don't account for the direction of remanent magnetisation relative to the present day earth field which will ultimately determine the total magnetisation of the rocks; however the Koenigsberger ratio provides an indication of which rocks will be more prone to remanent magnetisation complications. Koenigsberger ratios plot as diagonal lines on log-log plots. Figure 4.28 can be roughly divided into two parts: the massive sulphides and ultramafic rocks dominantly have susceptibilities $> 6 \times 10^{-3}$ SI and NRM intensities > 0.4 A/m. Mafic igneous, felsic igneous, metamorphic, and sedimentary rocks all have susceptibilities $< 6 \times 10^{-3}$ SI and NRM intensities < 0.4 A/m. Granitoid rocks overlap the boundary between these two divisions. In all groups, and for the dataset as a whole, increasing susceptibilities are associated with proportionally larger increases in NRM intensities resulting in higher Koenigsberger ratios with increasing susceptibilities. Mafic igneous rocks are plotted according to whether they are inferred to have an intrusive or extrusive origin. While there is no significant difference in properties between

these two subgroups in Figure 4.27, Figure 4.28 indicates that most of the intrusive gabbros and dolerites have NRM intensities and Koenigsberger ratios 1-2 orders of magnitude higher than basalts. There is significant overlap in property ranges between the assorted mafic igneous rocks and metamorphic rocks shown in both Figure 4.27 and Figure 4.28, so it is possible that many of the metamorphic rocks had mafic igneous protoliths. The metamorphic rocks also overlap slightly with the felsic volcanic rocks suggesting some felsic components.

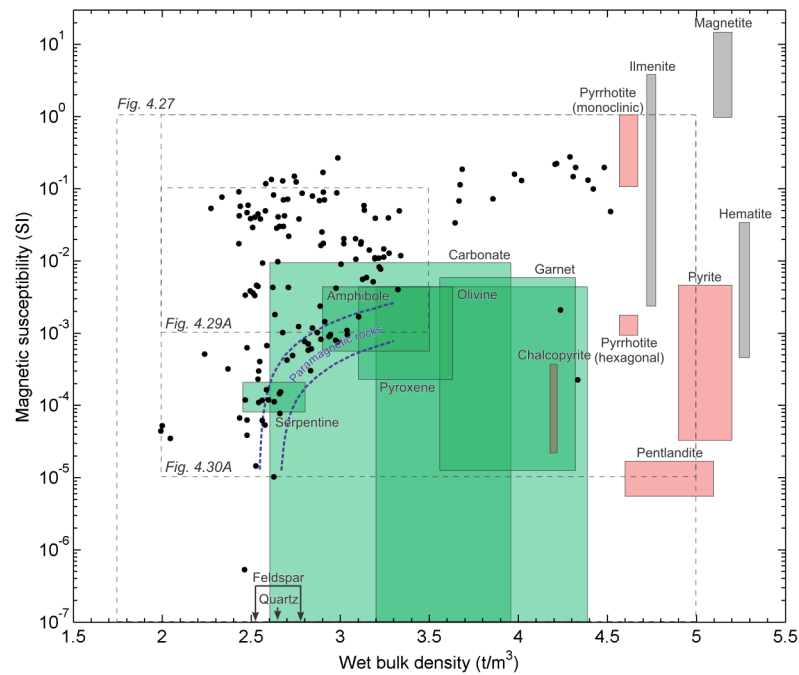


Figure 4.26. Densities versus magnetic susceptibilities for all samples in this study plotted with expected property ranges of associated minerals. Boxes indicate range of published literature values for selected minerals common in Archean granite-greenstone terranes and Ni-sulphide deposits and reflect compositional and property variability (Bleil and Petersen, 1982; Clark, 1997; Hunt et al., 1995; Johnson and Olhoeft, 1984; Telford et al., 1990; Wohlenberg, 1982). Silicates and carbonates are in green, sulphides in red, and oxides in grey. Feldspars and quartz are diamagnetic so have slight negative susceptibilities that cannot be accommodated on a logarithmic scale. The field of common paramagnetic rocks defined by Henkel (1994) corresponds well with the lowest susceptibilities observed in silicate rocks in this study. Dashed boxes outline the areas covered in the more detailed figures to follow.

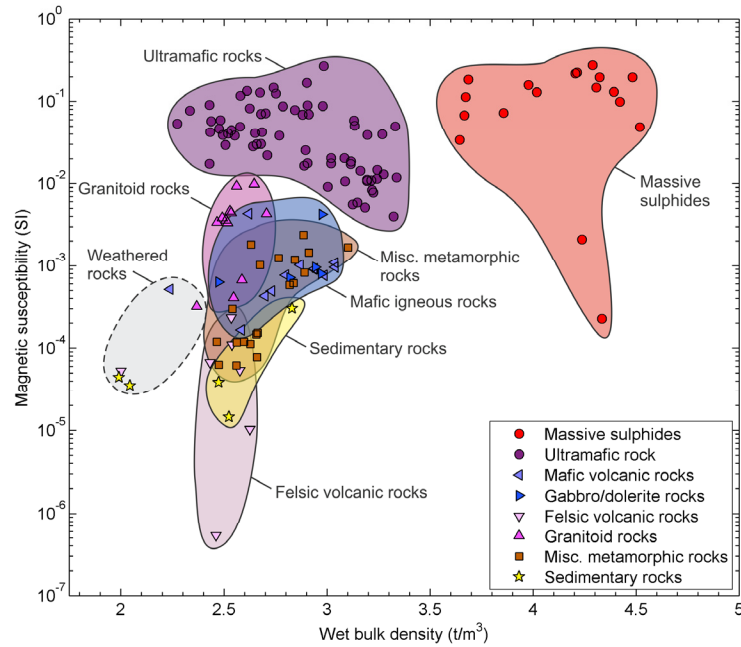


Figure 4.27. Densities and magnetic susceptibilities plotted by rock type for samples from this study. All samples are coloured by protolith rock type (if discernable) regardless of sulphide content or alteration. Miscellaneous metamorphic rocks include all rocks that are too fine-grained, deformed or altered to accurately identify by visual inspection.

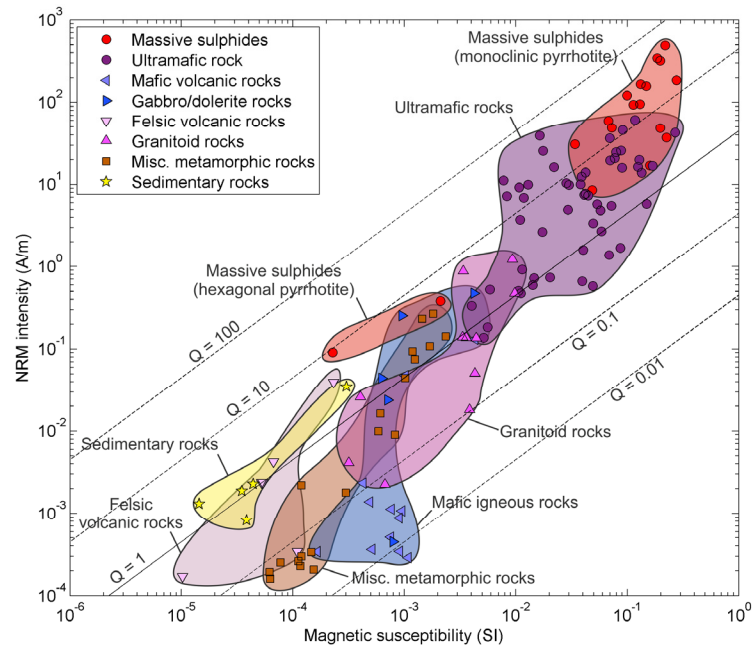


Figure 4.28. Magnetic susceptibilities and NRM intensities plotted by rock type for samples from this study. All samples are coloured by protolith rock type (if discernable) regardless of sulphide content or alteration. Diagonal lines are lines of constant Koenigsberger (Q) ratios as indicated. There is a strong correlation between susceptibility and NRM. Massive sulphides and ultramafic host rocks are distinguished by their high magnetic susceptibilities and highest total magnetisation. All other rocks show considerable overlap in NRM intensities, Q ratios, and magnetic susceptibilities. Several samples inferred to be affected by drilling or lightning IRM have been omitted.

The property ranges associated with ultramafic rocks in Figure 4.27 and Figure 4.28 are larger than most other lithological variations due to the wide variety of mineralogical changes accommodated by ultramafic rocks. There is insufficient information available in this study to identify all possible alteration, metamorphic, and mineralisation trends associated with ultramafic rocks, but the primary controls can be assessed. Visual inspection suggests that all ultramafic rock samples collected in this study are either serpentinised or contain olivine, and this is supported by the bimodal distribution in physical properties (Figure 4.17 and Figure 4.18) and by XRD analysis (Table 4.1). Figure 4.29 shows all ultramafic rocks with < 5 vol. % sulphides, plotted according to their dominant mineralogy. Serpentinised ultramafic rocks have significantly lower densities, and higher susceptibilities and NRM intensities than the olivine-bearing rocks but have similar Koenigsberger ratios. The observed serpentinisation corridor is linear in both plots and in Figure 4.29A is bounded by two empirical linear mixing lines. They appear curved because the susceptibility axis is logarithmic but the density axis is linear. Comparison between Figure 4.26 and Figure 4.29A confirms that the densest olivine-bearing samples lie within the field of natural olivine and that the serpentinised rocks lie on a mixing trend between olivine, serpentine and magnetite. The larger BHP Billiton dataset includes additional measurements for komatiitic ultramafic rocks and for various carbonated ultramafic rocks with talc, chlorite, and carbonate assemblages. There is insufficient control on the physical property relationships in these samples as they were not observed in this study, but their range is plotted in Figure 4.29A.

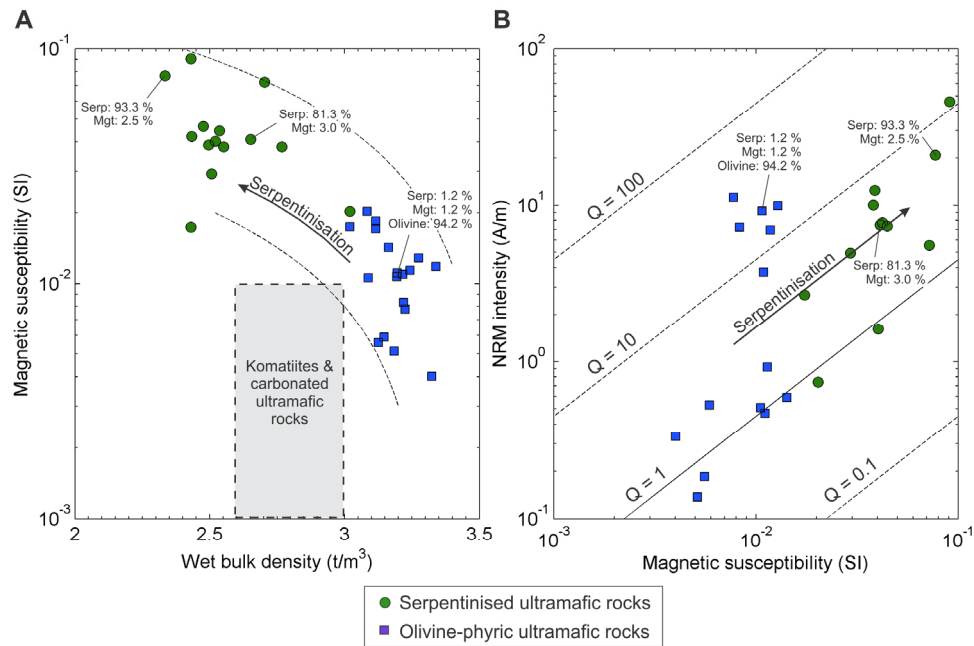


Figure 4.29. Cross-plots of density and magnetic properties associated with serpentinised and olivine-bearing ultramafic rocks. Only samples with < 5 vol. % sulphides are shown. Olivine, magnetite and serpentine contents determined by XRD analysis are indicated where available (0 % abundances are omitted for clarity). A. Density versus susceptibility. Serpentinisation increases susceptibility and decreases density. Dashed lines indicate a potential serpentinisation 'corridor'. The lines are linear mixing lines, but appear curved due to the use of log-linear axes. The field of komatiites and carbonated ultramafic rocks includes talc, chlorite, and carbonate altered rocks not observed in this study, but indicated in the BHP Billiton data (Figure 4.17 and Figure 4.18). B. Susceptibility versus NRM intensity. Diagonal lines indicate constant Koenigsberger (Q) ratios as indicated. Serpentinisation increases both susceptibility and NRM intensity, but appears to do so with approximately constant Q ratios ≥ 1 . Several samples inferred to be affected by drilling IRM have been omitted.

The other major control on the physical properties of ultramafic rocks is their sulphide content as demonstrated in Figure 4.30. Here, all ultramafic rocks are plotted according to their sulphide content, in addition to the massive sulphide samples. For samples with < 5 vol. % disseminated sulphides there is very little change in properties with increasing sulphide contents. The serpentinisation corridor identified in Figure 4.29A is preserved in Figure 4.30A for these samples, and the presence or absence of serpentinisation remains the dominant control on the properties. As the disseminated sulphide content increases above 10-20 vol. % the samples begin to show increased densities and susceptibilities away from the serpentinisation corridor. This trend may be associated with a slight increase in NRM intensities and Koenigsberger ratios (Figure 4.30B), but ultramafic rock samples with minimal sulphides can still show high susceptibilities, NRM intensities, and Koenigsberger ratios. Comparison between Figure 4.26 and Figure 4.30A shows that the sulphide-rich samples trend towards the physical properties associated with monoclinic pyrrhotite, but don't get to magnetic susceptibilities quite as high as pure monoclinic pyrrhotite. This may indicate the

influence of less magnetic hexagonal pyrrhotite. Emerson et al. (1999) reported monoclinic to hexagonal pyrrhotite ratios of ~1:1 for the Rocky's Reward deposit. The two massive sulphide samples with magnetic susceptibilities $< 10^{-2}$ SI both contain visible pentlandite in a pyrrhotite-dominant host, similar to most other massive sulphide samples, however they come from isolated thin (< 60 cm thick) massive sulphide lenses. Thermomagnetic analysis of one of the samples (Figure 4.19E) and comparison between Figure 4.26 and Figure 4.30 indicates that the form of pyrrhotite dominant in these samples is hexagonal pyrrhotite, resulting in low susceptibilities and NRM intensities, but relatively high Koenigsberger ratios (3-10).

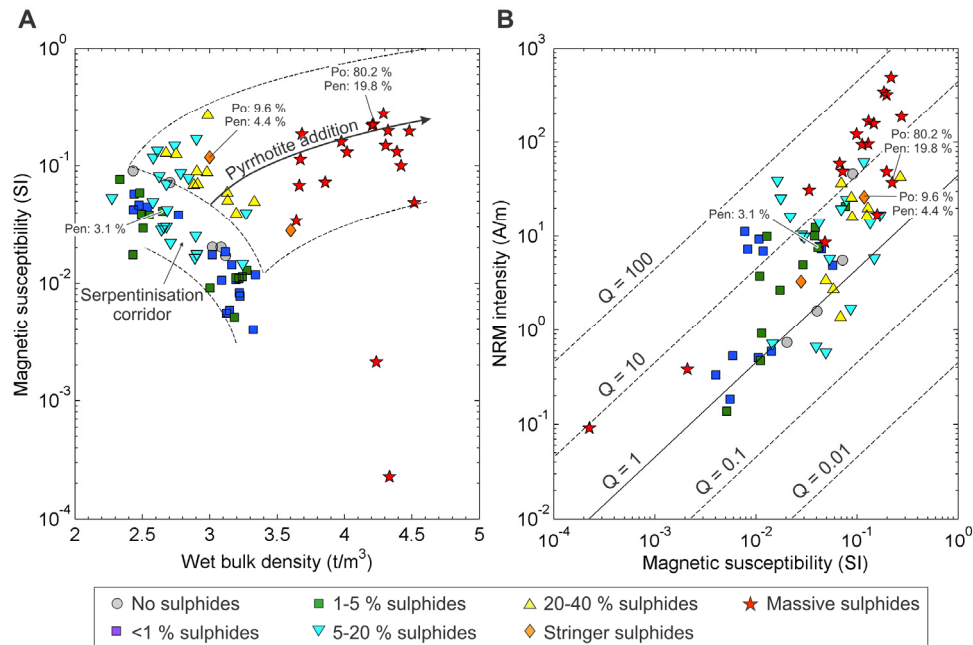


Figure 4.30. Cross-plots of density and magnetic properties associated with ultramafic rocks and massive sulphides plotted according to sulphide content. Samples are plotted regardless of alteration style. Sulphide contents (Po = pyrrhotite; Pen = pentlandite) determined by XRD analysis are indicated where available. A. Density versus susceptibility. Ultramafic rocks with < 5 -10 vol. % disseminated sulphides lie in the same serpentinisation corridor identified in Figure 4.29A so appear to be primarily controlled by alteration style. Increasing sulphide contents > 10 -20 vol. % are associated with an increase in density and susceptibility that trends towards monoclinic pyrrhotite. The dashed bounding lines on the sulphide trend are linear mixing lines with pure monoclinic pyrrhotite of different susceptibilities. B. When susceptibility is plotted against NRM intensity the relationships between properties and sulphide content are not as strong. NRM intensities, Q ratios, and magnetic susceptibilities all tend to increase with increasing sulphide content, but with significant overlap (also see Figure 4.14). Diagonal lines indicate constant Koenigsberger (Q) ratios as indicated. Several samples inferred to be affected by drilling IRM have been omitted.

4.4 DISCUSSION

The rocks surrounding the Leinster Ni-sulphide deposits are associated with a huge range of mass and magnetic properties that reflect the accumulation of multiple episodes of alteration, metamorphism and deformation. Despite their complex history, their physical

properties are distinctive with large physical property contrasts associated with particular lithologies, alteration styles, and mineralisation. These contrasts make these deposits, and similar ones around the world, highly favourable for exploration using potential field geophysical methods. To accurately interpret observed geophysical responses over exploration targets it is important to understand the physical properties that control the observed geophysical responses at known deposits. The data presented in this study can be summarised by a physical property discriminant diagram analogous to those used to subdivide igneous rocks based on chemical analyses (Cox et al., 1979; Le Bas et al., 1992; Winchester and Floyd, 1977). The discriminant diagram presented in Figure 4.31, and described below, captures most of the physical property relationships observed in this study. It provides a visual representation of the typical property ranges that could be used in geophysical modelling. It might also provide a first pass automated classification for *in situ* down-hole logging of physical properties when those techniques become more commonly applied in minerals exploration. In Chapter 7 it is used to develop predictive 3D geological models based on the physical property models recovered from gravity and magnetic inversions.

4.4.1 Massive sulphides

Massive sulphides at Leinster have the most extreme properties, but encompass a limited volume of rocks. They typically consist of 80-95 vol. % pyrrhotite, < 20 vol. % pentlandite, and minor chalcopyrite, pyrite, and magnetite. Monoclinic pyrrhotite (Fe_7S_8) is the only ferromagnetic sulphide present, but antiferromagnetic hexagonal pyrrhotite (Fe_9S_{10}) is expected in roughly a 1:1 ratio (Emerson et al., 1999). All massive sulphides have high densities $> 3.6 \text{ t/m}^3$ and extreme Koenigsberger ratios (3-50). Such high Koenigsberger ratios are suspicious and are commonly inferred to indicate drilling IRM overprints (de Wall and Worm, 2001), but the four massive sulphide samples subjected to AF demagnetisation in this study showed no evidence of drilling IRM, including a sample with a Koenigsberger ratio of 22. The magnetic susceptibility and NRM intensity of the massive sulphide samples is controlled by their hexagonal/monoclinic pyrrhotite ratio, although minor magnetite is present. Massive sulphides dominated by hexagonal pyrrhotite can have susceptibilities and NRM intensities as low as $0.1 \times 10^{-3} \text{ SI}$ and 0.1 A/m , similar to any possible host rock. Those with dominantly monoclinic pyrrhotite will have susceptibilities up to $280 \times 10^{-3} \text{ SI}$ and NRM intensities up to 700 A/m , significantly higher than all host rocks. Massive sulphide bodies rich

in hexagonal pyrrhotite may not be associated with aeromagnetic anomalies, but monoclinic pyrrhotite dominant massive sulphides may cause aeromagnetic anomalies. Self-demagnetisation may also be significant in these most extremely magnetic rocks (Clark and Emerson, 1999). All significant volumes of massive sulphides will be associated with gravity anomalies.

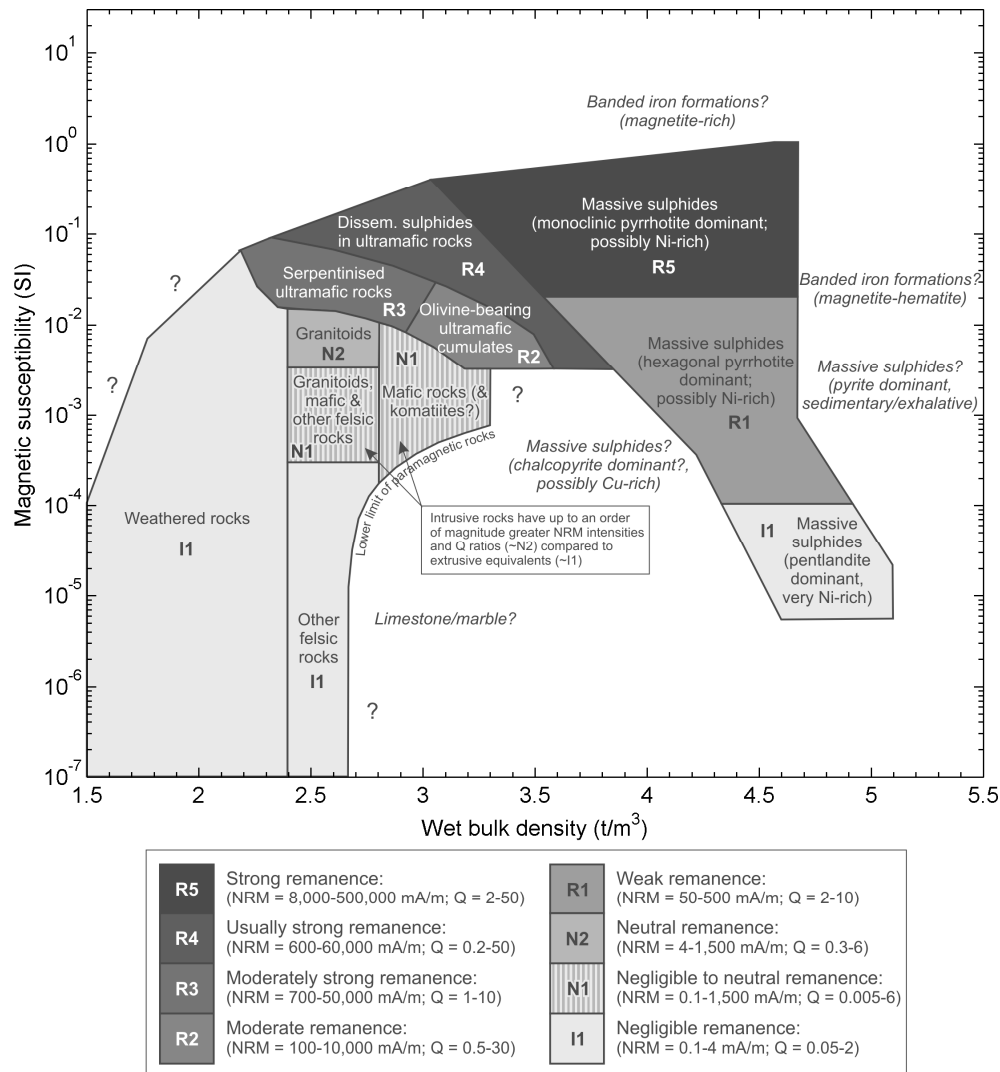


Figure 4.31. A physical property discriminant diagram for rocks found in the Leinster area. Densities and susceptibilities provide the greatest discrimination of rocks, but secondary information may be obtained from remanent magnetisation. Remanent magnetisation classifications are initially based on whether Koenigsberger (Q) ratios are generally < 1 (I = induced), \approx 1 (N = neutral), or > 1 (R = remanent) and subsequently on the intensity of NRM (numbers 1-5). The diagram is an interpretation based on the relationships observed in this study, and the physical properties of end-member minerals depicted in Figure 4.26. The terms mafic and felsic apply to igneous rocks and metamorphic or sedimentary rocks derived from predominantly mafic or felsic components. Igneous rocks in the two N1 fields with vertical striped shading have different remanent magnetisation characteristics depending on whether the rocks are intrusive (granitoids, gabbros, dolerites) or extrusive. Intrusive rocks have higher remanence and tend towards R2, whereas extrusive equivalents tend towards I1. The lower limit of paramagnetic rocks is taken from Henkel (1994). Italicised text outside the coloured fields indicate inferred positions for several rock types not observed in this study. Question marks indicate areas where the boundaries are poorly defined due to a lack of samples.

Hexagonal pyrrhotite is the stable high temperature phase above 260-290° C but can be converted to ferrimagnetic monoclinic pyrrhotite relatively easily at low temperatures (Rochette et al., 1990). McCall et al. (1995) report both hexagonal and monoclinic pyrrhotite in peridotite-hosted nickel sulphide deposits in the Widgiemooltha area south of Kambalda and infer that the type of pyrrhotite present is related to the temperature of metamorphism, with hexagonal pyrrhotite more commonly present in higher temperature metamorphic rocks. Previous workers have reported that the peak metamorphic grade at Perseverance reached middle-amphibolite facies (< 550 °C) but decreased northwards (Barrett et al., 1977; Binns et al., 1976; Gole et al., 1987). The higher grades at Perseverance may have promoted more hexagonal pyrrhotite formation than in more northerly deposits. However, Bennett and Graham (1980) and O'Reilly et al. (2000) suggest that the rate of cooling may have more of a control, with monoclinic pyrrhotite forming during slow equilibration, and hexagonal pyrrhotite preserved by fast cooling.

Directions of remanent magnetisation cannot be conclusively identified in this study due to the lack of fully oriented samples. The abundance of pyrrhotite in the massive sulphide samples and their potentially high susceptibilities and NRM intensities may also lead to complications with anisotropy of magnetic susceptibility and remanent magnetisation (Dunlop and Özdemir, 1997). The AF demagnetisation intensities shown in Figure 4.20 are consistent with multidomain pyrrhotite with grain sizes > 1.6 µm (Soffel, 1977) and indicate that NRM in the massive sulphide samples has a low coercivity (O'Reilly et al., 2000). All three of the measured small circles lie within 20° of the present day earth field, and one contains the present field orientation. These findings are all consistent with the possibility that the massive sulphide samples may be prone to acquisition of VRM from the present day earth field (Dunlop and Özdemir, 1997). Such VRM would serve to increase the apparent total magnetic intensity of aeromagnetic anomalies, relative to what would be observed from a purely induced magnetisation, without significantly changing the geometry of the anomalies. If the observed NRM is not a VRM then the most extreme outcomes are represented by the orientations in the small circles that lie at the greatest angle to the present day earth field. The two samples with the lowest Koenigsberger ratios have small circles entirely within the upper hemisphere, and the orientations furthest from the present field would be approximately orthogonal to the present earth field. Such directions would contribute little to the observed total magnetic field anomalies. In contrast, for sample D1101.1 the most extreme orientation would have a reversed

direction relative to the present earth field and its high NRM intensity and Koenigsberger ratio would cause a large decrease in the observed magnetic anomaly relative to the expected induced magnetic reduced. If a large volume of such sulphides were present they could cause significant problems with modelling and inversion techniques that neglect the effect of remanent magnetisation.

4.4.2 Ultramafic rocks

The most voluminous magnetic rocks in the Leinster area are the various ultramafic rocks, and the Leinster area is dominated by the large Perseverance Ultramafic Complex (Figure 4.2). As demonstrated in Figure 4.29 and Figure 4.30 the physical properties of the ultramafic rocks are controlled by two main processes: 1) serpentinisation, and 2) presence of sulphides. Additional controls may be imposed by carbonation reactions and different ultramafic protoliths.

Serpentine versus olivine

Serpentinisation represents the hydration of ultramafic rocks and involves the replacement of olivine with serpentine minerals, magnetite and frequently brucite. The process commonly maintains the ultramafic protolith MgO/SiO_2 ratio, allowing classification of the protolith, so the associated decrease in density must be related primarily to an increase in volume (Coleman, 1971). Relict igneous olivine is preserved in the core of the Perseverance Ultramafic Complex but prograde amphibolite-grade metamorphic olivine has also been formed from previously serpentinised ultramafic rocks and may locally have undergone retrograde serpentinisation (Barnes et al., 1988; Gole et al., 1987; Hill et al., 1990). These two overlapping and competing processes may complicate the spatial distribution of serpentinised versus olivine-bearing ultramafic rocks, but the samples collected in this study indicate that many ultramafic rocks that have minimal sulphides (<10 vol. %) can be classified according to their olivine and serpentine contents. The serpentinisation trend identified in Figure 4.29 corresponds well with that calculated and observed by Henkel (1976).

Thermomagnetic analysis indicates that both serpentine- and olivine-bearing groups contain multidomain magnetite with or without titanomagnetite. The presence of multidomain magnetite prevents thermomagnetic analysis from conclusively identifying single domain magnetite. Monoclinic pyrrhotite is a minor component in those samples that contain

sulphides. Those that contain olivine (either igneous or metamorphic in origin) have densities $\sim 3.2 \text{ t/m}^3$, susceptibilities $\sim 10 \times 10^{-3} \text{ SI}$, NRM intensities from 100-10,000 mA/m, and Koenigsberger ratios of 0.5-30. Those that contain visible serpentine have generally been completely serpentinised and have densities $\sim 2.6 \text{ t/m}^3$, susceptibilities $\sim 40 \times 10^{-3} \text{ SI}$, NRM intensities from 700-50,000 mA/m, and Koenigsberger ratios of 1-10. As for the massive sulphide samples, the most extreme Koenigsberger ratios may indicate drilling IRM overprints and two samples with Koenigsberger ratios of 23 and 51 and several with Koenigsberger ratios of 1-7 are associated with clear drilling IRM (these have been removed from the susceptibility versus NRM intensity cross-plots). However samples D1704.1 and D1018.1 in Figure 4.22 have Koenigsberger ratios of 12 and 17 and show no evidence of drilling IRM.

The character of the NRM in the ultramafic rocks is complicated by the presence of VRM and drilling IRM overprints in many samples. Most of the olivine-bearing samples subjected to AF demagnetisation are inferred to have at least some component of drilling IRM (e.g., Figure 4.22C-D) which is more easily acquired by multidomain magnetite (Audunsson and Levi, 1989). Where observed in this study such overprints are magnetically soft and easily removed with peak AF strengths of $< 10 \text{ mT}$, consistent with the findings of others (Audunsson and Levi, 1989; Özdemir and Dunlop, 1988). Grains with such low coercivities would be highly susceptible to acquisition of VRM parallel to the present earth field when in the ground, however no clear candidate VRM components were preserved in the olivine-bearing samples analysed here. Several of the samples contain a magnetically harder remanence that may represent a surviving ChRM (Figure 4.22C-D, Figure 4.25). The demagnetisation intensities in these samples show the more gradual decay associated with single domain or pseudo single domain magnetite (Clark, 1997; Dunlop and Özdemir, 1997). The higher coercivities of these components are unlikely to allow acquisition of VRM at present ambient temperatures, but the inferred ChRM could have been acquired when the rocks were heated at any stage of their history. These ChRM components include small circles entirely within the upper hemisphere, and small circles that cross the horizon Figure 4.25 and lie $> 10\text{-}30^\circ$ from the present earth field direction.

The story is similar for the serpentinised ultramafic rocks. Many samples have clear drilling IRM overprints that are demagnetised with peak fields $< 10 \text{ mT}$ (Figure 4.22A-B) and their low coercivity grains are again likely to have held VRM parallel to the earth field when in

the ground. Several samples contain low coercivity remanent magnetisation at angles $> 20^\circ$ from the sample axis that are unlikely to be the result of drilling IRM. An example is D1704.1 from the Rocky's Reward host rocks in Figure 4.22E-F which has a single NRM component oriented at 40° to the sample axis that is demagnetised to $< 2\%$ by peak fields < 12 mT; the sharp decay is indicative of multidomain magnetite. When rotated into geographic coordinates the small circle associated with this component contains the present earth field direction and it likely represents a VRM acquired *in situ* (Figure 4.24). Such VRM components may not have been erased by drilling IRM due to the use of less magnetised drill core barrels. This sample is particularly noteworthy because it demonstrates the possibility of extreme Koenigsberger ratios (17) in magnetically soft multidomain magnetite. Accumulations of such rocks would dramatically amplify positive magnetic anomalies giving rise to erroneously high susceptibility estimates if remanent magnetisation is ignored in geophysical modelling. However, it is the only sample to show this characteristic. As for the olivine-bearing samples, higher coercivity ChRM components are preserved in many of the serpentinised samples. These also show the more gradual decay of demagnetisation intensities associated with single domain or pseudo single domain magnetite (Clark, 1997; Dunlop and Özdemir, 1997).

All the NRM components shown in Figure 4.23 to Figure 4.25 come from different localities and separate ultramafic bodies along a 16 km strike length (Figure 4.1 and Figure 4.2). Thermomagnetic analysis indicates the presence of multidomain magnetite in all samples analysed. The AF demagnetisation intensity curves indicate low coercivities commonly associated with multidomain magnetite (Clark, 1997; Dunlop and Özdemir, 1997) in many, if not all samples, and the multidomain magnetite appears to carry either drilling IRM or VRM components. Samples of both serpentinised and olivine bearing ultramafic rocks also show higher coercivity components that have not been replaced by IRM or VRM. The decay of the demagnetisation intensities of these inferred ChRM components is indicative of pseudo single domain or single domain magnetite (Clark, 1997; Dunlop and Özdemir, 1997). This is consistent with other studies of komatiite NRM. For example, Yoshihara and Hamano (2004) analysed various komatiitic rocks from southern African greenstone belts and found that, despite greenschist metamorphism and extensive serpentinisation, reliable primary grain growth remanent magnetisation was preserved in pure single domain magnetite. At Leinster the distribution of this pseudo single or single domain magnetite does not seem to be controlled solely by the presence of serpentine or olivine so must be attributable to the original ultramafic

protoliths and their local metamorphic, cooling and alteration histories. Separating these affects would require a more comprehensive dataset with detailed petrographic analysis.

Despite their wide distribution in a wide variety of complexly folded and metamorphosed rocks it is notable that nearly all the possible ChRM small circles are contained between declinations of 180° and 320° and inclinations from 45° down to vertically upward. As shown in Figure 4.25, the declinations are roughly perpendicular to the dominant regional strike ($\sim 160^{\circ}$). In the Leinster area most of the rocks are near vertical and face east in the opposite direction to the remanence vectors. The only two samples that can be reoriented in this study indicate that serpentinised portions of the Perseverance Ultramafic Complex may show moderate reverse to intermediate polarity NRM. Similar small circles that cross the horizon are observed in both serpentinised and olivine-bearing rocks in the core of the Perseverance Ultramafic Complex, but olivine-bearing samples from its margins show small circles entirely contained in the upper hemisphere that cannot contain reverse polarities. The preserved NRM orientations may be highly dependent on the exact thermo-chemical history in individual locations. It is important to note that known ultramafic bodies in the Agnew-Wiluna greenstone belt form discrete laterally continuous positive magnetic anomalies. This indicates that intense reverse polarities are spatially limited in extent and importance relative to induced susceptibilities and normal to intermediate polarity remanence.

Sulphide content

Figure 4.14 and Figure 4.30 show the relationships between the sulphide content of ultramafic rocks and physical properties. The sulphides almost exclusively consist of varying amounts of pyrrhotite and pentlandite, either disseminated or as stringer veins. Although there is a weak correlation the addition of $< 10\text{-}20$ vol. % sulphides only has a minimal influence of physical properties. Above $10\text{-}20$ vol. % the densities, susceptibilities, NRM intensities and Koenigsberger ratios all tend to increase, with densities showing the most significant variation. The distribution shown in Figure 4.30A suggests that the physical properties of the sulphide-bearing ultramafic rocks is highly dependent on whether the host rock is serpentinised or contains olivine. As discussed for the massive sulphide samples above, the physical properties of the sulphide rich samples should be controlled by the relative abundances of monoclinic pyrrhotite, hexagonal pyrrhotite and non-magnetic pentlandite. However for small quantities of

sulphides these variations may not be as significant as the affect of serpentinisation and are not clearly observed in this study.

The AF demagnetisation behaviour of samples with 10-40 vol. % sulphides is similar to that observed for ultramafic rocks with < 10 vol. % sulphides. Most samples have a low coercivity component with NRM directions < 20° from the sample axes indicative of drilling IRM, but several samples contain a higher coercivity component with small circles > 10° from the present earth field that likely represent ChRM. These include both styles of small circles shown in Figure 4.25: those that are entirely contained in the upper hemisphere, and those that are cross the horizon. As these samples contain both pyrrhotite and magnetite, thermal demagnetisation would be required to identify which is the carrier of the observed ChRM. None of the samples analysed show clear VRM although it may have been the original component replaced by the low coercivity drilling IRM

Other factors

Trends associated with ultramafic type and carbonation reactions add some tertiary complexity to the main trends described above (Table 4.5 and Table 4.6, Figure 4.15-Figure 4.18). The distinction between ultramafic protolith types is primarily based on the abundance of olivine versus parental melt and is reflected in the whole rock MgO content (Hill et al., 1990). However, with the exception of the core of the Perseverance Ultramafic Complex most ultramafic rocks in the district are serpentinised (Gole et al., 1987). The main histogram peaks for the different ultramafic protoliths in Figure 4.15 are associated with a range of densities from 2.6-2.9 t/m³, which is entirely within the range of serpentinised ultramafic densities observed in the samples collected in this study. The susceptibilities are more variable. Komatiitic rocks which lack olivine phenocrysts have much lower susceptibilities ($1-10 \times 10^{-3}$ SI) than the cumulate rocks sampled in this study ($3-100 \times 10^{-3}$ SI). There is limited physical property data for alteration styles in the ultramafic rocks other than serpentinisation. Talc, chlorite and carbonate alteration styles that are associated with carbonation of komatiitic flows and the margins of the cumulate lenses (Barnes et al., 1988; Gole et al., 1987; Hill et al., 1990) appear to be associated with intermediate densities ~ 2.9 t/m³ and low susceptibilities $\sim 1 \times 10^{-3}$ SI (Table 4.6, Figure 4.17, Figure 4.18). From this study it is unclear whether the similarity in properties between the komatiites and the talc, chlorite and carbonate alteration styles represents a lithological control on the style of alteration present or a genuine trend in physical

properties with alteration. Clark et al. (1992) found that moderate carbonate alteration does not significantly affect the physical properties of ultramafic rocks in the belt but intense talc-carbonate alteration reduces magnetic susceptibility. This would seem to suggest that there are both lithological and alteration controls behind the komatiite and carbonised ultramafic rock field indicated in Figure 4.29A

Clark et al. (1992) note that the observed magnetic anomaly amplitude associated with ultramafic rocks in the belt decreases northwards away from Perseverance in direct correlation with decreasing metamorphic grade. Bourne et al. (1993) found a similar correlation between metamorphic grade of ultramafic rocks and their magnetic susceptibility by comparing separate greenstone belts in the Yilgarn Craton. Similar positive correlations with metamorphic grade are well known for density (Emerson, 1990; Telford et al., 1990). Although virtually all rocks observed in this study were metamorphosed to similar amphibolite grades, such regional relationships may indicate the potential for more localised temperature controls on physical properties. The high grade metamorphism around Leinster undoubtedly contributed to the abundance of multidomain magnetite observed in thermomagnetic analysis and demagnetisation intensities. This in turn would explain the common occurrence of low coercivity IRM and VRM overprints.

4.4.3 Other greenstone and granitoid rocks

The number of samples of the various other greenstone and granitoid country rocks is more limited, but the variability of measured physical properties in those samples also appears to be more limited. The full range of densities observed for felsic volcanoclastic rocks through to gabbro and dolerite intrusive rocks spans $2.4\text{--}3.0\text{ t/m}^3$ and is consistent with established textbook values (e.g., Telford et al., 1990) despite the regional metamorphism. The measured susceptibilities show greater departures from textbook values but correlate well with measurements of similar rocks from other locations in the Yilgarn Craton (Bourne et al., 1993; Emerson et al., 1999). There is considerable overlap between different lithologies (Figure 4.27 and Figure 4.28), but the more extreme physical properties can be diagnostic. The highest magnetic susceptibilities ($> 3 \times 10^{-3}$ SI) are associated with granitoids. The lowest susceptibilities ($< 0.2 \times 10^{-3}$ SI) are associated with felsic volcanic and volcanoclastic rocks and their metamorphic or sedimentary derivatives. The highest densities ($> 2.75\text{ t/m}^3$) are associated with mafic igneous rocks or their metamorphic or sedimentary derivatives. The lowest densities

(< 2.4 t/m³) are restricted to weathered rocks that have undergone an increase in porosity through leaching.

An additional diagnostic layer can be considered when NRM measurements are included. In almost all cases, regardless of original composition, coarse grained intrusive rocks (e.g., granites, gabbros and dolerites) have an order of magnitude greater NRM intensity than their extrusive equivalents (felsic volcanics, basalts). The reason for this relationship is not immediately obvious as the finer-grained extrusive rocks should have more single domain magnetite which tends to carry a higher remanence (Clark, 1997). The stronger remanence observed in coarser magnetite versus finer-grained magnetite may be the result of different unblocking characteristics of each during metamorphism and metamorphism itself may have affected the rocks differently.

4.5 CONCLUSIONS

The mass and magnetic properties of Ni-sulphide mineralisation and its ultramafic host rocks, and surrounding greenstone and granitoid country rocks show a large variation that spans virtually the entire natural range of properties. Massive sulphides have the most extreme densities, but have extremely variable magnetic susceptibilities and NRM intensities depending on the proportion of ferromagnetic monoclinic pyrrhotite to antiferromagnetic hexagonal pyrrhotite. The influence is so dramatic that large accumulations of monoclinic pyrrhotite dominant massive sulphides will have strong magnetic anomalies, but equivalent volumes of hexagonal pyrrhotite dominant massive sulphides will have negligible magnetic anomalies. All would have strong gravity anomalies. Such sulphide accumulations are rare however, and most nickel exploration would focus on identifying the more voluminous prospective ultramafic host rocks. These show a wide range of densities but always have high magnetic susceptibilities and NRM intensities. The remaining country rocks have less distinct physical properties, but more extreme country rock densities and susceptibilities can be diagnostic. The intensity of NRM in country rocks appears to be primarily controlled by whether igneous rocks had an intrusive or extrusive origin, with intrusive rocks having higher NRM intensities. Many metamorphic and sedimentary rocks have properties similar to their precursor constituents. The observed density and susceptibility relationships have been summarised into a physical property discriminant diagram (Figure 4.31) that provides a visual display of the expected property controls and may provide allow a first pass classification of rock types based on physical properties that are

either measured during down-hole logging, or estimated from geophysical modelling and inversion (as applied in Chapter 7). The broad distinctions between rock types that can be made using densities and magnetic susceptibilities together confirms the need to integrate geophysical interpretations using magnetic and gravity data rather than treat each data set individually.

Remanent magnetisation is common in sulphide-bearing rocks, due to the abundance of both monoclinic and hexagonal pyrrhotite, and in most ultramafic rocks. Analysis of the character of the observed remanent magnetisation in these rocks indicates that most have low coercivity multidomain components prone to overprinting by VRM *in situ*, and drilling IRM during extraction. But many also contain a higher coercivity pseudo or single domain component that appears to preserve a ChRM from some time in the rocks' evolution. The declinations of these components are restricted to the SW quadrant, broadly perpendicular to the dominant strike. However, without fully oriented samples it appears that virtually all inclinations are possible and Koenigsberger ratios are extremely variable, so the importance of these ChRM components for geophysical interpretation is not clear. The regional magnetic anomalies are usually positive so remanent magnetisation only influences the positive magnitude of the anomalies, and not their sign. Although Koenigsberger ratios of up to 10 are measured in dolerite and granite country rocks, their remanence is generally of such low intensity and low coercivity that no reliable *in situ* components could be recovered and it is not expected to be important in geophysical interpretations.

4.6 REFERENCES

- Audunsson, H., and Levi, S., 1989, Drilling-induced remanent magnetization in basalt drill cores: *Geophysical Journal International*, v. 98, p. 613-622.
- Barnes, S. J., Hill, R. E. T., and Gole, M. J., 1988, The Perseverance ultramafic complex, Western Australia; the product of a komatiite lava river: *Journal of Petrology*, v. 29, p. 305-331.
- Barrett, F. M., Binns, R. A., Groves, D. I., Marston, R. J., and McQueen, K. G., 1977, Structural history and metamorphic modification of Archean volcanic-type nickel deposits, Yilgarn block, Western Australia: *Economic Geology*, v. 77, p. 1195-1223.
- Benn, K., Rochette, P., Bouchez, J. L., and Hattori, K., 1993, Magnetic susceptibility, magnetic mineralogy and magnetic fabrics in a late Archean granitoid-gneiss belt: *Precambrian research*, v. 63, p. 59-81.
- Bennett, C. E. G., and Graham, J., 1980, New observations on natural pyrrhotites; Part III, Thermomagnetic experiments: *American Mineralogist*, v. 65, p. 800-807.
- Beresford, S. W., Duuring, P., Rosengren, N. M., Fiorentini, M., Bleeker, W., Tait, M. A., Barley, M. E., Cas, R. A. F., and Wallace, H., 2004, Structural and stratigraphic reconstruction of the Agnew-Wiluna belt, Western Australia, *in* Beresford, S. W., Duuring, P., Fiorentini, M., Rosengren, N. M., Bleeker, W., Barley, M. E., Cas, R. A. F., Tait, M. A., and Wallace, H., eds., P710 final report: The structural and stratigraphic architecture of the Agnew/Wiluna Belt, WA: Melbourne, AMIRA International, p. 1-7.
- Beresford, S. W., and Rosengren, N. M., 2004, Komatiite-hosted Ni-Cu-PGE deposits of the Agnew-Wiluna greenstone belt - an overview, *in* Neumayr, P., Harris, M., and Beresford, S. W., eds., Gold and nickel deposits in the Archaean Norseman-Wiluna greenstone belt, Yilgarn Craton, Western Australia — a field guide, 2004/16, Geological Survey of Western Australia, p. 87-91.
- BHP Billiton Ltd., 2007, 2007 BHP Billiton Annual Report: Melbourne, BHP Billiton Ltd., p. 296.
- Binns, R. A., Gunthorpe, R. J., and Groves, D. I., 1976, Metamorphic patterns and development of greenstone belts in the eastern Yilgarn Block, Western Australia, *in* Windley, B. F., ed., The early history of the Earth: London, John Wiley and Sons, p. 303-313.
- Bleil, U., and Petersen, N., 1982, Magnetic properties of natural minerals, *in* Angenheister, G., ed., Physical properties of rocks, Vol. 1b: Berlin, Springer-Verlag, p. 308-365.
- Borradaile, G., 2003, Statistics of earth science data: Their distribution in space, time, and orientation: Berlin, Springer-Verlag, 351 p.

- Bourne, B. T., Trench, A., Dentith, M. C., and Ridley, J., 1993, Physical property variations within Archaean granite-greenstone terrane of the Yilgarn Craton, Western Australia; the influence of metamorphic grade: *Exploration Geophysics*, v. 24, p. 367-374.
- Butler, R. F., 1992, *Paleomagnetism: Magnetic domains to geologic terranes*: Boston, Blackwell Scientific Publications, 319 p.
- Cassidy, K. F., Champion, D. C., Krapež, B., Barley, M. E., Brown, S. J. A., Blewett, R. S., Groenewald, P. B., and Tyler, I. M., 2006, A revised geological framework for the Yilgarn Craton, Western Australia, 2006/8, Geological Survey of Western Australia, p. 9.
- Champion, D. C., and Sheraton, J. W., 1997, Geochemistry and Nd isotope systematics of Archaean granites of the Eastern Goldfields, Yilgarn Craton, Australia: implications for crustal growth processes: *Precambrian Research*, v. 83, p. 109-132.
- Clark, D. A., 1997, Magnetic petrophysics and magnetic petrology; aids to geological interpretation of magnetic surveys: *AGSO Journal of Australian Geology and Geophysics*, v. 17, p. 83-103.
- Clark, D. A., and Emerson, D. W., 1999, Self-demagnetisation; "the rock doctor": *Preview*, v. 79, p. 22-25.
- Clark, D. A., French, D. H., Lackie, M. A., and Schmidt, P. W., 1992, Magnetic petrology: Application of integrated rock magnetic and petrological techniques to geological interpretation of magnetic surveys: *Exploration Geophysics*, v. 23, p. 65-68.
- Coleman, R. G., 1971, Petrologic and geophysical nature of serpentinites: *Geological Society of America Bulletin*, v. 82, p. 897-918.
- Cox, K. G., Bell, J. D., and Pankhurst, R. J., 1979, *The interpretation of igneous rocks*: London, Allen and Unwin, 450 p.
- de Wall, H., and Worm, H. U., 2001, Recognition of drilling-induced remanent magnetization by Q-factor analysis: a case study from the KTB-drillholes: *Journal of Applied Geophysics*, v. 46, p. 55-64.
- Dunlop, D. J., and Özdemir, Ö., 1997, *Rock magnetism: fundamentals and frontiers*: Cambridge, University Press, 573 p.
- Duuring, P., Bleeker, W., and Beresford, S. W., 2004a, Major folding and remobilisation of nickel sulphides at Perseverance, Leinster, Western Australia, *in* Beresford, S. W., Duuring, P., Fiorentini, M., Rosengren, N. M., Bleeker, W., Barley, M. E., Cas, R. A. F., Tait, M. A., and Wallace, H., eds., *P710 final report: The structural and stratigraphic architecture of the Agnew/Wiluna Belt*, WA: Melbourne, AMIRA International, p. 73-124.
- Duuring, P., Bleeker, W., and Beresford, S. W., 2004b, Structural overview of the Agnew-Wiluna greenstone belt, Yilgarn Craton, Western Australia, *in* Beresford, S. W., Duuring, P., Fiorentini, M., Rosengren, N. M., Bleeker, W., Barley, M. E., Cas, R. A. F., Tait, M. A.,

- and Wallace, H., eds., P710 final report: The structural and stratigraphic architecture of the Agnew/Wiluna Belt, WA: Melbourne, AMIRA International, p. 23-72.
- Eisenlohr, B. N., 1989, The structural development and controls on mineralisation of the northern sector of the Norseman-Wiluna Belt, Western Australia: Unpub. Ph. D. thesis, University of Western Australia, 189 p.
- Emerson, D. W., 1990, Notes on mass properties of rocks; density, porosity, permeability: *Exploration Geophysics*, v. 21, p. 209-216.
- Emerson, D. W., and Macnae, J., 2001, Further Physical Property Data from the Archaean Regolith, Western Australia: *ASEG Preview*, June, p. 33-37.
- Emerson, D. W., Macnae, J., and Sattel, D., 2000, Physical properties of the regolith in the Lawlers area, Western Australia: *Exploration Geophysics*, v. 31, p. 229-235.
- Emerson, D. W., Martin, K., and Williams, P. K., 1999, Electrical, magnetic and mass properties of the nickeliferous komatiite sequence near Leinster, Western Australia: *Preview*, v. 81, p. 13-22.
- Emerson, D. W., and Yang, Y. P., 1997, Insights from laboratory mass property crossplots; "The Rock Doctor": *Preview*, v. 70, p. 10-14.
- Ferré, E. C., Wilson, J., and Gleizes, G., 1999, Magnetic susceptibility and AMS of the Bushveld alkaline granites, South Africa: *Tectonophysics*, v. 307, p. 113-133.
- Fowler, C. M., Stead, D., Pandit, B. I., Janser, B. W., Nisbet, E. G., and Nover, G., 2005, A database of physical properties of rocks from the Trans-Hudson Orogen, Canada: *Canadian Journal of Earth Sciences*, v. 42, p. 555-572.
- Freedman, D., and Diaconis, P., 1981, On the histogram as a density estimator: L_2 theory: *Zeitschrift für Wahrscheinlichkeitstheorie und verwandte Gebiete*, v. 57, p. 453-476.
- Giddings, J. W., Klootwijk, C., Rees, J., and Groenewoud, A., 1997, Automated AF-demagnetization on the 2G-Enterprises through-bore, cryogenic magnetometer: *Geologie en Mijnbouw*, v. 76, p. 35-44.
- Gole, M. J., Barnes, S. J., and Hill, R. E. T., 1987, The role of fluids in the metamorphism of komatiites, Agnew nickel deposit, Western Australia: *Contributions to Mineralogy and Petrology*, v. 96, p. 151-162.
- Grant, F. S., and West, G. F., 1965, *Interpretation theory in applied geophysics*: New York, McGraw-Hill, 584 p.
- Henkel, H., 1976, Studies of density and magnetic properties of rocks from northern Sweden: *Pure and Applied Geophysics*, v. 114, p. 235-249.
- Henkel, H., 1989, Petrophysical measurements in detailed bedrock mapping of crystalline Precambrian rocks: *IGA Bulletin*, v. 53, p. 173.

- Henkel, H., 1991, Petrophysical properties (density and magnetization) of rocks from the northern part of the Baltic Shield: *Tectonophysics*, v. 192, p. 1-19.
- Henkel, H., 1994, Standard diagrams of magnetic properties and density; a tool for understanding magnetic petrology: *Journal of Applied Geophysics*, v. 32, p. 43-53.
- Hill, R. E. T., Barnes, S. J., Gole, M. J., and Dowling, S. E., 1990, Physical volcanology of komatiites; a field guide to the komatiites of the Norseman-Wiluna Greenstone Belt, Eastern Goldfields Province, Yilgarn Block, Western Australia, 1, Excursion Guide Book - Geological Society of Australia, v. 1, p. 100.
- Hill, R. E. T., Barnes, S. J., Gole, M. J., and Dowling, S. E., 1995, The volcanology of komatiites as deduced from field relationships in the Norseman-Wiluna greenstone belt, Western Australia: *Lithos*, v. 34, p. 159-188.
- Hunt, C. P., Moskowitz, B. M., and Banerjee, S. K., 1995, Magnetic properties of rocks and minerals: *AGU Reference Shelf*, v. 3, p. 189-204.
- Hutchison, C. S., 1974, *Laboratory handbook of petrographic techniques*: New York, Wiley, 527 p.
- Jaireth, S., Hoatson, D., Jaques, L., Huleatt, M., and Ratajkoski, M., 2005, Nickel sulphide metallogenic provinces: resources and potential, *AusGeo News*, Geoscience Australia.
- Johnson, G. R., and Olhoeft, G. R., 1984, Density of rocks and minerals, *in* Carmichael, R. S., ed., *CRC handbook of physical properties of rock*: Boca Raton, Florida, CRC Press, p. 1-38.
- Kirkwood, T. B. L., 1979, Geometric means and measures of dispersion: *Biometrics*, v. 35, p. 908-909.
- Kirschvink, J. L., 1980, The least-squares line and plane and the analysis of palaeomagnetic data: *Geophysical Journal of the Royal Astronomical Society*, v. 45, p. 699-718.
- Kodama, K. P., 1984, Palaeomagnetism of granitic intrusives from the Precambrian basement under eastern Kansas: orienting drill cores using secondary magnetization components: *Geophysical Journal International*, v. 76, p. 273-287.
- Kontny, A., de Wall, H., Sharp, T. G., and Posfai, M., 2000, Mineralogy and magnetic behavior of pyrrhotite from a 260° C section at the KTB drilling site, Germany: *American Mineralogist*, v. 85, p. 1416-1427.
- Latham, A. G., Harding, K. L., Lapointe, P., Morris, W. A., and Balch, S. J., 1989, On the lognormal distribution of oxides in igneous rocks, using magnetic susceptibility as a proxy for oxide mineral concentration: *Geophysical Journal International*, v. 142, p. 179-184.
- Le Bas, M. J., Le Maitre, R. W., and Woolley, A. R., 1992, The construction of the Total Alkali-Silica chemical classification of volcanic rocks: *Mineralogy and Petrology*, v. 46, p. 1-22.

- Leshner, C. M., 1989, Komatiite-associated nickel sulfide deposits: Reviews in Economic Geology, v. 4, p. 45-101.
- Leshner, C. M., and Keays, R. R., 2002, Komatiite-associated Ni-Cu-PGE deposits: geology, mineralogy, geochemistry, and genesis, *in* Cabri, L. J., ed., The geology, geochemistry, mineralogy and mineral beneficiation of platinum-group elements. Special Volume 54, Canadian Institute of Mining, Metallurgy and Petroleum, p. 579-617.
- Libby, J. W., Stockman, P. R., Cervoj, K. M., Muir, M. R. K., Whittle, M., and Langworthy, P. J., 1998, Perseverance nickel deposit, *in* Berkman, D. A., and Mackenzie, D. H., eds., Geology of Australian and Papua New Guinean mineral deposits: Melbourne, Australasian Institute of Mining and Metallurgy, p. 321-328.
- Liu, S. F., Champion, D. C., and Cassidy, K. F., 2002, Geology of the Sir Samuel 1:250,000 sheet area, Western Australia, 2002/14, Geoscience Australia, p. 57.
- Liu, S. F., Griffin, T. J., Wyche, S., and Westaway, J., 1996, Sir Samuel, W.A. Sheet 3042, 1:100 000 Geological Map Series, Western Australia Geological Survey.
- Liu, S. F., Stewart, A. J., Farrell, T. R., Whitaker, A. J., and Chen, S. F., 2000, Solid geology of the North Eastern Goldfields, Western Australia, 1:500 000 scale map: Canberra, ACT, Canberra, AGSO.
- Martin, J. E., and Allchurch, P. D., 1975, Perseverance nickel deposit, Agnew, *in* Knight, C. L., ed., Economic geology of Australia and Papua New Guinea, 1. Metals: Melbourne, Australasian Institute of Mining and Metallurgy, p. 149-155.
- McCall, L. M., Dentith, M. C., Li, Z. X., and Trench, A., 1995, The magnetic signature of komatiitic peridotite-hosted nickel sulphide deposits in the Widgiemooltha area, Western Australia: Exploration Geophysics, v. 26, p. 66-77.
- Musgrave, R. J., Grewar, J., and Vega, M., 2006, Significance of remanence in Stawell goldfield aeromagnetic anomalies: Australian Journal of Earth Sciences, v. 53, p. 783-797.
- Myers, J. S., 1993, Precambrian history of the West Australian Craton and adjacent orogens: Annual Review of Earth and Planetary Sciences, v. 21, p. 453-485.
- Naldrett, A. J., and Turner, A. R., 1977, The geology and petrogenesis of a greenstone belt and related nickel sulfide mineralization at Yakabindie, Western Australia: Precambrian Research, v. 5, p. 43-103.
- O'Reilly, W., Hoffmann, V., Chouker, A. C., Soffel, H. C., and Menyeh, A., 2000, Magnetic properties of synthetic analogues of pyrrhotite ore in the grain size range 1-24 μm : Geophysical Journal International, v. 142, p. 669-683.
- Özdemir, Ö., and Dunlop, D. J., 1988, Crystallization remanent magnetization during the transformation of maghemite to hematite: Journal of Geophysical Research, v. 93, p. 6530-6544.

- Pinto, M. J., and McWilliams, M., 1990, Drilling-induced isothermal remanent magnetization: *Geophysics*, v. 55, p. 111-115.
- Puranen, R., 1989, Susceptibilities, iron and magnetite content of Precambrian rocks in Finland, Tutkimusraportti - Geologian Tutkimuskeskus = Report of Investigation - Geological Survey of Finland, p. 51.
- Rochette, P., Fillion, G., Mattéi, J. L., and Dekkers, M. J., 1990, Magnetic transition at 30-34 Kelvin in pyrrhotite: insight into a widespread occurrence of this mineral in rocks: *Earth and Planetary Science Letters*, v. 98, p. 319-328.
- Rödsjö, L., and Goodgame, V. R., 1999, Alteration of the Mt. Keith nickel sulphide deposit, *in* Stanley, C. J., et al., ed., *Mineral deposits; processes to processing*: Rotterdam, Balkema, p. 779-782.
- Rosengren, N. M., Beresford, S. W., Hayward, N., and Cas, R. A. F., 2004, The structural and stratigraphic architecture of the Mt Keith domain, Agnew-Wiluna greenstone belt, Western Australia, *in* Beresford, S. W., Duuring, P., Fiorentini, M., Rosengren, N. M., Bleeker, W., Barley, M. E., Cas, R. A. F., Tait, M. A., and Wallace, H., eds., *P710 final report: The structural and stratigraphic architecture of the Agnew/Wiluna Belt, WA*: Melbourne, AMIRA International, p. 167-206.
- Schön, J. H., 2004, *Physical properties of rocks: Fundamentals and principles of petrophysics*: Oxford, Elsevier, 583 p.
- Soffel, H., 1977, Pseudo-single-domain effects and single-domain multidomain transition in natural pyrrhotite deduced from domain structure observations: *Journal of Geophysics*, v. 42, p. 351-359.
- Stewart, A. J., 2001, Leonora, W.A., Sheet SH51-01, 2nd Ed., 1:250 000 Geological Map Series, AGSO - Geoscience Australia.
- Telford, W. M., Geldart, L. P., and Sheriff, R. E., 1990, *Applied Geophysics*: New York, Cambridge University Press, 770 p.
- Trofimovs, J., Tait, M. A., Cas, R. A. F., McArthur, A., and Beresford, S. W., 2003, Can the role of thermal erosion in strongly deformed komatiite-Ni-Cu-(PGE) deposits be determined? *Perseverance, Agnew-Wiluna Belt, Western Australia: Australian Journal of Earth Sciences*, v. 50, p. 199-214.
- Van der Voo, R., and Watts, D. R., 1978, Palaeomagnetic results from igneous and sedimentary rocks from the Michigan Basin borehole: *Journal of Geophysical Research*, v. 83, p. 5844-5848.
- Vanderhor, F., and Flint, R. B., 2001, 1:500 000 Interpreted bedrock geology of Western Australia, Geological map, Geological Survey of Western Australia.
- Whitaker, A. J., 2003, The geophysical characteristics of granites and shear zones in the Yilgarn Craton, and their implications for gold mineralisation, *in* Blevin, P. L., Jones, M.,

- and Chappell, B. W., eds., *Magma to mineralisation; the Ishihara symposium, 2003/14*, Geoscience Australia, p. 129-133.
- Wilson, S. A., Raudsepp, M., and Dipple, G. M., 2006, Verifying and quantifying carbon fixation in minerals from serpentine-rich mine tailings using the Rietveld method with X-ray powder diffraction data: *American Mineralogist*, v. 91, p. 1331-1341.
- Winchester, J. A., and Floyd, P. A., 1977, Geochemical discrimination of different magma series and their differentiation products using immobile elements: *Chemical Geology*, v. 20, p. 325-343.
- Wohlenberg, J., 1982, Density of minerals, *in* Angenheister, G., ed., *Physical properties of rocks*, Vol. 1b: Berlin, Springer-Verlag, p. 66-113.
- Yoshihara, A., and Hamano, Y., 2004, Paleomagnetic constraints on the Archean geomagnetic field intensity obtained from komatiites of the Barberton and Belingwe greenstone belts, South Africa and Zimbabwe: *Precambrian Research*, v. 131, p. 111-142.
- Zijderveld, J. D. A., 1967, A.C. demagnetization of rocks: Analysis of results, *in* Collinson, D. W., Creer, K. M., and Runcorn, S. K., eds., *Methods in palaeomagnetism*: Amsterdam, Elsevier, p. 254-286.

Chapter 5: An automated approach for building geological constraints for potential field inversions using sparse observations¹

5.1 INTRODUCTION

Inversion of geophysical data seeks to extract a model, or suite of models, representing the subsurface physical property contrasts that can explain an observed geophysical dataset. Due to the inherent non-uniqueness of inversions, any recovered property distribution is only one of an infinite number of possible distributions that could explain the observed data. The most desirable solutions are those that can explain the observed geophysical data and also reproduce known geological features; a goal that can only be achieved by including any available geological information into the inversions as constraints.

There are two approaches that can be used to include these geological constraints, based on the type of geological information available and the geological problem being addressed. A hypothesis-testing approach supplies a full 3D model of geological observations and interpretations to the inversion to test the hypothesis that those interpretations are consistent with the geophysical data (McGaughey, 2007; McInerney et al., 2007; Oldenburg and Pratt, 2007). Typically a qualitative assessment of the result is made based on how far the recovered inversion model deviated from the supplied interpretations in order to explain the observed geophysical data. However, in portions of the model that have low sensitivity to the geophysical data and no geological controls it may be possible to recover a property distribution that explains the observed geophysical data but is consistent with a flawed geological model. There may be no indication that the result is incorrect. This is problematic for gravity and magnetic data which are inherently non-unique due to the behaviour of potential fields. The gravity and magnetic responses decay with distance-squared and distance-cubed, respectively, so the sensitivity of subsurface model cells to surface geophysical data decreases dramatically with depth in the model. The amount of geological information available, and therefore the reliability of any 3D models produced also decreases significantly with depth below surface. In the areas where more reliable constraints are required, less

¹ A version of this chapter will be submitted for publication. Williams, N.C., and Oldenburg, D.W. An automated approach for building geological constraints for potential field inversions using sparse observations.

reliable constraints are provided. In addition, as geological interpretations are required prior to performing any hypothesis-testing inversions, a significant amount of geological knowledge and interpretation must be available, and a significant time commitment is required to build the models before any inversion results are obtained.

An alternate approach is to supply all available raw geological information to the inversion to recover a prediction about the subsurface distribution of geological features that may be required to satisfy both the known geological constraints and the observed geophysical data. This sparse data approach is particularly suited to problems where geological information is limited, sparsely distributed, or concentrated within restricted areas such as known ore bodies or along the ground surface. The limited and uneven distribution of data makes it difficult or impossible to build full 3D models that are reliable enough to be included in the hypothesis testing approach. Using the available sparse data also postpones much of the geological interpretation until after the inversions have been performed, reducing the lead time to recovering an inversion result and enabling the results of inversions to be used in decisions to acquire further geological and geophysical data or to assist with geological interpretation.

This chapter describes a method for preparing the geological constraints required for this sparse data approach, eliminating the need for interpreting geology in regions of a 3D model that have limited or no geological information on which to base the interpretations. Applying geological constraints in any geophysical inversion procedure requires solid knowledge of the physical properties of the rocks. The technique outlined here specifically makes that physical property knowledge the central link between the geological information available and the geological constraints to be applied. In regions where little geological information is available, accurate physical property information may be unavailable, but the ability to include rough physical property estimates allows creation of simple models of geological constraints. Routine acquisition of physical property measurements during ongoing work will be rewarded by more robust constraint models which will provide more reliable inversion results on which to base further data collection. The technique also seeks to: 1) reduce the number of software packages required to integrate a variety of spatial datasets into a single physical property model by reading directly from raw data files; 2) automate the process as much as possible; and 3) ensure that the model can be updated quickly and easily when additional data becomes available so as to improve the recovered subsurface predictions. A

demonstration version of the program with a basic graphical user interface has been developed using the Matlab programming package (Mathworks Inc.).

Although the implementation developed here is specifically targeted for use with the UBC–GIF GRAV3D and MAG3D gravity and magnetic inversion programs (Li and Oldenburg, 1996, 1998), a similar treatment of geological observations could be adapted to meet the requirements of other inversion algorithms requiring geological constraints. The key constraint types developed here includes a model of expected values, an indication of the reliability of those values, limits and the possible values in each cell, and a measure of how the recovered properties are expected to vary between cells. Such forms of constraints could be generalised across inversion platforms. In detail, the UBC–GIF inversion approach allows constraints to be assigned to each cell using four sets of parameters:

- A reference physical property which provides the best estimate of the actual physical property of the cell.
- A smallness weight, w_s , which provides an estimate of the reliability of the assigned reference physical property. The weight is a unitless value ≥ 1 with increasing values indicating higher confidence. The default value of unity indicates that the reference physical property is uncertain and should not be strongly enforced in the inversion.
- Lower and upper physical property bounds which provide absolute limits on the minimum and maximum property that can be assigned to the cell. These effectively represent a confidence interval on the supplied reference property.
- Smoothness weights controlling the variation in properties between each adjacent cell in each direction.

Where abundant geological information is available, a cell can be constrained by assigning a reference physical property with a high smallness weight and a tight bounds range. Cells with no geological information should be assigned some default reference physical property, a smallness weight of unity, and wide bounds that reflect the full range of possible physical properties. The inversion will recover a physical property model with properties for each cell that lie between the defined bounds, and are as close as possible to the supplied reference physical properties, while still reproducing the observed geophysical data. If possible, the

reference physical properties will be matched more closely in those cells that have the highest smallness weights.

5.2 METHOD OVERVIEW

The fundamental goal of this approach is to create a 3D physical property model, based only on sparsely distributed raw geological data and enforced only in areas where information is available, using a repeatable, automated process. The recovered physical property model can be used on its own to provide an additional tool to aid direct interpretation of subsurface geological data, or can be supplied to the UBC–GIF or other inversion programs as a constraining reference model. The inversion constraint parameters, including reference properties, smallness weights, and lower and upper property bounds, are all related so all are created at the same time using the same data. The discretisation of the model, including the sizes and positions of cells, is defined by a mesh file which is supplied to the model building routine.

There are two main classes of observation that can be utilised in building a physical property model from geological data: actual physical property measurements; and observations or interpretations of rock types or alteration styles. Actual physical property measurements are obviously the most directly related to building a physical property model; however they may not be collected systematically. Observations of geology are far more common. Since most geological units and rocks types have characteristic (but not necessarily unique) physical properties, observations of rock types and alteration may be used as a proxy for actual property measurements. A key component of building a physical property model that is partially based on rock type observations is to link the geological observations to appropriate physical property information. This is done early in the model building process via the creation of a physical property database for the model.

Once the physical property database is created, the model building routine can load the various data files containing those observations and extract or calculate the 3D coordinates at which the observations occur. The data files that can be supplied to the model building program are listed in Table 5.1. If the observation is a geological observation of rock or alteration types it is converted to a physical property estimate based on the physical property database. The model cells are populated by combining all of the most reliable property

measurements or estimates in each cell and extracting a statistical estimate of the mean physical property value within the cell. Any cell that contains no geological information is assigned default properties.

Table 5.1. List of the data types handled by the model building application. The data types are applied in the order of priority listed, which corresponds to their relative reliability within the model.

Priority	Data type	File formats	Description	Requires physical property database
1	Physical property measurements on surface samples	Column-delimited text files	Measurements taken on outcrop rocks or hand samples for which 3D coordinates are available	No
2	Physical property measurements on drill core	Column-delimited text files	Measurements taken on drill core samples, or by drill hole property logging tools, with position reported as a down-hole depth	No
3	Geology observations on drill core	Column-delimited text files	Observations of rock types and/or alteration styles taken on drill core samples, with position reported as a down-hole depth	Yes
4	Outcrop or surface geology maps	ESRI vector polygon shapefiles	A nontopological shape format of vector coordinates of polygons (Environmental Systems Research Institute, 1998) storing observations of rock types, geological unit names, or descriptions made on surface rocks	Yes
5	Basement or solid geology maps	ESRI vector polygon shapefiles	A nontopological shape format of vector coordinates of polygons (Environmental Systems Research Institute, 1998) storing interpretations of rock types or geological unit names expected at some position in the subsurface	Yes
6	3D models of geological units	UBC–GIF inversion model format text files	A 3D model of geological units bounded by well-defined contacts, stored as a set of lithology IDs for each cell in the model volume	No
7	3D models of geological domains	UBC–GIF inversion model format text files	A 3D model of geological domains that may span multiple geological map units, have poorly-defined boundaries, and distinct structural orientations or fabrics, stored as a set of domain IDs for each cell in the model volume	No

An optional final step expands the number of cells for which physical properties are assigned by extrapolating the properties outwards from data-bearing cells into adjacent cells based on prevalent structural orientations and the assumption that the physical properties will be roughly similar in adjacent cells. This assumption may be valid in some situations but not others, depending on the complexity of the geology, so the distance of extrapolation and the methods for determining the properties in the buffer cells are options for the user.

5.3 LINKING PROPERTY MEASUREMENTS TO INVERSION PROPERTY MODELS

Before assigning values for constraints in the inversions, it is necessary to review what values are actually needed for reference properties and bounds constraints. Due to the principal of superposition applying to potential fields, the combined gravity or magnetic response of a collection of sources will be the sum of the responses of each of the individual sources (Blakely, 1995). The collection of sources therefore has the same potential field response as a uniform body with the same total volume and the mean physical property of all the sources, as long as the body is far enough removed from the observation point that the distribution of properties within the body does not affect the potential field response of the body. The density of the whole collection must therefore be equal to the mean density of all of the individual sources regardless of the individual density values.

Synthetic forward and inverse modelling confirms that the mean property is the appropriate value for populating reference models, regardless of the form of the probability density function of the physical properties in the collection of sources each having the same individual volume. A synthetic magnetic susceptibility model was created using a mesh with uniform $200\text{ m} \times 200\text{ m} \times 100\text{ m}$ cells throughout except for one central cell which was replaced by 4 million cells, each $1\text{ m} \times 1\text{ m} \times 1\text{ m}$, representing the constituent magnetic sources of the original larger cell. These constituent cells were randomly populated using a lognormal (base 10) probability density function resembling a histogram of measured magnetic susceptibilities (approximate range of $1.6 \times 10^{-7}\text{ SI}$ to 1 SI , mean of $3.653 \times 10^{-3}\text{ SI}$: Figure 5.1 and Figure 5.2A). The magnetic response of the model was calculated. The resulting noise-free magnetic data were inverted using a mesh containing a single $200\text{ m} \times 200\text{ m} \times 100\text{ m}$ cell occupying the position of the original 4 million cells, to recover the bulk property for that single cell that best explains the calculated magnetic data. The magnetic susceptibility

recovered by the inversion for the single central cell was 3.644×10^{-3} SI which is clearly more consistent with the arithmetic mean of 3.653×10^{-3} SI than the median or geometric mean of 1.00×10^{-3} SI. The slight discrepancy can be attributed to slight variations in how well the original data were reproduced by the recovered model. Since the inversion will populate a cell with an estimate of the arithmetic mean of constituent components within the cell, the expected mean property for each cell is the most appropriate value to assign in the reference model.

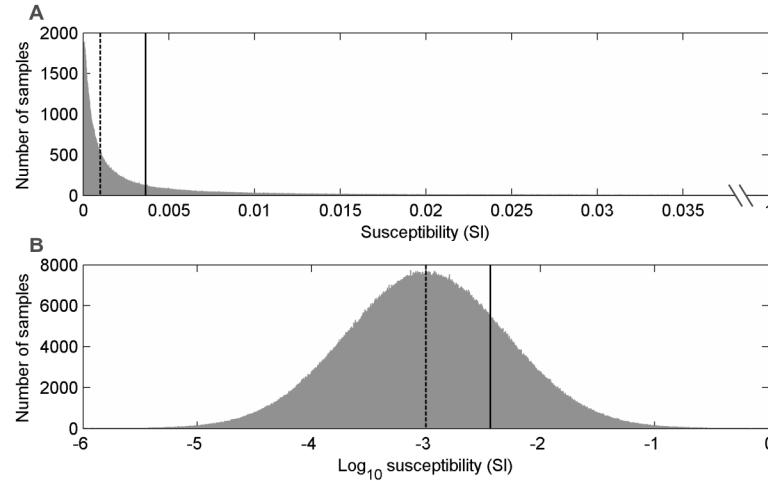


Figure 5.1. Histograms of the lognormal probability density function used to populate 4 million cells representing the constituent magnetic components of a single $200 \text{ m} \times 200 \text{ m} \times 100 \text{ m}$ cell in the model on linear (A) and \log_{10} (B) scales. Solid black line is the arithmetic mean of 3.653×10^{-3} SI; dashed black line indicates the median or geometric mean value of 1.00×10^{-3} SI.

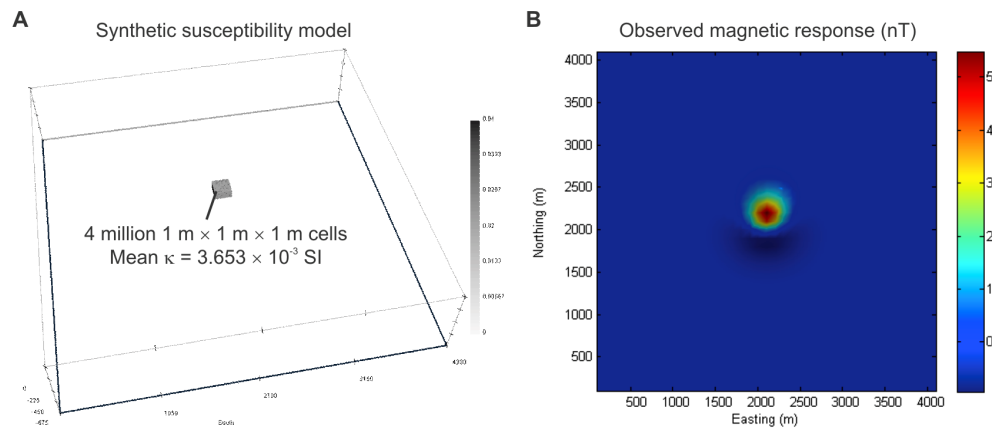


Figure 5.2. A. Synthetic susceptibility model with a central core of 4 million $1 \text{ m} \times 1 \text{ m} \times 1 \text{ m}$ cells (shown) populated with the synthetic susceptibilities shown in Figure 5.1, surrounded by a background of $200 \text{ m} \times 200 \text{ m} \times 100 \text{ m}$ cells with 0 SI susceptibility (hidden). B. Calculated magnetic response of the model in A. Inverting the magnetic response for the bulk property of a single $200 \text{ m} \times 200 \text{ m} \times 100 \text{ m}$ cell gives a susceptibility of 3.644×10^{-3} SI which is consistent with the mean value of 3.653×10^{-3} SI identified in histograms (Figure 5.1).

The central limit theorem provides the ability to estimate the mean of any population (and therefore any cell) based on a large enough subset of samples from that population,

without any knowledge or assumptions regarding the probability density function associated with the population (Borradaile, 2003; Devore and Peck, 1986). Any subset of samples taken from the population will provide an estimate of the mean of the population. Repeated sampling will give a normal distribution of estimates of the population mean, regardless of the underlying population distribution (Devore and Peck, 1986). An outcome of this property is that for any large single set of samples from the population, an approximate $100(1 - \alpha) \%$ confidence interval for the population mean can be obtained using:

$$\bar{x} \pm Z_{\alpha/2} \frac{\sigma}{\sqrt{n}}, \quad (n \geq 30) \quad 5.1$$

where \bar{x} is the sample mean, $Z_{\alpha/2}$ is the critical Z value for the confidence level, σ is the sample standard deviation, and n is the number of samples (Borradaile, 2003; Shi and Golam Kibria, 2007). For a 95 % confidence interval, the critical Z value is 1.96. Confidence intervals represent the most likely range containing the population mean at a given confidence level and can be used directly to assign bounds for each cell in the inversion constraint models.

If the number of samples is small (< 30), the central limit theorem no longer applies and a modification is required to derive an estimate of the confidence interval for the population mean. If the population is expected to be approximately normally distributed, as generally expected for densities, then a more reliable confidence interval for the population mean is obtained using:

$$\bar{x} \pm t_{\alpha/2, (n-1)} \frac{\sigma}{\sqrt{n}}, \quad (n < 30) \quad 5.2$$

where $t_{\alpha/2, (n-1)}$ is the upper tail $\alpha/2$ percentile Student t value for $n - 1$ degrees of freedom (Borradaile, 2003; Shi and Golam Kibria, 2007). For sample numbers near 30, equations 5.1 and 5.2 are roughly equivalent but $t_{\alpha/2, (n-1)}$ increases more rapidly as sample numbers decrease resulting in wider confidence intervals with fewer samples. For $n = 5$, the 95 % confidence level value for $t_{\alpha/2, (n-1)}$ is 2.57 which provides a significantly wider confidence interval than the factor of 1.96 obtained for $n \geq 30$.

Where only a small number of samples are available from a population that is expected to be skewed or lognormal, such as magnetic susceptibilities, other methods are needed to calculate reliable confidence intervals estimates for the population mean. Bootstrap methods

are the most effective (Efron and Tibshirani, 1993; Wang, 2001), but can be computationally intensive. A simpler approach is the median t test proposed by Shi and Golam Kibria (2007) which is based on the Student t modification outlined above but measures the variability of the sample relative to the more central sample median. Instead of calculating the standard deviation relative to the sample mean, \bar{x} , it is calculated relative to the sample median, \tilde{x} , using:

$$\tilde{s} = \sqrt{\frac{1}{n-1} \sum_{i=1}^n (x_i - \tilde{x})^2} \quad 5.3$$

The confidence interval is then calculated using

$$\bar{x} \pm t_{\alpha/2, (n-1)} \frac{\tilde{s}}{\sqrt{n}}, \quad (n < 30) \quad 5.4$$

Various simulation tests on synthetic lognormally distributed magnetic susceptibilities shows that the median t test provides wider confidence intervals than the Student t test for small sample sizes and is more likely to contain the true population mean.

The preceding analysis gives a set of numerical methods to translate raw physical property measurements into bulk estimates of physical properties for assigning to inversion model cells. Potential fields respond to the mean physical properties in any rock volume, so an estimate of the mean physical property for each cell is required in the reference model. Therefore, bounds indicate the confidence interval associated with the estimate of the mean physical property. They do not represent the most extreme individual measurements possible within each cell. The confidence interval can be established at any desired confidence level (e.g., 95 % or 99 %). Note that when assigning the bounds using a 95 % confidence interval, the actual mean property of the cell is expected to lie outside the specified bounds in 5 % of the cells. It is hoped that in those 5 % of cases, the actual property will still be close to the specified reference value. If this level of accuracy is not acceptable, then a higher confidence level should be used.

If a large number of samples ($n \geq 30$) are present within a cell then the central limit theorem provides the most reliable estimate of the confidence interval. If there is a small number of samples ($n < 30$), then a decision must be made based on the expected probability density function for the specific property. If the property is expected to be normally distributed,

such as densities, the Student t test is used. If the property is expected to be skewed or lognormal, as for magnetic susceptibilities, then the median t test is used. Since the constraints are based on the contents of each cell, geostatistical methods which estimate the property of a cell from surrounding data are not necessary. Likewise there is no need to apply any volume-scaling of variance as we are not interested in the variability within samples, but are only concerned with the reliability of our estimate of the mean.

5.4 CREATING A PHYSICAL PROPERTY DATABASE

If a user wishes to include geology maps, drilling logs, or a 3D geological model as constraints, a physical property database must be created to provide estimates of the physical properties associated with the observed geological labels. The database is created automatically from the following four data sources as depicted in Figure 5.3:

1. Physical property measurements and geology observations from surface samples
2. Physical property measurements and geology observations from drilling
3. A translation table that matches geology identifiers used in drilling logs to geology identifiers used in maps. This is necessary because drilling geology logs commonly use abbreviations and sometimes cryptic letter or number codes whereas maps tend to be more formal products with formal geological unit names, descriptions or identifiers.
4. Manually-specified properties for any geological rock types that are poorly sampled or difficult to measure properties on.

When creating the database, actual 3D coordinates of the observations are not required, only the co-location of property and geology observations is needed. The database assumes that the geology labels capture all characteristics that may control the physical properties of the rock, including weathering, metamorphism and alteration or mineralisation. If the geology labels apply to an inferred protolith rather than the actual rock, then any occurrences of the actual protolith will be assigned properties that more accurately represent the modified rock. Likewise, if the geology labels fail to capture major alteration or metamorphic characteristics, incorrect properties may be assigned. One approach to this latter problem is to concatenate separate lithology and alteration logging codes into a single label. Physical property

measurements and geology observations for surface samples will typically be available in a single database, spreadsheet or table which can be extracted easily.

1 Extract all physical property measurements everywhere

Surface sample measurements	
GEOLOGYCODE	DENSITY (G/CM ³)
Aod	2.93
Afv	1.75
Afv	2.35
Abm/Czl	1.99

Drill hole measurements			
HOLEID	FROM	TO	DENSITY (G/CM ³)
ADJD406	86.0	88.0	2.15
ADJD406	118.0	120.0	2.58
ADJD406	212.0	214.0	2.51
ADJD406	214.0	216.0	2.51

Drill hole geology logs			
HOLEID	FROM	TO	GEOLOGYCODE
LRC885	100.0	102.0	MA
LRC885	102.0	106.0	UK-
LRC885	106.0	110.0	MA
LRC885	110.0	112.0	FT

2 Link detailed geology codes to major rock types

Translation table	
MAP_LABEL	DRILLING/SAMPLE_CODES
Dacitic porphyritic volcanics	FP%
Basalt	MB%, MA%, Abb, Abv, Abmgrp
Basalt - Plagioclase Phyric	MB%, MA%, Abb, Abv, Abmgrp
Black Shale	SH, SB, SSH, \$SB

3 Calculate property estimates for each geology label

For reference property
Mean
For lower and upper bounds (only if sufficiently sampled)
Confidence intervals at all confidence levels

4 Add manually-defined properties where needed

Manual property estimates			
LABEL	LOWER_BOUND (G/CM ³)	REFERENCE (G/CM ³)	UPPER_BOUND (G/CM ³)
Aog	2.25	2.94	3.2
Cza	1.4	1.9	2.3
Czb	1.4	1.9	2.3
Czc	1.4	1.9	2.5

5 Completed physical property database

Physical property database					
LABEL	#SAMPLES	MEAN	68CI_LOWER	95CI_LOWER	...
Basalt	8562	2.90	2.90	2.89	...
FG	20	2.69	2.64	2.60	...
Granitoid/Gneiss	44	2.77	2.73	2.70	...
SH	53	2.86	2.82	2.78	...

Figure 5.3. Schematic depiction of the data inputs and stages for preparing the physical property database to be used to assign physical property estimates to geological observations throughout the model. 1. The data files are basic text files. Drilling data files must be interrogated to match the geology observations in one file to the property measurements in another file. 2. The translation table links the geology codes for surface samples and drilling logs to the labels used in maps. The wildcard '%' symbol matches all codes that start with the preceding letter combination to the corresponding map label. 3. The mean and confidence intervals on that mean at a range of confidence levels are calculated to provide estimates of the reference property and lower and upper bounds associated with all measurements for each geology label. 4. Manually-defined properties can be assigned for poorly sampled geology labels, or if the measurements are deemed inadequate for particular labels. 5. The finished physical property database provides a statistical summary of the physical properties associated with each geology label. Only a selection of the available statistics is shown.

5.4.1 Drilling information

Drilling observations and property measurements require more careful manipulation as they will typically be stored in separate databases or tables, one for physical property measurements at intervals down each hole, and another for geological observations at intervals

down each hole. Any duplicate entries are skipped. If a drill hole has been logged more than once, or by different people, observations along the hole may have been made on different or overlapping intervals. If overlapping intervals exist, where the end point of one interval lies below the starting point of another interval, all interval endpoints are extracted and sorted in depth order to create a new set of intervals that do not overlap. The observation or measurement associated with the shortest original observation interval that contains each new interval position is extracted (Figure 5.4). The shortest interval is used because it is assumed to represent the most detailed observation.

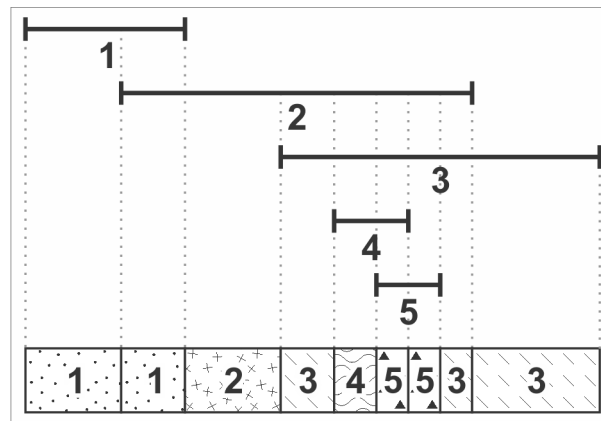


Figure 5.4. Schematic example showing how overlapping observation intervals in drill holes are handled. This may occur where multiple geologists have logged a hole, or where geological units and alteration assemblages have been logged independently. A new set of non-overlapping intervals is created from the end-points, and the observation associated with the shortest original interval at each position is extracted (bottom row).

It cannot be assumed that the physical properties will be recorded at the same locations as the geology observations, and they will likely be recorded on different interval lengths. This is especially common where regular sampling is employed to identify the density for every metre of rock, regardless of geological boundaries. To match measurements to the relevant geology observations, another reprocessing of interval lengths is performed as illustrated in Figure 5.5. All interval endpoints used on both the geology logs and the property logs are extracted and sorted to create all the shortest common interval lengths. The geology observation and property measurement (if any) corresponding to each subinterval are extracted and linked together for use in creating the physical property database.

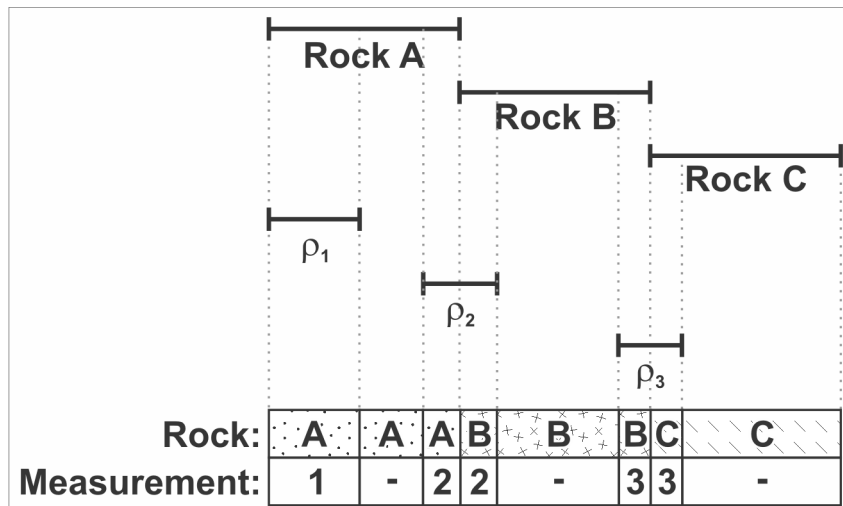


Figure 5.5. Schematic example showing how different geology observations (rocks A, B, and C) and property measurements (ρ_1 , ρ_2 , and ρ_3) are matched to correctly assign the measurements to the corresponding geological observations. A new set of non-overlapping intervals is created from all the interval end-points, and the observation associated with the shortest original interval at each position is extracted. Note that if a property measurement interval corresponds to more than one geology observation, that measurement will be applied to all relevant geology observations.

5.4.2 Translation table for geology labels

For the physical property database to apply to surface samples, drilling logs and geological maps, a facility is required to match any abbreviated geology codes and descriptors used for samples and geology logs with the more general or formal names commonly used in geological maps. This is accomplished via a text file translation table that specifies the geology labels used in the maps in one column, and in a second column any sample or drilling geology labels that correspond to those map labels (step 3 in Figure 5.3). The implementation presented here allows wildcards to be used in the matching of labels to enable all labels starting with certain letter combinations to be easily grouped together into a single more general map label. All physical property measurements from samples and drilling corresponding to each label (or wildcard) are combined and assigned to the identified map label.

5.4.3 Calculating physical property estimates for geology labels

All the observed properties associated with each geology label identified in surface samples, drilling, or the translation table are compiled. These provide the largest available sample of the properties associated with each geology label. They provide the best means of estimating the bulk properties associated with each label, assuming there is negligible spatial variability in properties associated with each label. Estimates of the mean and confidence intervals at a range of confidence levels are calculated for all property measurements

associated with each geology label. All statistical measures for each label are stored for future use, so that the physical property database only needs to be rebuilt when new data are added, and can be reused with different confidence level selections.

5.4.4 Manually-specified properties

If physical property measurements are scarce, or do not cover the full suite of required geological labels, it is possible to manually assign the reference property and lower and bounds associated with any geological label (step 4 in Figure 5.3). This is also useful if it is suspected that the measured properties for certain geological units are biased or unrepresentative. These manually-specified properties replace any automatically-calculated properties for those labels. Typically the manually-specified properties for each label, which are entered via a column-delimited text file, will be based on textbook property values, properties measured on similar rocks in other regions (although these measurements might be more usefully included in the drilling and sample data files and incorporated into the automatic property calculation), or by accessing some external physical property database such as the Mira Geoscience rock property database (<http://www.mirageoscience.com/rpds>; Parsons and McGaughey, 2007).

5.5 INPUT DATA TYPES

Once the physical properties for the geological labels are defined, the raw observation data can be imported and manipulated into the required format. Surface samples are again easy to include as the data will consist of a table of coordinates and physical property measurements that can be used directly.

5.5.1 Drilling information

The spatial position of drill hole traces are usually defined by a file containing drill hole collar coordinates and hole lengths and a file of down-hole positional surveys indicating the azimuth and inclination of the hole at various depths. The physical property observations may be recorded on any interval length down the hole so they are reprocessed in the same manner as described in Section 5.4.1 and Figure 5.4 to remove duplicate entries, and overlapping intervals. To adequately represent measurements reported over intervals each hole is resampled at a small user defined interval with any physical property observation at each resample point extracted. The 3D coordinates for the resample points are calculated using the standard

minimum curvature method based on the positions and orientations of the adjacent drill hole survey points (Sawaryn and Thorogood, 2005). Minimum curvature assumes that adjacent survey points along the hole are connected by a circular arc centred at a point on the plane in which the drill hole trace lies (Sawaryn and Thorogood, 2005). The resulting data consist of a list of 3D coordinates and physical property measurements along each drill hole. The same procedure is performed for the drilling geology logs, with the observed geology code at each resample point extracted and the 3D coordinates calculated for each resample point.

5.5.2 Maps

Map data is commonly stored in polygon format ESRI shapefiles or can be translated into the shapefile format in other software packages. Each polygon stored within the file contains coordinates for the geometry of the polygon, and attributes associated with the polygon. One of the attributes will be a geological label or descriptor which can be linked to the physical property database to extract a property estimate for that polygon. The Matlab Mapping Toolbox (Mathworks Inc.) contains a built in utility to read the polygons and their attributes from shapefiles. The easting and northing coordinates for each column of cells in the model are defined by the supplied mesh definition file. Within each column the vertical position of the map is determined from supplied topographic data and a user defined depth below topography. If an outcrop map is being used, the map should lie on the topographic surface and the depth below topography will likely be zero. A map of interpreted basement geology could be placed at any depth below the surface. Both outcrop and basement geology maps can be used together placed at different vertical positions in the model. Depending on the scale of the map and the complexity of the geology, the user defines the number of sampling points to be used in each cell. The geology label or descriptor contained in the map at each of these regularly spaced sample points in each cell is identified from the shapefile data using another Matlab utility (interpshapefile: Kearney, 2006). If desired, properties can be assigned to whitespace in the map where no geological labels are defined. Such whitespace may represent a particular formation that has been omitted from the map for clarity. The reference property for the map in each cell is taken as a weighted average of the relevant properties indicated in the physical property database based on the frequency with which each geology label is encountered within each cell. The lower and upper bounds for the map in each cell are defined by the minimum and maximum confidence interval limits associated with any of the

map geology labels identified in the cell as defined in the physical property database. This captures the full range of possibilities within the cell while also indicating the most likely value.

5.5.3 Three-dimensional geological and domain models

The purpose of this approach to building models from sparse constraints is to avoid the over interpretation required to build full 3D models in regions of minimal geological data. However, in some near-mine areas, enough subsurface geological information might be available to facilitate building a detailed geological model of units and contacts, or simple layered earth models might be beneficial where geological information is scarce. This information can provide a useful framework for populating a physical property model, and the position of geological boundaries and contacts, if known well, can be powerful in defining regions of similar physical properties. Some geophysical inversion model building software packages use the full 3D geological model as the only, and therefore most reliable, constraint (Guillen et al., 2004; McGaughey, 2007). The method presented here only uses available 3D models as the least reliable constraints; all data and observations are applied over the top of the interpreted 3D models.

A distinction is made between geological models, and less reliable domain models. Geological models are defined as full 3D models where individual rock types with specific physical properties are individually mapped and the positions and orientations of all contacts are well known and accurately represented in the model. The geological model, created in a specialised 3D modelling package, must be available in the model format used by the inversion with an integer geological unit ID number stored in each cell. A separate text definition file provides estimates of the lower bounds, reference property, upper bounds, and smallness weights for each geological unit identified by an ID number.

Domain models are defined as more poorly constrained 3D models in which the inferred domains include a variety of individual rock types with contacts that are poorly known or approximated. Following from the geological notion of structural domains, distinct structural orientations can be defined in each domain to direct the extrapolation of properties if required. Domains are particularly useful for assigning bounds on the physical properties of rocks in different regions of the model based on an understanding of the geological variability within those regions. One example is the transition from porous weathered material at surface

to lithified basement rocks at depth. The exact depth of weathering may not be known, but an inference can be made that weathering does not extend below a certain depth. Any cells above that depth may have the low densities of weathered rocks or the higher densities associated with basement rocks, whereas all cells below that depth must have the higher densities associated with lithified basement rocks, and therefore a more restricted range of properties. When such constraints are applied in an inversion, the observed geophysical data response will help refine the thickness and extent of the weathered unit as needed. This situation is common enough that an option is included to automatically build a weathering domain with a wider range of properties above a certain depth below the surface. This weathering domain will transgress any other defined domains or geological units, simplifying the 3D model building process.

Domains are defined within a 3D model in the same way as geological units, with an integer domain ID number stored in each cell and a definition file indicating the physical property estimates for each domain. An optional orientation definition file can be supplied to define the dominant structural orientations within each domain. These will define the shape and orientation of the ellipsoid to be used in extrapolating properties as described in detail in Section 5.7 and Figure 5.9. Properties defined in the geological and domain models are used as the default properties in the model where no other information is available.

5.6 ASSIGNING DATA PROPERTIES TO THE MODEL

By this stage all of the input data has been reduced to 3D coordinates and either a measured property value or estimates of the mean property value and confidence intervals. As indicated in Table 5.1, priority in each cell is given to point observations (either measurements or geological observations), then map interpretations, and finally the volumetric interpretations contained in 3D models. Each data type is associated with a user-defined maximum smallness weight (w_s) indicating the general reliability of that data type.

5.6.1 Point observations

If point observations are available within a cell there may be a mixture of physical property measurements and property estimates derived from geological observations. All the standard issues related to spatial sampling apply, and in most cases neither the distribution of measurements nor the distribution of geological observations will represent independent

random samples. Each of the data types will also be associated with particular sampling biases. Physical property measurements may only be made on mineralised, altered, or otherwise unusual rocks. Geological logs are commonly acquired more systematically, but may capture more detail about those unusual rocks than the more voluminous host or background rocks. Even when both data types are acquired systematically there may remain underlying spatial or geological trends that make one data type a more reliable predictor of the bulk physical properties of a cell.

To handle these sampling biases, each data type can be combined in a number of unbiased and biased ways, depending on how reliable the different data types are inferred to be, to recover an estimate of the reference property for that cell (Table 5.2). The first two methods provide reference property estimates that treat either each data point or each data type equally. The second two methods should be used if one data type is considered more reliable than the other, a choice that must be made by comparing the sampling distribution and the expected geological and physical property variability within the model. The final method assumes that each data type is representative and automatically emphasises the data type that provides the best sample distribution within a cell. If the available property measurements and estimates are well distributed in the cell and relatively unbiased, then all of the estimates will converge to a single bulk physical property estimate of that cell. Commonly this will not be the case, and two challenging examples of assigning reference properties with different numbers of measurements and geology observations are shown in Figure 5.6 and Figure 5.7. The figures demonstrate that there can be a significant variability in the reference properties recovered by the different methods when the cell is poorly sampled.

The spatial distribution of observations within a cell is a good indicator of how well the cell was sampled, and therefore provides a guide to how reliable any estimate of the reference property might be. The spatial distribution of surface sample and drilling data within the cell is determined by dividing the cell into blocks of a size that can be approximately represented by a single observation of either geology or physical properties; the default block size is 10 m × 10 m × 10 m, but this can be adjusted if more or less geological or property variability is expected such as for magnetic susceptibility measurements. Within each cell the proportion of blocks containing observations is determined to indicate the spatial distribution of those observations within that cell. Method 5 in Table 5.2 uses the calculated spatial distribution of measurements

and geology-based property estimates to decide which data type best samples the cell and should therefore be emphasised to recover the most reliable reference property (methods 3 or 4), or whether both data types sample the cell equally well and should be given equal weight by using method 2.

Table 5.2. Available methods for assigning reference properties to cells when the cells contain a combination of measurements from surface samples and drill holes and property estimates from drilling geology logs.

Method	Combination method	Calculation in each cell	Use
1	Treat each point observation equally	Combines all measurements and geology-based property estimates and assigns the mean as the reference property.	Measurements and geology-based estimates are equally reliable indicators of the cell properties. This indirectly emphasises the most common observation type without sacrificing any information.
2	Treat each data type equally	The reference property is taken as the value halfway between the mean measurement and the mean geology-based property estimate.	Measurements and geology-based estimates are equally reliable indicators of the cell properties. However, when one data type is underrepresented, it will be over-emphasised with this method. Since physical property measurements are generally less common than geology observations, this will usually provide a slight overemphasis on property measurements.
3	Prefer property measurements	Treats the mean of all geology-based property estimates as a single measurement. The reference property is the mean of all measurements.	The expected variability in properties within a cell is less than the expected geological variability. For example, multiple geological units are expected in each cell but the geology-based property estimates reflect a spatial property variability not observed within individual cells. If only a very small number of measurements are available, this also includes information from any geology-based estimates.
4	Prefer geology observations	Treats the mean of all measurements as a single geology-based estimate. The reference property is the mean of all geology-based property estimates.	The expected geologic variability within a cell is less than the expected property variability. For example, one geological unit with extremely varied properties is expected in cells. A district-based estimate of the unit's properties may be more reliable than any individual measurements within the cell. If only a very small number of geology-based estimates are available, this also includes information from any measurements.
5	Emphasise the observation type that best samples each cell	Calculates the proportion of each cell sampled by measurements and by geology observations. Uses the ratio of the sampling coverage of each data type to pick one of methods 2-4.	Avoid combining measurements and geology-based property estimates in cells where one type provides significantly better sampling of the cell than the other.

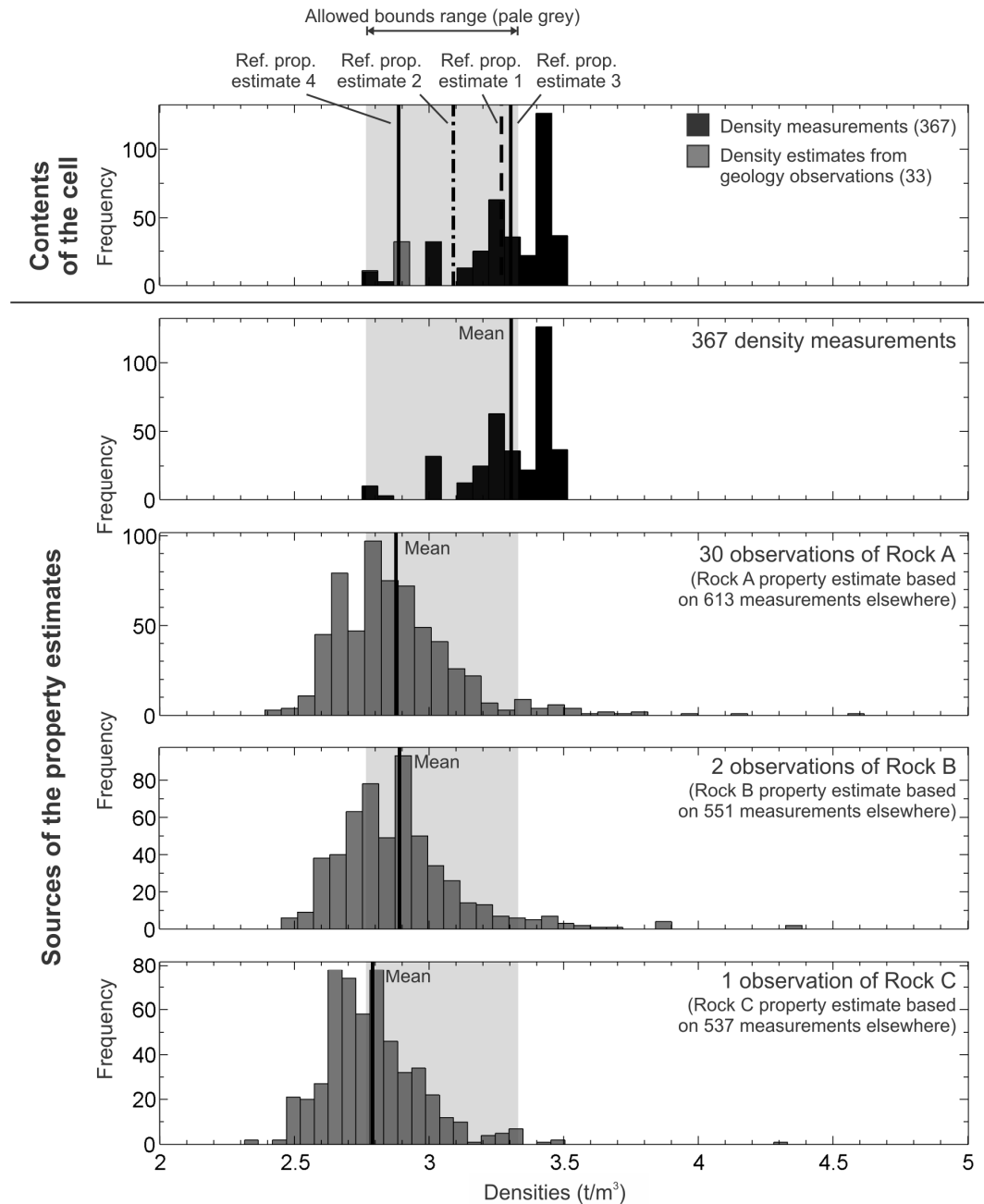


Figure 5.6. A real example of assigning properties to a cell that contains many more property measurements (367) than geology observations (33). Three different rock types were identified in the cell. Each of the geology observations is assigned the mean property associated with that rock type throughout the model as shown by the bottom three histograms. The recovered reference properties derived using the four methods listed in Table 5.2 provide significantly different results as shown at the top of the figure. The fifth method listed in Table 5.2 provides an automated way to pick from methods 2-4 for each cell. The shaded pale grey region indicates the range of bounds applied in the cell determined from the minimum and maximum confidence intervals within the cell. Estimate 1: The mean of all measurements and geology-based property estimates. This is the best estimate based solely on the available data. Estimate 2: Halfway between the mean measurement and the mean of all the geology-based estimates. As there are fewer geology observations, this biases towards the geology observations. Estimate 3: Emphasise the property measurements. This is the most appropriate estimate if the measurements are deemed more reliable than the geology observations. Estimate 4: Emphasise the geology-based property estimates. Given the available data this appears to underestimate the density; however it is the most appropriate method if geology observations are more reliable.

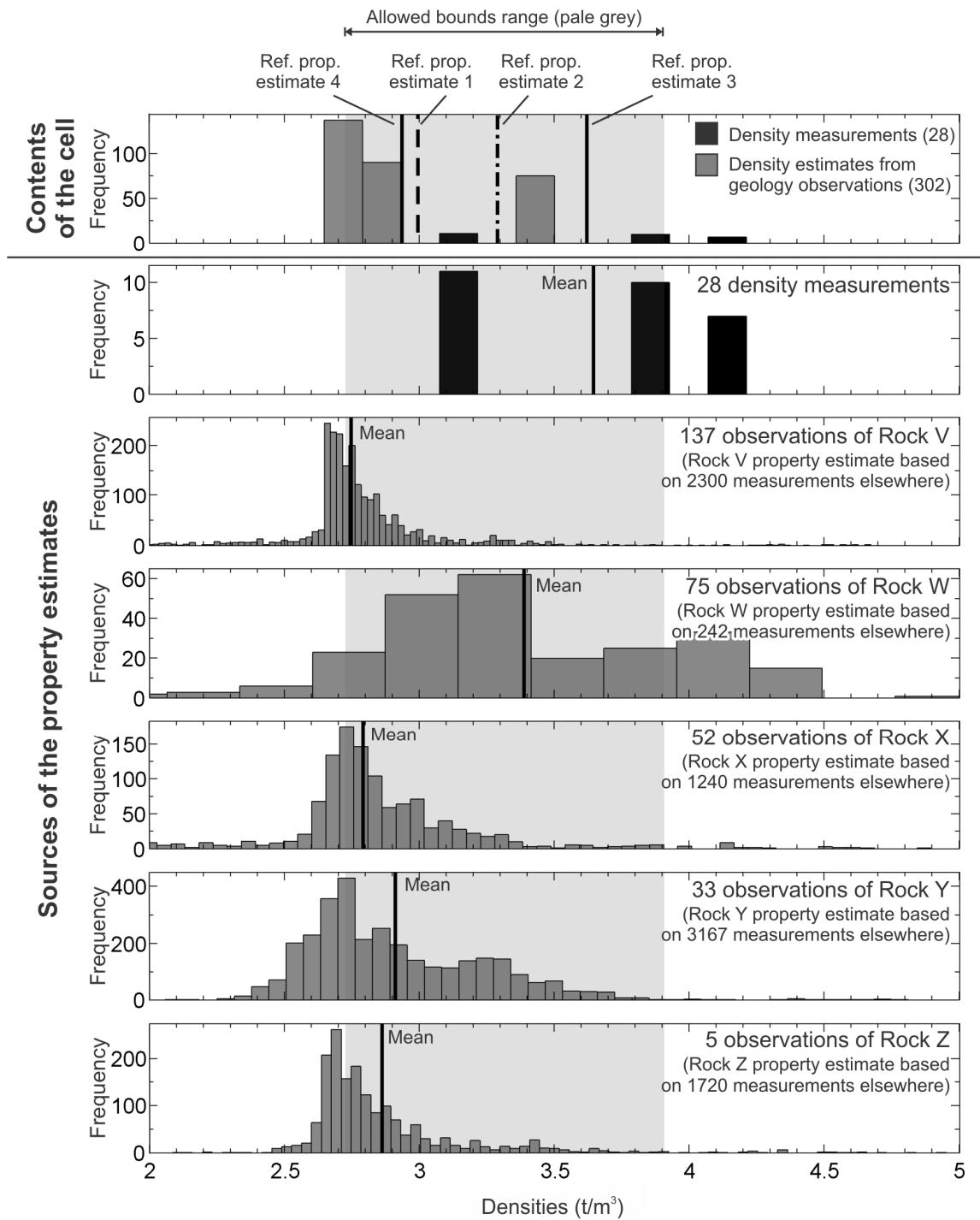


Figure 5.7. A real example of assigning properties to a cell that contains many more geology observations (302) than property measurements (28). Five different rock types were identified in the cell. The reference property estimates were derived in the same manner as for Figure 5.6 using the methods listed in Table 5.2. The shaded grey region indicates the range of bounds applied in the cell determined from the minimum and maximum confidence intervals within the cell. Estimate 1: The mean of all measurements and geology-based property estimates. This is the best estimate based solely on the available data. Estimate 2: This estimate lies halfway between the mean measurements and the mean of all the geology-based estimates. As there are fewer property measurements, this biases towards the measurements. Estimate 3: Emphasise the property measurements, however in this example the property measurements do not appear to be representative of the bulk composition of the cell and the result probably overestimates the desired reference property. Estimate 4: Emphasise the geology-based property estimates. In this example this is perhaps the best estimate.

The spatial distribution is also used to assign smallness weights to each cell indicating the reliability of the reference property for that cell (Figure 5.8). The data type with the most observations in the cell is identified and the maximum smallness weight associated with that data type is scaled by the spatial distribution using:

$$w_s = w_{s_{max}} - \left(\frac{n_{total} - n_{sampled}}{n_{total}} \right)^2 (w_{s_{max}} - 1), \quad 1 \leq w_s \leq w_{s_{max}} \quad 5.5$$

where w_s is the smallness weight assigned to the cell, $w_{s_{max}}$ is the maximum smallness weight associated with the dominant data type in the cell, $n_{sampled}$ is the number of blocks sampled in the cell, and n_{total} is the total number of blocks in the cell. The $w_{s_{max}} - 1$ term allows for the smallness weights having a minimum of unity rather than zero. The squared-weighting provides an intuitive measure of reliability, with the smallness weight increasing rapidly with the addition of a few more samples, but little penalty if only a small proportion of blocks in the cell are not sampled. A reference property is assigned even if there is only one observation in a cell, as it is assumed to be the best estimator of the property of the cell, but will be assigned a relatively low smallness weight by equation 5.5.

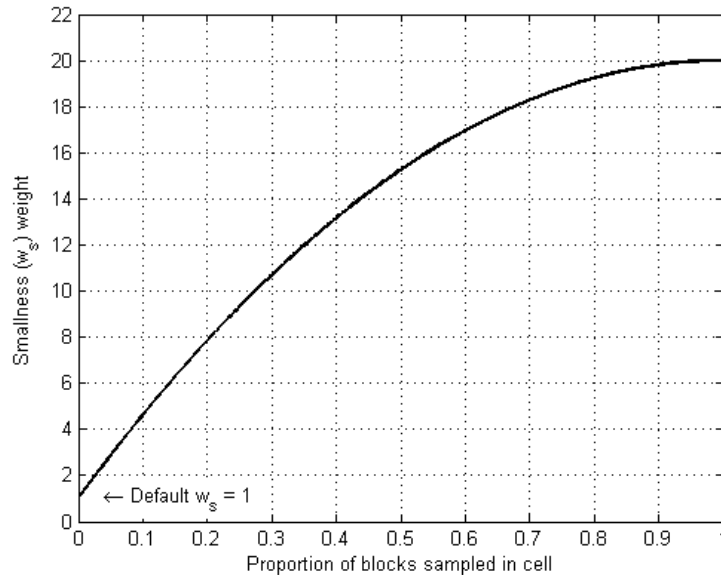


Figure 5.8. Example of assigning smallness weights to a cell based on the distribution of point observations within the cell. Each cell is divided into blocks and the number of blocks containing observations is counted as a proportion of the total number to indicate the spatial distribution of samples within the cell. Equation 5.5 defines the smallness weight as a function of the proportion of blocks sampled, ranging from the default weight of unity up to the maximum smallness weight associated with the particular data type (in this case 20).

Narrow, non-default property bounds are only assigned to a cell if the cell has been sufficiently sampled, with $n_{sampled}$ exceeding some threshold of n_{total} , such as 75 %. The bounds are taken as the minimum and maximum values of any of the confidence intervals calculated at the selected confidence level for all measurements or any geology label property estimates present in the cell. This gives the maximum expected range of properties given the variability observed within the cell. Although the confidence intervals are not specifically shown for the cell in Figure 5.6, the lower bound is defined by the lower 99.7 % confidence interval for Rock C and the upper bound is defined by the upper 99.7 % confidence interval for the property measurements. In Figure 5.7 the lower bound is defined by the lower 99.7 % confidence interval for Rock V and the upper bound is defined by the upper 99.7 % confidence interval for the property measurements.

5.6.2 Maps and 3D models

If no point observations are available, then the property estimates and smallness weight associated with geology map observations within the cell are used as determined in Section 5.5.2. Outcrop maps are favoured over basement geology because the outcropping rocks are more likely to have been directly observed. If still no data is found for the cell, then the cell retains its default property values as defined in the geological model, the domain model, or as specified by the user. Once this has been performed for every cell in the model, the model is complete and can be saved as a UBC–GIF reference model, weight model and bounds model files ready to be included in an inversion.

5.7 EXTRAPOLATING PROPERTIES

The constraining model created thus far is based only on the data and is only enforced where data is available. In data-rich areas a significant number of the cells may be constrained. However, in data-poor environments, such as early exploration stages, few cells will have constraints. An option is provided to extrapolate the observed data outwards a short distance into surrounding cells. Geostatistics provides several methods for extrapolating the observed data to populate model cells, however the general case of populating a 3D physical property model from varied and extremely irregularly-distributed observations of geology and properties across multiple geological units with varied structural trends, is a special case requiring computationally complex universal kriging (Rendu, 1981). Stationarity of the

property mean between cells in different areas of the model cannot be assumed in complex geological environments and regionally reliable models of property drift are difficult to devise. Calculating semivariograms and kriging an anisotropic 3D model of a million cells with even a few thousand property measurements or estimates (which may be available with only 10 well-sampled holes) is also computationally expensive. One simplifying approach might be to subdivide the model into subgroups of cells and apply random kriging to the properties of each cell in each subgroup assuming that samples are located randomly throughout each cell (Rendu, 1981). But it remains that in regions where observations are extremely sparse or even absent, kriging relies entirely on specific semivariogram models and drift functions that require geological knowledge that may not be available.

Given that the method proposed here is best suited to sparsely distributed observations, and to speed performance, a simpler statistical approach based on distance weighting is used. The results are quicker to obtain and in data-poor regions will be at least as reliable as poorly constrained geostatistical solutions. In data-rich regions, slower geostatistical methods may provide more accurate and robust solutions, and this provides an avenue for future development. The currently implemented method calculates an ellipsoidal buffer zone to represent the zone of influence around each data cell. Buffers are applied in all directions around all cells that contain point observations. For cells that only contain map data, buffers are only applied downwards and outwards as the maps are assumed to depict the rocks lying below the map. Buffers are not applied to domain or geological models as they have already populated a volume. The buffer zones are also truncated by any geological contacts defined in the 3D geology model so that properties are never extrapolated from one geological unit to another. An alternative to using buffers to extrapolate the properties prior to performing an inversion is to define smoothness weights to the cell faces that bound data-bearing cells to promote smooth extrapolation of properties during the inversion itself (Section 5.8).

5.7.1 Defining ellipsoidal extrapolation buffers

The buffer around each data-bearing cell is defined as an ellipsoid with three axes, the major **A**, intermediate **B**, and minor polar **C** axes, radiating from the centre of each data-bearing cell. The orientations of the three axes are derived from geological orientations supplied by the user, either for individual domains or for whole model, as defined in Figure 5.9. The **A** axis lies in the direction of any dominant fold hinge lines or principal stretching

directions, which at a small scale may be apparent as stretching or bedding-cleavage lineations within the dip plane. The **B** axis lies perpendicular to the **A** axis, within the dip plane. The polar **C** axis lies perpendicular to the dip plane containing the **A** and **B** axes. The orientations of the ellipsoid axes can be completely defined by three angles: the strike and dip of the plane, and the pitch of the fold hinge or lineation in that plane, as shown in Figure 5.9, using the three equations described by de Kemp et al.(2006):

$$\mathbf{A} = a \begin{pmatrix} \cos(plunge) \sin(trend) \\ \cos(plunge) \cos(trend) \\ -\sin(plunge) \end{pmatrix} \quad 5.6$$

$$\mathbf{B} = b(\mathbf{A} \times \mathbf{C}) \quad 5.7$$

$$\mathbf{C} = c \begin{pmatrix} \sin(dip) \sin(dipdirection) \\ \sin(dip) \cos(dipdirection) \\ \cos(dip) \end{pmatrix} \quad 5.8$$

where a , b , and c are the lengths of each axis, and the geometrical relationships relating various standard structural measures are:

$$plunge = \sin^{-1} [\sin(dip) \sin(pitch)] \quad 5.9$$

$$trend = strike + \cos^{-1} \left[\frac{\cos(pitch)}{\cos(plunge)} \right] \quad 5.10$$

$$dipdirection = strike + 90^\circ \quad 5.11$$

If all three axes are given the same length, $a = b = c$, then the buffer is a sphere. If $a = b > c$ then the ellipsoid depicts a uniform plate parallel to the strike and dip plane, and the pitch angle becomes redundant, which is useful if no information regarding the pitch is available.

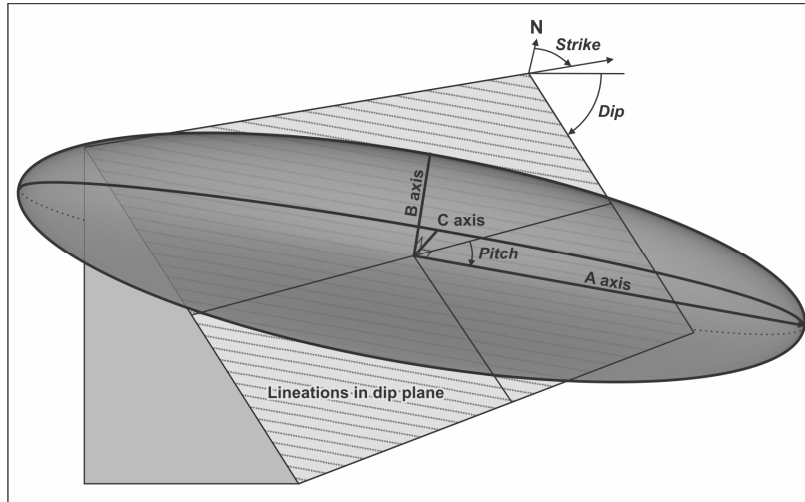


Figure 5.9. Definition of ellipsoidal buffer based on geological orientations. The orientations of the 3 ellipsoid axes, **A** (within dip plane, along lineations), **B** (within dip plane), and **C** (perpendicular upwards out of the dip plane), are derived from the three angles, strike, dip, and pitch. Strike is the clockwise angle (0-360°) from north such that the plane dips to the right when looking towards the strike azimuth (the right-hand rule). The dip is the angle (0-90°) of the plane below horizontal. The pitch is the angle (0-180°) of lineations below the strike line, within the dip plane. Lineations can represent actual stretching lineations and bedding-cleavage orientations, or may be estimates of local fold hinge lines. The length of each axis is estimated by the user according to the expected extent of the structural grain in each direction.

Cells are identified as being inside the ellipsoidal buffer zone if the distance from the centre of the buffer to the cell centre is less than the radius of the ellipsoid in that direction. The radius of the ellipsoid in the direction of each cell is calculated using the standard equation for an ellipsoid in spherical coordinates:

$$\frac{r^2 \cos^2 \theta \sin^2 \phi}{a^2} + \frac{r^2 \sin^2 \theta \sin^2 \phi}{b^2} + \frac{r^2 \cos^2 \phi}{c^2} = 1 \quad 5.12$$

which can be readily solved for the radius, r , in the direction of each cell with the coordinate origin being the centre of each data-bearing cell. In equation 5.12, ϕ is the polar angle, or colatitude, from the **C** axis and can be calculated for the vector \mathbf{v}_i from the centre of the data-bearing cell to each cell in the buffer using:

$$\phi = \cos^{-1} \left(\frac{\mathbf{C} \cdot \mathbf{v}_i}{|\mathbf{C}| |\mathbf{v}_i|} \right) \quad 5.13$$

The longitude, θ , is the angle from the **A** axis within the **A-B** plane:

$$\theta = \cos^{-1} \left(\frac{\mathbf{A} \cdot (\mathbf{v}_i - \mathbf{u}_i)}{|\mathbf{A}| |\mathbf{v}_i - \mathbf{u}_i|} \right) \quad 5.14$$

where:

$$\mathbf{u}_i = \text{proj}_{\mathbf{C}}(\mathbf{v}_i) = \mathbf{C}(\mathbf{C}^T \mathbf{C})^{-1}(\mathbf{C}^T \mathbf{v}_i) \quad 5.15$$

is the projection of vector \mathbf{v}_i onto the polar axis \mathbf{C} . The vector $\mathbf{v}_i - \mathbf{u}_i$ is therefore the component of vector \mathbf{v}_i that lies in the \mathbf{A} - \mathbf{B} plane.

Although it is possible to define a different ellipsoid orientation, shape and size for each individual cell in the model based on actual structural measurements in each cell, it may be more convenient to define these characteristics separately in different regions of the model. In the current implementation the orientations and shapes of the ellipsoids are defined within different structural domains within the model. The orientations are defined by the dominant strike, dip, and pitch in each domain. The ellipsoid shape is defined by the length of the \mathbf{B} and \mathbf{C} axes as a proportion of the major \mathbf{A} axis (b/a and c/a , respectively) based on the structural grain of each domain, such as the thickness, extent, and strain of geological units. In contrast, the ellipsoid sizes can be based on the quality of data contained within a cell. Some data types, such as maps, may be more representative over larger areas than other data types, such as surface sample point measurements. The maximum ellipsoid dimension, the length of the \mathbf{A} axis, should be set using an interpretation of the reliability of each data type and the variability of physical properties or geology at the scale being studied. Some of this information can come from experimental or synthetic semivariograms, or an understanding of the general size and extent of geological units. The two part definition of the buffers gives all buffers within a domain the same shape and orientation, but those cells with more reliable observations will have larger buffers than less reliable cells.

5.7.2 Assigning properties within single buffers

If no other data-bearing cells lie within a buffer, then the reference property of the data-bearing cell is applied as the best available estimate of the reference property for every cell in that buffer zone. Given that the confidence in that property estimate will decrease with distance from the data-bearing cell, the smallness weight assigned to each cell in the buffer is derived from the smallness weight associated with the data-bearing cell but weighted by the squared distance from the data-bearing cell using:

$$w_{s_i} = \left(\frac{d_i}{r_{\text{ellipsoid}}} \right)^2 (w_{s_{\text{default}}} - w_{s_0}) + w_{s_0} \quad 5.16$$

where w_{s_i} is the smallness weight assigned to cell i within the buffer, d_i is the distance from the central data-bearing cell to the centre of cell i , $r_{\text{ellipsoid}}$ is the radius of the ellipsoid in the direction of cell i as determined from solving Equation 5.12, and w_{s_0} is the smallness weight assigned to the central data cell. Equation 5.16 contains the same squared weighting used to assign smallness weights to an individual cell based on the spatial distribution of point samples within the cell.

If the central data-bearing cell was sufficiently sampled to have narrow, non-default bounds assigned, then bounds are assigned to every cell in the buffer; however, the same inverse-distance weighting is used to widen the bounds range as the confidence in the bounds decreases with increasing distance from the data-bearing cell until they reach default background values at the edge of the buffer:

$$b_i = \left(\frac{d_i}{r_{\text{ellipsoid}}} \right)^2 (b_{\text{default}} - b_0) + b_0 \quad 5.17$$

where b_i is the bound value (either upper or lower) for cell i , b_{default} is the default background bound value, and b_0 is the bound value associated with the data-bearing cell. So for a simple example where there are no adjacent data-bearing cells, the properties assigned to cells within the buffer are shown in Figure 5.10.

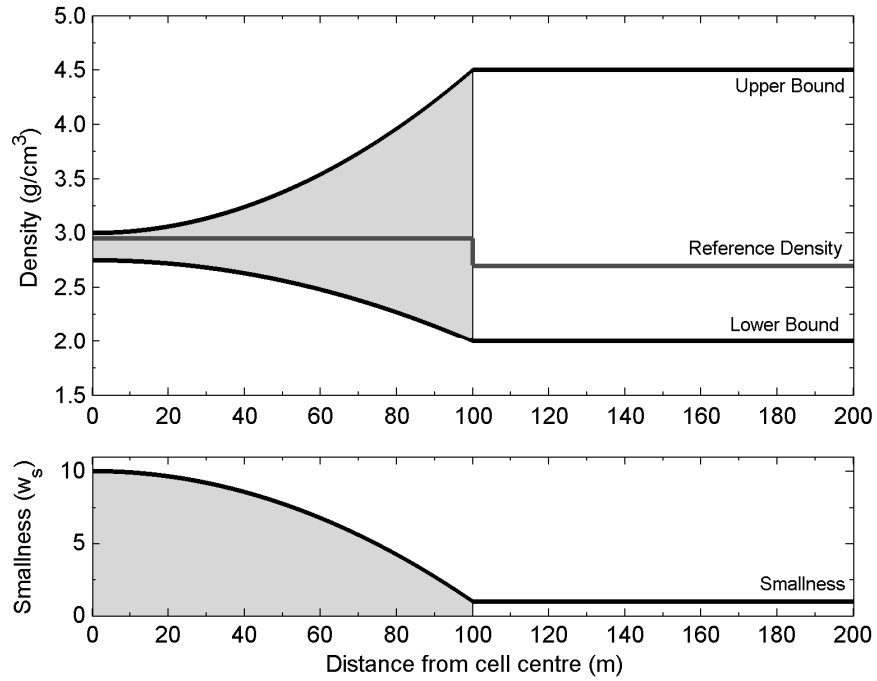


Figure 5.10. Unidirectional example of property values assigned within a 100-m-wide buffer surrounding a single data-bearing cell at 0 m. Within the buffer zone, shaded grey, all cells are assigned the reference property associated with the data-bearing cell, but have decreasing smallness weights and widening bounds as distance from the data increases and reliability of the property estimates decreases. Outside of the buffer zone (> 100 m) default values are used.

5.7.3 Assigning properties within overlapping buffers

If multiple data-bearing cells are present within a buffer zone, then the buffers around each of the data-bearing cells will overlap. Any cells that lie between data-bearing cells must take properties that reflect the influence of each of the data-bearing cells; however buffer cells that are closer to one data-bearing cell should more closely reflect the properties of that cell. The contribution of each data-bearing cell to the properties of each buffer cell is determined by the distance from each data-bearing cell, and the smallness weight (or reliability) associated with each data cell's properties. This suggests a weighted average property with weights derived from both distances and smallness values. To be consistent with the distance-squared weights used above, a reliability weight, R_{ij} , is calculated for each cell i in the buffer zone for the properties associated with each adjacent data-bearing cell j as defined by:

$$R_{ij} = \left(\frac{d_i}{r_{\text{ellipsoid}}} \right)^2 (w_{s_j} - 1) \quad 5.18$$

The $w_{s_j} - 1$ term adjusts the smallness weight of each data-bearing cell so that R_{ij} reaches a minimum of zero at the maximum buffer distance rather than the default smallness value of 1. This ensures that zero weighting is given to those distal cells. Where the buffers of n data-bearing cells overlap, the weighted average property p extracted for each cell i is:

$$p_i = \frac{\sum_{j=1}^n R_{ij} \cdot p_j}{\sum_{j=1}^n R_{ij}} \quad 5.19$$

where p_j is the property of the j th data-bearing cell. The smallness weight assigned to each buffer cell is just the maximum R_{ij} for that cell plus 1 to ensure that $R_{ij} = 0$ corresponds to $w_s = 1$, the default value.

The remaining issue is to define the deflation of the ellipsoid buffer required so that the buffer surrounding one data-bearing cell does not extend beyond any adjacent data-bearing cells. This ensures that each data-bearing cell influences only those cells closest to it. If more than one data-bearing cell is present within a buffer, the angle α_{ij} from the central data-bearing cell to each non-data-bearing cell, vector \mathbf{v}_i , and each data-bearing cell within the buffer, vector \mathbf{v}_j (Figure 5.11), is calculated:

$$\cos \alpha_{ij} = \frac{\mathbf{v}_i \cdot \mathbf{v}_j}{|\mathbf{v}_i| |\mathbf{v}_j|}. \quad 5.20$$

A new deflated buffer radius, $\tilde{r}_{\text{ellipsoid}_i}$, is calculated in the direction of all non-data-bearing cells i with angles $\alpha_{ij} < 90^\circ$ in the original ellipsoidal buffer using the cubed dot product as a weight function controlling the trade-off between the original ellipsoid radius, and the distance to the nearest data-bearing cell, d_j :

$$\tilde{r}_{\text{ellipsoid}_i} = \cos^3 \alpha_{ij} (d_j - r_{\text{ellipsoid}_i}) + r_{\text{ellipsoid}_i}, \quad \alpha_{ij} < 90^\circ. \quad 5.21$$

The cubed dot product tends to preserve the shape of more elongate ellipsoids better than lower powers do. The result is demonstrated in Figure 5.11 where a spherical buffer is deflated from its original radius to the distance to the nearest data-bearing cell. Cells that lie outside this new deflated radius in any direction will be removed from the buffer.

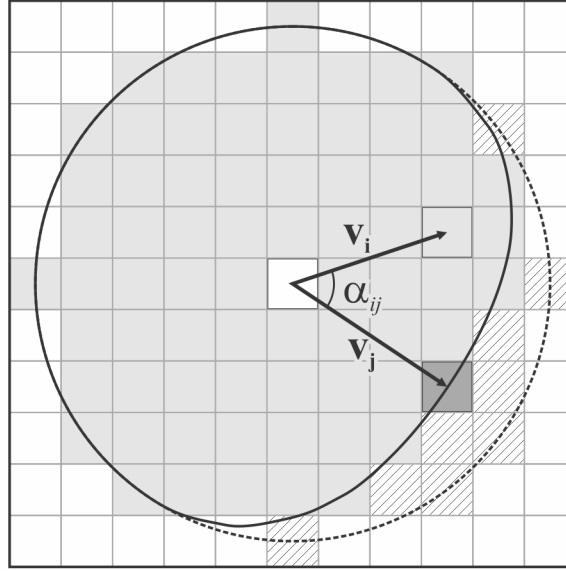


Figure 5.11. Two-dimensional example of how the size of a spherical buffer around a data-bearing cell (centre cell) is reduced when other data-bearing cells lie within the buffer zone. This is done to ensure that the buffer around each data-bearing cell only affects the cells closest to it. The cosine of angle α_{ij} , between each buffer cell i (light grey shading), and each data cell j (dark grey shading), is calculated using equation 5.20. A new buffer distance, $\tilde{r}_{\text{ellipsoid}_i}$ (solid outline; compare to the original user-defined buffer, $r_{\text{ellipsoid}}$, shown by the dotted line), is calculated using equation 5.21. Potential buffer cells that have an angle $\alpha_{ij} < 90^\circ$ and $d_i \geq \tilde{r}_{\text{ellipsoid}_i}$ are excised from the buffer zone (hatched cells). In practice the calculation is performed in three dimensions on arbitrary ellipsoidal buffers and works regardless how many data-bearing cells are present within the user-defined buffer zone and how complex their distribution may be, and ensures that the region of influence of a data-bearing cell never extends beyond another observation.

The adjusted buffer distances are calculated iteratively for each buffer cell-data cell pair within each buffer zone and the minimum deflated ellipsoid radius in every direction is retained. This ensures that the buffer zone, and therefore the central data-bearing cell's influence, never extends beyond adjacent data cells and the weighted properties calculated using Equation 5.19 only include those properties from the nearest data-bearing cells. Where many data-bearing cells lie with a buffer zone, the shape of the buffer can become quite complex as demonstrated in Figure 5.12. In the extreme case where the central data-bearing cell is surrounded on all sides by other data-bearing cells, the adjusted buffer distance around that cell becomes less than the distance between cells so the buffer contains no cells and no extrapolation occurs. Properties are only extrapolated where no other data is available, and the extrapolation only extends a relatively short distance outwards with sharply decreasing certainties (represented by the width of the assigned bounds, and the smallness weights applied) as distance from the data increases (Figure 5.13). For these reasons this method of populating the model gains some intelligence over standard geostatistical techniques.

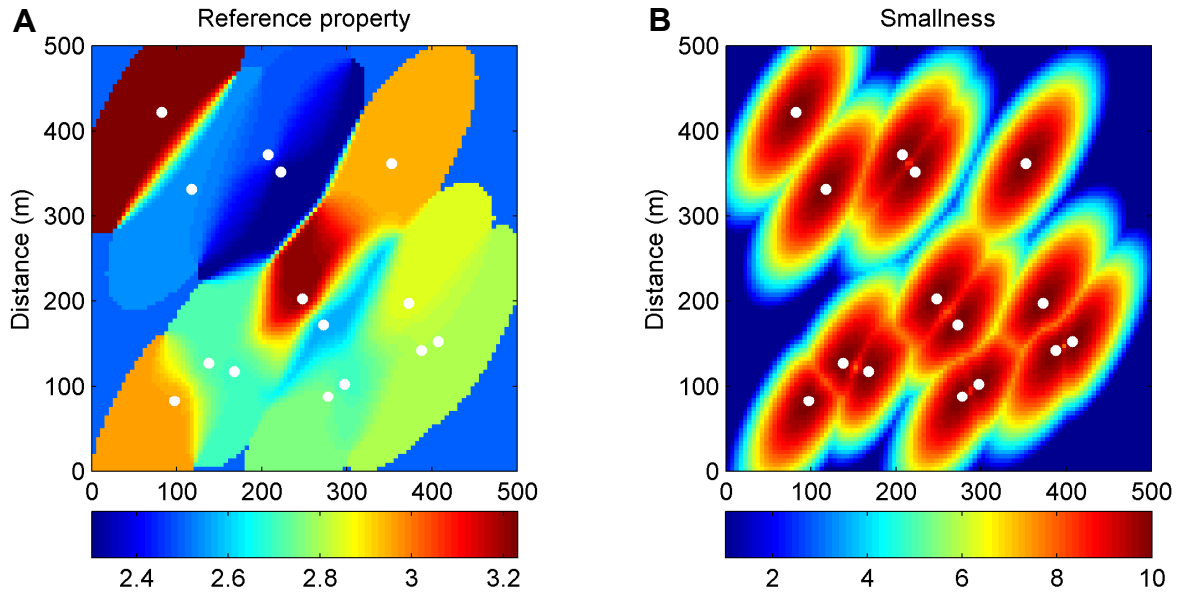


Figure 5.12. Example of ellipsoidal buffers surrounding 15 random data points in a slice through a 3D model. The slice consists of 5-m-wide cells in each direction. The data-bearing cells have randomly defined properties and their locations are marked by white dots. The ellipsoids are defined by: strike = 030° ; dip = 70° ; pitch = 45° ; a (major axis length) = 200 m; $b/a = 0.7$ (giving $b = 140$ m); and $c/a = 0.3$ ($c = 60$ m). A. Reference model properties. Where two or more data-bearing cells lie within the proposed buffer, the ellipsoid radius is deflated to the distance to the nearest data-bearing cell, and the reference properties of intervening buffer cells acquire a weighted average reference property from the adjacent cells. As a result, property gradients are observed between data-bearing cells. The steepness of the gradients depends on the separation between data cells and the difference in their properties. B. The smallness weights assigned to buffer cells decrease with distance from a maximum of 10 at the data-bearing cells to a background level of 1 which is reached at the edge of each buffer.

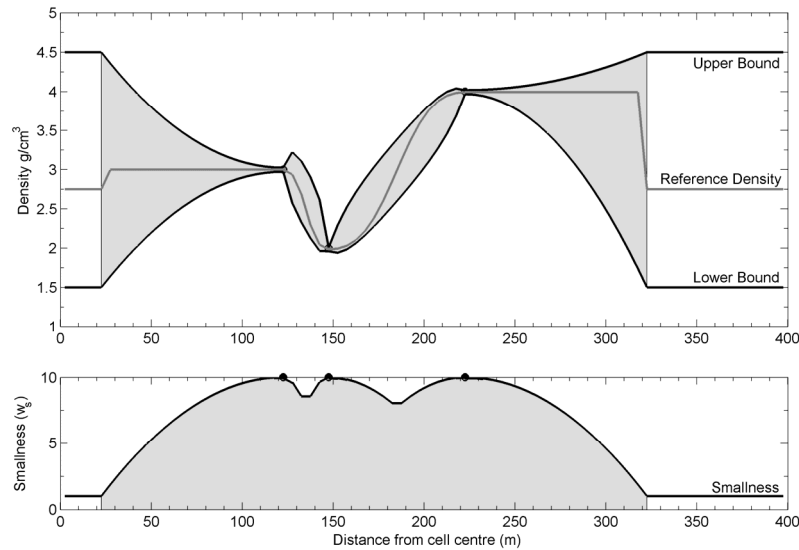


Figure 5.13. Unidirectional example of property values assigned within buffer zones surrounding three data-bearing cells marked with circles at 122.5 m, 147.5 m, and 222.5 m. At the data points, tight bounds and maximum smallness weights indicate a high confidence in the assigned properties. Between the three data-bearing cells the reference properties, bounds, and smallness weights are distance-squared-weighted averages. Intuitively the bounds and smallness weights reflect a maximum uncertainty in the properties at points halfway between data-bearing cells where it is most unclear which property should apply. To the left and right ends of the profile the bounds widen to default values, and uniform reference properties are assigned.

5.8 CALCULATING SMOOTHNESS WEIGHTS

The final type of constraint available for use in the UBC–GIF inversion programs are smoothness weights which define how smoothly the physical properties in the recovered inversion should vary between adjacent cells. The weights are assigned to each cell face in the model. Weights above the default value of unity promote smoothness whereas weights below unity promote sharper changes in the properties of the recovered model. There are three main geological scenarios to which smoothness weights can be usefully applied:

1. Allowing sharp changes in properties across geological contacts where they are known;
2. Promoting smooth extrapolation of properties away from observation locations into cells that lack observations, as an alternative to using buffers; and
3. Retaining the natural variability or roughness in physical properties observed in the reference model.

Each of these situations may arise individually, or in combination, as shown in a schematic example in Figure 5.14. If a 3D geology model is available it will usually contain boundaries separating rocks with different geological unit IDs. Cell faces across which unit IDs change can be identified and assigned a user-specified smoothness weight < 1 (Figure 5.14B) to allow the inversions to recover a sharp contact.

Section 5.7 describes a method for using buffers to extrapolate properties within the reference and bounds models. An alternative approach attempts to guide the inversion to perform the extrapolation by assigning smoothness weights > 1 to those cell faces that separate data-bearing cells from cells that contain no data. The inversion will then ensure that the properties in those adjacent cells lacking data will be assigned similar properties to the data-bearing cells if possible. The benefit to this more conservative approach is that it requires no assumptions regarding the form of the extrapolation function (geostatistical parameters, buffer shapes, sizes and orientations, etc.); however, the smoothness weights typically only propagate the properties a maximum of 1 or 2 cells outwards from data-bearing cells. The smoothness weights are set using the same approach as for geological contacts: the cell faces separating data-bearing cells from non-data bearing cells are identified and assigned a user-specified smoothness weight (Figure 5.14C).

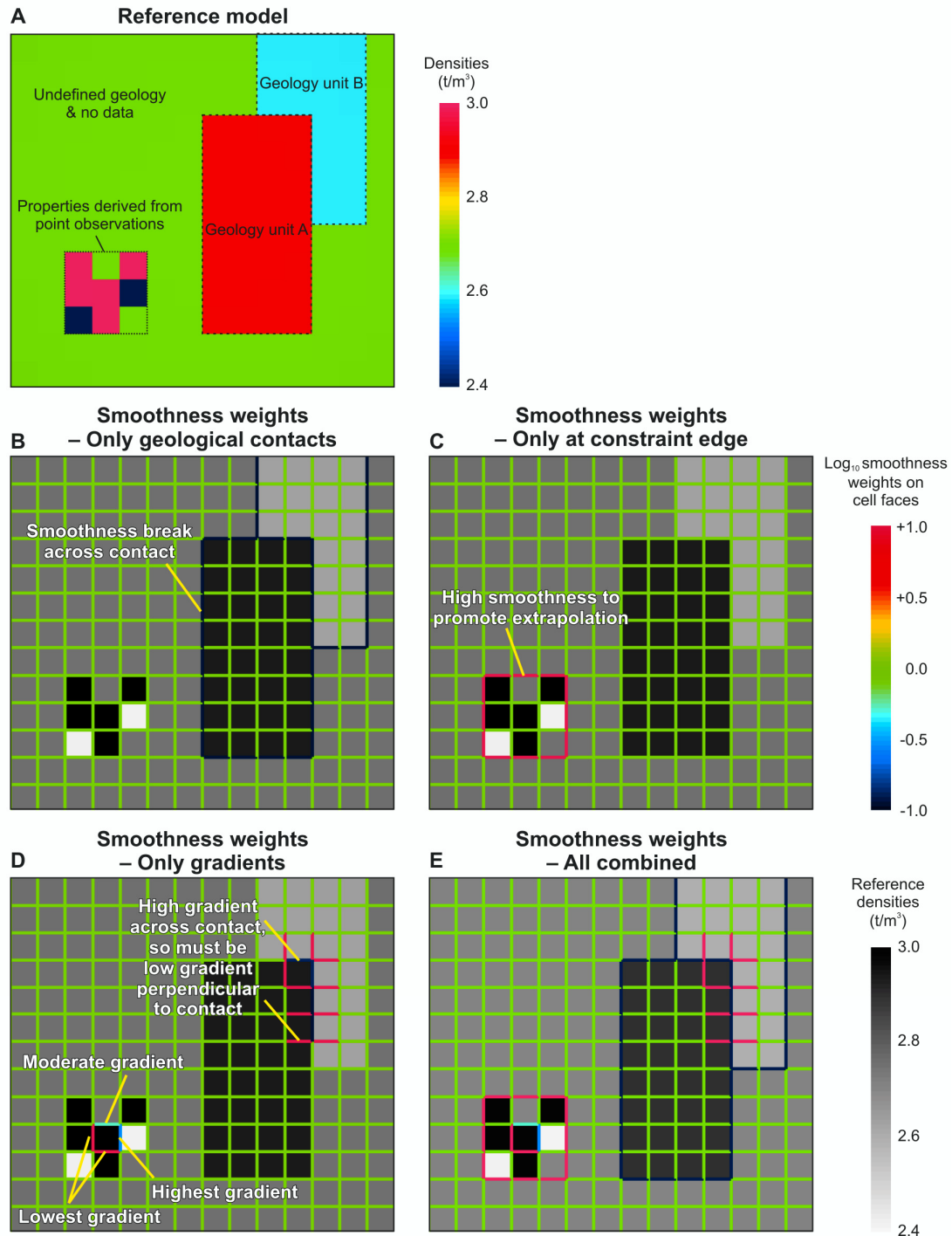


Figure 5.14. Schematic example demonstrating the uses of smoothness weights (coloured along cell faces) with respect to a reference model. A. Simple reference model consisting of two defined geological units in an unknown host rock. The host rock includes a patch of cells that have been constrained by point observations. The same model is used in all images, except with a greyscale colour map. B. Low smoothness weights (0.1) are assigned to all geological unit boundaries, defined by changes in the geological unit IDs, to allow sharp changes in properties across the boundaries. C. High smoothness weights (10) are assigned at the edge of constrained cells to promote extrapolation of the properties. D. Property gradients in the reference model are used to calculate smoothness weights that will help recover the variability in properties observed in the reference model. Smoothness weights are only applied to those cell faces surrounded by enough data-bearing cells to fully define their 3D property gradients. E. A combination of all three approaches seeks to capture the property variability, define geological boundaries, and extrapolate properties as appropriate.

5.8.1 Defining smoothness weights using reference model gradients

Since the smoothness weights determine how much properties should vary between cells and the reference model provides an estimate of the values of the properties in the cells, a good estimate of appropriate smoothness weights might be derived directly from the reference model. The method employed here uses the 3D property gradient calculated in each cell of the reference model to identify in which directions the property is changing. A mapping function converts the computed gradient vector components into appropriate smoothness weights.

The 3D property gradient is easily calculated for each cell based on the reference model properties in adjacent cells:

$$\mathbf{g} = \begin{bmatrix} \frac{\Delta\tilde{\rho}_x}{\Delta x} & \frac{\Delta\tilde{\rho}_y}{\Delta y} & \frac{\Delta\tilde{\rho}_z}{\Delta z} \end{bmatrix} \quad 5.22$$

where $\Delta\tilde{\rho}_x$ is the total magnitude of changes in properties across the cell's faces in the x direction calculated using a long difference between the adjacent cells, and Δx is the distance between cell centres. For a cell that is the i th cell in the x direction, the j th cell in the y direction, and the k th cell in the z direction the long difference is calculated using:

$$\Delta\tilde{\rho}_{x_{i,j,k}} = |\rho_{i-1,j,k} - \rho_{i,j,k}| + |\rho_{i,j,k} - \rho_{i+1,j,k}| \quad 5.23$$

$$\Delta\tilde{\rho}_{y_{i,j,k}} = |\rho_{i,j-1,k} - \rho_{i,j,k}| + |\rho_{i,j,k} - \rho_{i,j+1,k}| \quad 5.24$$

$$\Delta\tilde{\rho}_{z_{i,j,k}} = |\rho_{i,j,k-1} - \rho_{i,j,k}| + |\rho_{i,j,k} - \rho_{i,j,k+1}| \quad 5.25$$

and the distances are defined from the coordinates of the cell centres using:

$$\Delta x = |x_{i+1} - x_{i-1}| \quad 5.26$$

$$\Delta y = |y_{j+1} - y_{j-1}| \quad 5.27$$

$$\Delta z = |z_{k+1} - z_{k-1}| \quad 5.28$$

Absolute values are used throughout as it is only the magnitude of the change in properties that is important for defining the smoothness weights. This could be modified for implementation in other inversion algorithms where constraints can be supplied regarding whether the properties increase or decrease in a particular direction.

The gradient at the cell face can be derived using the actual difference in properties between the two adjacent cells, and an estimate of the property gradient in the two perpendicular directions obtained from averaging the property gradient components from the two adjacent cells in the x direction (Figure 5.15) using:

$$\mathbf{g}_{1,2} = \left[\frac{\Delta \rho_x}{\Delta x_{1,2}} \quad \frac{1}{2} \left(\frac{\Delta \tilde{\rho}_{y_1}}{\Delta y_1} + \frac{\Delta \tilde{\rho}_{y_2}}{\Delta y_2} \right) \quad \frac{1}{2} \left(\frac{\Delta \tilde{\rho}_{z_1}}{\Delta z_1} + \frac{\Delta \tilde{\rho}_{z_2}}{\Delta z_2} \right) \right] \quad 5.29$$

and likewise for cell faces in the y and z directions using:

$$\mathbf{g}_{1,2} = \left[\frac{1}{2} \left(\frac{\Delta \tilde{\rho}_{x_1}}{\Delta x_1} + \frac{\Delta \tilde{\rho}_{x_2}}{\Delta x_2} \right) \quad \frac{\Delta \rho_y}{\Delta y_{1,2}} \quad \frac{1}{2} \left(\frac{\Delta \tilde{\rho}_{z_1}}{\Delta z_1} + \frac{\Delta \tilde{\rho}_{z_2}}{\Delta z_2} \right) \right] \quad 5.30$$

$$\mathbf{g}_{1,2} = \left[\frac{1}{2} \left(\frac{\Delta \tilde{\rho}_{x_1}}{\Delta x_1} + \frac{\Delta \tilde{\rho}_{x_2}}{\Delta x_2} \right) \quad \frac{1}{2} \left(\frac{\Delta \tilde{\rho}_{y_1}}{\Delta y_1} + \frac{\Delta \tilde{\rho}_{y_2}}{\Delta y_2} \right) \quad \frac{\Delta \rho_z}{\Delta z_{1,2}} \right] \quad 5.31$$

Here the actual property gradient across cell faces is included where appropriate rather than the long difference operator:

$$\Delta \rho_x = |\rho_2 - \rho_1| \quad 5.32$$

$$\Delta \rho_y = |\rho_2 - \rho_1| \quad 5.33$$

$$\Delta \rho_z = |\rho_2 - \rho_1| \quad 5.34$$

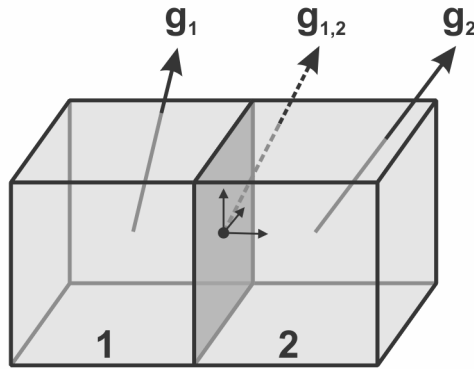


Figure 5.15. Schematic example of the physical property gradients necessary to define the smoothness weight for the cell face separating cells 1 and 2. The smoothness weight will be defined by the 3D property gradient $\mathbf{g}_{1,2}$ at the centre of the shaded face. Although the gradient in properties across the face is readily computed, no information regarding the change in properties in the perpendicular directions is available for a cell face. Instead, the components of the gradient in those two directions are derived from the average of those gradient components in the two adjacent cells, \mathbf{g}_1 and \mathbf{g}_2 .

Thus the gradient at each cell face consists of three components: an actual gradient in properties across the cell face, and two estimates of the gradients in properties in the orthogonal directions derived from averages of the adjacent cell-centred gradients.

It should be noted that the current implementation of the UBC–GIF inversion programs only allows the smoothness weights to be defined in directions orthogonal to the mesh axes (Li and Oldenburg, 1996, 1998), so it is only the x, y, and z components of the property change that are needed at each cell face in those directions. This also provides a definition of the meaning of a default smoothness weight of unity: the properties vary equally in each of the three mesh axis directions. This is equivalent to a property gradient in which all components have equal magnitude which occurs when:

$$\begin{aligned}\hat{\mathbf{g}}_x^2 + \hat{\mathbf{g}}_y^2 + \hat{\mathbf{g}}_z^2 &= 1 \\ \hat{\mathbf{g}}_x &= \hat{\mathbf{g}}_y = \hat{\mathbf{g}}_z = \frac{1}{\sqrt{3}}\end{aligned}\tag{5.35}$$

The calculated gradient at each cell face can be normalised to unit length to determine the relative magnitude of the property gradient in each direction:

$$\hat{\mathbf{g}}_{1,2} = \frac{\mathbf{g}_{1,2} + \frac{\varepsilon}{\sqrt{3}}}{\|\mathbf{g}_{1,2}\| + \varepsilon}\tag{5.36}$$

This normalisation includes a small stabilising factor, ε , which prevents numerical errors when the magnitude of the gradient is zero. This will occur when all adjacent cells have identical properties. In this situation, the properties vary equally in all directions and the gradient components should all have values of $1/\sqrt{3}$, giving rise to the extra scaling term in the numerator. For significant property gradients, these extra terms are negligible.

If a normalised gradient component is $< 1/\sqrt{3}$ then the properties vary more smoothly than the default values expect, and a smoothness weight > 1 could be used to encourage that smoothness in the inversion result. Likewise, if the normalised gradient component is $> 1/\sqrt{3}$ the properties change more sharply than the default smoothness weights suggest, and weights < 1 could be used to allow a sharp break in the recovered properties. This suggests a logarithmic mapping scheme, and testing shows that orders of magnitude changes in smoothness weights are required to significantly influence the models recovered from inversions. The scheme used

here creates a nearly linear mapping devised such that the maximum gradient component of 1 maps to a smoothness weight of 0.1, a gradient component of $1/\sqrt{3}$ obtained when all components are equal maps to a smoothness weight of unity, and the minimum gradient component of 0 maps to a smoothness weight of 10, as shown in Figure 5.16.

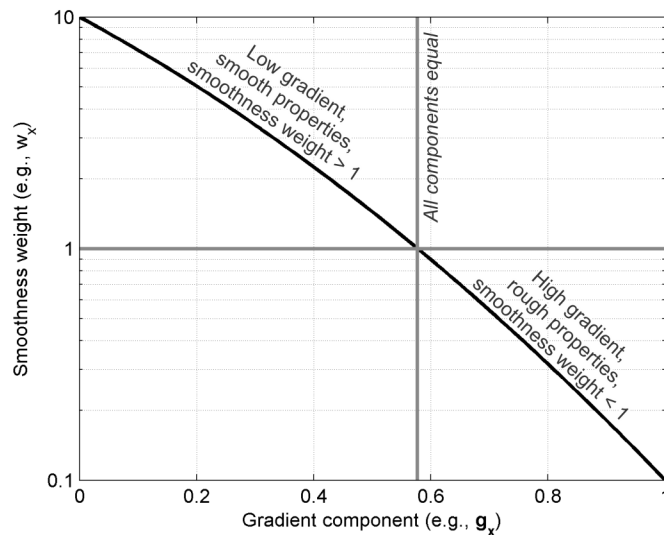


Figure 5.16. Mapping function to convert calculated gradient components into appropriate smoothness weights. The function is defined by the minimum and maximum smoothness weights to be assigned to the gradient components of 0 and 1 and by the default smoothness weight of unity associated with all gradient components being equal, $g_x = g_y = g_z = 1/\sqrt{3}$.

Although the calculation could be applied to every cell face, some additional checks need to be employed to ensure meaningful results. Reliable property gradients can only be calculated when all cells used in the calculation for a particular face contain data, so the calculation is only performed where enough data are available. An example is shown in Figure 5.14D. Only those cells in the interior of data-bearing regions are surrounded by sufficient data-bearing cells to fully define their 3D property gradients, and it is only the faces of those cells that are assigned smoothness weights. Figure 5.14D also demonstrates how using gradients to calculate the smoothness weights links the weights assigned to nearby cell faces. There is a sharp gradient in properties across the contact separating geological units A and B giving a high gradient component across the contact and a low smoothness weight. To accommodate the high gradient component, there must be a low gradient component in at least one of the orthogonal directions suggesting the properties vary more smoothly in that orthogonal direction, and so higher smoothness weights are applied to cell faces perpendicular to the contact.

5.9 EXAMPLE OF DEVELOPING GEOLOGICAL CONSTRAINTS

A case study example around the Perseverance komatiite-hosted nickel sulphide deposit in Western Australia was used to develop this sparse constraint model building program. Although the constraint models are demonstrated here, their application in gravity inversions is beyond the scope of this chapter and is covered in Chapter 7. The case study seeks to use all available geological information surrounding the deposit to create a density model for constraining gravity inversions. The model volume measures 8.3 km east-west \times 8.8 km north-south \times 4 km vertically and has a minimum cell size of 25 m \times 25 m \times 10 m. The case study is particularly useful because it includes a large number of physical property measurements and geological observations in and around the ore deposit, but very few observations > 1 km away from the mine site. The geology is complex with multiply deformed and metamorphosed units, many of which are relatively thin. The irregular data spacing and complex geology represents a challenging problem for traditional kriging techniques, and highlights the benefits of the simpler and faster method presented here for populating the model. The available data includes:

1. The Sir Samuel 1:100,000 scale outcrop geology map ESRI shapefile (Liu et al., 1996) created as part of regional mapping by the Geological Survey of Western Australia;
2. BHP Billiton basement geology shapefile interpretation (C. Perring, pers. commun., 2005);
3. BHP Billiton's district-wide drilling database containing $> 125,000$ density measurements and $> 290,000$ geology observations on $> 45,000$ drill holes (G. Thompson, pers. commun., 2005);
4. Density measurements on 30 variably weathered surface rocks from elsewhere in the district (Chapter 4); and
5. BHP Billiton's partial 3D geological model created from drilling and potential field interpretation (G. Thompson, pers. commun., 2005). The model captures the geometry and extents of the major rock types in a portion of the volume to be used in this example.

A simple 3D domain model was created for inclusion in the model building. It consists of a regolith and Quaternary cover domain with a wide range of densities down to a depth of 100

m below surface, overlying greenstone and granite domains separated by a steeply west-dipping fault and having more restrictive properties and different dominant structural orientations.

5.9.1 Basic model of surface constraints

Chapter 2 demonstrated that in areas where there is a strong physical property contrast between surface rocks and basement rocks, such as in deeply weathered terrain, providing a model that constrains the physical properties of surface rocks provides the most effective and easiest to implement constraint for enhancing the resolution of features at depth in inversions. The geophysical data are most sensitive to the physical properties of those surface rocks and so using surface constraints to improve the model at shallow levels can cause large changes at depth where the model is less sensitive to the geophysical data (Chapter 2). The most readily available constraints that can be applied to surface rocks are physical property estimates associated with surface mapping. These types of constraints are applicable to both prospect-scale delineation using company mapping, and regional scale targeting using government mapping. To demonstrate the approach for building a quick initial model of constraints using map data for greenfields exploration, an initial density model was created with minimal data. The model was built using only the geological survey's outcrop geology map shapefile (Figure 5.17A), the 30 surface sample density measurements, and estimates of physical properties based on literature values (Emerson et al., 2000; Telford et al., 1990) for 42 geology labels used in the outcrop geology map that had no available density measurements.

Figure 5.17. Constraint models recovered for the Perseverance case study area using readily available surface data only. A. Portion of the Sir Samuel outcrop geology map (Liu et al., 1996) over the 8.3 km east-west \times 8.8 km north-south volume of interest. The grey units represent mine infrastructure for which density estimates were not assigned. B. Resulting sparse constraint density reference model for the same area. The reference model clearly replicates the outcrop geology map with abundant low density weathered material with small patches of less-weathered basement outcrops of both granite (eastern half) and greenstone (western half). The large red region in the middle of the image corresponds to the region of mine infrastructure that was assigned default densities of 2.8 t/m^3 . As shown in D these are also associated with default, uncertain smallness weights. The dotted white line indicates the location of the slice depicted in C and D. C. Slice through the reference model showing the effect of extrapolating the map downwards using 100-m-wide spherical buffers. At these shallow levels the mesh cells are 10 m tall, so a layer of 10 cells is constrained accounting for 11.6 % of the 805,291 model cells that lie below topography. D. Assigned smallness weights indicating the reliability of the reference model values in each cell. This view shows the decreasing reliability as the buffers spread downwards away from the map surface. Default reliabilities are assigned wherever there are no physical property estimates available for the mapped geology, such as for the mine infrastructure. E-F. Lower and upper bounds indicating the 99.7 % confidence interval on the reference densities. Although the lower and upper bounds are shown with the same colour scale, this differs from the color scale used for the reference model.

With these data inputs, the sparse constraint model builder automatically created a reference model (Figure 5.17B-C), smallness (Figure 5.17D) and smoothness weights (not shown), and a 99.7 % confidence level bounds model, using spherical 100-m-wide buffers to extrapolate the map (Figure 5.17C-D), in less than 30 minutes. The resulting model contains geological constraints for 11.6 % of the 805,291 model cells that lie below topography and clearly reproduces the mapped geology with islands of denser basement outcrops amongst dominantly low density weathered material. As described above, the buffers are calculated to ensure that the strength of the constraints, defined by the smallness weights and bounds range, decreases with depth away from the mapped surface (Figure 5.17D).

5.9.2 Complete model of sparse 3D constraints

When all the available geological information is included, much tighter constraints can be imposed over a much larger proportion of the model. First, all the available geology observations and density measurements were combined to create a database of physical property estimates for the region. The entire district-wide drilling database was included, even though many of the observations lie outside the volume interest, to improve the quality of the calculated density estimates in the physical property database. This assumes that there is minimal spatial variability of the mean property associated with each individual geology label throughout the area. Measurements were available for 1110 unique drilling or surface sample logging codes. An additional 49 basement geology map labels were not identified in the drilling logs. By including these in the translation table they were automatically assigned properties based on analogous units in the drilling logs. Of the total of 1159 geology labels with property measurements, 995 had enough measurements to have confidence intervals calculated for use in assigning bounds. The same 42 manually-defined properties described above for the outcrop geology map were also included to complete the physical property database. There are an additional 158 geology labels identified in the drilling geology logs for which there are no physical property measurements available. Further research could manually identify property estimates for all of these labels to further refine the model; however it is useful to demonstrate the quality of the model that can be created with minimal manual interaction.

Although the entire database of > 45,000 holes was included in the physical property database calculation, only about 12,000 have geology observations within the volume of interest, and 6,600 have any density measurements within the volume of interest. Only this subset of geology and property observations was directly used to populate the model. The remainder merely provide more robust physical property estimates for the different rock types. Likewise, none of the surface sample density measurements lay within the inversion volume and so were automatically excluded from the resulting model.

In those cells that contained drilling measurements or geology observations the reference property was taken as the mean of all measurements and geology-based estimates in the cell (method 1 in Table 5.2). This decision was based on an interpretation that both geology and density measurements provide reliable estimates of the reference properties for the model. Geological units in the area are commonly greater than one cell width (> 25 m) wide, so the geological labels identified within a cell are expected to be reliable predictors of that cell's dominant rock type even where irregularly sampled. Simple 3D isotropic semivariogram analysis of all the density measurements suggests that they correlate over distances of up to 500 m (Figure 5.18A). This is consistent with the ranges inferred for 1D semivariograms computed along five well-sampled drill holes (drilled perpendicular to bedding) which show ranges of 200-400 m (Figure 5.18B). Analysis within selected individual cells shows that the reference properties obtained from geology estimates are frequently in good agreement with those obtained from physical property measurements. The most common exception is where abundant geology-based estimates within a cell indicate lower host rock densities, and the more limited number of density measurements indicate higher densities associated with sulphide ores (such as shown in Figure 5.7). The abundance of geological observations will minimise the effect of these outlier physical property measurements. Since both data types provide reliable properties, better results should be obtained by using all information equally. Different smallness weights were assigned to each data type to reflect the varying reliability of each, as indicated in Table 5.3. For point observations these smallness weights were scaled according to the spatial distribution of observations within each cell. Bounds were always calculated using 99.7 % confidence intervals.

In addition to the constraints imposed on near surface rocks by the outcrop map and basement map, a weathering and cover domain was automatically included to allow a wider

range of densities in the top 100 m than in the lithified basement below. The basement rocks were divided into two domains, granites and greenstones, separated by a major known fault. Various parameters were set in each domain as outlined in Table 5.4 based on regional knowledge. Buffers were used to extrapolate properties around data-bearing cells. The orientations and shapes of the ellipsoidal buffers are defined for each domain in Table 5.4. Note the distinct shape changes that are possible by changing only the dip and axis length ratios. The size of the buffers is defined by the length, a , of the **A** axis based on the reliability of the observation data type as indicated in Table 5.3 and Figure 1.18.

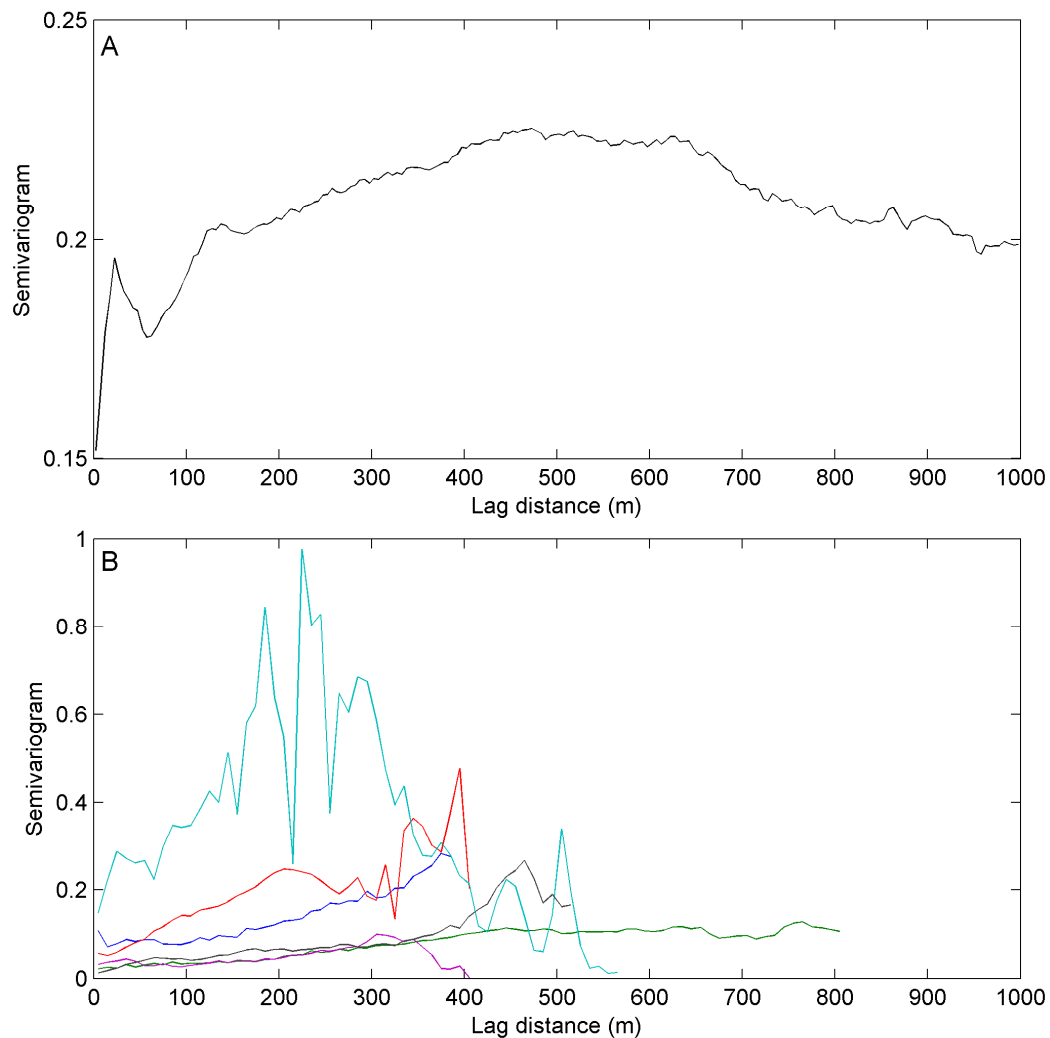


Figure 5.18. Experimental semivariograms of density in the case study area. A. Isotropic semivariogram of all 103,608 density measurements within the volume of interest. The significant nugget effect and noticeable hole-effects (showing reduced variances at lags of 55 m and 1000 m) are due to the multiple geological units present. However, there is a broad sill at lag distances of 500 m indicating some spatial correlation of densities up to that distance. B. One-dimensional semivariograms along each of the five best sampled drill holes. Despite their complexity, and the significant differences between the semivariograms, in all cases primary sills have a range of > 200 m.

Table 5.3. Parameters assigned to data types based on data reliability. The smallness weights associated with measurements and drilling geology observations are scaled to a minimum of 1 according to the spatial distribution of samples within each cell. Smallness weights for other data types are assigned directly. The maximum buffer size used (200 m) is based on the minimum range observed in density semivariograms (Figure 5.18). Buffer sizes all No buffering is applied to 3D models.

	Maximum smallness weight	Maximum length (<i>a</i>) of the major buffer axis (A)	Comments
Surface measurements	15	50 m	Measurements are accurate, but may not be representative of large areas due to heterogeneity of weathered rocks.
Drilling measurements	15	100 m	Some data entry errors in database, but sampled systematically on many holes. Usually restricted to basement rocks which are more predictable than weathered rocks.
Drilling geology observations	20	100 m	Very systematic and moderately detailed logging.
Outcrop geology map	20	100 m	Good lateral accuracy but doesn't capture vertical heterogeneity, so requires small amount of vertical extrapolation with buffers.
Basement geology map	10	200 m	Only an interpretation based on potential field interpretations correlated with drilling and surface mapping, but expected to capture the broad-scale features of the basement geology.
3D geology model	2	N/A	Primarily based on potential field interpretations, with minimal ground truthing.
3D domain model	2	N/A	Simplified version of the 3D geology model capturing the basic rock packages and a regionally-extensive boundary fault.

Table 5.4. Model building parameters assigned to each domain.

Parameter	Weathering/cover domain	Greenstone domain	Granite domain
Description	Properties may be similar laterally, but densities increase with depth in the regolith profile as porosity decreases.	Felsic, mafic and ultramafic rock packages have strong NNW strike, with a downward plunge to the NNW	Similar strain orientation to the greenstone belt, but less intense. Due to volume of granite, properties are expected to be relatively homogenous in all directions.
Lower bound (g/m ³)	1.80	2.40	2.55
Reference density (t/m ³)	2.10	2.90	2.75
Upper bound (g/m ³)	3.50	4.50	2.90
Buffers – dominant structural orientation	Flat lying circular plate	NNW-plunging, W-dipping ellipsoid	Sphere
Strike	160°	160°	160°
Dip	0°	75°	75°
Pitch (estimated from fold hinges)	135°	135°	135°
<i>b/a</i> axis length ratio	1.0	0.8	1.0
<i>c/a</i> axis length ratio	0.3	0.3	1.0

A view of the various resulting constraint models is shown in Figure 5.19, including reference model (A), smallness weights (B), lower bounds (C), upper bounds (D), and the dominant data type contained within each cell (E). Smoothness weights were also calculated using the reference property gradients, geological boundaries, and constraint extrapolation methods described in Section 5.8, but are difficult to visualise so are not shown. The model took under 3 hours to build from scratch, including all data management and importing stages. A breakdown of how constraints have been used within the model is listed in Table 5.5. In this example, 19.9 % of the 805,291 model cells that lie below topography have detailed constraints applied from point measurements, geology observations and maps.

Figure 5.19. Cutaway perspective views of the final constraint models. All images show the same view. A. Reference density model showing the expected densities for each cell based on all available data and buffer-based extrapolation. Labels schematically indicate the locations of some of the data types used but a more detailed identification of the data types is given in E. Geological structure is clearly present in the model and correlates extremely well with the company's wireframe surface interpretations (not shown and not included in the model building process). Several new features have been identified and mapped based on this density model (Figure 5.20) as it provides a new synthesis of the available data. B. Smallness weights assigned within the model. These indicate the inferred reliability of the reference densities assigned to each cell. The most reliable data clearly lie at the surface and in the core of the main region of drilling, and reliability decreases outwards from the available data until it reaches default values in the 3D models. C-D. Lower and upper bounds displayed with the same colour scale (but different from the reference model). Non-default bounds are only assigned in those cells that are adequately sampled. E. Indication of the dominant data type in each cell.

In addition to providing a powerful means for constraining inversions, the recovered reference model can even be used directly to make some inferences about the geology through synthesising a wide variety of geological observations into a common format: density. The model has raised several testable questions about the distribution of alteration at depth, and provides a quick 3D volume representation of the complicated stratigraphy and structure in the subsurface. Of particular note is the large dense mass at depth in the centre of the model shown in Figure 5.19A, and in more detail in Figure 5.20. In drilling logs it corresponds to an ultramafic adcumulate body with trace disseminated sulphides and negligible serpentinisation. It appears to be a less-altered equivalent of more serpentinised adcumulate rocks at shallower levels; however its volume and consistent high densities have not been previously recognised. Its extent has not been mapped previously, and it had not been included in the supplied 3D geological model. The density model is also capable of mapping structure due to the spatial correlation of observations, and an example is indicated in Figure 5.19A. The identified fold was known locally from manual interpretations and correlation of drill hole geology logs but not in enough detail to be included in the supplied 3D geological model. However in the reference model it is easily visualised and mapped in 3D due to its sharp density contrast.

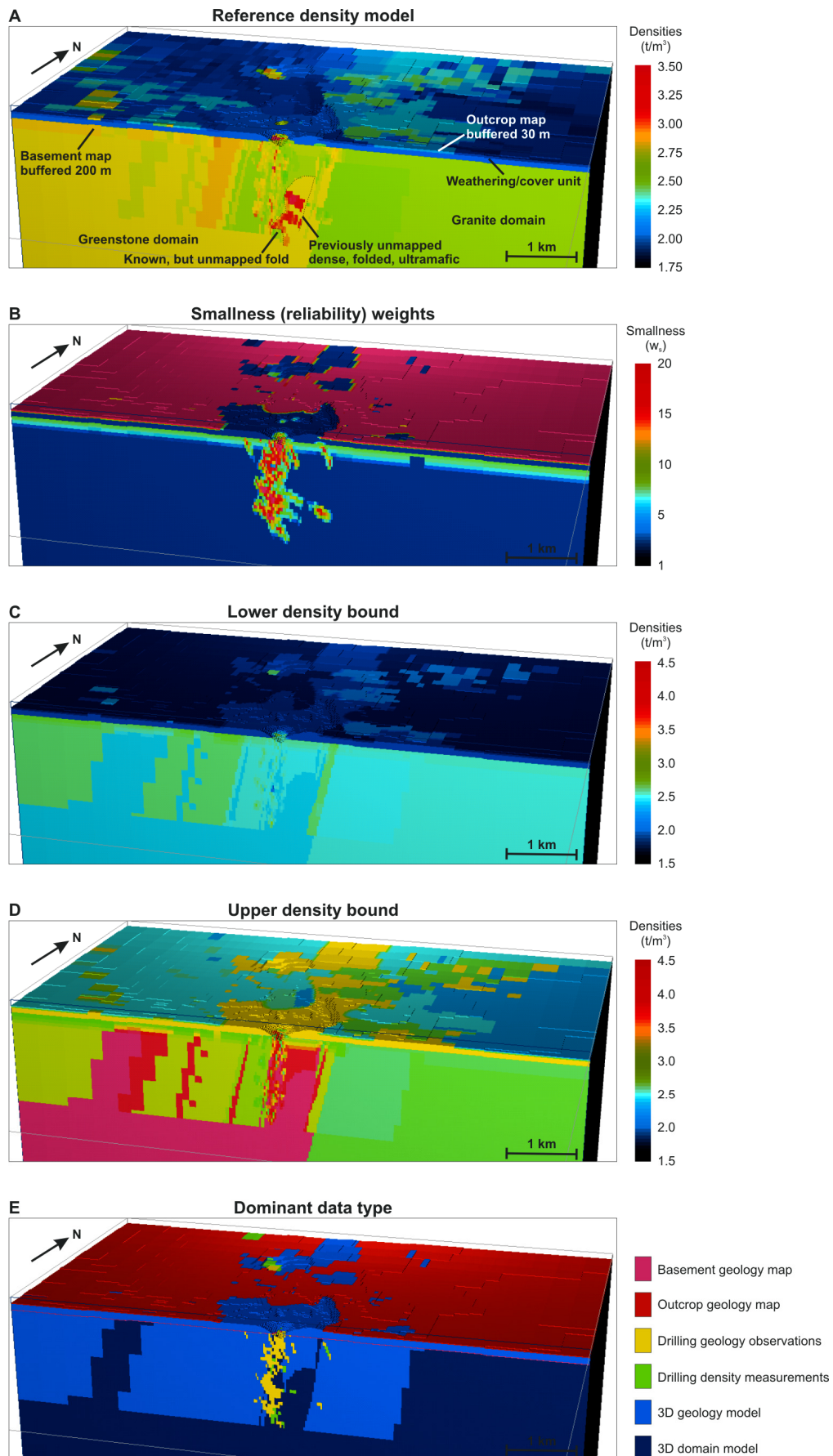


Table 5.5. Breakdown of the number of cells constrained with each data type and whether the constraint came directly from the data or via buffer extrapolation. The model contains 920,856 cells, but only 805,291 of those lie below topography; cells above topography were ignored in these totals. Of most importance is that 3.9 % of the model can be constrained using point or map data alone, and a total of 19.9 % of the model can be constrained by applying buffers around those observations. All cells outside the buffer zones are only constrained by the 3D models (to which buffers do not apply).

Type of data	Model cells containing data		Model cells with properties from buffer extrapolation		Total number of cells containing any constraints	
	Number	Percent	Number	Percent	Number	Percent
Surface sample density measurements ¹	0	0.0%	0	0.0%	0	0.0%
Drilling density measurements	2,322	0.3%	14,680	1.8%	17,002	2.1%
Drilling geology observations	9,122	1.1%	23,863	3.0%	32,985	4.1%
Outcrop map geology	8,417	1.0%	20,338	2.5%	28,755	3.6%
Basement map geology	11,743	1.5%	69,697	8.7%	81,440	10.1%
3D geology model	297,111	36.9%	N/A	N/A	297,111	36.9%
3D domain model	347,998	43.2%	N/A	N/A	347,998	43.2%
Total constrained by point or map observations	31,604	3.9%	138,563	16.0%	166,637	19.9%

¹ Surface samples are included in the table because 30 samples were used to help calculate the physical properties database, but all lay outside the actual volume of interest.

Despite the great depth (> 500-600 m below surface) of the dense adcumulate body its mass may make a significant contribution to the observed gravity data. That indicates a further use of such density models: forward modelling for survey design and sensitivity testing. Calculating the gravity response of the reference model may help determine the required gravity station spacing and lateral data extents required to image the observed density contrasts and spatial distribution in the subsurface.

5.10 SUMMARY

The sparse constraint model builder described here provides a quick and efficient means of producing data-based constraining models for geophysical inversions. Although specifically developed for use with the UBC–GIF inversion programs (UBC–GIF, 2005a, b), the treatment of the different types of geological information could be applied for use in any inversion or modelling algorithm. The procedure itself is primarily a data management routine to provide a systematic and repeatable way of combining geological observations and physical property measurements into a single, self-consistent model. Physical property data is integral to

the proposed technique, and this may be perceived as a limiting factor in applying the method in some areas, but physical properties provide the critical link between geology and observed geophysical responses and an understanding of the expected physical properties is a necessary component in any geophysical interpretation. By demonstrating an efficient link between physical property measurements and development of a constraining model for inversions, it should provide justification for acquiring more property measurements in the field. But as demonstrated above, the simplest constraining model for any area can be achieved during a desktop study with a public domain geology map and literature values for physical properties. Any additional data acquired during a work program can be rapidly included to continually improve the working constraint model for a given area. The reference model can also be used to calculate the predicted geophysical response of the currently known geology to identify whether additional geophysical targets may not have been adequately tested or determine appropriate geophysical survey designs.

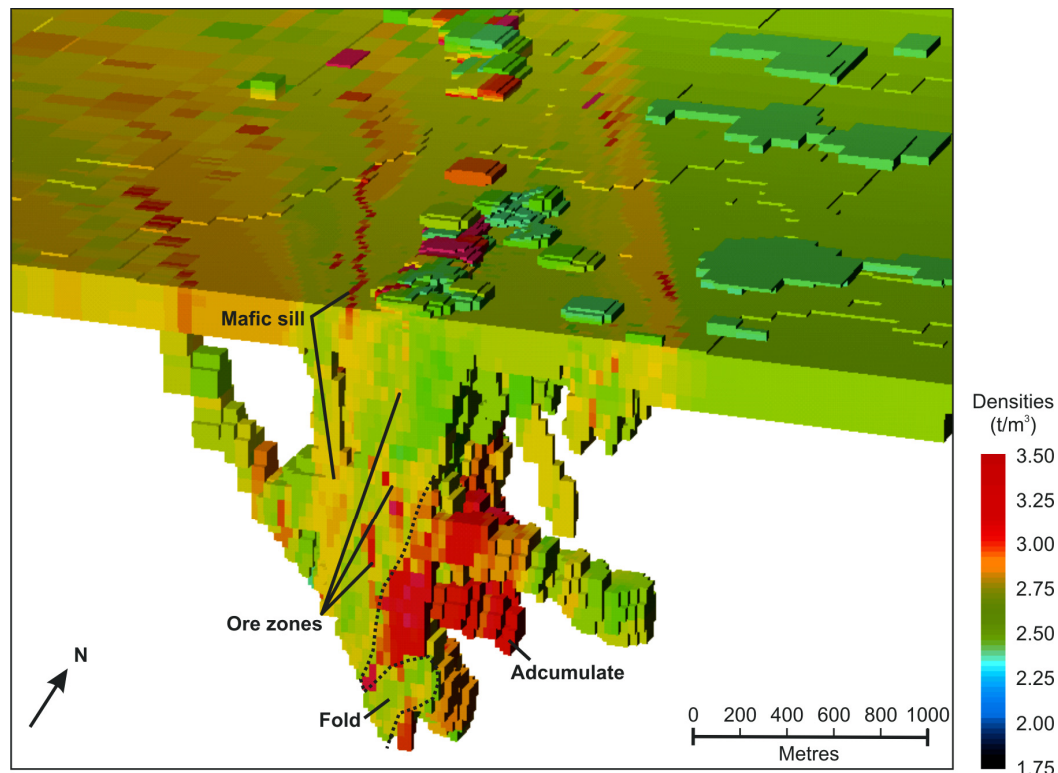


Figure 5.20. Cutaway perspective view along strike to the NNW zoomed to the central portion of Figure 5.19A. Only cells with densities $> 2.5 \text{ t/m}^3$ that were constrained by point or map observations are shown (information from the 3D models has been hidden), effectively displaying a model of expected basement densities. The 3D extent of the dense ultramafic adcumulate can be seen more clearly. It is 400 m thick and > 800 m tall with a 900 m strike length. A 200-m-wide fold is present below the adcumulate. A 25-m-wide NNW-trending, near vertical mafic sill identified in the basement map is apparent as a linear high density feature to the west of the adcumulate. Although barely thick enough to be captured at the scale of this model, the model indicates that it is vertically extensive. Massive sulphide ore zones are generally thinner than the 25-m-wide cells, but three short sections are visible in this model.

5.11 REFERENCES

- Blakely, R. J., 1995, Potential theory in gravity and magnetic applications: Cambridge, Cambridge University Press, 441 p.
- Borradaile, G., 2003, Statistics of earth science data: Their distribution in space, time, and orientation: Berlin, Springer-Verlag, 351 p.
- de Kemp, E. A., Schetselaar, E. M., and Sprague, K., 2006, 3-D symbolization of L–S fabrics as an aid to the analysis of geological structures: *Computers & Geosciences*, v. 32, p. 52-63.
- Devore, J., and Peck, R., 1986, Statistics: The exploration and analysis of data: St. Paul, Minnesota, West, 699 p.
- Efron, B., and Tibshirani, R., 1993, An introduction to the bootstrap: London, Chapman & Hall, 436 p. p.
- Emerson, D. W., Macnae, J., and Sattel, D., 2000, Physical properties of the regolith in the Lawlers area, Western Australia: *Exploration Geophysics*, v. 31, p. 229-235.
- Environmental Systems Research Institute, 1998, ESRI Shapefile Technical Description: <http://www.esri.com/library/whitepapers/pdfs/shapefile.pdf>, accessed 2 Nov 2007, Environmental Systems Research Institute.
- Guillen, A., Courrioux, P., Calcagno, P., Lane, R., Lees, T., and McNerney, P., 2004, Constrained gravity 3D litho-inversion applied to Broken Hill: ASEG 17th Geophysical Conference & Exhibition, Sydney, 15-19 August, 2004.
- Kearney, K., 2006, *interpshapefile*, MATLAB Central File Exchange: <http://www.mathworks.com/matlabcentral/fileexchange/>, accessed 5 Nov 2007.
- Li, Y., and Oldenburg, D. W., 1996, 3-D inversion of magnetic data: *Geophysics*, v. 61, p. 394-408.
- Li, Y., and Oldenburg, D. W., 1998, 3-D inversion of gravity data: *Geophysics*, v. 63, p. 109-119.
- Liu, S. F., Griffin, T. J., Wyche, S., and Westaway, J., 1996, Sir Samuel, W.A. Sheet 3042, 1:100 000 Geological Map Series, Western Australia Geological Survey.
- McGaughey, J., 2007, Geological models, rock properties, and the 3D inversion of geophysical data, *in* Milkereit, B., ed., Proceedings of Exploration 07: Fifth Decennial International Conference on Mineral Exploration, p. 473-483.
- McNerney, P., Goldberg, A., Calcagno, P., Courrioux, G., Guillen, A., and Seikel, R., 2007, Improved 3D geology modelling using an implicit function interpolator and forward modelling of potential field data, *in* Milkereit, B., ed., Proceedings of Exploration 07: Fifth Decennial International Conference on Mineral Exploration, p. 919-922.

- Oldenburg, D. W., and Pratt, D. A., 2007, Geophysical inversion for mineral exploration: A decade of progress in theory and practice, *in* Milkereit, B., ed., Proceedings of Exploration 07: Fifth Decennial International Conference on Mineral Exploration, p. 61-95.
- Parsons, S., and McGaughey, J., 2007, Rock property database system, *in* Milkereit, B., ed., Proceedings of Exploration 07: Fifth Decennial International Conference on Mineral Exploration, p. 933-938.
- Rendu, J.-M., 1981, An introduction to geostatistical methods of mineral evaluation: Johannesburg, South African Institute of Mining and Metallurgy, 84 p.
- Sawaryn, S. J., and Thorogood, J. L., 2005, A compendium of directional calculations based on the minimum curvature method: SPE Drilling & Completion, paper 84246, p. 24-36.
- Shi, W., and Golam Kibria, B. M., 2007, On some confidence intervals for estimating the mean of a skewed population: International Journal of Mathematical Education in Science and Technology, v. 38, p. 412-421.
- Telford, W. M., Geldart, L. P., and Sheriff, R. E., 1990, Applied Geophysics: New York, Cambridge University Press, 770 p.
- UBC–GIF, 2005a, GRAV3D version 3.0: A program library for forward modelling and inversion of gravity data over 3D structures: Vancouver, The University of British Columbia–Geophysical Inversion Facility, p. 46.
- UBC–GIF, 2005b, MAG3D version 4.0: A program library for forward modelling and inversion of magnetic data over 3D structures: Vancouver, The University of British Columbia–Geophysical Inversion Facility, p. 41.
- Wang, F. K., 2001, Confidence interval for the mean of non-normal data: Quality and Reliability Engineering International, v. 17, p. 257-267.

Chapter 6: Mapping subsurface alteration using gravity and magnetic inversion models¹

6.1 INTRODUCTION

Inversion of potential field data can readily provide models of the distribution of physical properties in the subsurface, but rigorous geological interpretation of those property models is challenging. For mineral exploration, qualitative interpretations may be based on associations expected for mineralisation or alteration, such as the existence of “coincident magnetic and density anomalies”. However, there is merit in assessing prospectivity more rigorously. Cross-plots of measured densities and susceptibilities can be used to help classify rock types and general alteration trends (Henkel, 1976; Puranen, 1989; Henkel, 1994), and can provide some rapid insights into the rock characteristics and allow some broad classifications. However they only provide a graphical rather than a quantitative approach. Cluster analysis techniques provide a more quantitative method for classifying rock types and alteration trends, but do not allow for any direct inclusion of information about geological processes and characteristics.

Quantitative methods for estimating mineralogy from remotely acquired reflectance spectra have been in use for more than two decades (Smith et al., 1985). These spectral unmixing techniques assume that a pixel’s observed reflectance spectra are linearly related to the abundance of various end-member components within that pixel and use inversion to extract the component abundances from the observed band reflectances (Van der Meer and De Jong, 2000). Two of the most troublesome issues with spectral unmixing techniques are selecting the appropriate end-member components (Theseira et al., 2003) and correlation or similarity between end-member responses (Van der Meer and De Jong, 2000). Various strategies have been proposed to mitigate these problems.

The unmixing approach may be applied to other data types, such as the densities and magnetic susceptibilities that are among the most commonly used geophysical datasets in mineral exploration. When limited to only two data, density and susceptibility, instead of multiple spectral bands the number of end-member components that can be uniquely resolved

¹ A version of this chapter has been published. Williams, N.C., and Dipple, G.M., 2007, Mapping subsurface alteration using gravity and magnetic inversion models, *in* Milkereit, B., ed., *Proceedings of Exploration 07: Fifth Decennial International Conference on Mineral Exploration*, p. 461-472.

becomes severely limited. One mitigation strategy, known as partial unmixing, is to only extract the abundances of those end-member components that are most relevant for the questions being addressed (Boardman et al., 1995). All other components are lumped together as a single component containing everything else (Boardman et al., 1995); in our implementation to follow, this component will be the “host rock”. This method is particularly appropriate for densities and susceptibilities as most common rock-forming minerals have very similar densities and susceptibilities. Extremely high densities and susceptibilities are generally due to the sulphides and oxides that are of direct importance to mineral exploration. This association also provides us a better understanding of which end-member components need to be included in the unmixing calculation, thus eliminating the need for complex component selection algorithms.

For Fe-oxide Cu-Au (IOCG) systems, Hanneson (2003) assumed that the physical properties of any rock were controlled by the abundance and physical properties of three end-member components: magnetite, combined hematite and sulphides, and the host rock (a fictitious pure end-member that contains no magnetite, hematite, or sulphides). He could then solve a simple system of three weakly non-linear equations for the abundance of each of the three end-members:

$$\kappa_{mgt} f_{mgt}^{\phi} + \kappa_{hem} f_{hem} + \kappa_{host} f_{host} = \kappa_{sample} \quad 6.1$$

$$\rho_{mgt} f_{mgt} + \rho_{hem} f_{hem} + \rho_{host} f_{host} = \rho_{sample} \quad 6.2$$

$$f_{mgt} + f_{hem} + f_{host} = 1 \quad 6.3$$

where κ is susceptibility, ρ is density, and f is the volume fraction of the component (from 0 to 1), κ_{sample} is the susceptibility of the sample, ρ_{sample} is the density of the sample, and ϕ is an empirical exponent that has been variously estimated at between 1.0 and 1.39 depending on the value of κ_{mgt} , the grain size of magnetite in the sample, and the method used for estimating f_{mgt} (see compilation by Schön, 2004).

Williams et al. (2004) showed that this method can be applied directly to the 3D density and susceptibility models derived from constrained gravity and magnetic inversions to map, in 3D, regions of anomalous hematite or sulphide accumulations which may be prospective for exploration. The physical properties included in a constraining reference model supplied to the

gravity and magnetic inversions are used to derive the properties expected for barren host rock within each mappable rock unit. For each inversion cell, the density and susceptibility recovered by the inversions is used to estimate the abundance of each of the three end-member components by solving the system of three equations outlined above and in Figure 6.1. The results can then be displayed as 3D maps of magnetite, hematite and sulphide, or barren host rock abundance.

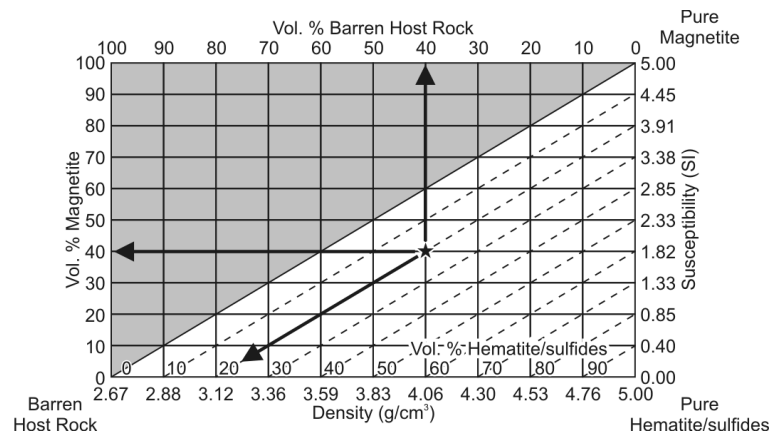


Figure 6.1. Graphical representation of equations 6.1-6.3 depicting how the density and susceptibility of a sample may be used to estimate the volume proportions of each of three end-members. Valid solutions are only possible in the white triangle. Modified from Hanneson (2003).

This method may provide an acceptable first pass estimate of sulphide abundance for many sulphide-rich deposit styles, but there are several deficiencies with this approach. One is that many more minerals contribute to the physical properties of the rocks than the three end-member system allows. Sericite alteration is common in volcanic hosted massive sulphide (VHMS) and IOCG systems and the ultramafic host rocks in many nickel sulphide deposits are strongly serpentinised. These low density phases complicate the systematics of the three-end-member mineralogy estimate by introducing a component that may have a lower density than the allowed host rock density. Such rocks have no possible solution in the three-end-member system (grey triangle in Figure 6.1). There also may be a range in the physical properties of each end-member mineral, or the properties of each mineral may be poorly known. The uncertainty associated with the physical properties recovered from inversions is also not taken into account.

To address these issues, a new method of estimating mineralogy from physical properties is developed here. The method follows the approach of Gordon and Dipple (1999) who applied linear programming techniques to estimate mineral abundances from whole rock chemistry compositions. Although not intended to replace direct observation, we first

demonstrate the applicability of our mineralogy unmixing method to different deposit styles, and test its accuracy, by applying it to actual measured densities and susceptibilities for drill core samples from the Perseverance komatiite-hosted nickel sulphide deposit in Western Australia's Archean Yilgarn Craton. We then apply the technique to the results of regional-scale geologically-constrained inversions (originally developed by Williams et al., 2004) around the Olympic Dam IOCG deposit in South Australia's Proterozoic Gawler Craton to assess the method's use in targeting and ranking prospective targets for exploration at depth and under cover.

6.2 METHOD

If the volume fraction of magnetite in a sample is less than about 0.1 (or 10 volume %), the empirical exponent ϕ in equation 6.1 contributes little and the system is approximately linear (Clark, 1997). Even for samples with > 0.1 volume fraction magnetite, a linear approximation only overestimates the abundance of magnetite slightly. For this reason, and the complexity and instability of nonlinear implementations (using quadratic programming methods), the linear approximation is deemed adequate. The general linear approximation of the system for n end-member components is:

$$\sum_{i=1}^n \kappa_i f_i = \kappa_{sample} \quad 6.4$$

$$\sum_{i=1}^n \rho_i f_i = \rho_{sample} \quad 6.5$$

$$\sum_{i=1}^n f_i = 1 \quad 6.6$$

where κ_i and ρ_i are the susceptibility and density of mineral or component i , f_i is the volume fraction of mineral or component i , and κ_{sample} and ρ_{sample} are the sample susceptibility and density. Thus when $n > 3$ the system is underdetermined and an exact solution for f cannot be obtained. In such underdetermined problems optimisation techniques can be applied to seek preferred solutions. Our use of linear programming is based on that presented by Gordon and Dipple (1999).

6.3 LINEAR PROGRAMMING

Linear programming is an optimisation method that seeks a solution that minimises some linear objective function subject to a finite number of linear inequality constraint equations. The inequality equations define an n -dimensional convex feasible region, or polytope, the vertices of which provide the set of possible solutions for the optimisation problem. The vertex that minimises the objective function is the optimal solution. For linear programming the standard form of equations is:

$$\min_{\mathbf{x}} F(\mathbf{x}) \text{ such that } \begin{cases} \mathbf{Ax} \leq \mathbf{b} \\ \mathbf{lb} \leq \mathbf{x} \leq \mathbf{ub} \end{cases} \quad 6.7$$

where $F(\mathbf{x})$ is an objective function of the unknowns, \mathbf{x} , of the form:

$$F(\mathbf{x}) = \mathbf{c}^T \mathbf{x} = c_1 x_1 + c_2 x_2 + \dots + c_n x_n \quad 6.8$$

\mathbf{A} is a matrix of coefficients to a set of inequality equations, \mathbf{b} represents limiting values, \mathbf{lb} and \mathbf{ub} are vectors of the lower and upper bounds on possible values of \mathbf{x} , and \mathbf{c} is a vector of coefficients defining the objective function.

Many linear programming algorithms are freely or commercially available. Throughout this work we use the CDD linear programming algorithm developed by Fukuda and Prodon (1996) after Motzkin et al. (1953) and interfaced to the Matlab software package (Mathworks Inc., Natick, Massachusetts) as CDDMEX by Torrisi and Baotic (2005). Tests mapping the possible solution space using this implementation provided consistent and stable results everywhere.

6.3.1 Inequality constraint equations

To be included in the linear programming routine, the equality equations 6.4-6.6 must be transformed into the form $\mathbf{Ax} \leq \mathbf{b}$ used in the linear programming equation 6.7. The equality equations are equivalent to the inequality equations:

$$\sum_{i=1}^n \kappa_i f_i \geq \kappa_{sample} \quad \text{and} \quad \sum_{i=1}^n \kappa_i f_i \leq \kappa_{sample} \quad 6.9$$

$$\sum_{i=1}^n \rho_i f_i \geq \rho_{sample} \quad \text{and} \quad \sum_{i=1}^n \rho_i f_i \leq \rho_{sample} \quad 6.10$$

$$\sum_{i=1}^n f_i \geq 1 \text{ and } \sum_{i=1}^n f_i \leq 1 \quad 6.11$$

From equations 6.9-6.11 and using the procedure for including uncertainties of Gordon and Dipple (1999), we derive the six inequality equations:

$$-\sum_{i=1}^n \kappa_i^{\max} \cdot f_i \leq -\kappa_{\text{sample}}^{\min} \text{ and } \sum_{i=1}^n \kappa_i^{\min} \cdot f_i \leq \kappa_{\text{sample}}^{\max} \quad 6.12$$

$$-\sum_{i=1}^n \rho_i^{\max} \cdot f_i \leq -\rho_{\text{sample}}^{\min} \text{ and } \sum_{i=1}^n \rho_i^{\min} \cdot f_i \leq \rho_{\text{sample}}^{\max} \quad 6.13$$

$$-\sum_{i=1}^n f_i \leq -(1 - \Delta v) \text{ and } \sum_{i=1}^n f_i \leq (1 + \Delta v) \quad 6.14$$

These are the fundamental equations used to calculate the mineral abundances and can readily be written in the $\mathbf{Ax} \leq \mathbf{b}$ form required for linear programming algorithms, with \mathbf{x} being a vector of the unknown component abundances f_i . The minimum and maximum susceptibility for each mineral or component are κ_i^{\min} and κ_i^{\max} , and the minimum and maximum densities are ρ_i^{\min} and ρ_i^{\max} . The minimum and maximum sample densities and susceptibilities of the form $\rho_{\text{sample}}^{\min}$ and $\rho_{\text{sample}}^{\max}$ reflect the range of observed values for a sample; typically these may be defined in terms of ± 2 standard deviations of measurements. The uncertainty defined by Δv allows the volume sum to vary within an appropriate number of significant figures; we set it to 0.001 or 0.1 vol. %.

Since the problem is underdetermined, the solution space may be infinitely large, and extra constraints may help refine the solution. The types of constraints available will vary depending on the deposit style and end-member components used, but will typically be based on limitations imposed by an understanding of the petrography and expected relationships between the minerals that might arise given a particular alteration or mineralisation style; this can come directly from ore deposit models. To be included in the calculation the constraints must be of the form $\mathbf{Ax} \leq \mathbf{b}$ and will generally be based on observations of the form: “alteration minerals are more abundant than ore minerals,” or “mineral A is always more common than mineral B,” or “the abundance of mineral A is proportional to the abundance of mineral B.” Specific examples will be given with the examples below.

In most linear programming implementations the lower and upper bounds on x are supplied to the linear programming algorithm as two vectors. The algorithms then transform the bounds vectors into additional inequality constraints of the form:

$$-x_i \leq -lb_i \text{ and } x_i \leq ub_i \quad 6.15$$

6.3.2 Model objective function

Every vertex of the polytope defined by the inequality constraint equations outlined above is a valid solution to the optimisation problem. The optimal solution returned by the linear programming algorithm is defined by the vertex that minimises the supplied objective function $F(\mathbf{x})$, so selection of an appropriate objective function is critical in recovering useful mineral estimates.

Due to the underdetermined nature of the mineral estimation problem for more than 3 components, an exact solution cannot be obtained. It is therefore unreasonable to expect the linear programming routine to provide a single ideal solution. Instead it is useful to define two objective functions that define the likely range of possibilities for a particular problem. For mineral exploration, an appropriate pair of objective functions would seek to minimise and maximise the abundance of ore sulphides thus providing an estimate of the range of ore sulphide abundances. Another pair of objective functions might seek to minimise and maximise the abundance of a particular alteration phase.

By only seeking the possible range of mineral abundances, rather than an exact solution, many more end-member components can be included in the unmixing calculation than the three equations allow; however, as the number of components increases and the problem becomes more underdetermined, the extracted range of mineral abundances will widen, possibly reducing the effectiveness of the estimate. Therefore it remains important to select only those end-member components that are most likely to control the physical properties of the rocks; this decision is best based on a geological understanding of the rocks. The abundance of minor phases not included in the calculation will add some small error to the calculated ranges of mineral abundances.

Standard linear programming algorithms minimise an objective function of the form shown in equation 6.8. Maximising the value of an unknown component abundance, x_i , is equivalent to minimising the value of $-x_i$. The coefficients, c_i , in the objective function

equation 6.8 are therefore +1 or –1 depending on whether that component should be minimised or maximised respectively.

6.4 APPLICATION TO DRILL CORE SAMPLES

To demonstrate how the mineral estimates are obtained, and their accuracy, we first apply the method to a set of 144 drill core and surface samples from the Leinster komatiite-hosted nickel sulphide deposits. The Leinster group includes the Perseverance, Rocky's Reward, and Harmony deposits which contain massive nickel sulphide basal horizons, disseminated intercumulus nickel sulphides, and tectonically remobilised sulphides, with a total underground resource of 33 Mt at 2.3 wt. % Ni and an open pit resource of 155 Mt at 0.6 % Ni (BHP Billiton Ltd., 2006). The sulphides are generally hosted within variously serpentinised Archean ultramafic cumulate and flow rocks within a regionally extensive greenstone belt that also includes basaltic and gabbroic rocks, felsic porphyry, volcanic and volcanoclastic rocks, and sedimentary rocks that have all been metamorphosed up to amphibolite grade (Gole et al., 1989; Libby et al., 1998). The greenstone belt is bounded by regional-scale fault systems which juxtapose the greenstones against several suites of voluminous granitoid rocks. The samples represent all major rock types in the area and all styles of nickel sulphide mineralisation, from weakly disseminated sulphides and sulphide stringers in ultramafic rocks to massive sulphides. Although detailed petrographic analysis of all the samples has not yet been completed, each sample has been visually classified in terms of its host rock, alteration styles, and sulphide abundance and style.

To measure densities, the samples were dried for two days at 110 °C, weighed, soaked in water for two days, weighed, and then weighed suspended in water. The susceptibility of each sample is the geometric mean of the susceptibilities of three 22 mm × 22 mm × 22 mm cubes that were analyzed on either a Digico susceptibility bridge (for lower susceptibilities) or an AGICO KLY-3 kappabridge (for higher susceptibilities). Measured densities and susceptibilities for each sample were compared to the observed sample mineralogy to ensure that the measurements showed appropriate magnitudes.

6.4.1 Components, their properties and bounds

The densities and susceptibilities are plotted in Figure 6.2 with the seven components that are most likely to control the physical properties in such rocks: magnetite, serpentine,

monoclinic and hexagonal pyrrhotite, pyrite, the nickel ore pentlandite, and barren host rock. It is noted that many other minerals with extreme physical properties may be present in small amounts, including chalcopyrite, ilmenite, chromite, and millerite, but their total abundance is generally < 2 vol. % and their exclusion will only add an equivalently small error to the result. In fact, many of these components will effectively be included in the estimates of other mineral components with similar properties: ilmenite and chromite will likely be included in the pyrite estimate; chalcopyrite will be partially included in the pentlandite estimate.

The extents of the boxes in Figure 2 indicate the range of expected properties for each component. The minerals' properties are based on published literature values (Table 6.1). The density range allowed for the barren host rock component spans the range of densities observed for least-altered lithologies in the area regardless of rock type; the susceptibility range for the barren host rock component extends to 7×10^{-3} SI, the typical upper limit of rocks lacking ferrimagnetic minerals (Clark, 1997).

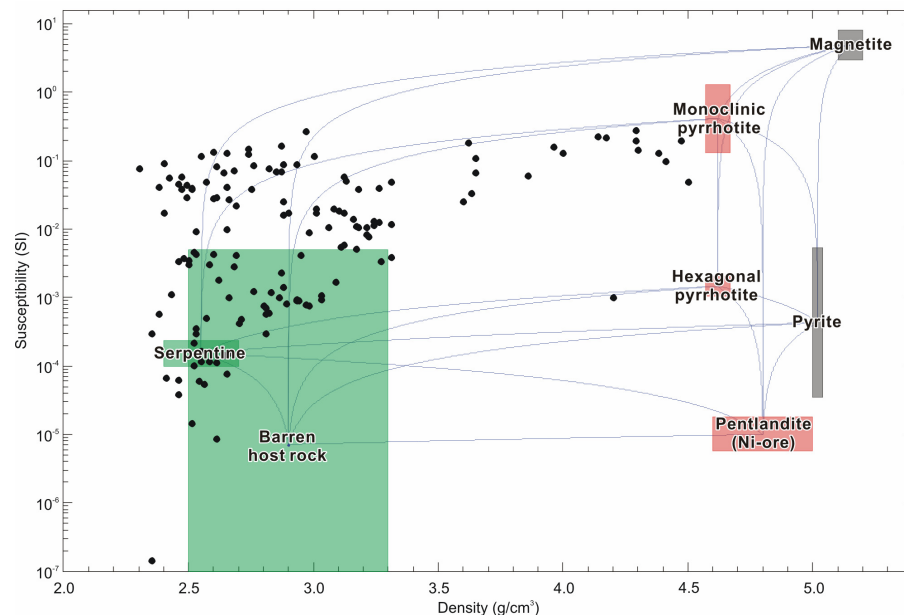


Figure 6.2. Densities and magnetic susceptibilities of the 144 drill core samples in this study (black circles), and seven controlling components. Blue lines represent linear mixing lines between the geometric mean properties of each of the components – they appear curved because of the logarithmic susceptibility scale.

Our goal for these samples is to estimate the possible range of sulphide abundance in each sample and compare the estimates to visual estimates of sulphide abundance to assess the effectiveness of the mineral estimates at classifying sulphidic rocks as anomalous. Once the relevant components expected in the samples have been identified (above; Table 6.1), the next

step is to identify the expected minimum and maximum abundance of each in the dataset. In general these may be 0.0 and 1.0 respectively (0 to 100 vol. %), but in many situations more restrictive ranges may be expected as shown for Leinster in Table 6.2. These values reflect many of the more extreme rocks that might exist; most rocks are unlikely to contain 100 vol. % serpentine or hexagonal or monoclinic pyrrhotite, so these upper and lower bounds are relatively loose.

Table 6.1. Summary of the physical properties of the components that will control the physical properties of rocks associated with komatiite-hosted nickel sulphide deposits. Where conflicting ranges are reported in the literature, a representative range is used.

Mineral	Minimum density (g/cm ³)	Maximum density (g/cm ³)	Minimum susceptibility (SI)	Maximum susceptibility (SI)	References
Barren host rock (allows for all likely host rock types)	2.5	3.3	1.00×10^{-8}	7.00×10^{-3}	Densities based on physical property measurements in this study; susceptibilities based on diamagnetic and paramagnetic minerals (Clark, 1997)
Serpentine	2.40	2.70	9.88×10^{-5}	2.38×10^{-4}	Chesterman and Lowe (1979), Bleil and Petersen (1982), Wohlenberg (1982)
Pyrite	5.00	5.04	3.50×10^{-5}	5.27×10^{-4}	Carmichael (1982), Hunt et al. (1995)
Pentlandite	4.60	5.00	5.62×10^{-6}	1.78×10^{-5}	Wohlenberg (1982), Emerson et al. (1999)
Hexagonal pyrrhotite (Fe ₉ S ₁₀)	4.57	4.67	1.05×10^{-3}	2.01×10^{-3}	Hunt et al. (1995), Emerson et al. (1999)
Monoclinic pyrrhotite (Fe ₇ S ₈)	4.57	4.67	0.13	1.30	Hunt et al. (1995), Clark (1997)
Magnetite	5.10	5.20	3	8	Telford et al. (1990), Clark (1997)
Term in equations 6.12 and 6.13	ρ_i^{\min}	ρ_i^{\max}	κ_i^{\min}	κ_i^{\max}	

Table 6.2. Expected minimum and maximum abundances of each mineral for rocks from the Leinster area.

Mineral	Abbreviation	Minimum abundance (vol. fraction)	Maximum abundance (vol. fraction)
Serpentine	serp	0.0	1.0
Pyrite	py	0.0	0.15
Pentlandite	pen	0.0	0.3
Hexagonal pyrrhotite	poH	0.0	1.0
Monoclinic pyrrhotite	poM	0.0	1.0
Magnetite	mgt	0.0	0.1

6.4.2 Objective functions

We then define the two objective functions that will be used to extract the range of feasible solutions. For nickel exploration we are most interested in the abundance of the nickel ore pentlandite, so we will select one objective function to extract the mineralogy containing the maximum possible abundance of pentlandite (all $c_i = +1$ are minimised, except $c_{pen} = -1$ is maximised):

$$F_1(\mathbf{x}) = \mathbf{c}^T \mathbf{x} = x_{mgt} - x_{pen} + x_{poH} + x_{poM} + x_{py} + x_{serp} + x_{host} \quad 6.16$$

The second objective function will reproduce a barren host rock with as few sulphides as possible by maximising the volume fraction of barren host rock present in each sample:

$$F_2(\mathbf{x}) = \mathbf{c}^T \mathbf{x} = x_{mgt} + x_{pen} + x_{poH} + x_{poM} + x_{py} + x_{serp} - x_{host} \quad 6.17$$

6.4.3 Additional constraint equations

Several additional constraints are available that can be included in the formulation. For this example the information comes from knowledge of the typical sulphide mineral assemblage and the serpentinisation reaction observed in the ultramafic rocks. Previous workers have reported typical pyrrhotite to pentlandite ratios of 3:1 (Martin and Allchurch, 1975), 7.5:1 (Emerson et al., 1999) and 11.5:1 (Duuring et al., 2007) for the Leinster nickel deposits. To encapsulate this range of variability in reported ratios we define a range of pyrrhotite to pentlandite ratios from 1:1 to 15:1 with the following two constraint equations

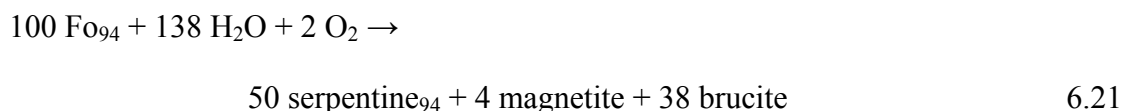
$$x_{pen} \leq x_{poH} + x_{poM} \quad 6.18$$

$$15x_{pen} \geq x_{poH} + x_{poM} \quad 6.19$$

which can in turn be included with equations 6.12-6.14 as two extra rows in the linear programming equation 6.7.

Most of the rocks that host mineralisation are ultramafic rocks that have undergone varying degrees of serpentinisation whereby primary igneous olivine is replaced by serpentine and magnetite in the presence of fluids. Barnes et al. (1988) report that primary igneous olivine at Leinster has an average composition of Fo₉₄ (Mg-number = $100 \times \text{MgO}/[\text{MgO} + \text{FeO}] = 94$). Such Mg-rich olivine is likely to hydrate to Mg-rich serpentine plus minor magnetite. Without electron microprobe analyses of the serpentine at Leinster, two possible balanced

serpentinisation reactions that provide a minimum and maximum amount of magnetite produced might be:



where Fo_{94} represents the primary igneous olivine, serpentine_{100} and serpentine_{94} represent serpentine with Mg-numbers of 100 and 94 respectively. Brucite $[\text{Mg}(\text{OH})_2]$ is a common alteration by-product of serpentinisation but has a similar density to serpentine (Wohlenberg, 1982) so for the mineral estimation calculations it is treated as part of the serpentine component. For each of these two equations the molar ratio of [(serpentine + brucite) / magnetite] can be converted to a mass ratio and then a volume ratio of [(serpentine + brucite) / magnetite] to define an approximate range of such ratios that is possible. Assuming that the alteration system is closed (no net mass or elemental loss), and that the compositions specified in reactions 6.20 and 6.21 represent the full compositional range of the minerals, then this calculation provides a range of serpentine to magnetite volume ratios that can be expressed as:

$$35x_{mgt} \leq x_{serp} \quad 6.22$$

$$150x_{mgt} \geq x_{serp} \quad 6.23$$

again, assuming that all brucite is included in the serpentine component. These two equations can also be added as additional rows with equations 6.12-6.14 in the linear programming equation 6.7.

In the mineral estimation calculation we provide no information regarding rock type or whether serpentinisation is present. Instead, by providing these constraints we are assuming that magnetite is only significant (>1 vol. %) in those samples where serpentinisation of ultramafic rocks has taken place. Where no serpentinisation has taken place but minor magnetite is present, such as in a granitic sample, this assumption fails and the calculation may give rise to an erroneous proportion of serpentine which, due to its low density, may allow an erroneous estimate of sulphide content resulting in a false positive anomaly. However, nearly

all of the sulphides are hosted in serpentinised ultramafic rocks, and this constraint is critical in correctly identifying sulphides in these samples.

6.4.4 Results

The equations, objective functions, and the 144 rock samples' property measurements are supplied directly to the linear programming routine as matrices. The results are presented in Figure 6.3. Each vertical bar represents one of the 144 individual rock samples. The bars are coloured by their actual sulphide content, either barren, trace disseminated sulphides, moderate disseminated sulphides, heavy disseminated sulphides, and massive sulphides. The tops and bottoms of each bar represent the solutions extracted using each of the two objective functions. The calculation clearly identifies the massive sulphide samples as having the most pentlandite, up to the upper bound of 0.3 vol. fraction, with correspondingly minimal silicate content, down to 0 vol. fraction. As the predicted sulphide content goes up, the predicted silicate content goes down.

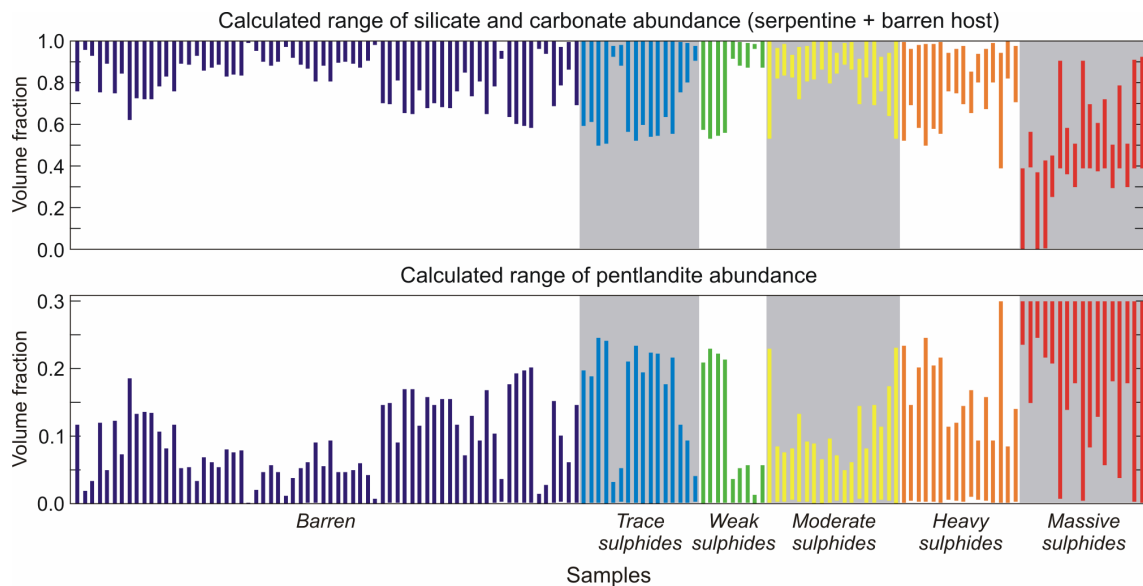


Figure 6.3. Results of the mineral estimate calculation on drill core samples from Leinster. Each vertical bar represents an individual sample and is coloured and grouped by its actual sulphide content. The tops and bottoms show the results obtained with each of the two objective functions thus defining the range of possibilities. As the actual sulphide content increases, the minimum abundance (bar bottoms) of pentlandite abundance tends to increase, and the maximum abundance (bar tops) of silicate and carbonate abundance tends to decrease.

There is significant variability in the heights of the bars in Figure 6.3, but there is much less variability in the position of the bottoms of the bars, or minimum abundances. These minimum abundances indicate what must be required to satisfy the imposed constraints, and can be used as an effective conservative estimate of mineral abundance. Our goal in this

assessment is to correctly identify ore sulphide-bearing samples based on their physical properties. The samples most likely to contain pentlandite would be those where the minimum predicted abundance of pentlandite is >0.001 volume fraction (the Δv threshold for significant figures defined above). Those most likely to contain ore sulphides (pyrrhotite + pentlandite) would have >0.001 volume fraction pyrrhotite + pentlandite. These criteria are shown in Figure 6.4 where in each panel the samples have been sorted in order of increasing minimum ore sulphide content (top) or increasing minimum pentlandite content (bottom), with the 0.001 volume fraction cut-off identify by dashed line. The samples are coloured as in Figure 6.3, only their order has been changed. Immediately one can see that the barren and trace sulphides (blues) plot to the left, whereas the samples with higher actual sulphide contents plot to the right.

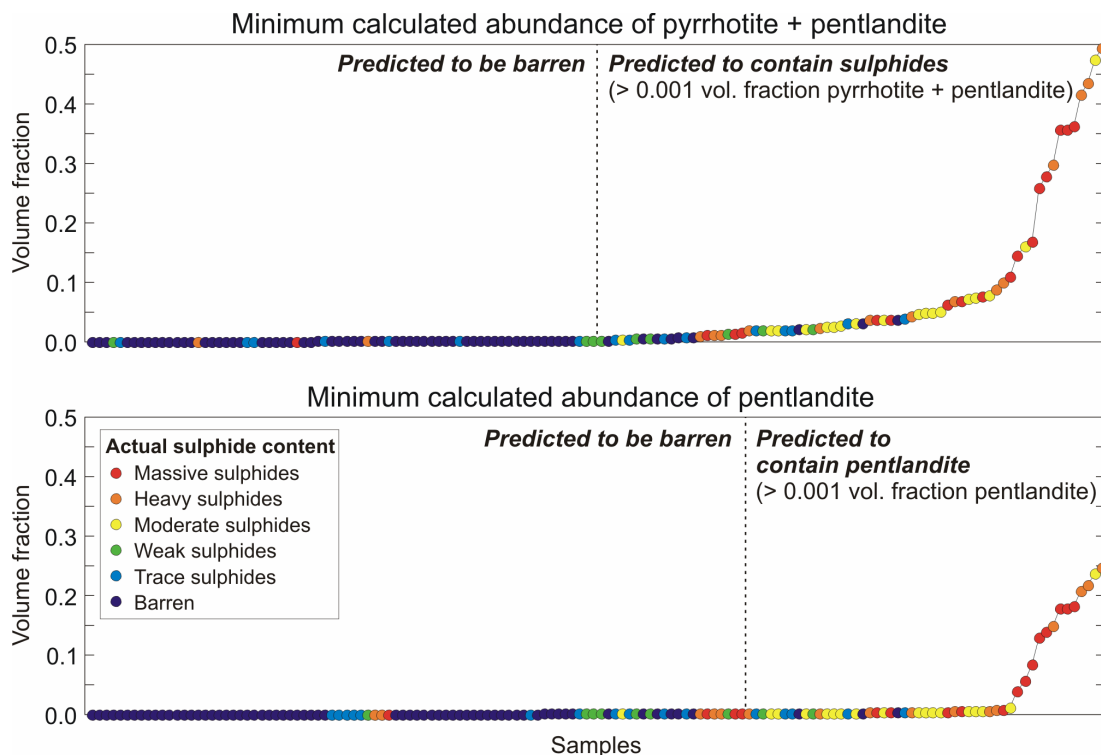


Figure 6.4. An alternate representation of the results from Figure 6.3. Here only the minimum abundances (bar bottoms) are shown (circles) coloured by actual sulphide content. The bars are sorted in order of increasing minimum predicted abundance of pyrrhotite and pentlandite (top) or pentlandite alone (bottom). Where the respective predicted abundances exceed 0.001 volume fraction (depicted by dashed lines), the samples can be flagged as anomalous and worthy of follow-up. Either criteria can be used; for Figure 6.5 we use the pyrrhotite + pentlandite criteria to identify sulphide-bearing samples.

Using these criteria we can test the accuracy of the mineral estimate prediction for barren and sulphide-bearing samples (Figure 6.5). A more conservative estimate would focus only on those samples that must contain pentlandite (Figure 6.4, bottom), however this will

miss many of the pyrrhotite-rich samples that surround and are associated with ore. More than 85 % of barren samples are correctly predicted to be barren, and 81 % of sulphide-bearing samples are correctly predicted to contain sulphides. The success rate increases as the actual sulphide content increases. Using >0.001 volume fraction pentlandite would reduce the number of false positives but increase the number of sulphide-bearing samples that are misidentified as barren.

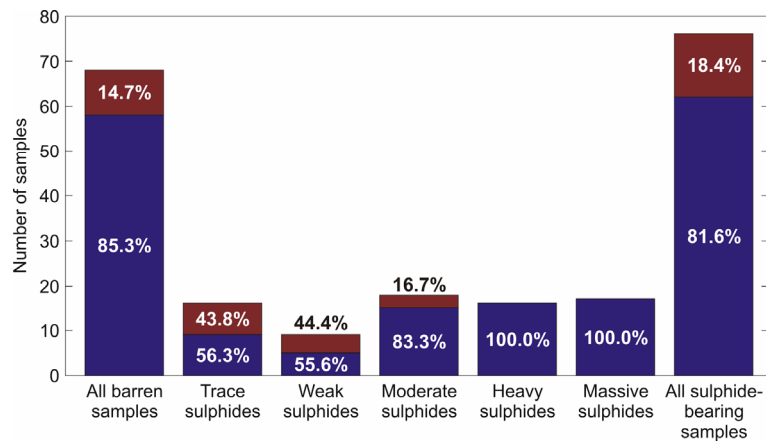


Figure 6.5. Graph showing the accuracy of the mineral predictions when using a cut-off of 0.001 volume fraction pyrrhotite and pentlandite (top of Figure 6.4). Each bar represents the listed group of samples based on visual estimates of sulphide content. Blue segments indicate the proportion of successful predictions for that group. Brown segments show where the predictions were incorrect, i.e., sulphide-bearing samples that were predicted to be barren (false negative) or barren samples predicted to contain sulphides (false positive).

6.4.5 Summary

The high success rate for identifying sulphide-bearing samples based only on knowledge of densities and susceptibilities is very encouraging. Using a cut-off criterion based on the minimum abundance of ore sulphides results in minimal false positives, where barren rocks are incorrectly identified as sulphide-bearing, yet has a high success rate at identifying actual sulphide-bearing rocks.

6.5 APPLICATION TO 3D INVERSION MODELS

In practice the mineral estimates are better suited to situations where visual inspection of the rocks is impossible. One such situation might be where wireline down hole logs of density (or gamma-gamma density) and susceptibility have been recorded but core has been lost, has deteriorated, or is inaccessible. A more general application of the mineral estimates applies to densities and susceptibilities derived for the subsurface using geophysical modelling and inversion techniques.

Gravity and magnetic inversions are becoming standard practice in many mineral exploration programs and are one of the few ways in which 3D information can be inferred from buried rocks. Interpreting the 3D density and magnetic susceptibility models derived using inversions is challenging due to the number of factors that can influence the physical properties of a particular rock or rock type. Measurements of physical properties on samples can supply some information on the physical properties expected for particular rocks and alteration or mineralisation styles. However, in ancient or complex hydrothermal and metamorphic terrains such measurements may not be representative of all possible geological processes in the region, and the rocks may be deeply buried preventing direct access and measurement anyway. In such scenarios, an estimate of mineralogy derived from inferred physical properties, a general understanding of the processes the rocks may have been exposed to, and knowledge of ore deposit models may provide a useful targeting tool for focusing future exploration efforts.

6.5.1 Olympic Dam

Here we present an example of how the mineral estimation can be applied to the results of regional-scale gravity and magnetic inversions over the Olympic Cu-Au province north of Adelaide along the eastern margin of the Gawler Craton in South Australia. Despite negligible Proterozoic outcrop, and thick Proterozoic to Cambrian basinal cover sequences, it is highly prospective for Proterozoic Cu-Au mineralisation. It hosts the giant Olympic Dam iron oxide Cu-Au-U-Ag-REE (IOCG) deposit which contains total resources of 4430 Mt at 1.1 % Cu, 0.4 kg/t U₃O₈, 0.5 g/t Au, and 2.2 g/t Ag (BHP Billiton Ltd., 2006), as well as two significant new IOCG discoveries in the last decade at Prominent Hill (Belperio and Freeman, 2004) and Carrapateena (Fairclough, 2005), northwest and south, respectively, of this study's area of interest. Olympic Dam consists of a large (>3 km diameter) accumulation of hematite-chalcopyrite-bornite-magnetite mineralisation hosted by a 7 km × 5 km areal extent breccia complex within a granitic batholith, below a minimum of 260 m of younger transported cover rocks (Reeve et al., 1990; Skirrow et al., 2002). The batholith is one of several large Paleoproterozoic to Mesoproterozoic granitoid suites in the Olympic province, which also includes a core of Archean granulite facies rocks underlying various metamorphosed volcanic and sedimentary sequences intruded by or associated with the granitoid suites (Daly et al., 1998).

Gravity and magnetic inversions were prepared by Williams et al. (2004) using the UBC–GIF inversions software GRAV3D and MAG3D (Li and Oldenburg, 1996, 1998) and publicly available regional gravity and magnetic data (Geophysical Archive Data Delivery System: <http://www.geoscience.gov.au/gadds/>). These inversions covered a region of 150 km × 150 km to a depth of 10 km centered on the Olympic Dam deposit, and used 1 km × 1 km and 0.5 km tall cells (0.5 km³) throughout. As described by Williams et al. (2004), a basic reference model of expected geology, based on the basement geology interpretation by Direen and Lyons (2002), was used to constrain the inversions and physical properties were defined for each of the 10 rock units in the model based on physical property measurements on drill core samples (N. Direen, unpub. data, 2002).

The goal of our present study is to assess whether mineralogical maps can be derived from density and magnetic susceptibility models recovered by the inversions and whether such maps might add value to the recovered inversion results. Our study was not seeking to identify candidate exploration targets and no ground validation of the results has been conducted except by correlation with the locations of known copper deposits and prospects. The work presented here should be considered a proof of concept rather than a formal exploration outcome for the Olympic Cu-Au province.

6.5.2 Estimating mineral abundances from inversion models

Component properties

Mineralogy estimates can be obtained from density and magnetic inversion models using a similar approach to that described above for drill core samples. For IOCG systems the dominant minerals controlling the physical properties of the rocks will be magnetite, hematite, chalcopyrite, pyrite, and the low density alteration phase sericite, plus the barren host rock component that contains all other silicate and carbonate minerals. The properties of these minerals are outlined in Table 6.3. Although generally a mixture of white micas with densities of 2.7–3.0 g/cm³ (Chesterman and Lowe, 1979), intensely sericitised rocks are likely to have lower densities due to increased porosity as a result of mass loss to the acidic fluids responsible for the sericitisation. Table 6.3 therefore shows our estimated properties for intensely sericitised rocks in this region.

Table 6.3. Summary of the physical properties of common minerals associated with iron oxide copper gold (IOCG) deposits. Where conflicting ranges are reported in the literature, a representative range is used.

Mineral	Minimum density (g/cm ³)	Maximum density (g/cm ³)	Minimum susceptibility (SI)	Maximum susceptibility (SI)	References
Sericite	2.10	2.30	1×10^{-5}	1×10^{-3}	Estimated (see text below)
Pyrite	5.00	5.04	3.50×10^{-5}	5.27×10^{-4}	Carmichael (1982), Hunt et al. (1995)
Chalcopyrite	4.18	4.22	2.30×10^{-5}	4.02×10^{-4}	Hunt et al. (1995)
Hematite	5.24	5.30	1.00×10^{-4}	4.02×10^{-2}	Carmichael (1982), Hunt et al. (1995)
Magnetite	5.10	5.20	3	8	Telford et al. (1990), Clark (1997)

For an unaltered or minimally altered rock the primary control on the rock's physical properties is its lithology. In a geologically-constrained potential field inversion the user will have supplied a 3D model of expected physical properties for each cell to guide the inversion towards a solution that is consistent with the geology. This 3D reference model will be based on any existing knowledge of the geology of the area, including mapping, drilling, structural interpretation and conceptual models. The inversion will recover a physical property model that is as close as possible to the reference model while still reproducing the observed geophysical data. Due to the size of the model, the size of the cells, and the lack of detailed knowledge of the true geology within the model, the reference model will only represent coarse-scale geological features, >10-20 km across at the scale of this study, and is unlikely to represent more localised hydrothermal alteration and mineralisation. The densities defined in the reference model, $\bar{\rho}_{host}$, can therefore be used as an estimate of the barren host rock properties for each inversion cell. The range of susceptibilities is defined by the range of susceptibilities expected for rocks containing only silicate and carbonate minerals.

Uncertainties

When applied to drill core samples (above), uncertainties associated with the physical properties of minerals, barren host rock component, or samples could readily be defined in terms of measurement ranges or standard deviations. The inversion cells are orders of magnitude larger than the individual core samples that actual property measurements were made on so it is necessary to adjust the uncertainties to allow for the volume scaling of variance. A geostatistical analysis of a large physical property database would provide an

understanding of the magnitude of the reduction in variance for a particular suite of rocks, but such data is rarely available at the scale (up to 10s or 100s of kilometres) of inversion models.

The range of allowable host rock end-member densities, $\bar{\rho}_{host} \pm \Delta\rho_{host}$, will be reduced by bulk averaging of the rock and will converge towards the mean rock density, $\bar{\rho}_{host}$, with increasing cell volumes. The value of $\Delta\rho_{host}$ can therefore be reduced for large cell volumes. The uncertainty in the accuracy of the physical properties recovered by the inversion is more problematic. The reduction in variance associated with increasing rock volumes would be partially compensated for by an increase in the uncertainty associated with the physical properties recovered by inversion compared to direct measurement.

Objective functions

Two objective functions are defined to extract a possible range of mineral abundances with one extreme represented by the maximum possible abundance of the copper ore chalcopyrite:

$$F_1(\mathbf{x}) = \mathbf{c}^T \mathbf{x} = x_{mgt} + x_{hem} - x_{cpy} + x_{py} + x_{ser} + x_{host} \quad 6.24$$

and the other represented by the maximum abundance of the barren host rock component

$$F_2(\mathbf{x}) = \mathbf{c}^T \mathbf{x} = x_{mgt} + x_{hem} + x_{cpy} + x_{py} + x_{ser} - x_{host} \quad 6.25$$

Additional constraints

Since no information is available regarding the absolute maximum and minimum abundances of each of the six components within 0.5 km³ cells, default lower and upper bounds of 0 and 1, respectively, are used for each component. One additional constraint is included based on the premise that alteration is more common than mineralisation. In particular it is expected that the amount of chalcopyrite will always be less than the amount of hematite in any sample (Reeve et al., 1990), so we apply a constraint of the form

$$x_{cpy} \leq x_{hem} \quad 6.26$$

Results

In general the method is unable to clearly differentiate between chalcopyrite-, pyrite-, and hematite-bearing rocks at the scale of 0.5 km³ inversion model cells. This might be

expected based on the IOCG ore deposit model and the constraint imposed by equation 6.26, but is also an artefact of the scale of observation and minimising the objective functions. The calculation is more likely to include hematite to explain a dense cell as the volume of the higher density hematite required to explain the high density cell is lower than the volume of the lower density chalcopyrite and pyrite required. Since IOCG ore bodies commonly contain all three minerals we usually display images of hematite + sulphide abundance which will effectively identify the more volumetrically extensive hematite alteration zones that might contain and enclose IOCG mineralisation. Despite the lack of resolution of the individual minerals in this example, the result is more accurate than including a combined hematite-pyrite-chalcopyrite end-member that would have extremely broad uncertainty in its expected physical properties of 4.18-5.3 g/cm³ and 2.30×10^{-5} to 4.02×10^{-2} SI (from Table 6.3).

The maps in Figure 6.6 show calculated abundances of magnetite, sericite, and hematite + sulphide at the inferred basement surface derived from drill hole intersections. Following the method used for drill core samples above where the minimum calculated abundances were used to provide an effective conservative estimate of sulphide content, we will focus on the minimum calculated hematite + sulphide abundances for the Olympic province inversions obtained when the abundance of barren host rock is maximised. This identifies areas where the supplied reference model of properties and therefore the available geological understanding, and the supplied constraints are insufficient to explain the gravity and magnetic anomalies, and so some hematite and sulphides are required.

In Figure 6.6, the largest and richest hematite and sulphide calculated anomaly exactly coincides with the Olympic Dam deposit, but the calculation also identified potential hematite and sulphide accumulations near several other copper prospects. Some prospects do not show evidence of hematite and sulphide accumulations in this calculation, but are associated with anomalous magnetite accumulations; these may represent low-grade copper targets, or prospects where copper zones lie below the inferred basement surface. There are also some areas that show potential for hematite and sulphides where no known copper has been identified during previous exploration; these may represent hematite-rich rocks with no copper sulphides, areas where the geological understanding is incorrect, or genuine prospective targets.

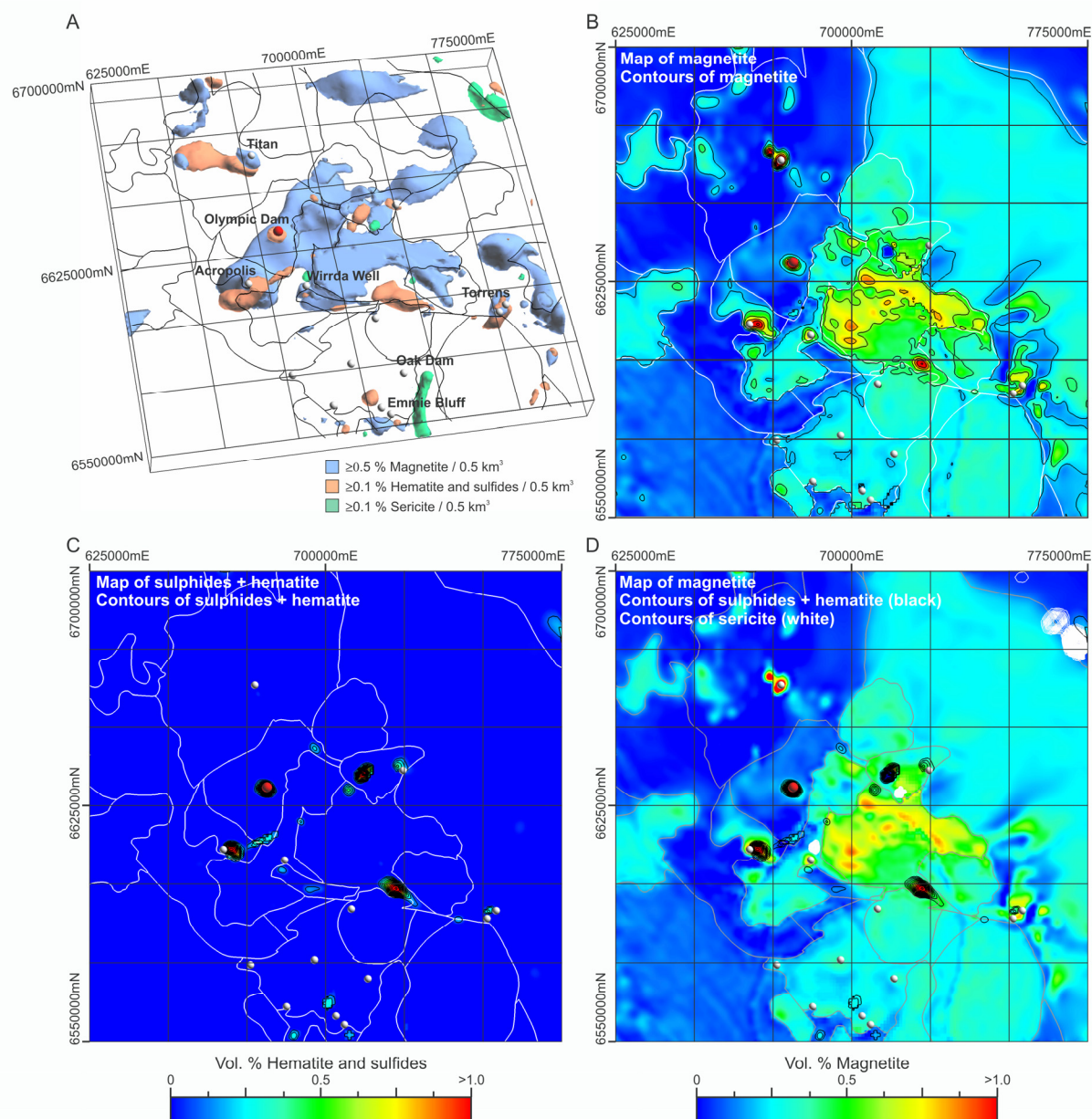


Figure 6.6. A. Perspective view of a 3D alteration map of the inversion volume. Brown surfaces enclose all cells with >0.1 vol. % hematite or sulphides; green surfaces enclose cells with >0.1 vol. % sericite; blue surfaces enclose cells with >0.5 vol. % magnetite. Black lines indicate unit boundaries used in reference model; red spheres indicate mines/deposits, small spheres indicate prospects/occurrences, with the main occurrences labelled. B. Calculated magnetite abundance on the basement surface with 0.2 % contours of magnetite shown in black, and unit boundaries shown in white. C. Calculated hematite + sulphide abundance on the basement surface with 0.1 % contours of hematite + sulphides shown in black and unit boundaries shown in white. D. Calculated magnetite abundance on the basement surface with 0.1 % contours of hematite + sulphides shown in black, 0.1 % contours of sericite shown in white, and unit boundaries shown in grey.

By converting the physical properties recovered by the inversion into a mineralogical model the results can be interpreted and prospective areas ranked with respect to the IOCG mineral system model. High quality targets will have larger, richer predicted accumulations of hematite and sulphides within or adjacent to magnetite accumulations (Bastrakov et al., 2002),

possibly with local sericite alteration. Lower quality targets might have small or less abundant hematite and sulphide zones or greater separation from adjacent magnetite accumulations.

6.6 CONCLUSIONS

Reliable estimates of mineral abundances can be extracted from physical property measurements by including an understanding of the minerals most likely to control the physical properties of the rocks, a small number of geological constraints, and allowing for measurement uncertainty. Maps of the extracted minimum abundances provide realistic first-pass estimates of the distribution of minerals at depth and under cover when applied to geologically-constrained gravity and magnetic inversion results. These results can help identify target areas for further data acquisition or sampling when interpreted with an understanding of likely ore deposit models. The accuracy of the maps depends on

- the quality and resolution of the gravity and magnetic data,
- the accuracy of the geologic reference model used to constrain the inversions,
- the resolution of the inversions,
- how representative the selected suite of minerals or components is,
- the accuracy of lower and upper bounds on mineral abundances,
- the accuracy of the mineralogical constraints used, and
- the level of uncertainty allowed in the calculation.

If improvements can be made at any of these stages, such as developing an improved geological understanding after drilling a hole, then those improvements should be included in an updated iteration of the mineral estimation process.

As these estimates are based on only two data they are underdetermined, and the extracted range of possible mineral abundances may be large. The best solution to this problem is to include additional data. An unlimited number of geophysical or geological datasets can be included in the calculation by adding equations similar to equations 6.9 and 6.10. These will make the calculation less underdetermined and enhance the resolution of each end-member component. Obvious candidate datasets include resistivity or conductivity, chargeability, and seismic velocities. Unfortunately many of these datasets may have nonlinear relationships to

mineral abundances, and depend on characteristics other than mineral abundances, such as the connectivity of conductive minerals. Such complexities may require the use of nonlinear, or quadratic, programming techniques.

6.7 REFERENCES

- Barnes, S.J., Hill, R.E.T., and Gole, M.J., 1988, The Perseverance ultramafic complex, Western Australia; the product of a komatiite lava river: *Journal of Petrology*, v. 29, p. 305-331.
- Bastrakov, E.N., Skirrow, R.G., and Barovich, K.M., 2002, Towards discriminating Cu-Au mineralised from barren hydrothermal systems using fluid chemistry: Gawler Craton 2002 - State of Play, Adelaide, 5-6 December, Department of Primary Industries and Resources South Australia, Exploration Data Package 10.
- Belperio, A., and Freeman, H., 2004, Common geological characteristics of Prominent Hill and Olympic Dam; implications for iron oxide copper-gold exploration models: *AusIMM Bulletin*, v. 6, p. 67-75.
- BHP Billiton Ltd., 2006, 2006 BHP Billiton Annual Report: Melbourne, BHP Billiton Ltd., 256 p.
- Bleil, U., and Petersen, N., 1982, Magnetic properties of natural minerals, *in* Angenheister, G., ed., *Physical properties of rocks*, Vol. 1b: Berlin, Springer-Verlag, p. 308-365.
- Boardman, J.W., Kruse, F.A., and Green, R.O., 1995, Mapping target signatures via partial unmixing of AVIRIS data: *Proceedings of the Fifth JPL Airborne Earth Science Workshop*, JPL Publication 95-1, v. 1, p. 23-26.
- Carmichael, R.S., 1982, Magnetic properties of minerals and rocks, *in* Carmichael, R.S., ed., *Handbook of physical properties of rocks*, Volume II: Boca Raton, Florida, CRC Press, p. 230-287.
- Chesterman, C.W., and Lowe, K.E., 1979, *The Audubon Society field guide to North American rocks and minerals*: New York, Alfred A. Knopf, 850 p.
- Clark, D.A., 1997, Magnetic petrophysics and magnetic petrology; aids to geological interpretation of magnetic surveys: *AGSO Journal of Australian Geology and Geophysics*, v. 17, p. 83-103.
- Daly, S.J., Fanning, C.M., and Fairclough, M.C., 1998, Tectonic evolution and exploration potential of the Gawler Craton, South Australia: *AGSO Journal of Australian Geology and Geophysics*, v. 17, p. 145-168.
- Direen, N., and Lyons, P., 2002, Geophysical interpretation of the Central Olympic Cu-Au province: 1:500,000 scale map sheet, Geoscience Australia.
- Duuring, P., Bleeker, W., and Beresford, S.W., 2007, Structural modification of the komatiite-associated Harmony nickel sulfide deposit, Leinster, Western Australia: *Economic Geology*, v. 102, p. 277-297.

- Emerson, D.W., Martin, K., and Williams, P.K., 1999, Electrical, magnetic and mass properties of the nickeliforous komatiite sequence near Leinster, Western Australia: *Preview*, v. 81, p. 13-22.
- Fairclough, M., 2005, Geological and metallogenic setting of the Carrapateena FeO-Cu-Au prospect; a PACE success story: *MESA Journal*, v. 38, p. 4-7.
- Fukuda, K., and Prodon, A., 1996, Double description method revisited, *in* Deza, M., Euler, R., and Manoussakis, I., eds., *Combinatorics and computer science*: Berlin, Springer, 1120, p. 91-111.
- Gole, M.J., Barnes, S.J., and Hill, R.E.T., 1989, The geology of the Agnew nickel deposit, Western Australia: *CIM Bulletin*, v. 82, p. 46-56.
- Gordon, T.M., and Dipple, G.M., 1999, Measuring mineral abundance in skarn; II, A new linear programming formulation and comparison with projection and Rietveld methods: *The Canadian Mineralogist*, v. 37, p. 17-26.
- Hanneson, J.E., 2003, On the use of magnetics and gravity to discriminate between gabbro and iron-rich ore-forming systems: *Exploration Geophysics*, v. 34, p. 110-113.
- Henkel, H., 1976, Studies of density and magnetic properties of rocks from northern Sweden: *Pure and Applied Geophysics*, v. 114, p. 235-249.
- Henkel, H., 1994, Standard diagrams of magnetic properties and density; a tool for understanding magnetic petrology: *Journal of Applied Geophysics*, v. 32, p. 43-53.
- Hunt, C.P., Moskowitz, B.M., and Banerjee, S.K., 1995, Magnetic properties of rocks and minerals: *AGU Reference Shelf*, v. 3, p. 189-204.
- Li, Y., and Oldenburg, D.W., 1996, 3-D inversion of magnetic data: *Geophysics*, v. 61, p. 394-408.
- Li, Y., and Oldenburg, D.W., 1998, 3-D inversion of gravity data: *Geophysics*, v. 63, p. 109-119.
- Libby, J.W., Stockman, P.R., Cervoj, K.M., Muir, M.R.K., Whittle, M., and Langworthy, P.J., 1998, Perseverance nickel deposit, *in* Berkman, D.A., and Mackenzie, D.H., eds., *Geology of Australian and Papua New Guinean mineral deposits*: Melbourne, Australasian Institute of Mining and Metallurgy, p. 321-328.
- Martin, J.E., and Allchurch, P.D., 1975, Perseverance nickel deposit, Agnew, *in* Knight, C.L., ed., *Economic geology of Australia and Papua New Guinea*, 1. Metals: Melbourne, Australasian Institute of Mining and Metallurgy, p. 149-155.
- Motzkin, T.S., Raiffa, H., Thompson, G.L., and Thrall, R.M., 1953, The double description method, *in* Kuhn, H.W., and Tucker, A.W., eds., *Contributions to theory of games*, Vol. 2: Princeton, Princeton University Press, p. 51-73.

- Puranen, R., 1989, Susceptibilities, iron and magnetite content of Precambrian rocks in Finland, Tutkimusraportti - Geologian Tutkimuskeskus = Report of Investigation - Geological Survey of Finland, 90, 51 p.
- Reeve, J.S., Cross, K.C., Smith, R.N., and Oreskes, N., 1990, Olympic Dam copper-uranium-gold-silver deposit, *in* Hughes, F.E., ed., *Geology of the mineral deposits of Australia and Papua New Guinea*, v. 2: Melbourne, The Australian Institute of Mining and Metallurgy, p. 1009-1035.
- Schön, J.H., 2004, *Physical properties of rocks: Fundamentals and principles of petrophysics*: Oxford, Elsevier, 583 p.
- Skirrow, R.G., Bastrakov, E., Davidson, G.J., Raymond, O.L., and Heithersay, P., 2002, The geological framework, distribution and controls of Fe-oxide Cu-Au mineralisation in the Gawler Craton, South Australia: Part II - Alteration and mineralisation, *in* Porter, T.M., ed., *Hydrothermal iron oxide copper-gold & related deposits: A global perspective*, volume 2: Adelaide, PGC Publishing, p. 33-47.
- Smith, M.O., Johnson, P.E., and Adams, J.B., 1985, Quantitative determination of mineral types and abundances from reflectance spectra using principal components analysis: *Proceedings of the Fifteenth Lunar and Planetary Science Conference, Part 2, Journal of Geophysical Research*, v. 90 (Supplement), p. C797-C804.
- Telford, W.M., Geldart, L.P., and Sheriff, R.E., 1990, *Applied Geophysics*: New York, Cambridge University Press, 770 p.
- Theseira, M.A., Thomas, G., Taylor, J.C., Gemmell, F., and Varjo, J., 2003, Sensitivity of mixture modelling to end-member selection: *International Journal of Remote Sensing*, v. 24, p. 1559-1575.
- Torrìsi, F., and Baotic, M., 2005, CDDMEX - Matlab interface for the CDD solver: <http://control.ee.ethz.ch/~hybrid/cdd.php>.
- Van der Meer, F., and De Jong, S.M., 2000, Improving the results of spectral unmixing of Landsat Thematic Mapper imagery by enhancing the orthogonality of end-members: *International Journal of Remote Sensing*, v. 21, p. 2781-2797.
- Williams, N.C., Lane, R., and Lyons, P., 2004, Towards 3D maps of alteration under cover: Regional constrained 3D inversion of potential field data from the Olympic Cu-Au province, South Australia: *Preview*, p. 30-33.
- Wohlenberg, J., 1982, Density of minerals, *in* Angenheister, G., ed., *Physical properties of rocks*, Vol. 1b: Berlin, Springer-Verlag, p. 66-113.

Chapter 7: Geologically-constrained gravity and magnetic inversions over the Agnew-Wiluna greenstone belt and Perseverance nickel deposit, Western Australia¹

7.1 INTRODUCTION

The Yilgarn Craton in Western Australia provides a typical example of the challenge facing mineral explorers in mature mineral provinces. Although exploration has been hugely successful in the Yilgarn Craton, and specifically the Eastern Goldfields, over the last 150 years, it is thought that a majority of the outcropping ore deposits have already been identified. However, more than 95 % of the Archean basement rocks are covered by regolith and transported cover (Griffin, 1990). Continued exploration success in such covered environments requires an “expansion of the search space” to include those buried rocks (Whiting, 2006).

One possible solution comes from the use of 3D inversions of magnetic and gravity data to obtain subsurface predictions of the distribution of physical properties required to explain observed geophysical data. These techniques have become common in mineral exploration in recent years. For exploration seeking large targets with highly anomalous mass or magnetic properties relative to their host rocks, 3D inversions that honour only the supplied magnetic and/or gravity data can provide useful guides for targeting drill holes or follow-up data acquisition. Application of these techniques have led to some new ore discoveries such as the Prominent Hill iron oxide copper gold deposit in South Australia (Macdonald, 2002; Hart and Freeman, 2003) and extensions to existing ore bodies such as at the Raglan nickel deposit in Québec (Watts, 1997). However, the ease and completeness of “default” inversion solutions gives them an unwarranted air of validity. Due to the non-uniqueness of the solutions there may be significant discrepancies between the actual subsurface and the representation recovered by default inversions. There may be infinitely many physical property models that explain the observed geophysical data, and the default result obtained using only mathematical constraints is just one such possibility.

¹ A version of this chapter will be submitted for publication. Williams, N.C., and Oldenburg, D.W. Geologically-constrained gravity and magnetic inversions over the Agnew-Wiluna greenstone belt and Perseverance nickel deposit, Western Australia.

The non-uniqueness of the inverse problem provides an important opportunity to include other geological information to obtain an earth model consistent with both geological and geophysical observations; a reliable solution demands it. By including geological information, potential field inversions can be constrained to provide only those solutions which reproduce the observed geophysical data, honour the known or expected geology, and satisfy the mathematical constraints. The geological information can come in any form: mapping, drilling, sampling, structural studies, 2D cross sections or 3D model interpretations, or other geophysical data. All commercially available gravity and magnetic inversion packages allow the use of geological constraints; the difficulty arises in how to effectively include the necessary information.

Some work has already been done assessing the use of geological constraints in inversions for mineral exploration (Phillips, 1996; Phillips and Oldenburg, 2002; Marquis et al., 2003; Guillen et al., 2004; Williams et al., 2004; Ash et al., 2006; Farquharson et al., 2008; Fullagar et al., 2008; and Chapter 2 of this study) but few of the published works provide detailed descriptions or guidelines on how the geological constraints were derived, implemented, and tuned. In many cases the solutions are heavily customised to a specific set of data and provide little guidance for more general problems. The challenges faced and time required to create these tailor-made constraints may make it impractical for most mineral explorers to apply them in their regular work programs. Farquharson et al. (2008) point out that another reason for the lack of use of geological constraints in mineral exploration inversions is the possible perception that geophysical data are less useful once targets have been identified and the acquisition of detailed geological data has commenced. If true, this suggests that the ongoing value of gravity and magnetic inversion results, and of geophysical data in general, in an integrated exploration program has still not been adequately demonstrated.

This study aims to provide clear examples, at different observation scales, of how geological information can be included into geophysical inversions to recover holistic predictions of the subsurface geology consistent with all existing knowledge in an area. Geological interpretations of the results will be presented to demonstrate the benefits and limitations of the approach. A number of inversion algorithms have been adopted in the mineral exploration industry, namely the University of British Columbia – Geophysical Inversion Facility (UBC–GIF) GRAV3D and MAG3D packages (Li and Oldenburg, 1996,

1998a), the University of Utah Consortium for Electromagnetic Modeling and Inversion GRMAG3D package (Portniaguine and Zhdanov, 1999, 2002), the Bureau de Recherches Géologiques et Minières (BRGM) & Intrepid Geophysics GeoModeller package (Guillen et al., 2004) and the Fullagar Geophysics VPmg package (Fullagar and Pears, 2007; Fullagar et al., 2008). Each of the programs has benefits and limitations and may be suited to slightly different problems and sets of geological data. This study uses the UBC–GIF GRAV3D and MAG3D inversion packages, partially due to their more common usage within the industry, but also because they are particularly well suited to early stages of exploration where prior geological knowledge is limited.

The examples in this study are all from the Agnew-Wiluna greenstone belt in the Eastern Goldfields Superterrane of Western Australia's Yilgarn Craton, but the techniques are equally applicable in other areas where similar data sources exist. The Eastern Goldfields boasts several key characteristics that make it suitable for such use, primarily:

- A sizeable endowment of nickel sulphide mineralisation with a pronounced gravity and magnetic signature, and abundant gold mineralisation
- A variety of rock types with moderately large physical property contrasts
- Well mineralised and understood localities, such as the Perseverance nickel deposit, and wide areas of covered and poorly known rocks with high potential for additional mineralisation
- Availability of large amounts of high quality geological and geophysical data, at a range of scales, courtesy of WMC Resources and subsequently BHP Billiton, Geoscience Australia (GA), and the Geological Survey of Western Australia (GSWA)

Regional-scale geologically-constrained inversions are applied to identify the general crustal architecture associated with the highly prospective Agnew-Wiluna greenstone belt and surrounding areas, and aid 3D geological mapping. The inversions are assessed on their effectiveness at identifying how deep the greenstone belts extend, the characteristics of the structures controlling their margins and whether they can identify if the prospective greenstone belts extend under cover. District-scale inversions are applied to map the geometry and extents of the greenstone rocks that host the gold and nickel deposits. At the deposit scale, inversions are applied to identify stratigraphic horizons or units that may be favourable hosts for

extensions of the main sulphide ore zone at depth at the Perseverance nickel sulphide deposit near Leinster. Even though the Perseverance deposit is a well-developed and data-rich mine environment, subsets of the available geological data are also used to simulate the results that might be obtained when applying geologically-constrained inversions at earlier stages of exploration around the deposit

7.2 GEOLOGY AND ARCHITECTURE OF THE EASTERN GOLDFIELDS

Despite poor outcrop (commonly < 5 %: Griffin, 1990), the Yilgarn Craton contains an inordinately large proportion of Australia's known mineral wealth. It is composed of greenstone belts, containing metavolcanic and metasedimentary rocks, several granitoid suites, and granitic gneiss, all with ages generally ranging from 3.05 to 2.62 Ga (Myers, 1993). According to the most recent classification by Cassidy et al. (2006) the craton is an agglomeration of at least six terranes (Figure 7.1), each comprising several domains. Each domain represents a dismembered fragment of relatively contiguous stratigraphy. The terranes are bounded by regional scale fault systems which predominantly follow north to north-northwest trends. The craton is thought to have amalgamated during a period of intense granitic intrusion between 2.76 and 2.62 Ga, and had stabilised by around 2.5 Ga (Myers, 1995). The western half of the craton is known as the Youanmi Terrane and may have acted as the core on which all other terranes were accreted (Griffin et al., 2004; Cassidy et al., 2006).

The craton-wide north-south Ida Fault System separates the Youanmi Terrane from the Eastern Goldfields Superterrane (EGST) to the east. The EGST contains a majority of the Yilgarn Craton's greenstone belts and comprises three terranes; from west to east the Kalgoorlie, Kurnalpi, and Burtville Terranes. This study focuses on the northern portion of the Kalgoorlie Terrane, in particular the Agnew-Wiluna greenstone belt. The Kalgoorlie Terrane is bounded to the east by the Ockerburry Fault System and the Kurnalpi Terrane. The limited extent of outcropping Archean basement rocks (Figure 7.2) makes surface-based exploration challenging. To compensate, several basement geology interpretations integrating surface mapping and 2D gravity and magnetic interpretations have been published (Liu et al., 2000; Vanderhor and Flint, 2001; Whitaker and Bastrakova, 2002). The interpretation by (Liu et al., 2000) is shown in Figure 7.3, and provides a more informative view of the current understanding of the geology in the northern portion of the Kalgoorlie Terrane and in particular the Agnew-Wiluna greenstone belt.

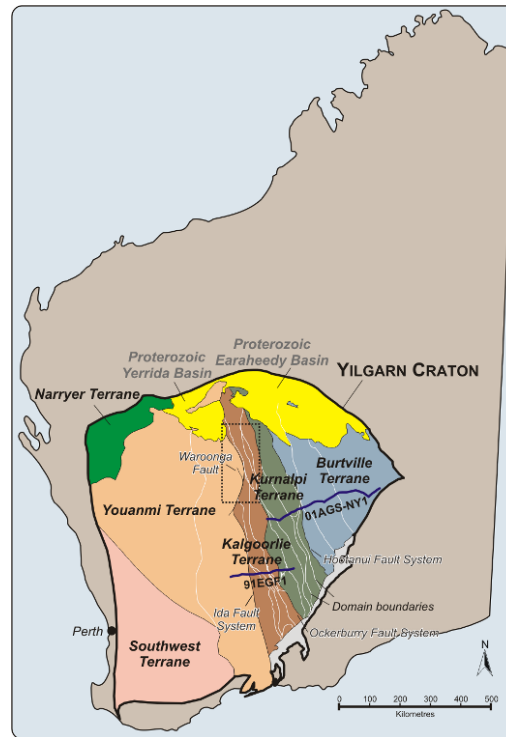


Figure 7.1. Terranes (coloured polygons) and domains (white boundaries) of the Archean Yilgarn Craton as defined by Cassidy et al. (2006). Blue lines show the locations of two deep reflection seismic lines, 91EGF1 (Goleby et al., 1993) through Kalgoorlie and 01AGS-NY1 (Goleby et al., 2003) through Leonora and Laverton (Figure 7.4). Dotted black box surrounds the Agnew-Wiluna greenstone belt.

Two long, roughly east-west oriented deep reflection seismic traverses provide much of the available information regarding the gross 3D architecture of the EGST (Figure 7.4). The southern traverse, 91EGF1 near Kalgoorlie (Goleby et al., 1993), covers 213 km from the eastern edge of the Youanmi Terrane, over the Ida Fault System and the Kalgoorlie Terrane, and into the Kurnalpi Terrane. The northern traverse, 01AGS-NY1 near Leonora and Laverton (Goleby et al., 2003), covers 430 km from the eastern edge of the Kalgoorlie Terrane, across the Kurnalpi Terrane and much of the Burtville Terrane. Although further from this study's area of interest, the southern line may be particularly relevant as it provides some of the only 3D geometrical constraints on the Kalgoorlie Terrane.

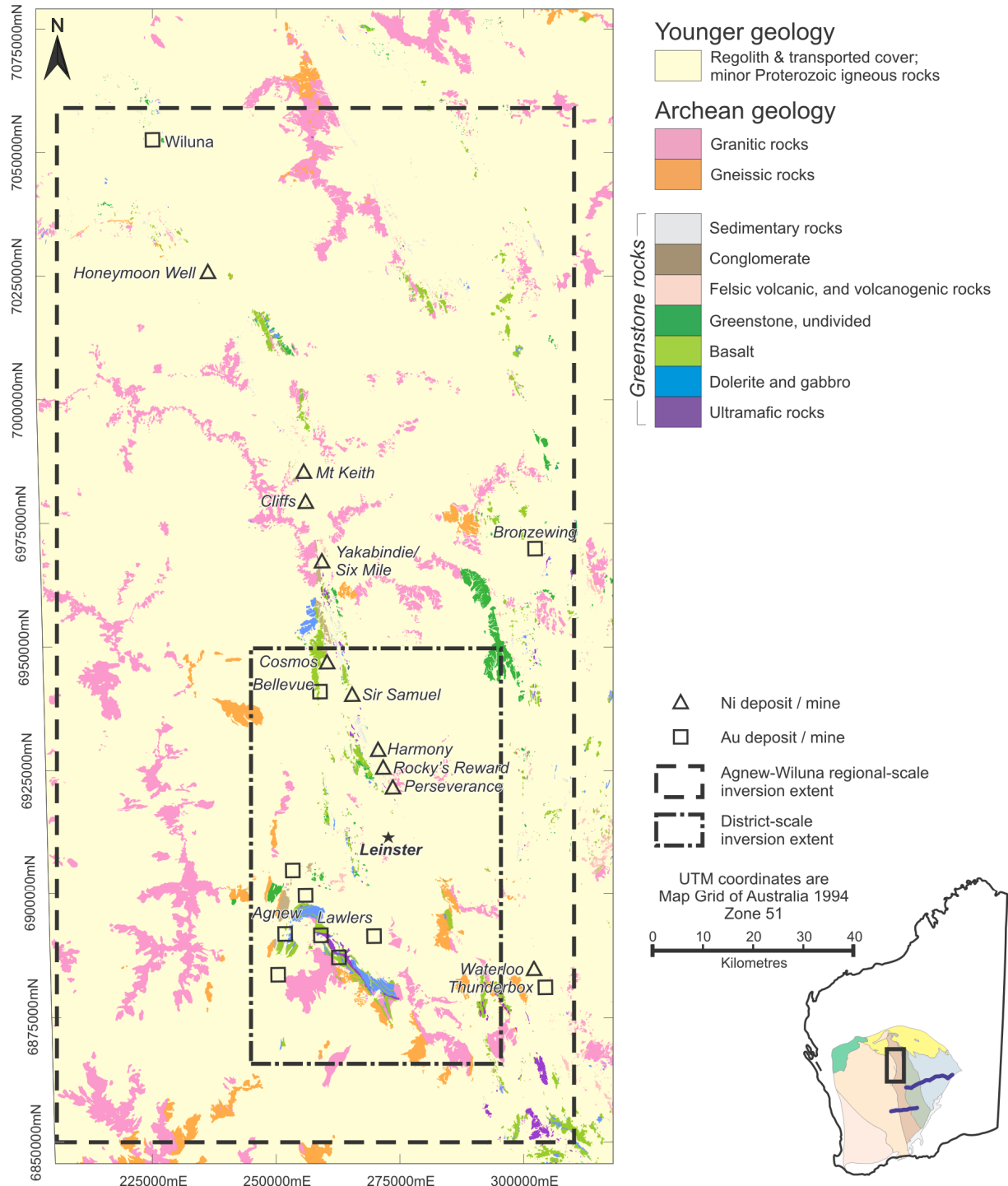


Figure 7.2. Outcropping Archean basement rocks of the Agnew-Wiluna greenstone belt and surrounding areas, simplified from the 1:100,000 scale map compilation by the GSWA (2004). The extents of the Agnew-Wiluna regional-scale inversion volume and the district-scale inversion volume are shown, but the full extent of the Perseverance deposit-scale inversion lies under the Perseverance deposit marker.

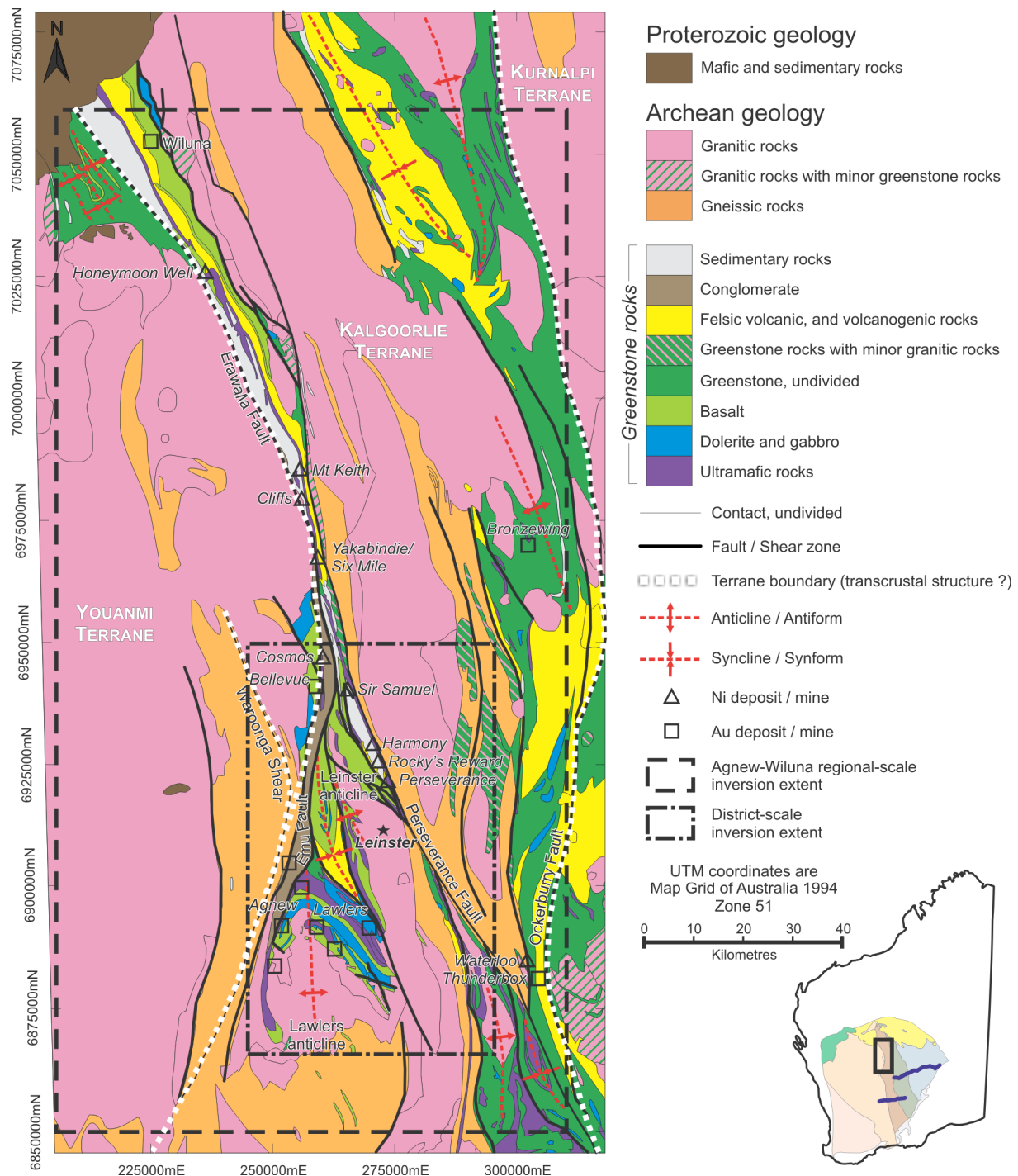


Figure 7.3. Basement geology of the Agnew-Wiluna greenstone belt simplified from the 1:500,000 scale interpretation by Liu et al. (2000). Terrane boundaries from Figure 7.1 and Cassidy et al. (2006) are shown. Note the division of gold deposits into the western domains, and nickel deposits into the eastern domains of the Agnew-Wiluna belt, and the structural complexity and attenuation within the belt. The extents of the Agnew-Wiluna regional-scale inversion volume and the district-scale inversion volume are shown, but the full extent of the Perseverance deposit-scale inversion lies under the Perseverance deposit marker.

The seismic data identifies the Moho at between 33 and 46 km depth; the depths increase to the east and north (Swager et al., 1997; Goleby et al., 2003). In the southern line, both east- and west-dipping transcrustal structures are present, but in the north only west-dipping transcrustal structures are observed (Goleby et al., 2003). The southern seismic line clearly images the Ida Fault, dipping about 30° to the east and continuing to depths of 25-30 km, forming a sharp western boundary to the EGST (Goleby et al., 1993; Swager et al., 1997). The EGST is inferred to have dropped down about 5 km along the Ida Fault System relative to the Youanmi Terrane (Swager, 1997; Goleby et al., 2003). In the EGST both seismic lines show low-angle, gently east-dipping shear zones that separate the greenstone belts from inferred uniform felsic gneiss basement below (Swager et al., 1997; Goleby et al., 2004). In the southern line these coalesce into a single regional detachment surface, whereas no such detachment surface is observed in the northern line (Goleby et al., 2003). Along the southern line the greenstones are generally 4-7 km thick (Swager et al., 1997), whereas along the northern line they range from 4-9 km thick down to < 1 km thick in places (Goleby et al., 2004). The greenstones are commonly intruded by granites, and local domes of exposed felsic gneiss basement occur where the overlying greenstones have been tectonically dismembered and eroded, especially in the northern traverse. In general, the greenstones appear to show a trend of increasingly variable thickness and increasingly patchy lateral extents further north in the EGST.

7.2.1 Geology of the Agnew-Wiluna greenstone belt

The Agnew-Wiluna greenstone belt is the smaller of two greenstone belts in the northern Kalgoorlie Terrane, the other being the Yandal greenstone belt 50 km to the east. Both belts are well endowed with gold, but only the Agnew-Wiluna belt is known to contain significant nickel resources. The Agnew-Wiluna belt is between 2 and 20 km wide, and extends over 200 km north-south. It is surrounded to the west and east by voluminous granitoid rocks.

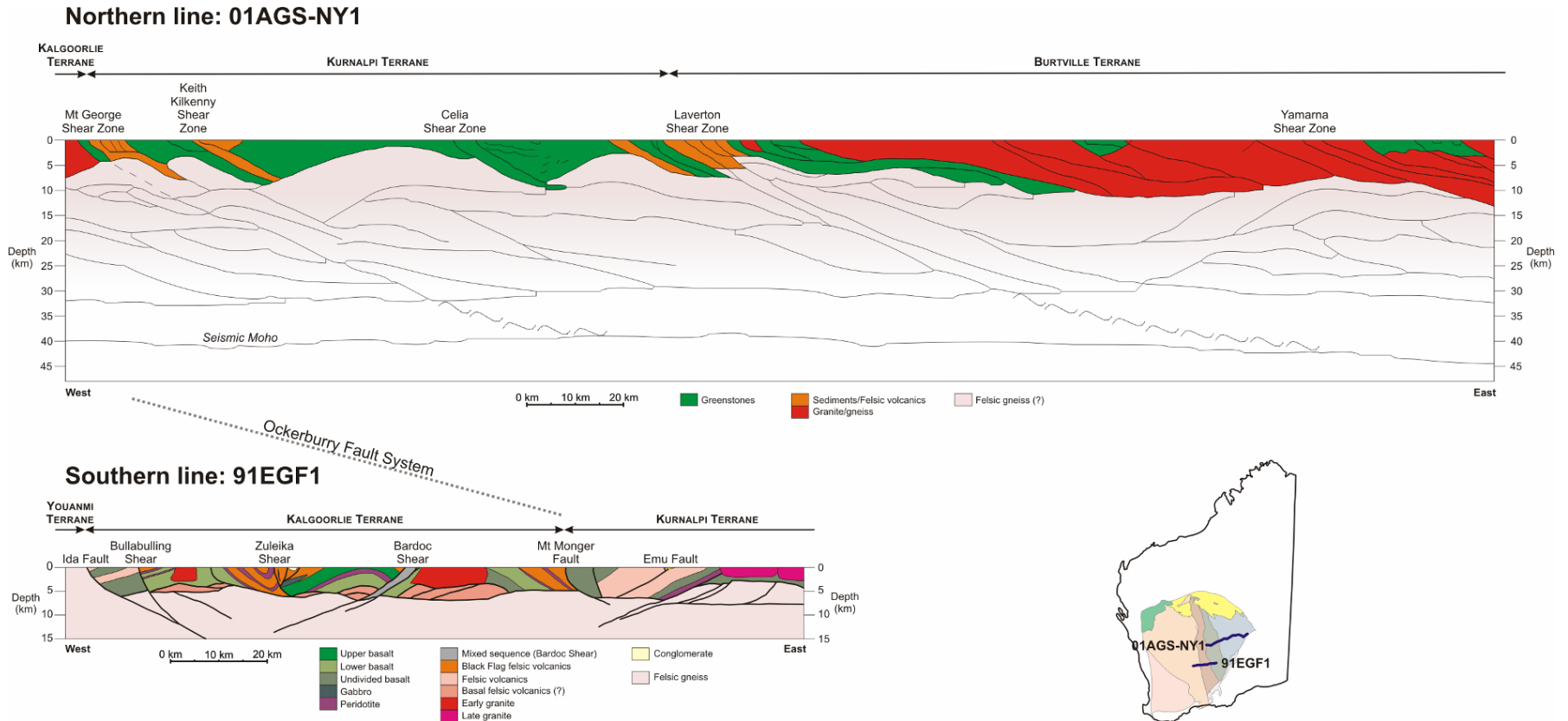


Figure 7.4. Deep reflection seismic profiles across the EGST. The western portion of 01AGS-NY1 is shown with interpretation adapted from Goleby et al. (2004); 91EGF1 is shown with interpretation modified from Goleby et al. (1993). Transcrustal fault systems or shear zones mark the terrane boundaries defined by Cassidy et al. (2006) as shown in Figure 7.1 and reproduced in inset. The northern line mainly shows the Kurnalpi Terrane, and the southern line mainly shows the Kalgoorlie Terrane. Greenstones of the EGST appear to thin and become more variable in thickness to the north. The northern line also lacks both the regional detachment surface at the base of the greenstones and the west-dipping structures common in the southern line (Cassidy et al., 2003). Both lines are reproduced at the same scale with no vertical exaggeration.

The western boundary of the Agnew-Wiluna belt corresponds to the Ida Fault System, the western edge of the EGST. In the north it is represented by the steeply east-dipping Erawalla Fault. In the south the western boundary is more complex, and may variously be attributed to the Miranda or Emu Faults, or the west-dipping Waroonga Shear Zone which has been inferred to truncate the top of the east-dipping Ida Fault System in this area (Groenewald et al., 2001; Liu et al., 2002; Blewett, 2004). Extension along the Ida Fault system around 2,660 Ma is thought to have accommodated development of late sedimentary basins deposited on pre-folded greenstone sequences along the western edge of the Agnew-Wiluna belt (the Scotty Creek and Jones Creek Conglomerates; Blewett et al., 2004; Blewett and Czarnota, 2007b).

The eastern margin of the Agnew-Wiluna belt is controlled by the Perseverance Fault which is associated with a strongly sheared granitoid inferred to be up to 6 km wide (Liu et al., 2002). The Perseverance Fault is thought to be a major crustal structure, and several authors have interpreted it to be a terrane boundary (Myers, 1993; Brown et al., 2001). The more recent classification by Cassidy et al. (2006) places the Perseverance Fault as a domain boundary. The fault passes < 1 km east of the Perseverance nickel deposit, where it is vertical to steeply southwest dipping, but it is generally considered to be a continuation of the east-dipping craton-wide Keith-Kilkenny Shear Zone imaged in the northern seismic line (Liu et al., 2002; Henson and Hitchman, 2004). The relationship between the Perseverance Fault and the Ida Fault System at depth is unknown. The main geographic, and possibly stratigraphic, domains within the belt include the Agnew-Lawlers domain south and west of the Leinster anticline, the Mt Keith-Perseverance domain along the Perseverance Fault, and the Wiluna domain at the northern end of the belt.

The metamorphic grade increases from prehnite-pumpellyite and lower-greenschist facies near Wiluna through middle-greenschist facies at Mt Keith up to lower- to middle-amphibolite facies (~550 °C) at Perseverance (Binns et al., 1976; Barrett et al., 1977; Gole et al., 1987). The primary igneous mineralogy of the komatiitic rocks, intrusive or extrusive ultramafic rocks with > 18 wt. % MgO (Leshner and Keays, 2002), has been considerably altered by multiple stages of metamorphism, and serpentinisation. Serpentinisation involves hydration reactions that convert olivine into magnetite and serpentine, with a dramatic increase in volume and magnetic susceptibility, and a decrease in density (Henkel, 1991). Amphibolite-

grade metamorphism of previously serpentinised ultramafic rocks has created abundant metamorphic olivine at the expense of magnetite and serpentine, but the metamorphic olivine has also commonly undergone later serpentinisation (Hill et al., 1990), further complicating the physical properties.

The stratigraphy of the Agnew-Wiluna greenstone belt includes three ultramafic associations: komatiite – felsic volcanic, komatiite – black shale, and komatiite – basalt, all below the unconformable sedimentary Jones Creek Conglomerate (Naldrett and Turner, 1977; Eisenlohr, 1989; Liu et al., 2002; Beresford et al., 2004; Beresford and Rosengren, 2004). Naldrett and Turner (1977) identified a Lower Greenstone sequence, exposed in the hinges of the Lawlers and Leinster Anticlines and between Yakabindie and Kathleen Valley, that consists of gabbros, and tholeiitic and high-Mg basalts, below sedimentary rocks; and an Upper Greenstone sequence along the eastern edge of the Agnew-Wiluna belt that consists of felsic volcanics and volcanoclastics, shales and cherts, basalts, more felsic volcanoclastics, and ultramafic flows intruded by mineralised dunite pods. This framework has been built upon by subsequent authors and correlated with adjacent greenstone belts, including the southern Kalgoorlie Terrane and the Agnew-Wiluna belt (Brown et al., 2001; Cassidy et al., 2002).

Although felsic facies are present in the upper greenstone sequences throughout the Kalgoorlie Terrane, only along the eastern edge of the Agnew-Wiluna belt are they associated with komatiitic rocks and rich nickel mineralisation. A characteristic of the komatiite – felsic volcanic association in the Agnew-Wiluna belt is the presence of large, up to 700-m-wide and 2-km-long, adcumulate dunite lenses amongst thin spinifex-textured komatiite flows. The dunite lenses host, or are adjacent to, most of the known nickel occurrences in the belt in particular at Perseverance and Mt Keith, two of the world's largest komatiite-hosted Ni-Cu-(PGE) deposits. The Perseverance Ultramafic Complex (PUC), representing the main ultramafic lens containing the dunite core, is depicted in Figure 7.5 with its characteristic komatiite – felsic volcanic association. There has been much debate regarding intrusive versus extrusive origin for the dunite lenses, with an original intrusive interpretation (Burt and Sheppy, 1975; Martin and Allchurch, 1975; Naldrett and Turner, 1977), then an extrusive interpretation (Barnes et al., 1988; Dowling et al., 1990; Hill et al., 1995), and more recently a subvolcanic intrusive reinterpretation (Trofimovs et al., 2003; Beresford et al., 2004; Rosengren et al., 2005). The host felsic volcanics in the komatiite – felsic volcanic association

were emplaced from 2,742-2,706 Ma (R.I. Hill and I.H. Campbell, unpub. data, cited in Libby et al., 1998; Duuring et al., 2004b) the youngest providing a maximum age for the komatiites. This age corresponds well with the 2,705 Ma age of komatiites and associated felsic volcanics at Kalgoorlie (Nelson, 1997), indicating a possible time correlative horizon along the length of the Kalgoorlie Terrane (Cassidy et al., 2002).

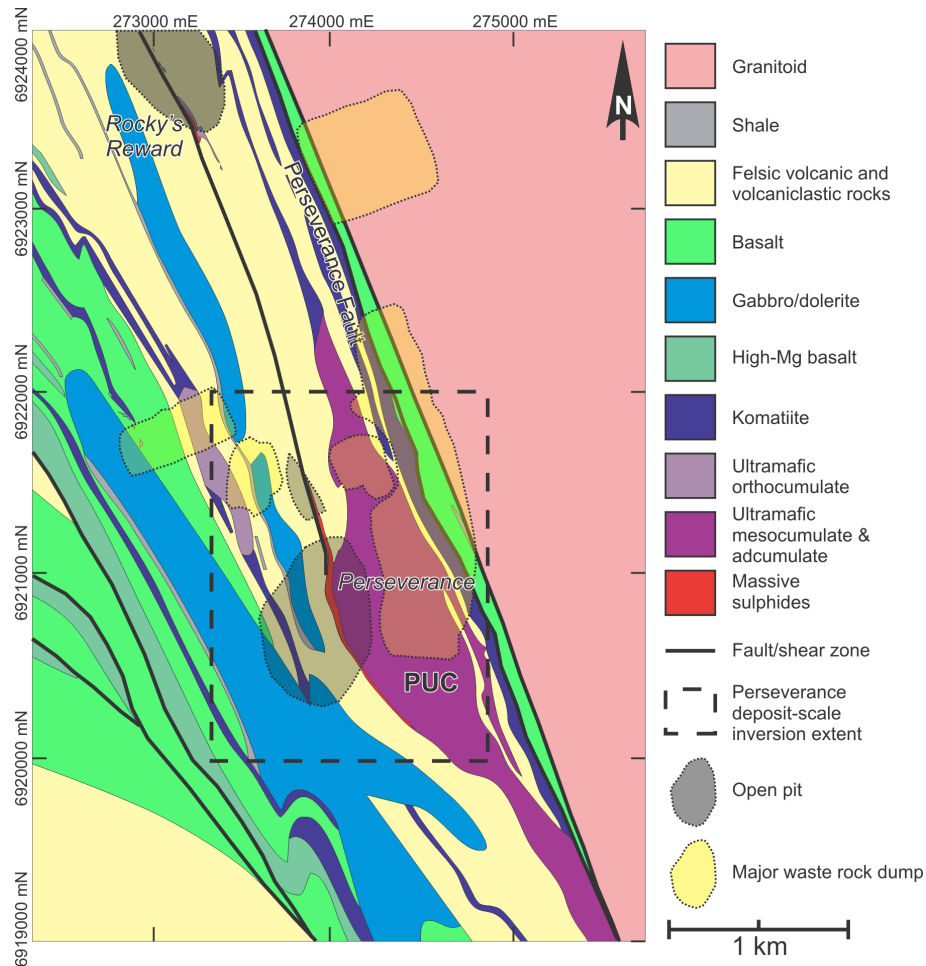


Figure 7.5. Basement geology surrounding the Perseverance Ni-deposit showing the deposit-scale inversion core. The Perseverance Ultramafic Complex (PUC) containing the dunite core is marked as are the major mine infrastructure features. Simplified from BHP Billiton internal data (C. Perring, unpub. map, 2005).

The komatiite – black shale association only occurs in the eastern Agnew-Wiluna belt near the Sir Samuel Ni-Cu-(PGE) prospect 14 km north of Perseverance along the Perseverance Fault. It is inferred to represent deep marine facies equivalents of sedimentary and volcanoclastic rocks near Perseverance (Trofimovs et al., 2003). The komatiite – basalt association is restricted to the western domains of the Agnew-Wiluna belt, especially near Agnew and Lawlers where it is associated with younger (< 2,660 Ma) mesothermal gold deposits (Groves et al., 2000; Blewett and Czarnota, 2007a), but no nickel deposits.

The Agnew-Lawlers domain to the west shows large NNW-trending upright folds, including the Lawlers Anticline, Mt. White Syncline, and Leinster Anticline, intruded by 2,666 Ma granitoids (Eisenlohr, 1989; Fletcher et al., 1998; Duuring et al., 2004b; Blewett and Czarnota, 2007b). The Mt Keith-Perseverance domain contains strongly deformed, complexly folded, and sheared rocks. It is closely associated with the Perseverance Fault and its associated structures, and contains the most attenuated stratigraphy where the greenstone belt reaches its narrowest point in the vicinity of Mt Keith (Eisenlohr, 1989; Duuring et al., 2004b). The separation between the gold-bearing versus nickel-bearing, or equivalently the komatiite – basalt association versus the komatiite – felsic volcanic association, is either the north-northwest-plunging Leinster Anticline which is intruded by the Leinster Granodiorite (Eisenlohr, 1989; Duuring et al., 2004b), or the eastern limb of the anticline along the Sir Samuel Fault (Liu et al., 2002).

7.2.2 Mineral deposits of the Agnew-Wiluna greenstone belt

The Agnew-Wiluna greenstone belt contains four of the world's 15 largest nickel sulphide deposits, Mt Keith, Perseverance, Yakabindie, and Honeymoon Well, which represent the majority of the world's large komatiite-hosted Ni-Cu-(PGE) deposits (Jaireth et al., 2005). The Perseverance deposit is part of the Leinster group which also includes the Rocky's Reward and Harmony deposits. The group contains massive nickel sulphide basal horizons (Type I: Leshner and Keays, 2002), disseminated intercumulus nickel sulphides (Type IIb), and tectonically remobilised sulphides (Type V), with a total underground resource of 31 Mt at 2.3 wt. % Ni and an open pit resource of 155 Mt at 0.6 % Ni (BHP Billiton Ltd., 2007). The disseminated nickel sulphide deposits at Mt. Keith (Type IIb) have a total open pit resource of 393 Mt at 0.5 wt. % Ni (BHP Billiton Ltd., 2007). Yakabindie and Honeymoon Well are similar high tonnage, low grade disseminated sulphide deposits (Type IIb) that have yet to be developed. Additional massive nickel sulphide deposits (Type I and Type V) exist in the belt, notably Cosmos and Cliffs, and several nickel resources are still being assessed, such as Sir Samuel. All of the known nickel deposits, except Cosmos, lie along the eastern corridor containing the komatiite – felsic volcanic association and its komatiitic flows and subvolcanic dunite intrusive bodies. The Cosmos deposit appears to be hosted in a komatiite – felsic volcanic sequence, but is the first major nickel deposit to be found in the western domains of the Agnew-Wiluna belt (Langworthy, 2004).

The rocks that host the Agnew-Wiluna nickel sulphide deposits are either thin komatiite flows (Cosmos and Cliffs), or komatiitic cumulate and dunite lenses or pods (Mt Keith, Perseverance, Yakabindie, and Honeymoon Well). Massive sulphide bodies at Perseverance are generally less than 5 m thick, and contain pyrrhotite (80 vol. %), pentlandite (< 8 vol. %), with the remainder consisting of pyrite, chalcopyrite, and magnetite (Duuring et al., 2004a). The disseminated ore body at Perseverance, defined by a 1 wt. % Ni shell, is up to 50 m wide and can contain up to 45 vol. % sulphides, mainly pyrrhotite and pentlandite, with minor pyrite and chalcopyrite (Duuring et al., 2004a). Post-emplacement deformation and metamorphism can remobilise the sulphides, commonly into surrounding host rocks.

All known gold deposits are located in the Agnew-Wiluna belt's western domains. The only current producing mines are in the Agnew, Lawlers, and Wiluna camps, but there are several historically significant producers (Sir Samuel, Bellevue and Kathleen Valley) and a number of undeveloped resources (Lake Way and additional resources at Kathleen Valley). Agnew is the largest group of deposits with a total resource of 15.3 Mt at 5.9 g/t Au (Gold Fields Ltd., 2007); Lawlers has 6.8 Mt at 3.2 g/t Au (Barrick Gold Corp., 2005), and Wiluna has 4.2 Mt at 5.7 g/t Au (Apex Minerals NL, 2007) although gold has been extracted around Wiluna since 1896 (Liu et al., 2002).

The Agnew-Wiluna greenstone belt has substantial potential for further gold and nickel deposits to be found. Near mine exploration has sustained gold mining in the belt for over 110 years. The komatiitic rocks within the eastern portion of the greenstone belt contain regularly spaced nickel deposits of either Type I or Type IIb mineralisation, associated with a time correlative komatiite horizon, but the structural and stratigraphic complexities in the belt have hindered identification of continuations of the horizon. Type IIb disseminated mineralisation is known to occur in large dunite lenses in the belt, but massive Type I and remobilised Type V nickel sulphide mineralisation may occur anywhere within or surrounding komatiitic rocks (Fiorentini et al., 2007). For example, the Cosmos Deeps deposit consists of massive nickel sulphides at a depth of 400 m that have either been remobilised, or tectonically removed from their parent komatiite such that they lie wholly enclosed by felsic volcanic rocks (Langworthy, 2004). Continued exploration will target these small but high grade bodies at depth throughout the belt. In addition, the Cosmos and Cosmos Deeps deposits are located within western

portion of the belt and may indicate potential new nickel exploration areas (Langworthy, 2004).

7.3 PHYSICAL PROPERTIES

The critical link between geological and geophysical interpretation is the physical properties of the rocks and minerals involved. Geophysical inversions require input of physical property knowledge at two stages. Physical property information is required when defining geological constraints. But even in greenfields exploration where there is no prior geological knowledge, an understanding of physical properties is needed to interpret inversion results. Without an expectation of what the physical properties should be it is difficult to assess the validity of recovered physical property models. A lack of physical property knowledge also hinders assessment of which features and physical property contrasts may represent prospective horizons or target regions. In established projects and mines, large databases of physical properties are usually available. Densities are required for ore reserve estimates, and magnetic susceptibilities are regularly gathered during exploration as an aid for mapping and logging. Knowledge of physical properties in near-mine environments may be useful in constraining and interpreting inversions in similar data-poor greenfields areas and this approach is used in this study.

Chapter 4 provides a detailed description of the physical properties of rocks in the southern portion of the Agnew-Wiluna greenstone belt and the Leinster nickel deposits. A summary of the densities and magnetic susceptibilities is presented in Table 7.1. The data show that there are some clear physical property contrasts between certain rock types, but there are also some strong similarities in physical properties. The most dense and magnetic rocks are invariably the sulphide-rich rocks, especially the massive sulphides. The large standard deviations for the densities and susceptibilities of the sulphide-rich rocks reflects the variety of sulphide types and abundances in the area, including disseminated to massive nickeliferous sulphidic rocks with abundant pentlandite and magnetic pyrrhotite, as well as sedimentary and metamorphic sulphide-bearing rocks which contain mostly non-magnetic pyrite with minor pyrrhotite. Although sulphide-bearing rocks could be expected to dominate the potential field responses, they occur in such limited volumes that they will not usually be imaged directly. Of the more voluminous rock types, the ultramafic rocks show the most variable densities and susceptibilities depending on their alteration and metamorphic history as outlined above; they

have the highest susceptibilities, but moderate densities. The densest common rocks are the basalts, gabbros and dolerites. They have moderate to low susceptibilities and there is little difference in properties between the different types. Some of the sedimentary rocks have unusually high densities and susceptibilities which are likely attributable to the presence of dense and magnetic diagenetic and metamorphic sulphides and oxides, and recrystallisation during metamorphism. Most of the remaining rocks have very similar properties.

Although the available physical property data represents a large database, it is far from complete. The most notable issue is the irregular sampling of different rock types. Although granitoid rocks constitute > 75 % of the interpreted geology in Figure 7.3, < 0.1 % of the available physical property measurements are on granitoid rocks. This poor sampling gives mean and median granitoid densities (2.63 and 2.57 t/m³ respectively) lower than typical values of 2.65-2.70 t/m³ inferred for the Yilgarn Craton (Goleby et al., 1993; Bell, 2002). Due to access limitations, the granitoid samples collected in this study came from surface outcrops which may have had slightly increased porosity due to weathering, or from drill core intersections of sheared granitoid, and so are unlikely to be fully representative. The pelite and shale rocks have densities which extend to extremely high values > 4.0 t/m³; although not observed in this study, these samples likely contained abundant hydrothermal sulphides. The supplied density measurements may have been preferentially made on sulphide-rich examples in the vicinity of ore zones, or the apparent sulphidic nature of pelites and shales may be common in the region. The properties for iron formations are significantly lower than those expected for true iron formations. These samples may not be representative, but iron formations are rarely observed in regional mapping.

Table 7.1. Statistical summary of densities and magnetic susceptibilities for different rock types observed in the southern Agnew-Wiluna greenstone belt. The data include measurements taken in this study and those supplied by BHP Billiton.

Rock type	Samples	Density (t/m ³)				Magnetic susceptibility ($\times 10^{-3}$ SI)				
		Mean \pm st. dev.	10 th percentile	Median	90 th percentile	Samples	Mean \pm st. dev.	10 th percentile	Median	90 th percentile
Sulphide-rich rock	10,365	3.85 \pm 0.68	2.78	4.02	4.60	420	25.6 \pm 71.6	0.290	6.04	65.0
Ultramafic	63,102	2.80 \pm 0.27	2.54	2.76	3.11	18,177	19.2 \pm 47.7	0.340	5.89	55.6
Basalt	2,084	2.97 \pm 0.25	2.73	2.95	3.21	4,705	2.70 \pm 22.5	0.110	0.770	2.69
Gabbro & dolerite	506	2.96 \pm 0.24	2.72	2.96	3.15	347	1.16 \pm 1.73	0.210	0.780	1.84
Intermediate intrusive	0	-	-	-	-	9	3.21 \pm 3.48	0.272	1.47	8.43
Granitoid	33	2.63 \pm 0.18	2.45	2.57	2.87	33	0.944 \pm 1.34	0.00242	0.460	3.64
Gneiss	24	2.83 \pm 0.25	2.56	2.82	2.92	34	2.25 \pm 1.16	0.00977	2.30	3.66
Pegmatite	416	2.71 \pm 0.21	2.56	2.65	2.90	214	2.02 \pm 8.23	0.0300	0.470	2.52
Felsic volcanic/volcaniclastic rock	6,053	2.76 \pm 0.28	2.64	2.72	2.97	4,753	1.76 \pm 5.75	0.0700	0.690	3.16
Fine-grained metamorphic rock	9,676	2.86 \pm 0.32	2.66	2.78	3.15	8,072	2.98 \pm 23.6	0.0900	0.600	2.74
Pelite and shale	1,287	3.13 \pm 0.56	2.72	2.91	4.15	7,796	4.87 \pm 22.5	0.150	1.22	8.40
Sandstone and psammitic rock	78	2.84 \pm 0.37	2.63	2.76	3.24	195	2.20 \pm 4.73	0.400	1.10	4.03
Conglomerate	2	2.23 \pm 0.34	1.99	2.23	2.47	2	<0.0001	<0.0001	<0.0001	<0.0001
Chert	68	3.09 \pm 0.33	2.76	3.06	3.54	1,091	5.40 \pm 16.3	0.196	1.27	9.46
Iron formation	14	2.45 \pm 0.39	1.98	2.24	2.97	4	2.91 \pm 2.56	0.660	2.02	6.20
Regolith & Quaternary cover	15	2.27 \pm 0.28	1.92	2.29	2.74	977	3.18 \pm 7.18	0.110	0.900	7.93

The magnetic response of a rock is derived from two main constituents, a component induced by the earth's present magnetic field, and an intrinsic remanent magnetisation that reflects the rock's history. The Koenigsberger ratio:

$$Q = \frac{|\mathbf{NRM}|}{\kappa |\mathbf{H}_0|} \quad 7.1$$

indicates the proportion of remanent magnetisation $|\mathbf{NRM}|$ to induced magnetisation which is the product of the magnetic susceptibility, κ , and the earth field intensity $|\mathbf{H}_0|$. Values < 1 indicate induced magnetisation is dominant; values > 1 indicate that remanent magnetisation is dominant. Magnetic surveys measure the component of the sum of the two constituents that lies in the direction of the earth's magnetic field. The UBC–GIF magnetic inversion code does not account for remanent magnetisation so Koenigsberger ratios $\ll 1$ are assumed. The physical property analyses performed in Chapter 4 indicate that extreme remanent magnetisation ($Q > 10$) is common in the nickeliferous massive sulphides and moderate remanent magnetisation ($Q > 2-5$) is found within the ultramafic rocks, whether serpentinised or not. Most other rocks generally have Koenigsberger ratios < 1 , although local examples of Koenigsberger ratios > 1 can be found in some granites and intrusive mafic rocks.

The direction of the remanent magnetisation is also important, and is not reflected by Koenigsberger ratios. Where the remanent magnetisation component is in the direction of the earth's field the observed magnetic response will be larger, and therefore susceptibilities recovered by UBC–GIF inversions may be greater than measured induced susceptibilities. If the remanent magnetisation component is in the reverse direction to the earth's field, then the observed magnetic response will be lower and recovered susceptibilities will be less than measured susceptibilities. The remanent magnetisation component will have little effect on recovered susceptibilities if it is perpendicular to the earth's field. Koenigsberger ratios also do not distinguish primary remanent magnetisation from various secondary overprints. The results in Chapter 4 indicate that a large number of sulphide-rich and ultramafic rock samples exhibit viscous remanent magnetisation acquired from the present day earth field. These components lie parallel to the present earth field. Inversions will typically assign these rocks higher susceptibilities than those measured on samples. Other samples that did not show evidence of overprinting show a range of angles to the present day earth field which could complicate the recovered inverse models. However, as the magnetic sulphide-rich rocks are so rare, the

magnetic ultramafic rocks are generally very thin features relative to the size of cells in the regional- and district-scale inversions, and the observed magnetic anomalies are all positive, the effects of remanent magnetisation are expected to be minimal for these models. The smaller deposit-scale inversions specifically aim to map the distribution of the ultramafic bodies so remanent magnetisation must be considered in these models.

7.4 AGNEW-WILUNA GREENSTONE BELT GEOPHYSICAL DATA

The publicly available magnetic and gravity data available for the Agnew-Wiluna greenstone belt, extracted from the Australian Geophysical Archive Data Delivery System (GADDS, 2006), is shown in Figure 7.6 and Figure 7.7. The aeromagnetic data are a compilation of multiple surveys that were generally collected along 400-m-spaced east-west flight lines over the last 25 years and were stitched together in an 80 m grid using the Gridmerge program (Intrepid Geophysics) with the Australia Wide Array of Geomagnetic Stations used as a control on the merging process (Milligan et al., 2001; P. Milligan, written commun., 2006). Publicly available ground gravity data over the Yilgarn Craton varies in quality and spacing having been collected during numerous surveys over the last 35 years. Gravity stations in the Agnew-Wiluna area have a median spacing of 2.3 km and this severely limits the possible resolution in the regional- and district-scale gravity inversions. The available gravity data will generally only be able to resolve features that are > 4 km in size, and the signal associated with smaller features may be aliased such that they appear larger.

The most prominent features in the magnetic data are elongate (< 35 km long) thin (< 1 km wide) northwest to north-east trending magnetic highs; based on mapping and expected physical properties these correlate with the location of near-surface ultramafic bodies. The adjacent magnetic lows are likely associated with near-surface mafic and felsic volcanic, volcanoclastic, and sedimentary rocks within the greenstones. Granitoid rocks are frequently associated with intermediate magnetic responses and show various streaky or mottled textures depending on whether they have been sheared or not.

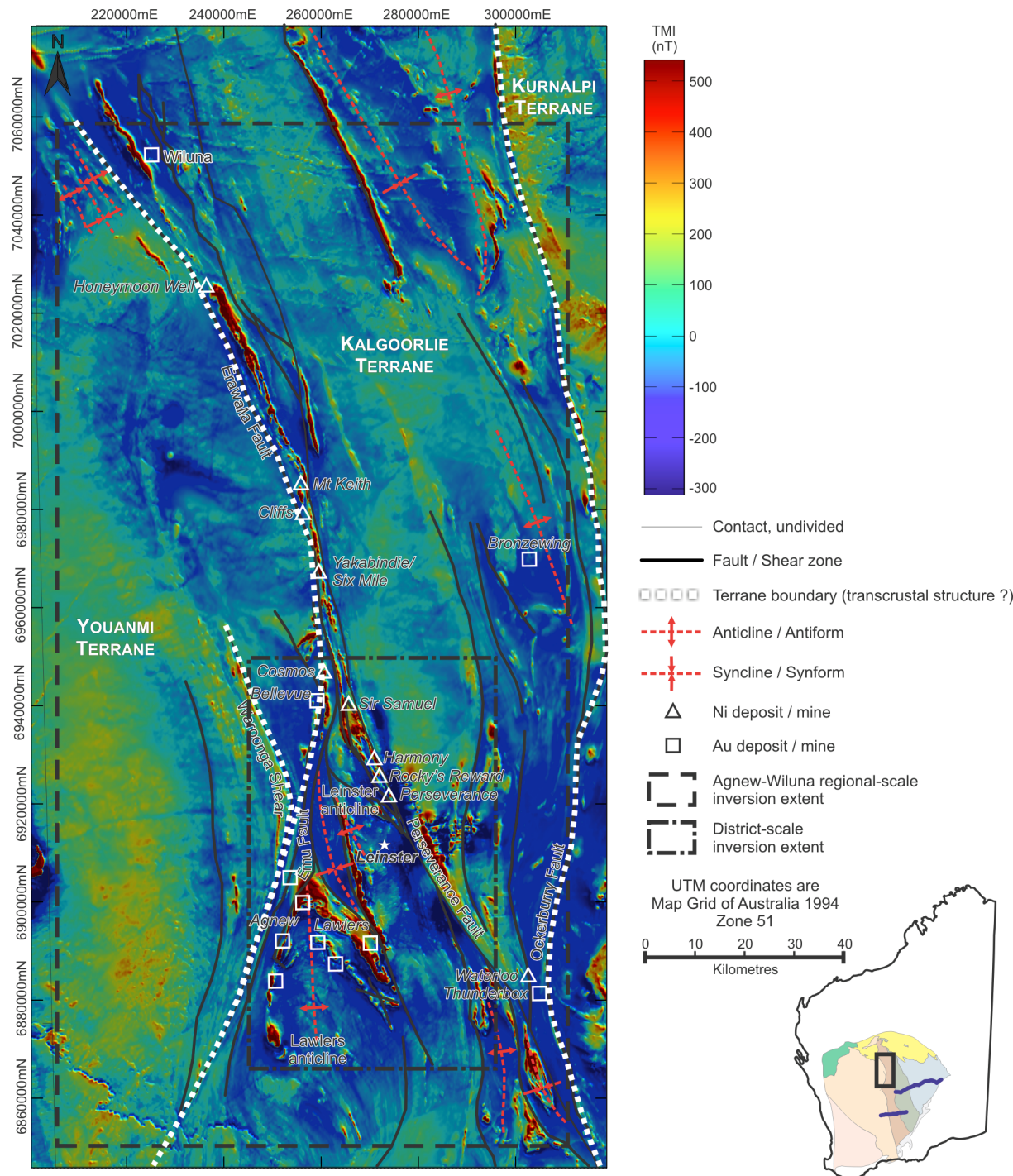


Figure 7.6. Total magnetic intensity data over the Agnew-Wiluna greenstone belt. The area is the same as in Figure 7.3 and the same geology outlines and annotations are included for reference. The data is from an 80-m-spaced grid of a mosaic of government aeromagnetic data that was flown at an average of 100 m elevation (GADDS, 2006). Comparison with Figure 7.3 shows that the magnetic data delineates ultramafic rocks well (high) with other rocks in the greenstone belt generally having low magnetic responses, and the adjacent granites having a moderate response. It is also effective at identifying the fine structure associated with both granites and greenstones.

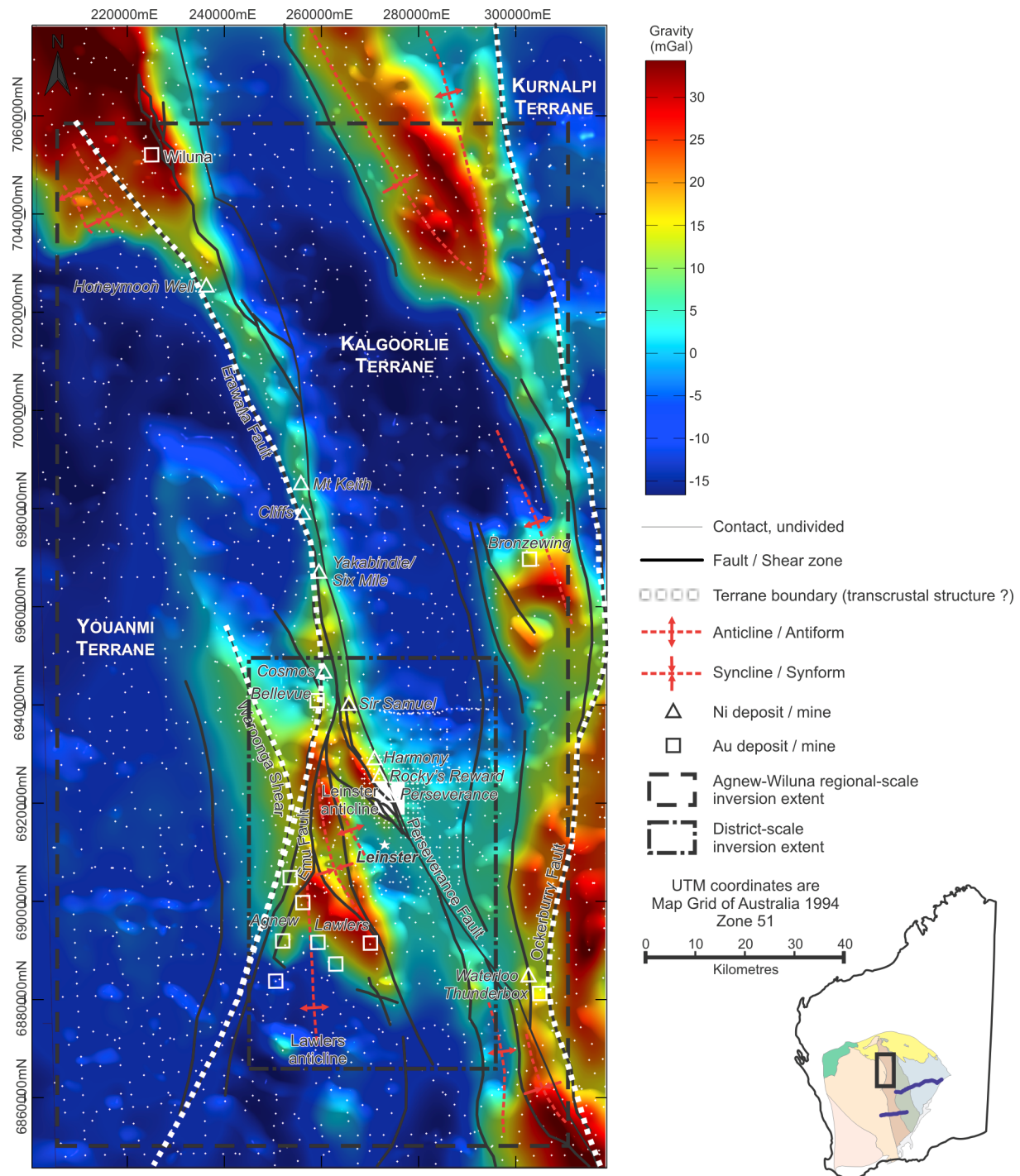


Figure 7.7. Bouguer gravity data over the Agnew-Wiluna greenstone belt. The area is the same as in Figure 7.3 and the same geology outlines and annotations are included for reference. The data are dominantly government ground gravity stations (GADDS, 2006) but the patch of data surrounding the Perseverance deposit are ground data supplied by BHP Billiton (pers. commun., 2004). The displayed data have been fully terrain corrected using a 2.67 t/m^3 Bouguer slab and terrain correction density. The gravity data have been gridded for display, but the actual observation points (white dots) are used in the inversion. The gravity emphasises the dense mafic rocks within the greenstone belt.

Gravity highs appear to delineate the gross geometry of the greenstone belt well despite the low data resolution. Closer examination reveals that the gravity highs are offset from the magnetic highs and correlate well with mapped occurrences of higher density mafic rocks within the belt. The granites bounding the greenstone belt show characteristic gravity lows. Little other information is evident from qualitative interpretation of the gravity data; however its ability to differentiate mafic rocks from the less dense felsic volcanic and granitic rocks demonstrates its importance for mapping the most voluminous rock types in the region.

BHP Billiton provided additional geophysical data for this research, including detailed 40-m-spaced flight line aeromagnetic data over the Leinster district (supplied on a 10 m grid), and a 2,267 station ground gravity survey over the Perseverance deposit with a core data spacing of 50 to 200 m. These data are shown in Figure 7.9 and Figure 7.8 in comparison to the existing basement geology interpretation from Figure 7.5. The data show the same relationships identified in Figure 7.6 and Figure 7.7. Mafic rocks within the greenstone belt west of the Perseverance and Rocky's Reward deposits are delineated by the gravity data but have no magnetic response. Ultramafic rocks, including the PUC, are associated with weak gravity lows but moderate to strong magnetic highs. Both the gravity and magnetic data show significant artefacts due to mine infrastructure, workings and development. Attempts to remove these features by modelling or filtering (as demonstrated by Jackson et al., 2004) had only partial success. Instead, upward continuation of the data removed much of the noise and the remaining low responses are managed using geological-constraints in the inversions. Remaining artefacts should be manifest as small shallow anomalies.

More problematic is the lack of gravity data over a 0.5 km² area above the Perseverance open pit. The pit lies directly over the main massive sulphide ore body and, based on synthetic forward modelling, this excludes the possibility of directly imaging the thin massive sulphide ore zones in the gravity inversions. Instead, the gravity and magnetic inversions are used primarily as a mapping tool to delineate the mafic and ultramafic units at depth to provide an indication of the location of favourable horizons for drilling and down-hole electromagnetic methods.

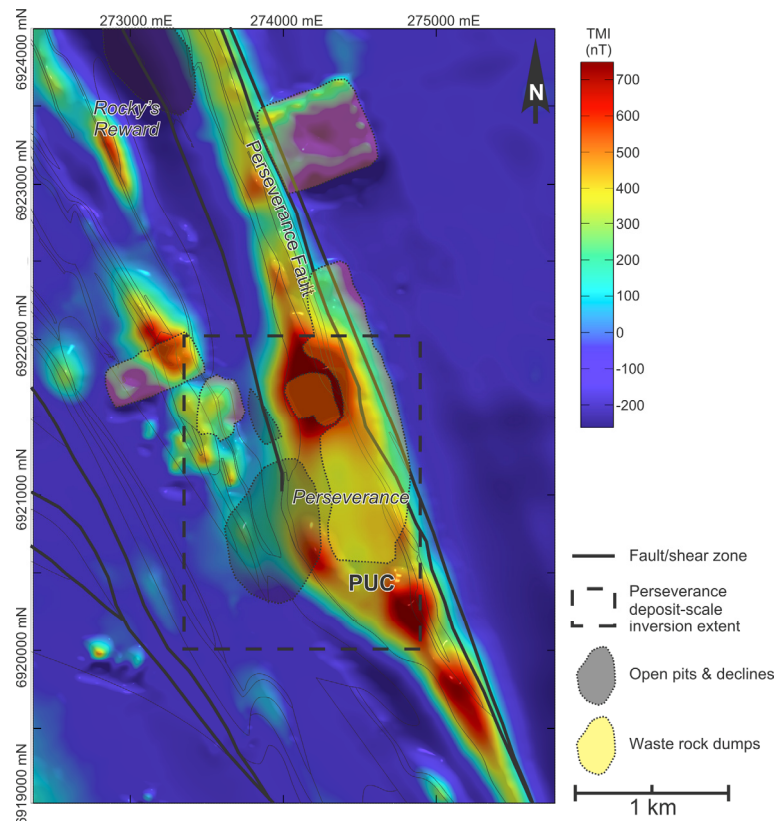


Figure 7.8. Total magnetic intensity response over the Perseverance deposit. Image shows the same area as in Figure 7.5, with the same geology outlines and annotations for reference. The data was supplied as a 10 m grid which was down-sampled for use in the inversions. There is significant noise from mine infrastructure, but these short wavelength features should be resolved as near surface anomalies in the inversion and are not expected to cause major problems. Of most importance is the variable response of the Perseverance Ultramafic Complex (PUC), with a less magnetic dunite core and more magnetic serpentinised margins, and the strong delineation of the ultramafic rocks along the Perseverance Fault. There is no response from the mafic rocks west of the deposits.

7.5 UBC–GIF INVERSION BACKGROUND

The details of the inversion method implemented by the UBC–GIF MAG3D and GRAV3D programs are covered in Li and Oldenburg (1996; 1998a) and the MAG3D and GRAV3D user manuals (UBC–GIF, 2005a, b). It is also discussed in detail in Chapters 2 and 3. Aspects of the UBC–GIF inversion algorithm relevant to this study are briefly summarised here. The algorithm poses the inverse problem as an optimisation problem that seeks a single discrete physical property model that satisfies a measure of model form and has a geophysical response that reproduces the supplied geophysical data. The model is defined by a rectangular mesh of rectangular prism cells. A single mean property value is assigned to each cell. The misfit between the observed geophysical data and the predicted response is normalised by an estimate of the standard deviation of the noise associated with each datum. This ensures that noise or uncertainty in the data is not reproduced within the model.

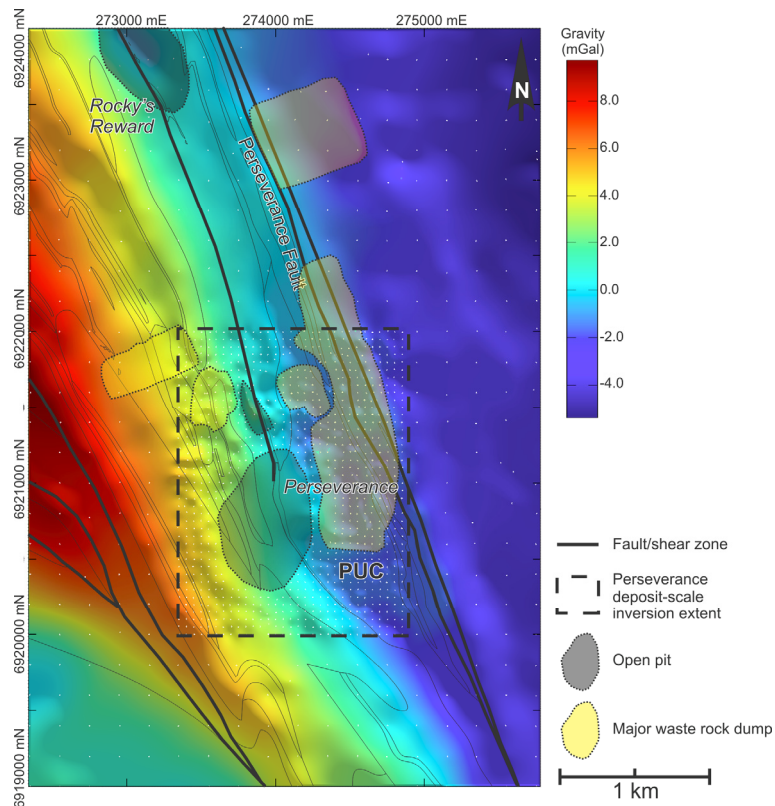


Figure 7.9. Gravity response over the Perseverance deposit. Image shows the same area as in Figure 7.5, with the same geology outlines and annotations for reference. The gravity data includes a complete terrain correction using Bouguer slab and terrain correction densities of 2.2 t/m^3 as determined using the method of Nettleton (1939). Data has been gridded for display, but the original data points (white dots) are used in the actual inversions. The displayed data is not upward continued so as to show the full detail available, but the inverted data was upward continued by half a cell width (12.5 m). No gravity data could be collected in the Perseverance open pit which lies directly over the primary ore body. Note the gravity low over the Perseverance Ultramafic Complex (PUC), and the high gravity response associated with the mafic rocks to the west.

The model form is measured by a model objective function that seeks a model with qualities of both smoothness and smallness, or closeness, to a supplied reference property model. The reference model is defined by the user to contain best estimates of the arithmetic mean physical property in each cell. How closely the recovered model should match the reference model is defined by a set of smallness weights which are unitless scalar values ≥ 1 . Higher values are used to seek a recovered model that more closely matches the reference model. With slightly different formulations of the model objective function, smoothness can be measured in slightly different ways. Previous versions of the software only used a formulation which measured how smoothly the difference between the recovered model and the reference model varied between individual cells. This “smooth-model difference” formulation is best employed where a full 3D geological model is supplied as a reference model. Newer versions of the software include a “smooth model” option which measures how smoothly the recovered

model varies between individual cells. This formulation is best applied where geological information is sparse, such as in early stage mineral exploration problems, as it allows extrapolation of observations into the rest of the model. The smooth model formulation is used exclusively throughout this study.

The user can specify a smoothness weight for each cell face in each axis direction (east, north, and vertical) to indicate whether the model properties should vary more (values > 1) or less (values between 0 and 1) smoothly. The magnitudes of the various weights are less important than their relative values, and the balance between smoothness and smallness. This balance can be further modified for the whole model using a set of α coefficients, or equivalent smoothness length scales, that define the relative smoothness in each direction.

A final requirement of the recovered model is that the property in each cell lies within strictly enforced lower and upper bounds. Whereas the objective function imposes relatively soft constraints that promote a particular model form if it can be accommodated by the geophysical data, bounds are a hard constraint imposed regardless of the geophysical data requirements. Bounds are the most powerful form of constraint but must be applied with care.

There are few published examples showing effective methods for incorporating geological constraints in UBC–GIF gravity and magnetic inversions. The examples that do exist focus on specific problems and types of data. For instance, Welford and Hall (2007) and Cella et al. (2007) build layered geological constraints based on available reflection seismic data and use these to constrain regional-scale gravity inversions. Although seismic data is available to the south of the current study area near Leonora, it is too far removed to be directly applied in this study. For local, deposit-scale modelling, Farquharson et al. (2008) apply geostatistical kriging of densities estimated from geochemical analyses along drill holes to develop a 3D density reference model to constrain their gravity inversions. Abundant drilling observations at the deposit scale are available in this study, but are restricted to the ore zones so kriging would only provide accurate constraints for the limited number of cells intersected by drilling. Phillips (1996) derives geological constraints from physical property measurements along drill core and applies average measurements to only those model cells intersected by the drill holes. This more general approach will be expanded on and applied to all available geological information in this study.

7.6 METHODS

Inverse modelling of gravity and magnetic data will be performed at three scales. The details of the core volumes, data areas, and padding zones for the three scales are listed in Table 7.2. The regional-scale models are developed to address questions about the architecture of the greenstone belts, their thickness, and their relationships to surrounding granitoids. District-scale inversions attempt to delineate orientations, extents, and geological associations of greenstone rocks in the Agnew-Leinster area. Deposit-scale models are used to aid near-mine exploration and 3D mapping around the Perseverance nickel mine. At each scale geological constraints will be built from the available geological information and included in the inversions to enhance the quality of the recovered models. The information available and the data sources are summarised in Table 7.3.

7.6.1 General inversion procedure

A detailed workflow for preparing gravity and magnetic inversions with constraints is presented in Chapter 3 and is the basis for the method summarised here. The same general procedure was used for all inversions in this study. Realistic limits were placed on the depth extent of each model. The regional-scale gravity and magnetic model extend to 30 km, the expected depth at which the Curie temperature of magnetite (580 °C) is reached based on an average geothermal gradient of ~18 °C/km (Weber et al., 2005). Magnetite is likely to be paramagnetic below this depth and will contribute little to the observed magnetic response. The district-scale models extend to 10 km depth as this should be sufficient to include the full depth of any greenstone rocks which rarely > 9 km thick in the seismic data (Figure 7.3). The deposit-scale inversion model is 2 km deep to capture the core volume surrounding the known and projected limits of the Perseverance ore body and the PUC. The cell sizes in each model were defined based on the total size of the model and the resolution required to address the specified goals of each scale of inversion.

Data area and mesh padding cells

As discussed in Chapter 3, precautions must be taken to ensure that anomalies and sources located near the edges of the model core are handled correctly. Because potential field data captures responses associated with sources in all directions surrounding the observation location, these geometries must be accommodated in the mesh and data extents. By using data

that extend beyond the core by a distance equal to the depth of the core, most of any contained anomaly wavelengths should be adequately captured. This extra data may contain information about sources that also lie outside the specified core volume. Padding cells are included around the core and extend beyond the edge of the supplied data by a distance equal to the depth of the core. The specific extents for the inversions in this study are identified in Figure 7.2.

Table 7.2. Details of the core, data and padding for each scale of inversion. The core contains the main volume of interest. The data area and padding zones are designed to accommodate sources and anomalies near the edge of the core as described in the text. All coordinates are in UTM Map Grid of Australia zone 51 J.

	Regional scale	District scale	Deposit scale
Core volume			
Size (east × north)	103 km × 208 km	50.6 km × 83.6 km	1.5 km × 2.0 km
Maximum depth below surface	30.8 km	10.6 km	2.0 km
Most common cell size (east × north × vertical)	1,000 m × 1,000 m × 500 m	400 m × 400 m × 200 m	25 m × 25 m × 25 m *
Number of cells	1.11 million	1.42 million	427,000
Southwest corner	207,000 mE, 6,850,000 mN	245,400 mE, 6,865,400 mN	273,350 mE, 6,920,000 mN
Northeast corner	310,000 mE, 7,058,000 mN	296,000 mE, 6,949,000 mN	274,850 mE, 6,922,000 mN
Data area			
Size (east × north)	165 km × 270 km	72 km × 105 km	5.5 km × 6.6 km
Median data spacing	Grav.: 2,260 m Mag.: 1,000 m (gridded)	Grav.: 2,300 m Mag.: 400 m (gridded)	Grav.: 50 m ** Mag.: 25 m (gridded)
Elevation of data (including upward continuation)	Grav.: 1,000 m Mag.: 500 m	Grav.: 200 m Mag.: 200 m	Grav.: 12.5 m Mag.: 40 m
Number of data	Grav.: 5,514 Mag.: 31,654	Grav.: 2,917 Mag.: 35,720	Grav.: 1,901 Mag.: 11,020
Southwest corner	176,000 mE, 6,819,000 mN	234,700 mE, 6,854,700 mN	271,000 mE, 6,917,700 mN
Northeast corner	341,000 mE, 7,089,000 mN	306,700 mE, 6,959,700 mN	277,000 mE, 6,924,300 mN
Padding volume			
Size (east × north)	227 km × 332 km	93.4 km × 126.4 km	9.6 km × 10.1 km
Total number of cells	1.97 million	2.23 million	1.15 million
Southwest corner	145,000 mE, 6,788,000 mN	224,000 mE, 6,844,000 mN	269,300 mE, 6,915,950 mN
Northeast corner	372,000 mE, 7,120,000 mN	317,400 mE, 6,970,400 mN	278,900 mE, 6,926,050 mN

* Most cells in the deposit-scale model are 25-m-tall, but cells above the lowest topographic point are only 10 m tall to better reproduce topography around the Perseverance mine site.

** The gravity data is patchy in places and no gravity data is available for 0.5 km² over the Perseverance open pit.

Table 7.3. Summary of the data used in this study and their sources. The regional- and district-scale modelling uses publicly available data with the exception of corporate physical property data provided by BHP Billiton. The local-scale models use the best available data.

Data type	Regional- and district-scale inversions	Deposit-scale inversions
Gravity data	<ul style="list-style-type: none"> Government ground gravity data. Median spacing = 2.3 km. Source: Australian Geophysical Archive Data Delivery System (GADDs, 2006). 	<ul style="list-style-type: none"> Government ground gravity data. Median spacing = 2.3 km. Source: Australian Geophysical Archive Data Delivery System (GADDs, 2006). BHP Billiton ground gravity data around Leinster. Minimum spacing = 50 m. Source: BHP Billiton (pers. commun., 2004).
Magnetic data	<ul style="list-style-type: none"> Government gridded aeromagnetic data. Average 100 m altitude, 400 m line-spacing. Source: Australian Geophysical Archive Data Delivery System (GADDs, 2006). 	<ul style="list-style-type: none"> Government gridded aeromagnetic data. Average 100 m altitude, 400 m line-spacing. Source: Australian Geophysical Archive Data Delivery System (GADDs, 2006). BHP Billiton gridded aeromagnetic data around Leinster. Average 40 m altitude, 40 m line-spacing. Source: BHP Billiton (pers. commun., 2004).
Topography	<ul style="list-style-type: none"> Shuttle Radar Topography Mission public domain 3 arc second (~83 m) data. Source: USGS (2007) and Farr et al. (2005). 	<ul style="list-style-type: none"> Shuttle Radar Topography Mission public domain 3 arc second (~83 m) data. Source: USGS (2007) and Farr et al. (2005). BHP Billiton topography contours (pers. commun. 2004).
Physical properties	<ul style="list-style-type: none"> Lab measurements on 157 surface and drill core samples from the southern Agnew-Wiluna greenstone belt collected in this study and described in Chapter 4. BHP Billiton database of > 100,000 density measurements and > 50,000 susceptibility measurements from drill core in the Leinster area. Described in Chapter 4. Source: BHP Billiton (pers. commun., 2005). 	
Surface geology map	<ul style="list-style-type: none"> Geological survey 1:100,000 scale outcrop map series compilation for the East Yilgarn. Source: GSWA (2004) 	
Drilling geology logs	<ul style="list-style-type: none"> None 	<ul style="list-style-type: none"> BHP Billiton drill hole collars, surveys, and geology logging codes for holes in the Leinster area. Source: BHP Billiton (pers. commun., 2005).

Regional data trends

An assumption of any inversion model is that all of the supplied data can be reproduced within the parameter space defined by the mesh. Data contributions from sources outside the padded mesh must be estimated and removed from the data. The regional-removal procedure of Li and Oldenburg (1998b) was used throughout this study. This procedure has the benefit of modelling the source positions and providing a regional response that is based on an actual potential field response rather than some mathematical filter. The three local meshes listed in Table 7.2 are nested in such a way that the larger meshes can be used to calculate the external

data contributions for the smaller meshes. However, an additional large initial inversion is required to determine the external data contributions for the regional-scale model. This initial inversion mesh was designed in accordance with the padding and data guidelines outlined above and, including padding cells, covered a total area of $536 \text{ km} \times 574 \text{ km}$ to a depth of 40 km. The depth corresponds to the approximate thickness of the crust in the seismic reflection data (Figure 7.4). The data for this initial inversion was prepared in the same way as for all models (see below), and the inversions were run using the same approach used throughout this study including basic geological constraints from surface mapping and a layered earth domain model. As the data for this initial inversion did not have their own regional trend removed, the result is only useful for determining the regional trend for the local models listed in Table 7.2, and it will not be presented here.

Data preparation

The magnetic data was only available in gridded form with either 80-m-spacing for the government data, or 10-m-spacing for the deposit scale BHP Billiton data. For each scale of inversion the data was upward continued to a height of half the width of the smallest mesh cells and trimmed to the extent listed in Table 7.2. This removed short wavelength anomalies that could not be accommodated by the smallest cell sizes used in the inversion. The gridded magnetic data was down-sampled using a spline-based interpolator to extract a single data value over the centre of every column of cells in the mesh. For the specified cell size this gives the maximum resolution using the fewest data. An uncertainty of $5 \text{ nT} \pm 5 \%$ of the observation value was specified for each observation. Although a regional data trend was removed from the data, this does not account for the average data level which indicates whether the residual data are higher or lower than the regional trend, or the datum relative to which the original data were reported. This average level cannot be accommodated in the inversions as it relates to sources outside the mesh so this mean level was removed by subtracting the mean value from each dataset. At each scale of inversion the average data level was then adjusted in increments of $\pm 50\text{-}100 \text{ nT}$ so as to minimise the occurrence of spurious source features within the padding cells as indicated in Chapter 3. Typically a bias of +50 to +200 nT was appropriate.

The gravity data were available as original ground observation stations with standard gravity reduction and simple Bouguer slab corrections applied using a density of 2.67 t/m^3 . This correction density was acceptable for the larger scale models where the topography is

basically flat: the entire topographic relief is less than a single model cell height. Complete terrain corrections were calculated using an automated Hammer terrain correction with the same density. For the deposit-scale data, preliminary gravity inversions using a Bouguer slab and terrain correction density of 2.67 t/m^3 showed a strong correlation between the recovered density distribution and the applied terrain corrections. High density anomalies were recovered directly below locations where significant terrain corrections had been added to the data. The standard correction density of 2.67 t/m^3 is thought to be too high given the presence of up to 70 m of low density ($\sim 2.0\text{-}2.2 \text{ t/m}^3$) regolith, and waste rock dumps of low density ($\sim 1.8 \text{ t/m}^3$) crushed rock up to 40 m tall (Figure 7.9 and Figure 7.10). The profile method of Nettleton (1939) was used to determine the densities associated with topographic features on three profiles across the deposit (Figure 7.10). For each profile the gravity data was processed using a suite of different Bouguer slab and terrain correction densities. A correction density of 2.2 t/m^3 provides the least correlation between the topography and the fully terrain corrected gravity data, and the deposit-scale data was reprocessed using this value for the Bouguer slab and Hammer terrain correction.

The gravity data in the district- and deposit-scale datasets were upward continued to half the cell width to remove small wavelength features. Upward continuation to a height of a full cell width was required for the regional-scale and initial inversions as preliminary inversions with lower levels of upward continuation recovered noisy models. This is likely due to the presence of several patches of very closely spaced data that cannot be adequately represented by the coarse cell size. The BHP Billiton data and recent government data were assigned a data uncertainty of 0.03 mGal. Older government data were assigned uncertainties of 0.05-0.1 mGal based on supplied accuracy estimates (GADDS, 2006). The gravity data contain a mean data level that indicates that the data are significantly more negative than the IGSN71 absolute gravity datum to which the observations are tied (GADDS, 2006), as indicated in the vertical axis of Figure 7.10. This negative anomaly cannot be reproduced within the inversions and is removed by subtracting the mean gravity value from each dataset.

Inversion settings

The inversion calculation is performed in two stages. The first stage calculates the sensitivity relationships between each cell and each observation. The calculation uses the mesh definition, observations, and topography data. A distance weighting function is also calculated

during this stage. It is a more rigorous version of the depth weighting function described by Li and Oldenburg (1996; 1998a) and is presented in the inversion user manuals (UBC–GIF, 2005a, b). The distance weighting function provides a better representation of the data sensitivity where topography is present or where the supplied data is irregularly distributed or contains gaps.

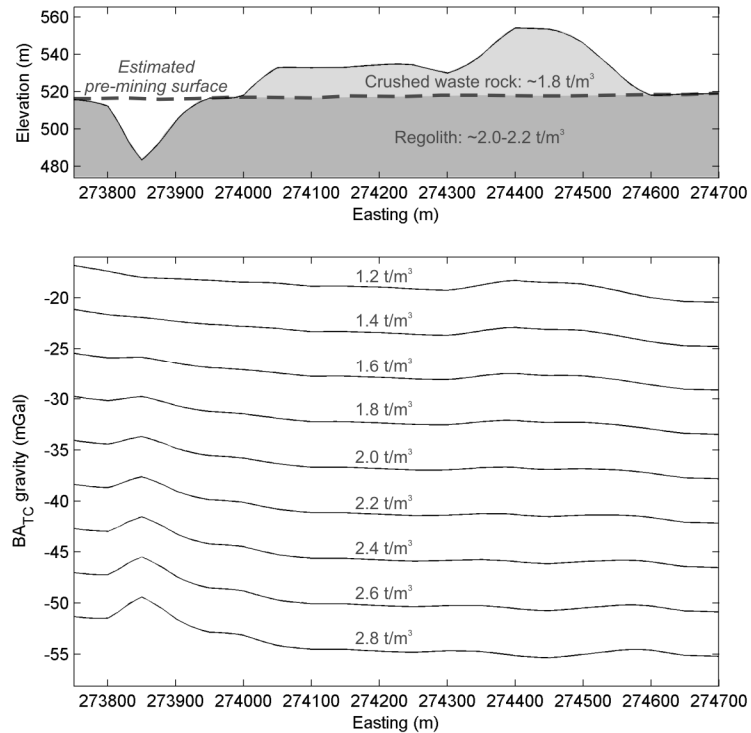


Figure 7.10. Application of the Nettleton (1939) method to determine an appropriate Bouguer slab and terrain correction density for one profile across the deposit. The total topographic relief is ~ 70 m and includes a concrete-lined underground decline and a crushed rock waste pile. Pervasive low density regolith is developed to ~ 70 m below the pre-mining surface. Bouguer slab and terrain corrections were applied to the data using the suite of correction densities shown. The most appropriate correction density is that which minimises correlations between topography and the gravity value. A value of ~ 2.0 t/m^3 is suggested along this profile, but slightly higher densities around 2.2 t/m^3 are required on other profiles. The left and right ends of the profile have northing coordinates of 6,921,400 mN and 6,922,000mN.

The second stage of the inversion process is the actual inversion calculation. This is performed using the result of the prior sensitivity calculation and the observations. There are a number of tuning parameters that can be set for each inversion. The most critical are length scales that determine the relative proportions of smallness to smoothness relative to the size of the cells used in the mesh. As suggested in the inversion user manuals (UBC–GIF, 2005a, b) a value of $2\times$ the width of the smallest cells in each mesh was applied in each direction in all inversions.

7.6.2 Geological constraints

The data-based approach for deriving geological constraints for mineral exploration problems is described in Chapters 2 and 3. A direct 3D physical property representation of the raw geological observations is constructed in a format consistent with the requirements of the inversions. All constraints are constructed using the automated GIFTtools:ModelBuilder package developed in Chapter 5 using the user manual presented in Appendix B, and both should be consulted for details on the technique. The discussion below will focus on the issues and decisions regarding the development of the constraints used in this study. The primary sources of geological constraints in this study are density and magnetic susceptibility measurements, outcrop maps, and drilling geology logs (Table 7.3). Some additional inferences on the general architecture and structural trends are based on map patterns, existing seismic data interpretations (Figure 7.4), and background geological understanding (Section 7.2). This knowledge will be used as a framework for the more detailed observations. The full set of constraints employed in the inversions is summarised in Table 7.4.

Physical properties

Constraints imposed using a reference model or bounds are specified in terms of expected physical property values. Where sufficient located measurements are contained within individual cells in a model it is relatively straightforward to assign physical property constraints for those cells. The reference model value in each cell would be the arithmetic mean of the measured values. The lower and upper bounds represent limits on the possible range of that mean value, so reasonable values can be assigned based on the calculated confidence interval on the mean at a particular confidence level (i.e., 95 %). This method is automatically applied in the ModelBuilder software to create constraints along drill holes where physical property measurements are available in the deposit-scale inversion model.

Geological observations of rock types within a cell, from maps or drilling without corresponding measurements of physical properties, provide just as important information as raw property measurements, but must be converted to estimates of the physical properties associated with the observed rocks. This can be done manually or automatically depending on the information available and the problem to be addressed.

Table 7.4. Summary of the geological constraints used in all inversions in this study. See text for details.

Constraint	Regional-scale inversions	District-scale inversions	Deposit-scale inversions
Physical property estimates	<ul style="list-style-type: none"> Manually assigned based on deposit-scale measurements 	<ul style="list-style-type: none"> Manually assigned based on deposit-scale measurements 	<ul style="list-style-type: none"> Automatically calculated based on deposit-scale measurements Manual estimates for regolith and transported cover in surface map
Domain models	<ul style="list-style-type: none"> 2 layer model 	<ul style="list-style-type: none"> 2 layer model 	<ul style="list-style-type: none"> 2 regions ('west' and 'east') divided by inferred Perseverance Fault Automatic regolith domain to 70 m below pre-mining surface
Maps	<ul style="list-style-type: none"> Surface geology map, Archean basement only 	<ul style="list-style-type: none"> Surface geology map, Archean basement only 	<ul style="list-style-type: none"> Surface geology map, regolith and basement
Drilling property measurements	<ul style="list-style-type: none"> Only used to estimate map properties 	<ul style="list-style-type: none"> Only used to estimate map properties 	<ul style="list-style-type: none"> Used to estimate map and drilling geology properties Used directly in the model where they exist
Drilling geology logs	<ul style="list-style-type: none"> Not used 	<ul style="list-style-type: none"> Not used 	<ul style="list-style-type: none"> Used wherever available
Smallness weights	<ul style="list-style-type: none"> Domains: 1-5 Map: 5 	<ul style="list-style-type: none"> Domains: 1-2 Map: 5 	<ul style="list-style-type: none"> Domains: 1 Map: 5 Drilling measurements: 10 Drilling geology: 5
Smoothness weights	<ul style="list-style-type: none"> Use reference property gradients where possible Smoothness at edge of data cells Smoothness at edge of buffers 	<ul style="list-style-type: none"> Use reference property gradients where possible Smoothness at edge of data cells Smoothness at edge of buffers 	<ul style="list-style-type: none"> Use reference property gradients where possible Smoothness at edge of data cells Smoothness at edge of buffers
Aspect ratios (east:north:vertical)	<ul style="list-style-type: none"> 2:5:1 	<ul style="list-style-type: none"> 2:5:1 	<ul style="list-style-type: none"> Regolith: 2:2:1 West of fault: 1:2:1 East of fault: 1:1:1
Inverse distance weight scaling	<ul style="list-style-type: none"> Yes 	<ul style="list-style-type: none"> Yes 	<ul style="list-style-type: none"> Yes
Buffer-based extrapolation distance	<ul style="list-style-type: none"> Surface map: < 500 m (1 cell height) 	<ul style="list-style-type: none"> Surface map: < 500 m (~2 cell heights) 	<ul style="list-style-type: none"> Surface map: < 100 m Drilling measurements: < 100m Drilling geology logs: < 200 m
Buffer shape	<ul style="list-style-type: none"> Spherical 	<ul style="list-style-type: none"> Spherical 	<ul style="list-style-type: none"> Cover: Flat plate West of fault: NNE-plunging ellipsoid East of fault: Spherical

Manually-specified estimates of the reference property value (the expected value) and the lower and upper bounds for different rock types can be applied directly within the model wherever those rock types are observed. This is best suited to problems where: 1) limited physical property information is available for a given rock type; 2) spatial variability in the properties associated with a rock type is considerable; and 3) the number of distinct rock types is small enough that assigning properties manually is practical. This manual approach is employed to translate outcrop map observations into property constraints in the regional- and district-scale inversions. A list of all 216 Archean basement rock codes encountered in the outcrop map was generated, and properties assigned based on the summary in Table 7.1. The values used for the most commonly encountered rock codes are listed in Table 7.5. Most of the mapped rock codes are only slight variants of the main rock types listed in Table 7.1, so there was significant duplication of property estimates which simplified the task. Reference properties were assigned using the mean value, and bounds were assigned based on the 10th and 90th percentile values. Where possible, estimates of the properties for those rock types with limited measurements (such as the granite and gneiss densities) were augmented with information from typical published values. No constraints were applied if a reasonable property estimate could not be made for a rock type.

If a large database of physical property measurements is available, the number of individual rock types is large, and the available measurements are expected to capture most of the variability in properties associated with each rock type, then the property estimates may be calculated automatically. In this study, this automatic method is used only for geological observations from mapping and drilling in the deposit-scale model where the spatial variability of properties within different rock types is expected to be small. The ModelBuilder software combines all coincident physical property measurements and geological observations and all physical property measurements related to each rock type are used to calculate the mean value for that rock type and a confidence interval on that mean at a 95 % confidence level. The estimates are then applied throughout the model: the mean of the reference property estimates for geological observations in a cell is used to define the reference property value for that cell, and the most extreme confidence intervals are applied as the bounds.

Table 7.5. Manually-assigned physical property estimates for the most commonly encountered basement rock codes identified in the supplied surface geology map (GSWA, 2004). These properties were used in the initial regional-removal inversion as well as the regional- and district-scale models. Property estimates are mostly based on Table 7.1. Due to the height of the cells used in these larger models (> 500 m) relative to the thickness of the regolith (< 70 m) rock codes associated with regolith can be ignored. The descriptions are simplified from Riganti and Groenewald (2004).

GSWA map rock code	Description	Density (t/m ³)			Magnetic susceptibility ($\times 10^{-3}$ SI)		
		Lower bound	Reference	Upper bound	Lower bound	Reference	Upper bound
_C/A-g	Colluvium & weathered granitoid	2.50	2.65	2.87	0.002	0.5	5
_R-d-pg	Silcrete & weathered granitoid	2.50	2.65	2.87	0.002	0.5	5
_R-g-pg	Sand over granitoid	2.50	2.65	2.87	0.002	0.5	10
_R-z-u	Silica caprock over ultramafic rock	2.54	2.76	3.11	0.3	20	300
A-b	Mafic rock	2.54	2.80	3.24	0.05	1	70
A-bb	Basalt	2.73	2.95	3.21	0.1	0.8	5
A-bba	Basalt, aphyric	2.73	2.95	3.21	0.1	0.8	5
A-bbg	Basalt, amygdaloidal	2.73	2.95	3.21	0.1	0.8	5
A-bs	High-Mg basalt	2.70	2.95	3.21	0.1	2	20
A-f	Felsic volcanic & volcanoclastic rocks	2.64	2.72	2.97	0.05	0.7	5
A-fn	Felsic volcanic & volcanoclastic rocks	2.64	2.72	2.97	0.05	0.7	5
A-g	Granitoid	2.50	2.65	2.87	0.002	0.5	5
A-gg	Granodiorite	2.50	2.70	2.90	0.002	1	10
A-gm	Biotite monzogranite	2.50	2.65	2.90	0.002	1	10
A-gmd	Biotite monzogranite	2.50	2.65	2.90	0.002	1	10
A-gmp	Porphyritic monzogranite	2.50	2.65	2.90	0.002	1	10
A-gna	Granitoid	2.50	2.65	2.87	0.002	0.5	5
A-gr	Syenogranite	2.50	2.65	2.87	0.001	0.5	10
A-gtp	Tonalite	2.55	2.75	2.95	0.002	1	10
A-mbba	Amphibolite (from basalt)	2.73	2.90	3.21	0.1	0.6	5
A-mgsn	Foliated & gneissic granite	2.56	2.80	2.92	0.01	2.3	10
A-mgss	Foliated granitoid	2.50	2.65	2.87	0.002	0.5	5
A-mu	Ultramafic rock	2.54	2.76	3.11	0.3	20	300
A-od	Dolerite	2.72	2.96	3.15	0.2	0.8	5
A-og	Gabbro	2.72	2.96	3.15	0.2	0.8	5
A-s	Sedimentary rock	2.50	2.75	3.25	0	1	10
A-up	Peridotite	2.54	2.76	3.11	0.3	20	300
A-xmgss-mba	Foliated granite with minor mafic rock	2.50	2.80	3.24	0.002	1	70

For the deposit-scale inversion model, the available physical property database was able to provide reference property and bounds density estimates for 1018 individual map and drilling geology codes (most representing only slight variants of more general rock types). Fewer magnetic susceptibility measurements are available so reference property and bounds estimates were calculated for only 238 of the map and drilling codes. Mapping codes that had

too few measurements to reliably calculate physical property estimates were assigned manual estimates from Table 7.5, augmented by property estimates for regolith using Emerson et al. (2000) and Telford et al. (1990). Where both physical property measurements and estimates derived from geological observations are present in the same cell the values are combined to give the best possible property constraints.

Domain models

The simplest geological constraint that can be applied in an inversion is a uniform model identifying an expected reference property value and bounds on that value. Such a constraint is implicitly applied in every default UBC–GIF inversion by the defined default reference property and bounds values. It provides no spatial information and is unlikely to be restrictive. A logical progression is to specify different default reference property and bounds values in different parts of the model. This is achieved within the ModelBuilder software by supplying a domain model consisting of a basic 3D model in which each cell is assigned a domain ID. A look-up table links each domain ID to a set of default properties to be used in the absence of more detailed observations.

Simple layered earth domain models were created for the larger-scale models based on the geometries observed in the seismic data (Figure 7.4). Although the seismic lines lie south of all the inversion models, they suggest that the greenstones in the EGST east of the Ida Fault System are generally < 9 km thick, and commonly < 4 km in the north. Profile forward modelling of potential field data by Dentith et al. (1992b), Bell (2002), and Peschler et al. (2004) provide similar thickness estimates for greenstone sequences throughout the Yilgarn Craton. In the regional-scale model, an upper layer with a depth of 12 km was created to accommodate the possible presence of greenstone sequences with higher and more variable densities and susceptibilities (Table 7.6). A second layer to a depth of 30 km was assigned more restrictive properties consistent with the felsic gneiss and granulite rocks expected to be dominant at depth. In the district scale models (Table 7.7) which extend to 10 km depth, a more subtle layered domain model was created with a layer to 6 km depth likely to contain greenstones, based on the average depth estimates of Dentith et al. (1992b), Bell (2002) and Peschler et al. (2004). Below that, constraints were set so that dense and magnetic greenstone rocks can be accommodated, but granitoid and felsic gneiss rocks are more likely.

Table 7.6. Densities and magnetic susceptibilities assigned to domains in the regional-scale domain model.

Layer	Gravity inversions (density, t/m ³)				Magnetic inversions (susceptibility, ×10 ⁻³ SI)			
	Lower bound	Reference	Upper bound	Smallness weight (unitless)	Lower bound	Reference	Upper bound	Smallness weight (unitless)
0-12 km: Possible greenstone rocks	2.55	2.7	3.3	2	0	2	2000	1
12-30 km: Felsic gneiss and granulite	2.6	2.7	2.8	5	0	1	60	1

Table 7.7. Densities and magnetic susceptibilities assigned to domains in the district-scale domain model.

Layer	Gravity inversions (density, t/m ³)				Magnetic inversions (susceptibility, ×10 ⁻³ SI)			
	Lower bound	Reference	Upper bound	Smallness weight (unitless)	Lower bound	Reference	Upper bound	Smallness weight (unitless)
0-6 km: Likely greenstone rocks	2.55	2.7	3.5	1	0	2	300	1
6-10 km: Rare greenstone rocks. Mostly granitoid, gneiss and granulite	2.6	2.7	3.1	2	0	0.5	60	2

Domains can also identify portions of a model that may be affected by weathering and therefore contain significantly different properties. ModelBuilder can automatically create such a domain using a blanket layer of a certain thickness below topography or by assigning a user-defined surface of the maximum depth to basement. The domain truncates any other domains. Regolith in the Yilgarn Craton penetrates up to 150 m but more commonly 70 m (Dentith et al., 1992a; Anand and Paine, 2002). This information is consistent with observations in drill holes near the Perseverance mine. As this depth is significantly less than the height of cells used in the regional- and district-scale inversions (200-500 m) a weathering domain is not included in those models. But a 70-m-thick regolith domain is included in the deposit-scale inversions below a pre-mining topographic surface. The reference property is assigned as the default basement rock value to minimise the recovered regolith thickness, but the lower bound is relaxed to allow low density regolith material if required. Below the regolith domain, the basement was divided into western and eastern domains based on the inferred position of the Perseverance Fault. West of the fault greenstone rocks are expected; east of the fault granitoid and gneissic rocks are expected. The properties of the deposit-scale domain model are summarised in Table 7.8.

Table 7.8. Densities and magnetic susceptibilities assigned to domains in the deposit-scale domain model.

Layer	Gravity inversions (density, t/m ³)				Magnetic inversions (susceptibility, ×10 ⁻³ SI)			
	Lower bound	Reference	Upper bound	Smallness weight (unitless)	Lower bound	Reference	Upper bound	Smallness weight (unitless)
0-70 m: Possible regolith and transported cover	1.6	2.80	3.5	1	0	0	100	1
Below 70 m, west of Perseverance Fault: Likely greenstone rocks	2.55	2.80	3.5	1	0	2	400	1
Below 70 m, east of Perseverance Fault: Likely granitoid or gneiss	2.55	2.65	2.8	1	0	1	20	1

Domains also carry the connotation of structural domains and the ModelBuilder includes functionality to assign different structural orientations within different domains. This usage will be discussed in Section 7.6.3.

Maps

Mapping is the most readily available source of information for geological constraints. Even in greenfields exploration areas, basic surface maps may be available from government surveys and previous investigators in an area. The ESRI shapefile format is a standard digital storage format for polygon-based maps. ModelBuilder includes a capability to interpolate a supplied polygon shapefile, draped on a topographic surface or at a particular depth, onto an inversion mesh and populate cells with the appropriate physical property estimates. Within each cell, nine regularly spaced points of the map are interrogated to identify the rock code at each point. A weighted average reference property is assigned based on the frequency of occurrence of each rock code in the cell, and the most extreme bounds estimates observed in the cell are assigned as the bounds for that cell. Cells which contain rock codes for which no property estimates are available are left with the default constraint values.

A digital compilation of government survey 1:100,000 scale surface maps (GSWA, 2004) was used at all scales of inversion in this study, and provided the primary constraints for the regional- and district-scale inversions. Although basement geology interpretations are available for the region (Ferguson, 1998; Liu et al., 2000; Liu et al., 2002; Whitaker and Bastrakova, 2002; C. Perring, unpub. map, 2005), they were not used to provide constraints in this study. Since basement map interpretations are commonly based on 2D interpretation of

potential field data, using them to constrain potential field inversions can merely reinforce the existing interpretations. Basement geology interpretations also lack depth information. Features interpreted in the maps may actually lie at different levels within the crust so it is not clear at what depth the basement map constraints should be applied.

Drilling

Drilling provides the only way to develop geological constraints based on direct observation in the subsurface. Physical property measurements from drilling near the Perseverance mine are used to assign physical property estimates at all model scales, and are used directly as located constraints in the deposit-scale inversion. Geological logs from drilling provide another critical constraint for the deposit-scale inversions. Information from drilling geology logs is applied in a similar way to that used for map information. The ModelBuilder software calculates the trace of each available drill hole using the standard minimum curvature method (Sawaryn and Thorogood, 2005) and interrogates the drill hole logs at regular intervals down each hole, nominally every 20 cm. The geological observation at each sample point is assigned the appropriate physical property estimate. A bulk property estimate is assigned to each cell using all available property measurements and estimates in that cell.

Densities versus density contrasts

The UBC–GIF gravity inversion software recovers density contrasts, not true densities so constraints must be supplied as density contrasts rather than true densities. Density contrasts are obtained by subtracting some background density value from the reference model and bounds. Notionally, the background density value should be the average density in the ground contained by the mesh, but it is also related to the average data level within the original gravity data. Although a regional trend and the mean gravity value must be subtracted from the data to remove any influence from outside the specified mesh, this also removes any link between the background data level and the Bouguer slab and terrain correction densities. The appropriate background density is determined using a suite of at least three geologically-constrained inversions processed using different background density conversions, as demonstrated in Chapter 3. One inversion is run after subtracting an estimate of the average density in the volume from the density constraints and additional inversions are run after subtracting that background density $\pm 0.05 \text{ t/m}^3$ from the original constraints. The recovered models are

compared and the background density that gives the most even and realistic distribution of densities within the recovered model is chosen. This method is particularly effective when surface map constraints are used: the recovered surface densities will be lower than the densities at depth if the background density was too high and vice versa. In the regional- and district-scale inversions a background density of 2.70 t/m^3 was deemed the most appropriate. This corresponds well with the estimated average density in each volume. A background density of 2.80 t/m^3 was identified for the deposit scale inversions, but this is also consistent with the expected average density given the high proportion of mafic and dunite rocks in the model. Densities can be obtained from the recovered inversion models by adding back the same background density, and all models presented have undergone this conversion.

Remanent magnetisation

The physical property data presented in Chapter 4 indicate that remanent magnetisation is common in the ultramafic and sulphide-rich rocks around Perseverance. In the regional- and district-scale inversions, the volume of remanently magnetised rocks is relatively small compared to the size of the models so the effect of remanent magnetisation, although present, seems to be small. However, the deposit-scale model is expected to contain a large volume of ultramafic rocks and is specifically designed to map their distribution. A majority of the ultramafic rock samples measured in Chapter 4 contained some viscous remanent magnetisation parallel to the present-day magnetic field with a mean Koenigsberger ratio of 7.0. In an induced magnetisation inversion, as performed by the UBC–GIF algorithm, such remanent magnetisation is accommodated by unrealistically high recovered susceptibility values. Preliminary inversions recovered apparent susceptibilities >2-3 times larger than the measured susceptibilities in areas where ultramafic rocks were expected. As a result, geological constraints based only on measured susceptibilities will have values too low to be accommodated by the inversion which may even fail to obtain a solution.

A simple workaround is to include the effect of expected remanent magnetisation into the susceptibility estimates applied as constraints. If all remanent magnetisation is parallel to the present day earth field direction equation 7.1 can be rearranged as:

$$Q\kappa H_0 = \text{NRM} \quad 7.2$$

The total magnetisation is the sum of the induced and remanent magnetisation intensities:

$$\begin{aligned}
\mathbf{M} &= \mathbf{M}_I + \mathbf{NRM} \\
&= \kappa \mathbf{H}_0 + Q\kappa \mathbf{H}_0 \\
&= \kappa(1 + Q) \mathbf{H}_0
\end{aligned}
\tag{7.3}$$

The susceptibility constraints and model are then presented as apparent susceptibilities, $\tilde{\kappa}$, that include the true measured susceptibility and the apparent susceptibility attributed to remanent magnetisation:

$$\tilde{\kappa} = \kappa(1 + Q) \tag{7.4}$$

In the deposit-scale inversion this is achieved by multiplying all susceptibilities measured in ultramafic rocks by a factor of $1 + Q$, where $Q = 7$ is the average measured Koenigsberger ratio for ultramafic rocks determined in Chapter 4, prior to populating the constraint models. This approach does not allow for reverse polarity remanent magnetisation, nor any remanent magnetisation in other rock types, so only provides a partial solution, but is sufficient to extract useable models.

7.6.3 Regularisation parameters

The constraints outlined above provide the detailed geological information to be used in the inversions, however less tangible constraints can also be applied using the mathematical constructs of smallness and smoothness weights.

Smallness weights

Smallness weights are used to indicate confidence in the supplied reference property. Typical values range from 1 (limited reliability) to 20 (highly reliable), but are affected by the settings used for other parameters, especially the smoothness weights. Since some data types will be more reliable than others, smallness weights are initially based on the type of data used in a cell. For point-based data types, including drilling property measurements and geology observations, the ModelBuilder software automatically scales the specified smallness weight by a measure of the distribution of samples within each cell to indicate that well-sampled cells are more reliable than poorly sampled cells. In domain models, smallness weights can be specified differently in different domains to indicate how reliable the estimated reference property is (Table 7.6-Table 7.8).

Smoothness weights

Smoothness weights identify whether the change in recovered properties across a cell face should be smooth or sharp. The ModelBuilder software can calculate smoothness weights from the property gradients present in the reference model. High smoothness weights (1-10) are assigned to faces where the reference model properties vary smoothly, and low smoothness weights (0.1-1) are assigned to faces where the reference model properties change more sharply. This helps implement the reference model more accurately and can allow recovery of sharp breaks in the smooth property distributions where such gradients are observed in the available geological data. Moderate smoothness weights (2) are specified on faces that separate cells that contain geological constraints from those that do not. This helps to extrapolate observations outwards in the inversions. These methods were used in all inversions.

Distance scaling of smallness and smoothness weights

The default distance weighting described in Section 7.6.1 is a necessary mathematical constraint in cells that lack geological information as it allows features to be recovered at depth. It works by allowing larger deviations from the specified reference model as sensitivity to the data decreases with distance. This has an undesirable side-effect for cells that contain actual geological constraints and are situated far from the geophysical data. Usually this only occurs where constraints exist below about 100 m, as may be common for drilling data. By allowing large deviations from the reference model, geological constraints are not enforced as strongly at great depths and may be ignored by the inversion. This can be remedied by multiplying the desired smallness and smoothness weights in those cells containing reliable observation-based constraints by the squared inverse of the distance weight associated with those cells. This effectively turns off the depth weighting in those cells. Since distance weighting is itself an inverse function of distance (values $\ll 1$) this will transform the smallness and smoothness weights into large values ($\gg 1$). This does not mean that constraints in cells at great distances from the geophysical data are more reliable than those at shorter distances; it merely applies the constraints equally regardless of distance. Distance scaling of smallness and smoothness weights for cells containing geological constraints can be applied automatically in the ModelBuilder software, and is used in all inversions in this study. However, only the original unscaled smallness weights are shown in any of the figures, as these reflect the actual geological reliability.

Aspect ratios

A particular challenge involved in modelling greenstone belts using potential field data comes from their typical geometry. As depicted in the seismic reflection data (Figure 7.4) greenstone sequences are often relatively thin supracrustal features that resemble plate-like bodies. The gravity response of a plate-like feature is just a constant and the magnetic response is zero. Only the edges of a plate give a response that can be modelled with potential field data. As a result, where greenstone belts are laterally extensive and show little variation in internal composition or thickness, they cannot be reliably recovered in an inversion without additional information. Chapter 2 showed that the best way to facilitate recovery of such geometries is to specify the aspect ratio expected for features in different domains within the model. The aspect ratios defined in each domain are indicated in Table 7.4. ModelBuilder automatically adjusts the smoothness weights within each domain to effectively produce the desired aspect ratios using the method presented in Chapter 2.

7.6.4 Extrapolating constraints

So far a robust set of constraints have been described based solely on the geological observations and appropriate inferences about how those properties might vary spatially. In data-rich environments many such constraints might be available, and highly constrained models can be created. Where geological observations are scarce or sparsely distributed, the number of cells containing observation-based constraints might be quite small. Although smooth model inversions will provide some extrapolation it will be subtle and is performed without orientations derived from geological observations. It is useful to expand the number of constrained cells in a geologically-reasonable way prior to the inversion. Geostatistical kriging provides one option for extrapolating measured property values between observation locations or drill holes, and this approach has been successfully demonstrated for mineral exploration inversions by Farquharson et al. (2008). However, 3D kriging is less effective where data are scarce or restricted to particular positions in a model such as the ground surface.

The ModelBuilder software provides an alternate approach for extrapolating the geological constraints using distance weighting functions inside ellipsoidal buffers around each constrained cell. The shape of the buffers is calculated from observed or inferred structural orientations, including the strike, dip, and pitch, specified within each domain. The maximum size of the buffers is specified according to the data type since observations of some data types

(such as maps) might be more widely applicable than others (individual physical property measurements). The whole process is managed automatically once the shape and size of the buffers is specified; the buffers used at each scale in this study are described in Table 7.4. The resulting extrapolated models can effectively represent geometries associated with dipping strata. Due to the size of the cells relative to the buffer size, the buffers have only a moderate influence at the larger scales. They double the number of constrained cells at the regional scale and triple the number constrained cells at the district scale. At the deposit scale, where the buffers are relatively large compared to the cell sizes, they increase the number of cells constrained by observations by a factor of 7.

7.6.5 Predictive rock models

Based on the physical property data in Chapter 4 and described in Section 7.3, there are distinct differences in the physical properties associated with some rock types in the Agnew-Wiluna greenstone belt. Ignoring the volumetrically negligible sulphide-bearing rocks, the most magnetic rocks are the ultramafic rocks, whether serpentinised or not. The next most magnetic rocks are granitoids, although the inversion results indicate that there are some gneissic rocks in the region with moderately high magnetic susceptibilities that were not sampled in the physical property work carried out in this study. The densest rocks are usually the mafic and mafic-derived rocks. Regolith comprises the least dense group of materials. A physical property discriminant diagram was presented in Chapter 4 based on the available petrophysics. A simplified version (Figure 7.11) will be used to classify the densities and susceptibilities recovered from the inversions into a 3D rock model.

Lithological classification of inversion models offers several important benefits. It translates the physical property models into a form that can be directly compared to mapping or other geological interpretations. This can identify problem areas in the model. It also more clearly identifies any new knowledge gained from the inversions. Such classifications also combine the information present in two independent datasets into a single model, maximising the information available. Susceptibility models readily identify the magnetic ultramafic rocks, and density models readily identify the mafic rocks, but only when the two models are combined can the dense and magnetic olivine-bearing ultramafic rocks be identified. This is important in the Agnew-Wiluna greenstone belt where such rocks are associated with the four largest nickel sulphide deposits: Perseverance, Mt. Keith, Yakabindie and Honeymoon Well.

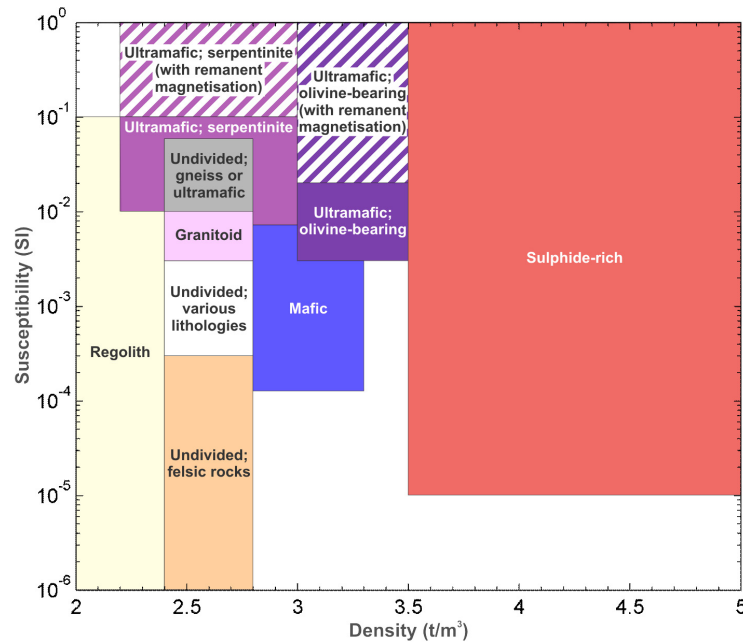


Figure 7.11. Simplified discriminant diagram for identifying certain distinct lithologies based on densities and susceptibilities. This classification assumes that sulphides and alteration are insignificant, and that inversion cells do not contain a mix of lithologies. The striped regions allow for higher apparent susceptibilities in ultramafic rocks due to the presence of viscous remanent magnetisation. The figure is adapted from Chapter 4.

Although there are many challenges associated with classifying physical property models the classification used here attempts to minimise the impact of many of these issues. The classification is based on identifying the most anomalous rocks in various categories. This helps avoid the extreme non-uniqueness present when classifying cells that contain a mix of lithologies. Mixing of different rock types will generally homogenise the properties of a cell towards the global median values of around 2.7 t/m^3 and $1 \times 10^{-3} \text{ SI}$. Such properties could be associated with a large range of different rock types and no attempt is made to classify these rocks. Rocks with more anomalous properties will only be identified as such if they are relatively pure. It is assumed that minimal sulphides and alteration (other than serpentinisation) are present in the rocks.

The available physical property data are unlikely to represent all possible rocks within the model and the classification cannot correctly identify rocks for which no physical property data are available. It is noted that the susceptibility models contain large moderately magnetic bodies at depth that are too voluminous to realistically be ultramafic rocks. They are instead inferred to represent gneiss or granulite; however, no reliable physical property data is available for these rocks. They are important enough that their presence is accommodated in the classification with estimated properties of $2.4\text{--}2.8 \text{ t/m}^3$ and $10\text{--}60 \times 10^{-3} \text{ SI}$, based primarily

on standard literature values (Kelso et al., 1993; Peschler et al., 2004). Likewise, there are no reliable property measurements for iron formations, which are likely to have high densities and extreme physical property values. These will likely be misidentified as sulphide-rich or ultramafic rocks, but due to the rare occurrence of iron formations in this area, the number of adversely affected cells will be minimal. Such general classification schemes are bound to misidentify some rocks so the results should be treated as best estimates consistent with the currently available physical property data, geophysical data, and geological constraints.

7.7 INVERSION MODELLING

Images of the actual geological constraints used in each inversion will be presented in this section together with the results from the constrained inversions. Although only one final density or magnetic susceptibility model is presented at each scale, it represents the most reliable model available and includes the best available representation of the features that were observed in a suite of inversions performed with slightly different inversion parameters and constraints. They provide a best estimate of the subsurface properties consistent with the available geological knowledge and geophysical data. Any improvement in the existing knowledge and data will improve the quality and reliability of the models.

7.7.1 Regional-scale: Agnew-Wiluna greenstone belt

As indicated in the surface geology map in Figure 7.2, there are very few outcropping Archean basement rocks in the Agnew-Wiluna greenstone belt region. The reference model and smallness weights applied in the surface layer of the gravity and magnetic inversions are shown in Figure 7.12 and Figure 7.13, respectively. Non-default bounds and smoothness weights were also used as described in Sections 7.6.2 and 7.6.3, but examples of these constraints are only shown for the deposit-scale inversions (Section 7.7.3). A basic layered earth model defined the default densities throughout the model, with aspect ratios indicating the expected north-south dominant strike. Spherical 500-m-diameter buffers were used to extrapolate the observed surface constraints; however given the $1 \text{ km} \times 1 \text{ km} \times 500 \text{ m}$ cell size this only propagated the surface values vertically down one cell. The results of the constrained gravity and magnetic inversions are depicted as a series of horizontal property slices at different depths in Figure 7.14 and Figure 7.15, respectively. Three cross sections through the density and susceptibility models, at Wiluna, Mt. Keith, and Lawlers, are shown in Figure 7.16.

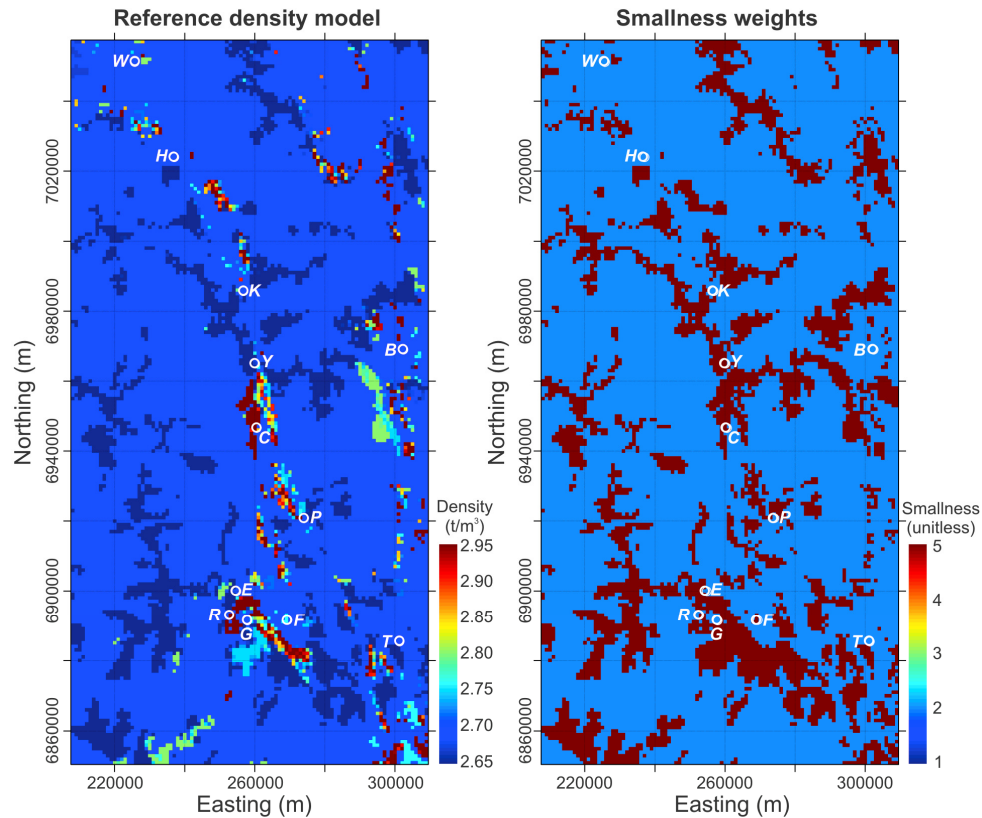


Figure 7.12. The surface layer of the reference density model and smallness weights used to constrain the regional-scale gravity inversion. The constraints are based on surface mapping, a basic layered earth model, and best estimate physical properties. The densities are converted to density contrasts using a background density of 2.70 t/m^3 ; this value was also used as the default reference property where no geological information was available. The smallness weights indicate the relative reliability of the supplied reference model: blue cells are effectively unconstrained (default values); brown cells contain mapped basement outcrops. Regolith is ignored in this model as the expected $< 70\text{-m}$ -depth of weathering is negligible compared to the 500 m cell heights. Locations of selected mines/deposits are indicated with white circles: W = Wiluna; H = Honeymoon Well; K = Mt. Keith; B = Bronzewing; Y = Yakabindie; C = Cosmos; P = Perseverance; E = Emu (Agnew group); R = Redeemer (Agnew group); F = Fairyland (Lawlers group); G = Great Eastern (Lawlers group); T = Waterloo.

The density model captures the long continuous traces of the greenstone belts, especially their dense mafic and mafic-derived rock facies (Figure 7.14). A continuous density low cuts through the middle of the southern part of the belt, and correlates with the position of the Leinster Granodiorite in surface mapping and continues to depths of $> 5 \text{ km}$. The Agnew and Lawlers gold deposits coincide with the thickest portions of the greenstone belt as imaged in the density model. This same association is observed for the Wiluna gold deposits in the north. A long moderate density lineation in the west of the model correlates with the position of the Waroonga Shear Zone and extends to $> 10 \text{ km}$ depth. The hook-like feature at its northern end seems to indicate folding of the shear zone, or an irregular control imposed on granitoid emplacement by a pre-existing structure (Figure 7.14).

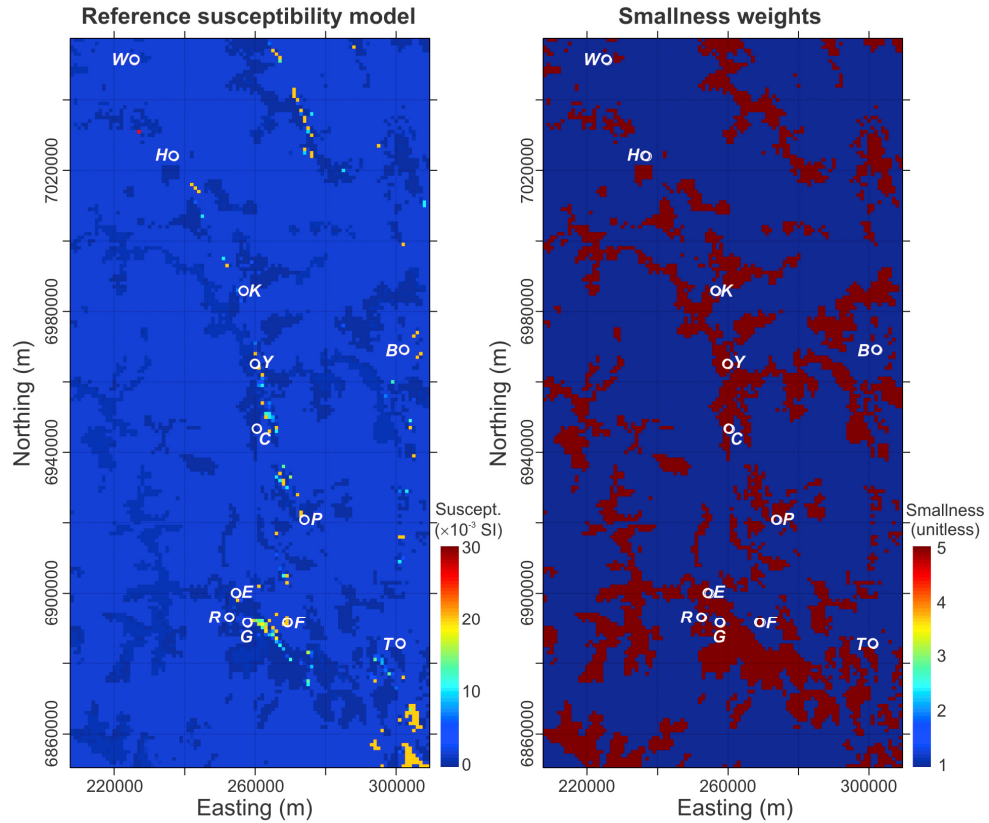


Figure 7.13. The surface layer of the reference susceptibility model and smallness weights used to constrain the regional-scale magnetic inversion. The surface layer of the constraints are based on surface mapping, a basic layered earth model, and best estimate physical properties. A default susceptibility of 0 SI was used wherever geological information was lacking. The smallness weights indicate the relative reliability of the supplied reference model: blue cells are effectively unconstrained (default values); brown cells contain mapped basement outcrops. Regolith is ignored in this model as the expected <70-m-depth of weathering is negligible compared to the 500 m cell heights. Locations of selected mines/deposits are indicated with white circles: W = Wiluna; H = Honeymoon Well; K = Mt. Keith; B = Bronzewing; Y = Yakabindie; C = Cosmos; P = Perseverance; E = Emu (Agnew group); R = Redeemer (Agnew group); F = Fairyland (Lawlers group); G = Great Eastern (Lawlers group); T = Waterloo.

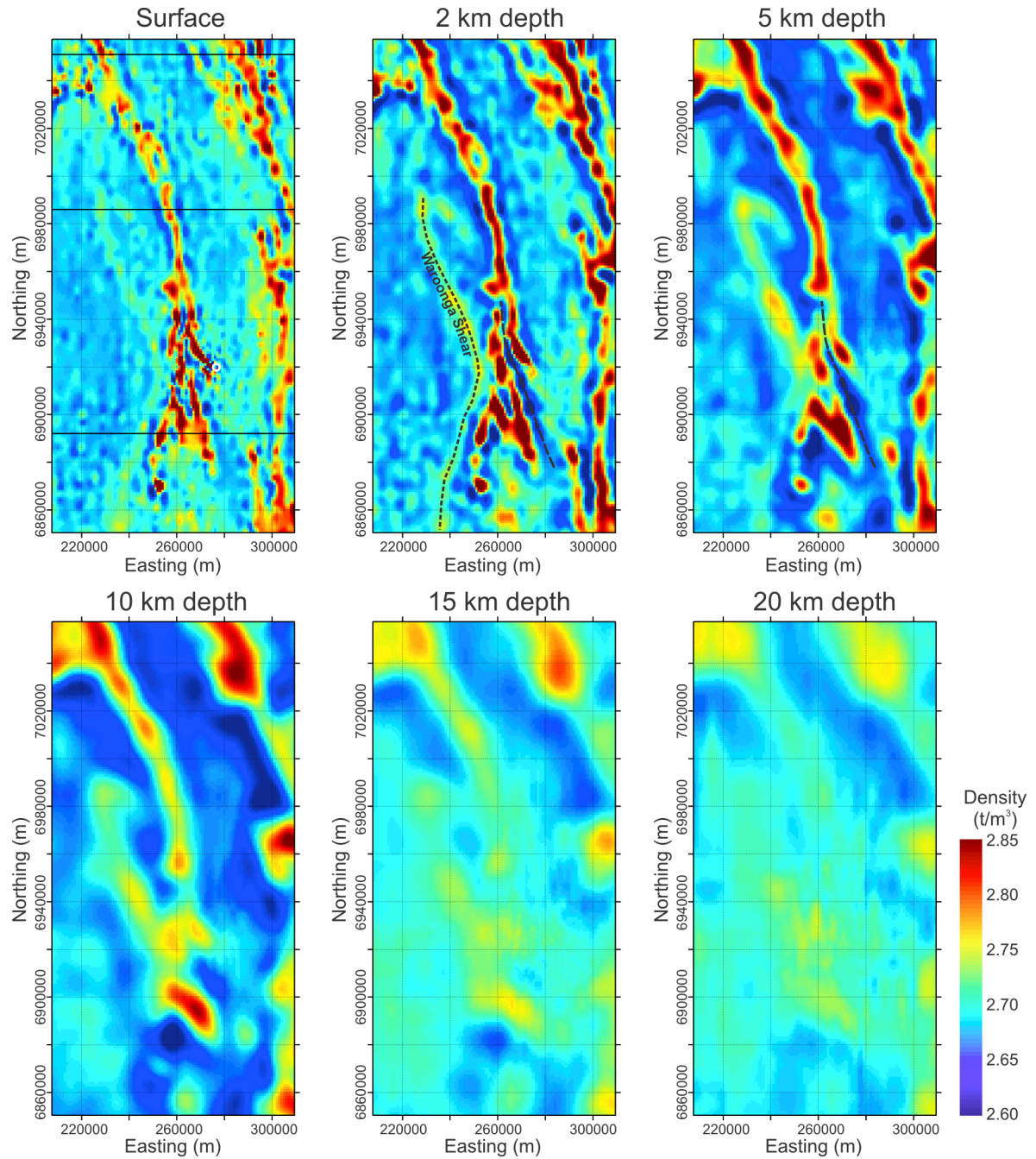


Figure 7.14. Horizontal slices at increasing depths through the regional-scale geologically-constrained gravity inversion model. The surface slice marks the position of the Perseverance deposit with a white circle, and the three black lines indicate the positions of the cross sections shown in Figure 7.16. The gravity inversions primarily map the extent of the denser mafic and mafic-derived rocks, which appear to be well imaged to ~5 km depth. The deepest parts of the greenstone belt are apparent in the 10-15 km depth slices at Lawlers (6,890,000mN) and north of Wiluna (7,050,000mN). No significant features below 15 km are required by the gravity data. At shallower levels there are clear discontinuities between the density highs suggesting significant structural and stratigraphic complexity. The notable linear density feature in the western half of the model with an east-facing hook at its northern end is inferred to represent the Waroonga Shear Zone. From 2-5 km a low density lineation (marked) is inferred to mark the extent of the Leinster Granodiorite. The colour scale is clipped to contain 99 % of values.

The susceptibility models (Figure 7.15) show small, discontinuous highly magnetic features, inferred to represent shallow ultramafic rocks, with broader, more continuous, moderately magnetic features at depth inferred to represent more magnetic gneiss and granulite rocks. Due to the higher resolution of the magnetic data, there is significantly more detail recovered in the magnetic susceptibility model at shallower levels. The thin ultramafic rock units are resolved to depths of up to 2-3 km, but if they exist at greater depths they are generally too small to be resolved by the magnetic data. Low susceptibility lineations are inferred to represent magnetite destruction, both mechanical and hydrothermal, along fault and shear zones. Some complex structure can be inferred from these features down to ~5 km depth. At greater depths only the wider shear zones can be resolved, so it is not possible to classify the importance of the structures based solely on their depth extent. The Waroonga Shear Zone is evident to at least 5 km depth, and appears to migrate west with increasing depth indicating a westward dip (see also Henson and Hitchman, 2004). Portions of the Perseverance Fault can be traced to at least 5 km depth but without any obvious dip. Its position is not as clearly defined at greater depths. The only significant feature in the susceptibility model below 5 km depth is the distinction between higher susceptibility rocks to the west ($10\text{--}50 \times 10^{-3}$ SI) and the lower susceptibility rocks to the east ($< 15 \times 10^{-3}$ SI) in the deeper slices and in the Lawlers cross section (Figure 7.16). This is inferred to be a characteristic difference between the basement rocks of the Youanmi Terrane (west) and Kalgoorlie Terrane (east). The boundary is inferred to be the continuation of the Ida Fault System, but it is difficult to tightly define its position.

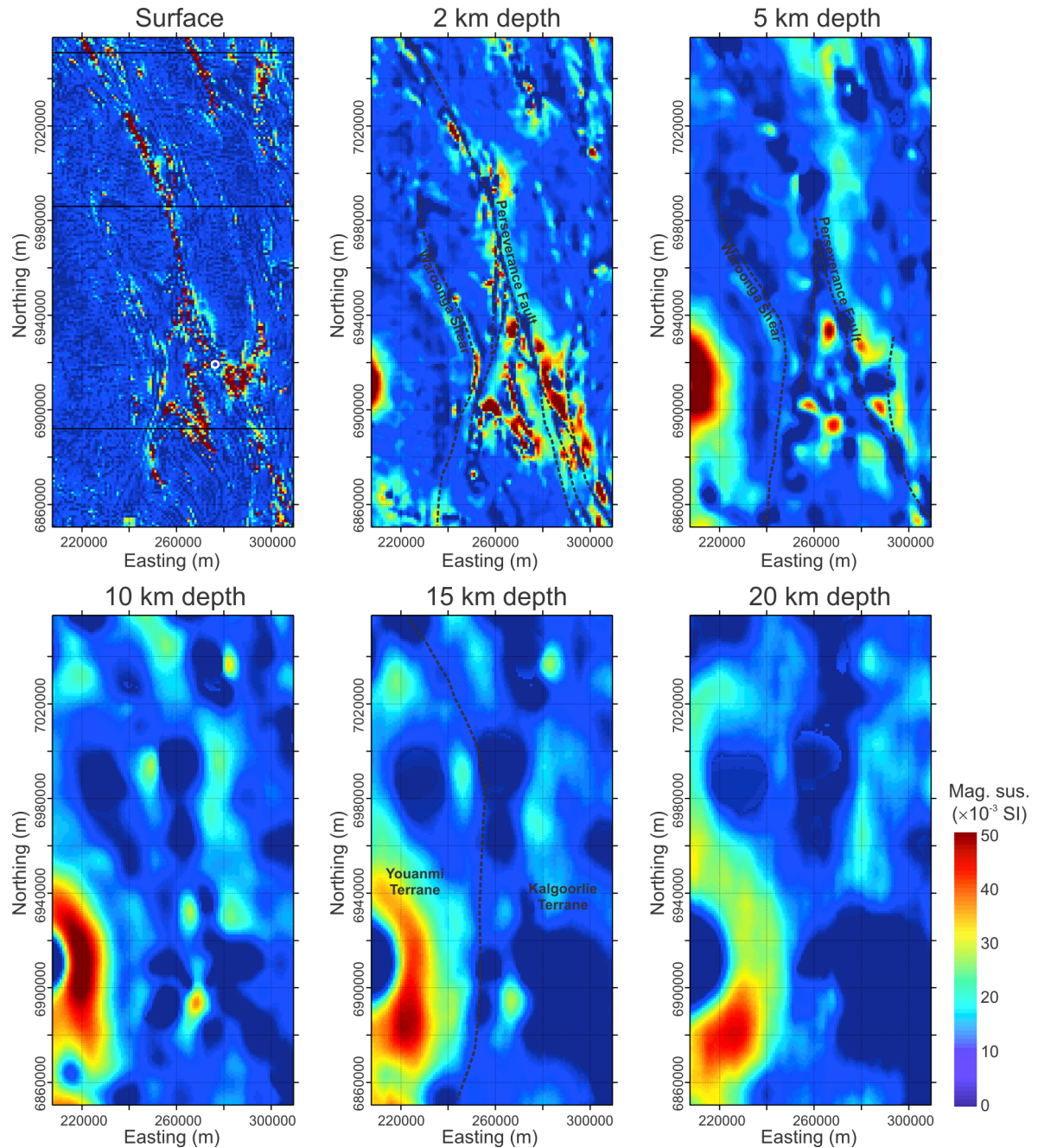


Figure 7.15. Horizontal slices at increasing depths through the regional-scale geologically-constrained magnetic inversion model. On the surface slice, the position of the Perseverance deposit is marked with a white circle; the three black lines indicate the positions of the cross sections shown in Figure 7.16. The highly magnetic ultramafic bodies are relatively thin and are only imaged to < 2-3 km depth. A number of structures are clearly evident as magnetic lows from 2-5 km depth, including the Waroonga Shear Zone (c.f., Figure 7.14), the Perseverance Fault and several connecting faults and shears. The main feature evident below 10 km is the distinction between the more magnetic rocks to the west and the less magnetic rocks to the east, and this is inferred to be a characteristic distinction between the Youanmi and Kalgoorlie Terrane basement rocks, separated by the Ida Fault System. The colour scale is clipped to contain 99 % of values.

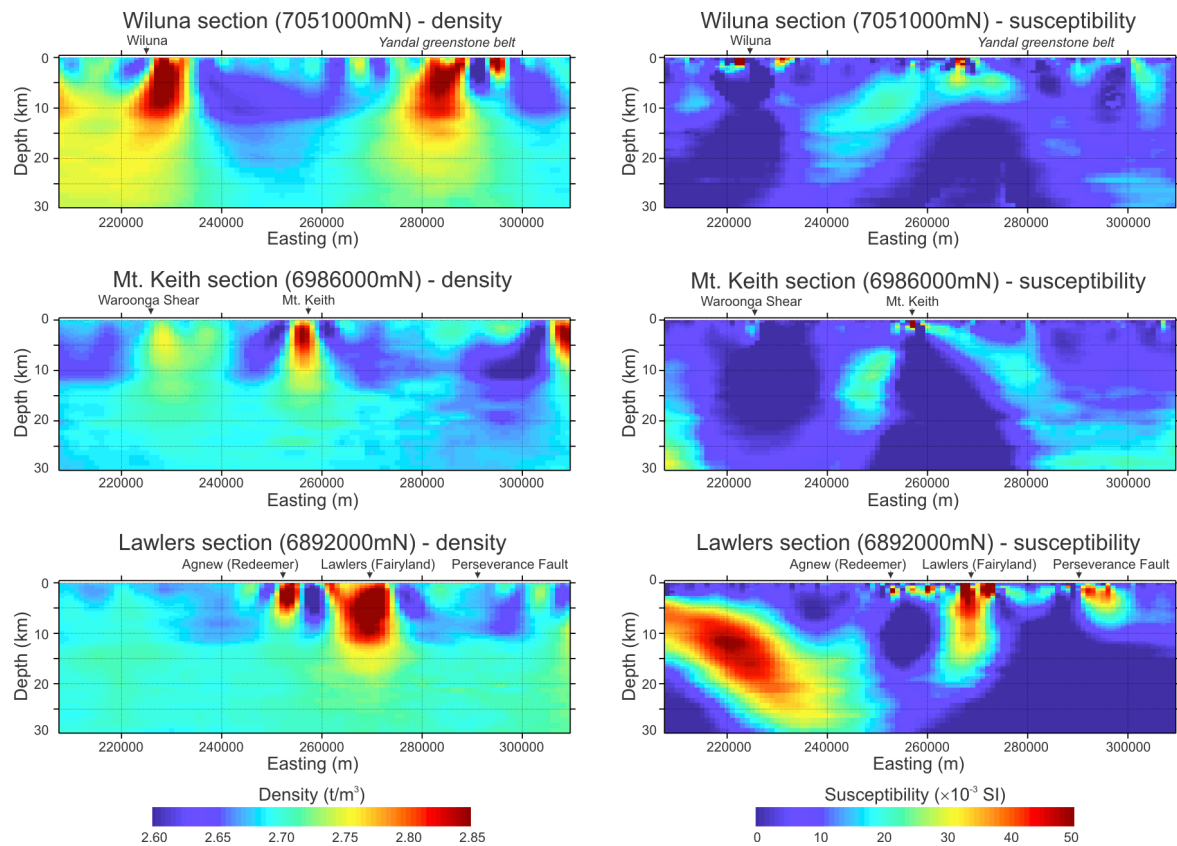


Figure 7.16. East-west cross sections through the regional-scale geologically-constrained gravity and magnetic inversions. Slices are arranged from north (top) to south (bottom), with the densities shown on the left and the susceptibilities shown on the right. The Wiluna and Lawlers sections pass through the thickest parts of the greenstone belt; the Mt. Keith section is one of the most attenuated parts of the belt. In the Wiluna section the density anomalies below Wiluna and the Yandal greenstone belt show diffuse excess masses below 12 km which may indicate the continuation of the greenstone rocks below the 12 km depth indicated by the layered earth constraints. The rest of the Agnew-Wiluna greenstone belt is comfortably accommodated above 10-12 km depth. The limited extent and depth resolution of the highly magnetic ultramafic rocks is indicated by the small magnetic anomalies at shallow levels in the susceptibility models.

Figure 7.17 shows the predicted rock types using the physical property classification in Figure 7.11. Comparison of the predicted geology model with the existing basement geology interpretation in Figure 7.3 shows good agreement in the distribution of the ultramafic and mafic rocks within the greenstone belts. The basement geology interpretation in Figure 7.3 was not included as a constraint in the inversions, and may contain features at different levels of the crust. Comparison with the surface geology map in Figure 7.2 demonstrates the ability of the model to predict greenstone extensions under cover. Only 20 cells in the whole model were classified as dense and magnetic unserpentinised ultramafic rocks. As these rocks are known to exist in association with most of the major nickel deposits in the belt, in the form of olivine-cumulate ultramafic rocks, these might provide prospective exploration targets. One occurrence is actually identified at the Perseverance nickel deposit, and consists of several cells

directly under the black circle around the Perseverance deposit in Figure 7.17 (~6,920,000 mN). Two more occurrences lie close to Perseverance, 3 km southwest (visible) and 3 km northwest (below the displayed map slice), and these are refined in the district-scale modelling. Two additional occurrences include one cell in the hinge of the Lawlers anticline, and several cells in the southern lobe of ultramafic rocks at 251,500 mE and 6,870,500 mN.

The distribution of mafic and ultramafic rocks is more clearly shown in Figure 7.18, which displays the surface projection of all predicted mafic and ultramafic rocks. This further highlights the quality of the correlation with the existing basement geology interpretation in Figure 7.3 which must also be interpreted as a surface projection of the geology. One difference is the apparent identification of a region of ultramafic rocks 10 km southeast of Perseverance. This feature will be discussed in detail in the district scale inversion results where it is more clearly resolved. Figure 7.18 also shows the maximum thickness of the predicted mafic and ultramafic rocks along the length of the Agnew-Wiluna greenstone belt. This emphasises the increasing thickness of the mafic-ultramafic sequence at the northern and southern ends of the belt at Wiluna and Lawlers, respectively, as suggested in Figure 7.16. These thicker portions of the belt are associated with most of the known gold deposits. The thinnest portions of the greenstone belt are at Cosmos and north of Mt. Keith.

The cross sections in Figure 7.17 do provide subtle indications of the orientations and positions of some of the major structures in the region. As noted above, the Waroonga Shear Zone seems to be imaged in the Mt. Keith section as a west-dipping structure to about 10 km depth, separating a weakly magnetic (felsic) unit from more magnetic rocks to the west. A similar west-dipping structure in the Lawlers section just west of the Redeemer gold deposit may be the southern continuation of the Waroonga Shear Zone; it flattens out at about 10 km depth. On the east side of the belt, there is a wedge of low magnetic susceptibility material (Figure 7.16) classified as undivided felsic rock (Figure 7.17) directly below the mapped trace of the Perseverance Fault. It continues from the southern edge of the model to north of Mt. Keith. The wedge appears to be bounded to the west and east by west- and east-dipping structures, respectively. Both are near vertical at shallow levels, but flatten somewhat with increasing depth. Near the Perseverance mine, the Perseverance Fault is known from drilling to be nearly vertical, consistent with the orientation observed for this structure at shallow depths within the model.

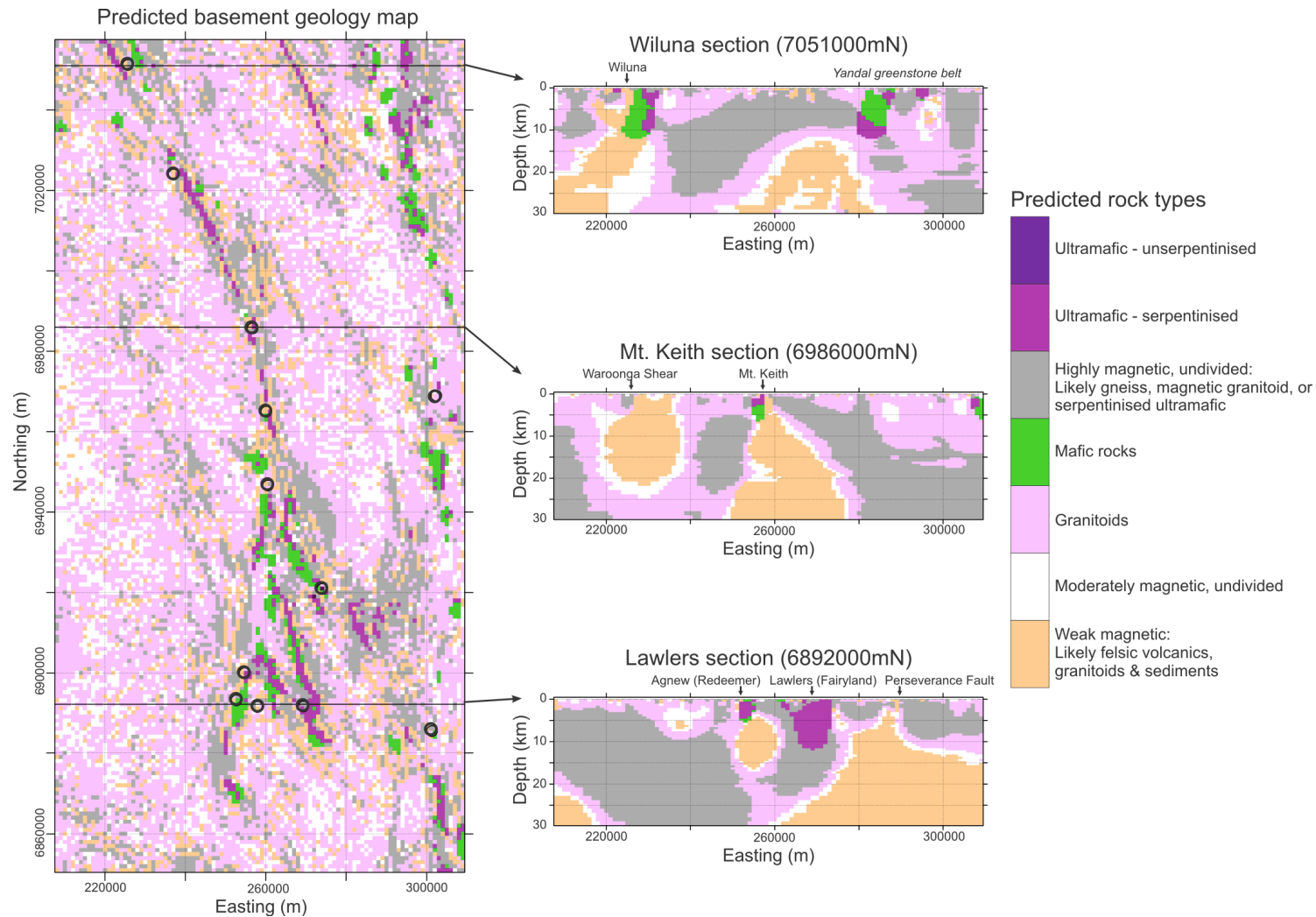


Figure 7.17. Predicted rock model for the Agnew-Wiluna greenstone belt based on the available geophysical data, geological constraints, and physical property data. Each cell in the inversion models has been classified using Figure 7.11 based on the recovered densities and susceptibilities and assuming minimal alteration and sulphides are present. Cells containing a mixture of rock types are assumed to fall in the various undivided categories depending on their relative susceptibilities. The basement geology map contains the predicted rock type in the surface layer of cells (0-500 m depth). Black circles indicate the locations of selected deposits identified in Figure 7.2 and Figure 7.12. The cross sections are in the same positions as in Figure 7.16. The map shows a good correlation with the traditional basement geology interpretation in Figure 7.3.

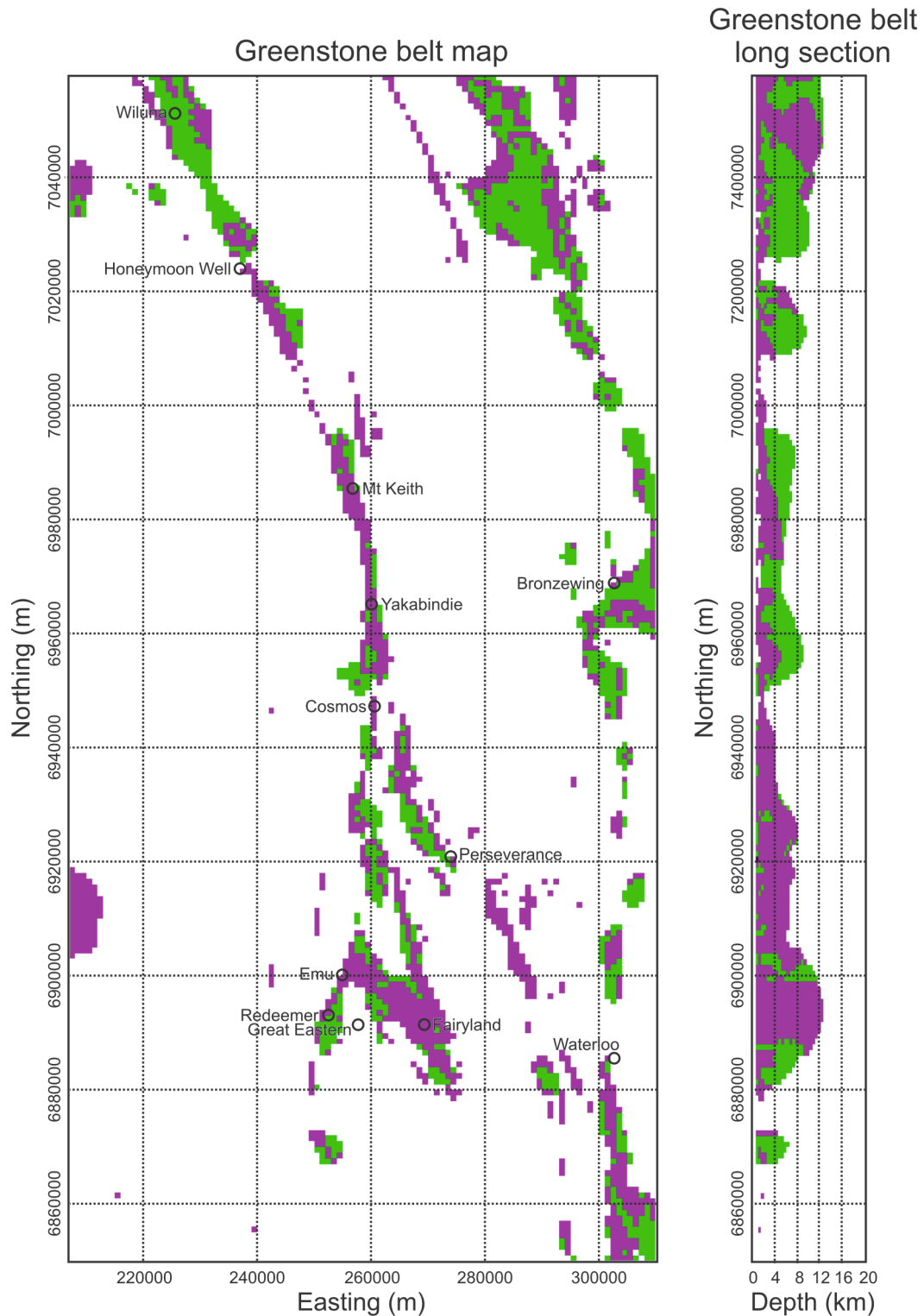


Figure 7.18. Predicted distribution of mafic and ultramafic rocks throughout the Agnew-Wiluna greenstone belt based on the rock model presented in Figure 7.17. The map shows the surface projection of all predicted mafic and ultramafic rocks regardless of depth and is coloured by according to whether mafic (green) or ultramafic (purple) rocks are the shallowest occurring in each position. The long section shows the maximum thickness of mafic and ultramafic rocks along the length of the Agnew Wiluna greenstone belt, coloured as viewed from the east. The thickest greenstones are at the north (Wiluna) and south (Agnew/Lawlers) ends. Most of the known gold deposits are associated with these thick greenstone piles.

7.7.2 District-scale: Agnew-Leinster district

The district-scale inversions seek to map the southern portion of the Agnew-Wiluna greenstone belt in more detail, and identify any stratigraphic or structural relationships between the nickel-bearing Mt. Keith-Perseverance domain and the gold-bearing Agnew domain. The surface layers of the reference models and smallness weights used are shown in Figure 7.19 and Figure 7.20 for the gravity and magnetic inversions, respectively. Non-default bounds and smoothness weights were also used as described in Sections 7.6.2-7.6.3, but are not shown. Buffers provide a slight extrapolation of the map constraints prior to the inversion. The 500 m radius is slightly larger than one cell width (400 m) so the buffers expand the constraints laterally as well as vertically. This can be seen in the figures where regions of outcrop are outlined by a ring of lower smallness weights.

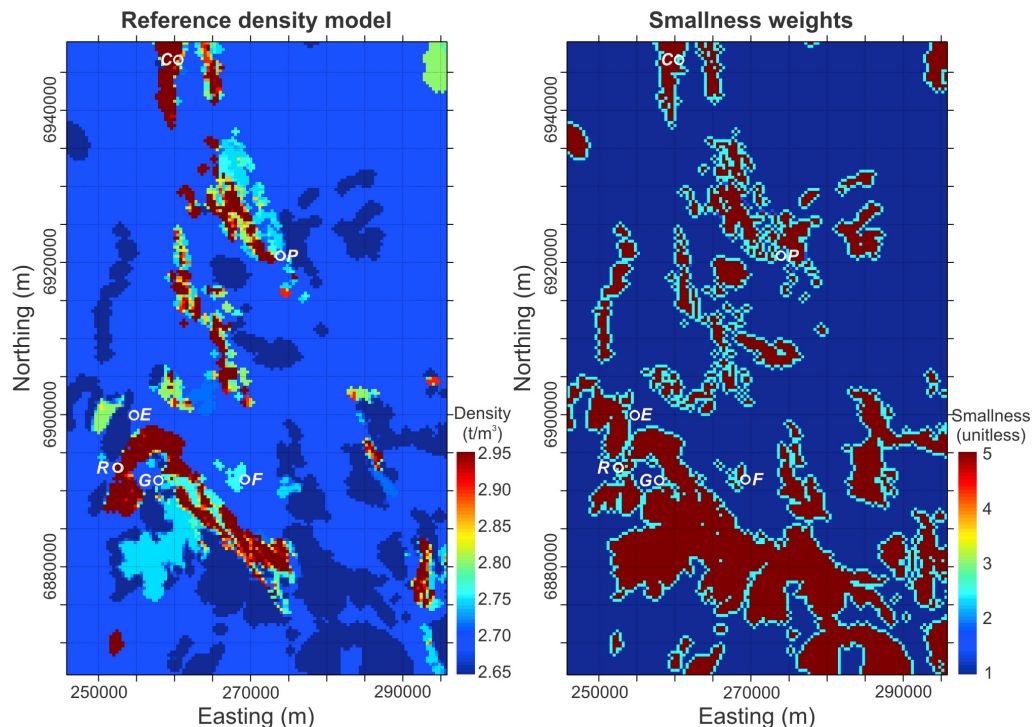


Figure 7.19. The surface layer of the reference density model and smallness weights used to constrain the district-scale gravity inversion. The constraints are based on surface mapping, a basic layered earth model, and best estimate physical properties. The densities are converted to density contrasts using a background density of 2.70 t/m^3 ; this background value was used as the default reference property where no geological information was available. The smallness weights indicate the relative reliability of the supplied reference model: blue cells are effectively unconstrained (default values); brown cells contain mapped basement outcrops. The cyan cells indicate cells where the properties have been extrapolated outwards using 500-m-radius buffers; these cells are assigned slightly lower smallness weights to reflect their lower reliability. Regolith is ignored in this model as the depth of weathering is negligible compared to the 200 m cell heights. Locations of selected mines/deposits are indicated with white circles: C = Cosmos; P = Perseverance; E = Emu (Agnew group); R = Redeemer (Agnew group); F = Fairyland (Lawlers group); G = Great Eastern (Lawlers group).

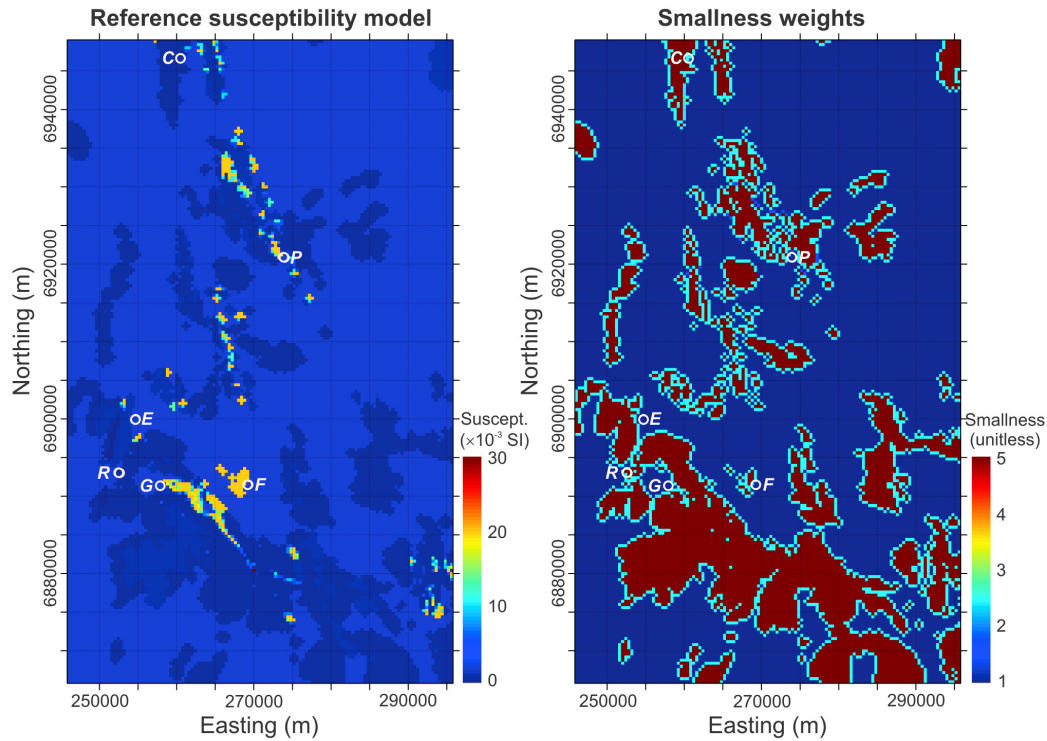


Figure 7.20. The surface layer of the reference susceptibility model and smallness weights used to constrain the district-scale magnetic inversion. The constraints are based on surface mapping, a basic layered earth model, and best estimate physical properties. The smallness weights indicate the relative reliability of the supplied reference model: blue cells are effectively unconstrained (default values); brown cells contain mapped basement outcrops. The cyan cells indicate cells where the properties have been extrapolated outwards using 500-m-radius buffers; these cells are assigned slightly lower smallness weights to reflect their lower reliability. Regolith is ignored in this model as the depth of weathering is negligible compared to the 200 m cell heights. Locations of selected mines/deposits are indicated with white circles: C = Cosmos; P = Perseverance; E = Emu (Agnew group); R = Redeemer (Agnew group); F = Fairyland (Lawlers group); G = Great Eastern (Lawlers group).

The gravity inversion results at this scale provide a useful example of the impact of the geological constraints. Figure 7.19 shows a comparison of the density models recovered using a default, geologically-unconstrained gravity inversion, and the geologically-constrained inversion. Since the gravity data are unevenly distributed, and widely spaced in some areas, the default result tends to identify individual, isolated density anomalies scattered throughout the model. Adding constraints from mapping and aspect ratios causes these distinct anomalies to link into coherent bodies, consistent with mapped trends. The layer-based constraints help focus the recovered anomalies into realistic shapes and volumes. The model shows a vertical slice in the position of the Lawlers cross section (also in Figure 7.24), which passes through some of the best outcrop in the district. The default inversion result provides a very poor reproduction of the mapped surface geology, and doesn't reproduce outcropping dense gabbro in the area, a representative sample of which has a measured density of 2.97 t/m^3 . Including the mapping constraints ensures that these outcropping rocks are reproduced in the result and

shows that they can only be accommodated if they are relatively thin and underlain by a less dense unit. This is consistent with their location near the hinge of the Lawlers Anticline, thus providing a more reliable depiction of the 3D geology.

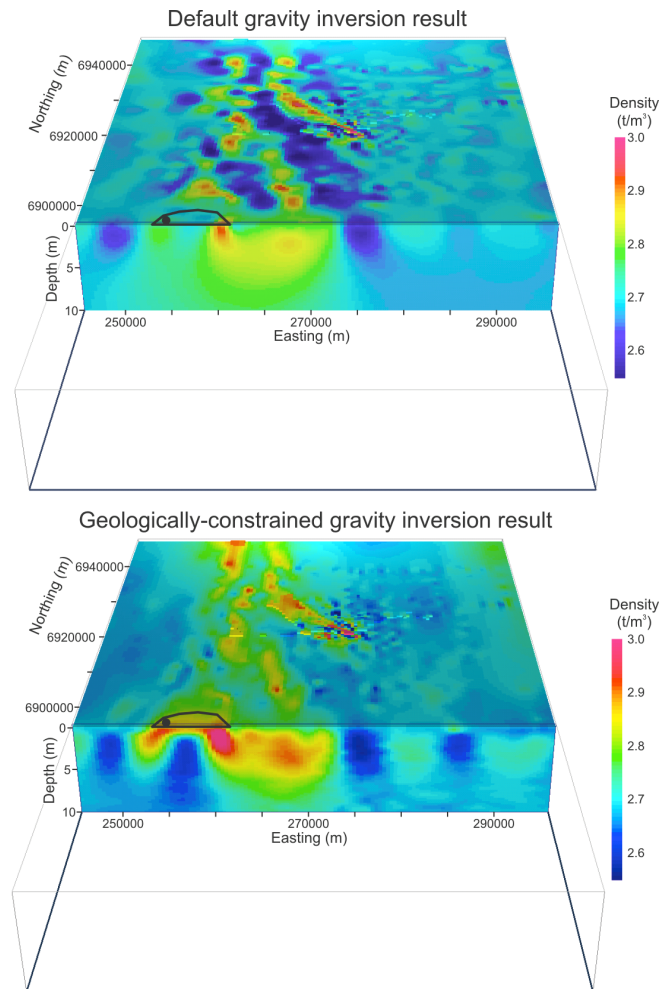


Figure 7.21. Comparison of the improvement gained by including geological constraints in the district-scale gravity inversion. The top model shows the default, geologically unconstrained result. The bottom model shows the result when constraints from mapping, a layered earth model, and aspect ratios are included. Both models explain the observed gravity data equally well, and the same view is shown for both with the same colour scale. Density contrasts have been converted to densities using a background density of 2.7 t/m^3 in both models. The area outlined in black contains outcropping gabbroic rocks; the black circle marks the location of an outcropping gabbro sample collected in this study with a measured density of 2.97 t/m^3 . This unit is not recovered in the default inversion result.

The district-scale models are depicted as horizontal slices in Figure 7.22 (density) and Figure 7.23 (susceptibility) and four cross sections in Figure 7.24. Comparison of the model slices (Figure 7.22-Figure 7.23) with the locations of outcrop (Figure 2.18-Figure 7.20) shows that both the density and susceptibility models delineate buried features and link isolated outcrops in a realistic manner. Although the model cell size is smaller, the gravity stations have the same 2.3 km spacing as for the regional inversion so there will be relatively little

improvement in the resolution of the density model. It shows many of the same features identified in the regional-scale results above. The Waroonga Shear Zone is visible, although its position close to the western edge of the model limits any geometrical interpretation. The density slices and Perseverance cross section (Figure 7.24) clearly map the large density low inferred to represent the Leinster Granodiorite. It is also intersected in the Leinster cross section where it may underlie many of the greenstone rocks and continue to > 6 km depth between 260,000-275,000 mE. Another feature that appears to be well mapped is a moderate density low along the western margin of the greenstone belt just east of the Waroonga Shear Zone. This correlates with limited outcrops of the late sedimentary basin Jones Creek Conglomerate. The model suggests that it is relatively continuous below the regolith and is < 2 -3 km thick. A final noteworthy feature is the apparent thickening of denser mafic rocks to up to 5 km in the Miranda section below and west of the late basin. The Miranda section passes through a region with almost no outcrop (c.f. Figure 2.18) near the southern shore of Lake Miranda, just south of the small Miranda gold deposits (Cams and Scorpion).

The magnetic susceptibility model (Figure 7.23) maps most of the known ultramafic rocks, and provides some resolution down to > 2 km depth. As for the regional-scale results, there are many low susceptibility linear structures, inferred to represent faults and shears, that are evident to depths of < 5 km. Even though more detail is available, it is more difficult to accurately mark the traces of some of the structures due to the large number present, and their complex relationships. The Waroonga Shear Zone and Perseverance Fault are clear to > 2 km depth, and there are several structures apparent along the western margin of the greenstone belt near the late basin inferred in the density model which may be associated with the Ida Shear Zone. The Lawlers Fairyland gold deposit on the Lawlers cross section (Figure 7.24) lies between two thin high susceptibility features, likely ultramafic bodies. In existing basement map interpretations (Figure 7.3) these features are placed in faulted contact with each other and this appears evident from the map slices through the susceptibility model (275,000 mE, 6,890,000 mN). The Lawlers cross section, however, shows two limbs connecting in a synformal structure with a hinge at 2-6 km depth and no significant vertical offset. There is also evidence that the eastern limb, which continues northwards into the Leinster cross section west of Leinster town, is itself the western limb of an antiformal structure that closes further east. This suggests the possibility of sinistral strike-slip faulting of pre-existing folds and provides an improved understanding of the 3D architecture beneath the Lawlers gold deposits.

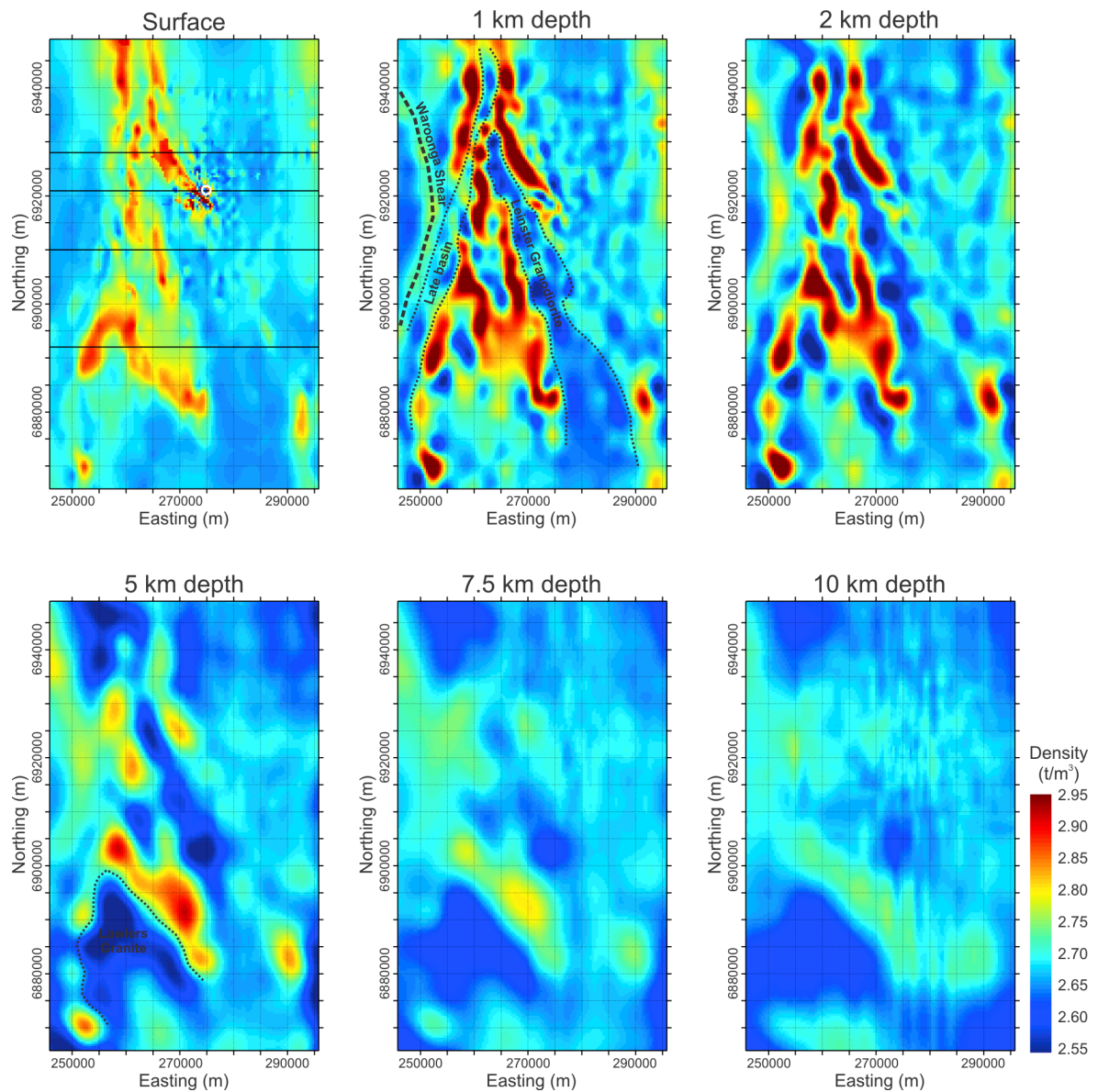


Figure 7.22. Horizontal slices at increasing depths through the district-scale geologically-constrained gravity inversion model. On the surface slice, the Perseverance deposit is marked with a white circle; black lines indicate the positions of the cross sections shown in Figure 7.24. The dense mafic and mafic-derived rocks are well imaged to > 5 km depth; the deepest parts extend to 8-9 km depth. Density lows associated with the inferred Leinster Granodiorite and late basin are roughly outlined where present at shallow levels. The Lawlers Granite in the hinge of the Lawlers Anticline is clearest below 2 km depth. The Waroonga Shear Zone is imaged to > 5 km depth. The colour scale is clipped to contain 99 % of values.

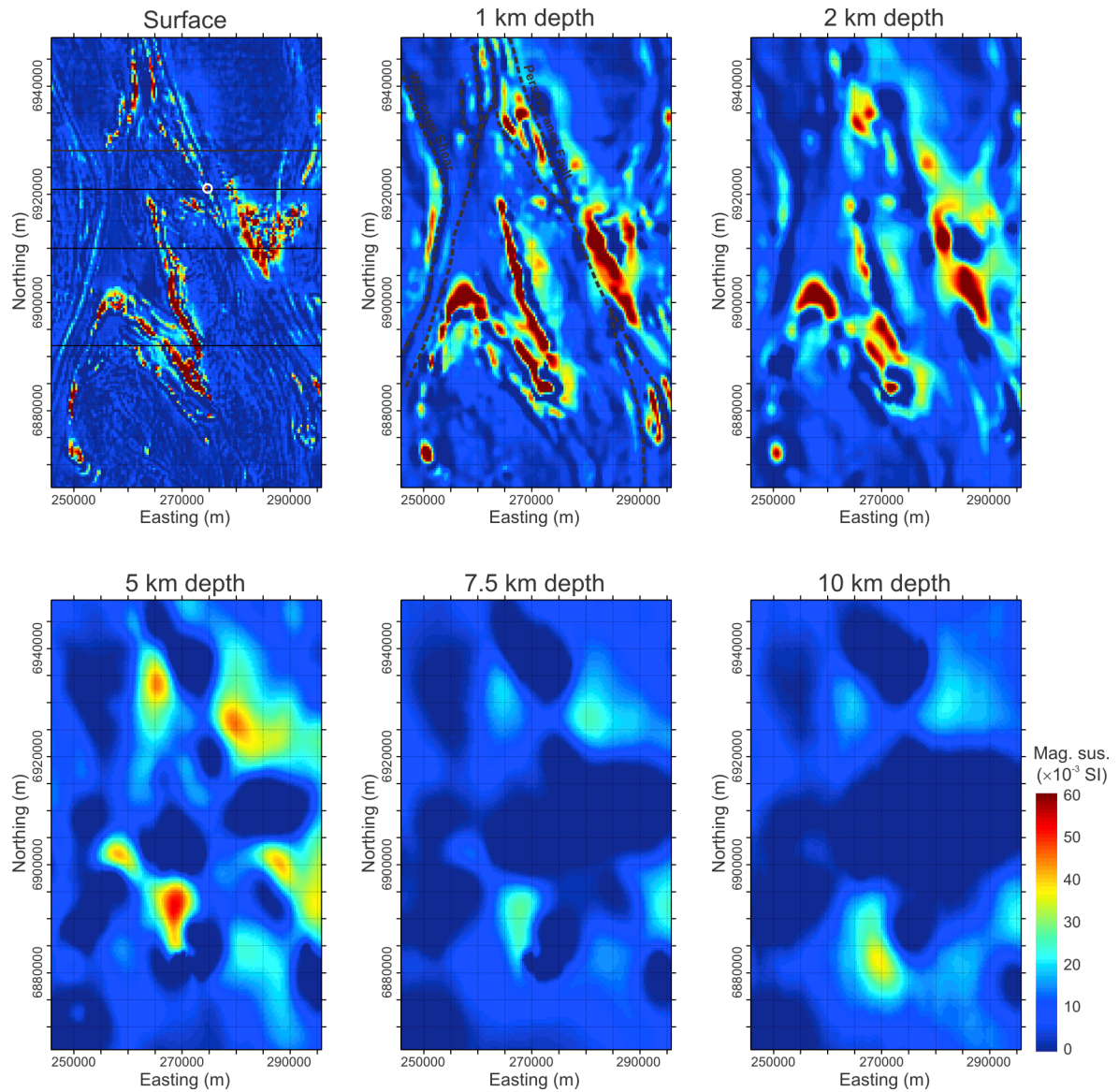


Figure 7.23. Horizontal slices at increasing depths through the district-scale geologically-constrained magnetic inversion model. On the surface slice, the position of the Perseverance deposit is marked with a white circle; black lines indicate the positions of the cross sections shown in Figure 7.24. The highly magnetic ultramafic bodies are relatively thin and are only imaged to < 2-3 km depth; they are too small to be imaged at greater depths. A number of structures are clearly evident as magnetic lows to similar depths, including the Waroonga Shear Zone (c.f., Figure 7.14), the Perseverance Fault, several structures along the western boundary, and other connecting faults and shears. These are more difficult to trace at greater depths. The colour scale is clipped to contain 99 % of values.

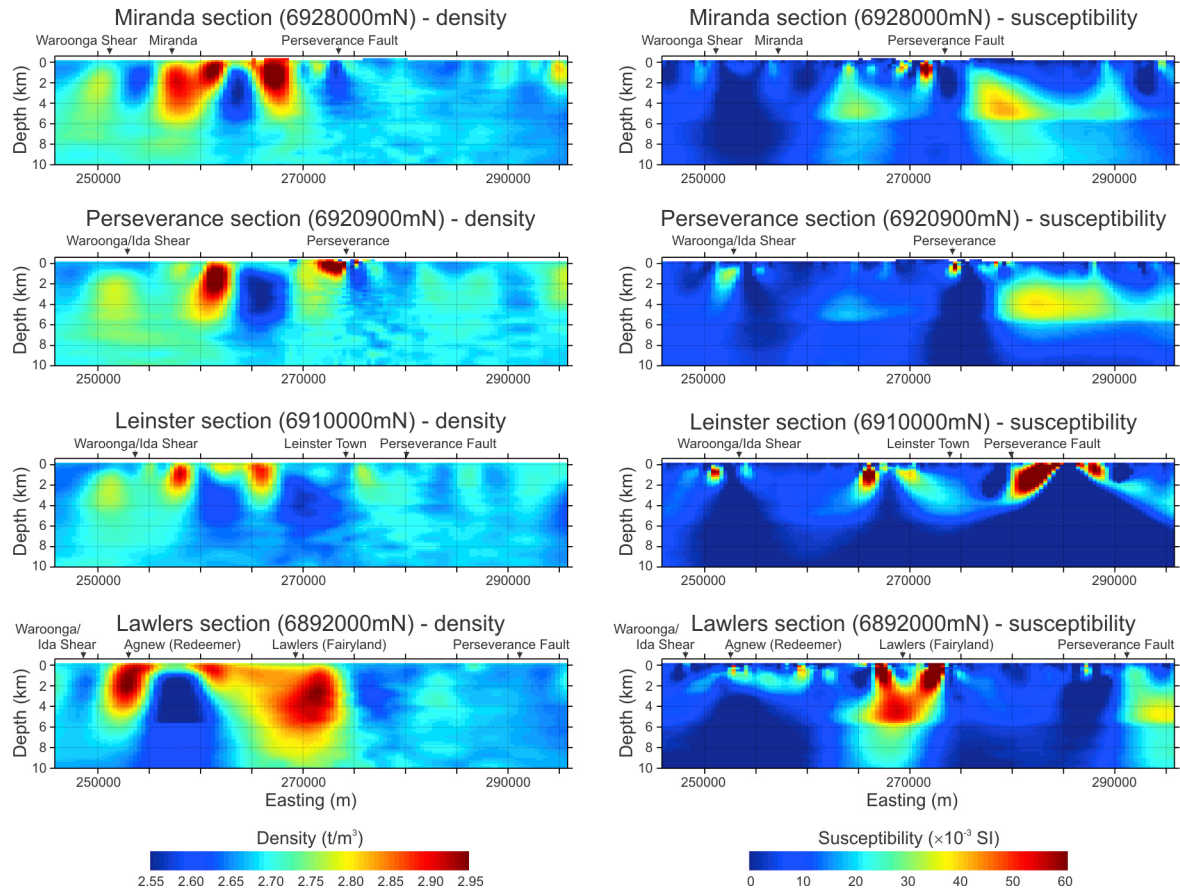


Figure 7.24. East-west cross sections through the district-scale geologically-constrained gravity and magnetic inversions. Slices are arranged from north (top) to south, with the densities shown on the left and the susceptibilities shown on the right. The Miranda section passes just south of the small Miranda gold deposits on the south shore of Lake Miranda. The Perseverance section contains the Perseverance deposit, and crosses the Leinster Granodiorite inferred to separate the west and east portions of the greenstone belt. The Leinster section also crosses the Leinster Granodiorite, two ultramafic bodies west of the town of Leinster, and a large magnetic body east of the Perseverance Fault. The Lawlers section crosses the most voluminous portion of the greenstone belt below the Fairyland gold deposit.

The basement geology map and cross sections predicted from the results are shown in Figure 7.25. The map again shows a good correlation with existing basement geology interpretations (Figure 7.3). One difference is the identification of several pods of mafic and ultramafic rocks at depth below cover, especially along the west edge of the belt under the inferred position of the late sedimentary basin (from Figure 7.22). In the Miranda cross section near the Miranda gold deposits, there is a 6-km-wide mafic and ultramafic body identified to 6 km depth that corresponds to the density anomaly identified in Figure 7.24. In the predicted basement geology map, which shows the layer of cells to 200 m below the surface, the feature is only 2-km-wide. This suggests that most of the body continues below the inferred position of the late sedimentary basin. A similar, but smaller mafic-ultramafic package is predicted below regolith and the late basin 17 km south of Miranda in the Leinster section (near Mosquito

Well). Since there is no distinct sedimentary rock classification due to the mix of properties and lithologies, the late basin is represented as various low density undivided or granitic rocks, depending on the recovered susceptibilities. Because of this classification, it is not possible to distinguish the sedimentary rocks from surrounding granitic rocks, but where the sedimentary rocks seem to be underlain by the mafic-ultramafic sequence on the Miranda section, the basin is predicted to be 600-800 m thick.

In the regional models, the location of the Perseverance Fault was associated with a wedge of low susceptibility undivided felsic rocks (Figure 7.17). The wedge is present in the district-scale result, but shows a more complicated geometry. In the Lawlers section in the vicinity of the Perseverance Fault, the wedge is bounded by a vertical structure and a shallow west-dipping structure 4-5 km to the west. In the Leinster section the wedge is very narrow and only visible to 5 km depth; structures that surface further east are prominent, possibly associated with the edge of the adjacent Yandal greenstone belt. The Perseverance section shows the clearest depiction of the structures bounding the wedge, and it continues into the Miranda section. The Waroonga Shear Zone is not as well resolved as in the regional-scale models, but seems to be associated with a west-dipping structure in all sections. In the Leinster section the Waroonga Shear Zone is also associated with a felsic wedge. The east-dipping structure bounding the eastern edge of the wedge may correlate with the Ida Shear Zone, the western boundary of the Kalgoorlie Terrane, but it is not clearly observed in other sections.

Large volumes of ultramafic rock like that predicted in the Lawlers cross section are unusual in the Yilgarn Craton. Given the recovered densities in the body are $2.85\text{--}3.0\text{ t/m}^3$, with susceptibilities of $25\text{--}50 \times 10^{-3}\text{ SI}$, the classification seems justified. However, a more realistic possibility is that the body contains a mix of highly magnetic ultramafic rocks and weakly magnetic mafic rocks, and the inversion lacks the resolution to distinguish the two. The feature could also contain gabbro or dolerite intrusions which Chapter 4 showed may contain weak-moderate remanent magnetisation that could increase their apparent susceptibility.

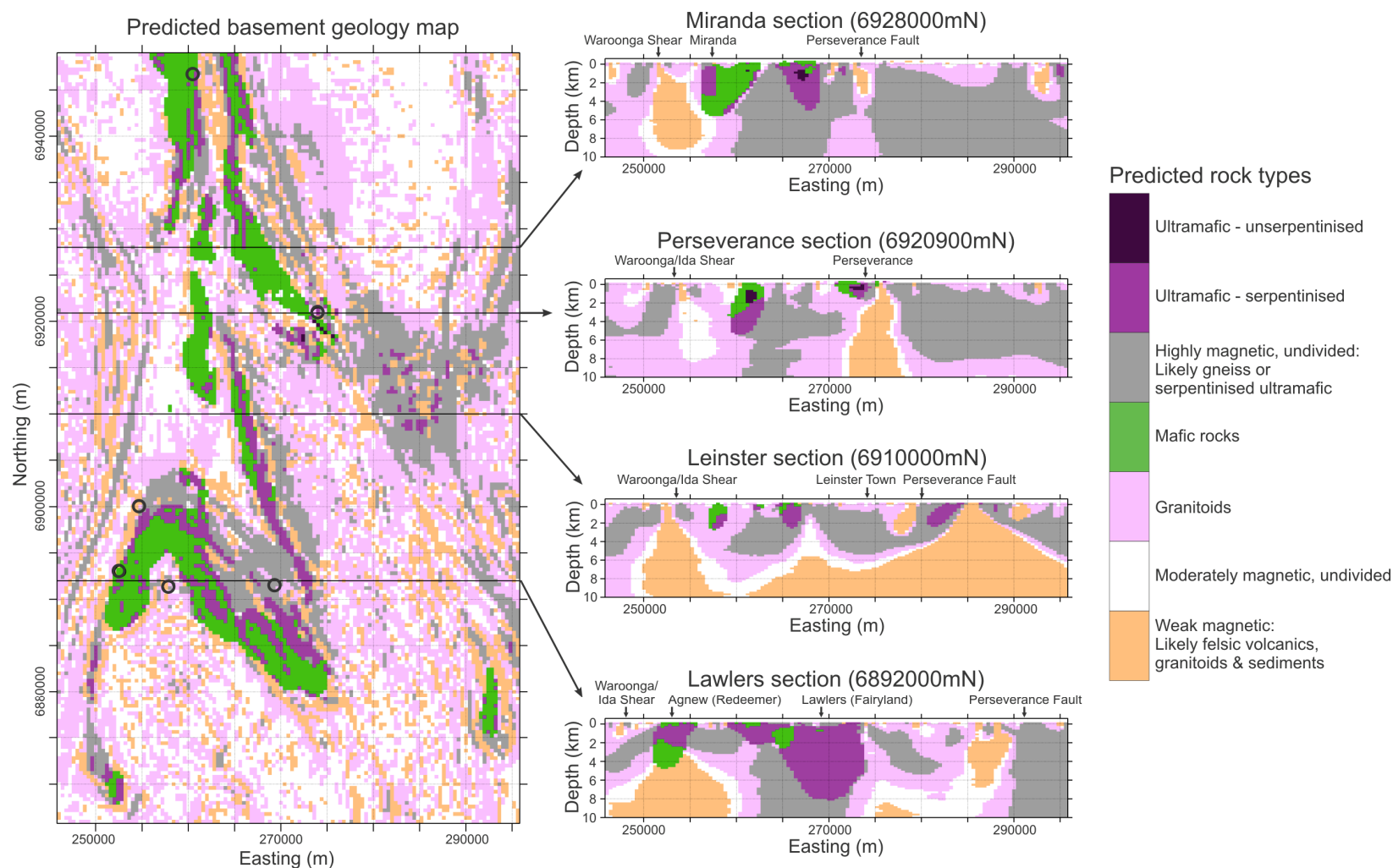


Figure 7.25. Best estimate predicted rock model for the southern Agnew-Wiluna greenstone belt based on the available geophysical data, geological constraints, and physical property data. Each cell in the inversion models has been classified using Figure 7.11 based on the recovered densities and susceptibilities and assuming negligible alteration and sulphides are present. Cells containing a mixture of rock types are assumed to fall in the various undivided categories depending on their relative susceptibilities. The basement geology map contains the predicted rock type in the surface layer of cells within the model. Black circles indicate the locations of the selected deposits identified in Figure 7.2 and Figure 2.18. The cross sections are in the same positions as in Figure 7.24. The map shows a good correlation with the traditional basement geology interpretation in Figure 7.3.

Figure 7.26 shows the surface projection of all predicted mafic and ultramafic rocks from Figure 7.25 and correlates well with the existing basement geology interpretation in Figure 7.3. The extent of the buried mafic-ultramafic sequence at Miranda is well delineated (west of 260,000 mE at ~6928000 mN) and appears to connect to the mafic-ultramafic sequence that hosts the Bellevue and Kathleen Valley gold deposits and the Cosmos nickel deposit. The map also depicts the surface projection of all of the densest, most magnetic rocks in the belt – those classified as unserpentinised ultramafic rocks. As for the regional-scale model, they still have a fairly limited distribution in the district model, but more are identified. The shallowest occurrences surround the Perseverance deposit. The locations of some of these features, entirely surrounded by mafic rocks, indicate that some may more likely be attributed to mafic intrusive bodies with weak-moderate remanent magnetisation, consistent with explanation for the voluminous ultramafic rocks in the Lawlers section.

The Leinster cross section in Figure 7.25 and the map in Figure 7.26 further define the region of apparently ultramafic rocks identified in the regional-scale model (Figure 7.18) 10 km southeast of Perseverance. It lies between Simpsons Well and Allan's Bore, 5 km east of 11 Mile Well. The top of the feature is within 200-400 m of the surface and the bottom extends to depths of 1.4-2.8 km. Within the body the inversions indicate densities of $\sim 2.69 \text{ t/m}^3$ and susceptibilities up to $110 \times 10^{-3} \text{ SI}$. It appears to have a shallow westerly dip and may be truncated by the Perseverance Fault to the west. A 15-km-long linear anomaly is clearly visible in the magnetic data in this area, subparallel to the Perseverance Fault (Figure 7.6). There is no associated gravity anomaly. Although the magnetic anomaly has the same shape, size and intensity as any associated with known ultramafic rocks, it has the same detailed short-wavelength mottled texture as surrounding granitic rocks. The nearest mapped basement outcrop is a small patch of granite 4 km east-southeast of the anomaly (Liu et al., 1996).

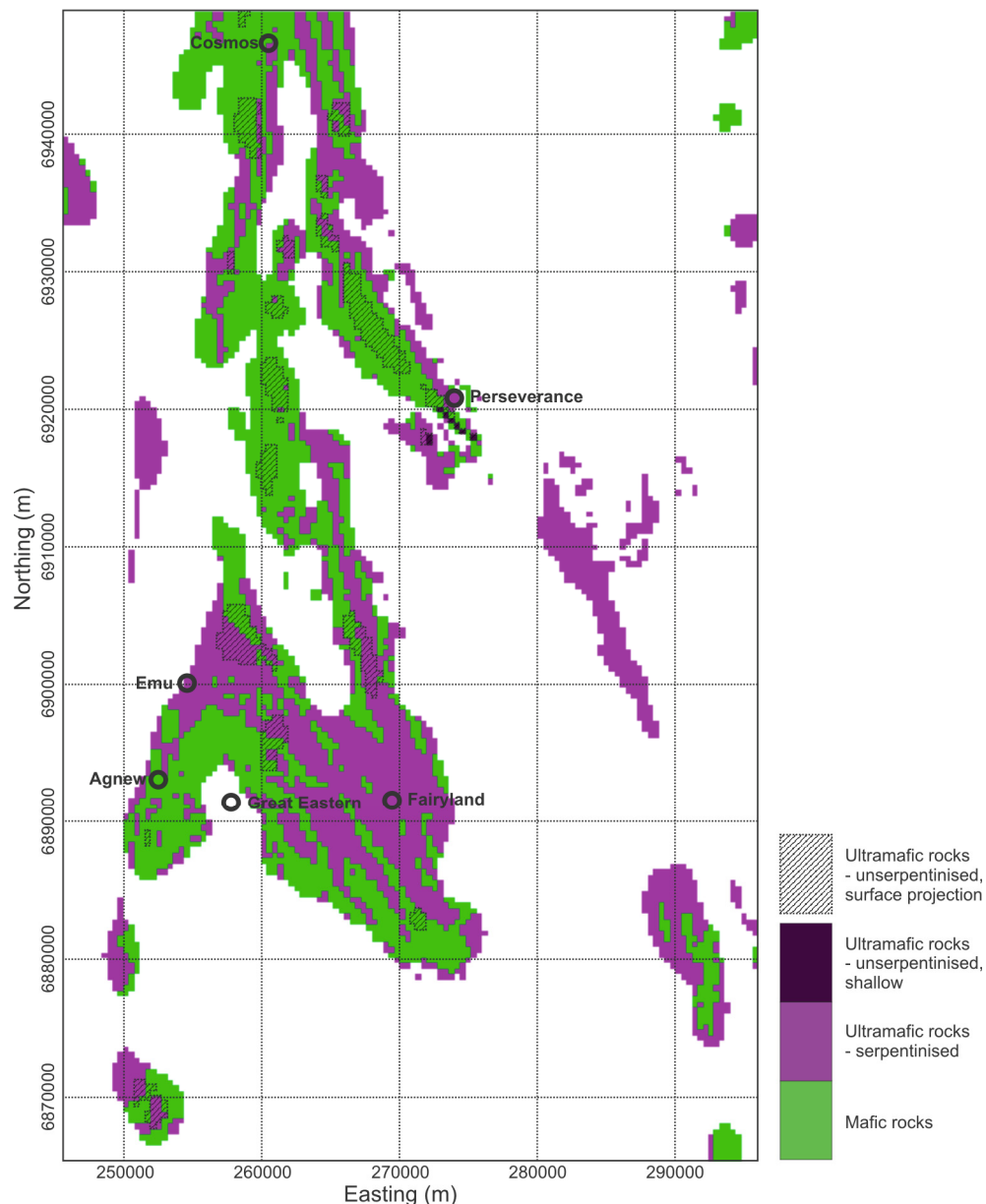


Figure 7.26. Predicted distribution of mafic and ultramafic rocks throughout the Agnew-Leinster district based on the rock model presented in Figure 7.25. The map shows the surface projection of all predicted mafic and ultramafic rocks and is coloured by according to whether mafic or ultramafic rocks are the shallowest occurring in each position. All other rock types are ignored. The surface projection of all of the densest and most magnetic rocks, interpreted to be unserpentinised ultramafic rocks, is also shown.

7.7.3 Deposit-scale: Perseverance nickel deposit

At Perseverance, the nickel-rich massive sulphide ore is generally < 5 m thick, less than the width of the cells being used in the inversions, so is unlikely to be imaged. The larger, more diffuse disseminated nickel-sulphide zones have only a subtle physical property contrast to their host ultramafic rocks (Chapter 4) and would only be 2-3 cells wide, so are also unlikely to be resolved, especially given the lack of gravity data over the open pit. The goal of these

inversions at Perseverance is therefore to map the large physical property contrasts associated with the mafic rocks, felsic volcanic and volcanoclastic rocks, and the variously serpentinised ultramafic host rocks. As there is a large existing database of drilling, geology core logs, and physical property data, a significant step is synthesising all the available data into common density or susceptibility models, and identifying regions within the models where the existing knowledge cannot adequately explain the available geophysical data.

The rich dataset also provides an opportunity to compare the inversion results that can be obtained for a real problem using different amounts of geological constraints. Three models will be presented for both the gravity and magnetic inversions. Default inversion models were prepared using default settings without including any prior geological knowledge. Since the most commonly available geological constraints come from surface information, another set of models is presented with constraints derived from available surface geology. A final set of models was created using the same surface constraints in combination with all drilling information including geology logs and physical located physical property measurements.

For the default models, aspect ratios of 1:1:1 were employed everywhere with default reference model, smallness and smoothness weights, and bounds. The surface constraints used in both the surface-constrained model and fully-constrained models were derived from the same surface geology map compilation used in the regional- and district-scale inversions (GSWA, 2004). Since the height of the near-surface cells in the models (10 m) is significantly less than the estimated thickness of regolith (70 m), it was necessary to augment the manual physical property estimates used in the regional- and district-scale models with estimates for various regolith materials based on Emerson et al. (2000) and Telford et al. (1990). Estimates of the densities and extents of the major mine infrastructure features, waste rock piles, ore stockpiles, and made ground, were also included. The same surface constraints were used in both the surface- and fully-constrained inversions. Map views of the surface constraints for the whole model volume, including padding cells, are shown in Figure 7.27 for the gravity inversions and in Figure 7.28 for the magnetic inversions. The padding cells are included in these figures to provide the local context surrounding the small core volume that will be shown in subsequent figures. The surface geology is dominated by low density, generally low susceptibility regolith, with small outcrops of high density, low susceptibility mafic rocks to the west, and outcrops of granitic rocks with moderate density and susceptibility to the east.

Flat ellipsoidal buffers were used to extrapolate the surface map properties up to 100 m laterally, but only 30 m down. A regolith domain allows for lower densities in the cover rocks, while requiring higher basement densities at depth.

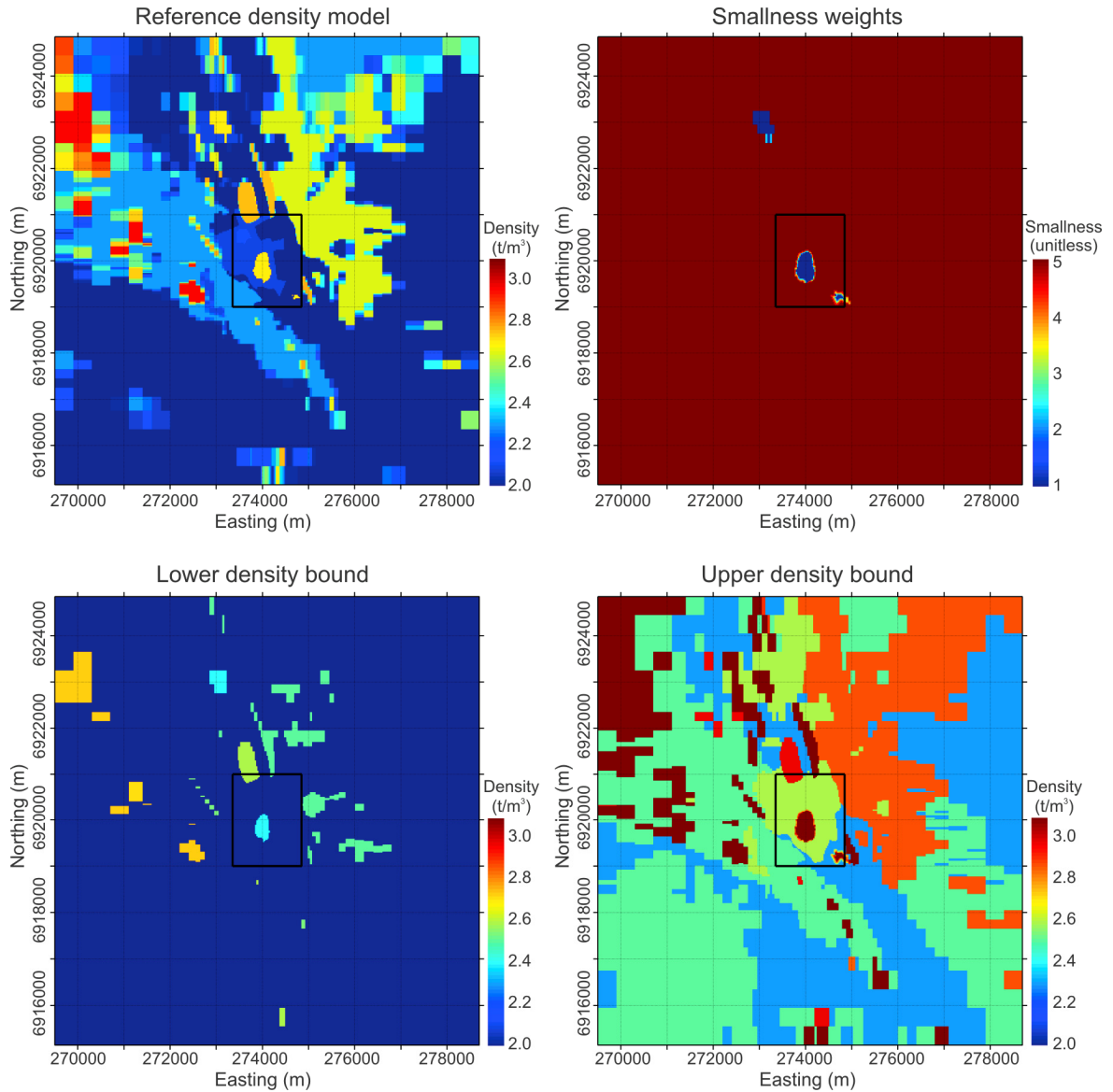


Figure 7.27. Surface map constraints for the deposit-scale gravity inversions. The constraints are based on 1:100,000 series surface maps (GSWA, 2004) with density estimates based on Table 7.1, augmented with literature values for regolith. The maps cover the full inversion area, including padding zones. The core volume centred on the Perseverance open-pit is outlined in black; subsequent figures will only show this core volume. Blue regions in the smallness weight model lack reliable constraints.

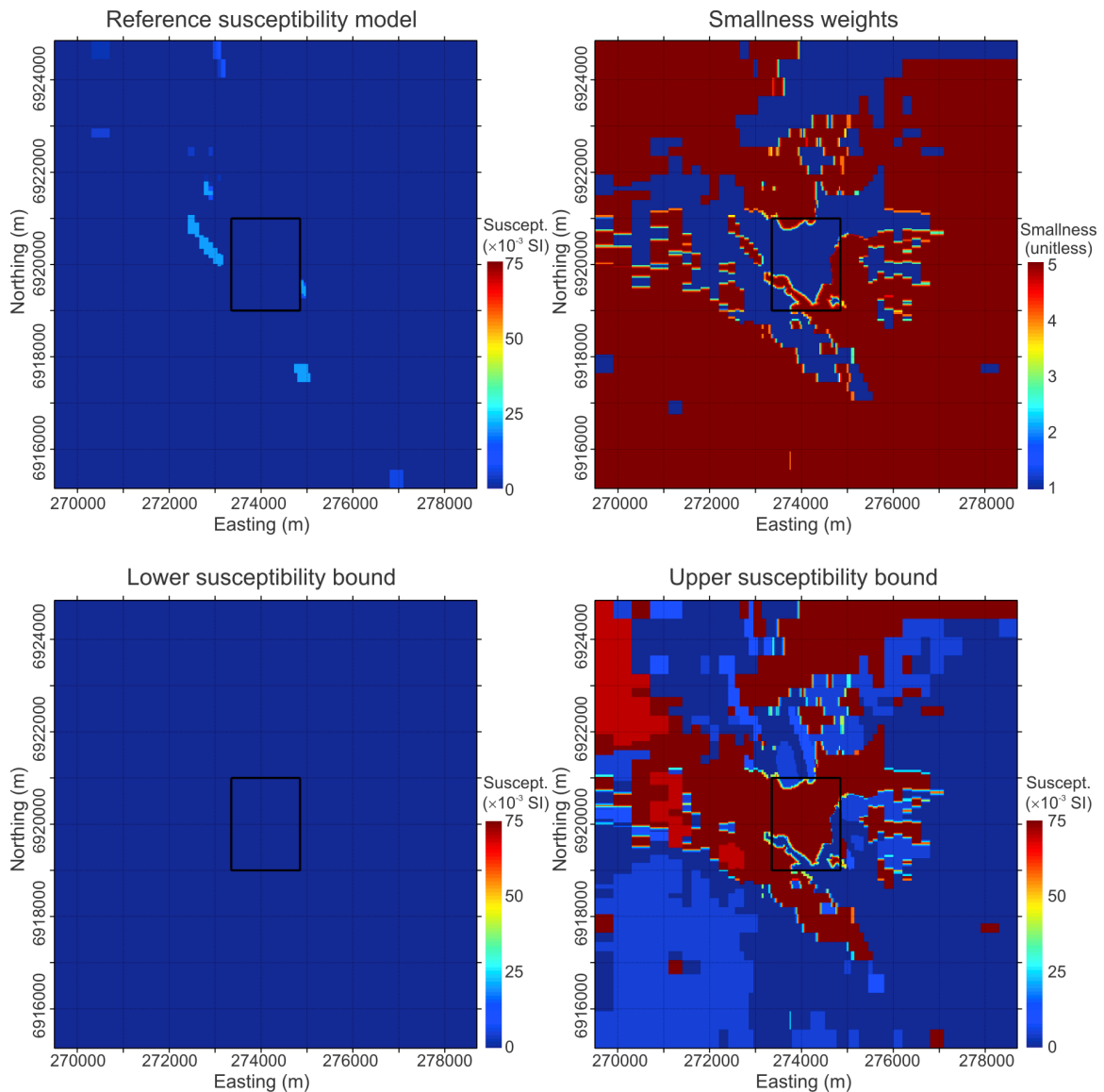


Figure 7.28. Surface map constraints for the deposit-scale magnetic inversions. The constraints are based on 1:100,000 series surface maps (GSWA, 2004) with susceptibility estimates based on Table 7.1, augmented with literature values for regolith. The maps cover the full inversion area, including padding zones. The core volume centred on the Perseverance open-pit is outlined in black; subsequent figures will only show this core volume. There is less detail than for the density constraints in Figure 7.27, due to the more limited susceptibility data. Blue regions in the smallness weight model lack reliable constraints.

By including all of the available drilling information, detailed constraint models can be created, especially when applying buffer-based extrapolation of the properties prior to inversion. The use of buffers increases the number of cells for which non-default constraints are available by a factor of 7 (Table 7.9). The full extrapolated constraints used in the gravity and magnetic inversions are shown in Figure 7.29 and Figure 7.30, respectively. Even prior to running the inversions, the constraint models provide a unique view of some of the geological features at Perseverance. The density reference model in Figure 7.29 shows several known geological features including the dense dunite core in the centre of the PUC, and maps a fold

intersected by only limited drilling at a depth of 1500 m. It also shows patches of the dense massive sulphides and thin subvertical mafic and ultramafic units west of the Perseverance open pit. These are clearly too small to be represented in the potential field data, but are significant features nonetheless.

Table 7.9. Percentage of the 1,027,324 below ground cells in the full padded deposit-scale density model with various non-default constraints, with and without buffer extrapolation. The sizes and shapes of the buffers are indicated in Table 7.4. The drilling geology logs are considered to be the most widely applicable constraint and so use up to 200-m-radius buffers, dramatically increasing the number of constrained cells.

Constraint type	Surface constraints only		Surface and drilling constraints	
	Without buffers	Including buffers	Without buffers	Including buffers
None	91.2 %	91.2 %	89.6 %	75.4 %
Regolith domain	7.6 %	4.8 %	7.6 %	4.6 %
Surface map	1.2 %	4.0 %	1.2 %	4.0 %
Drilling geology logs	N/A	N/A	1.3 %	13.4 %
Drilling property measurements	N/A	N/A	0.3 %	2.7 %
Cells with constraints based on mapping or drilling	1.2 %	4.0 %	2.8 %	20.0 %

As discussed in Section 7.6.2, remanent magnetisation is significant in the ultramafic rocks at Perseverance and introduces complications for the magnetic inversions. The constraints depicted in Figure 7.30 reflect true susceptibilities for all units other than ultramafic rocks, and estimated apparent susceptibilities for the remanently magnetised ultramafic rocks. As a result there are some relatively extreme values $> 100 \times 10^{-3}$ SI. Despite this, several geological features are apparent in the reference model, including: moderately magnetic serpentinised ultramafic rocks of the PUC at shallow levels east of the open pit; strongly magnetic ultramafic rocks close to the inferred position of the Perseverance Fault; weakly magnetic olivine-rich dunite core below 1000 m depth; and the nearly non-magnetic mafic and felsic volcanic and volcanoclastic rocks west of the open pit.

Calculating the magnetic response of the reference model provides insight as to how the known geology relates to the observed magnetic data (Figure 7.31). Despite the complications with remanent magnetisation, the reference model can already explain much of the observed magnetic data, including the most of the main PUC anomaly, prior to performing any inversions. However, the difference between the observed data and the response predicted by the reference model (Figure 7.31) shows some important discrepancies. These subtle features may identify previously unknown details about the subsurface that can only be resolved using inversion.

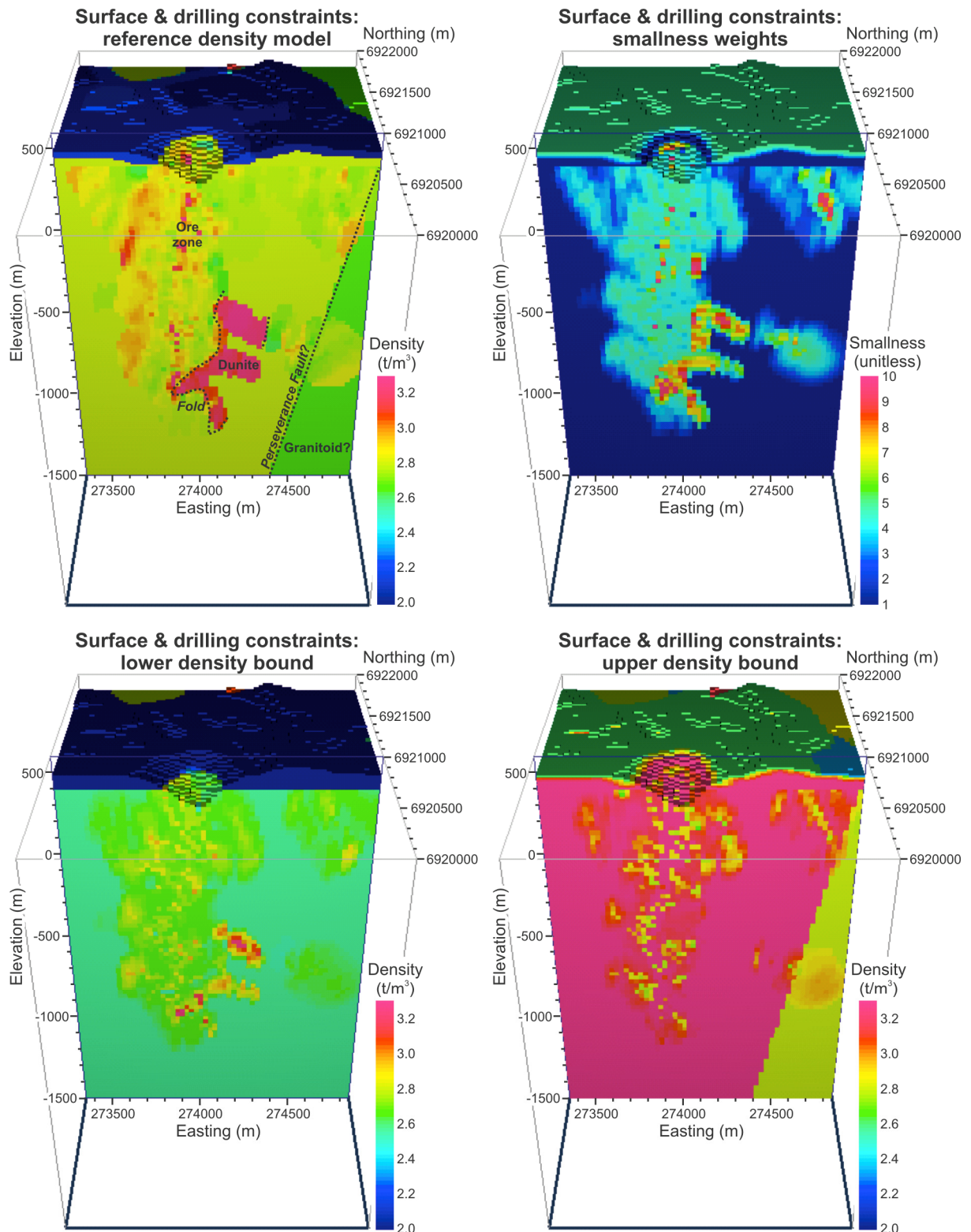


Figure 7.29. Density constraint models for the core of the Perseverance inversion volume based on drilling geology logs, density measurements and surface information. The observation-based constraints were extrapolated using the ellipsoidal buffers indicated in Table 7.4. The models show considerable complexity but reproduce much of the known geology, including a large dense dunite core at depth > 1 km, thin subvertical mafic and ultramafic bodies west of the open pit, and even patches of the massive sulphide ore zone.

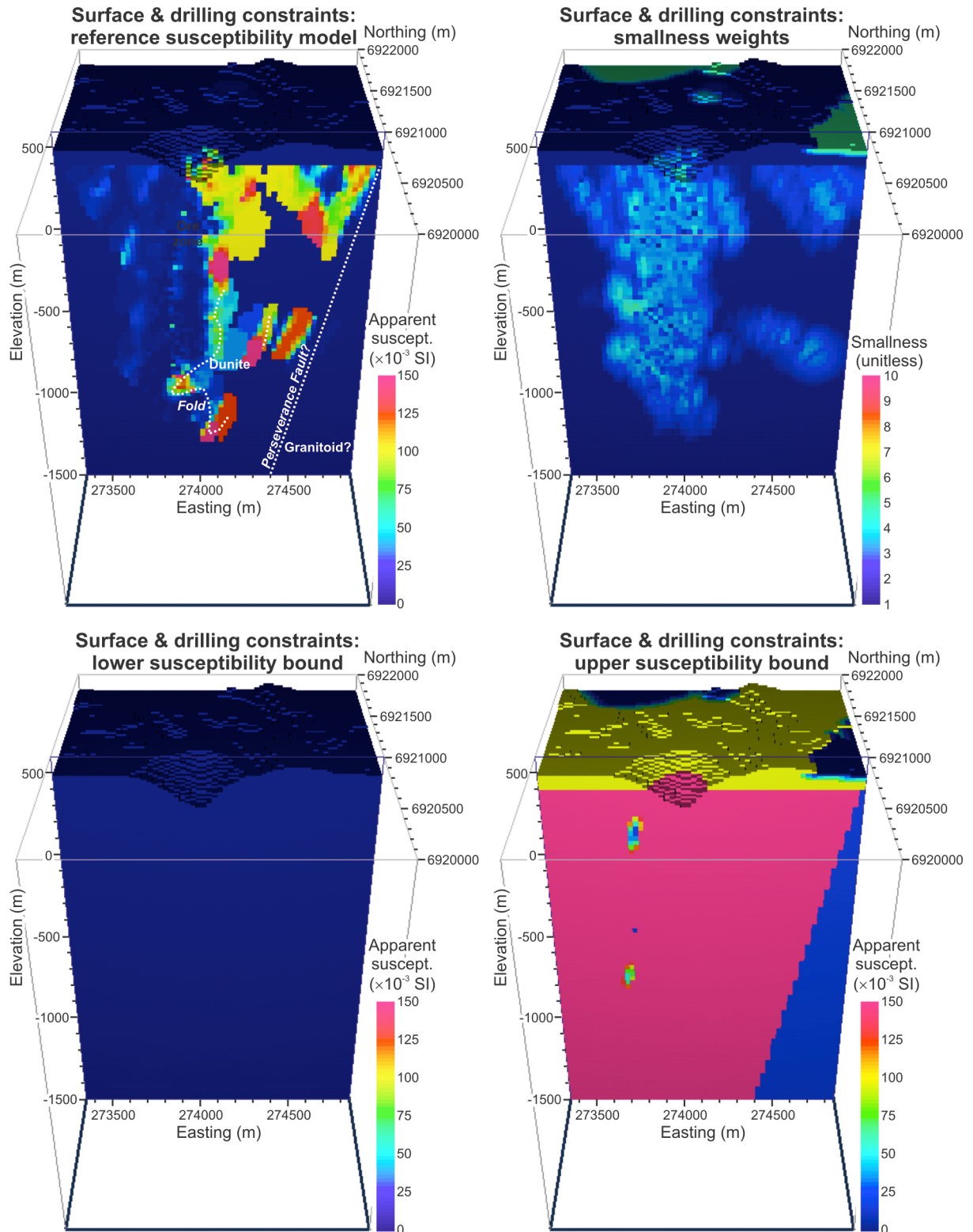


Figure 7.30. Apparent magnetic susceptibility constraint models for the core of the Perseverance inversion volume based on drilling geology logs, density measurements and surface information. Susceptibility measurements associated with ultramafic rocks were adjusted to allow for ubiquitous viscous remanent magnetisation with an average Koenigsberger ratio of 7 to give the apparent susceptibilities shown. The observation-based constraints were extrapolated using the ellipsoidal buffers indicated in Table 7.4. The models show considerable complexity but reproduce much of the known geology, including a large weakly magnetic dunite core at depth > 1 km below more magnetic serpentinised ultramafic rocks.

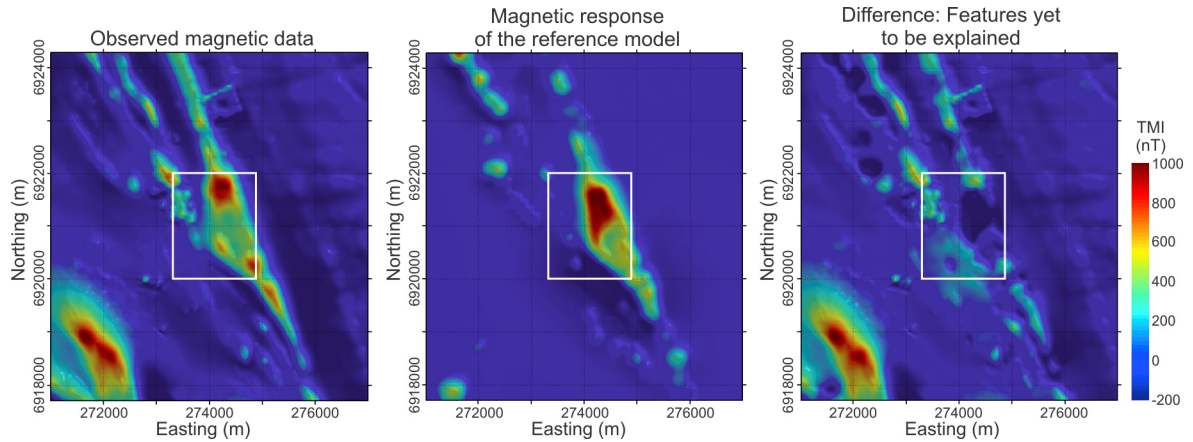


Figure 7.31. Comparison of the observed magnetic data with the magnetic response of the full reference model based on drilling and surface information. Even with the application of buffers and the approximation required to allow for remanent magnetisation in ultramafic rocks, the reference is roughly consistent with the observed magnetic data. The difference between the two indicates which features have not yet been explained by existing knowledge, and will need to be accounted for by the inversion. The white box shows the core inversion volume.

The results of the inversions at Perseverance are shown in Figure 7.32, including the default, geologically-unconstrained models, the models constrained by surface data only, and the models constrained by the best available geological data from mapping and drilling. It is clear that as increasing levels of constraints are included, the detail recovered in the models increases, but much of the enhanced detail is merely a reproduction of the supplied geological knowledge. This knowledge will only be modified if inconsistent with the geophysical data; if accurate it should be preserved in the recovered model results. The model recovered without geological constraints is very bland and only captures the major features: a large low density, highly magnetic body, likely to represent serpentinised ultramafic rocks, surrounded by some higher density, less magnetic mafic and possibly ultramafic rocks at shallow levels.

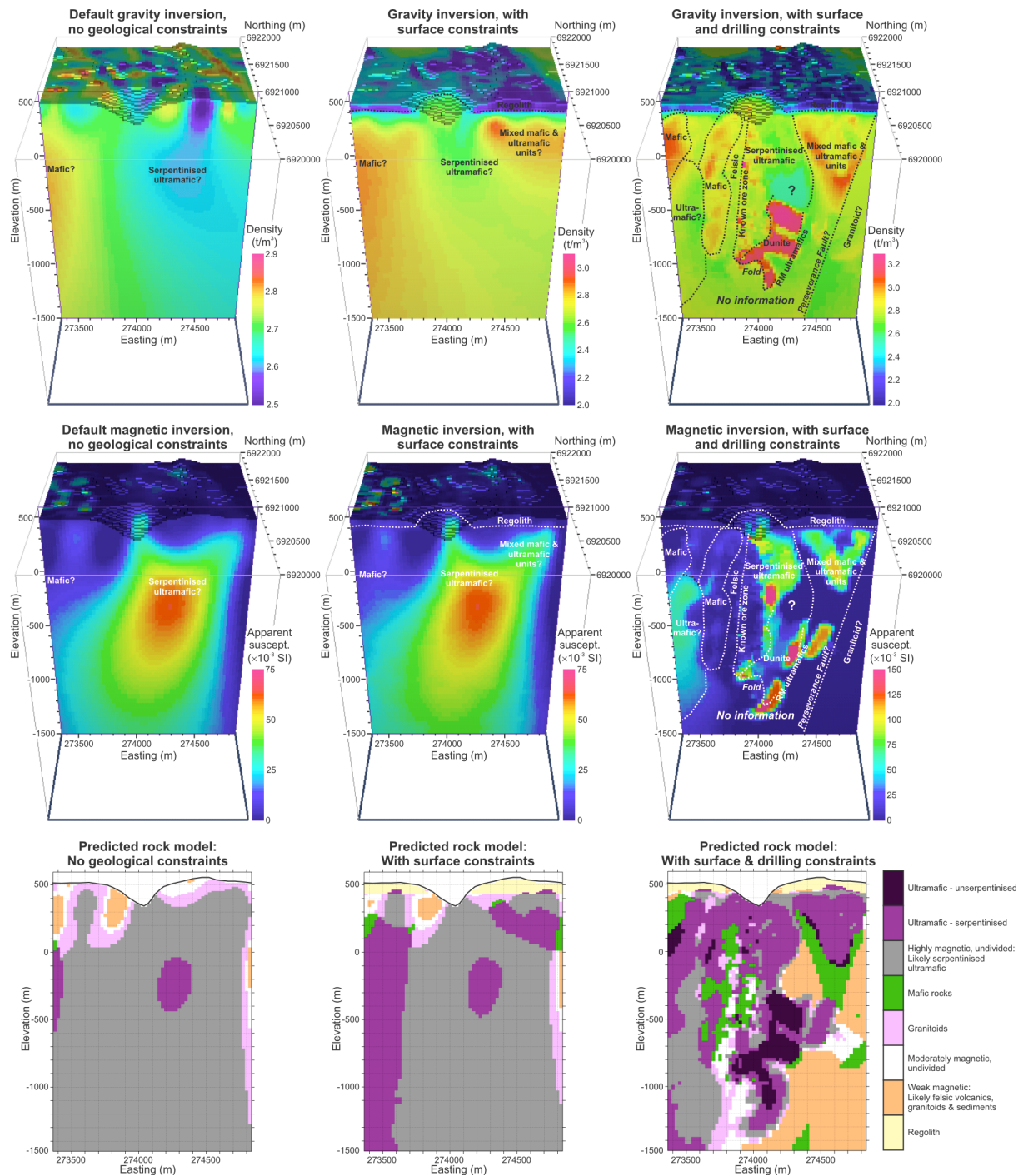


Figure 7.32. Results of the Perseverance gravity and magnetic inversions, with interpreted geology. The top row shows density models, the middle row show apparent susceptibility models (including an unknown component of remanent magnetisation), and the bottom row shows predicted rock models using the classification in Figure 7.11. The left column shows the default results with no geological constraints. The middle column shows results when surface constraints from mapping are used. The right column shows the best possible constraints from all available mapping and drilling. Each set of models is interpreted qualitatively based on relative properties in the top two rows, and quantitatively in the bottom row. Due to the complications associated with remanent magnetisation, the results should be treated as indicative given the current geological and geophysical knowledge. The colour scale for each physical property model is clipped to contain 99 % of the values in that model; the different colour scales emphasise the geometrical similarities and differences. All models satisfactorily reproduce the supplied geophysical data.

Surface constraints enhance the recovered density model to up to 500 m below surface by ensuring accurate reproduction of the low density regolith material that strongly influences the ground gravity data. Although not evident in this figure, the inversion actually recovers some variability in the thickness of regolith within the padding cells, giving a reasonably accurate depth-to-basement model. The surface constraints improve the resolution of the high density, variable susceptibility material east of the open pit and shift the main anomaly, inferred to represent a large serpentinised ultramafic body, slightly to the west. By applying estimates of the densities of the major mine infrastructure features as constraints, the inversion accurately handles the shallow anomalies attributed to the infrastructure. This is especially important for the waste rock dump east of the open pit which contributes a large low density anomaly from surface to great depth. Using the constraints, the waste rock dump anomaly can be completely contained within the dump, improving resolution of the dense rocks below. Given that the constraints, based on government surface mapping and some physical property estimates, cost nothing to obtain, the density result is clearly a large improvement on the default unconstrained result even with the lack of gravity data over the open pit.

The inversions that used all available geological information as constraints provide the most detailed models. As indicated for magnetic model in Figure 7.31, the reference models can actually explain much of the observed geophysical data. There are only relatively minor differences between the result in Figure 7.32 and the density and apparent magnetic susceptibility reference models in Figure 7.29 and Figure 7.30. The most notable enhancements from the reference models are the apparent recovery of a subvertical ultramafic unit at depth, west of the open pit, and the improved definition of the mafic and ultramafic rocks east of the open pit. Both were subtly present in the less constrained model results, but are much more clearly defined in the fully-constrained result.

Figure 7.32 includes both qualitative and quantitative geological interpretations estimates. The qualitative interpretations are based on relative physical property relationships, and provide a basic understanding of the model. These may be useful as they have filtered out some of the excessive detail in the model. However, the same rock model classifier employed for the regional- and district-scale models is also applied to obtain quantitative results. The results are more complicated to interpret, and should be treated with caution due to the known presence of remanent magnetisation, which can introduce geometrical artefacts. One problem

that is noted is that, in this particular area, it seems that the felsic (orange) and granitic rock (pink) classifications are reversed. Granite is known to be present along the eastern edge of the model beyond the Perseverance Fault, but the classifier indicates undivided felsic rocks. Likewise, felsic rocks are known to exist below the open pit in the footwall of the ore zone, but these rocks are classified as more magnetic granitic rocks. This indicates that the physical properties in this small area are slightly different from those in the district, and reflects the limited amount of petrophysical data available for the granitic rocks. Nevertheless, the predicted rock models do capture many of the more important features. They map out the extent of the dunite core, the mafic and felsic rocks below and west of the pit, the low density granitic/felsic rocks beyond the Perseverance Fault, and the mixed mafic and ultramafic rocks east of the Perseverance open pit.

There are some limitations to the results that become evident within the predicted rock model. The fact that the large dense dunite core is not evident in the less constrained models indicates that despite its size and extreme properties it is too deep to be detected with the existing ground gravity data. This is further confirmed in the fully-constrained inversion where the three fingers of dunite are not joined into a single continuous unit, as is likely. The geophysical data contain no additional information about the body, so the inversion has merely reproduced the supplied geological observations without adding any detail. Furthermore, the predicted felsic rock directly above the dunite core between -300 and 0 m elevation is highly unlikely, and again reflects the lack of information in the gravity data due to the hole in the data above the open pit. A zone of mafic rocks is predicted between 273,900-274,000 mE which is known from drilling not to be correct. It is merely an artefact of a mixture of measurements of high density nickel sulphide ore and low density serpentinised ultramafic rocks within individual cells when building the constraints. This shows that the predicted rock models can only be accurate where there is negligible mixing of rock types within each cell.

7.8 DISCUSSION

7.8.1 Limitations

The two most fundamental limitations on the interpretations in this study are the sparse distribution of gravity stations (with a median spacing of 2.3 km throughout the belt), and the limited physical property data for some rock types. The large gaps between gravity stations

limit the resolution to features that are $> \sim 3\text{--}4$ km across. They might also lead to aliasing of the gravity responses, which may make anomalies appear broader than they really are and may increase the apparent depth at which the source features are placed in the inversions. Geological constraints minimise the impact of aliasing, but more detailed gravity data would improve the quality and resolution of the models.

All constraints and interpretations were based on measurements on drill core within and around the Leinster nickel deposits, augmented by a modest number of samples of surface rocks throughout the district. Insufficient physical property measurements for some rock types limit the effectiveness of the constraints by reducing the accuracy of physical property estimates, and requiring wider, less certain property bounds for those rock types. The deposit scale inversions are affected by remanent magnetisation, but with representative remanent magnetisation and susceptibility measurements a reliable reference model of apparent susceptibilities can be created. Based on the limited remanent magnetisation measurements available a constant Koenigsberger ratio of 7 was applied to all ultramafic rocks. However, Chapter 4 indicates that there is considerable variability in the Koenigsberger ratios associated with different ultramafic rock types and alteration overprints. A more detailed understanding of the remanent magnetisation could be used to tailor the apparent susceptibilities in different portions of the model according to the known geology, to create more reliable models for handling such remanent magnetisation.

The predicted rock models show further complications due to limitations in the available physical property data. The isolated ultramafic bodies predicted in Figure 7.26 might more realistically be magnetic gneiss or granitic rocks, but too few physical property measurements are available for these rocks despite their abundance in the region. There are also only limited measurements of remanent magnetisation in the various mafic rocks. The data in Chapter 4 suggest that mafic intrusive rocks can contain notable remanent magnetisation, but it is not clear how pervasive and intense this really is. If common, then many of the predicted dense and magnetic ultramafic rocks identified in this study could actually be mafic intrusive rocks with remanent magnetisation, and this could change exploration models and targets in the region. The ambiguity associated with mixed lithologies within a single cell is irresolvable, so even with the most reliable physical property data, predicted rock models cannot be accurate where there is significant mixing of lithologies within individual cells.

A final limitation comes from the potential field data itself. Features can only be resolved within the inversions if they have anomalies contained in the supplied geophysical data. Given the depths of the models used at all scales, only large features with significant physical property contrasts will be recovered at depth. This is evident from the map slices through the regional- and district-scale models (Figure 7.15 and Figure 7.23), where the abundant thin elongate ultramafic rocks observed at shallow levels cannot be resolved below 3-5 km depth. Those rocks may continue to greater depths, but will never be accurately resolved by potential field data. The large deep features that can be resolved will generally have long wavelength anomalies indistinguishable from the long wavelength anomalies contributed by sources outside the inversion volume that must be removed by regional-residual separation. It is impossible to know the correct regional trend to remove, but use of geologically-constrained regional removal inversions, such as used here, is likely to give the most geologically-realistic regional responses. There will always be considerable ambiguity associated with features at great depths and synthetic data sensitivity modelling, in 2D and 3D, should be employed wherever the existence of deep features needs to be tested.

7.8.2 Geological interpretations

Regional- and district-scale models

Although the limitations indicated above must be acknowledged at all times, the recovered models provide useful predictions of the subsurface geology that are consistent with all currently available geological observations. As more geological, petrophysical and geophysical data becomes available, the quality of the models can be improved. However, there are already strong similarities to the existing basement geology interpretations. The 3D models add value by depicting the full 3D subsurface geometry. This allows 3D structural interpretation, mapping extensions of bodies below other units, and gives depth and thickness estimates throughout the greenstone belt (Figure 7.18). The thickness of the mafic-ultramafic sequences appears to increase to the south and to the north. The thinnest parts of the belt, < 2-km-thick, are near Cosmos, Honeymoon Well, and north of Mt. Keith. The thickest parts of the belt appear to extend to 10-12 km depth near Lawlers and Wiluna. The northwards trend of decreasing thickness of the greenstones in the EGST between Kalgoorlie and Leonora was implied by the seismic data (Figure 7.4), but can now be extended north to around Cosmos.

The thickest accumulations of greenstone rocks within the belt broadly correlate with the locations of most known gold deposits, notably at Wiluna and Agnew-Lawlers. Even gold deposits outside these two productive areas are associated with locally thickened greenstone packages; beneath the historic Bellevue and Kathleen Valley deposits near Cosmos, the greenstones are 4-8 km thick. If the mafic-ultramafic sequences were a source of gold, then it is reasonable to expect gold deposits to form in thick mafic-ultramafic sequences. Alternatively, gold mineralising fluids sourced from the mantle could have followed the same deep crustal structures that facilitated and controlled emplacement of thick mafic-ultramafic packages. This is consistent with evidence from observations in major gold districts and from the seismic data (Eisenlohr et al., 1989; Goleby et al., 2004; R. Blewett, pers. commun., 2008).

The results also indicate considerable variability in the thickness of the greenstones. Thin greenstones near Cosmos are < 8 km away from the relatively thick accumulations near the Bellevue and Kathleen Valley gold deposits to the south and north, respectively. In the Agnew-Lawlers region Figure 2.19 and the Lawlers cross section in Figure 7.24 show that outcropping mafic rocks near the hinge of the Lawlers Anticline are extremely thin (< 1 km) and underlain by a large low density, weakly magnetic granitoid intrusion. However, within 3-4 km west, north, and east, the greenstones thicken to > 8-10 km. This variability is consistent with the geometry of the greenstones in the northern seismic line in the adjacent Kurnalpi Terrane (Figure 7.4) and as determined from 2D gravity profile modelling by Peschler et al. (2004). It contrasts with the relatively constant thickness of greenstones imaged in the southern Kalgoorlie Terrane by the southern seismic line.

A thick accumulation of mafic and ultramafic rocks is identified beneath regolith and the late basin Jones Creek Conglomerate near the small Miranda gold deposits. The deposits include Cams and Scorpion and were mined for several years in the 1990's. Cams had an initial proven reserve of 0.4 Mt at 4.7 g/t and gold was hosted in sheared basalt 25-100 m below surface (Rohde, 1997). Identification of a more voluminous mafic-ultramafic sequence, apparent strike continuity with the rocks that host gold deposits at Bellevue and Kathleen Valley, an association with the late sedimentary basin, and proximity to the major structures bounding the greenstone belt, provide many similarities between the Miranda area and the richly mineralised Agnew area.

A goal of this study was to clarify the relationship between the gold-bearing komatiite – basalt association in the Agnew-Lawlers domain and the nickel-bearing komatiite – felsic volcanic association in the Mt. Keith-Perseverance domain. Previous workers have inferred the dividing line to be either the Leinster Anticline, intruded by the Leinster Granodiorite, or the Sir Samuel Fault (Eisenlohr, 1989; Liu et al., 2002; Duuring et al., 2004b). The NW linear trend of the Leinster Granodiorite may indicate that it intruded along a pre-existing structure that might have divided the two domains. However, mafic rocks are evenly distributed on both sides of the intrusion (Figure 7.18 and Figure 7.26) and gold deposits appear to coincide with thicker mafic-ultramafic accumulations regardless of geographic location. The distribution of felsic volcanic rocks may be more critical for identifying areas prospective for nickel, but since the felsic volcanic rocks and black shales have similar physical properties to the surrounding granitic rocks they are difficult to map reliably. They are depicted as patchy zones of undivided weakly magnetic felsic rocks and undivided highly magnetic rocks in the basement geology maps (Figure 7.17 and Figure 7.25). Since there is neither a fundamental difference in the character of the two domains nor any preserved evidence of a major structural divide it is possible that the distribution of the felsic volcanic rocks is merely controlled by their original depocentres.

Isolated pods of serpentinised ultramafic rocks were predicted below cover outside the expected boundaries of the greenstone belt, such as 10 km southeast of Perseverance and west of the Waroonga Shear Zone (Figure 7.26). There are two possible explanations for these features. Their recovered properties are completely consistent with serpentinised ultramafic rocks, and they could represent previously unrecognised pods of ultramafic rocks covered by a veneer of granitic rocks to account for the texture in the detailed magnetic data. However, most other ultramafic rocks in the Agnew-Wiluna belt are intimately associated with dense mafic rocks, and there is no evidence of higher density mafic rocks near these features. Alternatively, they could strongly represent magnetic granitic or gneissic rocks with normal polarity remanent magnetisation required to reproduce the susceptibilities recovered by the inversion. Existing basement geology maps classify these areas as either gneiss or foliated granite, consistent with this interpretation (Liu et al., 2000; Whitaker and Bastrakova, 2002). However, the pod southeast of Perseverance lies just west of several more thin zones of predicted ultramafic rocks which are interpreted as greenstones in existing basement geology maps. The available data cannot conclusively resolve the identity of these features. Measurement of the

direction and intensity of remanent magnetisation for foliated granite and gneiss samples might confirm whether they are capable of producing such magnetic anomalies.

Structure within the greenstone belt is variably resolved. The magnetic models delineate a large number of faults within the greenstone belt, and many correlate with mapped faults in the area. However, the models don't provide clear indications of the dips of the structures, either due to lack of resolution or because the faults are actually subvertical at shallow levels. The district-scale model does provide confirmation of the 3D geometry associated with the folds in the Agnew-Lawlers domain, including the Lawlers Anticline, Mt. White Syncline, and Leinster Anticline. The Lawlers Anticline is particularly well resolved in the gravity inversion models where it is intruded by the low density Lawlers Granite, whereas the Leinster Anticline is better resolved in the magnetic inversion models due to the more abundant thin ultramafic rocks. Beneath the Fairyland gold deposit at Lawlers, the 3D models provide a clear view of a NNW-trending upright synform (the southern extension of the Mt. White Syncline; Figure 7.24) that appears to be cut by a NNW-trending sinistral strike-slip fault whose displacement is only apparent in map view (Figure 7.23). Blewett and Czarnota (2007a) recognise this structural pattern throughout the EGST and have inferred that regional folding about NNW trends developed during the D4a structural event (2655-2650 Ma) and was overprinted by sinistral-strike slip faulting – especially along tightened fold limbs – during the D4b event (2650 Ma). This nicely demonstrates how 3D geometries recovered in inversions can be incorporated into a tectonic framework for an area.

The faults and shears that bound the greenstone belt are more challenging to resolve. Once they penetrate below the greenstone rocks, they juxtapose various granitic and gneissic rocks with very similar physical properties, so there is little contrast to provide a gravity or magnetic response. The best resolved structure is the Waroonga Shear, which is imaged as a west-dipping structure to at least 10 km depth in both the density and susceptibility models. In the Leinster cross section of the district-scale model (Figure 7.24) it appears to mark the western boundary of a low susceptibility wedge. The eastern boundary could mark the position of the east-dipping Ida Shear Zone, but it is not clearly observed elsewhere in the models. The Ida Fault System may control the notable contrast in magnetic properties between the Youanmi and Kalgoorlie Terrane basement rocks observed in the regional-scale magnetic inversions (Figure 7.15).

The eastern boundary of the southern Agnew-Wiluna belt is also associated with a low susceptibility wedge of undivided felsic rocks in the vicinity of the Perseverance Fault. The exact relationship between the Perseverance Fault and this wedge is not clear in the models, but it raises the possibility that the wedge lies between west- and east-dipping faults that merge along the eastern-edge of the belt. At the Perseverance mine drilling indicates that the western-most splays of the Perseverance Fault dip steeply ($\sim 80^\circ$) west, but it is usually inferred to be part of the east-dipping Keith-Kilkenny Shear Zone (Liu et al., 2002; Henson and Hitchman, 2004). The only significant westerly-dipping structure identified in the Kalgoorlie Terrane is the Bardoc Shear Zone in the Kalgoorlie area (Figure 7.4). Henson and Hitchman (2004) proposed that the Bardoc Shear Zone continues north into the Agnew-Wiluna greenstone belt, and linked it to the Sir Samuel Fault, west of the Perseverance mine. Since the inversion models show little evidence for a major crustal structure in the vicinity of the Sir Samuel Fault, it is proposed that the west-dipping Bardoc Shear Zone does continue into the Agnew-Wiluna and merges with the east-dipping Perseverance Fault about 25 km southeast of the Perseverance mine near the southern edge of the belt to form the observed structural wedge along the boundary. The merging of these faults would explain the 6-km-wide zone of sheared granitic rock described by Liu et al. (2002) along parts of the Perseverance Fault trace, and reconciles the west-dipping fault observed at Perseverance with the east-dipping continuation to the south. Henson and Hitchman (2004) also proposed that the Bardoc Shear Zone continues north to Wiluna. The regional-scale inversion results do seem to identify two west-dipping structures below and to the east of the Wiluna gold deposits (Figure 7.25), one of which could be the continuation of the Bardoc Shear Zone.

Deposit-scale models

In the deposit-scale results the challenges associated with remanent magnetisation are managed well by casting the magnetic inversion constraints and models as apparent susceptibilities that include a susceptibility component attributed to remanent magnetisation. The results may be less reliable, but still provide an acceptable representation of the known geology, and clarify the extents of several mafic and ultramafic units that are not adequately represented by the available drilling data. Even aside from the remanent magnetisation issues, the impact of including geological constraints is clear. Surface-based constraints enhance shallow anomalies, especially in the gravity inversions since the ground gravity data are

strongly influenced by the large near-surface density variations associated with regolith. An additional benefit of surface constraints is that they can accommodate the spurious features associated with mine infrastructure. By building inversion constraints using reasonable physical property estimates for infrastructure features such as waste rock dumps, ore stock piles and tailings ponds, the inversions can actually model any discrepancies from those estimates. It is clear from Figure 7.32 that the most detailed and reliable inversion results are those that include all the available geological information.

7.9 CONCLUSIONS

This chapter provides an integrated geological and geophysical study of the rocks associated with the Agnew-Wiluna greenstone belt at regional-, district-, and deposit scales. The study used the UBC–GIF gravity and magnetic inversion algorithms to extract 3D physical property models at each scale. The UBC–GIF algorithms are flexible enough to include variable amounts of geological information from a wide range of sources, without the need for developing full 3D geological models prior to performing the inversions. At the regional and district scales, only relatively limited geological data is available, primarily from surface mapping, but at the deposit scale detailed deep drilling provides additional 3D information. The constraints were built using the semi-automated procedure developed in Chapter 5, so are entirely reproducible, quick to obtain, and easy to update when additional information becomes available. By incorporating geological constraints from this available data, the physical property models recovered by the inversions are consistent with the available geological information as well as the geophysical data. Access to a representative physical property database is critical for developing reliable constraints and also allows the recovered physical property models to be translated back into predicted rock models that can form the basis for 3D geological interpretations.

Using these techniques, new 3D basement geology maps for the Agnew-Wiluna greenstone belt were derived at regional and district scales using publicly available data. These 3D maps are consistent with existing 2D basement geology interpretations, but have the added benefit of providing 3D predictions. An outcome of this is a new model of the thickness of mafic and ultramafic rocks within the greenstone belt which indicates that the thickest portions of the greenstone belt are the north and south ends at Wiluna and Lawlers, respectively. It is noted that most of the known gold deposits are associated with the thicker packages of

greenstone rocks, > 4 km thick, possibly explaining the abundance of gold at Wiluna and Agnew/Lawlers. It is postulated that gold-bearing fluids may have utilised the same structures that facilitated emplacement of voluminous mafic-ultramafic sequences. The belt thins considerably towards the Cosmos nickel deposit. Additional regions of thick mafic-ultramafic sequences are identified below cover in several places in the models, particularly near the south shore of Lake Miranda. Not only is there little outcrop in the area, but the modelling suggests that the voluminous mafic-ultramafic sequence there extends below the relatively thin Jones Creek Conglomerate late basin. The Miranda area has a couple of small historic gold mines and shares many features with the more richly endowed Agnew deposits, including proximity to the bounding structures and late basin along the west side of the greenstone belt.

Some outcrops of mafic rocks are shown to be very thin features underlain by voluminous granitic intrusions, such as in the hinge of the Lawlers Anticline. The results, especially the magnetic inversion models, clearly map the locations of several faults within the greenstone belt, but provide only limited information about the structures that extend into the underlying granitic and gneissic rocks below due to minimal physical property contrasts. The models confirm interpretations of the 3D geometry and even the timing of folding and faulting in the Lawlers area. The boundary between the Youanmi terrane to the west and the Kalgoorlie terrane is not clearly resolved; however the magnetic results suggest that the basement of the Youanmi Terrane is slightly more magnetic than the Kalgoorlie Terrane basement. A relatively shallow westerly dip is predicted for the Waroonga Shear Zone. The eastern boundary of the belt appears to coincide with a wedge of low susceptibility material bounded by west- and east-dipping faults. The only major west-dipping fault currently known in the Kalgoorlie Terrain is the Bardoc Shear Zone near Kalgoorlie. It is proposed that Bardoc Shear Zone continues northwards and merges with the east-dipping Perseverance fault in the southern portion of the belt creating a wide, complex shear zone along the eastern margin of the belt. This updates position of the Bardoc Shear Zone inferred by Henson and Hitchman (2004).

The deposit scale results are complicated by remanent magnetisation and gaps in the available gravity data, but do provide some additional information about the subsurface geology. With appropriate physical property knowledge it is possible to handle the complexities introduced by some types of remanent magnetisation as demonstrated in this example. The detailed reference models created from the extensive drilling database actually

reproduce much of the observed geophysical response, so the inversions are used to model the smaller geophysical anomalies that cannot yet be explained by the known geology. As a result, the shape and position of several small mafic and ultramafic bodies adjacent to the Perseverance deposit are mapped in more detail, and may provide new targets for further data acquisition. But even when such rich drilling databases are unavailable, the use of geological constraints from surface mapping can improve the resolution of near surface anomalies.

7.10 REFERENCES

- Anand, R.R., and Paine, M., 2002, Regolith geology of the Yilgarn Craton, Western Australia: implications for exploration: *Australian Journal of Earth Sciences*, v. 49, p. 3-162.
- Apex Minerals NL, 2007, Annual Report 2007: Perth, Apex Minerals NL, 88 p.
- Ash, M.R., Wheeler, M., Miller, H., Farquharson, C.G., and Dyck, A.V., 2006, Constrained three-dimensional inversion of potential field data from the Voisey's Bay Ni-Cu-Co deposit, Labrador, Canada: SEG Annual Meeting, New Orleans, October 1-6, p. 1333-1337.
- Barnes, S.J., Gole, M.J., and Hill, R.E.T., 1988, The Agnew nickel deposit, Western Australia; Part I, Structure and stratigraphy: *Economic Geology*, v. 83, p. 524-536.
- Barrett, F.M., Binns, R.A., Groves, D.I., Marston, R.J., and McQueen, K.G., 1977, Structural history and metamorphic modification of Archean volcanic-type nickel deposits, Yilgarn block, Western Australia: *Economic Geology*, v. 77, p. 1195-1223.
- Barrick Gold Corp., 2005, Annual Report 2005: Toronto, Barrick Gold Corp., 136 p.
- Bell, B., 2002, Application of potential field data to constrain three-dimensional geological modelling in the Leonora-Laverton transect area, *in* Cassidy, K.F., ed., *Geology, geochronology and geophysics of the north eastern Yilgarn Craton, with an emphasis on the Leonora-Laverton transect area*: Geoscience Australia, Record 2002/18, p. 75-82.
- Beresford, S.W., Duuring, P., Rosengren, N.M., Fiorentini, M., Bleeker, W., Tait, M.A., Barley, M.E., Cas, R.A.F., and Wallace, H., 2004, Structural and stratigraphic reconstruction of the Agnew-Wiluna belt, Western Australia, *in* Beresford, S.W., Duuring, P., Fiorentini, M., Rosengren, N.M., Bleeker, W., Barley, M.E., Cas, R.A.F., Tait, M.A., and Wallace, H., eds., *P710 final report: The structural and stratigraphic architecture of the Agnew/Wiluna Belt, WA*: Melbourne, AMIRA International, p. 1-7.
- Beresford, S.W., and Rosengren, N.M., 2004, Komatiite-hosted Ni-Cu-PGE deposits of the Agnew-Wiluna greenstone belt - an overview, *in* Neumayr, P., Harris, M., and Beresford, S.W., eds., *Gold and nickel deposits in the Archaean Norseman-Wiluna greenstone belt, Yilgarn Craton, Western Australia — a field guide*: Geological Survey of Western Australia, Record 2004/16, p. 87-91.
- BHP Billiton Ltd., 2007, 2007 BHP Billiton Annual Report: Melbourne, BHP Billiton Ltd., 296 p.
- Binns, R.A., Gunthorpe, R.J., and Groves, D.I., 1976, Metamorphic patterns and development of greenstone belts in the eastern Yilgarn Block, Western Australia, *in* Windley, B.F., ed., *The early history of the Earth*: London, John Wiley and Sons, p. 303-313.
- Blewett, R.S., 2004, A 5Qs synthesis and predictive mineral discovery, *in* Blewett, R.S., and Hitchman, A.P., eds., *Project Y2 Final Report: 3D geological models of the eastern Yilgarn Craton*: Perth, Predictive Mineral Discovery Cooperative Research Centre, p. 165-257.

- Blewett, R.S., Cassidy, K.F., Champion, D.C., Henson, P.A., Goleby, B.S., Jones, L., and Groenewald, P.B., 2004, The Wangkathaa Orogeny: an example of episodic regional 'D2' in the late Archaean Eastern Goldfields Province, Western Australia: *Precambrian Research*, v. 130, p. 139-159.
- Blewett, R.S., and Czarnota, K., 2007a, A new integrated tectonic framework of the Eastern Goldfields Superterrane: *Proceedings of Geoconferences Kalgoorlie '07 Conference*, Geoscience Australia Record 2007/14, p. 27-32.
- Blewett, R.S., and Czarnota, K., 2007b, Tectonostratigraphic architecture and uplift history of the Eastern Yilgarn Craton, Module 3: Terrane Structure, Project Y1-P763: *Geoscience Australia, Record 2007/15*, 114 p.
- Brown, S.J.A., Krapež, B., Beresford, S.W., Cassidy, K.F., Champion, D.C., Barley, M.E., and Cas, R.A.F., 2001, Archaean volcanic and sedimentary environments of the Eastern Goldfields Province, Western Australia — a field guide: *Western Australia Geological Survey, Record 2001/13*, 66 p.
- Burt, D.R.L., and Sheppy, N.R., 1975, Mount Keith nickel sulphide deposit, *in* Knight, C.L., ed., *Economic geology of Australia and Papua New Guinea*, 1. Metals: Melbourne, Australasian Institute of Mining and Metallurgy, p. 159-168.
- Cassidy, K.F., Blewett, R.S., Champion, D.C., and Goleby, B.R., 2003, Northeastern Yilgarn seismic reflection survey: implications for orogenic Au systems, *in* Goleby, B.R., Blewett, R.S., Groenewald, P.B., Cassidy, K.F., Champion, D.C., Jones, L.E.A., Korsch, R.J., Shevchenko, S., and Apak, S.N., eds., *The 2001 northeastern Yilgarn deep seismic reflection survey*: *Geoscience Australia, Record 2003/28*, p. 127-143.
- Cassidy, K.F., Champion, D.C., Fletcher, I.R., Dunphy, J.M., Black, L.P., and Claoue-Long, J.C., 2002, Geochronological constraints on the Leonora-Laverton transect area, north eastern Yilgarn Craton, *in* Cassidy, K.F., ed., *Geology, geochronology and geophysics of the north eastern Yilgarn Craton, with an emphasis on the Leonora-Laverton transect area*: *Geoscience Australia, Record 2002/18*, p. 37-58.
- Cassidy, K.F., Champion, D.C., Krapež, B., Barley, M.E., Brown, S.J.A., Blewett, R.S., Groenewald, P.B., and Tyler, I.M., 2006, A revised geological framework for the Yilgarn Craton, Western Australia: *Geological Survey of Western Australia, Record 2006/8*, 9 p.
- Cella, F., Fedi, M., Florio, G., Grimaldi, M., and Rapolla, A., 2007, Shallow structure of the Somma-Vesuvius volcano from 3D inversion of gravity data: *Journal of Volcanology and Geothermal Research*, v. 161, p. 303-317.
- Dentith, M.C., Evans, B.J., Paisch, K.F., and Trench, A., 1992a, Mapping the regolith using seismic refraction and magnetic data: results from the Southern Cross Greenstone Belt, Western Australia: *Exploration Geophysics*, v. 23, p. 97-104.
- Dentith, M.C., House, M., Ridley, J.R., Trench, A., and Dooley, J.C., 1992b, Three-dimensional structure of greenstone belts in Western Australia; implications for gold exploration: *Exploration Geophysics*, v. 23, p. 105-109.

- Dowling, S.E., Hill, R.E.T., and Sheppy, N.R., 1990, Komatiites and the Mt. Keith nickel deposit, Agnew-Wiluna greenstone belt: *Exploration Research News / CSIRO Division of Exploration Geoscience*, v. 3, p. 13.
- Duuring, P., Bleeker, W., and Beresford, S.W., 2004a, Major folding and remobilisation of nickel sulphides at Perseverance, Leinster, Western Australia, *in* Beresford, S.W., Duuring, P., Fiorentini, M., Rosengren, N.M., Bleeker, W., Barley, M.E., Cas, R.A.F., Tait, M.A., and Wallace, H., eds., P710 final report: The structural and stratigraphic architecture of the Agnew/Wiluna Belt, WA: Melbourne, AMIRA International, p. 73-124.
- Duuring, P., Bleeker, W., and Beresford, S.W., 2004b, Structural overview of the Agnew-Wiluna greenstone belt, Yilgarn Craton, Western Australia, *in* Beresford, S.W., Duuring, P., Fiorentini, M., Rosengren, N.M., Bleeker, W., Barley, M.E., Cas, R.A.F., Tait, M.A., and Wallace, H., eds., P710 final report: The structural and stratigraphic architecture of the Agnew/Wiluna Belt, WA: Melbourne, AMIRA International, p. 23-72.
- Eisenlohr, B.N., 1989, The structural development and controls on mineralisation of the northern sector of the Norseman-Wiluna Belt, Western Australia: Unpub. Ph. D. thesis, University of Western Australia, 189 p.
- Eisenlohr, B.N., Groves, D., and Partington, G.A., 1989, Crustal-scale shear zones and their significance to Archaean gold mineralization in Western Australia: *Mineralium Deposita*, v. 24, p. 1-8.
- Emerson, D.W., Macnae, J., and Sattel, D., 2000, Physical properties of the regolith in the Lawlers area, Western Australia: *Exploration Geophysics*, v. 31, p. 229-235.
- Farquharson, C.G., Ash, M.R., and Miller, H.G., 2008, Geologically constrained gravity inversion for the Voisey's Bay ovoid deposit: *The Leading Edge*, v. 27, p. 64-69.
- Farr, T.G., Rosen, P.A., Caro, E., Crippen, R., Duren, R., Hensley, S., Kobrick, M., Paller, M., Rodriguez, E., and Roth, L., 2005, The Shuttle Radar Topography Mission: *Reviews in Geophysics*, v. 45, RG2004, p. 33.
- Ferguson, K.M., 1998, Mineral occurrences and exploration potential of the North Eastern Goldfields: Geological Survey of Western Australia, Report 63, 40 p.
- Fiorentini, M., Rosengren, N., Beresford, S., Grguric, B., and Barley, M., 2007, Controls on the emplacement and genesis of the MKD5 and Sarah's Find Ni-Cu-PGE deposits, Mount Keith, Agnew-Wiluna Greenstone Belt, Western Australia: *Mineralium Deposita*, v. 42, p. 847-877.
- Fletcher, I.R., Mikucki, J.A., McNaughton, N.J., Mikucki, E.J., and Groves, D.I., 1998, The age of felsic magmatism and lode-gold mineralization events in the Lawlers area: Yilgarn craton, Western Australia [abs.]: *Geological Society of Australia Abstracts*, v. 49, p. 146.
- Fullagar, P.K., and Pears, G.A., 2007, Towards geologically realistic inversion, *in* Milkereit, B., ed., *Proceedings of Exploration 07: Fifth Decennial International Conference on Mineral Exploration*, p. 444-460.

Fullagar, P.K., Pears, G.A., and McMonnies, B., 2008, Constrained inversion of geologic surfaces—pushing the boundaries: *The Leading Edge*, v. 27, p. 98-105.

GADDS, 2006, Geophysical Archive Data Delivery System:
<http://www.geoscience.gov.au/gadds/>.

Gold Fields Ltd., 2007, Annual Report 2007: Johannesburg, Gold Fields Ltd., 266 p.

Gole, M.J., Barnes, S.J., and Hill, R.E.T., 1987, The role of fluids in the metamorphism of komatiites, Agnew nickel deposit, Western Australia: *Contributions to Mineralogy and Petrology*, v. 96, p. 151-162.

Goleby, B.R., Blewett, R.S., Groenewald, P.B., Cassidy, K.F., Champion, D.C., Korsch, R.J., Whitaker, A.J., Jones, L.E.A., Bell, B., and Carlson, G., 2003, Seismic interpretation of the northeastern Yilgarn Craton seismic data, *in* Goleby, B.R., Blewett, R.S., Groenewald, P.B., Cassidy, K.F., Champion, D.C., Jones, L.E.A., Korsch, R.J., Shevchenko, S., and Apak, S.N., eds., *The 2001 northeastern Yilgarn deep seismic reflection survey: Geoscience Australia, Record 2003/18*, p. 85-112.

Goleby, B.R., Blewett, R.S., Korsch, R.J., Champion, D.C., Cassidy, K.F., Jones, L.E.A., Groenewald, P.B., and Henson, P., 2004, Deep seismic reflection profiling in the Archaean northeastern Yilgarn Craton, Western Australia; implications for crustal architecture and mineral potential: *Tectonophysics*, v. 388, p. 119-133.

Goleby, B.R., Rattenbury, M.S., Swager, C.P., Drummond, B.J., Williams, P.R., Sheraton, J.E., and Heinrich, C.A., 1993, Archaean crustal structure from seismic reflection profiling, Eastern Goldfields, Western Australia: Australian Geological Survey Organisation, Record 1993/15, 54 p.

Griffin, T.J., 1990, Eastern Goldfields Province, *in* *Geology and mineral resources of Western Australia: Western Australia Geological Survey, Memoir 3*, p. 77-119.

Griffin, W.L., Belousova, E.A., Shee, S.R., Pearson, N.J., and O'Reilly, S.Y., 2004, Archean crustal evolution in the northern Yilgarn Craton: U-Pb and Hf-isotope evidence from detrital zircons: *Precambrian Research*, v. 131, p. 231-282.

Groenewald, P.B., Painter, M.G.M., and McCabe, M., 2001, East Yilgarn Geoscience Database, 1:100 000 geology of the north Eastern Goldfields Province - an explanatory note: Western Australia Geological Survey, Report 83, 99 p.

Groves, D.I., Goldfarb, R.J., Knox-Robinson, C.M., Ojala, J., Gardoll, S., Yun, G.Y., and Holyland, P., 2000, Late-kinematic timing of orogenic gold deposits and significance for computer-based exploration techniques with emphasis on the Yilgarn Block, Western Australia: *Ore Geology Reviews*, v. 17, p. 1-38.

GSWA, 2004, East Yilgarn DVD: Western Australia 1:100,000 geological information series, Department of Industry and Resources.

- Guillen, A., Courrioux, P., Calcagno, P., Lane, R., Lees, T., and McInerney, P., 2004, Constrained gravity 3D litho-inversion applied to Broken Hill: ASEG 17th Geophysical Conference & Exhibition, Sydney, 15-19 August.
- Hart, J., and Freeman, H., 2003, Geophysical responses of the Prominent Hill Fe-Cu-Au-U deposit: ASEG 16th Geophysical Conference & Exhibition, Adelaide, South Australia, 16-19 February.
- Henkel, H., 1991, Petrophysical properties (density and magnetization) of rocks from the northern part of the Baltic Shield: *Tectonophysics*, v. 192, p. 1-19.
- Henson, P., and Hitchman, A.P., 2004, An integrated geological and geophysical 3D map for the EYC, *in* Blewett, R.S., and Hitchman, A.P., eds., Project Y2 Final Report: 3D geological models of the eastern Yilgarn Craton: Perth, Predictive Mineral Discovery Cooperative Research Centre, p. 39-89.
- Hill, R.E.T., Barnes, S.J., Gole, M.J., and Dowling, S.E., 1990, Physical volcanology of komatiites; a field guide to the komatiites of the Norseman-Wiluna Greenstone Belt, Eastern Goldfields Province, Yilgarn Block, Western Australia: *Excursion Guide Book - Geological Society of Australia*, v. 1, 100 p.
- Hill, R.E.T., Barnes, S.J., Gole, M.J., and Dowling, S.E., 1995, The volcanology of komatiites as deduced from field relationships in the Norseman-Wiluna greenstone belt, Western Australia: *Lithos*, v. 34, p. 159-188.
- Jackson, J., Pears, G.A., and Fullagar, P., 2004, Minimisation of the Gravity Response from Mine Infrastructure: An Example from Sons of Gwalia Mine, WA: ASEG 17th Geophysical Conference & Exhibition, Sydney, 15-19 August.
- Jaireth, S., Hoatson, D., Jaques, L., Huleatt, M., and Ratajkoski, M., 2005, Nickel sulphide metallogenic provinces: resources and potential: *Geoscience Australia, AusGeo News*, n. 79.
- Kelso, P.R., Banerjee, S.K., and Teyssier, C., 1993, Rock magnetic properties of the Arunta Block, central Australia, and their implication for the interpretation of long-wavelength magnetic anomalies: *Journal of Geophysical Research, B, Solid Earth and Planets*, v. 98, p. 15,987-15,999.
- Langworthy, P.J., 2004, Cosmos Nickel Project, Kathleen Valley, *in* Neumayr, P., Harris, M., and Beresford, S.W., eds., Gold and nickel deposits in the Archaean Norseman-Wiluna greenstone belt, Yilgarn Craton, Western Australia — a field guide: *Geological Survey of Western Australia, Record 2004/16*, p. 109-115.
- Leshner, C.M., and Keays, R.R., 2002, Komatiite-associated Ni-Cu-PGE deposits: geology, mineralogy, geochemistry, and genesis, *in* Cabri, L.J., ed., The geology, geochemistry, mineralogy and mineral beneficiation of platinum-group elements: *Canadian Institute of Mining, Metallurgy and Petroleum, Special Volume 54*, p. 579-617.

- Li, Y., and Oldenburg, D.W., 1996, 3-D inversion of magnetic data: *Geophysics*, v. 61, p. 394-408.
- Li, Y., and Oldenburg, D.W., 1998a, 3-D inversion of gravity data: *Geophysics*, v. 63, p. 109-119.
- Li, Y., and Oldenburg, D.W., 1998b, Separation of regional and residual magnetic field data: *Geophysics*, v. 63, p. 431-439.
- Libby, J.W., Stockman, P.R., Cervoj, K.M., Muir, M.R.K., Whittle, M., and Langworthy, P.J., 1998, Perseverance nickel deposit, *in* Berkman, D.A., and Mackenzie, D.H., eds., *Geology of Australian and Papua New Guinean mineral deposits*: Melbourne, Australasian Institute of Mining and Metallurgy, p. 321-328.
- Liu, S.F., Champion, D.C., and Cassidy, K.F., 2002, Geology of the Sir Samuel 1:250,000 sheet area, Western Australia: *Geoscience Australia, Record 2002/14*, 57 p.
- Liu, S.F., Griffin, T.J., Wyche, S., and Westaway, J., 1996, Sir Samuel, W.A. Sheet 3042: 1:100 000 Geological Map Series, Western Australia Geological Survey.
- Liu, S.F., Stewart, A.J., Farrell, T.R., Whitaker, A.J., and Chen, S.F., 2000, Solid geology of the North Eastern Goldfields, Western Australia: 1:500 000 scale map, Canberra, AGSO.
- Macdonald, J., 2002, The role of geoscience in attracting investment: World Mines Ministries Forum, Toronto, 13-15 March.
- Marquis, R., Bois, D., and McGaughey, J., 2003, Quantitative geology using 3D common-earth modeling: PDAC 2003, Toronto, March 9-12.
- Martin, J.E., and Allchurch, P.D., 1975, Perseverance nickel deposit, Agnew, *in* Knight, C.L., ed., *Economic geology of Australia and Papua New Guinea*, 1. Metals: Melbourne, Australasian Institute of Mining and Metallurgy, p. 149-155.
- Milligan, P.R., Minty, B.R.S., Luyendyk, T., and Lewis, A., 2001, Comparisons of total magnetic intensity grids, combined using Gridmerge, with two independent datasets: *Geoscience Australia, Record 2001/43*, 47 p.
- Myers, J.S., 1993, Precambrian history of the West Australian Craton and adjacent orogens: *Annual Review of Earth and Planetary Sciences*, v. 21, p. 453-485.
- Myers, J.S., 1995, The generation and assembly of an Archaean supercontinent; evidence from the Yilgarn Craton, Western Australia: *Geological Society Special Publications*, v. 95, p. 143-154.
- Naldrett, A.J., and Turner, A.R., 1977, The geology and petrogenesis of a greenstone belt and related nickel sulfide mineralization at Yakabindie, Western Australia: *Precambrian Research*, v. 5, p. 43-103.

- Nelson, D.R., 1997, Evolution of the Archaean granite-greenstone terranes of the Eastern Goldfields, Western Australia: SHRIMP U-Pb zircon constraints: *Precambrian Research*, v. 83, p. 57-81.
- Nettleton, L.L., 1939, Determination of density for reduction of gravimeter observations: *Geophysics*, v. 4, p. 176-183.
- Peschler, A.P., Benn, K., and Roest, W.R., 2004, Insights on Archean continental geodynamics from gravity modelling of granite-greenstone terranes: *Journal of Geodynamics*, v. 38, p. 185-207.
- Phillips, N.D., 1996, Geophysical inversion in an integrated exploration program: examples from the San Nicolás deposit: Unpub. Masters thesis, University of British Columbia, 237 p.
- Phillips, N.D., and Oldenburg, D.W., 2002, Geophysical inversion in an integrated mineral exploration program: examples from the San Nicolás deposit: SEG Annual Meeting, Salt Lake City, October 6-10.
- Portniaguine, O., and Zhdanov, M.S., 1999, Focusing geophysical inversion images: *Geophysics*, v. 64, p. 874-887.
- Portniaguine, O., and Zhdanov, M.S., 2002, 3-D magnetic inversion with data compression and image focusing: *Geophysics*, v. 67, p. 1532-1541.
- Riganti, A., and Groenewald, P.B., 2004, East Yilgarn geoscience database - updated rock codes: Western Australia Geological Survey, Record 2004/13, 73 p.
- Rohde, C., 1997, Annual Report: Miranda Project, Cams/Scorpion: Western Australia Department of Industry and Resources, Open File Report A55158, 120 p.
- Rosengren, N.M., Beresford, S.W., Grguric, B.A., and Cas, R.A.F., 2005, An intrusive origin for the komatiitic dunite-hosted Mount Keith disseminated nickel sulfide deposit, Western Australia: *Economic Geology*, v. 100, p. 149-156.
- Sawaryn, S.J., and Thorogood, J.L., 2005, A compendium of directional calculations based on the minimum curvature method: SPE Drilling & Completion, paper 84246, p. 24-36.
- Swager, C.P., 1997, Tectono-stratigraphy of late Archaean greenstone terranes in the southern Eastern Goldfields, Western Australia: *Precambrian Research*, v. 83, p. 11-42.
- Swager, C.P., Goleby, B.R., Drummond, B.J., Rattenbury, M.S., and Williams, P.R., 1997, Crustal structure of granite-greenstone terranes in the Eastern Goldfields, Yilgarn Craton, as revealed by seismic reflection profiling: *Precambrian Research*, v. 83, p. 43-56.
- Telford, W.M., Geldart, L.P., and Sheriff, R.E., 1990, *Applied Geophysics*: New York, Cambridge University Press, 770 p.
- Trofimovs, J., Tait, M.A., Cas, R.A.F., McArthur, A., and Beresford, S.W., 2003, Can the role of thermal erosion in strongly deformed komatiite-Ni-Cu-(PGE) deposits be determined?

- Perseverance, Agnew-Wiluna Belt, Western Australia: Australian Journal of Earth Sciences, v. 50, p. 199-214.
- UBC–GIF, 2005a, GRAV3D version 3.0: A program library for forward modelling and inversion of gravity data over 3D structures: The University of British Columbia–Geophysical Inversion Facility, 46 p.
- UBC–GIF, 2005b, MAG3D version 4.0: A program library for forward modelling and inversion of magnetic data over 3D structures: The University of British Columbia–Geophysical Inversion Facility, 41 p.
- USGS, 2007, USGS Seamless Data Distribution System: <http://seamless.usgs.gov/>.
- Vanderhor, F., and Flint, R.B., 2001, 1:500 000 Interpreted bedrock geology of Western Australia: Geological map, Geological Survey of Western Australia.
- Watts, A., 1997, Exploring for nickel in the 90s, or ‘til depth us do part’, *in* Gubins, A.G., ed., Proceedings of Exploration 97: Fourth Decennial International Conference on Mineral Exploration, 97, p. 1003–1014.
- Weber, U.D., Kohn, B.P., Gleadow, A.J.W., and Nelson, D.R., 2005, Low temperature Phanerozoic history of the Northern Yilgarn Craton, Western Australia: Tectonophysics, v. 400, p. 127-151.
- Welford, J.K., and Hall, J., 2007, Crustal structure of the Newfoundland rifted continental margin from constrained 3-D gravity inversion: Geophysical Journal International, v. 171, p. 890-908.
- Whitaker, A.J., and Bastrakova, I.V., 2002, Yilgarn Craton aeromagnetic interpretation: 1:1 500 000 Map, Geoscience Australia.
- Whiting, T.H., 2006, Tomorrow's exploration challenges for today's megaminer(s): Australian Earth Science Convention, Melbourne, 2-6 July, GSA Conference Abstract Series, p. 63-64.
- Williams, N.C., Lane, R., and Lyons, P., 2004, Towards 3D maps of alteration under cover: Regional constrained 3D inversion of potential field data from the Olympic Cu-Au province, South Australia: Preview, p. 30-33.

Chapter 8: Conclusions

8.1 SUMMARY OF RESEARCH

Integrating geological information with physical property knowledge can enhance the reliability of 3D gravity and magnetic inversion models for mineral exploration applications as demonstrated in this thesis. The approach is based on the limited geological information that is available during early-stage or greenfields exploration programs and avoids the need for geological interpretations that cannot be substantiated directly by the available observations. This method has been used previously by Phillips (1996) and Farquharson et al. (2008); however, this thesis provides the first rigorous documentation of the types of geological observations that can be used, how the observations are most effectively utilised, and details the benefits that can be expected.

8.1.1 Use of geological constraints

The synthetic gravity inversion example in Chapter 2 clearly demonstrates the importance of including basic geological constraints from surface mapping and physical property measurements in geophysical inversions. Not only are these constraints the most readily available, they can provide the greatest improvement in the accuracy of the model, both qualitatively and quantitatively. These surface constraints may cost nothing to obtain where surface mapping has been previously undertaken by government agencies, researchers or explorers, and reasonable physical property estimates can be made based on neighbouring regions or existing databases. They should be included in every inversion. Regolith can show a strong density contrast with basement rocks, so it is just as important to include constraints based on cover material as it is to include constraints based on basement rock outcrops. At regional and district scales where cover is too thin to be effectively modelled, specifying the properties associated with basement outcrops may be the only constraint available, but can still make a significant contribution, as demonstrated in Chapter 7.

The benefits of including drilling-based constraints are proportional to the amount of drilling information available. A small number of drill holes with detailed physical property information can refine the recovered model adjacent to the holes, but will have limited impact on the whole model (Chapter 2). A large drilling database, as used in the deposit-scale inversions in Chapter 7, can provide tight constraints in a larger volume and is necessary to

recover detail at depth. Basic 3D models, such as the layered earth models used in Chapter 7, provide a useful way to restrict the range of properties in particular areas where conceptual geological knowledge indicates that certain features may or may not be present. With careful choice of constraints these regions can be allowed to favour a particular physical property distribution without excluding other possibilities.

Although using constraints based solely on geological observations can create extremely reliable constraint models, in most exploration contexts these observations will only occupy a limited number of cells, and so may not have as much influence on the whole model as might be expected. In these situations it can be beneficial to extrapolate the observations based on observed or expected geological trends. The new approach proposed in Chapter 5 makes the logical assumption that physical properties may be correlated over larger distances along strike and down dip than perpendicular to the dip plane. It calculates ellipsoidal buffers based on specified geological orientations, and populates cells within those buffers in a way that takes into account as much information as is available surrounding that cell. Although not a substitute for detailed geostatistical analysis and kriging, this method is quick, efficient and works where data are too sparsely distributed for more rigorous geostatistical methods to be used. Application of this buffering method in Chapter 2 demonstrates that such buffers can dramatically enhance the contribution of even limited drilling information.

This study identified and rectified several limitations to the standard implementation of some parameters in the UBC–GIF inversions, especially regarding the use of geological constraints. The current UBC–GIF implementation uses the concept of length scales to facilitate recovery of geological trends within an inversion model. These length scales, in the east, north and vertical directions, are a global measure applied to the whole model at once. Since length scales do not represent a clear geological concept, this study introduced the idea of aspect ratios which describe the shape of the expected geological units. The judicious use of the existing length scale and smoothness weight parameters described in Chapter 2 allows different aspect ratios to be assigned in different parts of a model without changing the core algorithm. By accommodating variations in geological trends and orientations within the earth, this approach provides greater flexibility for linking the geometries of recovered models to the expected geological trends. It also addresses a fundamental ambiguity of potential field data which poorly resolve flat lying features.

The study also clearly identified the two ways in which reference models can be included in the UBC–GIF algorithm, and the uses of each method. The ‘smooth model difference’ approach has been the default functionality built into the inversion codes for many years, and ensures that differences between the recovered model and the reference model are smoothly distributed over a number of adjacent cells. As a result, wherever there is a sharp change in properties in a reference model, there will be a sharp change in the recovered properties. This approach is ideal for hypothesis-testing inversions where every cell is assigned a non-default reference property value based on a full 3D model of surface-bounded geological units (Oldenburg and Pratt, 2007). The approach favoured in this study is a ‘smooth model’ approach which ensures that the recovered model itself varies smoothly. This promotes extrapolation of geological constraints into adjacent cells that lack geological observations. This approach is necessary when geological observations are sparsely distributed. The only previously documented use of the smooth model style of inversion was by Phillips (1996) because it was not an explicit option in the UBC–GIF algorithm. Instead it had to be implemented using restrictive bounds and a zero reference model everywhere, thus losing the flexibility of applying smallness weights to indicate geological information with variable reliability in different parts of a reference model. The benefit of the smooth model approach for implementing sparse geological constraints is evident from the results presented in Chapters 2 and 7. As a result of this work the UBC–GIF inversion code has now been modified to allow a user choice of smooth model difference or smooth model inversions when using a non-default reference model.

A final challenge encountered in the standard implementation of the UBC–GIF inversion codes was the interaction between depth or distance weighting and non-default reference models. It was noted in Chapter 2 that depth or distance weighting is actually a soft mathematical constraint that allows larger differences between the reference model and the recovered model as depth or distance from the geophysical observations increases. Although it is a necessary constraint where no other information is available it has the effect of reducing the influence of actual geological constraints in the reference model, especially at depth. The solution proposed in this study is to multiply the desired smallness and smoothness weights associated with cells containing geological information by the squared inverse of the depth or distance weighting associated with those cells, w_z^{-2} . This effectively turns depth or distance

weighting off in those cells that contain geological constraints, and ensures that the inversions reproduce both the observed geology and the observed geophysical data.

8.1.2 Physical properties

Geological constraints can only be as reliable as the observations on which they are based and are critically dependent on reliable physical property information. Similar rock types have widely varying physical properties depending on the specific hydrothermal and metamorphic history of the rocks. Therefore physical property measurements must be acquired in any complex or ancient terrane. Even a relatively small number of new measurements can be used to validate an existing dataset, as demonstrated in Chapter 4.

If magnetic inversions are to be used, then it is critical to assess the importance of remanent magnetisation in the area. It is commonly assumed that remanent magnetisation is negligible, as required by the UBC–GIF magnetic inversion algorithms, but measurements of remanent magnetisation in Chapter 4 show that significant viscous remanent magnetisation is common in ultramafic rocks in the Agnew-Wiluna greenstone belt. This suggests that remanent magnetisation should be considered in magnetic inversions in all Archean granite-greenstone terranes. Although several approaches have been proposed to accommodate remanent magnetisation in inversions (Paine et al., 2001; Li et al., 2004; Shearer, 2005; Lelièvre et al., 2006), all combine the induced susceptibility and remanent magnetisation components into a single magnetisation measure. As a result they are incompatible with constraints based directly on measured susceptibilities or measured remanent magnetisation. In situations where remanent magnetisation exists and is subparallel to the earth field direction, measured susceptibilities and Koenigsberger ratios can be used to create apparent susceptibility constraints which can be used within the inversions, as demonstrated in Chapter 7. The technique will not work where remanent magnetisation directions differ significantly from the earth field direction, but does allow for viscous remanent magnetisation which is common in many rocks (Dunlop, 1983; Yu and Tauxe, 2006).

The mineral estimation technique presented in Chapter 6 provides a powerful way to convert physical properties into mineralogy predictions, using petrographic constraints. The method has an extremely high success rate for predicting sulphide-rich rocks based on their physical properties. When applied to geologically-constrained inversion models in the Olympic Dam region of South Australia, it correctly identified many known copper deposits and several

potential new exploration targets. Despite its potential value, the technique was not applied to the Agnew-Wiluna greenstone belt inversions in Chapter 7 for a number of reasons. The technique is best suited to the hypothesis-testing style of inversion where a full 3D model of geological units is used to constrain the inversion, rather than the sparse data-based approach used in Chapter 7. When a full 3D lithological model is used to constrain the inversion the mineralogy estimates quantify the alteration or mineralisation required to explain deviations of the recovered models from the supplied lithological model. The technique also assumes that the volumes of alteration and mineralisation span multiple (> 3 -5) cells in the recovered models. This is not the case in the Agnew-Wiluna greenstone belt where serpentinisation and sulphide mineralisation are relatively thin features associated with relative thin ultramafic rocks. The technique could possibly be employed to estimate the mineralogy in the deposit scale inversion models where alteration and mineralisation occupy a larger proportion of the model. However, given the depth of the Perseverance deposit, the limited gravity data, and the presence of remanent magnetisation, it was decided that a lithological mapping approach would be more reliable.

8.1.3 Performing inversions

The basic steps for performing UBC–GIF inversions have been covered in existing literature (Li and Oldenburg, 1995, 1996, 1998; UBC–GIF, 2005a, b) and in various examples (Phillips, 1996; Oldenburg and Pratt, 2007; Welford and Hall, 2007; Farquharson et al., 2008), but conflicting approaches have been suggested and there has been no single comprehensive description of all stages of the process. To address these inconsistencies, a workflow is presented in Chapter 3 that covers all aspects of preparing, running and assessing UBC–GIF inversion. The workflow is based on the existing documentation, augmented by details from the procedures used in developing the inversions presented in Chapters 2 and 7. The workflow provides a standard “best practice” procedure that clearly establishes the key requirements for reliable gravity and magnetic inversions. Some of the key contributions of the new workflow include:

- How to define an appropriate mesh and depth of investigation, data extents, data spacing, cell sizes, and padding cells for a particular problem.

- Clarification of the gravity data processing required, with fully terrain corrected data preferred. Simple Bouguer slab data may be acceptable in situations where terrain corrections are expected to be minimal.
- An approach to reconcile the need to upward continue potential field data to suit the cell sizes being used, while avoiding the use of gridded data to prevent introducing artificial data points.
- Guides for identifying appropriate background data levels for gravity and magnetics data, and the relationships between gravity data, densities, and density contrasts. These relationships are critically important when correlating physical properties obtained from inversions with actual measurements.
- Identification of the need to use the more rigorous ‘distance weighting’ instead of the standard ‘depth weighting’ that has been the default recommendation. Distance weighting handles topography and irregularly spaced data appropriately. Depth weighting is an approximation that works for regular gridded data on a completely flat surface.
- Proposal of two new methods for linking geological geometries to the mathematical coefficients controlling the measures of smallness and smoothness. The use of aspect ratios is preferred and is demonstrated in Chapter 2 and 7.
- Outline of how hypothesis-based constraints using a full 3D model can be created in the Gocad modelling package, and how data-based constraints can be created in the GIFtools:ModelBuilder package developed in Chapter 5.
- Detailed guide for assessing the quality of recovered inversions models, and whether they have satisfied all necessary criteria to be considered plausible models of the physical property distribution.

8.1.4 Geological interpretation of inversion results

New 3D basement geology interpretations for the Agnew-Wiluna greenstone belt at regional and district scales were developed and presented in Chapter 7. These new interpreted geological models offer an improvement over existing 2D basement geology interpretations because they place the interpreted features at appropriate depths within the model, rather than

displaying only their surface projection. They also only classify those cells in the model that have distinct physical properties, so help indicate where ambiguity is present in the interpretation. Although such classifications are bound to suffer from misclassification in some areas, the results appear to be broadly equivalent to existing basement geology interpretations. Since they can be obtained relatively quickly, cheaply, and automatically, they provide a means for explorers to develop their own basement geology interpretations to use as a framework for more detailed data acquisition and modelling.

One outcome of the modelling is a prediction of the thickness of the mafic-ultramafic rock packages along the length of the Agnew-Wiluna belt. The modelling highlights the decreasing mafic-ultramafic thickness and volume northwards to Cosmos, and the increasing thickness and volume beyond Cosmos towards Wiluna. It also identifies a spatial relationship between most of the known gold deposits and thick mafic-ultramafic sequences. It could be argued that the emplacement of these more voluminous mafic-ultramafic packages was controlled by major crustal structures, and these pre-existing structures provided conduits for focussed fluid flow associated with gold mineralisation.

The ability of the geologically-constrained inversions to map below cover is demonstrated by the delineation of a non-outcropping mafic-ultramafic sequence below and south of Lake Miranda. The area lies along the western edge of the greenstone belt, in the corridor that typically contains the late extensional basin Jones Creek Conglomerate (Liu et al., 2000). However, the inversion models suggest that the relatively thin (< 200-400 m) regolith and basement conglomerate are underlain by a voluminous 6-km-thick mafic-ultramafic succession. This association is similar to that observed for the Agnew gold deposits further south with voluminous thick mafic-ultramafic rocks juxtaposed against late basin conglomerates controlled by extensional structures which may have focussed fluid flow. Although some gold was mined from shallow non-outcropping mafic rocks at the Cams and Scorpion deposits in the 1990s (Rohde, 1997), the inversion models indicate that the mafic-ultramafic rocks extend for several kilometres beneath cover and could demonstrate potential for follow-up exploration in the area.

The modelling provides variable resolution of the faults bounding the greenstone belt. Along the western margin, the Waroonga Shear Zone is resolved as a west-dipping structure to 10 km depth. The Ida Fault System that marks the western edge of the Kalgoorlie Terrain is not

well resolved but may mark the boundary between more magnetic basement in the Youanmi Terrane from less magnetic basement in the Eastern Goldfields Superterrane. Along the eastern edge of the greenstone belt there is evidence that the Perseverance Fault is composed of separate west- and east-dipping structures that merge 25 km southeast of Perseverance and continue northwards to beyond Mt. Keith. The east-dipping structure likely correlates with the Keith-Kilkenny Shear Zone (Liu et al., 2002; Henson and Hitchman, 2004). The only major west-dipping structure in the Kalgoorlie Terrane is the Bardoc Shear Zone (Goleby et al., 1993). Henson and Hitchman (2004) infer that the Bardoc Shear Zone does continue into the Agnew-Wiluna belt, and the modelling in this study shifts their interpreted location several kilometres east to the edge of the greenstone belt.

The models also capture some of the structural detail within the belt, despite the limitations imposed by sparse gravity stations:

- Beneath the Fairyland deposit at Lawlers the 3D models define a large upright NW-trending synform cut by a NW-trending sinistral strike-slip fault. This relationship is consistent with the existing structural framework and deformation history (Blewett and Czarnota, 2007) which can be used to date the development of those structures to ~2655-2650 Ma.
- The shape of the Lawlers Anticline is more clearly defined and outcropping mafic rocks in its hinge are shown to be surprisingly thin (< 1-2 km).
- Complex fault patterns are identified by the magnetic models, but these are difficult to trace away from the magnetic ultramafic rocks because of the poor resolution in the gravity data.

At the deposit scale, surrounding the Perseverance nickel deposit, the lack of gravity data over the large open pit limits the effectiveness of the inversions, but several important results are still apparent. The inclusion of surface geological observations clearly improves the resolution of density anomalies in the top 500 m, and should enhance the definition of subsurface exploration targets where better geophysical data coverage is available. Inclusion of surface constraints in the inversions can also help derive reasonable depth-to-basement estimates which can be factored into targeting decisions. The addition of detailed drilling information did help identify several mafic and ultramafic bodies that were previously poorly

defined, and indicate that existing drilling may not have sufficiently tested those portions of the model. Perhaps an unexpected outcome was the ability to use the constructed geological reference models to predict the observed geophysical data directly prior to performing any inversions. The forward modelled response of a reference model can be compared to available data to determine which geophysical anomalies cannot yet be explained by the model and may benefit from more detailed modelling and data acquisition. This may also provide information for geophysical survey design in near-mine environments by helping to identify the data spacing and coverage required to more accurately define a particular feature.

8.2 LIMITATIONS OF THE RESEARCH AND METHODS

This thesis analysed the existing UBC–GIF inversion codes to identify how they can be most efficiently used for mineral exploration problems. It was not intended to modify the functionality of the UBC–GIF algorithm directly. The existing functionality is sufficiently flexible to include a large amount of varied types of geological information and these capabilities have not previously been fully demonstrated in published research. Although this thesis has identified several methods for improving the reliability of inversion models using geological constraints, the biggest limitation on the methods and results remains that imposed by the non-uniqueness of potential field data and inversion.

It is clear from the geologically-constrained inversion models results presented in Chapter 2 and Chapter 7 that even when most of the conceivably available geological information is included, the recovered predictions of the subsurface physical property distributions are not definitive. The number of models that can reproduce an observed potential field dataset is limitless. Even when reliable geological constraints are applied in $> 25\%$ of a model, representing a higher proportion than will usually be available in early-stage exploration programs, the models still lack geological definition and retain considerable ambiguity and fuzziness. This is to be expected from the simple relationship that eliminating even 99.9 % of an infinite number of possible models still leaves an infinite number of models. The problem is not just the use of sparsely distributed constraints. Using a hypothesis-testing approach to develop a full 3D model of constraints will only test a small number of the possible models, and may not eliminate any of those models; an infinite number of hypotheses may remain untested. Including geological constraints in a gravity or magnetic inversion will never fully define the actual subsurface geology, and any expectation that this will be the case

is unrealistic. The purpose of geological constraints is to ensure that the (possibly infinite) set of models is limited to only those that can explain all of the geological observations as well as the geophysical data. The best possible inversion result is one that cannot be dismissed for being inconsistent with some piece of geological knowledge. The only way such a model can be recovered is by including all available geological knowledge as constraints. In doing so, the inversions may provide reliable predictions about subsurface features demanded by the geophysical data that are not explained by existing geological knowledge.

Given the extreme non-uniqueness associated with inversion, reliable results cannot be obtained where the geophysical data is limited. The results presented in Chapter 7 are hampered by the wide gravity station spacing averaging 3.2 km across the Agnew-Wiluna greenstone belt. Such wide spacings are typical of public gravity data across Australia (Figure 8.1). The resolution of inversions is fundamentally limited by the resolution of the original geophysical data. Widely spaced data can also alias geophysical anomalies. For potential field data this will usually result in broader and deeper source features being recovered in the inversions in place of the smaller shallower features that are actually present. Geological constraints help to remove some of the ambiguity associated with aliasing, but the availability of geological observations themselves is limited. It is therefore critical that adequate geophysical data is collected for the specific problem being addressed. The existing 2.3-km-spaced gravity data can only be expected to map features $> \sim 4$ km across, based on the Nyquist Theorem. If a nickel exploration program in the Agnew-Wiluna greenstone belt seeks to map the locations of the ~ 700 -m wide ultramafic adcumulate lenses that are known to host sulphide-rich ore bodies in the belt, then the Nyquist Theorem suggests that the spacing of gravity stations should be < 350 m. Spatial correlation of data over an area may allow for slightly wider spacing. Standard 400-m flight line aeromagnetic data flown perpendicular to geological strike meets this criterion but may not make the fundamental distinction between the mafic rocks, felsic volcanic and volcanoclastic rocks, and granitoids, so is insufficient for mapping on its own.

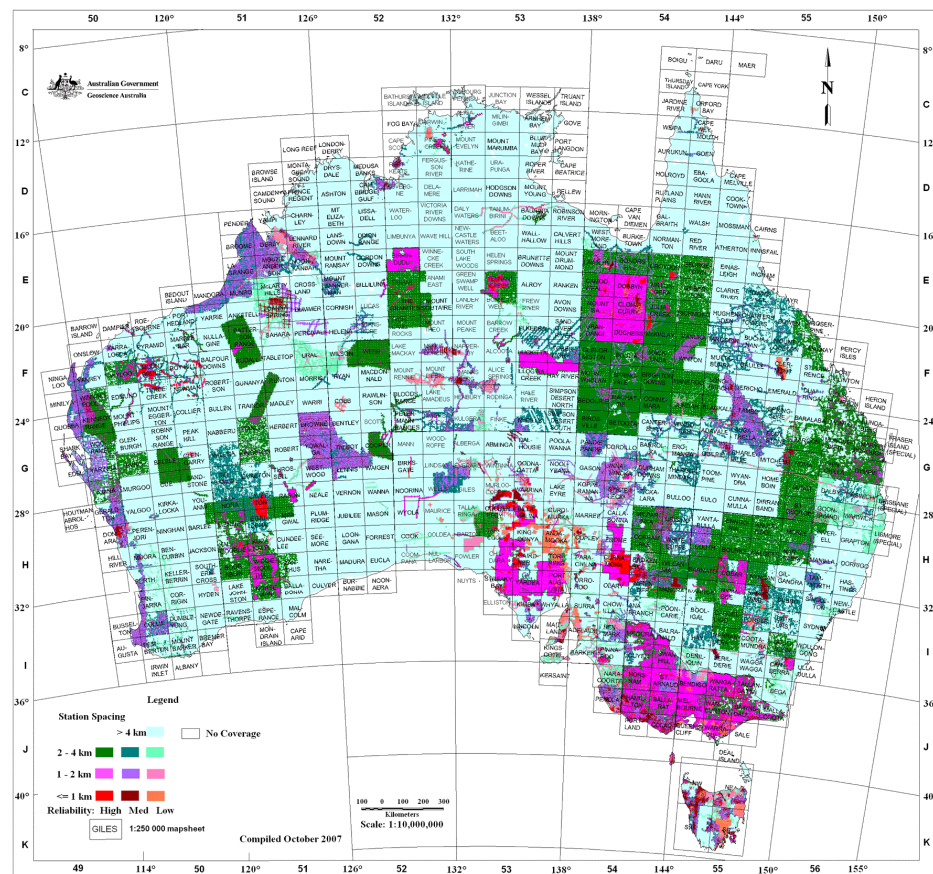


Figure 8.1. Publicly available ground gravity station coverage over Australia as of October 2007 from Geoscience Australia (2007). The average gravity station spacing is > 2-4 km across the continent; areas with < 1 km station spacing are extremely rare. The Agnew-Wiluna greenstone belt is contained in the Wiluna, Sir Samuel, and Leonora map sheets between 26-29 °S and 120-121.5 °E.

The inversion methods presented in this study assume that only relatively limited geological information is available or that the information is restricted to surface rocks or clusters of drill holes. If a large amount of geological information is available, with detailed structural mapping and measurements, regularly-spaced drill holes and a strong 3D understanding of the geometry of the subsurface, then other inversion approaches must be considered. Other inversion algorithms with different regularisation measures and geological constraint options may provide alternate solutions, and the choice may depend on the type of problem being addressed (Silva et al., 2001). Assessment of the suitability of each inversion approach for different exploration problems will require additional research.

Although a large component of software development was required to achieve the goals of this thesis, including development of the GIFtools:ModelBuilder software in Chapter 5 and Appendix B, and the mineralogy estimator in Chapter 6, this was not a software development thesis. The programs have been created to fulfill a research purpose, and are not presented as

robust deployable packages. All efforts have made to ensure correctness of the solutions; the ModelBuilder code has been tested by several different researchers with diverse datasets. Further programming and development work may be required to ensure the software can be deployed reliably. The software is presented as proof of concept research code and should be treated as such when used.

8.3 FUTURE RESEARCH OPPORTUNITIES

Although many types of geological information have been discussed in this study, there are many more which have yet to be utilised to their full potential. Cella et al. (2007) and Welford and Hall (2007) have both demonstrated the use of seismic reflection interpretations as geological constraints in UBC–GIF inversions with some success. Further research should investigate the application of such information using the techniques presented in this study, including the use of smooth model inversion, removal of depth/distance weighting in geologically-constrained cells, and extrapolation of the constraints based on observed or inferred structural trends. At regional scales, seismic velocity models could be used to derive basic models of density constraints using estimated seismic velocity and density relationships (Ludwig et al., 1970; Christensen and Mooney, 1995). Although this technique has proved to be somewhat ineffective for 2D profile forward modelling of gravity data (Barton, 1986), inversions have the benefit that they can reconcile the estimated densities in a reference model with the observed gravity data, and so extract a more reliable model than can be achieved using only forward modelling.

The methods outlined in Chapter 5 for the extrapolation of physical properties within constraint models could also be enhanced to better incorporate observed structural measurements. Ideally the ellipsoidal buffers should be based on actual structural measurements in each cell containing observations. This can currently be achieved only for those cells that contain structural measurements. It would be useful if those observed orientations could be extrapolated into adjacent cells that lack structural measurements to guide the extrapolation of physical property constraints in those cells. This could be achieved by performing an initial phase of extrapolation of the structural measurements to create a 3D model of structural orientations. Alternatively, the GeoModeller structural modelling package (Intrepid Geophysics) performs a more robust extrapolation of structural observations. Either method would provide a suitable 3D model of structural orientations, based on actual

measurements, which could be used to define ellipsoidal buffers for extrapolating physical property constraints in GIFtools:ModelBuilder.

There are two main bottlenecks in the workflow for preparing gravity and magnetic inversions presented in Chapter 3: gridding and upward continuing the data; and determining data levels and density contrasts. Neither is directly related to the inversions but both issues may introduce significant errors in the results if not treated carefully. The solutions presented in Chapter 3 will work with any data and will minimise introduction of errors. However, both stages are time consuming and tedious. Gridding and upward continuing irregularly spaced data could be streamlined by the development of a quick, efficient, and accurate equivalent source gridding algorithm with characteristics of smoothness and smallness. Several attempts were made during the course of this thesis to develop such a methodology within the existing UBC–GIF inversion code, but small inaccuracies associated with topography and extremely irregular data spacing could not be overcome. Further research is required on this approach.

Identifying the background data level for magnetic and gravity data can be approximately achieved by using the mean data value, however iteration is required to test that choice. A more efficient solution would be to include the background data value as an extra parameter to be solved for in the inversion. In this way, the inversion would seek the data level that allows the inversion to recover the optimal small and smooth model. For gravity data, the background data level is related to the background density in the model, and knowledge of this background density is required to convert between observed densities and recovered density contrasts. By including the model in a non-zero half-space and solving for an appropriate background density and data level, it may be possible to solve the inversion directly for densities. This would avoid introducing errors converting measured densities into density contrast constraints, would simplify the inversion processes, and provide results that are easier to interpret directly.

A powerful way to manage the non-uniqueness of inversions is to combine the information contained in different geophysical datasets using joint or cooperative inversion. This is an active field of research and several techniques have been employed (Haber and Oldenburg, 1997; Bosch and McGaughey, 2001; Guillen et al., 2004; Lelièvre et al., 2007). The physical property data presented in Chapter 4 indicate that densities and susceptibilities can be highly correlated due to the action of specific geological processes. Chemical, thermal,

pressure, and stress gradients are common drivers for geological processes, and these gradients will commonly impose variations on physical properties consistent with those gradients. This leads to two relationships that might be exploited to relate different physical properties.

The first is a geometrical relationship that indicates that physical properties tend to change in the same physical positions, without knowledge of the magnitude or sign of the gradient. Examples might be alteration fronts, lithological contacts, or faults, across which both properties may change. This approach for inversions has been described by Haber and Oldenburg (1997) and Lelièvre et al. (2007) for simple examples, but has not yet been applied to complex real examples where detailed geological constraints are available for both sets of properties. Such an approach would ensure that the physical property models recovered for two different datasets shared a common structure or geometry while also satisfying explicit geological observations. Having reliable constraints on the value of two different properties in a cell, and a common property gradient direction should provide a much stronger constraint on the inversion than either of the properties or the geometry alone.

The second relationship is a statistical correlation between physical properties imposed by specific geological processes. Igneous differentiation provides a strong positive correlation between density and susceptibility; serpentinisation of ultramafic rocks provides a strong negative correlation. However some geological processes affect some properties more than others, for instance addition of nickel sulphide assemblages to serpentinised ultramafic rocks primarily increases the densities of the rocks but may have a variable effect on susceptibilities. Because the correlation is different for different processes, and different processes may have occurred in different areas, a general correlation cannot be applied to relate two separate inversions. However it might provide a useful soft constraint to indicate that particular correlations are favoured in particular regions of a model where certain geological processes have been identified, or where particular physical property thresholds are satisfied. Serpentinisation only occurs in ultramafic rocks, so the negative correlation between densities and susceptibilities associated with serpentinisation could be encouraged in areas where ultramafic rocks have been identified, or where the rocks have the high susceptibilities typical of ultramafic rocks. Such subtle constraints may be difficult to implement and control in inversions, but form an important basis for the intuition that a geologist uses when building an understanding of rocks.

Finally, this thesis does not attempt to assess the benefits and limitations of other inversion algorithms. Instead it focuses on how to maximise the value of inversions with relatively limited geological constraints using the flexible approach provided by the UBC–GIF algorithms utilising smooth and small least-squares (L_2 -norm) regularisation. Future research should compare UBC–GIF inversion results prepared using the procedures and geological constraints outlined in this thesis to those obtained using equivalent geological information in other inversion algorithms and approaches, such as those provided by GeoModeller (Guillen et al., 2004), VPmg (Fullagar et al., 2008), GRMAG3D (Portniaguine and Zhdanov, 1999, 2002), or other non-commercialised approaches that implement different regularisation methods. Such comparisons are necessary to help identify the particular problems and datasets that can be solved most efficiently and effectively with each inversion approach.

8.4 CONCLUDING STATEMENT

Geologically-constrained 3D inversions of gravity and magnetic data provide a practical means to predict subsurface geology. The techniques presented in this thesis demonstrate the effectiveness of inversions for identifying exploration targets, and mapping stratigraphy and structure at depth and below cover. In many situations basic but useful constraints can be developed from publicly available or pre-existing data with minimal additional expense.

On their own, however, inversions cannot replace integrated exploration programs because of their insurmountable non-uniqueness, especially under the restrictions imposed by limited geological and geophysical data. Instead, the goal of geophysical inversions is to identify and delineate significant subsurface features and provide a holistic framework into which other exploration datasets can be integrated to develop enhanced targeting techniques. The inclusion of reliable, observation-based geological constraints in inversions will always enhance the detail and quality of subsurface predictions. However, those predictions must be combined with geological experience, mapping, drilling, structural analysis, geochemistry, mineral system models, fluid-flow modelling, and integrated geophysical techniques. The results can then be used to develop quantitative exploration risk models on which to base targeting decisions.

8.5 REFERENCES

- Barton, P.J., 1986, The relationship between seismic velocity and density in the continental crust - a useful constraint?: *Geophysical Journal International*, v. 87, p. 195-208.
- Blewett, R.S., and Czarnota, K., 2007, A new integrated tectonic framework of the Eastern Goldfields Superterrane: *Proceedings of Geoconferences Kalgoorlie '07 Conference*, Geoscience Australia Record 2007/14, p. 27-32.
- Bosch, M., and McGaughey, J., 2001, Joint inversion of gravity and magnetic data under lithologic constraints: *The Leading Edge*, v. 20, p. 877-881.
- Cella, F., Fedi, M., Florio, G., Grimaldi, M., and Rapolla, A., 2007, Shallow structure of the Somma–Vesuvius volcano from 3D inversion of gravity data: *Journal of Volcanology and Geothermal Research*, v. 161, p. 303-317.
- Christensen, N.I., and Mooney, W.D., 1995, Seismic velocity structure and composition of the continental crust: A global view: *Journal of Geophysical Research*, v. 100, p. 9761-9788.
- Dunlop, D.J., 1983, Viscous magnetization of 0.04-100 μm magnetites: *Geophysical journal of the Royal Astronomical Society*, v. 74, p. 667-687.
- Farquharson, C.G., Ash, M.R., and Miller, H.G., 2008, Geologically constrained gravity inversion for the Voisey's Bay ovoid deposit: *The Leading Edge*, v. 27, p. 64-69.
- Fullagar, P.K., Pears, G.A., and McMonnies, B., 2008, Constrained inversion of geologic surfaces—pushing the boundaries: *The Leading Edge*, v. 27, p. 98-105.
- Geoscience Australia, 2007, Gravity station coverage over Australia, October 2007: <http://www.ga.gov.au/minerals/research/methodology/geophysics/acquisition.jsp>, accessed August 2008.
- Goleby, B.R., Rattenbury, M.S., Swager, C.P., Drummond, B.J., Williams, P.R., Sheraton, J.E., and Heinrich, C.A., 1993, Archaean crustal structure from seismic reflection profiling, Eastern Goldfields, Western Australia: Australian Geological Survey Organisation, Record 1993/15, 54 p.
- Guillen, A., Courrioux, P., Calcagno, P., Lane, R., Lees, T., and McNerney, P., 2004, Constrained gravity 3D litho-inversion applied to Broken Hill: ASEG 17th Geophysical Conference & Exhibition, Sydney, 15-19 August.
- Haber, E., and Oldenburg, D., 1997, Joint inversion: a structural approach: *Inverse Problems*, v. 13, p. 63-78.
- Henson, P., and Hitchman, A.P., 2004, An integrated geological and geophysical 3D map for the EYC, *in* Blewett, R.S., and Hitchman, A.P., eds., *Project Y2 Final Report: 3D geological models of the eastern Yilgarn Craton*: Perth, Predictive Mineral Discovery Cooperative Research Centre, p. 39-89.

- Lelièvre, P.G., Oldenburg, D.W., and Phillips, N., 2006, 3D magnetic inversion for total magnetization in areas with complicated remanence: SEG Technical Program Expanded Abstracts, v. 25, p. 953-957.
- Lelièvre, P.G., Phillips, N.D., and Oldenburg, D.W., 2007, Joint and Cooperative Inversion Strategies for Mineral Exploration: American Geophysical Union, Fall Meeting 2007, abstract# NS43A-07.
- Li, Y., and Oldenburg, D.W., 1995, Separation of regional and residual magnetic field data: SEG Annual Meeting expanded technical program abstracts with biographies, v. 65, p. 791-794.
- Li, Y., and Oldenburg, D.W., 1996, 3-D inversion of magnetic data: Geophysics, v. 61, p. 394-408.
- Li, Y., and Oldenburg, D.W., 1998, 3-D inversion of gravity data: Geophysics, v. 63, p. 109-119.
- Li, Y., Shearer, S., Haney, M., and Dannemiller, N., 2004, Comprehensive approaches to the inversion of magnetic data with strong remanent magnetization: SEG 74th Annual International Meeting Expanded Abstracts, p. 1191–1194.
- Liu, S.F., Champion, D.C., and Cassidy, K.F., 2002, Geology of the Sir Samuel 1:250,000 sheet area, Western Australia: Geoscience Australia, Record 2002/14, 57 p.
- Liu, S.F., Stewart, A.J., Farrell, T.R., Whitaker, A.J., and Chen, S.F., 2000, Solid geology of the North Eastern Goldfields, Western Australia: 1:500 000 scale map, Canberra, AGSO.
- Ludwig, W.J., Nafe, J.E., and Drake, C.L., 1970, Seismic refraction, *in* Maxwell, A.E., ed., The Sea, v. 4: New York, Wiley, p. 53-84.
- Oldenburg, D.W., and Pratt, D.A., 2007, Geophysical inversion for mineral exploration: A decade of progress in theory and practice, *in* Milkereit, B., ed., Proceedings of Exploration 07: Fifth Decennial International Conference on Mineral Exploration, p. 61-95.
- Paine, J., Haederle, M., and Flis, M., 2001, Using transformed TMI data to invert for remanently magnetised bodies: Exploration Geophysics, v. 32, p. 238-242.
- Phillips, N.D., 1996, Geophysical inversion in an integrated exploration program: examples from the San Nicolás deposit: Unpub. Masters thesis, University of British Columbia, 237 p.
- Portniaguine, O., and Zhdanov, M.S., 1999, Focusing geophysical inversion images: Geophysics, v. 64, p. 874-887.
- Portniaguine, O., and Zhdanov, M.S., 2002, 3-D magnetic inversion with data compression and image focusing: Geophysics, v. 67, p. 1532-1541.
- Rohde, C., 1997, Annual Report: Miranda Project, Cams/Scorpion: Western Australia Department of Industry and Resources, Open File Report A55158, 120 p.

- Shearer, S.E., 2005, Three-dimensional inversion of magnetic data in the presence of remanent magnetization: Unpub. Masters thesis, Colorado School of Mines, 148 p.
- Silva, J.B.C., Medeiros, W.E., and Barbosa, V.C.F., 2001, Potential-field inversion: Choosing the appropriate technique to solve a geologic problem: *Geophysics*, v. 66, p. 511-520.
- UBC–GIF, 2005a, GRAV3D version 3.0: A program library for forward modelling and inversion of gravity data over 3D structures: The University of British Columbia–Geophysical Inversion Facility, 46 p.
- UBC–GIF, 2005b, MAG3D version 4.0: A program library for forward modelling and inversion of magnetic data over 3D structures: The University of British Columbia–Geophysical Inversion Facility, 41 p.
- Welford, J.K., and Hall, J., 2007, Crustal structure of the Newfoundland rifted continental margin from constrained 3-D gravity inversion: *Geophysical Journal International*, v. 171, p. 890-908.
- Yu, Y., and Tauxe, L., 2006, Acquisition of viscous remanent magnetization: *Physics of The Earth and Planetary Interiors*, v. 159, p. 32-42.

Appendix A: Mass and magnetic property measurements

Table A.1. Physical property measurement sample locations. UTM coordinates are given in Map Grid of Australia Zone 51 coordinates relative to the Australian Height Datum. The *in situ* orientation of the sample is indicated for drill hole samples. Surface samples were unoriented.

Sample ID	Hole ID	Depth from (m)	Depth to (m)	Easting (m)	Northing (m)	Elevation (m)	Down-hole plunge direction (°)	Down-hole plunge (°)
D0101	LPU937-1	247.34	247.68	273829.5	6921097.6	-810.7	65	44
D0102	LPU937-1	256.85	257.09	273835.7	6921100.5	-817.4	65	45
D0104	LPU937-1	262	262.3	273839.0	6921102.0	-821.0	65	45
D0203	LPU938-5	5.6	6	273606.7	6920986.8	-630.4	76	40
D0204	LPU938-5	60.4	60.7	273647.0	6920996.8	-666.1	76	41
D0206	LPU938-5	66.7	67	273651.6	6920997.9	-670.1	76	41
D0208	LPU938-5	104.7	105	273679.0	6921004.5	-695.7	77	43
D0209	LPU938-5	108.7	109.1	273682.0	6921005.2	-698.3	77	43
D0210	LPU938-5	110.3	110.6	273683.1	6921005.5	-699.4	77	43
D0212	LPU938-5	202.35	202.8	273748.3	6921020.8	-762.5	77	44
D0213	LPU938-5	209	209.4	273753.0	6921021.8	-767.2	76	44
D0215	LPU938-5	219.2	219.5	273760.1	6921023.5	-774.2	77	44
D0216	LPU938-5	258.7	259	273787.3	6921030.2	-802.0	75	46
D0217	LPU938-5	261.2	261.5	273789.0	6921030.6	-803.8	74	46
D0218	LPU938-5	279.5	279.7	273801.1	6921034.2	-817.1	72	46
D0219	LPU938-5	284.1	284.5	273804.1	6921035.2	-820.5	72	46
D0222	LPU938-5	314.3	314.6	273823.3	6921042.2	-842.7	70	47
D0223	LPU938-5	318.7	319	273826.2	6921043.2	-845.8	70	47
D0401	LPU941-19	239.27	239.78	273876.8	6920850.4	-796.9	82	53
D0402	LPU941-19	247.61	247.94	273881.8	6920851.1	-803.3	82	53
D0403	LPU941-19	249.6	249.93	273882.9	6920851.3	-805.1	82	53
D0501	LPU954-3	36.53	36.91	273918.8	6920539.6	-484.2	54	25
D0503	LPU954-3	52.42	52.86	273930.4	6920548.2	-491.0	52	26
D0505	LPU954-3	85.77	86.12	273953.6	6920567.0	-505.7	50	26
D0601	LPU954-4	22.43	22.69	273913.8	6920514.8	-475.0	99	17
D0603	LPU954-4	33.73	34.02	273924.5	6920513.2	-478.4	99	17
D0701	LPU954-5	85.05	85.35	273901.2	6920664.6	-505.4	37	22
D0702	LPU954-5	86.14	86.87	273902.0	6920665.5	-506.0	37	22
D0703	LPU954-5	88.42	88.68	273903.1	6920667.0	-506.8	37	22
D0801	LPU954-8	27.4	27.68	273917.9	6920509.9	-475.5	106	15
D0901	LPU954-10	79.93	80.1	273933.3	6920553.4	-513.4	52	34
D0904	LPU954-10	81.37	81.67	273934.3	6920554.2	-514.2	52	34
D1001	LPU966-48	2.8	3.1	274028.3	6920677.8	-343.0	69	10
D1002	LPU966-48	4.5	4.7	274029.8	6920678.3	-343.3	69	10
D1003	LPU966-48	9.5	9.8	274034.4	6920680.1	-344.1	69	10
D1004	LPU966-48	16.8	17.15	274041.2	6920682.6	-345.2	69	10
D1005	LPU966-48	44.6	44.9	274066.8	6920692.1	-350.0	69	10
D1007	LPU966-48	98	98.4	274116.1	6920710.4	-359.9	70	11
D1009	LPU966-48	109.5	109.8	274126.6	6920714.3	-362.2	70	12
D1011	LPU966-48	144.7	145.1	274158.9	6920726.2	-369.6	70	13
D1012	LPU966-48	150.5	150.8	274164.2	6920728.2	-370.9	70	13
D1014	LPU966-48	184	184.4	274194.9	6920739.7	-378.1	69	13
D1015	LPU966-48	223.7	224.05	274230.7	6920753.9	-387.4	68	15
D1018	LPU966-48	308.9	309.2	274305.1	6920787.1	-412.3	65	19
D1020	LPU966-48	394.4	394.75	274376.0	6920822.8	-444.1	62	24
D1022	LPU966-48	414.8	415.15	274392.3	6920831.5	-452.6	62	25
D1023	LPU966-48	423	423.35	274398.8	6920835.1	-456.1	62	25
D1024	LPU966-48	489.95	490.35	274450.9	6920864.0	-486.7	62	30
D1025	LPU966-48	493	493.3	274453.2	6920865.2	-488.2	62	30
D1026	LPU966-48	498.1	498.5	274457.1	6920867.3	-490.8	63	30
D1036	LPU966-48	791.7	791.95	274677.4	6920980.6	-648.0	63	30
D1101	LPU976-105	171.63	171.89	274045.0	6921267.4	-313.2	30	17
D1102	LPU976-105	172.06	172.3	274045.2	6921267.7	-313.3	30	17
D1103	LPU976-105	172.3	172.57	274045.4	6921267.9	-313.4	30	17
D1105	LPU976-105	196.67	196.89	274057.0	6921288.2	-320.3	30	16
D1202	LSD788	121.7	122.12	274741.2	6919973.5	402.5	70	59
D1206	LSD788	146.23	146.58	274752.9	6919977.5	380.5	70	59

Sample ID	Hole ID	Depth from (m)	Depth to (m)	Easting (m)	Northing (m)	Elevation (m)	Down-hole plunge direction (°)	Down-hole plunge (°)
D1207	LSD788	170.2	170.53	274764.1	6919980.6	360.7	74	62
D1301	LSD853	143.23	143.56	272335.5	6925287.0	322.5	104	53
D1302	LSD853	143.86	144.11	272335.9	6925286.9	322.0	104	53
D1401	LSD861	356.1	356.42	272354.0	6925146.6	209.1	78	55
D1402	LSD861	357.05	357.3	272354.5	6925146.7	208.5	78	55
D1501	LSD862	293.54	293.8	272360.8	6925157.4	267.2	79	51
D1503	LSD862	294.03	294.26	272361.1	6925157.5	266.8	79	51
D1505	LSD862	297.77	298.17	272363.4	6925158.0	263.9	79	51
D1601	LSD870	241.3	241.6	272418.3	6925009.5	299.4	77	57
D1602	LSD870	241.6	241.87	272418.5	6925009.6	299.2	77	57
D1604	LSD870	260.51	260.81	272428.5	6925011.9	283.0	77	57
D1606	LSD870	261.34	261.6	272428.9	6925012.0	282.4	77	57
D1701	LSD872	295.62	295.96	272411.7	6925000.8	260.2	84	54
D1704	LSD872	312.62	313	272422.3	6925001.8	248.0	85	53
D1705	LSD872	320.03	320.39	272426.7	6925002.2	242.3	85	53
D1801	LSD889	339.63	340.01	272384.1	6925027.8	193.3	84	66
D1902	LSD894	96.42	96.63	269245.2	6933238.0	397.2	71	61
D1904	LSD894	116.57	117.12	269254.5	6933241.2	379.5	71	61
D1905	LSD894	117.74	118.09	269255.0	6933241.4	378.5	71	61
D1906	LSD894	118.09	118.51	269255.2	6933241.5	378.2	71	61
D2001	LSD903	245.11	245.44	269298.8	6933207.3	271.8	74	61
D2006	LSD903	283.34	283.69	269316.5	6933213.7	239.4	62	61
D2102	LSD912	204	204.6	274633.5	6920729.5	392.5	83	54
D2112	LSD912	357.79	358.21	274727.3	6920739.5	271.0	84	51
D2205	LSD922	131.1	131.4	274628.8	6921862.9	364.5	237	76
D2207	LSD922	161	161.3	274622.6	6921858.9	335.5	238	76
D2209	LSD922	173.3	173.55	274620.1	6921857.4	323.7	239	76
D2211	LSD922	224.5	224.85	274609.2	6921851.1	273.7	240	76
D2213	LSD922	238.3	238.7	274606.2	6921849.4	260.6	240	76
D2214	LSD922	260.4	260.65	274601.5	6921846.7	239.0	241	76
D2216	LSD922	272.1	272.45	274599.0	6921845.3	227.9	241	76
D2217	LSD922	275.2	275.5	274598.4	6921844.9	224.6	241	76
D2218	LSD922	310.7	311.05	274590.7	6921840.7	190.0	241	76
D2220	LSD922	320.5	320.95	274588.6	6921839.5	180.5	241	76
D2301	LSD946	1467.7	1468.11	273508.5	6921303.1	-794.4	87	48
D2304	LSD946	1493.72	1494.15	273526.1	6921303.9	-813.7	88	47
D2306	LSD946	1496.72	1497.05	273528.1	6921303.9	-815.7	88	47
D2310	LSD946	1498.49	1498.77	273529.3	6921304.0	-817.1	88	47
D2311	LSD946	1498.85	1499.43	273529.6	6921304.0	-817.5	88	47
D2313	LSD946	1501.68	1502.05	273531.5	6921304.0	-819.4	88	47
D2316	LSD946	1506.5	1506.76	273534.8	6921304.2	-822.9	88	47
D2317	LSD946	1508.3	1508.6	273536.0	6921304.2	-824.2	88	47
D2320	LSD946	1512	1512.28	273538.6	6921304.3	-826.8	88	46
D2401	LSD958	160.55	160.83	268447.7	6934496.5	313.4	198	84
D2402	LSD958	160.83	161.03	268447.7	6934496.4	313.2	198	84
D2503	LSD959	341.23	341.47	267843.3	6934829.5	148.7	33	75
D2601	LSD965	250.47	250.75	268151.3	6934725.2	254.8	86	63
D2603	LSD965	255.69	256	268153.7	6934725.3	250.2	86	63
D2604	LSD965	266.01	266.53	268158.4	6934725.6	241.0	86	63
D2606	LSD965	269.68	269.94	268159.9	6934725.7	237.6	86	63
D2607	LSD965	288.5	288.8	268168.5	6934726.3	221.0	86	63
D2611	LSD965	302.72	303.02	268174.9	6934726.7	208.4	86	63
D2701	LSD970	301.07	301.4	268069.1	6935056.1	219.7	87	58
D2801	LSD984	59.66	59.92	273242.5	6923541.2	472.4	323	47
D2802	LSD984	60.7	60.95	273242.0	6923541.8	471.6	323	47
S0101	Surface	-	-	266542.0	6903872.0	526.0	-	-
S0201	Surface	-	-	264150.0	6903050.0	512.0	-	-
S0301	Surface	-	-	262531.0	6902387.0	512.0	-	-
S0401	Surface	-	-	259427.0	6901178.0	531.0	-	-
S0601	Surface	-	-	255703.0	6897438.0	516.0	-	-
S0602	Surface	-	-	255750.0	6897244.0	509.0	-	-

Sample ID	Hole ID	Depth from (m)	Depth to (m)	Easting (m)	Northing (m)	Elevation (m)	Down-hole plunge direction (°)	Down-hole plunge (°)
S0701	Surface	-	-	261202.0	6920745.0	512.0	-	-
S0801	Surface	-	-	259272.0	6938846.0	470.0	-	-
S0802	Surface	-	-	259278.0	6939017.0	474.0	-	-
S0803	Surface	-	-	259278.0	6939017.0	474.0	-	-
S0901	Surface	-	-	255539.0	6952102.0	489.0	-	-
S1001	Surface	-	-	259587.0	6954376.0	501.0	-	-
S1002	Surface	-	-	259838.0	6954376.0	504.0	-	-
S1003	Surface	-	-	259794.0	6954345.0	501.0	-	-
S1201	Surface	-	-	261807.0	6955794.0	525.0	-	-
S1401	Surface	-	-	273504.0	6951411.0	503.0	-	-
S1402	Surface	-	-	273602.0	6951367.0	498.0	-	-
S1501	Surface	-	-	264613.0	6944816.0	520.0	-	-
S1801	Surface	-	-	266177.0	6933610.0	472.0	-	-
S1901	Surface	-	-	258238.0	6896785.0	530.0	-	-
S1902	Surface	-	-	258238.0	6896785.0	530.0	-	-
S2001	Surface	-	-	258481.0	6899054.0	487.0	-	-
S2002	Surface	-	-	258481.0	6899054.0	487.0	-	-
S2101	Surface	-	-	254619.0	6896040.0	495.0	-	-
S2201	Surface	-	-	256389.0	6888584.0	473.0	-	-
S2301	Surface	-	-	255218.0	6894087.0	484.0	-	-
S2501	Surface	-	-	272529.0	6906972.0	499.0	-	-
S2502	Surface	-	-	272529.0	6906972.0	499.0	-	-
S2601	Surface	-	-	252708.0	6900822.0	496.0	-	-
S2701	Surface	-	-	252101.0	6899916.0	490.0	-	-

Table A.2. Physical property measurements acquired in this study. The analytical procedures are described in Chapter 4. The reported values indicate the appropriate bulk properties obtained from 3-5 specimen measurements per sample (vector mean, geometric mean, arithmetic mean as required). Negative NRM inclinations lie above the horizontal. The values k , δ , and α_{95} are standard uncertainty estimates for the vector averaged NRM orientation measurements: k is the precision and increases for more reliable orientations; δ is the angular dispersion, and decreases for more reliable orientations; α_{95} is the angular standard deviation in degrees and represents the radius of a small circle containing 95 % of measured orientations. Q is the Koenigsberger ratio. Negative porosities indicate inaccuracies in the measurement of associated parameters when the true porosity is small; these may be due to not using vacuum saturation methods.

ID	Description	NRM declination (°)	NRM inclination (°)	k	δ	α_{95} (°)	NRM intensity (mA/m)	Susceptibility ($\times 10^{-3}$ SI)	Q	Dry bulk density (g/cm ³)	Wet bulk density (g/cm ³)	Grain density (g/cm ³)	Porosity (%)
D0101	Serpentinised ultramafic mesocumulate with moderately disseminated sulphides	199	-72	157.0	5.3	9.9	5848.02	148.84	0.85	2.74	2.74	2.73	-0.2
D0102	Massive Ni-sulphide	74	-61	146.3	5.5	10.2	8551.77	48.59	3.79	4.50	4.52	4.54	0.8
D0104	Serpentinised ultramafic mesocumulate with moderately disseminated sulphides	103	-63	13.4	18.1	35.1	721.10	14.64	1.06	3.24	3.24	3.24	0.0
D0203	Moderately feldspar-phyric rock	2	-57	23.8	13.6	25.9	0.21	0.15	0.03	2.66	2.66	2.66	-0.2
D0204	Amphibolite-garnet mafic rock	72	-25	13.0	18.4	35.6	47.70	1.02	1.01	2.85	2.87	2.88	0.9
D0206	Amphibolite-garnet mafic rock	104	33	1.0	71.2	180.0	1.38	0.49	0.06	2.71	2.73	2.75	1.3
D0208	Fine-grained amphibole-quartz-feldspar-biotite schist	300	-8	9.5	21.6	42.4	16.26	0.61	0.57	2.82	2.84	2.86	1.5
D0209	Pegmatite	283	-8	1.5	56.1	180.0	0.34	0.11	0.07	2.52	2.54	2.55	1.2
D0210	Fine-grained biotite-quartz-feldspar schist	324	-25	12.0	19.2	37.2	9.93	0.58	0.37	2.81	2.82	2.83	0.7
D0212	Felsic porphyry, few feldspar-quartz phenocrysts	293	-62	6.6	26.0	52.5	0.26	0.11	0.05	2.61	2.63	2.65	1.5
D0213	Felsic porphyry, few feldspar-quartz phenocrysts	211	-54	85.9	7.1	13.4	0.30	0.12	0.05	2.58	2.60	2.61	0.9
D0215	Felsic porphyry, few feldspar-quartz phenocrysts	214	-62	84.7	7.2	13.5	0.23	0.12	0.04	2.55	2.56	2.57	1.1
D0216	Fine-grained biotite-quartz-feldspar schist with few feldspar phenocrysts	312	-49	2.7	40.8	96.5	0.16	0.06	0.05	2.46	2.47	2.49	1.1
D0217	Fine-grained biotite-quartz-feldspar schist	258	-84	30.7	12.0	22.6	0.19	0.06	0.07	2.54	2.56	2.58	1.4
D0218	Moderately quartz-phyric rock	277	-62	3.4	36.5	81.2	0.34	0.15	0.05	2.64	2.66	2.68	1.5
D0219	Moderately quartz-phyric rock	268	-58	7.4	24.5	48.9	0.25	0.08	0.07	2.64	2.66	2.68	1.4
D0222	Ni-sulphide stringers and moderate disseminated sulphides in serpentinised ultramafic	220	-83	18.5	15.4	29.5	3281.91	28.13	2.51	3.60	3.60	3.58	-0.6
D0223	Ultramafic with talc laths and weakly disseminated sulphides	114	-76	257.2	4.1	7.7	1192.36	9.10	2.82	2.98	3.00	3.04	1.9
D0401	Ni-sulphide stringers and moderate disseminated sulphides in serpentinised bladed ultramafic	147	-78	98.7	6.7	12.5	26333.70	118.65	4.78	3.00	3.00	2.98	-0.2

ID	Description	NRM declination (°)	NRM inclination (°)	<i>k</i>	δ	α_{95} (°)	NRM intensity (mA/m)	Susceptibility ($\times 10^{-3}$ SI)	Q	Dry bulk density (g/cm ³)	Wet bulk density (g/cm ³)	Grain density (g/cm ³)	Porosity (%)
D0402	Serpentinised bladed olivine ultramafic with heavily disseminated sulphides	172	-59	50.3	9.3	17.6	16015.60	89.89	3.84	2.88	2.91	2.93	1.7
D0403	Massive Ni-sulphide	173	-45	27.4	12.7	24.0	91.15	0.23	8.65	4.31	4.33	4.39	1.8
D0501	Serpentinised ultramafic mesocumulate with moderately disseminated sulphides	198	77	54.9	8.9	16.8	1701.90	86.97	0.42	2.76	2.79	2.81	1.6
D0503	Serpentinised ultramafic mesocumulate with heavily disseminated sulphides	203	44	337.5	3.6	6.7	1383.10	68.90	0.43	2.86	2.88	2.90	1.2
D0505	Ultramafic adcumulate with moderate disseminated sulphides and olivine	123	-5	34.9	11.2	21.2	664.21	39.50	0.36	3.26	3.27	3.27	0.4
D0601	Massive Ni-sulphide and mafic rock breccia	238	-37	182.2	4.9	9.2	382.46	2.11	3.91	4.21	4.24	4.31	2.4
D0603	Serpentinised ultramafic mesocumulate with moderately disseminated sulphides	176	58	257.7	4.1	7.7	577.73	49.27	0.25	2.57	2.58	2.58	0.6
D0701	Massive Ni-sulphide breccia	106	-69	9.2	22.0	43.3	37230.00	224.36	3.58	4.14	4.21	4.43	6.5
D0702	Massive Ni-sulphide	267	86	63.8	8.3	15.6	48669.20	196.98	5.32	4.47	4.48	4.48	0.2
D0703	Serpentinised ultramafic mesocumulate with heavily disseminated sulphides	111	-81	316.1	3.7	6.9	42523.70	268.92	3.41	2.97	2.98	2.99	0.4
D0801	Massive Ni-sulphide and felsic rock breccia	170	17	136.7	5.7	10.6	16944.30	160.02	2.28	3.96	3.98	4.00	1.1
D0901	Serpentinised bladed olivine ultramafic with heavily disseminated sulphides	175	-61	122.2	6.0	11.2	2706.37	58.75	0.99	3.12	3.13	3.14	0.6
D0904	Serpentinised bladed olivine ultramafic with heavily disseminated sulphides	268	-77	57.4	8.7	16.4	3381.38	49.50	1.47	3.31	3.33	3.35	1.2
D1001	Ultramafic adcumulate with olivine and weakly disseminated sulphides	251	-37	2621.2	1.3	2.4	137.17	5.13	0.58	3.17	3.18	3.19	0.4
D1002	Ultramafic adcumulate with olivine and weakly disseminated sulphides	205	-51	57.4	8.7	16.4	921.52	11.39	1.74	3.24	3.24	3.24	0.0
D1003	Ultramafic adcumulate with olivine and weakly disseminated sulphides	218	-22	90.6	7.0	13.0	3735.28	10.93	7.37	3.21	3.22	3.21	0.2
D1004	Ultramafic adcumulate with olivine and weakly disseminated sulphides	189	-29	255.4	4.1	7.7	470.00	11.10	0.91	3.17	3.19	3.22	1.6
D1005	Ultramafic adcumulate with olivine and trace sulphides	228	-20	100.9	6.6	12.3	592.36	14.23	0.90	3.15	3.16	3.16	0.4

ID	Description	NRM declination (°)	NRM inclination (°)	<i>k</i>	δ	α_{95} (°)	NRM intensity (mA/m)	Susceptibility ($\times 10^{-3}$ SI)	Q	Dry bulk density (g/cm ³)	Wet bulk density (g/cm ³)	Grain density (g/cm ³)	Porosity (%)
D1007	Ultramafic adcumulate with olivine and trace sulphides	178	-36	567.1	2.8	5.2	528.03	5.88	1.93	3.12	3.15	3.19	2.1
D1009	Ultramafic adcumulate with olivine and trace sulphides	283	-40	596.1	2.7	5.1	508.69	10.57	1.04	3.06	3.09	3.12	1.7
D1011	Ultramafic adcumulate with olivine and weakly disseminated sulphides	281	-25	644.6	2.6	4.9	9908.82	12.87	16.59	3.26	3.27	3.29	0.8
D1012	Ultramafic adcumulate with olivine and trace sulphides	17	-61	69.1	8.0	14.9	184.54	5.58	0.71	3.11	3.13	3.15	1.4
D1014	Ultramafic adcumulate with olivine and trace sulphides	93	-14	607.1	2.7	5.0	11174.40	7.77	31.00	3.22	3.23	3.22	0.2
D1015	Ultramafic adcumulate with olivine and trace sulphides	234	-23	241.4	4.3	8.0	7229.84	8.30	18.77	3.21	3.22	3.22	0.2
D1018	Ultramafic adcumulate with olivine and trace sulphides	154	-28	699.3	2.5	4.7	6928.68	11.81	12.64	3.32	3.34	3.37	1.6
D1020	Ultramafic adcumulate with olivine and trace sulphides	278	-42	143.8	5.5	10.3	333.04	4.01	1.79	3.31	3.32	3.34	0.8
D1022	Serpentinised ultramafic mesocumulate with no sulphides	227	-44	157.1	5.3	9.9	738.84	20.29	0.78	3.02	3.02	3.01	-0.2
D1023	Ultramafic mesocumulate with olivine and trace sulphides	260	-17	183.5	4.9	9.1	9186.69	10.71	18.48	3.18	3.19	3.20	0.5
D1024	Felsic porphyry, abundant feldspar-quartz phenocrysts	184	2	21.4	14.4	27.4	4.24	0.07	1.36	2.41	2.43	2.45	1.7
D1025	Felsic porphyry, abundant feldspar-quartz phenocrysts	74	-4	2.6	41.8	100.9	39.35	0.23	3.66	2.52	2.54	2.56	1.5
D1026	Felsic porphyry, abundant feldspar-quartz phenocrysts	328	-62	1.7	53.3	180.0	2.38	0.05	0.95	2.56	2.58	2.59	1.3
D1036	Pegmatite	352	-42	5.7	28.0	57.4	0.17	0.01	0.36	2.61	2.63	2.64	1.0
D1101	Massive Ni-sulphide and mafic rock breccia	210	-16	42.3	10.2	19.2	157702.00	148.14	22.94	4.30	4.31	4.27	-0.7
D1102	Massive Ni-sulphide and mafic rock breccia	171	10	40.6	10.4	19.6	48944.60	72.51	14.55	3.85	3.86	3.84	-0.4
D1103	Massive Ni-sulphide and mafic rock breccia	158	0	169.6	5.1	9.5	186879.00	277.42	14.52	4.29	4.29	4.26	-0.7
D1105	Serpentinised ultramafic mesocumulate with moderately disseminated sulphides	201	44	183.3	4.9	9.1	13911.60	134.98	2.22	2.59	2.61	2.63	1.2
D1202	Ultramafic mesocumulate with trace sulphides and chlorite-biotite alteration	201	-81	60.6	8.5	16.0	4876.75	57.52	1.83	2.41	2.44	2.46	2.0
D1206	Serpentinised ultramafic adcumulate with weakly disseminated sulphides	207	-79	256.4	4.1	7.7	2665.90	17.38	3.30	2.40	2.43	2.47	3.0
D1207	Serpentinised adcumulate ultramafic with trace sulphides	100	-71	23.4	13.7	26.1	7722.69	42.23	3.94	2.38	2.43	2.50	4.7

ID	Description	NRM declination (°)	NRM inclination (°)	<i>k</i>	δ	α_{95} (°)	NRM intensity (mA/m)	Susceptibility ($\times 10^{-3}$ SI)	Q	Dry bulk density (g/cm ³)	Wet bulk density (g/cm ³)	Grain density (g/cm ³)	Porosity (%)
D1301	Massive Ni-sulphide	169	-79	829.1	2.3	4.3	121862.00	99.74	26.33	4.40	4.42	4.45	1.0
D1302	Massive Ni-sulphide	8	-67	303.0	3.8	7.1	166798.00	131.50	27.33	4.38	4.39	4.40	0.6
D1401	Serpentinised ultramafic mesocumulate with moderately disseminated sulphides	333	-81	2102.7	1.4	2.7	24623.30	79.16	6.70	2.82	2.84	2.88	2.3
D1402	Serpentinised ultramafic mesocumulate with moderately disseminated sulphides	1	-84	508.2	2.9	5.5	19585.60	70.34	6.00	2.63	2.68	2.74	4.0
D1501	Serpentinised ultramafic mesocumulate with heavily disseminated sulphides	263	-81	352.0	3.5	6.6	19983.70	128.40	3.35	2.65	2.68	2.70	1.6
D1503	Serpentinised ultramafic mesocumulate with heavily disseminated sulphides	20	-75	441.6	3.1	5.9	25832.00	87.95	6.33	2.93	2.98	3.05	3.9
D1505	Spotted ultramafic mesocumulate with moderately disseminated sulphides	318	-72	120.8	6.0	11.3	10369.30	28.41	7.86	2.60	2.64	2.70	4.0
D1601	Massive Ni-sulphide and ultramafic rock breccia	149	-84	144.6	5.5	10.3	59497.40	67.69	18.94	3.65	3.67	3.68	0.8
D1602	Massive Ni-sulphide and ultramafic rock breccia	167	-67	141.3	5.6	10.4	30877.90	33.94	19.60	3.63	3.64	3.66	0.8
D1604	Serpentinised ultramafic mesocumulate with moderately disseminated sulphides	175	-44	63.1	8.3	15.7	9855.68	30.00	7.08	2.61	2.66	2.72	4.0
D1606	Serpentinised ultramafic mesocumulate with heavily disseminated sulphides	155	-51	262.0	4.1	7.6	36415.40	69.82	11.24	2.86	2.91	3.01	5.0
D1701	Serpentinised ultramafic adcumulate with moderate disseminated sulphides	176	-67	906.0	2.2	4.1	16294.40	21.97	15.98	2.69	2.71	2.73	1.4
D1704	Serpentinised dunite adcumulate	133	-59	17.7	15.8	30.2	46185.30	90.78	10.96	2.40	2.43	2.46	2.5
D1705	Ultramafic adcumulate with moderate disseminated sulphides and chlorite-biotite- talc alteration	174	-53	517.3	2.9	5.4	39410.80	16.40	51.80	2.87	2.89	2.90	1.0
D1801	Serpentinised ultramafic mesocumulate with moderately disseminated sulphides	29	-79	588.0	2.7	5.1	16807.90	169.15	2.14	2.87	2.90	2.94	2.1
D1902	Ultramafic orthocumulate mixed with moderate disseminated sulphides	117	-66	7.1	25.0	50.1	25630.10	17.61	31.36	2.90	2.91	2.91	0.4
D1904	Massive Ni-sulphide	325	-77	327.1	3.7	6.8	344418.00	185.73	39.96	3.62	3.69	3.84	5.7
D1905	Massive Ni-sulphide	8	-78	131.2	5.8	10.8	492959.00	219.26	48.44	4.17	4.21	4.28	2.5
D1906	Massive Ni-sulphide	214	-56	90.9	6.9	13.0	321360.00	197.97	34.98	4.30	4.32	4.38	1.8

ID	Description	NRM declination (°)	NRM inclination (°)	<i>k</i>	δ	α_{95} (°)	NRM intensity (mA/m)	Susceptibility ($\times 10^{-3}$ SI)	Q	Dry bulk density (g/cm ³)	Wet bulk density (g/cm ³)	Grain density (g/cm ³)	Porosity (%)
D2001	Serpentinised ultramafic mesocumulate with moderately disseminated sulphides	182	-80	763.4	2.4	4.5	14008.10	42.24	7.15	2.65	2.69	2.73	2.8
D2006	Serpentinised ultramafic mesocumulate with weakly disseminated sulphides	195	-89	546.2	2.8	5.3	7499.46	41.06	3.94	2.65	2.65	2.65	0.0
D2102	Serpentinised ultramafic orthocumulate	100	-82	776.0	2.4	4.4	5553.44	72.13	1.66	2.68	2.70	2.72	1.3
D2112	Serpentinised ultramafic orthocumulate	82	-63	60.0	8.6	16.1	1607.12	40.29	0.86	2.51	2.52	2.53	0.9
D2205	Granitoid	25	-70	13.3	18.2	35.3	2.26	0.67	0.07	2.57	2.59	2.60	0.9
D2207	Granitoid (mafic)	113	-62	753.1	2.4	4.5	4.12	0.32	0.28	2.34	2.37	2.39	2.1
D2209	Granitoid	191	-71	171.8	5.0	9.4	18.04	3.85	0.10	2.48	2.49	2.50	0.9
D2211	Granitoid	237	-77	91.9	6.9	12.9	36.22	-	-	2.38	2.40	2.41	1.3
D2213	Granitoid	12	-78	311.9	3.7	7.0	136.08	4.44	0.66	2.53	2.54	2.54	0.4
D2214	Granitoid	249	-70	47.2	9.6	18.1	50.89	4.29	0.26	2.69	2.71	2.72	0.8
D2216	Amphibolite-rich mafic rock	154	-73	136.9	5.7	10.6	131.16	4.32	0.65	2.60	2.62	2.64	1.3
D2217	Granitoid	253	-73	28.7	12.4	23.4	137.62	3.60	0.82	2.50	2.51	2.52	0.7
D2218	Granitoid	175	-73	65.8	8.2	15.3	139.22	3.34	0.90	2.50	2.52	2.53	1.1
D2220	Granitoid	202	-68	74.8	7.7	14.4	26.03	0.41	1.38	2.53	2.55	2.56	1.1
D2301	Fine-grained amphibole- quartz-feldspar-biotite schist	33	-34	4.5	31.4	66.3	1.78	0.30	0.13	2.53	2.54	2.55	0.7
D2304	Fine-grained amphibole- quartz-feldspar-biotite schist	161	-15	29.3	12.3	23.2	93.36	1.19	1.69	2.83	2.84	2.85	0.5
D2306	Fine-grained amphibole- quartz-feldspar-biotite schist	66	-13	50.3	9.3	17.6	267.93	1.81	3.19	2.62	2.63	2.64	1.0
D2310	Fine-grained amphibole- quartz-feldspar-biotite schist	318	-9	62.0	8.4	15.8	107.22	1.69	1.37	3.09	3.10	3.10	0.4
D2311	Fine-grained amphibole- quartz-feldspar-biotite schist	131	-63	3.4	36.7	81.9	142.69	2.36	1.30	2.87	2.89	2.90	0.9
D2313	Fine-grained amphibole- quartz-feldspar-biotite schist	10	-43	1.6	55.1	180.0	8.97	0.82	0.23	2.89	2.89	2.89	0.0
D2316	Fine-grained amphibole- quartz-feldspar-biotite schist	294	-17	226.1	4.4	8.2	233.41	1.45	3.48	2.88	2.91	2.95	2.4
D2317	Fine-grained amphibole- quartz-feldspar-biotite schist	67	61	3.8	34.7	75.5	74.64	1.24	1.30	2.76	2.76	2.77	0.4
D2320	Fine-grained amphibole- quartz-feldspar-biotite schist	42	-40	75.9	7.6	14.3	44.18	1.02	0.93	2.66	2.68	2.69	1.4
D2401	Massive Ni-sulphide	162	-83	370.5	3.4	6.4	93962.40	113.43	17.85	3.64	3.67	3.73	2.1
D2402	Massive Ni-sulphide	211	87	141.7	5.6	10.4	96088.60	129.85	15.94	4.00	4.02	4.06	1.5
D2503	Serpentinised ultramafic mesocumulate with moderately disseminated sulphides	197	-69	193.8	4.8	8.9	61506.70	117.55	11.27	2.55	2.58	2.62	2.9
D2601	Serpentinised ultramafic mesocumulate with weakly disseminated sulphides	317	-81	121.3	6.0	11.2	4945.15	29.33	3.63	2.49	2.51	2.52	1.2

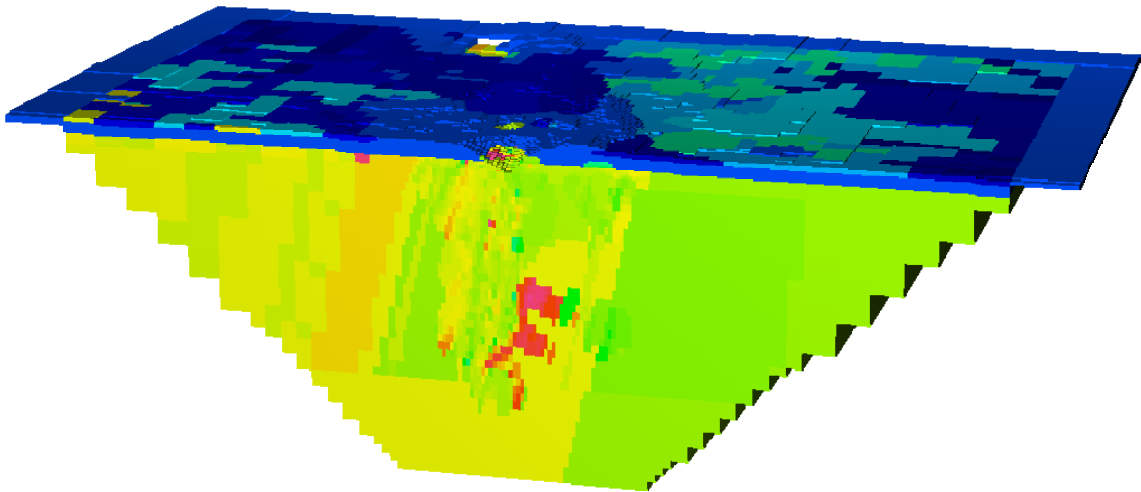
ID	Description	NRM declination (°)	NRM inclination (°)	<i>k</i>	δ	α_{95} (°)	NRM intensity (mA/m)	Susceptibility ($\times 10^{-3}$ SI)	Q	Dry bulk density (g/cm ³)	Wet bulk density (g/cm ³)	Grain density (g/cm ³)	Porosity (%)
D2603	Serpentinised ultramafic mesocumulate with weakly disseminated sulphides	168	-62	100.8	6.6	12.3	10030.50	38.11	5.67	2.51	2.55	2.60	3.6
D2604	Serpentinised ultramafic adcumulate with weakly disseminated sulphides	306	-85	47.9	9.6	18.0	12397.10	38.80	6.89	2.46	2.50	2.53	2.6
D2606	Serpentinised adcumulate ultramafic with trace sulphides	243	-56	43.4	10.1	18.9	7352.16	44.62	3.55	2.49	2.54	2.60	4.3
D2607	Serpentinised ultramafic adcumulate with moderate disseminated sulphides	297	80	32.3	11.7	22.1	5791.38	53.70	2.32	2.23	2.27	2.33	4.3
D2611	Serpentinised ultramafic mesocumulate with weakly disseminated sulphides	211	-59	39.3	10.6	19.9	20856.40	77.04	5.83	2.30	2.33	2.37	3.2
D2701	Serpentinised ultramafic with heavily disseminated sulphides and talc-anthophyllite	178	-66	574.7	2.8	5.1	16469.50	125.19	2.83	2.74	2.75	2.75	0.2
D2801	Weathered ultramafic	154	-77	512.7	2.9	5.5	21.91	0.58	0.82	2.38	2.44	2.54	6.4
D2802	Weathered ultramafic with net-textured sulphides	354	67	46.8	9.7	18.2	25.42	1.15	0.48	2.43	2.55	2.75	11.7
S0101	Weakly weathered dolerite	93	-51	3574.9	1.1	2.1	253.65	0.95	5.75	2.93	2.94	2.95	0.6
S0201	Strongly weathered fine grained felsic porphyry or volcaniclastic	86	-30	14.2	17.6	34.0	2.38	0.05	0.98	1.75	2.00	2.32	24.2
S0301	Moderately weathered fine grained felsic porphyry or volcaniclastic	111	-63	1622.0	1.6	3.1	3.10	0.00	125.23	2.35	2.46	2.63	10.5
S0401	Strongly weathered high Mg basalt/ultramafic?	322	66	44.7	9.9	18.7	0.36	0.51	0.02	1.99	2.24	2.63	24.4
S0601	Moderately weathered fissile dolerite	233	4	1.6	54.5	180.0	0.88	0.90	0.02	2.92	2.94	2.94	0.6
S0602	Weakly weathered dolerite	96	37	1.8	50.8	180.0	0.34	0.91	0.01	2.93	2.94	2.93	0.0
S0701	Moderately weathered felsic sediments near basalt	215	-26	84.1	7.2	13.5	1.88	0.03	1.16	1.85	2.04	2.28	18.8
S0801	Weakly weathered fine-grained basalt (Mt Goode Basalt)	264	17	10.0	21.0	41.2	2.34	0.43	0.12	2.70	2.70	2.69	-0.2
S0802	Moderately weathered coarse-grained basalt/gabbro with moderate meta-actinolite needles (Mt Goode Basalt)	117	-20	10.8	17.5	85.4	1.08	0.95	0.02	3.03	3.04	3.04	0.5
S0803	Weakly weathered basalt (Mt Goode Basalt)	340	4	2.0	47.8	134.5	0.29	1.09	0.01	3.03	3.04	3.04	0.2
S0901	Weakly weathered coarse-grained gabbro with possible anthophyllite (Kathleen Valley Gabbro)	347	28	177.0	5.0	9.3	23.68	0.71	0.72	2.81	2.82	2.82	0.0

ID	Description	NRM declination (°)	NRM inclination (°)	<i>k</i>	δ	α_{95} (°)	NRM intensity (mA/m)	Susceptibility ($\times 10^{-3}$ SI)	Q	Dry bulk density (g/cm ³)	Wet bulk density (g/cm ³)	Grain density (g/cm ³)	Porosity (%)
S1001	Weakly weathered medium-grained basalt/gabbro	81	-25	26.5	12.9	24.4	1.12	0.77	0.03	2.80	2.80	2.78	-0.9
S1002	Strongly weathered granite/granite conglomerate (Jones Creek Conglomerate?)	98	61	56.3	8.8	16.6	2.28	0.04	1.11	1.73	1.99	2.34	26.2
S1003	Minimally weathered granite from mine shaft, silicified (Jones Creek Conglomerate?)	113	79	4.2	32.7	69.8	0.82	0.04	0.46	2.46	2.47	2.48	0.5
S1201	Strongly weathered silicified cherty sedimentary rock - possible Mn crusts	287	-1	7.2	24.9	49.9	34.51	0.30	2.46	2.81	2.83	2.86	1.7
S1401	Fresh granite from Choolaweera Rocks	269	57	45.1	9.9	18.6	875.89	3.38	5.59	2.46	2.47	2.46	-0.2
S1402	Fresh granite from Choolaweera Rocks	46	-59	616.2	2.3	10.1	8874.47	4.63	41.30	2.52	2.53	2.53	0.5
S1501	Very fine grained basalt	53	-20	18.8	15.3	29.2	0.51	0.75	0.01	2.98	2.99	2.98	-0.2
S1801	Deeply weathered talcy ultramafic	32	2	3.9	29.3	180.0	32331.20	19.17	36.35	1.56	1.80	2.04	23.3
S1901	Fresh gabbro from Sunrise Birthday waste pile	210	52	1.3	59.7	180.0	473.16	4.23	2.41	2.95	2.98	3.00	1.7
S1902	Weathered gabbro from adjacent to Sunrise Birthday mine	310	-87	30.8	10.3	46.6	44.32	0.63	1.52	2.28	2.47	2.81	18.7
S2001	Moderately weathered actinolite-chlorite schist ultramafic	140	-2	3.4	36.4	80.9	0.56	0.73	0.02	2.77	2.80	2.86	3.2
S2002	Strongly weathered spinifex textured ultramafic, very soft, brittle, and fractured	46	-8	67.7	8.0	15.1	4.75	0.68	0.15	1.90	2.15	2.53	24.8
S2101	Weakly weathered coarse gabbro/dolerite	332	-6	54.4	9.0	16.9	0.45	0.79	0.01	2.97	2.97	2.97	0.0
S2201	Strongly weathered granite	137	70	1218.0	1.6	7.2	42.67	-	-	2.21	2.33	2.51	12.1
S2301	Moderately weathered granite/tonalite	136	-39	94.0	6.8	12.8	2.19	0.12	0.40	2.42	2.47	2.52	4.2
S2501	Moderately weathered granite	231	16	221.0	4.5	8.3	1226.15	9.33	2.83	2.54	2.56	2.59	2.1
S2502	Weakly weathered granite	130	-3	559.3	2.8	5.2	470.65	9.82	1.03	2.64	2.65	2.64	0.0
S2601	Moderately weathered schist (metabasalt?)	242	-57	275.0	4.0	7.4	0.34	0.17	0.04	2.55	2.59	2.63	3.1
S2701	Strongly weathered sediment/quartzite (Jones Creek Conglomerate?)	310	2	1.2	64.8	180.0	1.30	0.01	1.94	2.51	2.52	2.53	0.9

Appendix B: GIFtools:ModelBuilder user manual

GIFtools:ModelBuilder v1.0

A MATLAB package for building UBC–GIF models of geological constraints based on sparse observation data



User Manual

Nicholas C. Williams

Geophysical Inversion Facility & Mineral Deposit Research Unit

The University of British Columbia

September 2008

INTRODUCTION

Inversion of geophysical data seeks to extract a model, or suite of models, representing the subsurface physical property contrasts that can explain an observed geophysical dataset. As the observed geophysical data are a finite sampling of a continuous response, any recovered property distribution is only one of an infinite number of possible distributions that could explain the observed data. The most desirable solutions are those that can explain the observed geophysical data yet also reproduce known geological features; a goal that can only be achieved by including any available geological information into the inversions as constraints.

There are two approaches that can be used to include these geological constraints, based on the type of geological information available and the geological problem being addressed. A hypothesis testing approach supplies a full 3D model of geological observations and interpretations to the inversion to test the hypothesis that those interpretations are consistent with the geophysical data (McGaughey, 2007; McInerney et al., 2007; Oldenburg and Pratt, 2007). Typically a qualitative assessment of the result is made based on how far the recovered inversion model deviated from the supplied interpretations in order to explain the observed geophysical data. However, in portions of the model that have low sensitivity to the geophysical data and no geological controls it may be possible to recover a property distribution that explains the observed geophysical data and is consistent with a flawed geological model. There may be no indication that the result is incorrect. This is problematic for gravity and magnetic data which are inherently non-unique due to the behaviour of potential fields. The gravity and magnetic responses decay with distance-squared and distance-cubed, respectively, so the sensitivity of subsurface model cells to surface geophysical data decreases dramatically with depth in the model. The amount of geological information available, and therefore the reliability of any 3D models produced also decreases significantly with depth below surface. In the areas where more reliable constraints are required, less reliable constraints are provided. In addition, as geological interpretations are required prior to performing any hypothesis-testing inversions, a significant amount of geological knowledge must be available, and a significant time commitment is required before any inversion results are obtained.

An alternate approach is to supply all available raw geological information to the inversion to recover a prediction about the subsurface distribution of geological features that

may be required to satisfy both the known geological constraints and the observed geophysical data. This sparse data approach is particularly suited to problems where geological information is limited, sparsely distributed, or concentrated within restricted areas such as known ore bodies or along the ground surface. The limited and uneven distribution of data makes it difficult or impossible to build 3D models that are reliable enough to be included in the hypothesis testing approach. Using the available sparse data also postpones much of the geological interpretation until after the inversions have been performed, reducing the lead time to recovering an inversion result and enabling the results of inversions to be used in decisions to acquire further geological and geophysical data.

This manual describes a method for preparing the geological constraints required for this sparse data approach eliminating the need for interpreting geology in regions of a 3D model that have limited or no geological information on which to base the interpretations. Applying geological constraints in any geophysical inversion procedure requires solid knowledge of the physical properties of the rocks. The technique outlined here specifically makes that physical property knowledge the central link between the geological information available and the geological constraints to be applied. In regions where little geological information is available, accurate physical property information may be unavailable, but the ability to include rough physical property estimates allows creation of simple models of geological constraints. Routine acquisition of physical property measurements during ongoing work will be rewarded by more robust constraint models which will provide more reliable inversion results on which to base further data collection. The technique also seeks to: 1) reduce the number of software packages required to integrate a variety of spatial datasets into a single physical property model by reading directly from raw data files; 2) automate the process as much as possible; and 3) ensure that the model can be updated quickly and easily when additional data becomes available so as to improve the recovered subsurface predictions. A demonstration version of the program with a basic graphical user interface has been developed using the Matlab programming package (Mathworks Inc., Natick, Massachusetts).

This method for developing a model of sparse geological constraints is specifically targeted for use with the UBC–GIF GRAV3D and MAG3D gravity and magnetic inversion programs (Li and Oldenburg, 1996, 1998) which allow geological constraints to be enforced on a cell-by-cell basis within a discretised volume. As described in the UBC–GIF GRAV3D and

MAG3D inversion program manuals (UBC–GIF, 2005a, b), geological constraints are assigned to each cell by defining four sets of parameters:

- A reference physical property which provides the best estimate of the actual physical property of the cell.
- A smallness weight, w_s , which provides an estimate of the reliability of the assigned reference physical property. The weight is a unitless value ≥ 1 with increasing values indicating higher confidence. The default value of unity indicates that the reference physical property is uncertain and should not be strongly enforced in the inversion.
- Lower and upper physical property bounds which provide an absolute limit on the minimum and maximum property that can be assigned to the cell. These effectively represent a confidence interval on the supplied reference property at a certain confidence level.
- Smoothness weights controlling the variation in properties between each adjacent cell in each direction.

The property recovered by an inversion for a cell that contains abundant geological information can therefore be constrained by assigning a reference physical property with a high smallness weight and a tight bounds range. Cells with no geological information should be assigned some default reference physical property, a smallness weight of unity, and wide bounds that reflect the full range of possible physical properties. The inversion will recover a physical property model with properties for each cell that lie between the defined bounds, and are as close as possible to the supplied reference physical properties, while still reproducing the observed geophysical data. If possible, the reference physical properties will be matched more closely in those cells that have the highest smallness weights.

METHOD OVERVIEW

The fundamental goal of this approach is to create a 3D physical property model, based only on sparsely distributed raw geological data and enforced only in areas where information is available, using a repeatable, automated process. The recovered physical property model can be used on its own to provide an additional tool to aid direct interpretation of subsurface geological data, or can be supplied to the UBC–GIF inversion programs as a constraining

reference model. The inversion constraint parameters, including reference properties, smallness weights, and lower and upper property bounds, are all related so all are created at the same time using the same data. The discretisation of the model, including the sizes and positions of cells, is defined by a UBC–GIF format mesh file which is supplied to the model building routine.

There are two main classes of observation that can be utilised in building a physical property model from geological data: actual physical property measurements; and observations or interpretations of rock types or alteration styles. Actual physical property measurements are obviously the most directly related to building a physical property model, however they are rarely taken systematically. Observations of geology are far more common. Since many geological units and rocks types have distinctive physical properties, observations of rock types and alteration may be used as a proxy for actual property measurements. A key component of building a physical property model that is partially based on rock type observations is to link the geological observations to appropriate physical property information. This is done early in the model building process via the creation of a physical property database for the model.

Once the physical property database is created, the model building routine can load the various data files containing those observations and extract or calculate the 3D coordinates at which the observations occur. The data files that can be supplied to the model building program are listed in Table B.1. If the observation is a geological observation of rock or alteration types it is converted to a physical property estimate based on the physical property database. The model cells are populated by combining all of the most reliable property measurements or estimates in each cell and extracting a statistical estimate of the mean physical property value within the cell. Any cell that contains no geological information has default properties applied.

An optional final step expands the number of cells for which physical properties are assigned, if desired, by extrapolating the properties outwards from data-bearing cells into adjacent buffer cells as defined by structural orientations, based on the assumption that the physical properties will be roughly similar in adjacent cells. This assumption may be valid in some situations but not others, depending on the complexity of the geology, so the distance of extrapolation and the methods for determining the properties in the buffer cells are options for the user.

Table B.1. List of the data types handled by the model building application. The data types are applied in the order of priority listed, which corresponds to their relative reliability within the model.

Priority	Data type	File formats	Description	Requires physical property database
1	Physical property measurements on surface samples	Column-delimited text files	Measurements taken on outcrop rocks or hand samples for which 3D coordinates are available	N
2	Physical property measurements on drill core	Column-delimited text files	Measurements taken on drill core samples, or by drill hole property logging tools, whose position is reported as a down-hole depth	N
3	Geology observations on drill core	Column-delimited text files	Observations of rock types and/or alteration styles taken on drill core samples, or by drill hole property logging tools, whose position is reported as a down-hole depth	Y
4	Outcrop or surface geology maps	ESRI vector polygon shapefiles	A nontopological shape format of vector coordinates of polygons and attributes (Environmental Systems Research Institute, 1998) storing observations of rock types, geological unit names, or descriptions made on surface rocks	Y
5	Basement or solid geology maps	ESRI vector polygon shapefiles	A nontopological shape format of vector coordinates of polygons and attributes (Environmental Systems Research Institute, 1998) storing interpretations of rock types or geological unit names expected at some position in the subsurface	Y
6	3D models of geological units	UBC-GIF inversion model format text files	A 3D model of geological units bounded by well-defined contacts, stored as a set of lithology IDs for each cell in the model volume	N
7	3D models of geological domains	UBC-GIF inversion model format text files	A 3D model of geological domains that may span multiple geological map units have poorly-defined boundaries, and distinct structural orientations or fabrics, stored as a set of domain IDs for each cell in the model volume	N

USER MANUAL

REQUIREMENTS

The available installation of MATLAB must have access to the MATLAB Statistics Toolbox. If maps are to be used then the MATLAB Mapping Toolbox is also required. The ModelBuilder software is compatible with version MATLAB R2007b, but newer versions may also work.

INSTALLATION

The GIFtools:ModelBuilder is currently only available as a series of MATLAB language functions supplied as either *.p or *.m files. These need to be copied into a suitable program installation directory specified by the user. This directory then needs to be added to the MATLAB search path using the MATLAB menu command: File->Set Path. This allows the program to be run from any directory in MATLAB using the commands outlined below.

GETTING STARTED

The minimum requirements to get started building a model are a UBC–GIF format mesh file defining the model volume, and at least one source of data from Table B.1 to populate the model with some constraints. If maps, drilling geology logs, or a geological model are to be used to derive constraints, and no physical property measurements are available, then a table of manually estimated physical properties will also need to be supplied. All physical property measurements and estimates must be in the same units in all input data files. It is recommended that they all be in the same units as required for the inversions (g/cm^3 or t/m^3 for densities; SI for magnetic susceptibilities), however a basic functionality is built in to convert units using a multiplying factor (e.g., kg/m^3 to g/cm^3 or 1×10^{-3} SI to SI; see dialog box 3.1.0, p. 430).

ModelBuilder creates a set of output files in the current working directory during each run. These files include:

- Binary option files that store the settings from the current run as defaults for future runs
- Binary output files which can be used to shortcut some time-consuming steps in future runs. These include:
 - A file containing all drill hole traces
 - A file with all calculated property estimates
- Binary data files containing map sample points if maps are used. As one of the slowest parts of the process is interpolating the supplied maps, this data is saved in a reusable file. The files ('bmOutcropMapData.mat' or 'bmBasementMapData.mat') can be copied into any directory that uses the same mesh, map and sampling and the user will be prompted if they wish to use the existing data.

- Binary session file containing all of the loaded and processed data. This can be used to quickly rerun the model adjusting only a small selection of data-independent parameters (notably smoothness, smallness, and buffer parameters)
- Text log file summarising the settings used, and the data loaded
- Set of output model constraint files in inversion-ready formats

To manage these files it is recommended to arrange a set of project folders for each model with a folder containing common source data for the model, including meshes, drilling files, maps, surface sample files, etc., subdirectories for density- or magnetic susceptibility-specific data such as property estimates, and working directories to contain each model building run:

- Project Area A (containing common source data files for area A)
 - Density Models (containing density-specific data files for area A)
 - Model 1 working directory
 - Model 2 working directory
 - Magnetic Susceptibility Models
 - Model 1 working directory
 - Model 2 working directory
- Project Area B
 - ...

With the desired working directory selected, run the ModelBuilder program by invoking:

```
buildModel
```

By default ModelBuilder will load any pre-existing settings files to use as defaults. If these get corrupted (such as after crash), then ModelBuilder can be forced to delete pre-existing option files and start from scratch by invoking:

```
buildModel('clear')
```

MODEL BUILDER SETTINGS

This section describes the settings available during a program run. For clarity, each dialog box is numbered in order of appearance in a full model building run and will be described separately. Not all dialog boxes will display in any run, depending on user selections.

Likewise options may not be available on some dialog boxes when they do not apply, based on the user's previous choices. Depending on the options, four types of entries are possible:

1. Yes or no responses which should be reported as 'Y' or 'N' only (ignoring the quotation marks).
2. Numeric entries require the input of a number.
3. File name entries require a link to a file. This is best entered using copy and paste. Ninotech's free Path Copy⁷ utility adds a "Copy full path" option to the right-click context menu in Windows Explorer to ease this process. The full directory location of the file is not required if the file is located in the current working directory.
4. List selections with a number of options listed. Some lists allow multiple selections and others allow only single selections, as required. Use standard Windows CTRL-click and SHIFT-click methods to select multiple entries.

Default values will be present for each option to help indicate the type of entry required

1.0.0: Model building options

This is the main window, and defines the main options for the current run.

OPTIONAL: Path to MATLAB session file

If available, entering a MATLAB binary session filename here will skip all data loading and processing and skip directly to the model populating stage (11.0.0, p. 448). For large projects where only smallness weights, bounds options, or buffer extrapolation methods need changing, this can save much time. Any entry that does not link to an existing file will be ignored and this option skipped.

Path to UBC-GIF mesh file

This indicates the filename of the UBC–GIF mesh file that defines the model to be built. This is mandatory.

Paint in surface samples measurements

This option is used to paint any surface sample property measurements into the model. These can be any measurements that are associated with X, Y, Z coordinates.

Paint in drilling property measurements

⁷ Ninotech Path Copy website: <http://home.worldonline.dk/ninotech/freeutil.htm#pathcopy>

This option is used to paint any drilling property measurements into the model. These will be expressed as measurements at depths down a drill hole, and the orientation and position of the drill hole will be defined in separate collar and survey files.

Paint in drilling geology logs

This option is used to paint any drilling geology logs into the model. These will be expressed as observations of different geology labels at depths down a drill hole, and the orientation and position of the drill hole will be defined in separate collar and survey files. Property estimates for the labels must be available, either using manually-defined property estimates, or automatically calculated from available property measurements.

Paint in outcrop maps

An outcrop geology map in ESRI shapefile format can be included. It will be discretised and interrogated to identify observed geology labels for each cell on the map surface. To be applied to the model property estimates for the labels must be available, either using manually-defined property estimates, or automatically calculated from available property measurements.

Paint in basement maps

A basement geology map in ESRI shapefile format can be included. It will be discretised and interrogated to identify observed geology labels for each cell on the map surface. To be applied to the model property estimates for the labels must be available, either using manually-defined property estimates, or automatically calculated from available property measurements.

Paint a 3D geological model

A 3D geological model, built in Gocad, Geomodeller, or UBC–GIF Meshtools3D can be included to define default property values in part or all of the model. A geological model includes well-defined unit boundaries that must be preserved in the model. The model must already be in UBC–GIF model file format with lithology ID numbers assigned to each cell. A text definition file links each lithology ID to physical property estimates for each geological unit. A geological model can be treated as a more detailed 3D map in portions of the model, whereas a domain model provides the framework for the map (Table B.2). Both can be used as constraints at the same time.

Paint a 3D domain model

A 3D domain model, built in Gocad or UBC–GIF Meshtools3D can be included to define default property values in part or all of the model. A domain model includes poorly-known domain boundaries that can be modified in the model. The domains can also represent true structural domains with distinct bedding, structural orientations, or strain directions that can define preferred directions for the extrapolation of properties if buffers are used. The model must already be in UBC–GIF model file format with domain ID numbers assigned to each cell. A definition file links each domain ID to property estimates for that domain. An optional second orientation definition file can be supplied which defines the buffer orientation and shape for cells in each domain based on the observed structural orientations. A geological model can be treated as a more detailed 3D map in portions of the model, whereas a domain model provides the framework for the map (Table B.2). Both can be used as constraints at the same time.

Table B.2. Differences between 3D geological and domain models. They serve slightly different purposes and can be used to complement each other.

Concept	3D geological model	3D domain model
Detail	Typically high	Typically low
Contacts or boundaries	Sharp well defined boundaries	Unknown, poorly-defined, or approximated boundaries
Orientations	Structural orientations defined by host domain	Specific structural orientations (for buffers) or aspect ratios can be defined
Buffers and extrapolation	Buffers truncated by boundaries between rock types	Buffers may transgress domain boundaries
Physical properties	Usually well defined	Commonly poorly defined ranges of likely properties
Smoothness weights	Low values can be assigned along contacts to promote sharp property breaks	Domain boundaries are ignored by smoothness weight calculations

Apply buffers around data cells

In regions where few geological constraints are available it may be useful to extrapolate those constraints outwards away from the observation locations to fill more of the model space. This is done using ellipsoidal buffers oriented according to local geological trends. A single orientation can be defined for the whole model (19.0.0, p. 471), or in individual domains using a domain model (6.0.0, p. 437). A number of options are available for how the buffers are calculated (16.0.0 & 17.0.0, p. 461–466), and the distances that data can be extrapolated (18.0.0, p. 470). If buffers are used, then unbuffered versions of the models are also created.

2.0.0: Which constraints to build

This list box is used to select which types of constraint models should be created. The options are:

1. A UBC–GIF reference model of the estimated mean properties in each cell with smallness (w_s) weights to indicate confidence in the estimate;
2. A UBC–GIF bounds model indicating the lower and upper limits of the confidence interval associated with the reference properties;
3. A model of smoothness weights, w_x , w_y , w_z , across each cell face in each direction indicating how smoothly the recovered inversion model properties should vary across that cell face.

Although options one and two can be selected separately, the third option can only be selected if a reference model is selected because the smoothness weights are calculated based on gradients in the reference model.

3.0.0: Select a property

Use this list box to select which physical property the model will be based on: density, magnetic susceptibility, conductivity or chargeability. This option defines the default values to be used at various points in the model building process, although these default values can be modified later in the process. Selecting the density property also defines the expected physical property distribution function to be normal; all other properties are associated with fundamentally lognormal properties and slightly different statistical estimates are derived. It is important to note that conductivity and chargeability properties typically show non-linear relationships with observed geophysical responses. Since the GIFtools:ModelBuilder is based on linear relationships, the conductivity and chargeability models created using this method may not be valid. They are included for experimental uses.

3.1.0: Define properties

This dialog defines the default physical property values to be used in the model. If geological labels are being used, either in drilling geology logs or maps, then it also identifies files and methods for deriving physical property estimates for those geology labels.

Lowest possible measurement (for data validation)

To ensure only valid data are included in the model, this defines the minimum possible measurement for the selected physical property. All values lower than this will be rejected.

Highest possible measurement (for data validation)

To ensure only valid data are included in the model, this defines the maximum possible measurement for the selected physical property. All values higher than this will be rejected.

Conversion factor (to convert units)

This applies a simple multiplicative linear scaling factor which can be used to convert measurement units, if needed, to match the inversion requirements. Typically a default of 1.0 will be used to indicate no scaling is required. However, gravity inversions require densities in g/cm^3 or t/m^3 , so if supplied measurements are in kg/m^3 a scaling factor of 1e^{-3} will be required to convert the measurements to g/cm^3 . Likewise magnetic inversions require magnetic susceptibility in SI units; if the supplied measurements are in 1e^{-3} or 1e^{-5} , then a scaling factor of 1e^{-3} or 1e^{-5} is required. The conversion is applied to all measurements and estimates loaded from any file.

Reference property value

Only available if creating a reference model. This is the default background reference property where no data are available.

Prior property model for default reference property values

Only available if creating a reference model. A property model from a previous inversion, or one that has been scaled or modified in some way, can be supplied to define the default reference properties throughout the model. This will be used instead of the default reference value specified above. The model must be UBC–GIF model format. If using a model from a gravity inversion, it should contain actual densities, not density contrasts, so the prior recovered model has to have had some background density added to every cell.

Smallness (w_s) weight

Only available if creating a reference model. This is the default smallness (reliability) weight (usually 1) where no data are available.

Property lower bound

Only available if creating a bounds model. Default lower bound to be assigned in cells with no data, or insufficient data to adequately define bounds. Inversions will not recover values below this.

Property upper bound

Only available if creating a bounds model. Default upper bound to be assigned in cells with no data, or insufficient data to adequately define bounds. Inversions will not recover values above this.

3.2.0: Define property estimates

Only available if using drilling geology logs or maps This dialog defines how physical property estimates are defined for converting geological observations into physical properties. Properties can be defined from a table of manually-specified estimates which replace any automatically calculated estimates. They can also be calculated from available property measurements, or previously calculated estimates can be loaded from an existing file. If no files are specified and the ‘calculate property estimates’ option is turned off, then ModelBuilder will run without any property estimates and no drilling geology or map constraints will be applied. However, text files listing all the encountered geology codes will be created in the working directory, and these can be used to as a basis for defining manual property estimates.

OPTIONAL: Path to ASCII file of manually-defined properties

This text file contains estimates of appropriate bounds and reference properties for those geology labels that are either unsampled or poorly sampled for physical properties. These manually-defined property estimates replace any property estimates that may have been calculated using the automatic physical property database option (below). During every model building run that includes drilling geology logs or maps, a text file will be created in the working directory listing any geology labels for which no measured properties were available. These are candidates for assigning properties manually. Any entry that does not link to an existing file will be ignored and this option skipped.

Calculate property estimates from drilling logs or surface samples

This option automatically creates a physical property database from all available property measurements and geology observations for surface samples and drilling. For each geology label that has any measurements associated with it, statistical estimates of the mean property and confidence intervals on that mean are calculated at 68%, 95%, 99.7%, and 99.99% confidence levels. The results are stored in a MATLAB binary file that can be reused in future runs using the entry below. They are also reported in an ASCII text file with additional statistical measures including the standard deviation, median, and skewness

associated with the measurements for each geology label. The mean property estimate is used to assign reference properties, and the confidence intervals are used to assign bounds wherever the geological observation occurs within the model, either in drilling logs or maps.

OPTIONAL: Path to MATLAB file of all drilling and surface property data

If a property database has previously been calculated (above) it can be reused by linking to it here, avoiding recalculation. Be sure to select "N" for the option above, otherwise the database will be rebuilt. Any entry that does not link to an existing file will be ignored and this option skipped.

3.2.1: Property estimates data sources

Only available if calculating physical property estimates. The dialog defines the source data to be used to calculate the physical property estimates database.

Process surface sample measurements

Select this option to use a file of surface-sample property measurements and geology labels (no coordinates are required) to derive estimates of the properties associated with each code.

Process drilling logs & measurements

Select this option to use files of drilling property measurements and geology labels (no collar/survey files required) to derive estimates of the properties associated with each code

OPTIONAL: Path to geology label translation table

Geology labels used in maps often differ from those used in surface sample descriptions and drilling logs. A translation table file links surface-sample and drilling geology labels to map labels. For example, drilling logging codes such as 'Ab', 'Abb', and 'Abv' may all indicate basalts, and so might be grouped under the map-label 'Basalt; undifferentiated'. Doing so will apply all physical property measurements that are associated with 'Ab', 'Abb', and 'Abv' to also be associated with 'Basalt; undifferentiated'. It can also be used to group geology labels into broader categories that are expected to have similar physical properties. Continuing the example, drilling labels 'Abb' and 'Abv' may be more specific varieties of drilling label 'Ab' that still have similar properties. The labels 'Abb' and 'Abv' could therefore also be associated with 'Ab' and all measurements on 'Abb' and 'Abv' will be applied to 'Ab' as well.

Any entry for this option that does not link to an existing file will be ignored and this option skipped.

3.2.2: Property estimate source data files

Only available if calculating physical property estimates. The dialog defines the source data files to be used to calculate the physical property estimates database.

Path to surface sample data file

Only available if using surface sample measurements in the database calculation. This indicates a text column file containing surface-sample geology labels and property measurements. No coordinates are required. The input properties will be scaled by the conversion factor defined in 3.1.0 (p. 430).

Path to drilling geology logs file

Only available if using drilling measurements in the database calculation. This identifies the drilling geology log file for deriving estimates of the properties associated with each drilling geology label. No collar/survey files are required. Error checking is performed to remove duplicate entries, fix overlapping intervals, and replace point observations with short intervals to all resampling (below).

Path to drilling property logs file

Only available if using drilling measurements in the database calculation. This identifies the drilling property log file for deriving estimates of the properties associated with each drilling geology label. No collar/survey files are required. Error checking is performed to remove duplicate entries, fix overlapping intervals, and replace point observations with short intervals to all resampling (below). The input properties will be scaled by the conversion factor defined in 3.1.0 (p. 430).

Minimum drilling sample interval length for resampling

Only available if using drilling measurements in the database calculation. Drilling geology logs and property measurements are commonly reported over different length intervals. Geology logs tend to indicate the lengths of particular geological units or features; physical property measurements may be taken on regular sample intervals. The geology log intervals are therefore unlikely to match the measurement intervals. To link the two, the drill holes are resampled at a smaller interval and the geology label and measured property present

at each resample point are linked. The length of the resampling interval must be defined here. To adequately resample the observations the resampling interval should be less than half the average interval length.

3.3.0: Geology label bounds confidence level

Only available if creating a bounds model and using drilling geology logs or maps. The confidence level selected here is used to extract which confidence interval should be used to define the bounds for geology label property estimates. As bounds are an absolute constraint in the inversions, it is best to select a relatively high confidence level ($\geq 95\%$) to ensure accuracy. A higher confidence level will define a wider confidence interval and therefore wider bounds.

4.0.0: Constraint cropping options

For most problems, constraints should be applied throughout the mesh wherever they are available. However, in some circumstances it may be beneficial to limit the volume over which constraints are applied to the volume of the mesh that is sensitive to the data. This is generally the case where a regional data response has not been removed from the data, in which case the model's padding cells may need to accommodate extreme physical properties to adequately reproduce the observed data. If the constraints are to be cropped, the central region in which constraints are applied must be identified. Two options are available: 1) any cells lying directly below the surface extent of the geophysical data (Figure B.1B), or 2) a bowl-shaped region lying within the extent of the data (Figure B.1C).

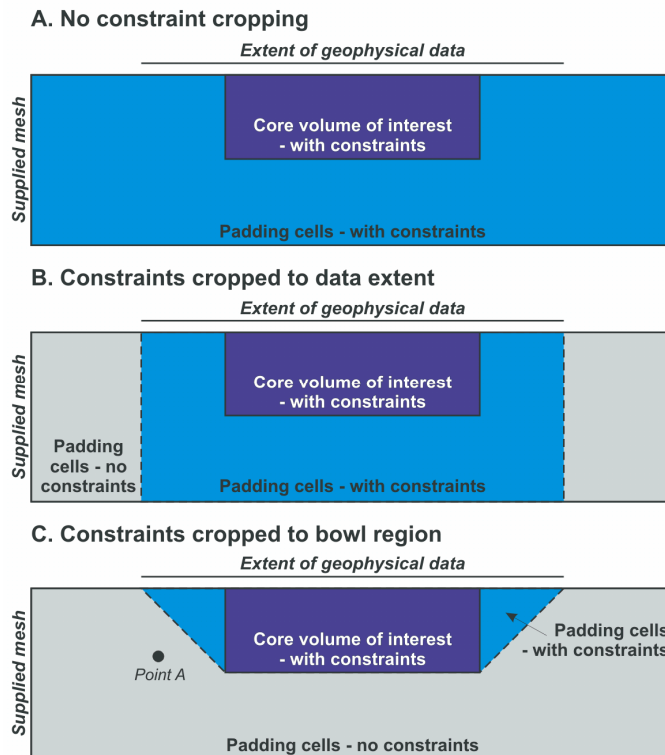


Figure B.1. Schematic 2D cross-section examples of the available constraint cropping options. The blue areas show the extent of constraints. A. Constraints are created throughout the entire supplied mesh. This is recommended for most problems. B. Constraints are limited to the region of the supplied mesh that lies directly below the available geophysical data. C. Constraints are only created within a bowl shaped region between the available geophysical data extent and some core volume of interest. A tight constraint supplied at Point A might not be able to be supported by the available geophysical data due because its depth may require data wavelengths that extend beyond the limit of the available geophysical data. This could cause distortions in the rest of the model.

4.1.0: Crop options

If constraints require cropping, either to the extent of the data or to a bowl region, additional information is required to define the constrained region.

Path to UBC-GIF geophysical data file

This identifies a UBC–GIF format geophysical data observation file that will be used. The data observation locations are used to define the lateral extent of the constraints within the model. The actual observation values in the file are ignored.

Path to mesh file over the core volume

This mesh defines the core volume of interest in the inversion volume. The lateral and vertical extents define the bottom of the bowl as shown in Figure B.1C. The cell sizes in the mesh definition file are not important.

5.0.0: Surface sample options

Only available if using surface sample measurements. If surface sample measurements are to be used, this dialog defines the data file and associated options.

Path to samples file

Identifies the surface sample data file containing X-Y-Z coordinates and property measurements. The input properties will be scaled by the conversion factor defined in 3.1.0 (p. 430).

Fix sample locations on topography surface

Use this option when all sample lie on the surface. Their vertical position will be adjusted to ensure that they lie in the top cell below the topography surface. Otherwise they may be unexpectedly cut off by the topography discretisation because they appear to lie in an “air” cell.

5.1.0: Topography options

Only available if using surface sample measurements and fixing the locations to the topography surface. This dialog boxes is used to define the topographic surface.

Path to UBC-GIF model file of topography

The discretisation of the topographic surface that will be used by the inversion is defined here using any recovered inversion model that used a topography file and the current mesh. The inversion will have stored a no-data-value in every cell above the topography surface. This is used to identify which is the top cell below the topographic surface.

Model file no-data-value

This is the no data value used in the supplied inversion model to indicate that a cell is above ground.

6.0.0: Domain model options

Only available if using a 3D domain model. A domain model specifies default property estimates and optional structural orientation for particular regions of the model.

Path to UBC-GIF model file of domains

A 3D domain model file linked to here will be a UBC–GIF format model file contains a unique index indicating which domain each cell belongs to. Every cell must be assigned a domain index, but those indexes not listed in the domain definition file will be ignored.

Path to domain definition file

This text file links the domain indexes to estimates of the lower and upper bounds and reference properties for each domain. The input properties will be scaled by the conversion

factor defined in 3.1.0 (p. 430). A smallness (w_s) weight is also assigned to indicate the confidence in those properties for each domain. The final three columns indicate the aspect ratio to be applied in each of the domains. These have default values of 1, 1, and 1 in the east-west, north-south, and vertical directions. The aspect ratio indicates the approximate shape of the expected bodies in a region. If bodies are expected to be 2 times wider (east-west) and 5 times longer (north-south) than they are tall, then an aspect ratio of 2:5:1 should be used in that domain. This effectively multiplies the specified length scales in that region by those values. If non-default aspect ratios are defined, then it is recommended that the length scales in the inversion input file control file are set to $2\times$ the cell widths. The aspect ratios are only applied if smoothness weights are being created, but must be present in the input file.

OPTIONAL: Path to domain orientations definition file

Only available if using buffers. The text file links the domain indexes to parameters that define the orientation and shape of the ellipsoid in each domain. Default buffer ellipsoids will be defined later for cells without an assigned domain or within the cover/weathering domain. Any entry for this option that does not link to an existing file will be ignored and this option skipped.

Include an automatic cover/weathering domain

This creates an additional domain above some depth in the model, overprinting all others, to represent cover rocks and/or weathering which commonly have unique physical properties.

6.1.0: Cover/weathering domain options

Only available if automatically including a cover/weathering domain. The extent and properties of the cover domain are specified here.

Path to UBC-GIF model file of topography OR basement level

The discretisation of the topographic or basement surface that will be used by the inversion is defined here using any recovered inversion model that used a topography file and the current mesh. The inversion will have stored a no-data-value in every cell above the topography surface. If an estimate of the basement surface topography is available as a UBC–GIF topography file it can be used in a rough inversion to recover a basement surface model which can be supplied here to define a more detailed base of cover and/or weathering.

Model file no-data-value

This is the no data value used in the supplied inversion model to indicate that a cell is above the topographic or basement surface.

Depth of cover below topography/basement surface

If a topography model was supplied rather than a basement surface model, this value should be the depth of cover/weathering below surface. If a basement model is included, this value should usually be zero.

Cover/weathering domain: Reference property value

Only available if creating a reference model. This defines the default reference property of the cover/weathering domain where no other data are available.

Cover/weathering domain: Smallness (w_s) weight

Only available if creating a reference model. This is the default smallness (reliability) weight of the cover/weathering domain where no data are available.

Cover/weathering domain: Aspect ratio – east-west

Only available if creating smoothness weights. Aspect ratios indicate the relative shape of bodies within the cover/weathering domain. Enter the relative width of the bodies here (≥ 1).

Cover/weathering domain: Aspect ratio – north-south

Only available if creating smoothness weights. Aspect ratios indicate the relative shape of bodies within the cover/weathering domain. Enter the relative length of the bodies here (≥ 1).

Cover/weathering domain: Aspect ratio – vertical

Only available if creating smoothness weights. Aspect ratios indicate the relative shape of bodies within the cover/weathering domain. Enter the relative thickness of the bodies here (≥ 1).

Cover/weathering domain: Lower bound

Only available if creating a bounds model. Default lower bound to be assigned in cover/weathering domain cells with no data, or insufficient data to adequately define bounds.

Cover/weathering domain: Upper bound

Only available if creating a bounds model. Default upper bound to be assigned in cover/weathering domain cells with no data, or insufficient data to adequately define bounds.

Trust drilling geology logs in cover/weathering domain

Only available if using drilling geology logs. Geologists sometimes ignore weathering when logging drill core or describing samples and try to identify the pre-weathering rock type. This protolith will have different physical properties from the weathered product, and will bias the model. This option prevents information from drilling geology logs being applied within the cover/weathering domain.

6.2.0: Cover/weathering internal orientation

Only available if automatically including a cover/weathering domain and using buffers. The orientations and shape of the ellipsoidal buffers to be applied in the cover domain is specified here as shown in Figure B.2. The actual size of the buffers, defined by the length of the major **A** axis, is based on the type of data in each cell (19.0.0, p. 470). If the cover/weathering domain is to represent weathering, a good estimate of the buffer orientation is a thin flat buffer resembling a plate. This can be defined with any strike and pitch, a dip of 0°, a b/a length ratio of 1.0 and a small c/a length ratio. If no dominant orientation can be inferred, then a default spherical buffer can be used. This is achieved by assigning any strike/dip/pitch combination and setting both the b/a and c/a length ratios to 1.0.

Dominant strike

This is the dominant strike of the cover rocks. The strike is specified as 0-360° from north, with the dip plane to the right of the strike direction. For example, a strike and dip of 045/45 SE would be represented as 045/45, whereas a strike and dip of 075/45 NW would be represented as 135/45.

Dominant dip

This is the dominant dip of the cover rocks below horizontal. It is specified as 0-90° and is assumed to be in a direction 90° to the right of the strike direction.

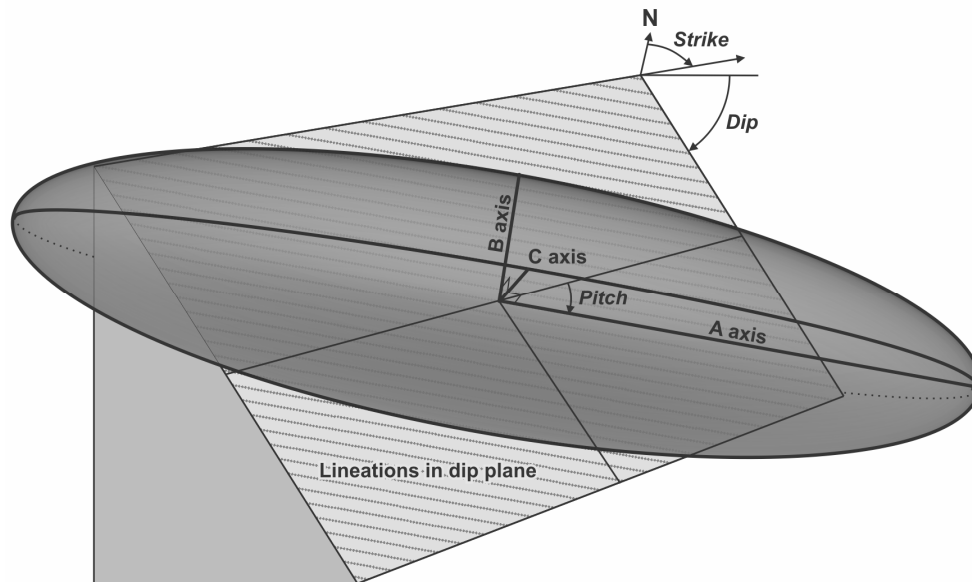


Figure B.2. Definition of ellipsoidal buffer based on geological orientations. The orientations of the three ellipsoid axes, **A** (within dip plane, along lineations), **B** (within dip plane, perpendicular to lineations), and **C** (perpendicular upwards out of the dip plane), are derived from the strike, dip, and pitch. Strike is the clockwise angle (0-360°) from north such that the plane dips to the right when looking towards the strike azimuth. The dip is the angle (0-90°) of the plane below horizontal. The pitch is the angle (0-180°) of lineations below the strike line, within the dip plane. Lineations can represent actual stretching lineations and bedding-cleavage orientations, or may be estimates of local fold hinge lines. The size of the buffer is defined by the length of the **A** axis which is defined by the data type, and the length ratios of the **B** axis to the **A** axis (b/a) and the **C** axis to the **A** axis (c/a) according to the strength and continuity of the structural grain in each direction.

Dominant pitch

This is the dominant pitch associated with any lineations, stretching, or fold axes in the dominant dip plane of the cover rocks/weathering. It is specified as 0-180° below horizontal away from the direction of strike. If no dominant pitch is expected, any value can be supplied here, and a value of 1.0 supplied for the b/a length ratio. This will recover a uniform plate oriented along the dip plane.

Intermediate axis length ratio (b/a)

This is the length of the **B** axis within the dip-plane, as a proportion (0-1) of the major **A** axis along-pitch buffer length. If the data type for a cell requires an **A** axis length of 100 m, a b/a ratio of 0.5 will give an intermediate **B** axis length of 50 m.

Minor axis length ratio (c/a)

This is the length of the **C** axis perpendicular to the dip-plane, as a proportion (0-1) of the major **A** axis along-pitch buffer length. If the data type for a cell requires an **A** axis length of 100 m, a c/a ratio of 0.5 will give a minor **C** axis length of 50 m.

7.0.0: Geological model options

Only available if using a 3D geological model. A geology model specifies default property estimates and boundaries for particular geological units within the model.

Path to UBC-GIF geology model file

A 3D geology model file linked to here will be a UBC–GIF format model file contains a unique index indicating which geological unit each cell belongs to. Every cell must be assigned a geological index, but those indexes not listed in the geology definition file will be ignored.

Path to geology definition file

This text file links the geology model indexes to estimates of the lower and upper bounds and reference properties for each geological unit. If a physical property database has been calculated, the estimates contained in it can be used to help manually define the properties for each of the geological units. A smallness (w_s) weight is also assigned to indicate the confidence in those properties for each unit. The input properties will be scaled by the conversion factor defined in 3.1.0 (p. 430).

8.0.0: Basement map options

Only available if using a basement geology map. Any number of ESRI polygon shapefiles can be imported and applied in the model as either outcrop or basement geology maps. The only difference between the treatment of basement geology maps and outcrop geology maps is their vertical placement within the model.

Path to UBC-GIF model file of topography OR basement level

The discretisation of the topographic or basement surface that will be used by the inversion is defined here using any recovered inversion model that used a topography file and the current mesh. The inversion will have stored a no-data-value in every cell above the topography surface. If an estimate of the basement surface topography is available as a UBC–GIF topography file it can be used in a rough inversion to recover a basement surface model which can be supplied here to define a more detailed base of cover and/or weathering.

Model file no-data-value

This is the no data value used in the supplied inversion model to indicate that a cell is above the topographic or basement surface.

Depth of map below topography/basement surface

If a topography model was supplied rather than a basement surface model, this value should be the approximate depth of basement below surface. If a basement model is included, this value should usually be zero.

Number of shapefiles to load

If the model crosses map boundaries then multiple maps can be loaded and tiled together. The number of maps must be entered here. A series of prompts will open one this dialog box is closed to identify the map files for each map. Load the shapefiles in order of their importance: load smaller, most detailed maps first, followed by larger less detailed maps.

UTM grid zone of the maps

The UTM grid zone associated with the maps is used in conversions between UTM and latitudes and longitudes. It must be entered in the form: 51 J.

Assign properties to whitespace or undefined portions of the map

Whitespace or undefined regions in a map might represent generic rocks or cover that could be assigned some estimated properties. If no properties are assigned then whitespace regions will be treated as not containing any data and will be assigned default property values.

Display maps

Selecting this option creates various plots of the model's position relative to the maps, and the resulting discretised map.

8.1.0: Map sampling detail

When using a map that was prepared at a more detailed scale than the current mesh can adequately represent, or in regions where the geology is complex, the geology map in each cell must be sampled in more detail to accurately identify which geological units are present. More detailed sampling gives a more accurate representation of the geology when multiple units are present within each cell; however the length of time required is multiplied by the number of samples required.

Low (1 sample per cell)

With this option only the mapped geology label in the centre of each cell is extracted. This is the fastest option and will adequately represent the geology if only one unit is expected to be dominant in each cell.

Medium (5 samples per cell)

A grid of five sample points, including the centre of the cell and points towards each horizontal corner is used. This will provide a reasonable sampling in most situations.

High (9 samples per cell)

The most detailed sampling method uses a regular grid of nine samples across each cell and provides the most accurate geological representation but takes nine times longer than for a single sample per cell.

8.2.0: Properties for map whitespace

Only available if indicated on the basement geology map options dialog box. If an estimate of the properties associated with rocks depicted as whitespace on a map is available it can be entered here. This will treat whitespace equally as another rock type.

Reference property

Only available if building a reference model. Indicate the reference property estimate to be associated with whitespace in the map.

Lower bound

Only available if building a bounds model. Indicate the lower bound or confidence interval on the estimate of the reference property to be associated with whitespace in the map.

Upper bound

Only available if building a bounds model. Indicate the upper bound or confidence interval on the estimate of the reference property to be associated with whitespace in the map.

9.0.0: Outcrop map options

Only available if using an outcrop geology map. Any number of ESRI polygon shapefiles can be imported and applied in the model as either outcrop or basement geology maps. The only difference between the treatment of basement geology maps and outcrop geology maps is their vertical placement within the model.

Path to UBC-GIF model file of topography level

The discretisation of the topographic surface that will be used by the inversion is defined here using any recovered inversion model that used a topography file and the current

mesh. The inversion will have stored a no-data-value in every cell above the topography surface.

Model file no-data-value

This is the no data value used in the supplied inversion model to indicate that a cell is above the topographic surface.

Depth of map below topography surface

If a topography model was supplied rather than a basement surface model, this value should be the approximate depth of basement below surface. If a basement model is included, this value should usually be zero.

Number of shapefiles to load

If the model crosses map boundaries then multiple maps can be loaded and tiled together. The number of maps must be entered here. A series of prompts will open one this dialog box is closed to identify the map files for each map. Load the shapefiles in order of their importance: load smaller, most detailed maps first, followed by larger less detailed maps.

UTM grid zone of the maps

The UTM grid zone associated with the maps is used in conversions between UTM and latitudes and longitudes. It must be entered in the form: 51 J.

Assign properties to whitespace or undefined portions of the map

Whitespace or undefined regions in a map might represent generic rocks or cover that could be assigned some estimated properties. If no properties are assigned then whitespace regions will be treated as not containing any data and will be assigned default property values.

Display maps

Selecting this option creates various plots of the model's position relative to the maps, and the resulting discretised map.

9.1.0: Map sampling detail

When using a map that was prepared at a more detailed scale than the current mesh can adequately represent, or in regions where the geology is complex, the geology map in each cell must be sampled in more detail to accurately identify which geological units are present. More detailed sampling gives a more accurate representation of the geology when multiple units are

present within each cell; however the length of time required is multiplied by the number of samples required.

Low (1 sample per cell)

With this option only the mapped geology label in the centre of each cell is extracted. This is the fastest option and will adequately represent the geology if only one unit is expected to be dominant in each cell.

Medium (5 samples per cell)

A grid of five sample points, including the centre of the cell and points towards each horizontal corner is used. This will provide a reasonable sampling in most situations.

High (9 samples per cell)

The most detailed sampling method uses a regular grid of nine samples across each cell and provides the most accurate geological representation but takes nine times longer than for a single sample per cell.

9.2.0: Properties for map whitespace

Only available if indicated on the outcrop geology map options dialog box. If an estimate of the properties associated with rocks depicted as whitespace on a map is available it can be entered here. This will treat whitespace equally as another rock type.

Reference property

Only available if building a reference model. Indicate the reference property estimate to be associated with whitespace in the map.

Lower bound

Only available if building a bounds model. Indicate the lower bound or confidence interval on the estimate of the reference property to be associated with whitespace in the map.

Upper bound

Only available if building a bounds model. Indicate the upper bound or confidence interval on the estimate of the reference property to be associated with whitespace in the map.

10.0.0: Drilling options

All options for using either drilling property measurements or geology observations are assigned with this dialog box. To be applied to the model, the drill hole traces must be defined.

These will be based on a collar file containing the collar location of each drill hole and its length, and a survey file which contains the drill hole direction at each survey point down each hole.

EITHER: Path to MATLAB drilling file

This file contains previously calculated drill hole traces, and significantly speeds processing time. Any entry that does not link to an existing file will be ignored and this option skipped.

OR: Path to collar file.

If traces have not previously been calculated, or need to be recalculated, then supply the drill holes' collar file here. This contains the X-Y-Z coordinates of the drill hole collars, and the total length of each hole.

PLUS: Path to survey file

If traces have not previously been calculated, or need to be recalculated, then supply the drill holes' survey file here. This contains the drill hole azimuth and inclination at survey points down each hole.

Path to property log file

Only available if using drilling property logs. Supply a text file of drilling property measurements, if needed. This may have already been supplied when calculating or loading the physical property database, in which case no entry is required.

Path to geology log file

Only available if using drilling geology logs. Supply a text file of drilling geology logs, if needed. This may have already been supplied when calculating or loading the physical property database, in which case no entry is required.

Interval for resampling

Because drilling geology logs and drilling property measurements are commonly reported over intervals, the drill holes are resampled at points to recover the geology code and measurement that applies to each point down hole. The resample interval should be less than the average reporting interval for the geology or property logs.

Display drill hole traces

This options will display a 3D plot of the loaded drill hole traces.

11.0.0: Method for assigning reference properties from point observations

Only available if creating a reference model and using both property measurements and drilling geology observations. Geological observations in each cell are converted into a list of the mean properties associated with each geology label as determined by the physical property database. Actual physical property measurements in the cell are also available as a list of numbers. Where both measurements and property estimates based on geology observations occur within a single cell, there are several ways in which they can be combined to recover a reference property for that cell. Fundamentally the choice depends on the expected relative variability of geology versus physical properties within the cell, and which type of data will provide a more representative reference property estimate for that cell. Consider two counter examples:

- The cell consists entirely of banded gneiss. Darker bands are more magnetic than the lighter bands. Within the cell there are five geological observations of “banded gneiss”. There are also 5 magnetic susceptibility measurements. The 5 measurements may represent all light coloured bands or all dark coloured bands, or a mixture. It is unlikely that those 5 measurements will provide an accurate representation of the physical properties in the cell because they are unlikely to represent the true proportions of light bands and dark bands. Throughout the whole model, however, there are 100 measurements on “banded gneiss” which could provide a statistically representative random sampling of the physical properties of the gneiss, and therefore the cell. In this situation, the geological variability is much lower (a single rock type) than the physical property variability (either high or low measurements) within the cell, and an estimate that favours the geological observations would provide the best reference property. This situation isn’t as unique as it might seem, and could equally apply to any bedded sedimentary rocks, altered or metamorphosed rocks, or most importantly, rocks containing uneven distributions of magnetic minerals or sulphides. The latter example is particular problematic because measurements might be preferentially made on the sulphidic rocks which provide the geophysical targets, and not on their more abundant host rocks.

- The cell consists of 4 geological units. There is a significant spread of physical properties associated with each of the units throughout the model, however, in this particular cell, the properties are nearly identical. Again, 5 property measurements and 5 geological observations are available. It would be expected that the 5 measurements would all be similar regardless of which unit they came from whereas the physical property estimates derived from the 5 geological observations may reflect the full spatial variability of the units and so provide a poor estimate of the properties within this particular cell. In this situation the geological variability is clearly greater than the physical property variability, and an estimate that favours the physical property measurements will be most effective.

For large numbers of well distributed measurements and observations, the cell will be well characterised regardless of the method used, and the estimates will all converge to some tight estimate of the appropriate reference property. The challenge occurs when there are small numbers of observations or measurements and high geological variability or high property variability, or both. In all cases, the bounds (if used) will be taken from the minimum and maximum confidence intervals associated with any geological observation or all of the physical property measurements.

Treat each point observation equally

This is the simplest option, it merely combines all available measurements and estimates based on geology observations and calculates the total mean value and assigns this as the reference property. This uses all the available information, but includes no interpretation as to which data type might be more reliable.

Emphasise the observation type(s) that best samples each cell (using one of the 3 methods below)

This option is not a calculation on its own, but provides an automated method for selecting a different one of the following options for each cell as required. The choice is based on the spatial distribution of each type of observation in each cell. The spatial distribution is determined by dividing each cell into a number of blocks, the size of which is set in dialog box 12.0.0 (below). The proportion of blocks containing samples of each data type is determined. If one data type samples significantly more volume of the cell than another data type, then that

data type is emphasised using the first or last option below. If the proportions differ by less than a third, then both data types sample the cell equally well and the middle option is used. Although this method attempts to remove any sampling bias in each cell it makes no interpretation about whether geology or physical properties are fundamentally more reliable estimators of the reference property.

Prefer property measurements (expect small property variability within cells)

This is the best option to use if property measurements always provide the best estimate of the properties of a cell. It should be used when there is a much larger geological variability than physical property variability, or when the property estimates based on geology observations contain a spatial variability that is not observed in individual cells. The mean of all geology-based property estimates in the cell is treated as a single property measurement. The reference property is then the mean of all the property measurements. This method ensures that if there is more than one property measurement, property measurements will be emphasised, if there is 1 measurement and 1 geology observation, the reference property will lie halfway between them, and if there are no property measurements, an estimate will still be recovered from the geological observations (if any).

Treat each data type equally (expect moderate variability in both)

With this method each data type is treated equally such that the recovered reference property lies halfway between the mean property measurement and the mean geology-based property estimate. If there are roughly equal numbers of observations of each data type, then this provides a very reliable estimate. However, if one of the data types has a much smaller number of samples than the other, then the underrepresented data type will be overemphasised using this method. This may still be desirable if the data type that is usually underrepresented is thought to be more reliable: this may commonly be the case for physical property measurements which are usually less common than geological observations.

Prefer geology observations (expect small geological variability within cells)

This is the best option to use if geological observations always provide the best estimate of the properties of a cell. It should be used when there is a much larger physical property variability than geological variability, or where individual physical property measurements are biased or otherwise not representative of the whole cell's properties. The mean of all property measurements in the cell is treated as a single geology-based property

estimate. The reference property is then the mean of all the geology-based property estimates. This method ensures that if there is more than one geological observation, geological observations will be emphasised, if there is 1 measurement and 1 geology observation, the reference property will lie halfway between them, and if there are no geological observations, an estimate will still be recovered from the physical property measurements (if any).

12.0.0: Spatial sampling requirements

Only available if using surface samples or drilling. Several functions require a measure of how well a cell is sampled spatially. This is a good indicator of the quality of observations within a cell, and therefore their reliability. The spatial sampling of each cell is determined by dividing the cell into cubic blocks of rock that can be approximately represented by a single point observation. The proportion of sample blocks that contain samples can then be used as a measure of the spatial distribution of those sample points. This may be used in any of these ways depending on the current suite of options:

- Determining how reference properties for each cell will be assigned
- Assigning smallness weights for each cell
- Determining if reliable bounds can be assigned

If bounds are being used then an additional threshold parameter must be defined to indicate what percentage of blocks need to be sampled before tight non-default bounds can be assigned to a cell based on its contents.

Sample block size

This is the length (in meters) of the side of the cube that can be approximately represented by a single property measurement or geology observation.

Adequate sampling threshold for each cell

Only available if using bounds. Each cell will be divided into sample blocks of the size defined above. The threshold defines the percentage of blocks that need to contain observations for the cell to have been adequately sampled. Only when this threshold is reached will tight bounds be applied

13.0.0: Bounds confidence level for point measurements

Only available if creating a bounds model and using surface sample or drilling measurements. The confidence level selected here is used to extract which confidence interval

should be used to define the bounds for a cell containing point observations from surface sample or drilling property measurements. As bounds are an absolute constraint in the inversions, it is best to select a relatively high confidence level ($\geq 95\%$) to ensure accuracy. A higher confidence level will define a wider confidence interval and therefore wider bounds. If drilling geology logs or maps are being used then the default confidence level will be the same as was used to define the confidence interval on geology label property estimates in 3.3.0 (p. 435).

14.0.0: Smallness (w_s) weights for each constraint type

Only available if using surface samples, drilling, or maps and creating a reference model. Smallness or w_s weights are used to indicate the reliability of the reference model property in each cell of the inversion cells. More reliable reference model properties should be associated with higher smallness weights. Less reliable smallness weights should be assigned lower smallness weights, or the default of unity. The ModelBuilder assigns smallness weights based on the reliability of the data type used to derive the reference properties. These values are set here for those data types that are being used.

Smallness weight (w_s) for surface measurements

This is the maximum smallness weight possible for a cell containing surface sample measurements. It will be scaled according to how thoroughly the cell has been sampled, as determined by the squared proportion of sample blocks containing measurements within the cell. The size of the sample blocks is defined in dialog box 12.0.0 (p. 451).

Smallness weight (w_s) for drilling measurements

This is the maximum smallness weight possible for a cell containing drilling measurements. It will be scaled according to how thoroughly the cell has been sampled, as determined by the squared proportion of sample blocks containing measurements within the cell. The size of the sample blocks is defined in dialog box 12.0.0 (p. 451).

Smallness weight (w_s) for drilling geology logs

This is the maximum smallness weight possible for a cell containing drilling geology logs. It will be scaled according to how thoroughly the cell has been sampled as determined by the squared proportion of sample blocks containing observations within the cell. The size of the sample blocks is defined in dialog box 12.0.0 (p. 451).

Smallness weight (w_s) for outcrop geology map

An outcrop geology map would usually have a higher reliability than a basement geology map because outcrop or surface geology is directly observable. No scaling is performed.

Smallness weight (w_s) for basement geology map

A basement geology map would usually have a lower reliability than an outcrop geology map because it is inferred or interpreted from indirect data sources. No scaling is performed.

Scale smallness or smoothness weights with depth or distance

Only available for density and magnetic susceptibility models. Depth or distance weighting in potential field inversions is necessary in many situations because there is no inherent depth information in the geophysical data. As implemented, the depth weighting effectively allows greater differences between the recovered model and the reference model as depth increases. This is desirable in areas where there are no geological constraints, but degrades the effectiveness of the reference model in areas where geological constraints are present and sensitivity to the geophysical data is low. Use this option to effectively turn off depth or distance weighting where constraints exist. When scaling is applied, the resulting smallness and smoothness weights can become large and quite complex (Figure B.3), but will ensure that constraints imposed using reference models, smallness weights, or smoothness weights are better reproduced at depth.

15.0.0: Weights to scale

Only available if scaling weights with depth or distance in density and magnetic susceptibility models and using creating smoothness models. The user can choose to scale smallness weights, smoothness weights, or both. Generally, scaling smallness weights has the most impact, but scaling smoothness weights can also be useful. If smoothness weights are not being used and the scale weights option was selected on dialog 14.0.0, then smallness weights will be automatically scaled.

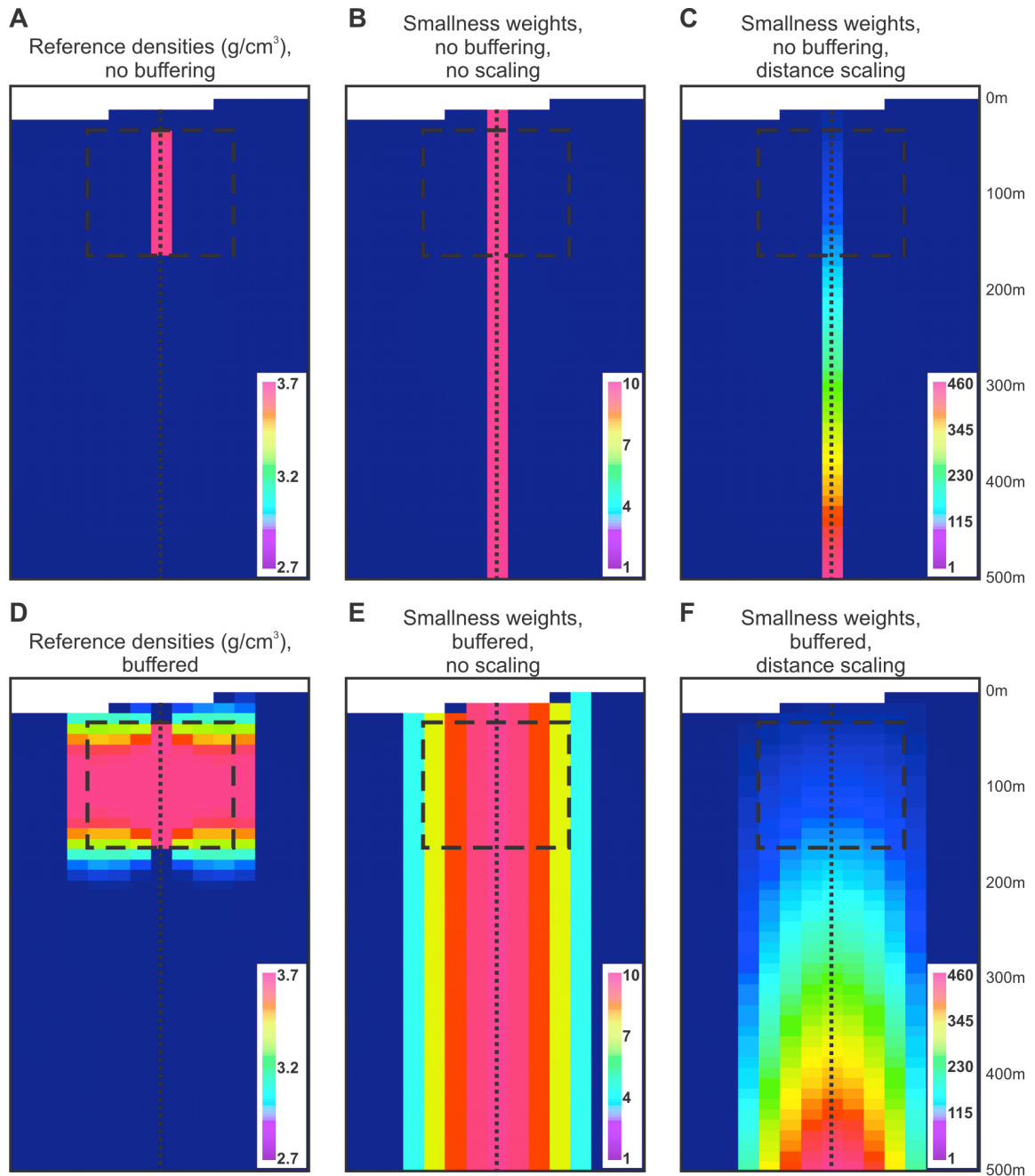


Figure B.3. Demonstration of distance weight scaling of smallness weights for a simple synthetic example with a single vertical drill hole (dotted line) passing through an anomalous block (outlined with dashed line). A-C show the constraint models obtained without using buffers; D-F show the constraint models when buffers are used. A. Reference model, with constraints assigned along the drill hole trace. B. Smallness weights assigned along the trace of the drill hole. Values of 10 are used where constraints exist and 1 where there are no constraints. C. Resulting smallness weights after the values from B are scaled by the distance weights. Although the increasing smallness weights suggests that confidence in the reference model is increasing with depth, this actually turns off distance weighting in these cells in the inversion so that the constraints are reproduced with the same confidence at deep and shallow levels. D. Reference model, with constraints assigned along the drill hole trace and 100 m buffers applied. E. Smallness weights assigned along the trace of the drill hole with 100 m buffers applied. Values of 10 are used where data exist and decrease through the width of the buffer until they reach default values of 1 where there are no constraints. F. Resulting smallness weights after the values from E are scaled by the distance weights to turn off distance weighting in the constrained cells.

15.1.0: Scaling applied in buffers

Turning off depth or distance weighting in cells with geological constraints ensures that those constraints will be honoured in the inversion model. Where the constraints are based directly on geological observations, this is completely desirable. However, if buffers have been used to extrapolate the data-based constraints, the constraints in those buffer zones may be less reliable because they are not based on direct observation. Full strength weight scaling will be applied to data-based constraints, but the intensity of the scaling used in the buffers can be adjusted here.

Full weight scaling in buffers

Full weight scaling is applied to constraints in buffers. This should only be used when the buffers are small relative to the size of cells and are expected to be highly reliable. The buffer properties at depth will be strongly reproduced in the recovered model.

Half-power weight scaling in buffers

Half-power depth or distance weights are used to scale the smallness and smoothness weights. These scaling weights are the square root of the full weights. Testing in both real and synthetic inversions suggests that this is the best setting to use for most problems. The constraints applied in buffers at depth have a strong influence on the model, but are not strictly enforced.

No scaling in buffers, scale data only

Only apply depth or distance weight scaling to constraints based directly on observations. No weight scaling is applied to buffers constraints. Buffer zones at depth will only have a weak influence of the recovered model. This may be the best option the buffers are extremely large, and therefore less reliable.

15.2.0: Type of weight scaling to apply

Here is where the type of scaling to apply is specified: distance weighting, depth weighting, or a hybrid weighting scheme. Generally the selection will be based on whether distance or depth weighting will be used in the inversion. However, using distance weighting with geological constraints in inversions where geophysical data has a highly irregular spatial distribution can give some undesirable results in shallow layers. These features typically manifest themselves in the recovered inversion model as spots or stripes of elevated properties

close to isolated geophysical observations. In such situations, a hybrid weighting scheme is recommended with depth weights specified in the inversion. The ModelBuilder then scales the smallness weights in such a way that they act as distance weights where no constraints exist and depth/distance weighting is turned off where constraints do exist. For smoothness weights (if being used) the depth weighting is turned off where constraints exist, but otherwise behaves normally in this hybrid scheme. The effect on constrained and unconstrained cells using the three types of scaling is summarised in Table B.3.

Table B.3. Summary of the effect of the three available types of weight scaling on constrained and unconstrained cells. Typically the choice of which scaling to apply will be based on whether distance or depth weighting will be used in the inversions. The hybrid method combines the best features of both and works best where there is a highly irregular spatial distribution of geophysical data.

	Smallness weights			Smoothness weights	
	Weighting specified in the inversion	Effective weighting for constrained cells in inversions	Effective weighting for unconstrained cells in inversions	Effective weighting for constrained cells in inversions	Effective weighting for unconstrained cells in inversions
1. Distance weighting scheme	Distance	None	Distance	None	Distance
2. Depth weighting scheme	Depth	None	Depth	None	Depth
3. Hybrid weighting scheme	Depth	None	Distance	None	Depth

15.3.0: How to determine weights

The weights can be calculated automatically or can be loaded from an existing weighting file if available. The required files are output by newer versions of the GZSEN3D or MAGSEN3D code, or are automatically saved after being calculated in by the ModelBuilder.

15.4.0: Distance weighting parameters

Only available if distance weights need to be calculated. The distance weighting parameters used to scale the smallness and/or smoothness weights must be defined here. By default they are set to estimated values for the current mesh. More accurate values may be obtained from the log files produced by GZSEN3D/MAGSEN3D. An example of how distance weight scaling is applied is shown in Figure B.3.

Distance weighting, r_0 (m)

This parameter is calculated by the inversion codes GZSEN3D/MAGSEN3D and is typically one quarter the smallest dimension of any cells. It can be obtained from the

inversion's sensitivity calculation log file (where it is written as 'rnot'). The default is a quarter of smallest cell dimension used in the model.

Distance weighting, beta or pwr

This parameter is determined by the inversion codes GZSEN3D/MAGSEN3D and depends on the type of geophysical data being used. It can be obtained from the inversion's sensitivity calculation log file (where it is written as 'pwr'). The default is 3 for magnetics and 2 for gravity.

UBC-GIF geophysical data file

The distance weights are based on the positions of the observation data points, so the data to be used in the inversion must be loaded. Identify the filename here.

Path to UBC-GIF model file of topography level

Distance weights should not be calculated above topography so the discretisation of the topographic surface that will be used by the inversion is defined here using any recovered inversion model that used a topography file and the current mesh. The inversion will have stored a no-data-value in every cell above the topography surface.

Model file no-data-value

This is the no data value used in the supplied inversion model to indicate that a cell is above the topographic surface.

15.5.0: Depth weighting parameters

Only available if depth weights need to be calculated. The depth weighting parameters used to scale the smallness and/or smoothness weights must be defined here. By default they are set to estimated values for the current mesh. More accurate values may be obtained from the log files produced by GZSEN3D/MAGSEN3D.

Distance weighting, z_0 (m)

This parameter is calculated by the inversion codes GZSEN3D/MAGSEN3D. The default value presented here is just half the height of cells in the center of the model, but is usually underestimates the appropriate value. The true value can be obtained from the inversion's sensitivity calculation log file (where it is written as 'znot').

Distance weighting, beta or pwr

This parameter is determined by the inversion codes GZSEN3D/MAGSEN3D and depends on the type of geophysical data being used. It can be obtained from the inversion's sensitivity calculation log file (where it is written as 'pwr'). The default is 3 for magnetics and 2 for gravity.

Path to UBC-GIF model file of topography level

Only available if an appropriate topography model file has not already been loaded.

Depth weights should not be calculated above topography so the discretisation of the topographic surface that will be used by the inversion is defined here using any recovered inversion model that used a topography file and the current mesh. The inversion will have stored a no-data-value in every cell above the topography surface.

Model file no-data-value

Only available if an appropriate topography model file has not already been loaded.

This is the no data value used in the supplied inversion model to indicate that a cell is above the topographic surface.

15.6.0: Identifying distance/depth weighting model files

Only available if loading the weights rather than calculating them. If the weights are to be loaded from existing files, then the locations of the files are specified here. These are output directly from newer versions of the GZSEN3D or MAGSEN3D programs or are saved when ModelBuilder calculates the values using dialog boxes 15.4.0 (p. 456) and 15.5.0 (p. 457).

Path to depth weighting file

Only available if using the depth or hybrid weighting scheme weighting. This file contains the required depth weights which must have been previously calculated (usually “depth_weight.txt”). “Air” cells must be marked with negative values.

Path to distance weighting file

Only available if using the distance or hybrid weighting scheme weighting. This file contains the required distance weights which must have been previously calculated (usually “dist_weight.txt”). “Air” cells must be marked with negative values.

16.0.0: Smoothness weight (w_x , w_y , w_z) options

Only available if building smoothness weights. Smoothness weights are used to define the magnitude of changes that can occur across each cell face in the three orthogonal directions within the inversion. Smooth variations are favoured across a cell face when assigned high smoothness weights (> 1). Sharper breaks across cell faces are favoured when assigned low smoothness weights (< 1). Examples of how the effect of some of these options using buffered and unbuffered models are shown in Figure B.4.

Gradient-based weights, logarithmic magnitude, M

The ModelBuilder employs a logarithmic weighting system based on the magnitude of property gradients present within the created reference model and a user-defined order of magnitude, M. Where strong gradients are present in a particular direction across a cell face, smoothness weights between 10^{-M} and 1.0 are created in that direction to allow a sharp break in properties, and elevated smoothness weights between 1.0 and 10^M are created in the two orthogonal directions. The default smoothness weight of 1.0 will be assigned wherever there are no geologic constraints in the reference model. Assigning a magnitude of 0 will turn this calculation off, while still allowing use of the following options. See Figure B.4C, G.

Include the supplied prior property model in gradient calculation

Only available if a default prior reference property model was supplied. This allows smoothness gradients to be calculated throughout the entire model, taking into account any property variations in the prior model. If the prior property model is included in the smoothness calculations, then the edge of constraints is the edge of the mesh and the next 2 options have no effect even if they are available.

Calculate smoothness weights within buffer zones

Only available if using buffers. If buffers have been used to extrapolate reference properties, a choice must be made whether to calculate the smoothness weights based on the raw constraint information, or on the extrapolated buffer constraints. Using the raw constraints might be more reliable as the buffers may introduce unrealistic non-geological property gradients in some parts of the model, which may be either too sharp or too smooth. However, the smoothness weights and reference model will be inconsistent if buffers are used on the reference model but not for the smoothness weights. See Figure B.4G.

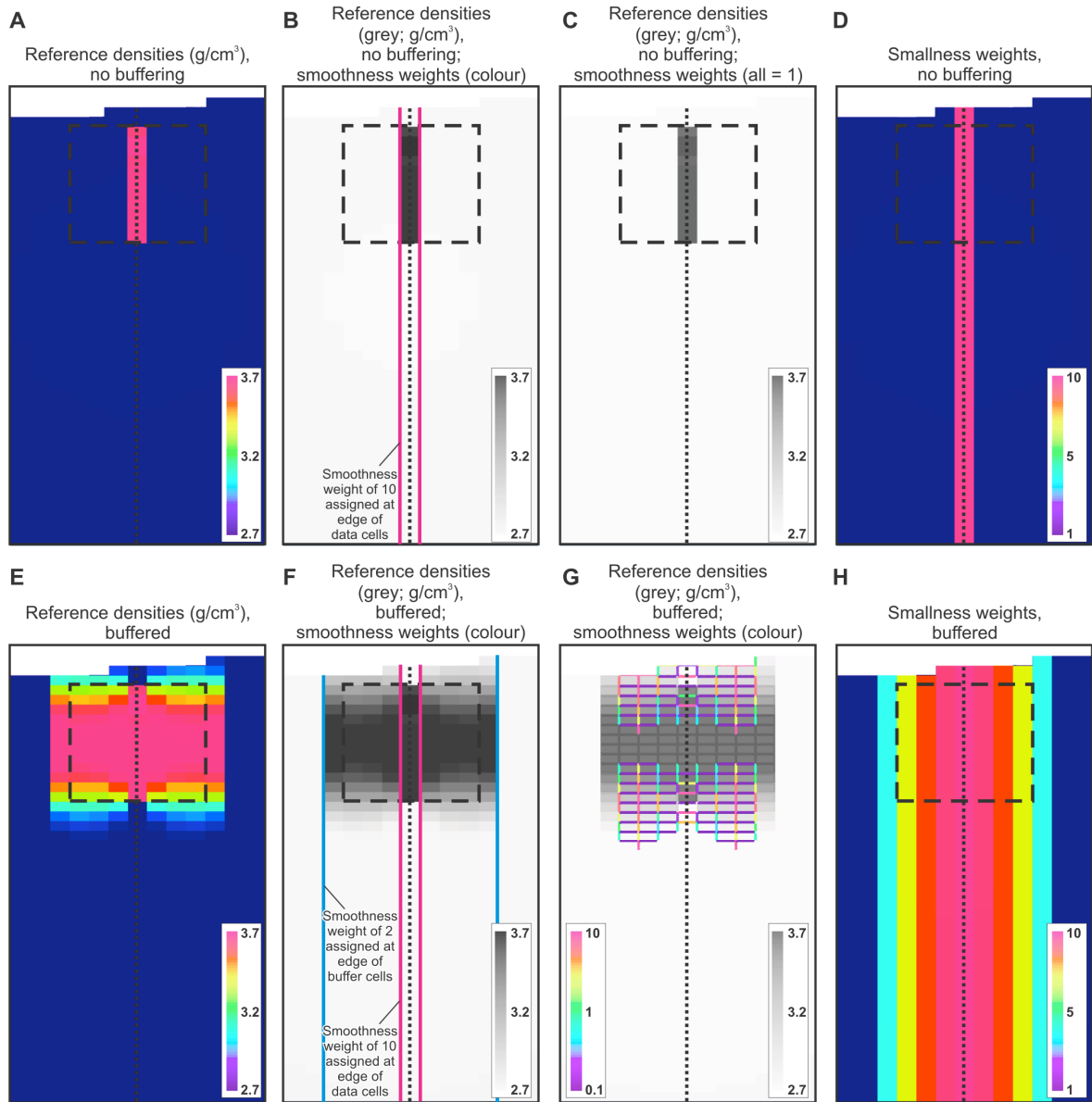


Figure B.4. Examples of how smoothness weights can be assigned for a simple synthetic example with a single vertical drill hole (dotted line) passing through an anomalous block (outlined with dashed line). The example is the same as used in Figure B.3, but without scaling applied. A-D show the constraint models obtained without using buffers; E-H show the constraint models when buffers are used. A. Reference model, with constraints assigned along the drill hole trace. B. Smoothness weights assigned at outer edge of data constraints. Only those cell faces with non-default smoothness weights are shown. C. Smoothness weights calculated by property gradients on the range 0.1-10. Note however, that all smoothness weights were assigned default values (1) because there were insufficient constraints to calculate a property gradient at any cell faces. A $3 \times 3 \times 3$ block of cells with constraints is required for a property gradient to be calculated. D. Smallness weights assigned along the trace of the drill hole. E. Reference model, with constraints assigned along the drill hole trace and extrapolated outwards 100 m in all directions. F. Smoothness weights assigned at outer edge of data constraints (10, pink) and at outer edge of buffer constraints (2, blue). Only those cell faces with non-default smoothness weights are shown. G. Smoothness weights calculated by property gradients on the range 0.1-10. Note that low values (blues) are typically oriented perpendicular to the drill hole and high values (red/oranges) are oriented parallel to the drill hole trace, promoting extrapolation outwards and a sharper boundary near the edge of the block. Only those cell faces with non-default smoothness weights are shown. D. Smallness weights assigned along the trace of the drill hole, decreasing with distance outwards in the buffer zone.

Smoothness weight assigned to outer edge of data constraints

This value will be assigned to all cell faces that separate data-bearing cells from unconstrained or buffer cells to help spread the constraints outwards (> 1) or truncate the constraints (< 1). The default smoothness weight of 1.0 provides slight outwards extrapolation of the data constraints, and effectively turns this option off. See Figure B.4B, F.

Smoothness weight assigned to outer edge of buffer constraints

Only available if using buffers. This value will be assigned to all cell faces that separate buffer cells from unconstrained cells to help spread the constraints outwards (> 1) or truncate the constraints (< 1). The default smoothness weight of 1.0 provides slight outwards extrapolation of the data constraints, and effectively turns this option off. See Figure B.4F.

Maximum smoothness weight across geological contacts

Only available if using a 3D geology model. Geological contacts, as defined in the 3D geology model, typically indicate a break in smoothness. To ensure all geological contacts are assigned as breaks with weights < 1 , enter the maximum allowed smoothness weight for contacts. All faces along contacts will have this weight or less as determined using the standard gradient calculation above. Use a large number ($> 10^M$) to turn this option off.

Maximum smoothness weight across cover/weathering domain boundary

If the cover/weathering domain represents weathering, it probably grades smoothly into the basement rocks below so enter a smoothness weight ≥ 1 . If it represents transported cover, perhaps on an erosional basement surface, it might have a sharp property break so enter a smoothness weight ≥ 1 . All faces along this boundary will have this weight or less as determined using the standard gradient calculation above. Use a large number ($> 10^M$) to turn this option off.

17.0.0: Method for calculating reference properties in buffers

Only available if using buffers and building a reference model with smallness weights. Buffers can be used to extrapolate constraints, including reference properties, smallness weights, lower and upper bounds, outwards from those cells containing data to adjacent cells. If only one data-bearing cell is present within a given buffer, properties are assigned to adjacent cells based on simple inverse distance weighting schemes. However, when two or more data-bearing cells lie within a given buffer zone, the buffers from each data-bearing cell

will overlap. Several options are available for how to assign properties to those cells that lie in the overlapping buffer zone between data-bearing cells. This list box allows the user to select the desired method for assigning reference properties.

1. Values from nearest-neighbour data cells

This option assigns the reference property of the nearest data-bearing cell to each cell in the buffers. If more than one data-bearing cell is at the same distance from a buffer cell, the mean of the reference properties of each data-bearing cell is taken. This is the simplest method, but does not include any information about the reliability of the constraints in each data-bearing cell, as defined by the smallness (w_s) weights. The smallness weight assigned to each buffer cell is the maximum smallness weight of all data-bearing cells that lie at the minimum distance to the buffer cell. Use this option if distance to observations is the only important criteria. The result will have sharp jumps in property wherever buffer cells become closer to a different data-bearing cell as demonstrated in Figure B.5.

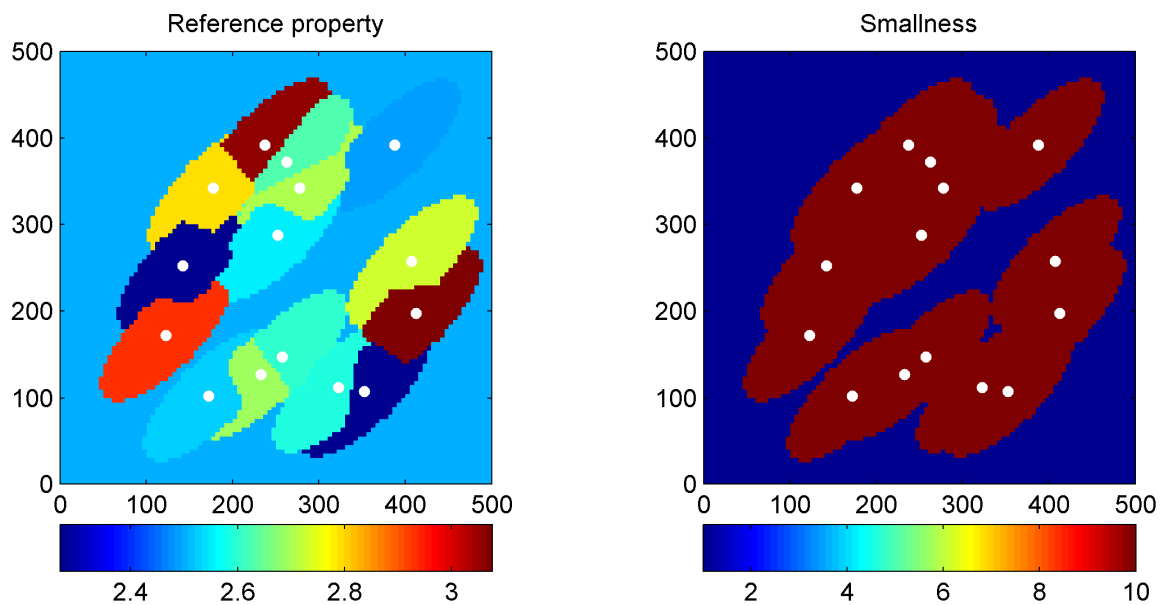


Figure B.5. Schematic example of ellipsoidal buffers applied around 15 random cells containing simulated surface sample property measurements (white dots) using the nearest neighbour buffer option. The reference property for each buffer cell is that of the nearest data-bearing cell, or an average if multiple data-bearing cells are at the same distance. The smallness weight is also that of the nearest data-bearing cell, or the maximum if multiple data-bearing are at the same distance.

2. Mean from the most reliable nearby data cells

This option uses a combination of distance and reliability weightings to extract the reference properties for a buffer cell from nearby data-bearing cells. The smallness weight associated with each data-bearing cell is weighted by inverse-distance from that cell to the background smallness weight at the edge of the buffer. This provides a reliability score that is used to identify which data-bearing cells have the most reliable influence on each buffer cell. Each cell in the buffer then takes the average of the reference properties from the data-bearing cells that contribute the highest reliability score to that cell. The smallness weight assigned to each buffer cell is the maximum distance-weighted smallness value contributed to that cell from adjacent data-bearing cells. This method uses both data reliability and distance from observations as criteria, but still results in sharp jumps in reference properties where the reliability score changes, as demonstrated in Figure B.6. This method has the advantage of not creating any property values that were not actually observed.

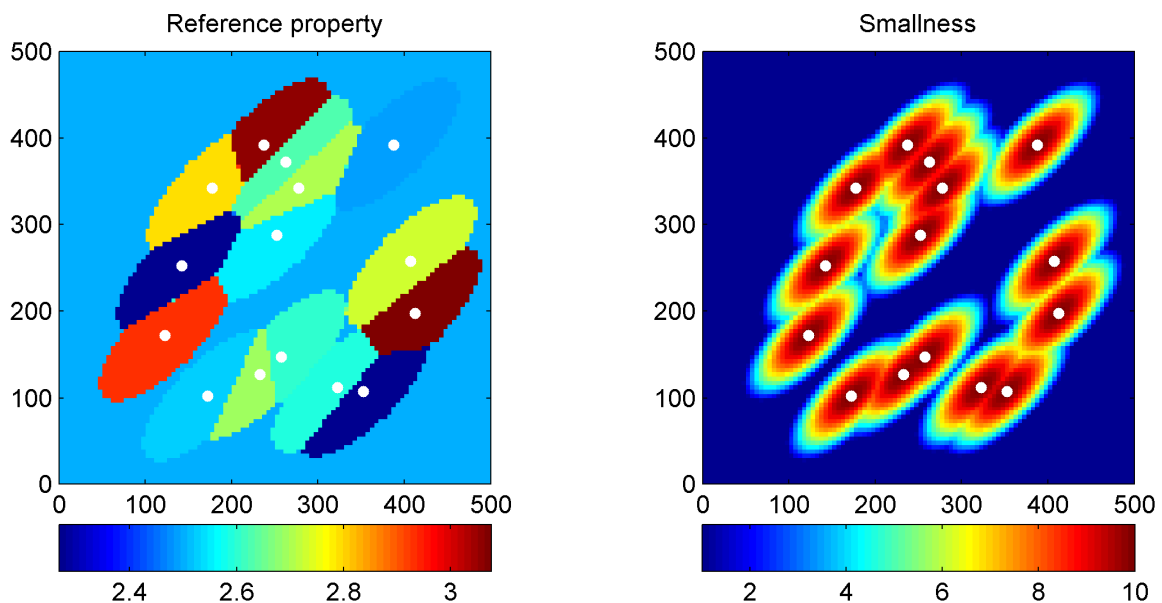


Figure B.6. Schematic example of ellipsoidal buffers applied around the same data as used in Figure B.5 except using the most reliable nearby data buffer option. The reference property for each buffer cell is the average property from the adjacent data-bearing cells that contribute the highest reliability score to each buffer cell. The reliability scores are obtained by applying an inverse distance weighting to the smallness weight associated with each data-bearing and reflects the decreasing reliability of observations with increasing distance. The smallness weight of each buffer cell is the highest distance-weighted smallness value from any of the adjacent data-bearing cells.

3. Smooth interpolation from nearby data cells using distance

This option calculates a smooth interpolation of reference properties by using a distance-weighted average of the reference properties of all adjacent data-bearing cells (Figure B.7). Each cell is assigned the maximum distance-weighted smallness value contributed by adjacent data-bearing cells. This option also includes an extra step which adjusts the position of the edge of each buffer to ensure that the influence exerted by one data-bearing cell never extends beyond another data-bearing cell in any direction.

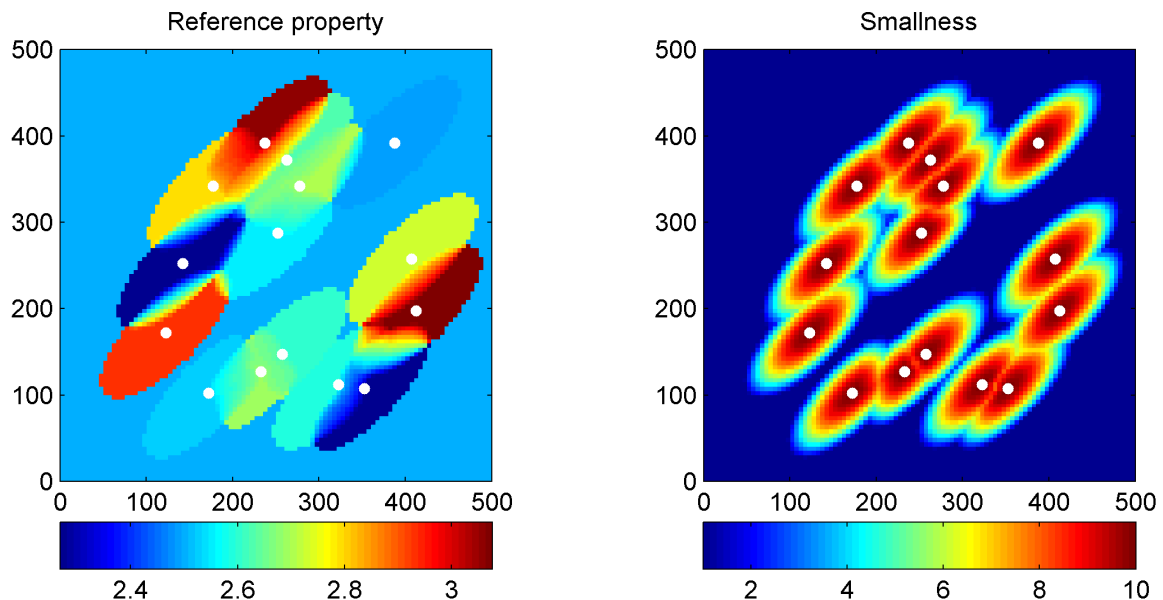


Figure B.7. Schematic example of ellipsoidal buffers applied around the same data as used in Figure B.5 except using the smooth interpolation option based on distance weights. The reference property for each buffer cell is a distance-weighted average from adjacent data-bearing cells. Since all adjacent data-bearing cells are used in the weighted average, the size of the buffers must be reduced so they never extend beyond another data-bearing cell in any direction. The smallness weight of each buffer cell is the highest distance-weighted smallness value from any of the adjacent data-bearing cells.

4. (Best) Smooth interpolation from nearby data cells using smallness weights & distance

This option calculates a smooth interpolation of reference properties by using a distance- and smallness-weighted average of the reference properties of all adjacent data-bearing cells (Figure B.8). Each cell is assigned the maximum distance-weighted smallness value contributed by adjacent data-bearing cells. This distance-weighted smallness values is also used derive a reliability score which is used for the weighted average reference property calculation. This option also includes an extra step which adjusts the position of the edge of each buffer to ensure that the influence exerted by one data-bearing cell never extends beyond another data-bearing cell in any direction. In situations where all data-types have similar smallness weights, the result will be similar to that obtained with reference model option 3, but provides a stronger distance-weighting; however, the result will also strongly indicate data reliability if there are differences in smallness weights between data types. This method is favoured because it uses all nearby data-bearing cells to derive a reference property estimate, not just those cells that satisfy certain criteria, and includes both distance and smallness criteria to derive the properties.

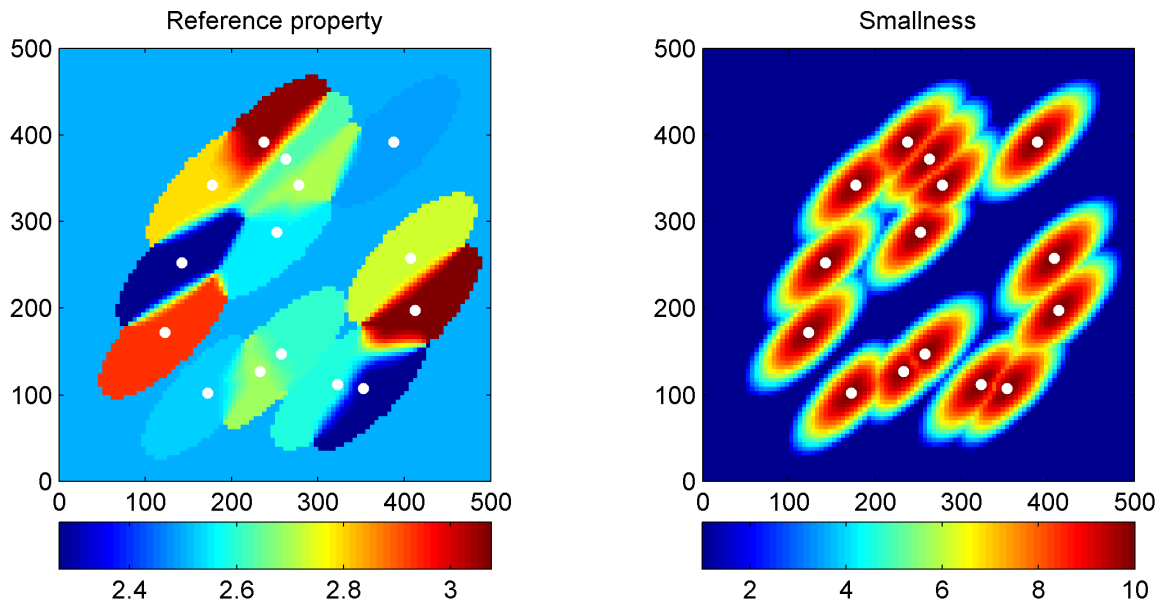


Figure B.8. Schematic example of ellipsoidal buffers applied around the same data as used in Figure B.5 except using the smooth interpolation option based on distance- and smallness-weights. The reference property for each buffer cell is a weighted average from adjacent data-bearing cells with the weights being the reliability scores associated with each data-bearing cell. The reliability scores are obtained by applying an inverse-distance weighting to the smallness weight associated with each data-bearing cell and reflects the decreasing reliability of observations with increasing distance. Since all adjacent data-bearing cells are used in the weighted average, the size of the buffers must be reduced so they never extend beyond another data-bearing cell in any direction. This is done prior to calculating the reliability scores. The smallness weight of each buffer cell is the highest distance-weighted smallness value from any of the adjacent data-bearing cells.

18.0.0: Method for calculating bounds in buffers

Only available if using buffers and building a bounds model. Buffers can be used to extrapolate constraints, including reference properties, smallness weights, lower and upper bounds, outwards from those cells containing data to adjacent cells. If only one data-bearing cell is present within a given buffer, properties are assigned to adjacent cells based on simple inverse distance weighting schemes. However, when two or more data-bearing cells lie within a given buffer zone, the buffers from each data-bearing cell will overlap. Several options are available for how to assign properties to those cells that lie in the overlapping buffer zone between data-bearing cells. This list box allows the user to select the desired method for assigning bounds within the buffers.

1. Most extreme bounds from nearest data

This is the most conservative option. It takes the most extreme bounds available from the nearest data-bearing cell as demonstrated in Figure B.9. Since wider bounds are commonly associated with cells with little knowledge, the bounds recovered using this method will be controlled by the distribution of those cells.

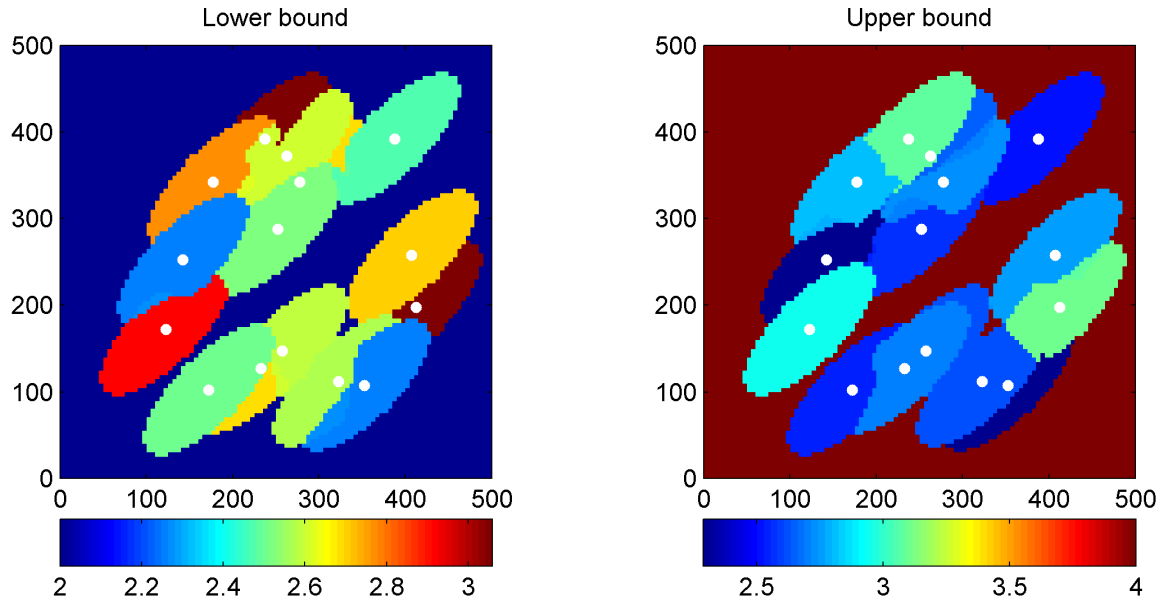


Figure B.9. Schematic example using ellipsoidal buffers to extrapolate bounds around the same data as used in Figure B.5. The bounds are derived from the most extreme bounds from the nearest data-bearing cells. This gives rise to sharp jumps in the bounds values when approaching a different data-bearing cell. There is no widening of bounds in the zone between two data-bearing cells where the uncertainty in properties is commonly the highest.

2. Smooth interpolation from nearby data cells using distance

This option produces a smooth interpolation of the bounds from adjacent data-bearing cells using a distance-weighted average (Figure B.10). This option also includes an extra step which adjusts the position of the edge of each buffer to ensure that the influence exerted by one data-bearing cell never extends beyond another data-bearing cell in any direction. The result has some appealing features in that the bounds widen slightly in the zone between two data-bearing cells reflecting the uncertainty in which properties should be applied when there is competing information. Bounds calculated in this way also lie somewhere between the tightest and widest bounds of adjacent data-bearing cells indicating a compromise in the confidence in each cell's properties.

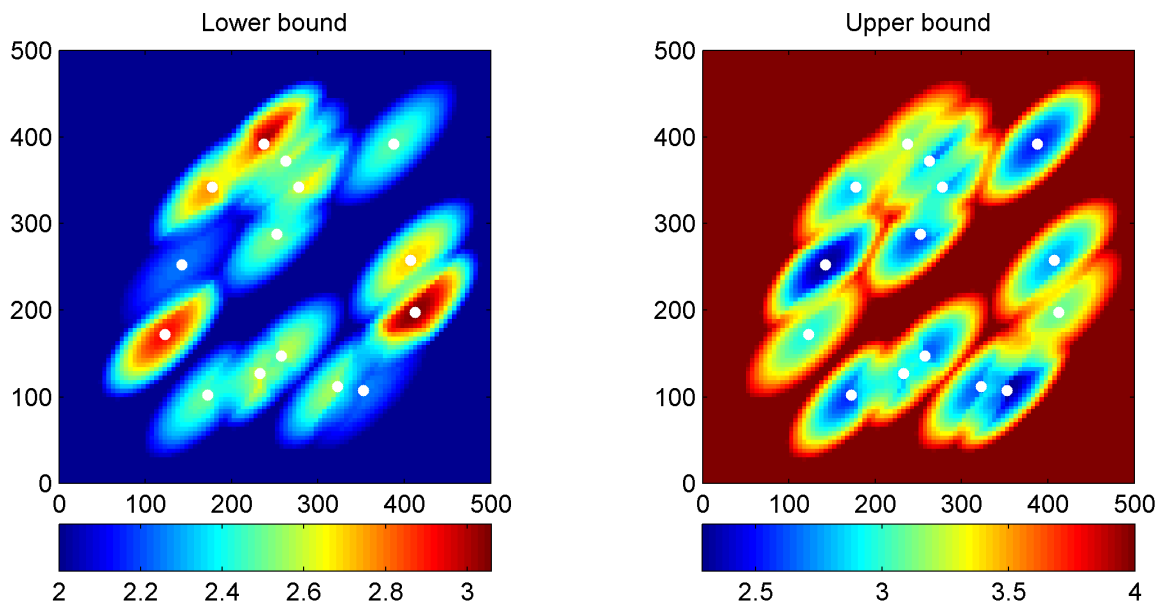


Figure B.10. Schematic example using ellipsoidal buffers to extrapolate bounds around the same data as used in Figure B.5. The bounds are a distance-weighted average from all adjacent data-bearing cells providing a smooth interpolation. Since all adjacent data-bearing cells are used in the weighted average, the size of the buffers must be reduced so they never extend beyond another data-bearing cell in any direction. There is a slight widening of bounds in the zone between two data-bearing cells where the uncertainty in properties is commonly the highest.

3. (Best) Smooth interpolation from nearby data cells using smallness weights & distance

Only available if building both a reference model with smallness weights and bounds.

This option produces a smooth interpolation of the bounds from adjacent data-bearing cells using a distance- and smallness-weighted average (Figure B.11). Because smallness weights are used to indicate data reliability, it requires a reference model to have been built. This option also includes an extra step which adjusts the position of the edge of each buffer to ensure that the influence exerted by one data-bearing cell never extends beyond another data-bearing cell in any direction. The result has some appealing features in that the bounds widen slightly in the zone between two data-bearing cells reflecting the uncertainty in which properties should be applied when there is competing information. Bounds calculated in this way also lie somewhere between the tightest and widest bounds of adjacent data-bearing cells indicating a compromise in the confidence in each cell's properties. In situations where all data-types have similar smallness weights, the result will be similar to that obtained with bounds option 2; however, the result will also strongly indicate data reliability if there are differences in smallness weights between data types. This method is favoured because it uses all nearby data-bearing cells to derive a reference property estimate, not just those cells that satisfy certain criteria, and includes both distance and smallness criteria to derive the bounds.

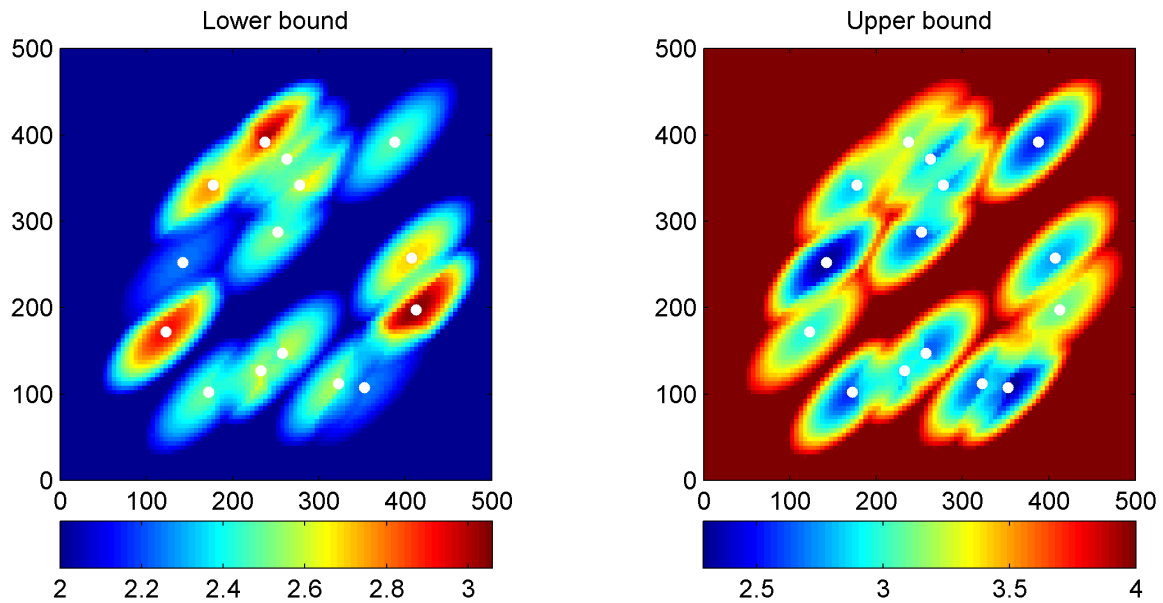


Figure B.11. Schematic example using ellipsoidal buffers to extrapolate bounds around the same data as used in Figure B.5. The bounds are a distance- and smallness-weighted average from all adjacent data-bearing cells providing a smooth interpolation that takes into account data reliability. Since all adjacent data-bearing cells are used in the weighted average, the size of the buffers must be reduced so they never extend beyond another data-bearing cell in any direction. There is a slight widening of bounds in the zone between two data-bearing cells where the uncertainty in properties is commonly the highest.

19.0.0: Maximum buffer distances

Only available if using surface samples, drilling, or maps and using buffers. Some data types are more widely applicable over an area than others. For instance, map information can apply over much larger distance than individual point property measurements. When buffers are applied to extrapolate properties outwards from observation locations, the size of the buffer ellipsoid, defined by the length of its major **A** axis (Figure B.2), is determined by the type of data present. The **A** axis lengths defined here will indicate the actual length of the buffer ellipsoid in the down-dip, along pitch direction. The length will be multiplied by the b/a and c/a ratios defined in the domain model definitions (6.0.0, p. 437) and the cover domain definition (6.2.0, p. 441) to obtain the lengths of the other two axes.

Maximum buffer distance for surface measurements

Maximum buffer distance for drilling measurements

Maximum buffer distance for drilling geology logs

Maximum buffer distance for outcrop geology map

Maximum buffer distance for basement geology map

20.0.0: Default buffer orientation

Only available if using buffers and their orientation has not been specified for every cell. The default buffer orientation to be used in the model is defined here, as shown in Figure 5.9. This orientation will be used wherever buffer orientations have not been defined using a domain model. The actual size of the buffers, defined by the length of the major **A** axis, is based on the type of data in each cell (19.0.0, p. 470). If no dominant orientation can be inferred, then a default spherical buffer can be used. This is achieved by assigning any strike/dip/pitch combination and setting both the b/a and c/a length ratios to 1.0.

Dominant strike

This is the dominant strike of the rocks. The strike is specified as 0-360° from north, with the dip plane to the right of the strike direction. For example, a strike and dip of 045/45 SE would be represented as 045/45, whereas a strike and dip of 075/45 NW would be represented as 135/45.

Dominant dip

This is the dominant dip of the rocks below horizontal. It is specified as 0-90° and is assumed to be in a direction 90° to the right of the strike direction.

Dominant pitch

This is the dominant pitch associated with any lineations, stretching, or fold axes in the dominant dip plane. It is specified as 0-180° below horizontal away from the direction of strike. If no dominant pitch is expected, any value can be supplied here, and a value of 1.0 supplied for the b/a length ratio. This will recover a uniform plate oriented along the dip plane.

Intermediate axis length ratio (b/a)

This is the length of the **B** axes within the dip-plane, as a proportion (0-1) of the major **A** axis along-pitch buffer length. If the data type for a cell requires an **A** axis length of 100 m, a b/a ratio of 0.5 will give an intermediate **B** axis length of 50 m.

Minor axis length ratio (c/a)

This is the length of the **C** axes perpendicular to the dip-plane, as a proportion (0-1) of the major **A** axis along-pitch buffer length. If the data type for a cell requires an **A** axis length of 100 m, a c/a ratio of 0.5 will give a minor **C** axis length of 50 m.

INPUT FILES AND DATA

A major component of the ModelBuilder is the input and management of a wide range of data files. The following section describes the data files and required formats. It is divided into subsections associated with each type of data that the ModelBuilder can use. The files associated with a particular data type are only required if that data type is to be included in the model.

All physical property units must be the same across all files. In general it is recommended that all physical property measurements and estimates be available in the same units as required for the inversions (e.g., g/cm³ or t/m³ for densities, SI for magnetic susceptibilities), however a basic functionality is built in to apply a multiplicative transformation for all input measurements to convert from kg/m³ to g/cm³, or to convert from 1×10^{-3} SI to SI (dialog box 3.1.0, p. 430).

MANDATORY FOR ALL MODELS

UBC–GIF mesh file

Description: This mesh file defines the mesh on which the geological constraining models will be built.

Format: A UBC–GIF format ASCII mesh file.

Header: None

FOR SURFACE SAMPLES (OR ANY SAMPLES THAT HAVE X-Y-Z COORDINATES):

Sample file (required)

Description: A tab-delimited ASCII text column file with coordinates and property measurements for surface samples.

Format: SAMPLEID X Y Z PROPERTY_MEASUREMENT

Header: The first line is ignored as column headings are assumed to be present.

FOR DRILLING

If either a drilling sample file or drilling geology file is used then a collar and survey file must be supplied. Data in any holes which lack collar and survey information will be ignored.

Collar file (required)

Description: A tab-delimited ASCII text column file with hole ID, collar coordinates and length of each drill hole.

Format: HOLE-ID X Y Z LENGTH

Header: The first line is ignored as column headings are assumed to be present.

Notes: Some error checking is done to remove duplicate collars. Any hole with zero length will be ignored even if survey information exists along the hole.

Survey file (required)

Description: A tab-delimited ASCII text column file with hole ID, collar coordinates and length of each drill hole.

Format: HOLE-ID DEPTH AZIMUTH INCLINATION

Header: The first line is ignored as column headings are assumed to be present

Notes: Azimuth is in clockwise degrees from north ($N = 0^\circ$, $E = 90^\circ$, etc.). Inclination is degrees above (positive) or below (negative) horizontal; downward directed holes require negative angles. Some error checking is done to remove duplicate surveys.

Drilling properties file (optional)

Description: A tab-delimited ASCII text column file with hole ID, depth interval and property measurement for samples along drill holes.

Format: HOLEID DEPTHFROM DEPTHTO PROPERTY_MEASUREMENT

Header: The first line is ignored as column headings are assumed to be present.

Notes: If any point measurements are present where DepthFrom = DepthTo, they are converted to short intervals centered on the location of the point measurement; but it is best if all entries represent intervals. Some error checking is done to remove duplicate entries and to fix overlapping intervals.

Drilling geology file (optional)

Description: A tab-delimited ASCII text column file with hole ID, depth interval and geology unit name/code for intervals along drill holes.

Format: HOLEID DEPTHFROM DEPTHTO GEOLOGYCODE

Header: The first line is ignored as column headings are assumed to be present.

Notes: There are no restrictions on the form of the geology codes (they may contain spaces, numbers, symbols, etc.), as long as they are consistent throughout all files. Some error checking is done to remove duplicate entries and to fix overlapping intervals.

Rock property data (required if a drilling geology file is used)

Description: Property data must be defined using any of the methods outlined in the section on Rock Properties Data (p. 477).

FOR OUTCROP OR BASEMENT MAPS

ArcView shapefile (1 or more required)

Description: A standard ESRI shapefile of map polygon data.

Format: Proprietary ESRI format

Header: Not applicable

Notes: Each shapefile can contain any number of attribute fields for each polygon. A selection box will appear prompting the user to select one of the character based attribute fields contained in the shapefile. The shapefile is expected to be in WGS84 latitude-longitude projection (or equivalent); however a basic conversion is done if the coordinates appear to be in UTM.

Topography/basement surface model file (required)

Description: A UBC–GIF format model file that indicates the discretised position of topography.

Format: UBC–GIF ASCII format model file

Header: None

Notes: Currently topography cannot be read directly from a standard topography file since it is important to use exactly the same surface triangulation as in the inversion model. To recover the same surface as used in the inversions, an actual inversion model is loaded and the No-Data-Values associated with above ground cells are used to locate the surface in the model. The model file can be any completed inversion model over the same mesh that the model will be created on. The values within the model are ignored, only the position of the surface, as defined by the UBC–GIF no-data-values within the model file. Alternatively it can be created in Meshtools by:

1. Load the mesh

2. Load the topography file
3. Edit->Add blocks
4. Enter a positive value
5. Move the X-Y-Z sliders to one extremity.
6. Check the dx box
7. Move the X-Y-Z sliders to the opposite extremity.
8. Click Set
9. Save the topography model using File->Save As

This process can also be used to create a basement surface file if points on the basement surface have been defined in a UBC–GIF topography format file.

Rock property data (required)

Description: Property data must be defined using any of the methods outlined in the section on Rock Properties Data (p. 477).

FOR A 3D DOMAIN MODEL

UBC–GIF model file of domain IDs (required)

Description: A UBC–GIF model file with unique identifying domain numbers indicating which domain each cell belongs to.

Format: UBC–GIF ASCII format model file

Header: None

Notes: The domain model can be made using the Add Blocks function in Meshtools, or from a more complex Gocad model exported to UBC-GIF model format, with a unique domain ID assigned to every cell in the model. While every cell must have an ID, not all of the ID numbers have to present in the accompanying domain definition file, thus allowing specific cells to be excluded from all domains (if no geological information is available for those areas). Any cells with a domain ID not specified in the definitions file will be assigned default properties and bounds.

Domain definition file (required)

Description: A tab-delimited ASCII text column file with domain ID, bounds, reference properties and smallness weights for each domain that is to be used in the model.

Format: DOMAIN_ID LOWER_BOUND REF_PROPERTY UPPER_BOUND WS
ASPECTRATIO_X ASPECTRATIO_Y ASPECTRATIO_Z COMMENTS

Header: The first line is ignored as column headings are assumed to be present.

Notes: The comments column is ignored but must be present; it is used to describe what the domain represents (e.g., “granites”). All other properties must be defined even if not required for the current model. The aspect ratios give an indication of the overall shape expected for geological bodies within each domain. If bodies are expected to be twice as wide (east-west) and 5 times as long (north-south) than they are tall, then they would be assigned an aspect ratio like 2:5:1. These aspect ratios effectively multiply the lengths scales specified in the inversion, in different portions of the model. Each of the domain ID numbers must be present in the domain model file.

Domain orientation file (optional)

Description: A tab-delimited ASCII text column file with domain ID and parameters defining the orientation of buffers within the domain as defined in Figure B.2.

Format: DOMAIN_ID STRIKE DIP PITCH B/A_AXIS_RATIO C/A_AXIS_RATIO

Header: The first line is ignored as column headings are assumed to be present.

Notes: The strike is specified as 0-360° from north, with the dip plane to the right of the strike direction. The dip is specified as 0-90° below horizontal and is assumed to be in a direction 90° to the right of the strike direction. The pitch is specified as 0-180° below horizontal away from the direction of strike. The b/a axis ratio is the length of the **B** axis within the dip-plane, as a proportion (0-1) of the major **A** axis along-pitch buffer length. The b/a axis ratio is the length of the **C** axis perpendicular to the dip-plane, as a proportion (0-1) of the major **A** axis along-pitch buffer length.

FOR A 3D GEOLOGICAL MODEL

UBC–GIF model file of geological unit IDs (required)

Description: A UBC–GIF model file with unique identifying geological unit numbers indicating which unit each cell belongs to.

Format: UBC–GIF ASCII format model file

Header: None

Notes: The geological model can be made using the Add Blocks function in Meshtools, or from a more complex Gocad model exported to UBC-GIF model format, with a unique

geological unit ID assigned to every cell in the model. While every cell must have an ID, not all of the ID numbers have to present in the accompanying geological model definition file, thus allowing specific cells to be excluded from all units (if no geological information is available for those areas). Any cells with a geological unit ID not specified in the definitions file will be assigned default properties and bounds.

Geological model definition file (required)

Description: A tab-delimited ASCII text column file with geological unit ID, bounds, reference properties and smallness weights for each geological unit that is to be used in the model.

Format: GEOLOGICAL_UNIT_ID LOWER_BOUND REF_PROPERTY UPPER_BOUND WS
COMMENTS

Header: The first line is ignored as column headings are assumed to be present.

Notes: The comments column is ignored but must be present; it is used to describe what the geological unit is (e.g., “granites”). Bounds must be defined even if a bounds model is not being built. Likewise, the reference property must also be defined. Each of the geological unit ID numbers must be present in the domain model file.

ROCK PROPERTIES DATA

If using drilling geology logs, or outcrop or basement maps, rock properties must be defined for the geological labels used. To assign these data into the model, a physical properties database is built containing estimates of the properties associated with each label. The properties of each geological label used in the database can be defined in one of two ways. First, a manually defined table of estimated properties for each unit can be supplied. These estimated properties can come from any number of sources such as textbooks (Carmichael, 1989; Telford et al., 1990; Hunt et al., 1995; Schön, 2004), regional studies or prior work, and external physical property databases (Parsons and McGaughey, 2007). Alternatively the properties can be calculated automatically for each unit based on all available physical property measurements associated with each unit from surface samples or drilling. This calculation is a supplementary procedure that usually only needs to be performed when new property measurements become available; the results are stored in a MATLAB binary file for future use. The reference property associated with each geology label is taken as the mean of all available measurements for that label. The bounds properties are taken as confidence intervals on that

mean at 68 %, 95 %, 99.7 or 99.99 % confidence levels, corresponding to 1, 2, 3, and 4 standard deviations respectively.

Any properties that are manually defined take precedence over those that are calculated automatically thus allowing the user to override automatically-calculated properties for particular units for which measurements are unreliable. In addition, because the geological unit names used in maps and drilling logs are usually different from the geological labels used in drilling and surface sample descriptions, an optional facility is included to translate drilling codes to map names (and vice versa).

Although each of the file types listed below are marked as optional, at least one must be used if drilling geology logs, or outcrop or basement maps are to be used. If a geology label is not listed in any of the property files then it will be ignored in the model.

Manually-assigned property file (optional)

Description: A four column tab-delimited ASCII text column file with geological names/codes of units and their user-assigned reference properties and lower and upper bounds.

Format: GEOLOGY_CODE LOWER_BOUND REF_PROPERTY UPPER_BOUND (COMMENTS)

The optional fifth column, for comments, is not strictly necessary but may be useful for identifying what references were used in picking a certain property value. Any entry in the fifth column must be preceded by the MATLAB comment character '%'.

Header: The first line is ignored as column headings are assumed to be present.

Notes: Bounds must be assigned even if a bounds model is not being built. Likewise, the reference property must also be assigned.

Measured surface sample properties (optional)

Description: A tab-delimited ASCII text column file with geology codes and property measurements for surface samples.

Format: GEOLOGY_CODE PROPERTY_MEASUREMENT

Header: The first line is ignored as column headings are assumed to be present.

Notes: This file, although seemingly similar to the surface sample property file defined above, is different in two respects. Firstly, this file does not contain coordinates; this allows the use of non-located property measurements. Secondly, this file does include the geology code whereas the other surface property file did not. For many cases the two files may contain the same list

of property measurements, but two different files are used to allow some greater flexibility in assigning properties.

Measured drilling properties (optional)

To be included, both drilling geology and property files are required, however as no X-Y-Z coordinates are necessary for this property calculation, no collar or survey files are required.

Drilling properties file (optional)

Description: A tab-delimited ASCII text column file with hole ID, depth interval and property measurement for samples along drill holes.

Format: HOLEID DEPTHFROM DEPTHTO PROPERTY_MEASUREMENT

Header: The first line is ignored as column headings are assumed to be present.

Notes: If any point measurements are present where DepthFrom = DepthTo, they are converted to short intervals centered on the location of the point measurement; but it is best if all entries represent intervals. Some error checking is done to remove duplicate entries and to fix overlapping intervals.

Drilling geology file (optional)

Description: A tab-delimited ASCII text column file with hole ID, depth interval and geology unit name/code for intervals along drill holes.

Format: HOLEID DEPTHFROM DEPTHTO GEOLOGYCODE

Header: The first line is ignored as column headings are assumed to be present.

Notes: There are no restrictions on the form of the geology codes (they may contain spaces, numbers, symbols, etc.), as long as they are consistent throughout all files. Some error checking is done to remove duplicate entries and to fix overlapping intervals.

Translation file (optional)

Description: A two column tab-delimited ASCII text column file with map unit names and a list of drilling geology codes that correspond to each map unit name. This is used to translate properties measured on drill logs to map units.

Format: MAPUNITNAME CODELIST

Header: The first line is ignored as column headings are assumed to be present.

Notes: Since map unit names are often different from drilling log unit names/descriptions, a facility is included to translate geology rock codes into map unit names. MAPUNITNAME is the name used for map units in the ArcView shapefiles (these can be obtained from the program from an initial run using maps but assigning no property information). CODELIST is a comma-space delimited list of geology codes corresponding to the map unit name. All entries are case-sensitive. Trailing wildcards ('%') can be used to match any codes starting with a particular word, phrase, or group of letters. The following example matches all codes that start with FP, \$FP, or exactly match Afv with the map unit name 'Felsic Extrusive':

MAPUNITNAME	CODELIST
Felsic Extrusive	FP%, \$FP%, Afv

The file is only useful if properties have been defined using at least one of the property files listed above. A particularly useful feature is that it can be used to link measurements associated with groups of drilling codes that are similar, even if maps are not used. For instance if 'Afv/FP' represents a mixture of codes Afv and FP, and both have similar properties, then all drilling measurements of Afv and of FP can be linked to the drilling code Afv/FP by including the line:

Afv/FP	Afv, FP
--------	---------

Care must be taken that no drilling code is listed in both the left column and the right column as this leads to circular logic.

OUTPUT FILES

Each run of the ModelBuilder produces a suite of output files containing the resulting models of constraints and additional documentation of the results. The files that are produced and the file names used depend on the options employed during each run. A text log file is always produced which includes an output of all options used, and summaries of all the constraints used. The general naming scheme includes information about what data types were used with abbreviations indicated in Table B.4, whether buffers were used, the date and time the file was produced, and information about what the file contains. The output files associated with each type of constraint are listed and described in the following section.

Table B.4. Output filename abbreviations and ID flags for different data types. The ID flags are used to identify which data types had the most influence on the properties assigned to each cell.

Data type	Filename abbreviation	Data type ID flag
Surface samples	SS	1
Drilling property measurements	DP	2
Drilling geology logs	DG	3
Outcrop geology map	OM	4
Basement geology map	BM	5
3D geology model	3G	0
3D domain model	3D	-1
No constraints		-1

REFERENCE MODEL AND WEIGHTS

A suite of files is created including the actual reference model, weighting files, and flag files that indicate the type of data used in each cell of the model. Unbuffered versions are always created. Buffered versions are only created if buffers were used.

UBC–GIF model of reference properties (*.den or *.mod) – unbuffered or buffered

These are standard reference property models in UBC–GIF model format. These should be used for viewing, and for magnetic and IP inversions. The unbuffered version only contains non-default properties in those cells that actually contained data. The buffered versions contain an extrapolated version of the same information according to the defined buffering parameters.

UBC–GIF model of reference property contrasts (*.den) – unbuffered or buffered

Only produced when a density model is created. These UBC–GIF model format reference property models contain density contrasts obtained by subtracting the default reference density from the assigned reference densities. These should be used in gravity inversions. The unbuffered version only contains non-default properties in those cells that actually contained data. The buffered versions contain an extrapolated version of the same information according to the defined buffering parameters.

UBC–GIF weighting files (*.w) – unbuffered or buffered

These UBC–GIF format weighting files contain smallness and smoothness weights (w_s , w_x , w_y , and w_z) suitable for use in inversions. The smallness weight section can be viewed by loading the file in the Meshtools3D model viewer in the normal way, but the smoothness weights can only be viewed using the Meshtools3D File->Cell Faces command. If smoothness weights have not been calculated from the reference model using the option on dialog 3.1.0 (p. 430), then default smoothness weights of unity will be included in this file, otherwise the actual

smoothness weights derived from the reference model will be included. The unbuffered and buffered versions of the weighting file will contain either the unbuffered or buffered smallness weights respectively. The file names will have a suffix to indicate whether smallness or smoothness or both types of weights were scaled with depth/distance, and an indication of whether distance, depth, or hybrid scaling was used. A version without scaling is also created with an ‘unscaled’ suffix.

UBC–GIF reference model data types

This UBC–GIF model (identified as refDataTypes) contains ID flags for each cell indicating the data type with the most observations in each cell, and therefore the data type which most influenced the resulting properties for that cell. The ID numbers are listed in Table B.4. No extrapolation is applied.

UBC–GIF reference model buffer data types

Only produced when using buffers. This UBC–GIF model (identified as refBufferDataTypes) contains ID flags for each cell indicating the data type that contributed most to the properties assigned in each cell used in a buffer. The ID numbers are listed in Table B.4. Since this model only identifies the data types within buffers, cells that actually contain observations are assigned an ID flag of -1 to indicate that they are not buffer cells.

BOUNDS MODEL

A suite of files is created including the actual bounds files, individual lower and upper bounds files for viewing, and flag files that indicate the type of data used in each cell of the model. Unbuffered versions are always created. Buffered versions are only created if buffers were used.

UBC–GIF bounds file – unbuffered or buffered

These are standard UBC–GIF bounds file. They contain two columns indicating the lower bound and upper bound for each cell in the model. These files can be used directly in magnetic inversions; however this format cannot be viewed in Meshtools3D. The unbuffered version only contains non-default bounds in those cells that actually contained data. The buffered versions contain an extrapolated version of the same information according to the defined buffering parameters.

UBC–GIF bounds contrasts file – unbuffered or buffered

Only produced when a density model is created. These contain the bounds from the model above, represented as density contrasts. They contain two columns indicating the lower bound contrast and upper bound contrast for each cell in the model. The contrasts are derived by subtracting the default reference density from the recovered bounds. These files can be used directly in gravity inversions; however this format cannot be viewed in Meshtools3D. The unbuffered version only contains non-default bounds in those cells that actually contained data. The buffered versions contain an extrapolated version of the same information according to the defined buffering parameters.

UBC–GIF model of lower bounds (lb) – unbuffered or buffered

These UBC–GIF format model files contain only the lower property bound for each cell as found in the above bounds files. They are suitable for viewing in Meshtools3D, but cannot be used in actual inversions because they lack the required upper bound column.

UBC–GIF model of upper bounds (ub) – unbuffered or buffered

These UBC–GIF format model files contain only the upper property bound for each cell as found in the above bounds files. They are suitable for viewing in Meshtools3D, but cannot be used in actual inversions because they lack the required lower bound column.

UBC–GIF bounds model data types

This UBC–GIF model (identified as `boundsDataTypes`) contains ID flags for each cell indicating the data type with the most observations in each cell, and therefore the data type which most influenced the resulting bounds for that cell. The ID numbers are listed in Table B.4. Since bounds are only applied if a cell has been sufficiently sampled, this model will differ from the model of reference data types identified above. No extrapolation is applied.

UBC–GIF bounds model buffer data types

Only produced when using buffers. This UBC–GIF model (identified as `boundsBufferDataTypes`) contains ID flags for each cell indicating the data type that contributed most to the properties assigned in each cell used in a buffer. The ID numbers are listed in Table B.4. Since this model only identifies the data types within buffers, cells that actually contain observations are assigned an ID flag of -1 to indicate that they are not buffer

cells. Since bounds are only applied if a cell has been sufficiently sampled, this model will differ from the model of reference data types identified above.

INFORMATIONAL TEXT FILES

Several additional text files are output at various stages to provide additional useful summary information.

Physical property summary file

Only produced when using maps or drilling geology logs. This file provides a tab-delimited text summary of the physical property database calculated by the ModelBuilder. It indicates the number of measurements associated with each geology label, the estimate mean reference property, and the lower and upper limits of the confidence intervals calculated at the full range of confidence levels. It also includes additional statistics for each geology label, that not used by the ModelBuilder but provide extra information to the user to enable an assessment of the reliability of the property estimates, and whether manually defined estimates may be required for particular labels. The filename includes the types of data included in the database (samples = surface sample measurements; drilling = drilling property logs and measurements; translated = geology label translation table) and the property it relates to.

List of geology labels without properties – drilling

Only produced when using drilling geology logs. This file provides a simple listing of all the geology labels encountered in drilling geology logs for which no physical property measurements were found. These labels are good candidates to be included in the manually-defined properties table until actual property measurements can be made for these rocks.

List of geology labels without properties – outcrop map

Only produced when using an outcrop map. This file provides a simple listing of all the geology labels encountered in the outcrop map shapefile for which no physical property measurements were found. These labels are good candidates to be included in the manually-defined properties table until actual property measurements can be made for these rocks.

List of geology labels without properties – basement map

Only produced when using a basement map. This file provides a simple listing of all the geology labels encountered in the basement geology map shapefile for which no physical

property measurements were found. These labels are good candidates to be included in the manually-defined properties table until actual property measurements can be made for these rocks.

MATLAB BINARY DATA FILES

A set of internal MATLAB format files are produced each run containing settings and data that can be utilised to speed up future runs. All can be safely deleted if no longer required.

ModelBuilder option files (bm*.mat)

These are internal data files used to store the options and parameters used in previous ModelBuilder runs. These will be loaded automatically to provide the default values in future runs to facilitate quick reproduction or updating of previous models. The files can be safely deleted manually if the settings are no longer required, or if the parameters get corrupted (after a crash) and need to be reset. They can also be removed automatically using the `buildModel('clear')` command.

ModelBuilder map data files (bmOutcropMapData.mat & bmBasementMapData.mat)

Only produced when using maps. The most time-consuming step in the ModelBuilder process can be interpolating the supplied map shapefiles, especially for large detailed maps. To make this process faster in subsequent runs over a particular area, ModelBuilder saves the interpolation (including the geology codes and coordinates at each sample point) and associated metadata into internal data files and saves these in the working directory. Any model that uses the same mesh, shapefiles, and number of sampling points can re-use these data files. They can be applied interchangeably to any physical property model, and can be copied to other directories if required. When assigning map data to a model, the ModelBuilder automatically identifies whether existing data files are present and prompts whether the existing data should be used.

Drilling traces file (drilling*.mat)

Only produced when using drilling property or geology logs. This file contains the 3D coordinates of all resample points along every drill hole trace, as calculated using the minimum curvature method (Sawaryn and Thorogood, 2005). Its filename contains the length of the resample interval used. The file can be loaded in dialog box 10.0.0 (p. 446).

Physical property database (aggregated*.mat)

Only produced when using maps or drilling geology logs. The complete physical property database is stored in this file with all the calculated property estimates. If drilling geology and property logs were used to create the database, then they are also saved in this file to remove the need to reprocess them. This file can be loaded in dialog box 3.2.0 (p. 432), but be sure to turn off the option to calculate the properties again.

Session file (buildModel_session*.mat)

This file contains all the geological and physical property data necessary to reproduce a model. It can be a very large file, but significantly speeds up the model building process. It can be loaded with the first option of the first dialog box (1.0.0, p. 427) and will allow the program to skip forward to dialog box 11.0.0 (p. 448) allowing the user to adjust parameters controlling smoothness and smallness weights, buffers, confidence intervals, and the assignment of reference properties for point data. The filename contains abbreviations indicating the types of data stored in the file; the abbreviations are as listed in Table B.4 (p. 481).

REFERENCES

- Carmichael, R.S., 1989, Magnetic properties of minerals and rocks, *in* Carmichael, R.S., ed., Practical handbook of physical properties of rocks and minerals: Boca Raton, Florida, CRC Press, p. 301-358.
- Environmental Systems Research Institute, 1998, ESRI Shapefile Technical Description: <http://www.esri.com/library/whitepapers/pdfs/shapefile.pdf>, accessed 2 Nov 2007, Environmental Systems Research Institute.
- Hunt, C.P., Moskowitz, B.M., and Banerjee, S.K., 1995, Magnetic properties of rocks and minerals: AGU Reference Shelf, v. 3, p. 189-204.
- Li, Y., and Oldenburg, D.W., 1996, 3-D inversion of magnetic data: Geophysics, v. 61, p. 394-408.
- Li, Y., and Oldenburg, D.W., 1998, 3-D inversion of gravity data: Geophysics, v. 63, p. 109-119.
- McGaughey, J., 2007, Geological models, rock properties, and the 3D inversion of geophysical data, *in* Milkereit, B., ed., Proceedings of Exploration 07: Fifth Decennial International Conference on Mineral Exploration, p. 473-483.
- McInerney, P., Goldberg, A., Calcagno, P., Courrioux, G., Guillen, A., and Seikel, R., 2007, Improved 3D geology modelling using an implicit function interpolator and forward modelling of potential field data, *in* Milkereit, B., ed., Proceedings of Exploration 07: Fifth Decennial International Conference on Mineral Exploration, p. 919-922.
- Oldenburg, D.W., and Pratt, D.A., 2007, Geophysical inversion for mineral exploration: A decade of progress in theory and practice, *in* Milkereit, B., ed., Proceedings of Exploration 07: Fifth Decennial International Conference on Mineral Exploration, p. 61-95.
- Parsons, S., and McGaughey, J., 2007, Rock property database system, *in* Milkereit, B., ed., Proceedings of Exploration 07: Fifth Decennial International Conference on Mineral Exploration, p. 933-938.
- Sawaryn, S.J., and Thorogood, J.L., 2005, A compendium of directional calculations based on the minimum curvature method: SPE Drilling & Completion, paper 84246, p. 24-36.
- Schön, J.H., 2004, Physical properties of rocks: Fundamentals and principles of petrophysics: Oxford, Elsevier, 583 p.
- Telford, W.M., Geldart, L.P., and Sheriff, R.E., 1990, Applied Geophysics: New York, Cambridge University Press, 770 p.
- UBC-GIF, 2005a, GRAV3D version 3.0: A program library for forward modelling and inversion of gravity data over 3D structures: The University of British Columbia-Geophysical Inversion Facility, 46 p.

UBC–GIF, 2005b, MAG3D version 4.0: A program library for forward modelling and inversion of magnetic data over 3D structures: The University of British Columbia–Geophysical Inversion Facility, 41 p.